Coastal Engineering- Waves, Beaches, Wave- Structure Interactions

T. Sawaragi

Coastal Engineering – Waves, Beaches, Wave-Structure Interactions

This Page Intentionally Left Blank

Coastal Engineering – Waves, Beaches, Wave-Structure Interactions

T. Sawaragi

Department of Civil Engineering, Osaka University,
Yamada-Oka 2-1, Suita 565, Osaka, Japan

1995

Further titles in this series:
Volumes 2, 3, 5–7, 9, 10, 12, 13, 15, 16A, 22 and 26 are out of print

This book in printed on acid-free paper.

Printed in The Netherlands

Preface

With the increasing demand for multi-purpose use of coastal sea areas in recent years, an in-depth understanding of nearshore currents, wave dynamics, sediment transport, and their mutual interaction with structures is becoming increasingly necessary. In addition, active and energetic research and development of new types of coastal and offshore structures and fishery structures have been conducted with much use of numerical calculation methods, which have progressed remarkably, together with hydraulic model experiments.

The science and technology of coastal and ocean engineering are closely related to harbour and fishery engineering, because they share a common basic knowledge. However, whereas various publications of coastal engineering, harbour engineering, and ocean engineering have described just the knowledge in their own respective fields, an inter-related and systematic presentation linking them together has yet to be attempted. This book is the first attempt to systematically combine the fields of coastal, ocean, harbour, and fishery engineering from an engineering viewpoint backed by hydrodynamics. Understanding the interaction of waves with structures and sediment, and predicting the associated responses of interest, underlie nearly every problem in coastal and ocean engineering. This is precisely the goal of this book. Although primarily intended for use as a special textbook for graduate students and senior practising engineers, it is hoped that this book will also serve as a useful reference and assist in the further development of this field. With these objectives in mind, each chapter deals with important problems to be solved in the near future. The references included in each chapter should aid students and practising engineers in further broadening their knowledge.

The original edition of this book was published in Japanese in May, 1991 by the Gihodo Publishing Company, Ltd. I am pleased to say that the Japanese version was well received by a large number of engineers and graduate students in Japan. This book is a revised translation of the Japanese edition.

The book comprises two parts. Part I is entitled "Fundamentals" and addresses very important areas for understanding Part II. Part I consists of Chapters 1 to 3. Chapter 1 presents the basic formulation of regular waves and random sea waves, including a review of potential flow hydrodynamics, two-dimensional linear wave theory, nonlinear wave transformation by means of numerical calculations, and random wave spectra and wave statistics. Chapter 2 presents the interaction of waves with structures. Wave boundary problems and numerical analyses are focused on, because remarkable progress in numerical calculation methods has made a great contribution to solving wave-structure interaction problems. Chapter 3 describes wave-caused currents, and the mechanism and basic principles of sediment transport.

Part II concerns Applications and comprises Chapters 4 to 8. This second part deals with (i) control methodology such as wave control, sand transport control, and motion control of moored structures, (ii) harbour tranquillity, and (iii) fishery structures. This part contains much important up-to-date information on structures and methodology, some of which are only now beginning to be developed. Chapter 4 examines the wave controlling functions

of various types of coastal structures. Chapter 5 develops various structures for controlling sediments such as groins, submerged breakwaters and sea-dykes with gentle slopes. Concepts of artificial beach nourishment are also described. Chapter 6 discusses structures for the use of ocean space. Chapter 7 investigates harbour tranquillity. It should be stressed that harbour tranquillity is discussed in terms of the magnitude of a ship's motion while the vessel is moored at a quay wall as well as disturbed wave heights correlated with the incident wave period and the natural period of the moored ship. Chapter 8 explores the hydraulic properties and fish gathering function of fishery structures such as artificial reefs, submerged and moored artificial habitats, a buoy-cable system for shellfish farming, and floating fishery cages for propagation and aquaculture facilities. These structures are presently attracting international attention.

I wish to acknowledge the devoted efforts of the ten authors of the original Japanese edition in writing this English edition. They were once under my supervision in accomplishing their doctoral dissertations and are now, at present, professors and associate professors of universities. Although very busy in teaching and research, they have earnestly devoted most of their off-duty hours to writing book. The sections that they have contributed correspond to the research subjects that they have extended from their doctoral dissertations and in which they are still seeking greater knowledge.

I am very grateful to I-ware Company, Ltd. for its great help in proofreading and editing the English. Mr. Akira Yoshikawa, the president of I-ware and also my nephew, is appreciated for his warm encouragement. In addition, I would also like to express my thanks to Gihodo Publishing Company, Ltd., publisher of the Japanese edition, who has generously allowed me to publish this English version.

Finally, I wish to acknowledge the efforts made by the dedicated staff at Elsevier Science in successfully publishing this book.

Toru Sawaragi
Editor in Chief

The Authors

T. Sawaragi   Member, the Science Council of Japan
                Professor of Civil Engineering,
                Osaka University, Suita, Osaka

K. Iwata   Chairman of Committee on Coastal Engineering, JSCE
                Professor of Civil Engineering,
                Nagoya University, Nagoya, Aichi

M. Kubo   Professor of Research Institute for Cargo Transportation,
                Kobe University of Mercantile Marine, Kobe, Hyogo

I. Deguchi   Associate Professor of Civil Engineering,
                Osaka University, Suita, Osaka

T. Nakamura   Associate Professor of Civil and Ocean Engineering,
                Ehime University, Matsuyama, Ehime

Y. Matsubara   Associate Professor of Civil Engineering,
                Tottori University, Tottori, Tottori

Y. Matsumi   Associate Professor of Social Systems Engineering,
                Tottori University, Tottori, Tottori

M. Nochino   Associate Professor of Civil Engineering,
                Osaka Institute of Technology, Osaka, Osaka

S. Aoki   Associate Professor of Architecture and Civil Engineering,
                Toyohashi University of Technology, Toyohashi, Aichi

N. Mizutani   Associate Professor of Civil Engineering,
                Nagoya University, Nagoya, Aichi

K. Saito   Assistant Professor of Research Institute for Cargo Transportation,
                Kobe University of Mercantile Marine, Kobe, Hyogo

This Page Intentionally Left Blank

Contents

Part I Fundamentals

Chapter 1 Basic Formulation of Sea Waves

Chapter 2 Wave Interactions with Structures and Hydrodynamic Forces

Chapter 3   Waves, Wave-Induced Currents and Sediment Transport

Part II   Applications

Chapter 4   Structures for Wave Control

Chapter 5   Structure for Controlling Sediment Movement

Chapter 6   Marine Structures for Ocean Space Utilization

Chapter 7   Harbour Tranquility

This Page Intentionally Left Blank

Chapter 1   Basic Formulation of Sea Waves

1.1 Introduction

Elucidating and understanding the characteristics of sea waves are requisites for the accurate evaluation of external forces in the design of coastal and offshore structures and in the prediction of beach deformations, etc. It is well known that sea waves can be classified into capillary waves, ultragravity waves, gravity waves, infragravity waves, long-period waves and trans-tidal waves in terms of the wave period and that sea waves also can be classified into deepwater waves, shallow water waves and very shallow water waves from the viewpoint of the relative water depth, h/L (h; the still water depth and L; the wavelength).

Research on the theoretical description of sea waves has been conducted for many years. The theory of permanent-type water waves was first investigated and has been developed from what is called a classical wave theory like that of the Airy wave, to a nonlinear wave theory such as a finite amplitude wave theory (e.g., Stokes wave theory). Recently, the theoretical treatment of non-permanent waves has been energetically investigated in order to bridge the gap between irregular sea waves and well-developed permanent-type wave theories. Owing to the rapid progress in numerical calculation using an electronic computer, numerical analysis based on nonlinear mathematical models is expanding, which enables wave kinematics of non permanent-type waves and fully-nonlinear waves to be evaluated even at the inception of wave breaking. This was considered almost impossible to pursue about two decades ago.

Since the analyses that will be described from Chapter 2 to Chapter 8 regarding wave transformation, wave force, sediment transport, and motions of structures are mainly based on a numerical wave analysis method, the main part of this chapter is devoted to the description of the numerical wave analysis method dealing with non permanent-types and, in some cases, fully-nonlinear wave theories as well such as the Airy wave, Stokes waves and long waves as permanent-type wave theories. The wave theories introduced in this chapter are based on the assumption of perfect fluid and employ mainly Eulerian equations of motion. The effect of fluid viscosity to wave motions is not discussed in this chapter. In Chapter 3, however, adopting Navier-Stokes equation, the wave motion in the bottom boundary layer is discussed.

Sea waves in the real sea are not regular, but irregular with different heights, periods, and propagation directions. Although theoretical approaches to the dynamical description of sea waves have been investigated and are being developed, we still do not have any reliable theory that can evaluate wave kinematics well in addition to water surface profiles from deepwater to near the shoreline. Accordingly, with regards to irregular sea waves, the spectral and statistical properties of a wave will be spotlighted in the latter part of this chapter.

1.2 Regular Wave Theory

A water wave theory is generally developed under the assumptions that the fluid is incompressible and inviscid, the wave motion is irrotational, and the wave is periodic and uniform in time and space with the period T and the wave height H. The basic hydraulic quantities regarding water waves are the still water depth h, the water surface profile η, the wave height H, the wave amplitude a ($=H/2$), the wavelength L, the wave celerity c, and

the wave period, T, as shown in Fig. 1.1. Important dimensionless quantities are the wave number k $(= 2\pi/L)$, the angular frequency σ $(= 2\pi/T)$, the shallowness or relative water depth h/L, and the wave steepness H/L.
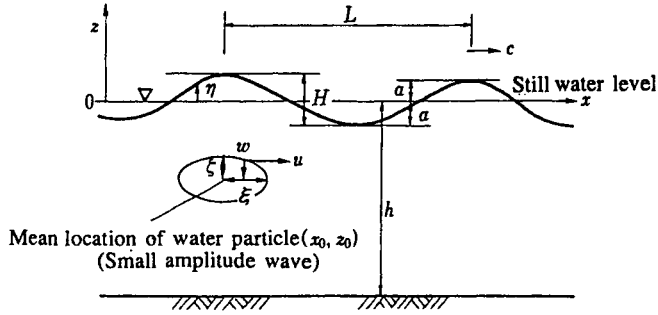
Fig. 1.1 Spatial wave profile and illustration of symbols

If the regular wave is periodic in time and space, then c, L and T satisfy

$$c = \frac{L}{T} \tag{1.1}$$

In developing a wave theory, conservation of the fluid mass provides the continuity equation, and the continuity equation gives rise to the basic differential equation of wave motion. The rectangular Cartesian coordinate system $O\text{-}x\text{-}y\text{-}z$ is employed here, in which O is at the still water surface, x is positive in the direction of wave propagation, z is positive upwards from the still water level and y forms a right-handed system with x and z. Employing incompressibility of the fluid, the continuity equation can be stated in terms of fluid velocities as

$$\frac{\partial u}{\partial x} + \frac{\partial v}{\partial y} + \frac{\partial w}{\partial z} = 0 \tag{1.2}$$

in which u, v, and w are the three components of a fluid particle velocity and refer to the partial differentiation with respect to the arguments.

The continuity equation in the cylindrical polar coordinate system is

$$\frac{\partial u_r}{\partial r} + \frac{\partial u_\theta}{r\partial \theta} + \frac{\partial w}{\partial z} = 0 \tag{1.3}$$

where, r is the perpendicular distance from a fluid particle to the z-axis, θ is the angle between the xz-plane and the plane containing the particle and the axis Oz, and u_r and u_θ are the r- and θ- components of a fluid particle velocity, respectively.

1.2.1 Velocity potential function and stream function

The rotational component of the fluid, Ω_x, Ω_y and Ω_z with respect to the x-, y- and z- axes are defined

$$\Omega_x = \frac{1}{2}\left(\frac{\partial u}{\partial z} - \frac{\partial w}{\partial x}\right), \ \Omega_y = \left(\frac{\partial v}{\partial x} - \frac{\partial u}{\partial y}\right), \ \Omega_z = \left(\frac{\partial w}{\partial y} - \frac{\partial v}{\partial z}\right) \tag{1.4}$$

Irrotationality of fluid motion yields

$$\Omega_x = 0, \ \Omega_y = 0, \ \Omega_z = 0 \tag{1.5}$$

If we define a function ϕ such that

$$u = \frac{\partial \Phi}{\partial x}, \ v = \frac{\partial \Phi}{\partial y}, \ w = \frac{\partial \Phi}{\partial z} \tag{1.6}$$

equation (1.5) is always satisfied. The function is referred to as the velocity potential function. The existence of a velocity potential ensures that the motion is irrotational. Substitution of Eq. (1.6) into Eq. (1.2) yields the well-known Laplace equation

$$\frac{\partial^2 \Phi}{\partial x^2} + \frac{\partial^2 \Phi}{\partial y^2} + \frac{\partial^2 \Phi}{\partial z^2} = 0 \tag{1.7}$$

In the cylindrical polar coordinates, the velocities in r, θ and z directions are given by

$$U_r = \frac{\partial \Phi}{\partial r}, \ U_\theta = \frac{\partial \Phi}{r\partial \theta}, \ W = \frac{\partial \Phi}{\partial z}, \tag{1.8}$$

and the Laplace equation becomes

$$\frac{\partial^2 \Phi}{\partial r^2} + \frac{\partial^2 \Phi}{r^2 \partial \theta^2} + \frac{\partial^2 \Phi}{\partial z^2} = 0 \tag{1.9}$$

In the case of a two-dimensional incompressible flow, the function defined with

$$u = \frac{\partial \psi}{\partial z}, \ w = -\frac{\partial \psi}{\partial x} \tag{1.10}$$

is referred to as a stream function. Then, noting $v = 0$ and using Eq. (1.10), the continuity equation (Eq. (1.2)) reduces to

$$\frac{\partial u}{\partial x} + \frac{\partial w}{\partial z} = \frac{\partial^2 \psi}{\partial x \partial z} - \frac{\partial^2 \psi}{\partial x \partial z} = 0 \qquad (1.11)$$

Existence of a stream function implies that the continuity relationship is satisfied. A stream function requires no assumption of irrotationality of the fluid motion, different from the velocity potential function. Also, it is well known that $\psi =$ const. defines a stream line. There can be, in general, no stream function for three-dimensional flows, with the exception of the axisymmetric flow. On the other hand, the velocity potential exists in any three-dimensional flow that is irrotational.

1.2.2 Green's theorem

Applying the divergence theorem of Gauss to a vector field, the vector field F and its divergence are defined

$$\iiint_V \operatorname{div} F \, d\tau = \oiint_S F \cdot n \, d\delta \qquad (1.12)$$

in which V is a closed region bounded by S, S is a simple closed surface, n is the vector normal to the surface, $d\tau$ is the small quantity of volume, $d\delta$ is the small quantity of area.

Now, let the x-, y- and z- components of vector F be X, Y and Z, respectively and let $F \cdot n$ be $F \cdot n = \lambda X + \mu Y + \nu Z$ ($\lambda = \cos(n,x)$, $\mu = \cos(n,y)$, $\nu = \cos(n,z)$), then, Eq. (1.12) is transformed to

$$\iiint_V \left(\frac{\partial X}{\partial x} + \frac{\partial Y}{\partial y} + \frac{\partial Z}{\partial z} \right) d\tau = \oiint_S \left(X \frac{\partial x}{\partial n} + Y \frac{\partial y}{\partial n} + Z \frac{\partial z}{\partial n} \right) d\delta \qquad (1.13)$$

Let scalar fields ϕ and ψ, together with $\nabla^2 \phi$ and $\nabla^2 \psi$, be defined throughout a closed region V bounded by a simple closed surface S and assume that ϕ and ψ, and their first and second derivatives are continuous. Replacing X with $\phi(\partial \psi / \partial x)$, Y with $\phi(\partial \psi / \partial y)$ and Z with $\phi(\partial \psi / \partial z)$ yields

$$\iiint_V \phi \nabla^2 \psi \, d\tau + \iiint_V \left(\frac{\partial \phi \partial \psi}{\partial x \partial x} + \frac{\partial \phi \partial \psi}{\partial y \partial y} + \frac{\partial \phi \partial \psi}{\partial z \partial z} \right) d\tau = \oiint_S \left(\phi \frac{\partial \psi}{\partial n} \right) d\delta \quad (1.14)$$

in which, $\partial / \partial n$ denotes the directional derivative along the outward normal to S and ∇^2 is three-dimensional Laplacian given as

$$\nabla^2 = \frac{\partial^2}{\partial x^2} + \frac{\partial^2}{\partial y^2} + \frac{\partial^2}{\partial z^2} \qquad (1.15)$$

Interchanging ϕ and ψ in Eq. (1.14)

$$\iiint_v \psi\nabla^2\phi\,\mathrm{d}\tau+\iiint_v\left(\frac{\partial\psi\partial\phi}{\partial x\partial x}+\frac{\partial\psi\partial\phi}{\partial y\partial y}+\frac{\partial\psi\partial\phi}{\partial z\partial z}\right)\mathrm{d}\tau=\oiint_s\left(\psi\frac{\partial\phi}{\partial n}\right)\mathrm{d}\delta \qquad (1.16)$$

Whence, by subtraction from Eq. (1.14)

$$\iiint_v\left(\phi\nabla^2\psi-\psi\nabla^2\phi\right)\mathrm{d}v=\oiint_s\left(\phi\frac{\partial\psi}{\partial n}-\psi\frac{\partial\phi}{\partial n}\right) \qquad (1.17)$$

Equations (1.14) and (1.17) are three-dimensional Green's theorems.

1.2.3 Bernoulli equation

Based on the assumption of irrotational motion and incompressible fluid, the governing equations of motion in the fluid for the x-, y- and z-planes are the Euler equations

$$\left.\begin{array}{l}\dfrac{Du}{Dt}=-\dfrac{1}{\rho}\dfrac{\partial p}{\partial x}\\[2mm]\dfrac{Dv}{Dt}=-\dfrac{1}{\rho}\dfrac{\partial p}{\partial y}\\[2mm]\dfrac{Dw}{Dt}=-\dfrac{1}{\rho}\dfrac{\partial p}{\partial z}-g\end{array}\right\} \qquad (1.18)$$

in which, ρ is the density of water, g is the gravitational acceleration, p is the pressure and t is time. D/Dt is the differential operator defined with

$$\frac{D}{Dt}=\frac{\partial}{\partial t}+u\frac{\partial}{\partial x}+v\frac{\partial}{\partial y}+w\frac{\partial}{\partial z} \qquad (1.19)$$

Employing the velocity potential function ϕ in place of u, v, and w, Eq. (1.18) is transformed to

$$\left.\begin{array}{l}\dfrac{\partial}{\partial x}\left(\dfrac{\partial\Phi}{\partial t}+\dfrac{1}{2}\left(\left(\dfrac{\partial\Phi}{\partial x}\right)^2+\left(\dfrac{\partial\Phi}{\partial y}\right)^2+\left(\dfrac{\partial\Phi}{\partial z}\right)^2\right)+\dfrac{p}{\rho}\right)=0\\[4mm]\dfrac{\partial}{\partial y}\left(\dfrac{\partial\Phi}{\partial t}+\dfrac{1}{2}\left(\left(\dfrac{\partial\Phi}{\partial x}\right)^2+\left(\dfrac{\partial\Phi}{\partial y}\right)^2+\left(\dfrac{\partial\Phi}{\partial z}\right)^2\right)+\dfrac{p}{\rho}\right)=0\\[4mm]\dfrac{\partial}{\partial z}\left(\dfrac{\partial\Phi}{\partial t}+\dfrac{1}{2}\left(\left(\dfrac{\partial\Phi}{\partial x}\right)^2+\left(\dfrac{\partial\Phi}{\partial y}\right)^2+\left(\dfrac{\partial\Phi}{\partial z}\right)^2\right)+\dfrac{p}{\rho}\right)=-g\end{array}\right\} \qquad (1.20)$$

Integrating the x-, y- and z- equations (Eq. (1.20)) and summarizing the integrated equations yield the following equation:

$$\frac{\partial \Phi}{\partial t} + \frac{1}{2}\left(\left(\frac{\partial \Phi}{\partial x}\right)^2 + \left(\frac{\partial \Phi}{\partial y}\right)^2 + \left(\frac{\partial \Phi}{\partial z}\right)^2\right) + gz + \frac{p}{\rho} = Q(t) \tag{1.21}$$

Equation (1.21) is called the unsteady form of the Bernoulli equation, or for brevity, simply the unsteady Bernoulli equation. The function $Q(t)$ is called Bernoulli term and is constant for steady flows. Now, if $Q(t)$ is included into $\Phi(t)$, Eq. (1.21) can be

$$\frac{\partial \Phi}{\partial t} + \frac{1}{2}\left(\left(\frac{\partial \Phi}{\partial x}\right)^2 + \left(\frac{\partial \Phi}{\partial y}\right)^2 + \left(\frac{\partial \Phi}{\partial z}\right)^2\right) + gz + \frac{p}{\rho} = 0 \tag{1.22}$$

1.2.4 Basic equation and boundary conditions

The fluid is assumed inviscid and incompressible and the wave motion is treated to be irrotational. In the case that the velocity potential Φ and the pressure p are the unknown functions, the basic equations in the Cartesian coordinate system are the Laplace equation (Eq. (1.7)) and the pressure equation (Eq. (1.22)). The boundary conditions to solve the basic equation are those imposed on the free surface and bottom.

(1) Boundary conditions at free surface

The kinematic and dynamic boundary conditions are required on the free surface. The dynamic condition states that the pressure on the free surface is uniform along the wave form. This condition is given as, with the unsteady Bernoulli equation (Eq. (1.22)),

$$\frac{\partial \Phi}{\partial t} + g\eta + \frac{1}{2}\left(\left(\frac{\partial \Phi}{\partial x}\right)^2 + \left(\frac{\partial \Phi}{\partial y}\right)^2 + \left(\frac{\partial \Phi}{\partial z}\right)^2\right) = 0 \qquad : z = \eta \tag{1.23}$$

in which, the atmospheric pressure p is assumed to be zero.

On the other hand, the kinematic condition states that there is no flow across the free surface. In another words, the component of the fluid velocity normal to the free surface is related to the local velocity of the free surface. Let the free surface be $F(x,y,z;t) = 0$, and then the kinematic condition is given as

$$\frac{DF}{Dt} = 0 \qquad : z = \eta \tag{1.24}$$

Since the free surface $F(x,y,z;t) = 0$ is equal to $\eta(x,y;t) - z = 0$, Eq. (1.24) becomes

$$\frac{\partial \Phi}{\partial z} = \frac{\partial \eta}{\partial t} + u\frac{\partial \eta}{\partial x} + v\frac{\partial \eta}{\partial y} \qquad : z = \eta \tag{1.25}$$

(2) Boundary condition at bottom

Under the condition that the bottom is fixed and impermeable, the bottom boundary condition is a kinematic one and is described with

$$\frac{\partial \Phi}{\partial z} = -\frac{\partial \Phi}{\partial x}\frac{\partial h}{\partial x} - \frac{\partial \Phi}{\partial y}\frac{\partial h}{\partial y} \qquad : z=-h \qquad (1.26)$$

In the special case that there is a body like a coastal or maritime structure in the wave field, the following condition should be satisfied on the surface of the body

$$\frac{\partial \Phi}{\partial n} = V_n \qquad (1.27)$$

in which n is the normal direction to the structure surface and V_n is the n-directed velocity component of the structure.

1.2.5 Water surface waves

We discuss here a two-dimensional progressive wave in constant water depth. The two-dimensional water wave boundary value problem is given from Eq. (1.7) and Eqs. (1.23) - (1.26).

governing equation:

$$\frac{\partial^2 \Phi}{\partial x^2} + \frac{\partial^2 \Phi}{\partial z^2} = 0 \qquad : \begin{array}{c} -h \leq z \leq \eta \\[6pt] -\infty \leq x \leq +\infty \end{array} \qquad (1.28)$$

boundary conditions:

$$\frac{\partial \eta}{\partial t} + \frac{\partial \Phi}{\partial x}\frac{\partial \eta}{\partial x} - \frac{\partial \Phi}{\partial z} = 0 \qquad : z=\eta \qquad (1.29)$$

$$\frac{\partial \Phi}{\partial t} + \frac{1}{2}\left(\left(\frac{\partial \Phi}{\partial x}\right)^2 + \left(\frac{\partial \Phi}{\partial z}\right)^2\right) + g\eta = Q(t) \qquad : z=\eta \qquad (1.30)$$

$$\frac{\partial \Phi}{\partial z} = 0 \qquad \text{(impermeable fixed condition)} : z=-h \qquad (1.31)$$

(1) Small-amplitude progressive wave theory (Airy wave theory)

Since the free surface boundary conditions (Eqs. (1.29) and (1.30)) are nonlinear, a general analytical solution cannot be obtained. Because of this, we assume that (i) the free surface variation η is very small, $O(\eta) = 0$, (ii) the wave motion is gentle and the square of the particle velocity is negligibly small, $O(u^2)<<O(u)$ and $O(w^2)<<O(w)$ and (iii) the water surface slope $\partial \eta/\partial x$ is very small, $O(\partial \eta/\partial x) = 0$, and the product of the particle velocity and $\partial \eta/\partial x$ is also small, $O(u\partial \eta/\partial x) = 0$. In addition, the Bernoulli constant $Q(t)$ is treated to be included into the velocity potential, $\Phi(x,y;t)$. Therefore, employing the above-cited assumptions, the nonlinear boundary conditions at free surface (Eqs. (1.29) and (1.30)) can be linearized as follows:

$$\frac{\partial \Phi}{\partial z} = \frac{\partial \eta}{\partial t} \qquad \qquad : z=0$$

$$\eta = -\frac{1}{g}\left(\frac{\partial \Phi}{\partial t}\right) \qquad : z=0$$

(1.32)

Eliminating η from the two equations in Eq. (1.32) yields

$$\frac{\partial \Phi}{\partial z} = -\frac{1}{g}\left(\frac{\partial^2 \Phi}{\partial t^2}\right) \qquad : z=0 \qquad (1.33)$$

Using Eq. (1.22), the water pressure p at the depth of z is derived as

$$p = -\rho \frac{\partial \Phi}{\partial t} - \rho g z \qquad (1.34)$$

The 1st term of Eq. (1.34) is the dynamic pressure caused by the wave motion, and the second term is the hydrostatic pressure.

(a) Shallow water waves (1/25<h/L<1/2)
   A progressive wave that is periodic in time and space and propagates over a horizontal bottom is treated in this section. With the given conditions that the wave height is H, the wave period is T and employing the method of separation of variables, the velocity potential function Φ that satisfies Eqs. (1.29), (1.30) and (1.31) is derived as

$$\Phi = \frac{H\sigma}{2k}\frac{\cosh k(h+z)}{\sinh kh}\sin k(x-ct) \qquad (1.35)$$

$$\sigma^2 = gk\tanh kh \qquad (1.36)$$

in which $k(= 2\pi/L)$ is the wave number, and $\sigma(=2\pi/T)$ is the angular frequency. Equation (1.36) describes the relationship between k and σ for a given water depth h. The wave celerity c and the wavelength L are derived from Eqs. (1.1) and (1.36)

$$c = \sqrt{\frac{g}{k}\tanh kh} \quad , \quad L = \frac{gT^2}{2\pi}\tanh kh \qquad (1.37)$$

Equations (1.36) and (1.37) state that the wavelength L increases with the increasing of the wave period T and therefore the wave celerity c also becomes larger with an increment of wave period T. Thus, Eq. (1.36), is called the "dispersion relationship equation", since it describes the manner in which a field of propagating waves consisting of many different frequencies will separate or disperse due to the different celerities of the various frequency components.

With the help of Eqs. (1.32), (1.34), (1.35) and (1.36), the water surface profile η and the wave pressure p are given as follows:

$$\eta = \frac{1}{2}H\cos k(x - ct) = \frac{1}{2}H\cos(kx - \sigma t) \tag{1.38}$$

$$p = \frac{1}{2}\rho g H \frac{\cosh k(h + z)}{\cosh kh}\cos(kx - \sigma t) \tag{1.39}$$

The horizontal and vertical components of water particle velocity u and w, respectively, are derived as follows with the use of Eqs. (1.6) and (1.35):

$$u = \frac{\partial \Phi}{\partial x} = \frac{1}{2}H\sigma\frac{\cosh k(h + z)}{\sinh kh}\cos(kx - \sigma t)$$

$$w = \frac{\partial \Phi}{\partial x} = \frac{1}{2}H\sigma\frac{\cosh k(h + z)}{\sinh kh}\sin(kx - \sigma t) \tag{1.40}$$

It can be understood that the phase difference between u and w is $\pi/2$. A water particle with a mean position of (x_0, z_0) will be displaced by the wave-caused pressures and the instantaneous water particle position $((x-x_0), (z-z_0))$ can be found by integrating the velocity with respect to time. The resulting water particle trajectory is

$$\frac{(x - x_0)^2}{\left(\dfrac{1}{2}H\dfrac{\cosh k(h + z_0)}{\sinh kh}\right)^2} + \frac{(z - z_0)^2}{\left(\dfrac{1}{2}H\dfrac{\sinh k(h + z_0)}{\sinh kh}\right)^2} = 0 \tag{1.41}$$

Equation (1.41) is the equation of an ellipse with semiaxes $H\cosh k(h+z_0)/2\sinh kh$ and $H\sinh k(h+z_0)/2\sinh kh$ in the x and z directions, respectively. Note that $H\cosh k(h+z_0)/2\sinh kh$ is larger than $H\sinh k(h+z_0)/2\sinh kh$.

The total wave energy consists of potential and kinetic energies. The total wave energy per unit area over one wavelength E is defined within the order of a^2 (a: wave amplitude)

$$E = E_p + E_k = \frac{1}{L}\int_0^L\int_0^\eta \rho g z\, dx dz + \frac{1}{L}\int_0^L\int_{-h}^0 \frac{1}{2}\rho(u^2 + w^2)\, dz dx \tag{1.42}$$

Substituting Eqs. (1.38) and (1.40) into Eq. (1.42) and assuming $\eta \equiv 0$ yield

$$E = \frac{1}{16}\rho g H^2 + \frac{1}{16}\rho g H^2 = \frac{1}{8}\rho g H^2 \tag{1.43}$$

Although small-amplitude waves do not transmit mass with their propagation across a fluid, water waves transmit energy as the trajectories of the water particles are closed. The rate of energy transfer is called the energy flux. The average energy flux over wave period $\overline{W}$ in the x-direction is defined within the order of a^2 (a; wave amplitude)

$$\overline{W} = \frac{1}{T} \int_0^T \int_{-h}^0 \left(-\frac{\partial \Phi}{\partial t} \right) u \mathrm{d}z \, \mathrm{d}t \tag{1.44}$$

Putting Eqs. (1.35) and (1.40) into Eq. (1.44) gives

$$\overline{W} = \frac{1}{16} \rho g H^2 c \left(1 + \frac{2kh}{\sinh 2kh} \right) \tag{1.45}$$

Equation (1.45) can be written

$$\overline{W} = Enc; \qquad n = \frac{1}{2}\left(1 + \frac{2kh}{\sinh 2kh} \right) \tag{1.46}$$

$$= Ec_g$$

in which, nc is the speed at which the energy is transmitted. This velocity is called the group velocity c_g. Within the small-amplitude wave theory, the total wave energy is transferred with the speed of c_g.

(b) Deepwater waves ($h/L>1/2$) and very shallow water waves ($h/L<1/25$)

The hyperbolic functions have deepwater and very shallow water asymptotes, and it is helpful to utilize them in order to obtain simplified forms of the equations describing wave motion.

In the case of deepwater waves ($h/L>1/2$), the following simplifications are usually done under the condition of $kh \to \infty$:

$$\left. \begin{aligned} \tanh kh &\to 1 \\ \sinh kh &\to \frac{1}{2}e^{kh} \\ \cosh kh &\to \frac{1}{2}e^{kh} \end{aligned} \right\} \tag{1.47}$$

In the case of very shallow water waves ($h/L<1/25$), the hyperbolic functions have the following asymptotic forms with $kh \to 0$:

$$\left. \begin{aligned} \tanh kh &\to kh \\ \sinh kh &\to kh \\ \cosh kh &\to 1 \end{aligned} \right\} \tag{1.48}$$

The mathematical descriptions of the wave properties regarding deepwater and very shallow water waves are very simplified, compared to those of shallow water waves, as shown in Table 1.1. From Table 1.1, it is seen that the trajectory of the water particle is a circle in the deepwater wave and a very flat ellipse in the very shallow water wave, as shown schematically in Fig. 1.2.

Table 1.1 Small amplitude wave theory

	Very shallow water wave $h/L < 1/25$	Shallow water wave $1/25 < h/L < 1/2$	Deepwater wave $h/L > 1/2$
Wave profile η	$\rightarrow$	$\eta = \dfrac{1}{2}H\cos(kx - \sigma t) = \dfrac{1}{2}H\cos\theta$	$\leftarrow$
Wave celerity c	$c = \sqrt{gh}$	$c = \dfrac{gT^2}{2\pi}\tanh\left(\dfrac{2\pi h}{L}\right)$	$c = \dfrac{gT}{2\pi}$
Wavelength L	$L = T\sqrt{gh}$	$L = \dfrac{gT^2}{2\pi}\tanh\left(\dfrac{2\pi h}{L}\right)$	$L = \dfrac{g}{2\pi}T^2$
Group velocity c_g	$c_g = c = \sqrt{gh}$	$c_g = \dfrac{1}{2}\left[1 + \dfrac{4\pi h/L}{\sinh 4\pi h/L}\right]$	$c_g = \dfrac{1}{2}c$
Particle velocity Horizontal compoennt u Vertical component w	$u = \dfrac{H}{2}\sqrt{\dfrac{g}{h}}\cos\theta$ $w = \dfrac{H\pi}{T}\left(1 + \dfrac{z}{h}\right)\sin\theta$	$u = \dfrac{H}{2}\dfrac{gT}{L}\dfrac{\cosh[2\pi(z+h)/L]}{\cosh(2\pi h/L)}\cos\theta$ $w = \dfrac{H}{2}\dfrac{gT}{L}\dfrac{\sinh[2\pi(z+h)/L]}{\cosh(2\pi h/L)}\sin\theta$	$u = \dfrac{\pi H}{T}\,e^{\frac{2\pi z}{L}}\cos\theta$ $w = \dfrac{\pi H}{T}\,e^{\frac{2\pi z}{L}}\sin\theta$
Particle acceleration Horizontal component $\dot{u}$ Vertical component $\dot{w}$	$\dot{u} = \dfrac{H\pi}{T}\sqrt{\dfrac{g}{h}}\sin\theta$ $\dot{w} = -2\pi\left(\dfrac{\pi}{T}\right)^2\left(1 + \dfrac{z}{h}\right)\cos\theta$	$\dot{u} = \dfrac{g\pi H}{L}\dfrac{\cosh[2\pi(z+h)/L]}{\cosh(2\pi h/L)}\sin\theta$ $\dot{w} = -\dfrac{g\pi H}{L}\dfrac{\sinh[2\pi(z+h)/L]}{\cosh(2\pi h/L)}\cos\theta$	$\dot{u} = 2H\left(\dfrac{\pi}{T}\right)^2 e^{\frac{2\pi z}{L}}\sin\theta$ $\dot{w} = -2H\left(\dfrac{\pi}{T}\right)^2 e^{\frac{2\pi z}{L}}\cos\theta$
Particle orbit Horizontal displacement ξ Vertical displacement ζ	$\xi = -\dfrac{HT}{4\pi}\sqrt{\dfrac{g}{h}}\sin\theta$ $\zeta = \dfrac{H}{2}\left(1 + \dfrac{z}{h}\right)\cos\theta$	$\xi = -\dfrac{H}{2}\dfrac{\cosh[2\pi(z+h)/L]}{\sinh(2\pi h/L)}\sin\theta$ $\zeta = \dfrac{H}{2}\dfrac{\sinh[2\pi(z+h)/L]}{\sinh(2\pi h/L)}\cos\theta$	$\xi = -\dfrac{H}{2}e^{\frac{2\pi z}{L}}\sin\theta$ $\zeta = \dfrac{H}{2}e^{\frac{2\pi z}{L}}\cos\theta$
Water pressure p	$p = \rho g(\eta - z)$	$p = \rho g\eta\dfrac{\cosh[2\pi(h+z)/L]}{\cosh(2\pi h/L)} - \rho g z$	$p = \rho g\eta\,e^{\frac{2\pi z}{L}} - \rho g z$

(a) Deepwater waves $\dfrac{h}{L} > \dfrac{1}{2}$

(b) Shallow water waves $\dfrac{1}{25} < \dfrac{h}{L} < \dfrac{1}{2}$

(c) Very shallow water waves $\dfrac{h}{L} < \dfrac{1}{25}$
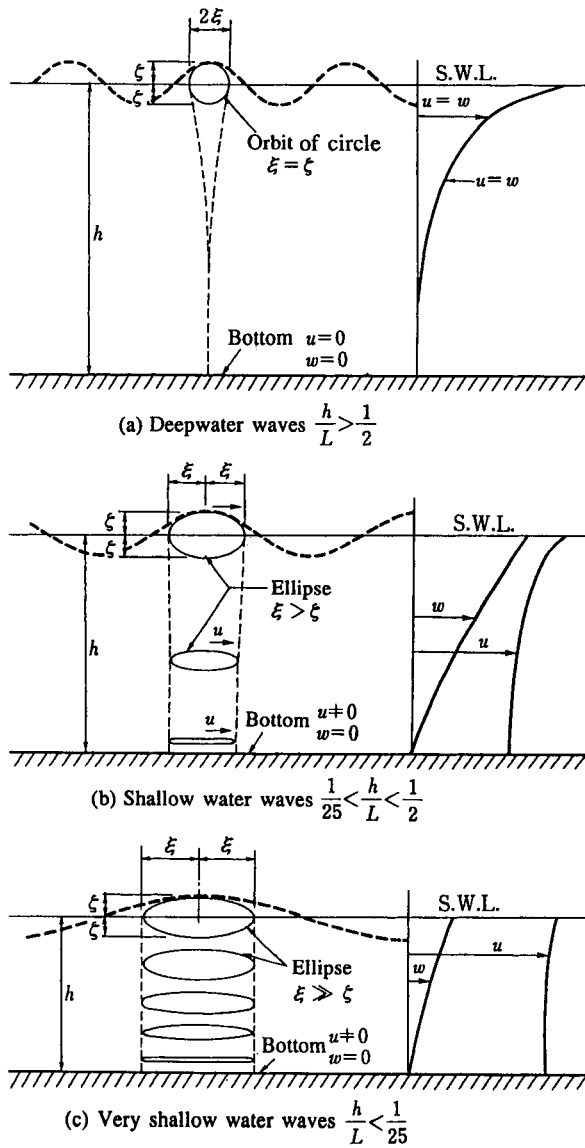
Fig. 1.2 Particle orbits and kinematics (small amplitude waves)

(2) Finite-amplitude progressive wave theory

It is known that the free surface boundary conditions cannot be linearized with the increasing of the wave steepness and wave height. For nonlinear boundary value problems, we can only derive approximate wave theories except for some special cases.

The methods to solve the nonlinear boundary value problem are classified into (i) analytical method (perturbation method, successive approximation method, etc.), (ii) numerical method (finite difference method, finite element method, boundary integral method, etc.) and (iii) graphical method (characteristics method, etc.). In this section, the perturbation method is first treated and the Stokes wave up to the 3rd-order will be described. Second, the Dean stream function method will be described.

(a) Stokes finite-amplitude wave theory

Stokes (1880) developed a nonlinear wave theory in order to approach the complete solution more closely, employing the perturbation method. Since then, higher order wave theories have been developed and Skjelbreia and Hendrickson (1960) derived up to the 5th-order approximate solution of the Stokes wave. Recently, Schwartz (1974) and Cokelet (1977) calculated much higher order Stokes waves, utilizing a large high-speed computer with a large capacity of memory.

The Stokes wave expansion method is formally carried out under the condition of $H/h \ll (kh)^2$ for $kh \ll 1$ and $H/L \ll 1$, and all wave properties (wave profile, velocity potential, wave celerity, etc.) are formulated with a power series with respect to H/L. Readers should refer to Skjelbreia and Hendrickson (1960) for a detailed derivation of the Stokes wave. In this section, the 3rd-order solution derived by Skjelbreia (1958) will be described. He expressed the velocity potential Φ, the water surface profile η, Bernoulli constant Q and the wave celerity c in the following series forms:

$$\frac{k\Phi}{c} = \left(\varepsilon A_{11} + \varepsilon^3 A_{13} \right) \cosh k(h+z) \sin (kx - \sigma t)$$

$$+ \varepsilon^2 A_{22} \cosh 2k(h+z) \sin 2(kx - \sigma t) \qquad (1.49)$$

$$+ \varepsilon^3 A_{33} \cosh 3k(h+z) \sin 3(kx - \sigma t)$$

$$k\eta = \varepsilon \cos(kx - \sigma t) + \varepsilon^2 B_{22} \cos 2(kx - \sigma t) + \varepsilon^3 B_{33} \cos 3(kx - \sigma t) \qquad (1.50)$$

$$kQ = \varepsilon^2 Q_3 \qquad (1.51)$$

$$kc^2 = Q_0 \left(1 + \varepsilon^2 Q_1 \right) \qquad (1.52)$$

in which, A_{11}, A_{13}, A_{22}, A_{33}, B_{22}, B_{33}, Q_0, Q_1 and Q_3 are unknown functions of kh, and ε is a perturbation parameter. Equation (1.49) satisfies the Laplace equation (Eq. (1.28)) and the bottom boundary condition (Eq. (1.31)). Equations (1.49) - (1.52) should satisfy the free surface boundary conditions (Eq. (1.29) and (1.30)). The boundary conditions at an unknown free surface $z = \eta$ are formally expanded as a Taylor series around $z = 0$.

$$\left(\eta_t + \Phi_x \eta_x - \Phi_z \right) + \sum_{n=1}^{n} \frac{\eta^n \partial^n}{n! \partial z^n} (\Phi_x \eta_x - \Phi_z) = 0 \quad : \quad z = 0 \qquad (1.53)$$

$$\left(g\eta + \Phi_t + \frac{1}{2} \left(\Phi_x^2 + \Phi_z^2 \right) \right) + \sum_{n=1}^{n} \frac{\eta^n \partial^n}{n! \partial z^n} \left(\Phi_t + \frac{1}{2} \left(\Phi_x^2 + \Phi_z^2 \right) \right) = Q \quad : \quad z = 0$$

$$(1.54)$$

Substitution of Eqs. (1.49) - (1.52) into Eqs. (1.53) and (1.54) leads to two equations involving undetermined coefficients, powers of parameter ε and powers of $\sin(kx\text{-}\sigma t)$ and $\cos(kx\text{-}\sigma t)$. These equations are grouped and sub-grouped according to the powers of $\sin(kx\text{-}\sigma t)$ and $\cos(kx\text{-}\sigma t)$. Since the equations must hold for any value of $(kx\text{-}\sigma t)$, the terms in each equation involving the same power of ε and the same power of $\sin(kx\text{-}\sigma t)$ or $\cos(kx\text{-}\sigma t)$ are set equal. This process produces 9 equations involving 9 unknown coefficients A_{11}, A_{13}, A_{22}, A_{33}, B_{22}, B_{33}, C_0, Q_1 and Q_3. The last unknown perturbation parameter has to be determined. The value of ε is usually obtained using the relationship

$$H = \eta_{\max} - \eta_{\min} \tag{1.55}$$

in which, H is the wave height, and $\eta_{\max}$ and $\eta_{\min}$ are the water elevation of wave crest and trough, respectively. Substitution of Eq. (1.50) into Eq. (1.55) yields

$$kH = 2\varepsilon + 2\varepsilon^3 B_{33} \tag{1.56}$$

Since $\varepsilon(<<1)$ can be taken as

$$\varepsilon = ka \tag{1.57}$$

Equation (1.53) is written

$$\frac{H}{2a} = 1 + a^2 k^2 B_{33} \tag{1.58}$$

The wave height H and the wave amplitude a hold the relationship given by Eq. (1.58). Thus, all the unknown coefficients (A_{11}, A_{13}, A_{22}, A_{33}, B_{22}, B_{33}, Q_0, Q_1 and Q_3) are determined and their values are all listed in Table 1.2.

Table 1.2 Coefficients (3rd-order)

$$A_{11} = 1/\sinh kh, \quad A_{22} = 3/8 \sinh^4 kh$$

$$A_{13} = -\frac{\cosh^2 kh(1 + 5\cosh^2 kh)}{8 \sinh^5 kh}, \quad A_{33} = \frac{13 - 4\cosh^2 kh}{64 \sinh^7 kh}$$

$$B_{22} = \frac{2\cosh^2 kh + 1}{4 \sinh^3 kh}\cosh kh, \quad B_{33} = \frac{3(8 \cosh^6 kh + 1)}{64 \sinh^6 kh}$$

$$Q_0^2 = g\tanh kh, \quad Q_1 = \frac{8 \cosh^4 kh - 8 \cosh^2 kh + 9}{8 \sinh^4 kh}$$

$$Q_3 = -1/(4\sinh kh \cdot \cosh kh)$$

The 3rd-order approximate solution contains the fundamental frequency component σ, second harmonic frequency component 2σ, and third harmonic frequency component 3σ. The water surface profile of the 3rd-order approximate solution steepens at a wave crest and flattens at a wave trough (see Fig. 1.5), compared to the small amplitude wave profile. It is known that the wavelength and the wave celerty of the 3rd-order approximation become larger than those of the small amplitude wave theory. The trajectory of the water particle of the 3rd-order Stokes wave is quite different from that of the small amplitude wave. That is, the trajectory of the water particle of the 3rd-order approximate theory never closes, as illustrated schematically in Fig. 1.3, and the water particles drift in the direction of the waves and move more rapidly at the surface than at the bottom. This is normally called "the mass transport velocity". Following the Lagrangian description, the mean mass transport velocity over one wave period $\bar{U}_l$ is

$$\bar{U}_1 = \frac{1}{2} c \left(\frac{2\pi}{L} \right)^2 a^2 \frac{\cosh 4\pi(h+z)/L}{\sinh^2 2\pi h/L} \tag{1.59}$$
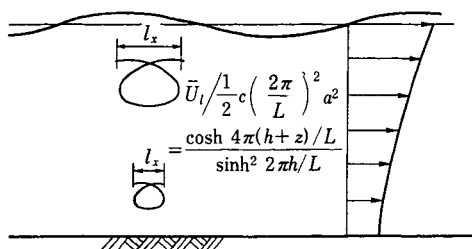
Fig. 1.3 Mass transport and mass transport velocity

(b) Dean stream function method (Dean 1965)
   Different from the perturbation method, the stream function method proposed by Dean belongs to the numerical method. The Dean stream function method is computationally simpler than the Chappelear method (1961).
   The coordinate system is moved with celerity of the wave c, thereby rendering the system steady. The stream function that strictly satisfies the basic equation (Eq. (1.28)) and the bottom condition (Eq. (1.31)) is described, in case of Nth-order, as

$$\psi = cz + \sum_{n=1}^{N} X(n)\sinh nks \, \cos nkx \tag{1.60}$$

in which, $ks = 2\pi(h+z)/L$, $kx = 2\pi h/L$, and $X(n)$ is the coefficient of the nth-order component. The use of Eq. (1.10) produces the equations regarding the particle velocity and the free surface profile.

$$u - c = -\frac{\partial \psi}{\partial z} = -c - \sum_{n=1}^{N} nk X(n) \cosh nks \, \cos nkx \tag{1.61}$$

$$w = \frac{\partial \psi}{\partial x} = -\sum_{n=1}^{N} nkX(n) \sinh\, nks \, \sin\, nkx \tag{1.62}$$

$$\eta = \frac{\psi(x,\eta)}{c} - \frac{1}{c} \sum_{n=1}^{N} X(n) \sinh\, nks \, \cos\, nkx \tag{1.63}$$

The free surface boundary conditions in the coordinate system moving with the wave celerity c are

$$\left.\begin{array}{l} \dfrac{\partial \eta}{\partial x} = \dfrac{w}{u-c} \\[3mm] g\eta + \dfrac{1}{2}\left(\left(\dfrac{\partial \psi}{\partial x}\right)^2 + \left(\dfrac{\partial \psi}{\partial z}\right)^2\right) = Q_s \end{array}\right\} \quad z=\eta \tag{1.64}$$

in which, Q_s is the Bernoulli constant.

The free surface is one stream line. Therefore, the water surface profile strictly satisfying the kinematic free surface boundary condition (1st equation in Eq. (1.64)) is, first of all, determined, and then $X(n)$ and L are determined so as to satisfy the dynamical free surface boundary condition (2nd equation in Eq. (1.64)) using the least square method. In numerical calculation, this condition is satisfied at i discrete points along the free surface profile, each point being denoted by i. According to the dynamic free surface boundary condition, all the Q_{si} should be equal to Q_s

$$Q_{si} = \left\{ \frac{\left(\dfrac{\partial \psi}{\partial x}\right)_i^2 + \left(\dfrac{\partial \psi}{\partial z}\right)_i^2}{2} \right\} + g\,\eta_i = Q_s \tag{1.65}$$

The iterative procedure is employed to determine $X(n)$ with use of Q_{si} . The measure of satisfaction of the dynamic free surface boundary condition is defined with E_l, which is the mean squared error to the boundary condition.

$$E_1 = \frac{2}{L} \int_0^{L/2} (Q_{si} - Q_s)^2 \, dx \cong \frac{1}{I} \sum_{i=1}^{I} (Q_{si} - Q_s)^2$$

$$Q_s = \frac{2}{L} \int_0^{L/2} (Q_{si}) dx \cong \frac{1}{I} \sum_{i=1}^{I} Q_{si} \tag{1.66}$$

For an exact solution E_l must be zero. It should be noted that the wave height H, the water surface profile η and η_i, must satisfy

$$\eta(0) - \eta(L/2) = H$$

$$\frac{2}{L} \int_0^{L/2} \eta(x) dx \cong \frac{1}{I} \sum_{i=1}^{I} \eta_i = 0 \tag{1.67}$$

Extension of this theory to waves near breaking has been done. In addition, this theory can be applied to regular measured wave profile η_m. Using the iterative method, the best-fit values of $X(n)$ and L of estimated wave profile η_p to the measured wave profile η_m are determined so as to minimize the error E^*

$$
\left.
\begin{aligned}
E^* &= E_1 + \lambda E_2 \\
E_1 &= \frac{1}{N}\sum_{i=1}^{N}\left(Q_{si} - Q_s\right)^2 \\
E_2 &= \frac{1}{N}\sum_{i=1}^{N}\left(\eta_{mi} - \eta_{pi}\right)^2
\end{aligned}
\right\}
\qquad (1.68)
$$

in which, λ is the Lagrange unfixed coefficient.

The water particle velocities on a gently sloping bottom have reportedly been evaluated well with the Dean stream function method (see Fig. 1.4), with the help of Eq. (1.68) (Koyama and Iwata 1988).
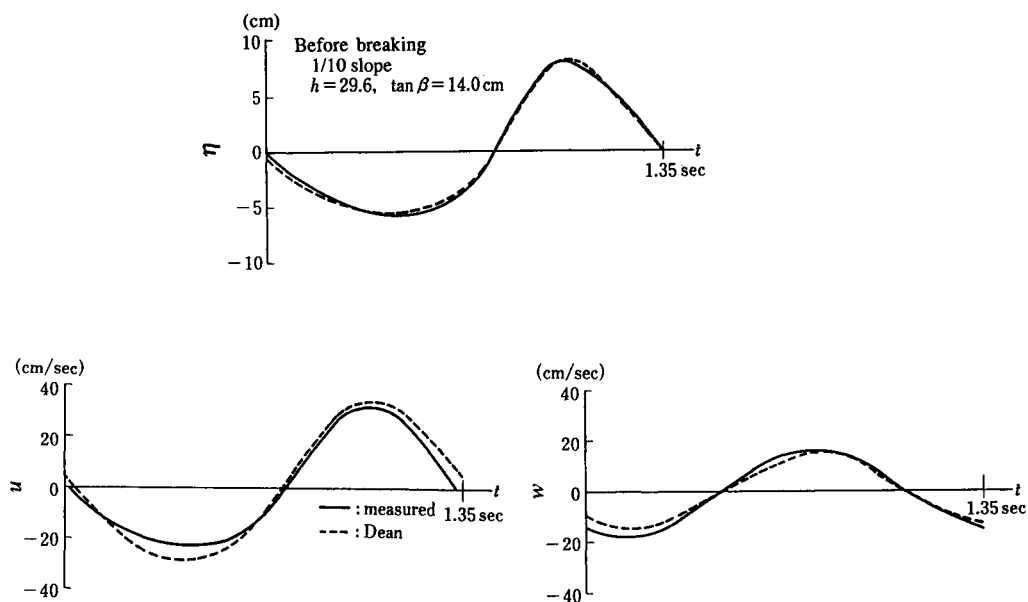
Fig. 1.4 Comparison between calculated values with the Dean stream function method and experimental values

(c) Applicable range of finite amplitude wave theory

Figure 1.5 shows one example of comparison of water surface profiles among laboratory experiments, the Stokes 2nd-order, 2nd-order cnoidal and small amplitude wave theories.
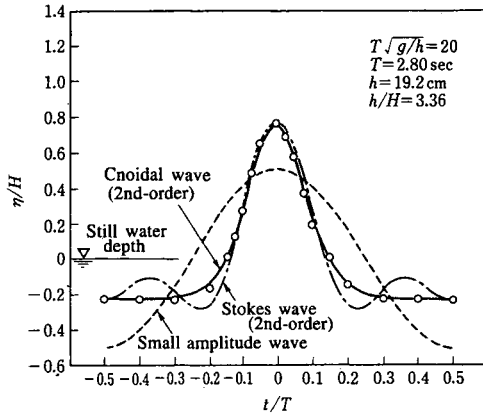
Fig. 1.5 Comparison of water surface profiles

It can be seen from the figure that the experimental value differs from the small amplitude wave, and that the Stokes wave differs from the measured value at the wave trough. The cnoidal wave, however, best fits the laboratory experiment. This is only one example of comparisons and different results will be obtained in different wave conditions. Generally speaking, the Stokes wave theory is applicable for waves under a large value of h/L and the cnoidal wave theory can be applied to waves under a small value of h/L. Using the Goda nonlinearity parameter Π (Goda 1985), Iwagaki (1987) has presented an elaborate graph (Fig. 1.6) that indicates the applicability range of various wave theories.
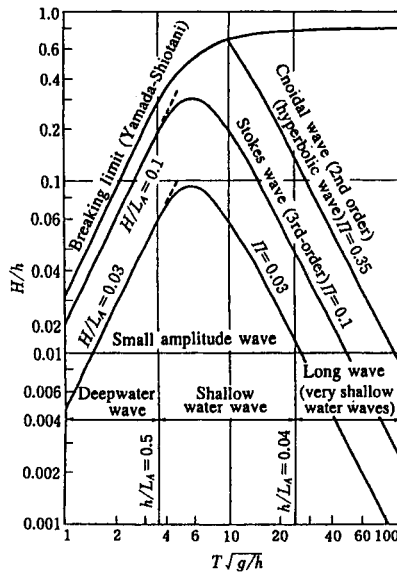
Fig. 1.6 Applicability range of various wave theories (Iwagaki 1987)

$$\Pi = \left(H/L_A\right)\coth^3\left(2\pi h/L_A\right) \tag{1.69}$$

in which, L_A is the wavelength of small amplitude wave. The applicable range of the small amplitude wave is $\Pi = 0.03$ for wave crest and $\Pi = 0.1$ for wave celerity and wavelength. It should be noted that each wave theory has its own applicability range that is limited by the wave steepness H/L, the relative water depth h/L and the nonlinear parameter Π.

(3) Standing wave theory
(a) Small amplitude wave theory
   The wave system comprised of two waves of the same period T and height H but propagating in the opposite direction is called the standing wave. The standing wave can be formed in the sea area seaward of a vertical wall by which an incident wave is perfectly reflected backward.
   For the linearized free surface boundary conditions (kinematic and dynamic free surface boundary conditions), the water surface profile of small-amplitude standing wave is

$$\left.\begin{aligned}\eta &= \frac{1}{2}H\cos(kx - \sigma t) + \frac{1}{2}H\cos(kx + \sigma t)\\ &= H\cos\sigma t\ \cos kx\end{aligned}\right\} \tag{1.70}$$

in which H is the incident wave and reflected wave height, k is the wave number, and s is the angular frequency. The amplitude of a standing wave varies with distance x and h becomes zero (minimum) at $x = (2n+1)L/4$ ($n = 0, 1, 2, ...$) which satisfies the relation of $\cos kx = 0$. The location at which h becomes zero is called the node. On the other hand, h becomes a maximum (H) at $x = (2n)L/4$ ($n = 0, 1, 2, ...$) which corresponds to $\cos kx = \pm 1$, which is called the antinode. Thus, the node and antinode are formed alternatively at the interval of $L/4$. The velocity potential, the horizontal and vertical velocities u and w, the horizontal and vertical displacements of the particle orbit from its mean position (x_0, z_0) x and z, and the water pressure p and the wave energy per unite area E are readily found to be

$$\Phi = -Hc\,\frac{\cosh k(h+z)}{\sinh kh}\sin\sigma t\cos kx$$

$$u = H\sigma\,\frac{\cosh k(h+z)}{\sinh kh}\sin\sigma t\sin kx$$

$$w = -H\sigma\,\frac{\sinh k(h+z)}{\sinh kh}\sin\sigma t\cos kx$$

$$\xi = H\,\frac{\cosh k(h+z_0)}{\sinh kh}\cos\sigma t\sin kx_0$$

$$\zeta = H\,\frac{\cosh k(h+z_0)}{\sinh kh}\cos\sigma t\cos kx_0 \tag{1.71}$$

$$p = \rho gH\,\frac{\cosh k(h+z)}{\cosh kh}\cos\sigma t\cos kx - \rho gz$$

$$E = \frac{1}{4}\rho gH^2$$

Inspection of Eq. (1.71) shows, as illustrated in Fig. 1.7, that $w = 0$ and $\zeta = 0$ at the antinodes (at $x = (2n-1)L/4$), and $u = 0$ and $\xi = 0$ at the nodes (at $x = nL/2$). The orbit of the water particle is a simple harmonic motion along a straight line, as illustrated in Fig. 1.7.
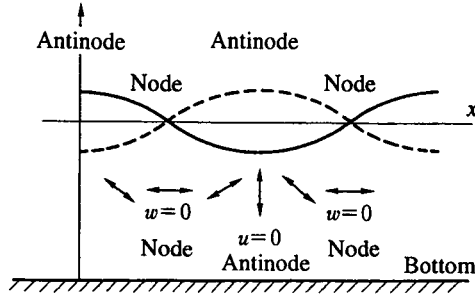
Fig. 1.7 Particle orbit of standing waves

(b) Finite amplitude wave theory

The small amplitude wave theory cannot be applied to waves by increasing of the wave height H. The finite amplitude wave theories of the Stokes-type ($1/25 < h/L < 1/2$) have been developed. Penny and Price (1952) derived the 2nd-order approximate solution, Tadjbakhsh and Keller (1960) developed the 3rd-order solution and Goda and Kakizaki (1968) derived the 4th-order solution by means of the perturbation method. In this section, the theoretical results of the 3rd-order approximate solution derived by Tadjbaksh and Keller (1960) are described:

$$\frac{\Phi}{a(g/k)^{1/2}} = A_1 + A_2 \cos\sigma t \cos kx + A_3 \sin 2\sigma t$$
$$+ A_4 \sin 2\sigma t \cos 2kx + A_5 \cos\sigma t \cos 3kx$$
$$+ A_5 \cos 3\sigma t \cos 3kx + A_6 \cos 3\sigma t \cos 3kx$$

$$\frac{\eta}{a} = \sin \sigma t \cos kx + B_1 \cos 2kx + B_2 \cos 2\sigma t \cos 2kx$$
$$+ B_3 \sin \sigma t \cos kx + B_4 \sin \sigma t \cos 3kx$$
$$+ B_5 \sin 3\sigma t \cos kx + B_6 \sin 3\sigma t \cos 3kx$$

$$\frac{L}{\left(gT^2/2\pi\right)} = \tanh kh \left(1 + C_1\right)^2$$

$$\frac{H}{a} = 1 + D_1$$

$$(1.72)$$

in which all the coefficients, A_1, A_2, A_3, A_4, A_5, A_6, B_1, B_2, B_3, B_4, B_5, B_6, C_1 and D_1 are listed in Table 1.3.

Table 1.3 Coefficients (3rd-order standing wave)

$$A_1 = ak\left(\beta_0 + \frac{1}{8}(w_0 - w_0^{-3})t\right) + \frac{(ak)^2}{2}\beta_2, \quad A_3 = -\frac{ak}{16}(3w_0 + w_0^{-3})$$

$$A_2 = \frac{w_0 \cosh k(h+z)}{\sinh kh}\cos\sigma t\cos kx,$$

$$A_4 = -\frac{3}{16}ak(w_0 - w_0^{-7})\frac{\cosh 2k(h+z)}{\cosh 2kh}, \quad A_5 = \frac{(ak)^2}{2}\cdot\beta_{13}\cdot\cosh 3k(h+z)$$

$$A_6 = \frac{(ak)^2}{2}\beta_{31}\cosh k(h+z), \quad A_7 = \frac{(ak)^2}{2}\beta_{33}\cosh 3k(h+z)$$

$$B_1 = \frac{ka}{8}(w_0^2 + w_0^{-2}), \quad B_2 = \frac{ka}{8}(w_0^{-2} - 3w_0^{-6}), \quad B_3 = \frac{(ka)^2}{2}b_{11}$$

$$B_4 = \frac{(ka)^2}{2}b_{13}, \quad B_5 = \frac{(ka)^2}{2}b_{31}, \quad B_6 = \frac{(ka)^2}{2}b_{33}$$

$$C_1 = \frac{(ak)^2}{64}(9w_0^{-8} - 12w_0^{-4} - 3 - 2w_0^4), \quad D_1 = \frac{(ak)^2}{256}(27w_0^{-12} + 27w_0^{-8} + 96w_0^{-4} - 63 + 11w_0^4 + 6w_0^8)$$

$$b_{11} = \frac{1}{32}(3w_0^{-8} + 6w_0^{-4} - 5 + 2w_0^4), \quad b_{13} = \frac{3}{128}(9w_0^{-8} + 27w_0^{-4} - 15 + w_0^4 + 2w_0^8)$$

$$b_{31} = \frac{1}{128}(3w_0^{-8} + 18w_0^{-4} - 5), \quad b_{33} = \frac{3}{128}(-9w_0^{-12} + 3w_0^{-8} - 3w_0^4 + 1)$$

$$\beta_{13} = \frac{1}{128\cosh 3kh}(1 + 3w_0^4)(3w_0^{-9} - 5w_0^{-1} + 2w_0^3)$$

$$\beta_{31} = \frac{1}{128\cosh 3kh}(9w_0^{-9} + 62w_0^{-5} - 31w_0^{-1})$$

$$\beta_{33} = \frac{1}{128\cosh 3kh}(1 + 3w_0^4)(-9w_0^{-13} + 22w_0^{-9} - 13w_0^{-5})$$

$w_0^2 = \tanh kh$, β_0 and β_2 = undetermined constants

(4) Partial standing wave

It is often seen in nature that when waves encounter obstacles, waves are reflected from the obstacle and some of the wave energy is absorbed by the obstacle and some is transmitted past the obstacle. Let us here assume that the incident wave has a height H_I and that of the reflected wave is smaller H_R. The wave periods of the incident and reflected waves will be the same. The total wave profile η_p seaward of the obstacle is

$$\begin{aligned}\eta_p &= \frac{H_I}{2}\cos(kx - \sigma t) + \frac{H_R}{2}\cos(kx + \sigma t) \\ &= \frac{1}{2}(H_I - H_R)\cos(kx - \sigma t) + H_R\cos\sigma t\cos kx\end{aligned}$$

(1.73)

Since the reflection is imperfect and the progressive wave whose height is $(H_I - H_R)$ exists, there are no true nodes and antinodes in a wave profile, which differs from the standing wave profile (Eq. (1.70)). This is called the partial standing wave. The maximum value $(\eta_p)_{max}$ and the minimum value $(\eta_p)_{min}$ correspond to the quasi-node and quasi-antinode, respectively;

$$\left(\eta_p\right)_{max} = \frac{1}{2}\left(H_I + H_R\right) \quad ; \text{quasi-antinode}$$

$$\left(\eta_p\right)_{min} = \frac{1}{2}\left(H_I - H_R\right) \quad ; \text{quasi-node}$$

(1.74)

The quasi-antinode and quasi-node are formed alternatively at the interval of $(1/4)L$. When the amplitude of the quasi-antinodes and quasi-nodes are measured by wave gages along the wave tank in laboratory experiments, the reflection coefficient K_R of the obstacle is defined as

$$K_R = \frac{H_R}{H_I} = \frac{\left(\eta_p\right)_{max} - \left(\eta_p\right)_{min}}{\left(\eta_p\right)_{max} + \left(\eta_p\right)_{min}}$$

(1.75)

The velocity potential of the partial standing wave is derived readily with use of Eq. (1.73),

$$\Phi = \frac{1}{2}\left(H_I - H_R\right)c\,\frac{\cosh k(h+z)}{\cosh kh}\sin\left(kx - \sigma t\right)$$

$$-H_R c\,\frac{\cosh k(h+z)}{\sinh kh}\sin \sigma t \cos kx$$

(1.76)

in which c is the celerity.

The finite amplitude wave theories of the partial standing wave of the Stokes wave-type have been investigated and discussed. Readers are referred to the references (Carry 1953; Goda and Abe 1964; Iwata and Tomita 1991)

1.2.6 Conservation of mass, momentum and energy flux

In the previous sections, wave motions propagating in uniform media of uniform depth are described. Waves propagating in a shallow water region receive various effects of surrounding environments such as changes in the water depth, river discharge, current and so on. Waves themselves bring about the change in the mean water level and wave-induced current.

In general, the change in water depth of a natural beach and resulting change in wave characteristics are small compared with the wavelength. The time scales of the change in the mean water level and wave-induced current are also far longer than wave period. Therefore, such phenomena as the changes in wave characteristics, mean water level and wave-induced current are usually discussed based on the depth and time averaged equations of conservation of mass, momentum and energy flux.

Longuet-Higgins and Stewart (1960) first derived the conservation of energy flux. The conservation of mass and momentum flux are derived by Whitham (1962) from the

conservation law of flux and by Phillips (1977) from the equation of continuity and Eulerian equation of motion. Mei (1983) also gave the expression for conservation of mass and momentum flux based on the Navier-Stokes equation and equation of continuity.

Here, we derive conservation of mass and momentum flux based on Navier-Stokes equation and the equation of continuity after Mei (1983). In the coordinate system where the x and y axes are taken on the still water surface and z axis upward from the still water, the equation of continuity and Naiver-Stokes equation are expressed as follows:

$$\frac{\partial \rho}{\partial t} + \frac{\partial}{\partial x}(\rho u) + \frac{\partial}{\partial y}(\rho v) + \frac{\partial}{\partial z}(\rho w) = 0 \tag{1.77}$$

$$\left. \begin{aligned} \frac{\partial}{\partial t}(\rho u) + \frac{\partial}{\partial x}(\rho u^2) + \frac{\partial}{\partial y}(\rho uv) + \frac{\partial}{\partial z}(\rho uw) &= -\frac{\partial p}{\partial x} + \mu \nabla^2 u \\[2mm] \frac{\partial}{\partial t}(\rho v) + \frac{\partial}{\partial x}(\rho uv) + \frac{\partial}{\partial y}(\rho v^2) + \frac{\partial}{\partial z}(\rho vw) &= -\frac{\partial p}{\partial y} + \mu \nabla^2 v \\[2mm] \frac{\partial}{\partial t}(\rho w) + \frac{\partial}{\partial x}(\rho uw) + \frac{\partial}{\partial y}(\rho vw) + \frac{\partial}{\partial z}(\rho w^2) &= -\rho g - \frac{\partial p}{\partial z} + \mu \nabla^2 w \end{aligned} \right\} \tag{1.78}$$

where ρ is the density of fluid, p is the pressure, (u, v, w) are the water particle velocities in x, y and z directions, μ is the molecular viscosity and $\nabla^2 = (\partial^2/\partial x^2 + \partial^2/\partial y^2 + \partial^2/\partial z^2)$. The time and depth averaged equation of conservation for mass and momentum flux are obtained by integrating these equations over a full depth and taking the time average. In the integration, the following so-called Leibnitz relation

$$\int_{-h}^{\eta} Df \mathrm{d}z = D\int_{-h}^{\eta} f \mathrm{d}z - f_{\eta}D\eta - f_{-h}Dh \tag{1.79}$$

and the boundary conditions at the free surface (Eqs. (1.23) and (1.25)) and at the bottom (Eq. (1.26)) are used. The expressions D and f in Eq. (1.79) are the linear operator (partial derivatives here) and the arbitrary quantity, respectively.

Here, we assume that (i) effect of viscosity and (ii) the bottom slope (∇h) and the wave steepness (kH) are small.

(1) Conservation of mass flux

To obtain a depth averaged continuity equation, we integrate Eq. (1.77) between a free surface ($z = \eta$) and a bottom ($z = -h$) by using Eq. (1.79) and boundary conditions of Eqs. (1.23), (1.25) and (1.26). Then we obtain the following equation:

$$\frac{\partial}{\partial t}\{\rho(h+\eta)\} + \frac{\partial}{\partial x}\int_{-h}^{\eta} \rho u \mathrm{d}z + \frac{\partial}{\partial y}\int_{-h}^{\eta} \rho v \mathrm{d}z = 0 \tag{1.80}$$

We assume here that the quantities relating to fluid motion f such as water particle velocity, pressure and so on are expressed as a sum of the time averaged component $\bar{f}$, wave component (phase-averaged component for regular waves) f_p and turbulent component f' as

$$f = \bar{f} + f_p + f' \tag{1.81}$$

Further, we define the following depth and time averaged velocity:

$$U = \bar{u} + \frac{1}{h + \overline{\eta}} \overline{\int_{-h}^{\eta} u_p \, dz} \; , \; V = \bar{v} + \frac{1}{h + \overline{\eta}} \overline{\int_{-h}^{\eta} v_p \, dz} \tag{1.82}$$

where u and v are the depth averaged velocity of the mean (wave-induced) current and $\overline{\eta}$ is the mean water level.

Substituting the relation of Eq. (1.81) for u, v and p in Eq. (1.80) and using the definition of U and V given by Eq. (1.82), we have the following conservation equation of mass flux:

$$\frac{\partial}{\partial t}\{\rho(h + \overline{\eta})\} + \frac{\partial}{\partial x}\{\rho U(h + \overline{\eta})\} + \frac{\partial}{\partial y}\{\rho V(h + \overline{\eta})\} = 0 \tag{1.83}$$

(2) Conservation of momentum flux

A vertical integration of the third equation of Eq. (1.78) by using boundary conditions (Eqs. (1.23), (1.25) and (1.26)) and the Leibnitz relation (Eq. (1.79)) gives the following relation:

$$\frac{\partial}{\partial t}(\rho w) + \frac{\partial}{\partial x}\int_{-h}^{\eta}\rho uw \, dz + \frac{\partial}{\partial y}\int_{-h}^{\eta}\rho vw \, dz = -\rho g(h + \eta)$$

$$+ \left[-p + \mu\frac{\partial w}{\partial z} - \mu\left(\frac{\partial w}{\partial x}\frac{\partial \eta}{\partial x} + \frac{\partial w}{\partial y}\frac{\partial \eta}{\partial y}\right)\right]_{\eta}$$

$$- \left[-p + \mu\frac{\partial w}{\partial z} - \mu\left(\frac{\partial w}{\partial x}\frac{\partial h}{\partial x} + \frac{\partial w}{\partial y}\frac{\partial h}{\partial y}\right)\right]_{-h}$$

$$+ \frac{\partial}{\partial x}\int_{-h}^{\eta}\mu\frac{\partial w}{\partial x}dz + \frac{\partial}{\partial y}\int_{-h}^{\eta}\mu\frac{\partial w}{\partial y}dz$$

By substituting the relation of Eq. (1.81) and taking the time average, we have the time averaged pressure at the bottom in the following form:

$$
\overline{P}_{-h} = \underbrace{\rho g\left(h+\overline{\eta}\right)}_{\text{①}} + \underbrace{\frac{\partial}{\partial x}\int_{-h}^{\eta}\overline{\rho\left(u_p w_p + u'w'\right)}\mathrm{d}z + \frac{\partial}{\partial y}\int_{-h}^{\eta}\overline{\rho\left(v_p w_p + v'w'\right)}\mathrm{d}z}_{\text{②}}
$$

$$
+ \left[\underbrace{\mu\overline{\frac{\partial w_p}{\partial z}}}_{\text{③}} - \underbrace{\mu\left(\overline{\frac{\partial w_p}{\partial x}\frac{\partial h}{\partial x} + \frac{\partial w_p}{\partial y}\frac{\partial h}{\partial y}}\right)}_{\text{④}}\right]_{-h} \qquad (1.84)
$$

$$
+ \underbrace{\frac{\partial}{\partial x}\int_{-h}^{\eta}\mu\overline{\frac{\partial\left(w_p+w'\right)}{\partial x}}\mathrm{d}z + \frac{\partial}{\partial y}\int_{-h}^{\eta}\mu\overline{\frac{\partial\left(w_p+w'\right)}{\partial y}}\mathrm{d}z}_{\text{⑤}}
$$

Table 1.4 is the comparison of the order of each term in the right hand side of Eq. (1.84) where a is the amplitude of an incident wave.

Table 1.4 Order of each term consisting the mean pressure at the bottom

①	②	③	④	⑤
$\rho g h$	$\rho k a^2 \sigma^2 h$	$\mu k a \sigma$	$\mu k a \sigma |\nabla h|$	$\mu k^2 a \sigma h$

According to the assumptions (i) and (ii) mentioned above, we can neglect 3rd to 5th terms in the right hand side of Eq. (1.84). The second term also becomes small compared with the first term and Eq. (1.84) is expressed in the following form:

$$
\overline{P}_{-h} = \rho g\left(h+\overline{\eta}\right) \qquad (1.85)
$$

By integrating the 1st and 2nd equations of Eq. (1.78) and using the relation given by Eqs. (1.81), (1.82) and (1.85), the following depth and time averaged conservation equations of the horizontal momentum flux are obtained:

$$
\frac{\partial}{\partial t}\left\{\rho U\left(h+\overline{\eta}\right)\right\} + \frac{\partial}{\partial x}\left\{\rho U^2\left(h+\overline{\eta}\right)\right\} + \frac{\partial}{\partial y}\left\{\rho U V\left(h+\overline{\eta}\right)\right\}
$$

$$
= -\rho g\left(h+\overline{\eta}\right)\frac{\partial\overline{\eta}}{\partial x} + \frac{\partial}{\partial x}\left(-S_{xx}+R_{xx}\right) + \frac{\partial}{\partial y}\left(-S_{xy}+R_{xy}\right) - \overline{\tau}_{bx}
$$

$$
\frac{\partial}{\partial t}\left\{\rho V\left(h+\overline{\eta}\right)\right\} + \frac{\partial}{\partial x}\left\{\rho U V\left(h+\overline{\eta}\right)\right\} + \frac{\partial}{\partial y}\left\{\rho V^2\left(h+\overline{\eta}\right)\right\} \qquad (1.86)
$$

$$
= -\rho g\left(h+\overline{\eta}\right)\frac{\partial\overline{\eta}}{\partial y} + \frac{\partial}{\partial x}\left(-S_{yx}+R_{yx}\right) + \frac{\partial}{\partial y}\left(-S_{yy}+R_{yy}\right) - \overline{\tau}_{by}
$$

where

$$S_{xx} = \overline{\int_{-h}^{\eta} \left(p + \rho u_p{}^2 \right) dz} - \frac{\rho g}{2} \left(h + \overline{\eta} \right)^2 - \frac{1}{\rho \left(h + \overline{\eta} \right)} \left(\overline{\int_{-h}^{\eta} \rho u_p dz} \right)^2$$

$$S_{yy} = \overline{\int_{-h}^{\eta} \left(p + \rho v_p{}^2 \right) dz} - \frac{\rho g}{2} \left(h + \overline{\eta} \right)^2 - \frac{1}{\rho \left(h + \overline{\eta} \right)} \left(\overline{\int_{-h}^{\eta} \rho v_p dz} \right)^2 \qquad (1.87)$$

$$S_{xy} = S_{yx} = \overline{\int_{-h}^{\eta} \rho u_p v_p dz} - \frac{1}{\rho \left(h + \overline{\eta} \right)} \left(\overline{\int_{-h}^{\eta} \rho u_p dz} \right) \left(\overline{\int_{-h}^{\eta} \rho u_p dz} \right)$$

$$R_{xx} = \overline{\int_{-h}^{\eta} \left(\mu \frac{\partial U}{\partial x} - \rho u'^2 \right) dz} \quad , \quad R_{yy} = \overline{\int_{-h}^{\eta} \left(\mu \frac{\partial V}{\partial y} - \rho v'^2 \right) dz}$$

$$R_{xy} = R_{yx} = \overline{\int_{-h}^{\eta} \left(-u' v' \right) dz} \qquad (1.88)$$

S_{xx}, S_{xy}, S_{yx} and S_{yy} given by Eq. (1.87) are the radiation stresses and R_{xx}, R_{xy}, R_{yx} and R_{yy} expressed by Eq. (1.88) are the lateral mixing terms resulting from turbulence. $\overline{\tau}_{bx}$ and $\overline{\tau}_{by}$ are the time averaged bottom shear stresses due to waves and current that will be discussed in detail in Chapter 3.

In the coordinate system shown in Fig. 1.8, the radiation stress is calculated by using a linear wave theory as follows:

$$S_{xx} = \frac{E}{2} \left\{ \frac{2 c_g}{c} \cos^2 \theta + \left(\frac{2 c_g}{c} - 1 \right) \right\}$$

$$S_{yy} = \frac{E}{2} \left\{ \frac{2 c_g}{c} \sin^2 \theta + \left(\frac{2 c_g}{c} - 1 \right) \right\} \qquad (1.89)$$

$$S_{xy} = S_{yx} = E \frac{c_g}{c} \cos \theta \sin \theta$$

where E is the wave energy density (Eq. (1.43)), c_g is the group celerity, c is the wave celerity and θ is the wave direction defined in Fig. 1.8. The expression of the radiation stress based on the finite amplitude wave theory has also been proposed (e.g., Longuet-Higgins 1975).
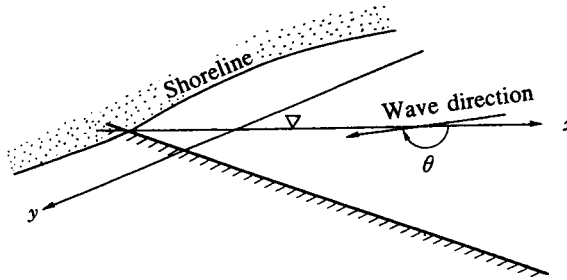
Fig. 1.8 Definition sketch of wave direction

The lateral mixing term is usually expressed by the gradient-diffusion type formula, the details of which will be mentioned in Chapter 3.

(3) Conservation of energy flux
Wave deformation due to changes in water depth in the presence of current is usually discussed by using conservation of wave number and energy flux. A profile of wave propagating in the direction of vector x is expressed by using a phase function $\chi(x,t)$ and an amplitude $a(x,t)$ as follows:

$$\eta(x,t) = a(x,t)\exp\{i\chi(x,t)\} \tag{1.90}$$

An equi-phase line of this wave is given by the equation $\chi(x,t)$ = const. Here, we define a wave number vector $k(= (k_x,k_y))$ and an angular frequency n by the following equations:

$$k = \left(k_x,k_y\right) = \nabla\chi \ , \ n = -\partial\chi/\partial t \tag{1.91}$$

From these equations, the following relations expressing the irrotational property of the wave number (Eq. (1.92)) and the conservation of the wave number (Eq. (1.93)) are obtained:

$$\nabla \times k = 0 \tag{1.92}$$

$$\partial k/\partial t + \nabla n = 0 \tag{1.93}$$

If the media that transmits waves is not uniform, for example, is moving at the speed of $U(x,t)$, the apparent angular frequency n is given by

$$n = \sigma(k) + k \cdot U(x,t) \tag{1.94}$$

where $\sigma(k)$ is the eigen angular frequency that satisfies the dispersion relation Eq. (1.36). In such a case, the conservation of angular frequency becomes

$$\partial k/\partial t + \nabla\{\rho(k) + k \cdot U(x,t)\} = 0 \tag{1.95}$$

In the steady state, Eq. (1.83) is expressed as follows:

$$\nabla\{\rho(k) + k \cdot U(x,t)\} = 0 \quad or \quad n = \sigma(k) + k \cdot U(x,t) = const. \tag{1.96}$$

Longuet-Higgins and Stewart (1960) and Phillips (1977) derived the following equation of conservation of wave energy density $E(= \rho g a^2/2)$.

$$\frac{\partial}{\partial t}\left[E - \frac{1}{2\rho(h+\overline{\eta})}\left\{\left(\overline{\int_{-h}^{\eta}\rho u_p dz}\right)^2 + \left(\overline{\int_{-h}^{\eta}\rho v_p}\right)^2\right\}\right]$$

$$+ \frac{\partial}{\partial x}\left[(\overline{u}+c_{gx})E - \frac{U}{2\rho(h+\overline{\eta})}\left\{\left(\overline{\int_{-h}^{\eta}\rho u_p dz}\right)^2 + \left(\overline{\int_{-h}^{\eta}\rho v_p}\right)^2\right\}\right]$$

$$+ \frac{\partial}{\partial y}\left[(\overline{v}+c_{gy})E - \frac{V}{2\rho(h+\overline{\eta})}\left\{\left(\overline{\int_{-h}^{\eta}\rho u_p dz}\right)^2 + \left(\overline{\int_{-h}^{\eta}\rho v_p}\right)^2\right\}\right] \qquad (1.97)$$

$$+ S_{xx}\frac{\partial \overline{u}}{\partial x} + S_{xy}\frac{\partial \overline{v}}{\partial x} + S_{yx}\frac{\partial \overline{u}}{\partial y} + S_{yy}\frac{\partial \overline{v}}{\partial y} = -D_i - D_b$$

Bretherton (1969) derived the following conservation equation of wave action (E/σ):

$$\frac{\partial}{\partial t}\left(\frac{E}{\sigma}\right) + \nabla\left\{(U+c_g)\left(\frac{E}{\sigma}\right)\right\} = 0 \qquad (1.98)$$

Phillips (1977) showed that both Eq. (1.97) and Eq. (1.98) are perfectly the same.

Wave deformation, wave-induced current and mean water level on a natural beach are calculated by using Eqs. (1.83), (1.84), (1.86) and (1.97) or (1.98), with the help of Eqs. (1.92) and (1.96) by adding a properly selected expression of wave energy loss caused by wave breaking to Eqs. (1.97) or (1.98).

1.2.7 Long waves in shallow water

As waves approach the shore, a wave number k and the relative water depth h/L decrease and the ratio of wave height to water depth H/h increases. The assumption of "small amplitude" does no longer hold for the waves in such a region. Propagating waves cannot maintain their profiles within a certain depth and they break and lose their energy. The conditions of wave breaking will be mentioned in **1.2.10** in detail.

Some waves of long wave periods (low frequency) can propagate into the shallow water region without breaking. Some of them are reflected from the shore to form a standing wave (leaky mode long wave). A certain part of them cannot propagate offshore as reflected waves and are trapped in the shallow water region to form edge waves. Miche (1944) gave the critical condition of wave breaking on the sloping beach in terms of a incident wave steepness in deepwater H_0/L_0 and a bottom slope $\tan\beta$.

$$\left(\frac{H_0}{L_0}\right)_c = \sqrt{\frac{\beta}{90°}}\frac{\sin^2\beta}{\pi} \qquad (1.99)$$

To express wave motion in such a region, two parameters, i.e., a relative water depth $\mu = kh$ and the ratio of wave height to water depth $\varepsilon = H/h$ or Ursell parmeter U_r defined as

$$U_r = (H/h)(1/(kh)^2) \approx HL^2/h^3 \qquad (1.100)$$

become important. According to the order of these parameters, approximate expressions of various degrees have been introduced (Mei 1983). For example, when $O(\mu)<<1$ and $O(\varepsilon)\sim1$, the following equations are used (Airy theory):

$$\frac{\partial \eta}{\partial t} + \frac{\partial (du)}{\partial x} + \frac{\partial (dv)}{\partial y} = 0 \tag{1.101}$$

$$\frac{\partial u}{\partial t} + u\frac{\partial u}{\partial x} + v\frac{\partial u}{\partial y} + g\frac{\partial \eta}{\partial x} = 0$$

$$\frac{\partial v}{\partial t} + u\frac{\partial v}{\partial x} + v\frac{\partial v}{\partial y} + g\frac{\partial \eta}{\partial y} = 0 \tag{1.102}$$

where d is the total depth ($=h+\eta$)

In this case, pressure becomes hydrostatic.

$$p = \rho g(\eta - z) \tag{1.103}$$

When $O(\mu) = O(\varepsilon)<1$, the fluid motion is expressed by a nonlinear dispersive wave theory (Boussinesq equation) in the following form:

$$\frac{\partial u}{\partial t} + u\frac{\partial u}{\partial x} + v\frac{\partial u}{\partial y} = -g\frac{\partial \eta}{\partial x} + \frac{h^2}{3}\left\{\frac{\partial}{\partial x}\left(\frac{\partial^2 u}{\partial x \partial t} + \frac{\partial^2 v}{\partial y \partial t}\right)\right\}$$

$$\frac{\partial v}{\partial t} + u\frac{\partial v}{\partial x} + v\frac{\partial v}{\partial y} = -g\frac{\partial \eta}{\partial y} + \frac{h^2}{3}\left\{\frac{\partial}{\partial y}\left(\frac{\partial^2 u}{\partial x \partial t} + \frac{\partial^2 v}{\partial y \partial t}\right)\right\} \tag{1.104}$$

The pressure is no longer hydrostatic

$$p = \rho g(\eta - z) + \frac{\rho}{2}(2hz + z^2)\left(\frac{\partial^2 u}{\partial x \partial t} + \frac{\partial^2 v}{\partial y \partial t}\right) \tag{1.105}$$

As has already been pointed out, nonlinear convection terms in Eqs. (1.102) and (1.104) steepen wave crests and a dispersion term in Eq. (1.104) (last term of right hand side of Eq. (1.104)) disperse waves into waves of different wavelengths. A so-called permanent wave such as a solitary wave and cnoidal wave whose profile has already shown in Fig. 1.5 can exist under a perfect balance of nonlinear and dispersive properties.

Equations (1.100) and (1.101) are usually solved by a method of characteristics. Carrier and Greenspan (1957) derived a solution of the standing waves formed by the normal incident and reflected very long waves on a sloping beach. Kobayashi et al. (1987) proposed a numerical procedure for solving swash oscillation on a rough sloping bottom.

The original Boussinesq equation is varied in the region of $O(\varepsilon) = O(\mu^2)<1$ or $U_r \approx 1$. Some modifications have been proposed to expand the applicability region of the Boussinesq equation toward a deeper region (Madsen et al. 1991). Recently, many

researchers utilize the Boussinesq equation to numerically predict regular and irregular wave transformations and wave-induced currents in shallow water regions.

On the other hand, when $O(\varepsilon) \ll 1$ and $O(\mu^2) \ll 1$, both nonlinear and dispersive terms become negligibly small and equations of continuity and motion are the following forms:

$$\frac{\partial \eta}{\partial t} + \frac{\partial(hu)}{\partial x} + \frac{\partial(hv)}{\partial y} = 0 \tag{1.106}$$

$$\frac{\partial u}{\partial t} = -g\frac{\partial \eta}{\partial x}, \ \frac{\partial v}{\partial t} = -g\frac{\partial \eta}{\partial y} \tag{1.107}$$

The pressure is again hydrostatic.

Classical theories of standing waves (leaky mode) and edge waves (trapped mode) on a sloping beach whose slope is $\tan\beta$ are derived based on Eqs. (1.106) and (1.107) assuming cross-shore and longshore wave profiles. Equations (1.108)-(1.112) are their surface profiles, water particle velocity and a dispersion relation if it exists.
Standing waves:

$$\eta(x, t) = aJ_0\left(2\sigma_s\sqrt{x/g\tan\beta}\right)\cos\sigma_s t \tag{1.108}$$

$$u(x, t) = a\sqrt{g/h}\, J_1\left(2\sigma_s\sqrt{x/g\tan\beta}\right)\sin\sigma_s t, \ v(x, t) = 0 \tag{1.109}$$

where σ_s is the angular frequency of standing waves, J_0 and J_1 are the Bessel functions of the 0th and 1st order.
Edge waves:

$$\eta(x, y, t) = a_n L_n\left(2k_{en}x\right)\exp\left(-k_{en}x\right)\cos\left(k_{en}y - \sigma_{en}t\right) \tag{1.110}$$

$$u(x, y, t) = \left(a_n g/\sigma_{en}\right)k_{en}\exp\left(-k_{en}x\right)\left\{2L_n'\left(2k_{en}x\right) - L_n\left(2k_{en}x\right)\right\}\sin\left(k_{en}y - \sigma_{en}t\right)$$
$$v(x, y, t) = \left(a_n g/\sigma_{en}\right)k_{en}\exp\left(-k_{en}x\right)L_n\left(2k_{en}x\right)\cos\left(k_{en}y - \sigma_{en}t\right) \tag{1.111}$$

$$\sigma_{en}^2 = gk_{en}(2n+1)\tan\beta \tag{1.112}$$

where a_{en} and k_{en} are the angular frequency and wave number of edge waves when the cross-shore modal number is n (= 0,1,2..) and L_n, L_n' are the Laguerre polynomial and its derivatives with respect to x.

If there is an obstacle in the direction of propagation of the edge waves that reflects them toward the opposite direction, propagated and reflected edge waves from standing edge waves with nodes and antinodes evenly distributed in the longshore direction. The surface profile and water particle velocity of standing edge waves are expressed as follows:

$$\eta(x,y,t) = a_n L_n(2k_{en}x)\exp(-k_{en}x)\cos k_{en}y \cos \sigma_{en}t \qquad (1.113)$$

$$u(x,y,t) = (a_n g/\sigma_{en})k_{en}\exp(-k_{en}x)\{2L_n(2k_{en}x) - L_n(2k_{en}x)\}\sin k_{en}y \sin \sigma_{en}t$$

$$v(x,y,t) = (a_n g/\sigma_{en})k_{en}\exp(-k_{en}x) L_n(2k_{en}x)\cos k_{en}y \cos \sigma_{en}t$$

$$(1.114)$$

1.2.8 Fundamental formulation for wave transformation

Many commentaries and explanations have so far been given. In this section, a derivation and a key to the solution of a mild slope equation that comprehensively describes wave transformation within the limit of linear wave theory are explained. Wave refraction, diffraction and shoaling are also discussed based on the mild slope equation.

(1) Conservation of energy

Conservation of energy of incompressible fluid in an arbitrary domain D is expressed as

$$\iint_\Gamma V_n E' d\Gamma + \frac{d}{dt}\iiint_D E dD = 0 \qquad (1.115)$$

where Γ is the surface of D, V_n is the outward relative velocity of Γ, E is the energy density, E' is the sum of E and p/ρ. We assume that the domain D is a vertical column between the free surface ($z = \eta$) and the bottom ($z = -h$) and that a velocity potential exists. Then Eq. (1.115) can be written by using the divergence theorem of Gauss, the Leibnitz theorem and the Euler equation of motion as follows:

$$\iint dx dy \int_{-h}^{\eta} -\frac{\partial \Phi}{\partial t}\left(\nabla^2 \Phi + \frac{\partial^2 \Phi}{\partial z^2}\right) dz = 0 \qquad (1.116)$$

where $\nabla = (\partial/\partial x, \partial/\partial y)$.

The domain of the integration of the x-y plane in Eq. (1.116) is arbitrary. Therefore the integrand in Eq. (1.116) is always zero. We further define the velocity potential of the form of $\Phi = \tilde{\Phi}(x,y,t)f(z,h)$, $h = h(x,y)$. Then we obtain the following expression of Φ through the boundary conditions Eqs. (1.25) and (1.26):

$$\nabla \cdot \int_{-h}^{\eta} f^2 \nabla \tilde{\Phi} dz - \tilde{\Phi}\int_{-h}^{\eta}\left(\frac{\partial f}{\partial z}\right)^2 dz + f\frac{\partial \eta}{\partial t}\bigg|_{z=\eta} + \tilde{\Phi}\nabla \cdot \int_{-h}^{\eta} f \nabla f dz - \tilde{\Phi}\int_{-h}^{\eta}(\nabla f)^2 dz = 0$$

$$(1.117)$$

Equation (1.117) strictly expresses the energy conservation under the assumption of $\Phi = f\tilde{\Phi}$.

(2) Reduction of mild slope equation

Variables are normalized in the following way:

$$\left(x^*, y^*, z^*\right) = \left(k_0 x,\ k_0 y,\ k_0 z\right),\quad t^* = \sigma t,\quad h^* = k_0 h$$

$$g^* = k_0 g / \sigma^2,\quad \tilde{\Phi}^* = \sigma \tilde{\Phi} / a_0 g$$

$$c^* = c/c_0,\quad \mu^* = k/k_0,\quad \nabla^* = \nabla/k_0,\quad \eta^* = \eta/a_0$$

where the variables with "*" are nondimensional variables, $\sigma^2 = gk\tanh kh$, $c_0 = \sigma/k$, a is the wave amplitude, σ is the angular frequency, k is the wave number and subscript "$_0$" refers to the quantities in deepwater.

Let the small parameter of deepwater be ε ($= k_0 a_0 \ll 1$), then the integral domain becomes $(-h^*, \varepsilon \eta^*)$. To integrate Eq. (1.117), we divide the integral domain into $(-h^*, 0)$ and $(0, \varepsilon \eta^*)$ and expand the later region to the Taylor expansion with respect to $z^* = 0$. The integration gives the following relation at the order of ε^0 through the assumption of $f = \cosh\mu^*(h^* + z^*)/\cosh\mu^* h^*$:

$$\nabla^* \cdot \left(c^* c_g^* \nabla^* \tilde{\Phi}^*\right) - (1-n)\tilde{\Phi}^* + \frac{\partial \eta^*}{\partial t^*} + \frac{1}{2}\tilde{\Phi}^* \nabla^* \left(c^{*2} \nabla^* n\right) - \frac{\tilde{\Phi}^*}{2c^{*2}}\left(\nabla^* c^{*2}\right)^2 \Xi = 0$$

$$\Xi = \frac{\left(6n - 1 - 3n^2\right)h^*}{4n - 2} - \frac{nh^{*2}}{2} + \frac{(2n-1)\left(\mu^* h^*\right)^2}{6} + \frac{1-n}{4} \tag{1.118}$$

$$n = \frac{1}{2}\left(1 + \frac{2\mu^* h^*}{\sinh\left(2\mu^* h^*\right)}\right),\qquad c_g^* = nc^*$$

Using the same normalization and the Taylor expansion, the kinematic boundary condition at the free surface also becomes

$$\frac{\partial \tilde{\Phi}^*}{\partial t} + \eta^* = 0 \tag{1.119}$$

The orders of 4th and 5th terms in Eq. (1.118) are $(\nabla^* h^* / \mu^* h^*)^2$ in shallow water and $(\nabla^* h^*)^2$ in very shallow water. These two terms are smaller than other terms whose orders are the unity. By neglecting these terms of small magnitude and eliminating η^* from Eqs. (1.118) and (1.119), the following unsteady mild slope equation is obtained:

$$\nabla \cdot \left(cc_g \nabla \tilde{\Phi}\right) - \sigma^2 (1-n)\tilde{\Phi} - \frac{\partial^2 \Phi}{\partial t^2} = 0 \tag{1.120}$$

When we further assume the periodic variation in time, e.g., $\tilde{\Phi}(x, y, t) = \tilde{\phi}(x, y)\exp(-i\sigma t)$, we finally obtain the following steady mild slope equation:

$$\nabla \cdot \left(cc_g \nabla \tilde{\phi}\right) + \sigma^2 \frac{c_g}{c}\tilde{\phi} = 0 \tag{1.121}$$

In the case of a constant water depth, Eq. (1.121) becomes a well-known Helmholtz equation:

$$\nabla^2 \tilde{\phi} + k^2 \tilde{\phi} = 0 \tag{1.122}$$

This equation contains a 2nd derivative with respect to space and is classified as an elliptic type equation. Under the requisite boundary conditions, the solution to Eqs. (1.121) or (1.122) is uniquely given in the objective domain.

(3) Methods for solving the mild slope equation

As mentioned before, both Eqs. (1.121) and (1.122) are elliptic type second-order partial differential equations. In order to solve these equations, therefore, appropriate boundary conditions must be given on all the boundaries of a domain of interest. The finite difference method (FDM) and the finite element method (FEM) are representative numerical methods to solve this kind of equation (e.g., Mei 1978; Yeung 1982). Although the FDM (e.g., Panchang et al. 1988) is a convenient and useful method, it is not suitable for the calculation of a wave field in the domain with a complicated configuration that requires a small mesh size to express the coastline. Moreover, it is sometimes difficult to compose an appropriate formula for a boundary condition that involves derivatives of unknown functions by using values at discrete points. On the other hand, the applicability of the FEM (e.g., Houston 1981) to the complex region is usually better than the FDM because we can arbitrarily take the size of each element. Furthermore, we do not have to pay any special attention to the boundary conditions.

In both the FDM and the FEM, the whole region of interest is divided into small segments and a large set of first-order algebraic equations is solved numerically where solutions are obtained at the discrete points such as grid points or nodes. Thus, although these methods usually give a fairly good approximate solution of the mild slope equation, they require a lot of memory on a computer and a lot of computing time when calculating a wave field in a large region. Therefore, they are not suitable for practical use except for when the water depth is locally changed.

Another useful method that transforms Eq. (1.121) into a set of first-order differential equations is proposed by Nishimura (1983). Equation (1.121) can be rewritten as

$$\nabla \cdot \left(cc_g \nabla \tilde{\Phi} \right) - \frac{c_g}{c} \frac{\partial^2 \tilde{\Phi}}{\partial t^2} = 0 \tag{1.123}$$

by using the relation $-\sigma^2 \tilde{\phi} e^{-i\sigma t} = \partial^2 \tilde{\Phi}/\partial t^2$. Applying the linearized dynamic free surface condition to Eq. (1.123), we get the following equations equivalent to Eq. (1.123):

$$\nabla \cdot \left(cc_g \nabla \tilde{\Phi} \right) + g \frac{c_g}{c} \frac{\partial \eta}{\partial t} = 0 \tag{1.124}$$

$$\frac{\partial \tilde{\Phi}}{\partial t} + g\eta = 0 \tag{1.125}$$

Furthermore, these equations can be expressed in terms of water particle velocities on a free surface in horizontal and vertical directions, u and v, and the surface displacement η:

$$\frac{\partial}{\partial x}\left(cc_g u\right)+\frac{\partial}{\partial y}\left(cc_g v\right)+g\frac{c_g}{c}\frac{\partial \eta}{\partial t}=0 \tag{1.126}$$

$$\frac{\partial u}{\partial t}+g\frac{\partial \eta}{\partial x}=0 \tag{1.127}$$

$$\frac{\partial v}{\partial t}+g\frac{\partial \eta}{\partial y}=0 \tag{1.128}$$

where, in order to derive Eqs. (1.127) and (1.128), we took the gradient of Eq. (1.125). Equation (1.126) is an energy conservation equation and Eqs. (1.127) and (1.128) correspond to the linearized equations of motion on a free surface. By using staggered mesh discretization in the FDM, the set of equations can be solved more easily than by solving Eq. (1.121) directly by using the FDM or FEM. In this method, calculations are carried out in the time domain and must be continued until a steady periodic solution is obtained. Transient wave motions have no meaning and it is sometimes difficult to decide whether the motions are steady or not.

(4) Approximation of the mild slope equation

In this section, we show some approximate mild slope equations which are easier to solve numerically.

(a) The WKB approximation (Elmore and Heald 1969)

Since the velocity potential $\tilde{\phi}$ in Eq. (1.121) is a complex number, it can be expressed as

$$\tilde{\phi}(x, y) = A(x, y)e^{iS(x, y)} \tag{1.129}$$

where $A(x,y)$ and $S(x,y)$ are real functions that represent the amplitude and the phase of the velocity potential, respectively. The water surface displacement η is expressed as $\eta=i\sigma A/ge^{iS}$. Substituting Eq. (1.129) into Eq. (1.121), the following two equations are derived from real and imaginary parts, respectively:

$$(\nabla S)^2 = k^2 + \frac{\nabla \cdot \left(cc_g \nabla A\right)}{cc_g A} \tag{1.130}$$

$$\nabla\left(A^2 cc_g \nabla S\right)=0 \tag{1.131}$$

Here, we assume that the gradients of A and cc_g are both small. We call this approximation the WKB approximation since the assumption that the inhomogeneity is gradual for the equation of wave propagation in inhomogeneous media is called the WKB approximation. By employing this approximation we can eliminate the last term of Eq. (1.130). Thus Eqs. (1.130) and (1.131) are reduced to

$$(\nabla S)^2 = k^2 \tag{1.132}$$

$$\nabla\left(A^2 c_g \frac{\nabla S}{|\nabla S|}\right) = 0 \tag{1.133}$$

Equation (1.132), which is called the eikonal equation in optics, means that the phase function S is determined by only the wave number k that is a function of water depth. Equation (1.133) shows that the divergence of the energy flux propagating in the direction of ∇S is zero, i.e., that the wave energy is conserved in the direction of the propagation. Now we take a curvilinear coordinate s as shown in Fig. 1.9 in the direction of the wave propagation that is same as the direction of vector ∇S.
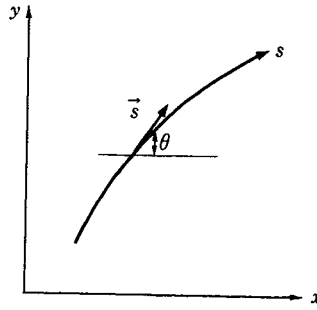
Fig. 1.9 Wave ray

From Eq. (1.132), ∇S is expressed as

$$\nabla S = k\vec{s} \tag{1.134}$$

where $\vec{s}$ is a unit vector tangent to the coordinate s and given as $\vec{s} =(\cos\theta, \sin\theta)$. Defining the wave number vector $\vec{k}$ as $\vec{k} = (k\cos\theta, k\sin\theta)$, Eq. (1.134) becomes

$$\nabla S = \vec{k} \tag{1.135}$$

This equation indicates that the wave number vector $\vec{k}$ is irrotational and therefore we obtain

$$\nabla \times \vec{k} = \frac{\partial}{\partial x}(k \sin \theta) - \frac{\partial}{\partial y}(k \cos \theta) = 0 \tag{1.136}$$

Furthermore, substituting Eq. (1.134) into Eq. (1.133), we get the energy conservation equation:

$$\frac{\partial}{\partial x}\left(A^2 c_g \cos \theta \right) + \frac{\partial}{\partial y}\left(A^2 c_g \sin \theta \right) = 0 \tag{1.137}$$

By using the FDM, we can calculate θ and A^2 at discrete grid points. Details of this method can be referred to in **3.5**.

Next, let us consider the change of $k\vec{s}$ in the direction of the wave propagation

$$\frac{dk\vec{s}}{ds} = \frac{d}{ds}(\nabla S) = \vec{s}\,\nabla(\nabla S) = \frac{\nabla S}{k}\nabla(\nabla S) = \frac{1}{2k}\nabla(\nabla S)^2 = \frac{1}{2k}\nabla k^2$$
$$= \nabla k \tag{1.138}$$

This equation indicates that if we know the value of $k\vec{s}\,(=\nabla S)$ at a certain point in the wave field, we can trace the wave propagation, the so-called wave ray, from the point as indicated in Fig. 1.10. Furthermore, since Eq. (1.133) can be written as

$$\nabla \cdot \left(A^2 c_g \frac{\nabla S}{|\nabla S|} \right) = \nabla \cdot \left(A^2 c_g \vec{s} \right) = \nabla A^2 \cdot c_g \vec{s} + A^2 \nabla \cdot \left(c_g \vec{s} \right)$$
$$= c_g \frac{dA^2}{ds} + A^2 \left(\frac{dc_g}{ds} + c_g \nabla \cdot \vec{s} \right) = 0 \tag{1.139}$$

we have

$$\frac{1}{A^2}\frac{dA^2}{ds} = -\frac{1}{c_g}\frac{dc_g}{ds} - \left(-\sin\theta\frac{\partial\theta}{\partial x} + \cos\theta\frac{\partial\theta}{\partial x} \right) \tag{1.140}$$
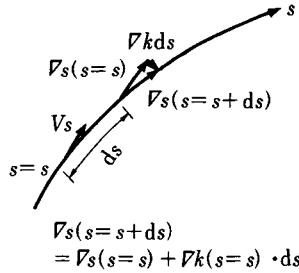
Fig. 1.10 Ray tracing

If we know a wave ray, we can compute the value of the right hand side of Eq. (1.140) and then the change of wave energy along the wave ray. If we omit the last two terms of Eq. (1.140), we get the relation, $A^2 c_g = \text{const.}$, which means that the first term of the right hand side represents the shoaling effect. On the other hand, the last two terms depend on the geometric pattern of wave rays and therefore represent the effect of refraction. Thus, by considering the energy change along the wave ray, we can split the effects of shoaling and refraction. The wave ray method is a method to calculate only the refraction effect along the wave ray taking advantage of this property. The last two terms of Eq. (1.140) are expressed by using the distance between adjacent rays, i.e., the separation distance b, as shown in Fig. 1.11:

$$-\sin\theta\frac{\partial\theta}{\partial x}+\cos\theta\frac{\partial\theta}{\partial y}=\frac{d\theta}{dn}=\frac{1}{b}\frac{db}{ds} \qquad (1.141)$$
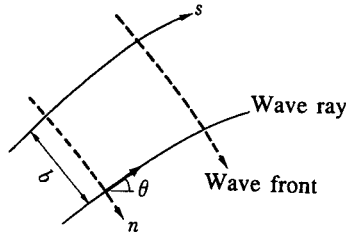
Fig. 1.11 Wave front and separation distance

Substituting this equation into Eq. (1.140) and integrating it, we have

$$A^2 c_g b = \text{const.} = A_0^2 c_{g0} b_0 \qquad (1.142)$$

where the subscript o denotes the values in deepwater. From Eq. (1.139), A is represented as

$$A = \sqrt{c_{g0}/c_g}\,\sqrt{b_0/b}\,A_0 = K_s K_r A_0 \qquad (1.143)$$

where $K_s = \sqrt{c_{g0}/c_g}$ and $K_r = \sqrt{b_0/b}$ are called the shoaling coefficient and refraction coefficient, respectively. Both of them represent the effects of the change of water depth. In particular, when the contours of water depth are all parallel to the x-axis, the wave properties do not change in the x-direction. Therefore, we get

$$k\cos\theta = \text{const.} = k_0\cos\theta_0 \qquad (1.144)$$

from Eq. (1.136) or (1.138), by which the angle of wave propagation θ can be readily calculated at any point. Furthermore, the refraction coefficient is given as

$$K_r = \sqrt{\sin\theta_0/\sin\theta} \qquad (1.145)$$

through Eq. (1.137) or (1.140).

(b) Parabolic approximation (Radder 1979)
   In the WKB approximation, we assume that the gradients of A and cc_g are both small. Now let us apply this approximation only in the x-direction. Equation (1.130) would be reduced to

$$\left(\frac{\partial S}{\partial x}\right)^2 + \left(\frac{\partial S}{\partial y}\right)^2 = k^2 + \frac{1}{cc_g A}\frac{\partial}{\partial y}\left(cc_g\frac{\partial A}{\partial y}\right) \qquad (1.146)$$

Moreover, assuming that the direction of wave propagation is nearly parallel to the x-axis, we can write

$$\frac{\partial S}{\partial x} = k + \varepsilon \qquad (1.147)$$

where ε represents a small value. By using this expression, $(\partial S/\partial x)^2$ is written as

$$\left(\frac{\partial S}{\partial x}\right)^2 = k^2 + 2k\varepsilon + \varepsilon^2 = k^2 + 2k\left(\frac{\partial S}{\partial x} - k\right) + \varepsilon^2 = 2k\frac{\partial S}{\partial x} - k^2 + \varepsilon^2 \qquad (1.148)$$

Neglecting the last term and substituting it into Eq. (1.146), we have

$$\left(\frac{\partial S}{\partial x}\right)^2 + 2k\frac{\partial S}{\partial x} = 2k^2 + \frac{1}{cc_g A}\frac{\partial}{\partial y}\left(cc_g\frac{\partial A}{\partial y}\right) \qquad (1.149)$$

The function $\tilde{\phi} = Ae^{iS}$, in which A and S satisfy Eq. (1.149) and (1.131) respectively, satisfies the following equation (Berkhoff et al. 1982):

$$\frac{\partial\tilde{\phi}}{\partial x} = \left[ik - \frac{1}{2kcc_g}\frac{\partial}{\partial x}\left(kcc_g\right)\right]\tilde{\phi} + \frac{i}{2kcc_g}\frac{\partial}{\partial y}\left(cc_g\frac{\partial\tilde{\phi}}{\partial y}\right) \qquad (1.150)$$

This is a parabolic type second-order partial differential equation and can be solved by the FDM as an initial value problem.

(c) Applicability of approximate equations

The equations obtained by the WKB or parabolic approximation are suitable for the calculation of a wave field in a large region compared with solving the mild slope equation directly by using the FDM or the FEM because the WKB or parabolic approximation equations need much less memory and time for computing. However, if the assumptions used to derive these equations are not valid, the equations give us wrong results. In the WKB approximation, when the last term of Eq. (1.130) cannot be eliminated, i.e., when the effects of diffraction and reflection are as large as those of shoaling and refraction, the equations derived by the WKB approximation are no longer useful. The typical example appears in the prediction of a wave field around a submerged semi-spherical mound, where the wave rays cross each other behind the mound. In the parabolic approximation, the diffraction effect resulting from a variation of wave amplitude in the y-direction which is nearly perpendicular to the direction of wave propagation is taken into account as indicated in Eq. (1.146). However, when a variation of wave amplitude in the x-direction becomes large, for example, when the reflection cannot be neglected, or when the angle between the

x-axis and the direction of wave propagation becomes large because of refraction, the equations derived by parabolic approximation collapse and sometimes give us less accurate results than those computed by the WKB approximation. In order to counteract this weakness, some modified methods have been proposed. For example, transforming Eq. (1.150) onto a curvilinear coordinate system that consists of wave rays and wave fronts is one of the useful methods (Tsay and Liu 1982).

1.2.9 Calculation method for nonlinear water waves

A water wave problem has a free surface boundary that moves with the water particle velocity. This velocity is one of the unknown variables. Therefore, the position of the free surface boundary is also an unknown variable before computation. The computation method for the two dimensional water wave used in this section is separated into two mathematical parts; boundary value problem and evolution problem. In this section, the fluid is assumed to be a perfect fluid and the flow to be irrotational. Thus, the velocity potential $\Phi = \Phi(x,z,t)$ exists and satisfies the Laplace equation.

$$\nabla^2 \Phi = 0 \tag{1.151}$$

Taking the partial derivation of the above equation with respect to time, another Laplace equation is given,

$$\nabla^2 \Phi_t = 0 \tag{1.152}$$

where subscript t indicates the derivation with respect to time. Equation (1.151) is the equation of the mass conservation and Eq. (1.152), the alternative to the Bernoulli equation. There are three types of boundaries; the free surface, bottom and the moving boundary. The moving boundary implies the incident boundary or the wave generator set at one end of the wave tank.

The boundary conditions at the bottom and the moving boundary are expressed as follows.

$$\frac{\partial \Phi}{\partial n} = q(t) \tag{1.153}$$

$$\frac{\partial \Phi_t}{\partial n} = q_t(t) \tag{1.154}$$

where n indicates the normal direction out of the fluid domain, and $q(t)$ and $q_t(t)$ are zeros at the bottom and are given functions at the moving boundary.

On the free surface, there are three unknown variables; the velocity potential, the partial derivatives of the velocity potential with respect to time q_t and the coordinates of free surface. These unknowns are given by the solutions of the evolution problem.

Observing the water particles on the free surface from the Lagrangian point of view, the kinematic free surface boundary condition gives the following equations.

$$\frac{dX}{dt} = \frac{\partial \Phi}{\partial x} \tag{1.155}$$

$$\frac{dY}{dt} = \frac{\partial \Phi}{\partial y} \tag{1.156}$$

where (X,Y) is the coordinate of a water particle on the free surface. On the other hand, the dynamic free surface condition gives

$$\Phi_t = -\frac{1}{2}(\nabla \Phi)^2 - gZ \tag{1.157}$$

The total derivative calculated by using Eq. (1.157) as follows:

$$\frac{\partial \Phi}{\partial t} = \frac{1}{2}(\nabla \Phi)^2 - gZ \tag{1.158}$$

where d/dt denotes the operator of the total derivative, which is rewritten in Eulerian form as:

$$\frac{d}{dt} = \frac{\partial}{\partial t} + u\frac{\partial}{\partial x} + w\frac{\partial}{\partial z} \tag{1.159}$$

Derivating the Eqs. (1.155), (1.156) and (1.158), the following equations are given:

$$\left.\begin{array}{l} \dfrac{d^2 X}{dt^2} = \Phi_{xt} + \Phi_x \Phi_{xx} + \Phi_z \Phi_{xz} \\[2mm] \dfrac{d^2 Z}{dt^2} = \Phi_{zt} + \Phi_x \Phi_{xz} + \Phi_z \Phi_{zz} \\[2mm] \dfrac{d^2 \Phi}{dt^2} = \Phi_x \dfrac{d^2 X}{dt^2} + \Phi_z \dfrac{d^2 Z}{dt^2} - g\Phi_z \end{array}\right\} \tag{1.160}$$

The Laplace equations, Eqs. (1.151) and (1.152), are solved by means of the boundary element method (BEM). The unknown variables are assumed to change linearly in the element. In the BEM, the normal derivatives of functions $\partial \Phi/\partial n$ and $\partial \Phi_t/\partial n$ are unknowns on the free surface, and the Φ and Φ_t are unknowns on both the bottom and the moving boundary. Therefore, the systems of linear equations corresponding to Eqs. (1.151) and (1.152) have the same coefficient matrices. We tested the accuracy and stability of this scheme by comparing numerically with the third-order Taylor expansion. This scheme showed good results.

On the first step of the computation, the second-order Taylor expansion is applied. In the calculation, the following condition (Longuet-Higgins and Cokelet 1976) is required.

$$\left(X^j - X^{j-1}\right)^2 + \left(Z^j - Z^{j-1}\right)^2 \geq \left(\left(\Phi_x^j\right)^2 + \left(\Phi_z^j\right)^2\right)\Delta t. \tag{1.161}$$

When the above condition breaks, e.g., near the wave breaking point, the time step is changed to a shorter one, so that Eq. (1.161) is satisfied. The computation starts from rest and the velocity potential is assumed to be zero at the initial condition on the free surface. This initial condition is physically existent. Therefore, the computation results are able to exist physically. In the calculation of Eqs. (1.155)-(1.160), the partial derivations of Φ with respect to x and z are obtained from the Φ and Φ_n solution of BEM.

Figure 1.12 shows the sequential change of the calculated wave profiles near the wave breaking point. The solid line indicates the computational results with 1/80 second time steps each. The computational results show the development of the plunging breaker. Figure 1.13 shows the velocity field.

$H_0/L_0 = 0.0186$ $H_b/H_0 = 1.488$ $\tan \beta = 1/10$
$h_b/L_0 = 0.0230$ $\xi = 0.600$

Distance from wave maker (m)

(time $t = 6.2$ sec $\sim t = 6.89$ sec)
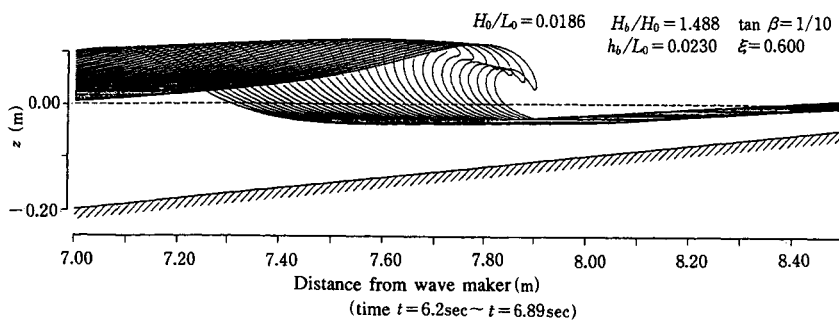
Fig. 1.12   Change in surface profile

$H_0/L_0 = 0.0201$
$H_b/H_0 = 1.423$ $\tan \beta = 1/15$
$h_b/L_0 = 0.0215$ $\xi = 0.393$

$\overrightarrow{1.0}$ m/sec

Distance from wave maker (m)
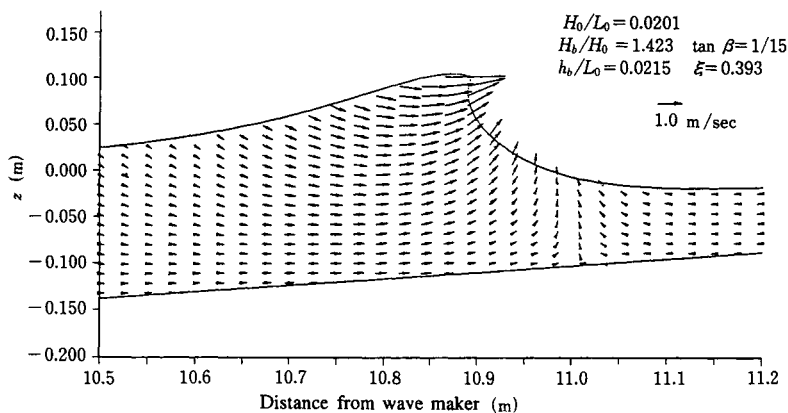
Fig. 1.13   Velocity field of nearly breaking zone

1.2.10 Wave breaking
(1) Breaking condition and limit

It is well known that waves break when they reach a critical state. Wave breaking is an extreme limit of the wave motion, which is under the strong and sensitive influence of the bottom configuration, disturbance of water surface, shapes of structures, etc.

So far, many mathematical models have been proposed to define wave breaking, some of which are, however, short of physical background.

(a) Progressive wave

Breaking conditions proposed for progressive waves are as follows. That is, the wave breaks (i) when the particle velocity at the wave crest becomes faster than the wave celerity, (ii) when waves peak up and the cusped crest has the angle of 120°, (iii) when the wave profile loses a symmetrical shape and the wave front becomes vertical, etc. The reliable and higher-order breaking limits proposed for progressive waves are

$$(H_0/L_0)_b = 0.142 : \text{deepwater waves (Michell 1893)} \tag{1.162}$$

$$(H/L)_b = 0.142 \tanh 2\pi h_b/L_b : \text{shallow water waves (Miche 1944)} \tag{1.163}$$

$$(H/h)_b = 0.83 : \text{solitary wave (Yamada 1957)} \tag{1.164}$$

in which, subsuffix b indicates the wave breaking limit. On the other hand, no reliable formula has been proposed for progressive waves on gentle slopes. In Japan, the empirical formula proposed by Goda (1985):

$$\left(H_b/L_0\right) = 0.17\left(1 - \exp\left(-1.5\pi\left(h_b/L_0\right)\left(1 + 15(\tan \beta)^{4/3}\right)\right)\right) \tag{1.165}$$

is popular. Here, $\tan\beta$ is the bottom slope.

(b) Standing wave

The breaking limit of the standing wave is derived under the condition that the vertical acceleration of a water particle at the loop becomes larger than the gravitational acceleration. The higher order and reliable breaking limits of a standing wave in a constant water depth are as follows:

$$(H_0/L_0)_b = 0.214 : \text{deepwater wave (Penny and Price 1952)} \tag{1.166}$$

$$(H/L)_b = 0.218 \tanh k_b h_b : \text{shallow water wave (Wiegel 1964)} \tag{1.167}$$

$$(H/L)_b = \frac{1}{\pi}\left(\frac{\coth^2 k_b h_b + 0.35\,\text{cosech}^2 k_b h_b - \coth k_b h_b}{0.296\,\text{cosech}^2 k_b h_b}\right)$$
$$\text{: shallow water wave (Kishi(1959))} \tag{1.168}$$

Some investigations of the breaking limit of a standing wave on a gentle slope have been conducted. However, a reliable breaking limit has not yet been proposed. This requires further investigation.

(c) Partial standing wave

Few investigations on the breaking limit of a partial standing wave has been conducted. The physical mechanism of wave breaking of the partial standing wave has not been clarified. The following empirical breaking limit has been proposed (Iwata and Kiyono 1985).

$$(H/L)_b = \left(0.218 - 0.076 \left(\frac{1 - K_R}{1 + K_R} \right) \tanh k_b h_b \right) \quad : \quad \text{shallow water wave} \quad (1.169)$$

in which, K_R is the reflection coefficient from the obstacle. Eq. (1.169) equals Eq. (1.163) in the case of no reflection ($K_R = 0$) and Eq. (1.169) is equal to Eq. (1.167) in the case of perfect reflection ($K_R = 1$).

(2) Breaker type

Breaker types are classified into four types:

(i) Spilling breaker: The limiting wave shape is not so unsymmetrical as in the case of the plunging breaker. The spilling breaker is characterized by the appearance of " white water" at the crest. The wave generally breaks gradually and turbulent water spills down front face of the wave.

(ii) Plunging breaker: This shows a very unsymmetrical profile with a steeper front face compared to the back surface. The crest curls over a large air-pocket. Air-entrained horizontal roller or vortex and splash usually follow.

(iii) Surging breaker: The wave peaks up as if to break in the manner of the plunging breaker, but when the base of the wave surges up the beach face with the resultant disappearance of the collapsing wave crest.

(iv) Collapsing breaker: This type of breaker is defined by Galvin (1968). The collapsing breaker occurs over the lower half of the wave. Minimal air-pockets and usually no splash-up follow. Bubbles and foam are formed.

The spilling, plunging and surging breakers can be classified in terms of the wave steepness in deepwater H_0/L_0 and the bottom slope $\tan\beta$ as shown in Fig. 1.14. Battjes (1978) has shown that the surf similarity parameter ξ_b defined with

$$\xi_b = \frac{\tan \beta}{\sqrt{H_b/L_0}} = \frac{1}{\sqrt{2\pi}} \frac{\tan \beta}{\sqrt{H_b/gT^2}} \quad (1.170)$$

can successfully classify the breaker type as follows:

$$\begin{array}{lll}
\text{spilling breaker :} & 0.4 > \xi_b \\
\text{plunging breaker :} & 0.4 < \xi_b < 2.0 & \quad (1.171) \\
\text{surging breaker :} & 2.0 < \xi_b
\end{array}$$

In Fig. 1.14, experimental results of breaker classification by Iverse (1952), and Patric and Wiegel (1955) are shown.
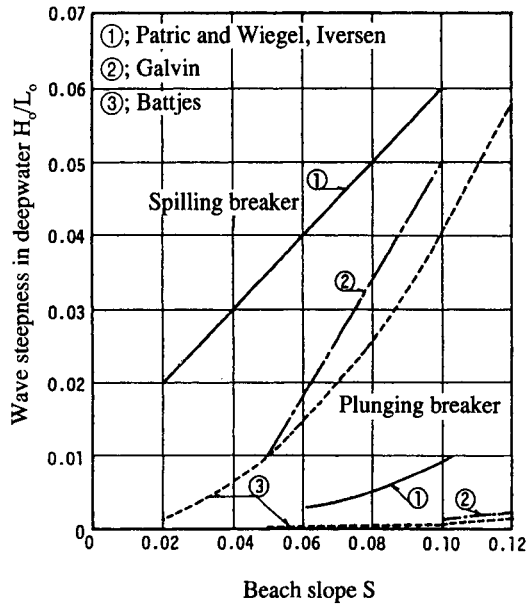
Fig. 1.14 Breaker classification

1.2.11 Wave deformation after breaking

The theoretical methods that evaluate variations of wave characteristics such as the wave height, water surface profile and wave kinematics after breaking have so far been investigated. Regarding the estimation of wave height variation, some theoretical models have succeeded in evaluating the laboratory and field data well. On the other hand, concerning the evaluation of the water surface profile after breaking, however, no reliable theoretical model has been proposed, even though a numerical calculation technique has remarkably progressed. This is one of the important problems requiring future investigation.

The theoretical approaches are mainly classified into (a) analytical method (b) energy method. The former directly solves the basic equation that includes a breaker-caused turbulence by means of a numerical calculation. The latter utilizes the law of conservation of energy flux, in which the energy dissipated by a wave breaking is taken into account. Detailed description and explanation of the energy method will be given in Chapter 3. In this section, one example of the analytical method is introduced.

First calculation of the wave deformation on a sloping bottom was carried out by Stoker (1948). He solved numerically the nonlinear shallow water wave (Eqs. (1.101) and (1.102)) with the use of the method of characteristics. However, he did not include the effect of the breaker-caused turbulence. Sawaragi and Iwata (1974) investigated the two-dimensional wave deformation after breaking and they first introduced the breaker-caused turbulence into the nonlinear shallow water wave theory,

$$\frac{\partial u}{\partial t} + u\frac{\partial u}{\partial x} + g\frac{\partial \eta}{\partial x} + \frac{\partial}{\partial x}\left\{m^2(\eta + h)^2(u/h)^2\right\} = 0$$

$$\frac{\partial \eta}{\partial t} + \frac{\partial}{\partial x}\left\{u(h + \eta)\right\} = 0$$

(1.172)

where, u is the x-component of the water particle velocity, η is the water surface profile, h is the still water depth, g is the gravitational acceleration, x is the horizontal axis and t is time. The term $(\partial/\partial x)\left\{m^2(h+\eta)^2(u/h)^2\right\}$ is the breaker-caused turbulence term and m is the turbulence intensity coefficient.

Figure 1.15 shows one example of comparison between data of laboratory experiments and theoretically estimated values with the use of Eq. (1.172). The figure clearly shows that theoretical values are in good agreement with experimental ones for an adequate value of M^* $(=m^2)$. The value of M^* in Fig. 1.15, however, depends on the breaker type and was not formulated theoretically. After their investigation, extensive research concerning breaker-caused turbulence has been conducted from laboratory experiments and field measurements. Details of breaker-caused turbulence will be discussed in Chapter 3.

Regarding the variation of the water surface profile after breaking, Sakai et al. (1986) tried to calculate numerically the broken wave after breaking. No theoretical model has succeeded in estimating the variation of the water surface profile after breaking. This problem also requires further investigation.
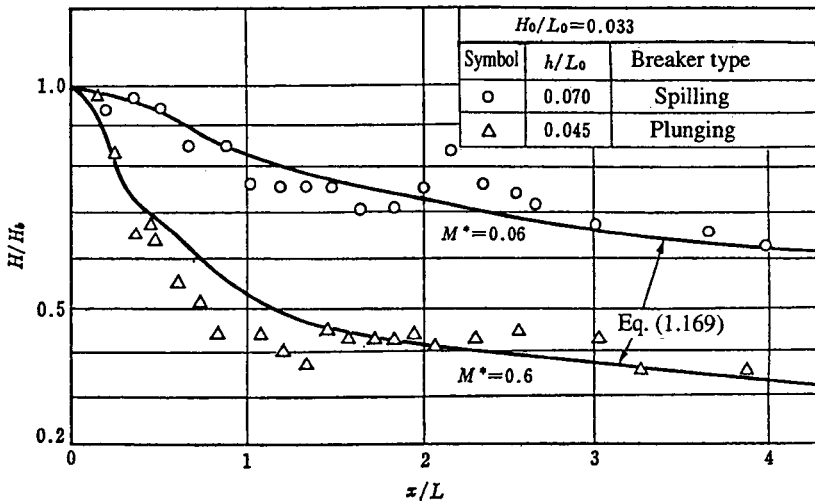
Fig. 1.15 Comparison of wave height variation between laboratory experiments and theoretically estimated values.

1.3 Description of Random Waves

Sea waves consist of many individual waves with different heights, periods and propagation directions. It is difficult, therefore, to discuss such random waves in a

deterministic manner on the basis of the equation of motion as used for regular waves. Characteristics of the random waves are usually discussed by means of either spectral analysis or wave-by-wave analysis. The spectral analysis provides the wave energy distribution in the domain of wave frequency, wave number or wave direction, assuming that the random waves are expressed by superimposing linearly a large number of regular waves with different amplitudes, frequencies and directions. In wave-by-wave analysis, the time series of the irregular surface elevation is first divided into a number of individual wave elements by either the zero-upcrossing method or the zero-downcrossing method, which assigns wave heights and wave periods for the individual waves. The statistical wave characteristics are discussed in terms of the distribution functions of these wave heights and wave periods. The statistics based on the wave-by-wave analysis are usually classified into three categories: short-term wave statistics, wave climate statistics and long-term wave statistics, corresponding to the time scale we are interested in. The short-term wave statistics deal with the waves observed over the period of several tens of minutes to one hour, where the wave characteristics are supposed to be stationary. The wave statistics over the period of about one month to one year is referred to as the wave climate statistics. The statistics based on the wave record over a long period such as several decades are termed the long-term wave statistics, which are also called the statistics for high waves or for extraordinary waves because the maximum value of the wave heights observed in the period of storm conditions are used as a variable.

Since the spectral analysis is based on the principle of linear superposition of sinusoidal waves, the amplitudes of the component waves are supposed to be small, which is the basic assumption of the linear wave theory. For the wave-by-wave analysis, each individual wave sampled is assumed to behave as it would be in a regular wave train. It is therefore easy to trace the individual waves as long as the interaction with neighbouring waves is negligible. Neither spectral analysis nor wave-by-wave analysis provides us with universal description for the hydrodynamic internal structure of irregular waves. Thus to take advantage of the features of these two methods, their combined use may be the best way as yet, even though a new comprehensive and precise theory that enables us to discuss the hydrodynamic internal structure is really what is hoped for.

1.3.1 Spectra of sea waves
(1) Frequency spectra

The water surface profile $\eta(x, y, t)$ of irregular waves, which varies both in time and in space, is expressed as

$$\eta(x, y, t) = \sum_{n=1}^{\infty} a_n \cos\left[\left(k_n \cos\theta_n\right)x + \left(k_n \sin\theta_n\right)y - 2\pi f_n t + \varepsilon_n\right] \qquad (1.173)$$

where a is the amplitude, k is the wave number, θ is the wave direction, f is the wave frequency, ε is the phase lag, and the subscript n indicates the n-th component wave.

When we observe the surface elevation at a fixed point in space, η yields a function of t. We now define the total energy density $E(f)$, which is related to the total energy of a component wave whose frequency lies between f and $f+\Delta f$:

$$E(f)\Delta f = \sum_{f}^{f+\Delta f} \frac{1}{2} a_n^2 \qquad (1.174)$$

The energy density spectrum $E(f)$ is sometimes simply called the wave spectrum (one-dimensional spectrum) and has a dimension of $(length)^2 \times (time)$. The generalized form of the energy spectrum density for wind waves is expressed as

$$E(f) = Af^{-m} \exp\left[-Bf^{-n}\right] \qquad (1.175)$$

There are a variety of standard spectra proposed for deepwater waves. Bretschneider-Mitsuyasu and Pierson-Moskowitz types are frequently used in Japan as theoretical spectra. Table 1.5 shows the values of the coefficients used in Eq. (1.175), A, m, B, and n, for several representative standard spectra. Although it is generally known that the wave spectra are significantly transformed in a shallow water region due to shoaling or wave breaking, the appropriate description for the shallow water wave spectra has not been established yet.

Table 1.5 Profiles of representative spectra

Proponent	A	B	m	n
Neumann (1953)	$0.39(2\pi)^{-1}(H_{1/3})^2(\overline{T})^{-5}$	$1.767(\overline{T})^{-2}$	6	2
Pierson – Moskowitz (1964)	$0.0081(2\pi)^{-4}g^2$	$-0.74(2\pi U_{19.5}/g)^{-4}$	5	4
Bretschneider (1969)	$0.430(\overline{H})^2(\overline{T})^4$	$0.675(\overline{T})^{-4}$	5	4
ITTS (1987)	$\alpha_1(2\pi)^{-5}g^2$	$4\alpha_1 g^2(2\pi)^{-4}(H_{1/3})^{-2}$	5	4
JONSWAP (1973)	$\alpha_2(2\pi)^{-4}g^2 r^{\exp\left[\frac{(f/f_p-1)}{2\sigma_f^2}\right]}$	$1.25(f_p)^{-4}$	5	4
Mitsuyasu (1975)	$0.258(H_{1/3})^2(T_{1/3})^{-4}$	$1.03(T_{1/3})^{-4}$	5	4

Remarks: $U_{19.5}$: wind speed measured at 19.5m above the sea surface, $\sigma_f = \begin{bmatrix} 0.07(f \le f_p) \\ 0.009(f > f_p) \end{bmatrix}$, $\alpha_1 = 0.0081\left\{T_{1/3}\sqrt{4g/H_{1/3}}/3.54(2\pi)\right\}^{-4}$, $\alpha_2 = 7.6 \times 10^{-2}(gF/U_{10}^2)$, $r=0.33$ U_{10}= Wind speed measured at 10.0m above the sea surface, F: fetch, $f_p = 3.5(g/U_{10})(gF/U_{10}^2)^{-3.33}$

(2) Directional wave spectra and wave number spectra

As seen in Eq. (1.173), wave energy scatters not only in the frequency domain but also in the wave direction domain. We thus define the directional wave spectrum (or two dimensional spectrum) $E(k,\theta)$ as in the following equation:

$$\sum_{k}^{k+\Delta k} \sum_{\theta}^{\theta+\Delta\theta} \frac{1}{2}a_n^2 = E(k, \theta)\, \Delta k\Delta\theta \qquad (1.176)$$

which refers to the total energy of component waves whose wave numbers and wave directions lie respectively between k and $k+\Delta k$ and between θ and $\Delta\theta$. The integration of $E(k,\theta)$ with respect to θ

$$E(k) = \int_0^{2\pi} E(k, \theta)\, d\theta \tag{1.177}$$

is referred to as a wave number spectrum. Using the dispersion relation, we can also write the directional wave spectrum as $E(f, \theta)$, in which the wave frequency f is used instead of wave number k. Similar to $E(k)$, we can obtain the frequency spectrum $E(f)$ by integrating $E(f,\theta)$ over the range $0 \le \theta \le 2\pi$.

For the purpose of engineering applications, $E(f, \theta)$ is often expressed as a product of the frequency spectrum $E(f)$ by the directional spreading function $h(\theta, f)$:

$$E(f,\theta) = E(f)h(\theta, f) \tag{1.178}$$

There are a variety of formulas proposed for $h(\theta, f)$. We here show two formulas proposed by Pierson et al. (1955), which is independent of f, and by Mitsuyasu et al. (1975):

$$h(\theta)\begin{cases} \dfrac{2}{\pi}\cos^2\theta : |\theta| \le \pi/2 \\ \\ \quad 0 \quad : |\theta| > \pi/2 \end{cases} \qquad \text{(Pierson et al. 1955)} \tag{1.179}$$

$$\begin{aligned} h(\theta, f) &= \left[\int_{\theta_{min}}^{\theta_{max}} \cos^{2S}\left(\frac{\theta}{2}\right) d\theta\right]^{-1} \cos^{2S}\left(\frac{\theta}{2}\right) \\ &= \left(\frac{1}{\pi} 2^{2S-1} \frac{\Gamma^2(S+1)}{\Gamma(2S+1)}\right)\cos^{2S}\left(\frac{\theta}{2}\right) \end{aligned}$$

(Mitsuyasu et al. 1975) (1.180)

where $\theta_{min} = -\pi$ and $\theta_{max} = \pi$. The parameter S in Eq. (1.180) represents the degree of concentration and is given by Goda and Suzuki (1975) as

$$S = \begin{cases} S_{max}(f/f_p)^5 : & f \le f_p \\ S_{max}(f/f_p)^{-2.5} : & f > f_p \end{cases} \tag{1.181}$$

in which f_p denotes the peak frequency of the spectrum and S_{max} is the maximum value of S and called the spreading parameter. Goda and Suzuki (1975) suggested letting $S_{max} = 10$ for wind waves, $S_{max} = 25$ for a swell with a short decay distance (with a relatively large wave steepness), and $S_{max} = 75$ for a swell with a long decay distance (with a relatively small wave steepness). Most of the formulas of the directional spectra are proposed for deepwater waves and have not been extended for shallow water waves.

1.3.2 Short-term statistics
(1) Distribution of water surface elevation

Providing that nonlinear interactions are small enough to assume that component waves are statistically independent, the probability distribution of the water surface elevation is considered to be a Gaussian distribution:

$$p(\eta) = \frac{1}{(2\pi m_0)^{1/2}} \exp(-\eta^2/2m_0) \tag{1.182}$$

from the central limit theorem, where we let $\overline{\eta} = 0$ and $m_0 = \overline{\eta^2}$ with $\overline{}$ indicating a time averaged quantity.

Representative statistical quantities of η are the mean water level $\overline{\eta}$, the standard deviation or root-mean-square value η_{rms}, the skewness $\sqrt{\beta_1}$ and the kurtosis β_2. These quantities are defined as

$$\left.
\begin{array}{cc}
\overline{\eta} = \dfrac{1}{N}\sum\limits_{i=1}^{N}\eta_i & \eta_{rms} = \left[\dfrac{1}{2}\sum\limits_{i=1}^{N}(\eta_i - \tilde{\eta})^2\right]^{1/2} \\
\sqrt{\beta_1} = \dfrac{1}{\eta^3_{rms}}\dfrac{1}{N}\sum\limits_{i=1}^{N}(\eta_i - \overline{\eta})^3 & \beta_2 = \dfrac{1}{\eta^4_{rms}}\dfrac{1}{N}\sum\limits_{i=1}^{N}(\eta_i - \overline{\eta})^4
\end{array}
\right\} \tag{1.183}$$

where η is sampled at an interval of Δt. The skewness $\sqrt{\beta_1}$ and the kurtosis β_2 are concerned with the shape of the probability distribution and take 0 and 3, respectively, for the Gaussian distribution. On the basis of field measurements at 40 locations along the coast of Japan, Kobune (1990) showed that these parameters take the values in the range $0.01 \le \sqrt{\beta_1} \le 0.1$ and $2.89 \le \beta_2 \le 3.18$. With wave heights increasing, the nonlinear effects become significant and the wave form becomes steeper at a wave crest and flatter at a wave trough, which gives a positive skewness and a kurtosis larger than 3.

(2) Distribution of Wave Heights

Provided that the irregular waves consist of the component waves only in a narrow frequency band with random initial phases, the probability distribution of wave heights is considered to be the Rayleigh distribution (Longuet-Higgins 1952):

$$p\left(\frac{H}{\overline{H}}\right)dH = \frac{\pi}{2}\left(\frac{H}{\overline{H}}\right)\exp\left\{-\frac{\pi}{4}\left(\frac{H}{\overline{H}}\right)^2\right\}dH \tag{1.184}$$

where $p(H/\overline{H})$ is the probability density function and $\overline{H}$ denotes the mean wave height. The statistical representative waves that we commonly use are the highest wave, the highest one-tenth wave, the highest one-third wave or the significant wave, and the mean wave. The highest wave denoted by H_{max} and T_{max} corresponds to the individual wave that has the largest wave height in a wave record. The highest one-tenth wave ($H_{1/10}$, $T_{1/10}$), the highest one-third wave or the significant wave ($H_{1/3}$, $T_{1/3}$) and the mean wave ($\overline{H}$, $\overline{T}$) are hypo-thetical waves that have the wave heights and periods given by averaging those of the particular individual waves. The wave height $H_{1/10}$ of the highest one-tenth wave is obtained by averaging wave heights larger than and equal to the $N/10$-th largest wave height among all the individual wave heights of N in the wave record, and the wave period $T_{1/10}$ of the highest one-tenth wave is given by averaging the wave periods of the corresponding waves. The wave height $H_{1/3}$ and the wave period $T_{1/3}$ of the significant wave are calculated in a similar manner to that for the highest one-tenth wave except that the $N/3$-th largest wave height is used instead of the $N/10$-th largest wave height. The mean wave height and the mean wave period are the mean values of the heights and periods of all the individual waves.

Assuming that the water surface elevation η and the wave height H in a wave record exhibit respectively the Gaussian distribution and the Rayleigh distribution, the representative quantities $H_{1/10}$, $H_{1/3}$, and η_{rms} are related to each other as follows:

$$\left.\begin{array}{lll} \overline{H}/H_{1/3} = 0.626 & H_{1/10}/H_{1/3} = 1.271 & \overline{H}/H_{1/10} = 0.4878 \\ \overline{H}/\eta_{rms} = 2.507 & H_{1/3}/\eta_{rms} = 4.004 & H_{1/10}/\eta_{rms} = 5.090 \end{array}\right\} \qquad (1.185)$$

Since the maximum wave height H_{max} increases as the number of individual waves N increases, H_{max} cannot be directly related to other representative wave heights but is given as a function of N

$$H_{max}/H_{1/3} \cong \frac{1}{a}(\ln N)^{1/2} + \gamma/2a(\ln N)^{1/2} \qquad (1.186)$$

where $a = 1.416$, γ is the Euler constant (≈ 0.5772), and ln denotes the natural logarithm. The standard deviation of $H_{max}/H_{1/3}$, $\sigma[H_{max}/H_{1/3}]$, is given as (Longuet-Higgins 1952)

$$\sigma\left[H_{max}/H_{1/3}\right] \cong \pi/2\sqrt{6}\,a(\ln N)^{1/2} \qquad (1.187)$$

which gives $H_{max}/H_{1/3} \cong 1.71$ for $N = 200$ and 1.93 for $N = 1000$.

The field observations in the coastal region of Japan says that the probability distribution of wave heights varies with the correlation coefficient between wave heights and wave periods, $r(H,T)$ (see Fig. 1.18)

$$r(H, T) = \frac{\sum\limits_{i=1}^{N}(H_i - \overline{H})(T_i - \overline{T})}{\sqrt{\sum\limits_{i=1}^{n}(H_i - \overline{H})^2}\,\sqrt{\sum\limits_{i=1}^{n}(T_i - \overline{T})^2}} \qquad (1.188)$$

Kobune (1990) showed that the Rayleigh distribution can be applied in the range $0.3 \leq r(H,T) \leq 0.7$. As waves approach the coastline, the probability distribution of H deviates from the Rayleigh distribution and accordingly the relations in Eq. (1.185) become no longer correct.

(3) Distribution of wave period

Bretschneider (1959) showed that the probability distribution of the square of a wave period is predicted well by the Rayleigh distribution for fully-developed wind waves, which yields

$$p\left(\frac{T}{\overline{T}}\right)dT = 2.7\left(\frac{T}{\overline{T}}\right)^3 \exp\left\{-0.675\left(\frac{T}{\overline{T}}\right)^4\right\}dT \qquad (1.189)$$

where $p(T/\overline{T})$ is the probability density function of wave periods and $\overline{T}$ is the mean wave period.

On the other hand, Longuet-Higgins (1975b) derived the theoretical probability density function for irregular waves having a narrow band spectrum
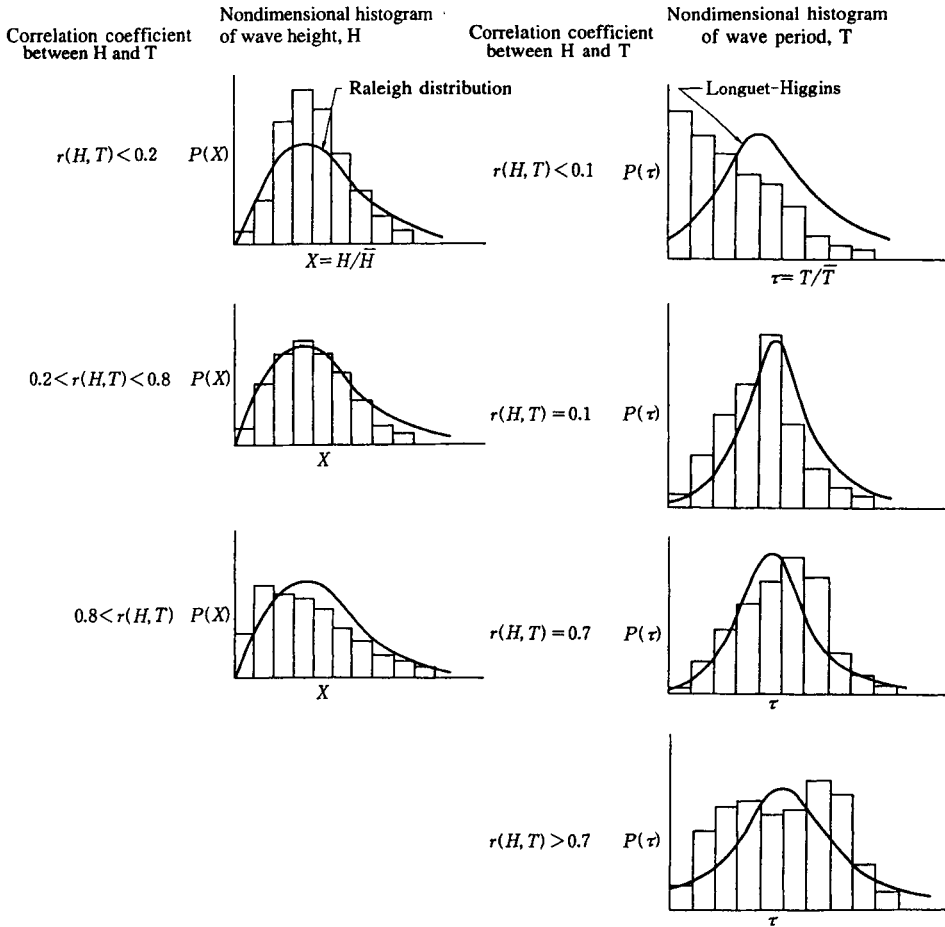
Fig. 1.16 Histograms of nondimensional wave height and period

$$p(\tau) = \frac{1}{2(1+\tau^2)^{3/2}}$$
$$\tau = \frac{T - \overline{T}}{v\overline{T}} \qquad v = \frac{m_0 m_2 - m_1^2}{m_1^2}$$

$$(1.190)$$

where v denotes the spectral width parameter. The parameters m_0, m_1 and m_2 are the zeroth, first and second spectral moments of the energy spectrum respectively, and given by

$$m_n = \int_0^\infty f^n E(f) \ df$$

$$(1.191)$$

Equation (1.190) says that the shape of the probability density function is significantly influenced by the spectral width parameter v. Goda (1978) used the new parameter, the period band width parameter, v_t, proposed by Longuet-Higgins (1975b)

$$\left.\begin{array}{l} v = \dfrac{\sqrt{3}}{2} IQR(\tau) \equiv v_t \\ IQR(\tau) = \tau_1 - \tau_3 \end{array}\right\} \qquad (1.192)$$

and apply it to Eq. (1.190) for v to show that Eq. (1.190) can be applied to irregular waves having relatively wide-band spectra. τ_1 and τ_3 in Eq. (1.192) correspond to τ at which the probability of occurrence of τ, $p(\tau < \tau_i)$, is equal to 1/4 and 3/4, respectively. According to these field observations in the coastal region of Japan, the probability distribution of wave periods is influenced by the correlation coefficient $r(H,T)$ between wave heights and wave periods, and the measured distribution shows good agreement with the theoretical distribution of Eq. (1.190) in the region $0.1 \leq r(H,T) \leq 0.7$.

The relations between the representative wave periods are approximately given as

$$T_{1/3}/\overline{T} = 0.9 \sim 1.4, \quad T_{1/10}/T_{1/3} = 0.9 \sim 1.1 \qquad (1.193)$$

by numerical simulations and field measurement (Goda and Nagai 1974).

(4) Joint probability distribution between wave heights, periods and directions

For the irregular waves having a narrow band spectrum, the joint probability distribution between wave heights, wave periods and wave directions have been discussed theoretically, making use of the envelope profiles of the time series of various quantities such as water surface elevation $\eta(t)$ and its time derivative. Longuet-Higgins (1975b) derived the joint probability density function $p(X,\tau)$ between wave heights $\left(X = H/\overline{H}\right)$ and wave periods $\left(\tau = T/\overline{T}\right)$ from the joint probability distribution of the envelope functions of $\eta(t)$ and $\dot{\eta}(t)$

$$p(X, \tau) = \left(\frac{\pi X^2}{4v}\right) \exp\left\{-\frac{\pi}{4} X^2 \left(1 + \frac{(\tau - 1)^2}{v^2}\right)\right\} \qquad (1.194)$$

The marginal distribution given by integrating Eq. (1.194) with respect to X over the region $0 \leq X \leq \infty$ provides the distribution function of τ shown in Eq. (1.190), while the integration with respect to τ over the region $0 \leq \tau \leq \infty$ gives the Rayleigh distribution for wave heights shown in Eq. (1.184).

Isobe (1987) provided two kinds of joint probability distributions between wave heights and wave directions of individual waves using the time series of $\eta(t)$, $u(t)$ and $v(t)$, which correspond to two different definitions of wave directions. The definitions used for the wave direction are (i) the horizontal direction of a water particle velocity vector under a wave crest, and (ii) the direction in which the horizontal water particle velocity becomes a maximum. They showed that these two definitions bring about a considerable difference in the probability density functions and accordingly in the joint probability distribution between wave heights and wave periods. They also suggested that we should carefully select the definition of wave direction suitable for the phenomena being considered when discussing the directional random waves through the wave-by-wave analysis.

Kwon et al. (1988) and Akai and Mizuguchi (1988) independently obtained the expressions for the joint probability density function between wave heights, wave periods (frequencies) and wave directions based on the above-mentioned definition (i), using the envelope functions of $\eta(t)$, $\dot{\eta}(t)$, $u(t)$ and $v(t)$. There are two differences between Kwon's and Akai's. One is that the covariance between $\dot{\eta}(t)$, $u(t)$, and $v(t)$ are taken into account in the former and are neglected in the latter. The other is that the wave period is used as a parameter representing the time scale in the former whereas the wave frequency is used in the latter to avoid theoretical problems in converting the wave frequency into a wave period. Here we show the Kwon expression

$$p(X,\tau,\theta) = \frac{\overline{\sigma}}{2^3} \frac{1}{r} \left(\frac{X}{\tau}\right)^2 exp\left[-\frac{\pi}{4\Delta} X^2\left\{A_{11} + A_{44}\overline{\sigma}^2(1-1/\tau)^2 + 2A_{14}\overline{\sigma}(1-1/\tau)\right\}\right]$$
$$\times \left[\frac{\sqrt{\Delta}}{A} + \frac{B'}{A^{3/2}} \frac{\pi}{2} exp\left(\frac{B'\pi}{4A\Delta} X^2\right)\left\{1 - p_r\left(-B'\sqrt{\frac{\pi}{2A\Delta}} X\right)\right\}\right]$$

where

$A = A_{22}cos^2\theta + A_{33}sin^2\theta/r^2 + 2A_{23}cos\theta sin\theta/r$
$B' = -(A_{12}cos\theta + A_{13}sin\theta/r + A_{24}\overline{\sigma}(1-1/\tau)cos\theta + A_{34}\overline{\sigma}(1-1/\tau)sin\theta/r)$
$\overline{\sigma} = 2\pi m_1/m_0$ (m_i ; the i-th moment of frequency spectrum)

$$pr(\xi) = \frac{1}{\sqrt{2\pi}}\int_\xi^\infty exp\left(-\frac{t^2}{2}\right)dt \tag{1.196}$$

Δ, r and A_{ij} ($i = 1$-4, $j = 1$-4) are expressed as

$$\begin{aligned}
\Delta &= 1 + 2r_{11}r_{12}r_{21} - r_{12}^2 - r_{21}^2 - r_{11}^2 - r_{10}^2 - 2r_{01}r_{10}r_{12}r_{21} \\
&\quad + 2r_{10}r_{01}r_{11} + r_{10}^2r_{21}^2 + r_{01}^2r_{12}^2 - r_{01}^2,
\end{aligned} \tag{1.195}$$

$$A_{11} = 1 + 2r_{11}r_{12}r_{21} - r_{12}^2 - r_{21}^2 - r_{11}^2,$$
$$A_{12} = r_{21}^2r_{10} + r_{01}r_{11} - r_{10} - r_{01}r_{12}r_{21},$$
$$A_{13} = r_{10}r_{11} + r_{12}^2r_{01} - r_{01}r_{12}r_{21} - r_{01},$$
$$A_{14} = r_{10}r_{12} + r_{01}r_{21} - r_{01}r_{11}r_{21} - r_{01}r_{11}r_{12},$$
$$A_{22} = 1 - r_{21}^2 - r_{01}^2,$$
$$A_{23} = r_{01}r_{10} + r_{12}r_{21} - r_{11},$$
$$A_{24} = r_{11}r_{21} + r_{01}^2r_{12} - r_{12} - r_{10}r_{01}r_{21},$$
$$A_{33} = 1 - r_{12}^2 - r_{10}^2,$$
$$A_{34} = r_{11}r_{12} + r_{10}^2r_{21} - r_{21} - r_{10}r_{21}r_{12},$$
$$A_{44} = 1 + r_{10}r_{01}r_{11} - r_{01}^2 - r_{11}^2 - r_{10}^2$$

$$\tag{1.197}$$

by using the following dimensionless covariances between the envelope functions (η_s,η_c), $(\dot{\eta}_s,\dot{\eta}_c)$, (u_s,u_c) and (v_s,v_c) of $\eta(t)$, $\dot{\eta}(t)$, $u(t)$ and $v(t)$, respectively:

$$\left.\begin{aligned}
r_{10} &= m_{10}/\sqrt{m_{00}m_{20}} & r_{01} &= m_{01}/\sqrt{m_{00}m_{02}} & r_{11} &= m_{11}/\sqrt{m_{20}m_{02}} \\
r_{12} &= m_{12}/\sqrt{m_{20}m_{22}} & r_{21} &= m_{21}/\sqrt{m_{02}m_{22}} & r &= \sqrt{m_{02}/m_{20}}
\end{aligned}\right\} \tag{1.198}$$

where m_{ij} $(i,j=0,1,2)$ is the covariance between the envelope functions.

$$
\left.
\begin{aligned}
m_{00} &=<\eta_c\eta_c>=<\eta_s\eta_s> & m_{10} &=<\eta_c u_c>=<\eta_s u_s> \\
m_{01} &=<\eta_c v_c>=<\eta_s v_s> & m_{20} &=<u_c u_c>=<u_s u_s> \\
m_{02} &=<v_c v_c>=<v_s v_s> & m_{11} &=<u_c v_c>=<u_s v_s> \\
m_{22} &=<\dot{\eta}_c\dot{\eta}_c>=<\dot{\eta}_s\dot{\eta}_s> & m_{12} &=<u_c\dot{\eta}_s>=-<u_s\dot{\eta}_c> \\
& & m_{21} &=<v_c\dot{\eta}_s>=-<v_s\dot{\eta}_c>
\end{aligned}
\right\}
\tag{1.199}
$$

Equation (1.195) yields the expression of Akai et al. if we take the x-axis as a principal direction and let the covariance between $\dot{\eta}(t)$, $u(t)$ and $v(t)$ be zero, and also yields Isobe's joint probability function between wave heights and wave directions based on the definition (i) for the wave direction if we integrate the equation with respect to τ over the range $0 \le \tau \le \infty$. The covariances in Eq. (1.199) are related to the directional spectrum as follows:

$$
\left.
\begin{aligned}
m_{00} &= \int_0^\infty \int_{-\pi}^\pi E(f,\theta)\,\mathrm{d}\theta\mathrm{d}f \\
m_{11} &= \int_0^\infty \int_{-\pi}^\pi b(f)^2 \sin\theta\cos\theta\, E(f,\theta)\,\mathrm{d}\theta\mathrm{d}f \\
m_{10} &= \int_0^\infty \int_{-\pi}^\pi b(f)\cos\theta\, E(f,\theta)\,\mathrm{d}\theta\mathrm{d}f \\
m_{01} &= \int_0^\infty \int_{-\pi}^\pi b(f)\sin\theta\, E(f,\theta)\,\mathrm{d}\theta\mathrm{d}f \\
m_{20} &= \int_0^\infty \int_{-\pi}^\pi b(f)^2 \cos^2\theta\, E(f,\theta)\,\mathrm{d}\theta\mathrm{d}f \\
m_{02} &= \int_0^\infty \int_{-\pi}^\pi b(f)^2 \sin^2\theta\, E(f,\theta)\,\mathrm{d}\theta\mathrm{d}f \\
m_{22} &= \int_0^\infty \int_{-\pi}^\pi (2\pi)^2 \left(f-\bar{f}\right) E(f,\theta)\,\mathrm{d}\theta\mathrm{d}f
\end{aligned}
\right\}
\tag{1.200}
$$

where $b(f)$ is the transfer function of water particle velocity from the water surface elevation based on the linear wave theory.

Figure 1.17 shows the joint probability distributions between wave heights, wave periods and wave directions under the condition that one of these parameters takes a value in a particular range shown in the figures, where both the isolines and the numerals indicate the number of waves out of 1000 waves. The isolines are calculated by applying Eq. (1.195) to the surface elevation $\eta(t)$ and the horizontal water particle velocities $u(t)$ and $v(t)$ measured on the coast of Awaji Island in Japan. The numerals are obtained by analyzing the measured surface elevation through the zero-downcrossing method and by assigning the wave directions on the basis of Isobe's definition (i). The agreement is good except for the region of the small relative period $\left(T/\overline{T} < 0.75\right)$.

(a) $-15° \leqq \theta < 15°$
Joint distribution of wave height and period

(b) $0.75 \leqq H/\bar{H} < 1.25$
Joint distribution of wave period and direction

(c) $0.75 \leqq T/\bar{T} < 1.25$
Joint distribution of wave period and direction
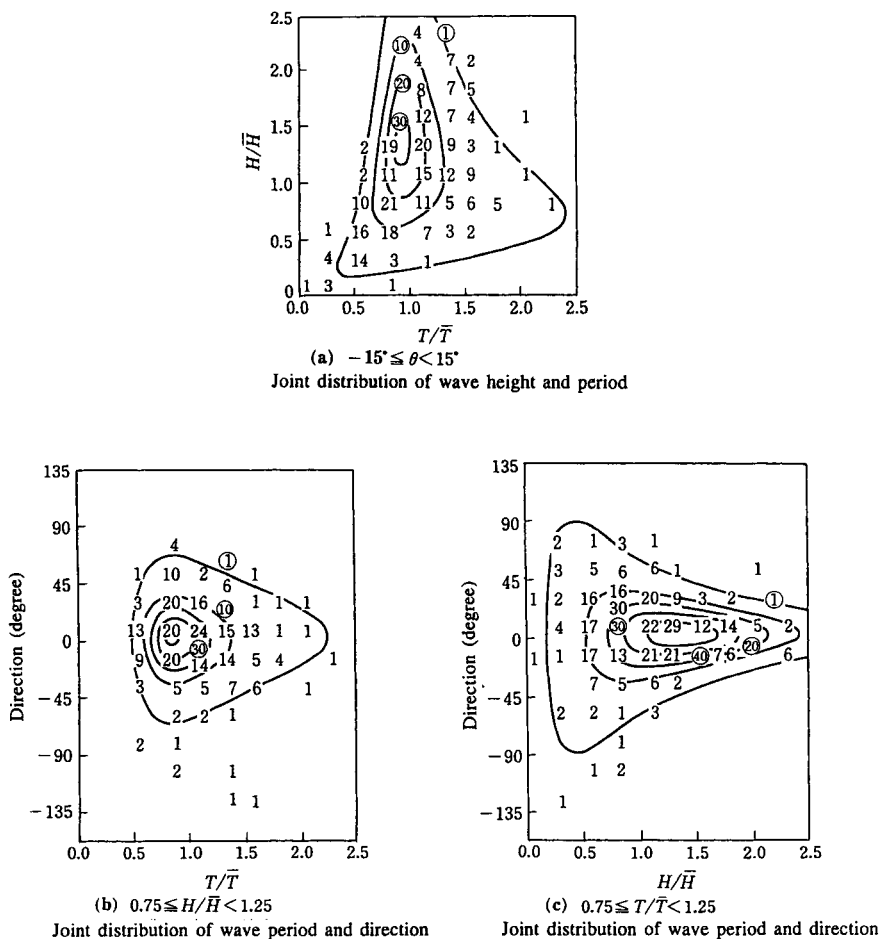
Fig. 1.17 Joint distribution of wave height, period and direction

(5) Wave grouping

It is generally known that high waves tend to be observed successively, showing alternate high wave groups and low wave groups. A succession of high waves whose wave heights exceed a specific wave height H^* is called a "run of high wave heights."

The number of waves contained in such a wave group is termed "run length" indicated by J_1 in Fig. 1.18. The "repetition of high waves" indicates the waves that lie between the first exceedance and the next, the number of which is termed "repetition length of high waves" or "total run length of high waves," shown by J_2 in the figure. Ewing (1973), Goda (1976) and Kimura (1980) theoretically investigated the statistical quantities such as probability distributions of the run length and total run length of high waves. Kimura's theory, which is accepted in practical use and in which the correlation between two

successive waves is taken into account, provides the probability distributions $p(J_1)$ and $p(J_2)$, the mean value $\bar{J}_1$ and $\bar{J}_2$, and the standard deviation $\sigma(J_1)$ and $\sigma(J_2)$, for the run length J_1 and the repetition length of high waves J_2:
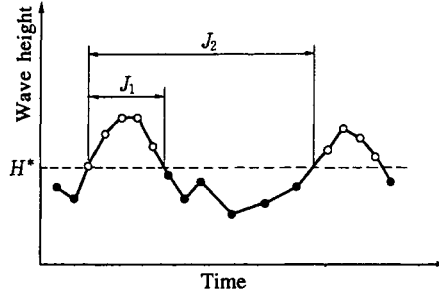
Fig. 1.18 Definition of run length and repetition length of high waves

$$\left.\begin{array}{l} p(J_1) = p_{22}^{j_1-1}(1 - p_{22}) \\[2mm] p(J_2) = \dfrac{(1 - p_{11})(1 - p_{22})}{(p_{11} - p_{22})}\left(p_{11}^{j_2-1} - p_{22}^{j_2-1}\right) \\[2mm] \bar{J}_1 = 1/(1 - p_{22}) \\[2mm] \bar{J}_2 = [1/(1 - p_{11})] + [1/(1 - p_{22})] \\[2mm] \sigma(J_1) = \sqrt{p_{22}}/(1 - p_{22}) \\[2mm] \sigma(J_2) = \left[\dfrac{1}{(1 - p_{11})^2} + \dfrac{1}{(1 - p_{22})^2} - \dfrac{1}{(1 - p_{11})} - \dfrac{1}{(1 - p_{22})^2}\right]^{1/2} \end{array}\right\} \qquad (1.201)$$

where

$$p(H_1, H_2) = \frac{4H_1 H_2}{(1 - 4\rho^{*2})H_{\text{rms}}^4}\exp\left[-\frac{1}{(1 - 4\rho^{*2})}\left(\frac{H_1^2 + H_2^2}{H_{\text{rms}}^2}\right)\right] \times I_0\left[\frac{4H_1 H_2 \rho^*}{(1 - 4\rho^{*2})H_{\text{rms}}^2}\right]$$

$$p_{11} = \int_0^{H^*}\int_0^{H^*} p(H_1, H_2)\,dH_1 dH_2 \bigg/ \int_0^{H^*} q(H_1)\,dH_1$$

$$p_{22} = \int_{H^*}^{\infty}\int_{H^*}^{\infty} p(H_1, H_2)\,dH_1 dH_2 \bigg/ \int_{H^*}^{\infty} q(H_1)\,dH_1$$

$$r_{HH} = \frac{E(2\rho^*) - (1 - 4\rho^{*2})K(2\rho^*)/2 - \pi/4}{(1 - \pi/4)}$$

In these equations, I_0 denotes the modified Bessel function, ρ^* is the correlation parameter, $K(\ )$ and $E(\ )$ are the complete elliptic integrals of the first and second kinds, respectively, and r_{HH} is the correlation coefficient between two successive wave heights, and $q(H_1)$ is the probability density function of H_1.

Funke and Mansard (1980) proposed the following new parameter GF (Groupiness Factor) to provide additional information of the wave grouping besides the run length and the repetition length of high waves:

$$\left. \begin{aligned} \text{GF} &= \left[\frac{1}{T_n} \int_0^{T_n} \left(E^*(t) - \overline{E}^* \right)^2 \mathrm{d}t \right]^{1/2} \Big/ \overline{E}^* \\ E^*(t) &= \frac{1}{T_p} \int_{-\infty}^{+\infty} \eta^2(t+\tau) Q(\tau) \, \mathrm{d}\tau \\ \overline{E}^* &= \frac{1}{T_n} \int_0^{T_n} E^*(t) \, \mathrm{d}\tau = m_0 = \overline{\eta^2} \end{aligned} \right\} \tag{1.202}$$

where T_n is the record length, η is the water surface elevation, T_p is the peak period of the wave spectrum, $E^*(t)$ is the smoothed instantaneous wave energy history (abbreviated SIWEH), τ is the time lag, and $Q(\tau)$ is the data window for which they recommended using the following function:

$$\left. \begin{aligned} Q(\tau) &= 1 - \left(|\tau|/T_p \right) &&: |\tau| \le T_p \\ &= 0 &&: |\tau| > T_p \end{aligned} \right\} \tag{1.203}$$

It has been pointed out that the wave grouping significantly influences mooring problems of floating structures, wave run-up heights on a slope (Mase et al. 1983), stability of rubble mounds or wave dissipating concrete blocks (Sawaragi et al. 1983), and overflowing phenomena over a dike due to waves (Kimura 1981). Iwata and Itoh (1986) also investigated the run length and the repetition length of breakers on gentle slopes.

1.3.3 Wave climate statistics
(1) Distribution function

Since there are no leading theories for the wave climate statistics, most of investigations have been performed on the basis of field data. Wave climate statistics deal with significant wave heights $H_{1/3}$, significant wave periods $T_{1/3}$, and wave directions. Although a variety of distribution functions have been proposed (Chakrabarti 1987), the Weibull distribution is often used as a distribution function of $H_{1/3}$ and $T_{1/3}$

$$P(X < x) = P(x) = \left\{ \begin{aligned} 1 - \exp\left[-\left\{ (x - x_c)/x_0 \right\}^r \right] &&: x \ge x_c \\ 0 &&: x < x_c \end{aligned} \right\} \tag{1.204}$$

where X indicates $H_{1/3}$ or $T_{1/3}$, x is a specific value of X, x_c denotes the minimum value of $H_{1/3}$ or $T_{1/3}$, x_0 is the scale parameter, and r is the shape parameter.

The Weibull distribution shows good agreement with field data except for both very large and small wave heights. The Port and Harbor Research Institute of the Ministry of Transport, Japan obtained the values of the parameters used in Eq. (1.204), $(H_{1/3})_0$, $(H_{1/3})_c$, r_H, $(T_{1/3})_c$, $(T_{1/3})_0$, and r_T for the 22 locations along the coast of Japan through field measurements, where r_H and r_T are the shape parameters for H and T, respectively. Kobune

(1990) investigated the annual variation of the monthly averaged values of the significant wave heights and periods observed on the coast of Japan, and obtained the relation

$$H_{1/3} = aT^3_{1/3} \qquad (1.205)$$

This is different from the relation $H_{1/3} \propto T^2_{1/3}$, which Bretschneider (1954) proposed for the short-term statistics. The parameter a in Eq. (1.205) takes 0.007 on the northern coast of the Sea of Japan, 0.006 on the western coast of the Sea of Japan, and 0.005 on the coast of the East China Sea.

(2) Duration of wave climate (Goda 1985)
   Kuwayama and Hogben (1984) derived the probability distribution for duration τ of the wave climate during which wave heights exceed a specific significant wave height $(H_{1/3})_c$ and also obtained the mean duration $\bar{\tau}$ of such a wave climate

$$\left.\begin{array}{l} P\left[\tau / H_{1/3} > \left(H_{1/3}\right)_c\right] = 1 - \exp\left[-C(\tau/\bar{\tau})^\alpha\right] \\[2mm] \bar{\tau} = A \Big/ \left\{-\ln Q\left[H_{1/3} > \left(H_{1/3}\right)_c\right]\right\}^\beta \end{array}\right\} \qquad (1.206)$$

assuming the probability distribution of $H_{1/3}$ to be the two-parameter Weibull distribution and letting $x_c = 0$ in Eq. (1.204). They also obtained the relations: $A = 35/r^{1/2}$, $\beta = 0.6r^{0.287}$, $C = [\Gamma(1+1/\alpha)]^\alpha$, $\alpha = 0.267\gamma[(H_{1/3})_c/\bar{H}_{1/3}]^{0.4}$, from the field measurements, where $\bar{H}_{1/3}$ denotes the mean value of $H_{1/3}$, $\Gamma(\ )$ is the Gamma function, and $Q[H_{1/3} > (H_{1/3})_c]$ is the probability of exceedance over $(H_{1/3})_c$. Furthermore, they suggested the estimation of the probability distribution for the duration τ' and the mean duration $\bar{\tau}'$, where τ' is the duration during which wave heights show smaller values than $(H_{1/3})_c$, by using the following parameters:

$$\left.\begin{array}{ll} \bar{\tau}' = \bar{\tau}(1-Q)/Q & \alpha' = 0.267r\left[(H_{1/3})_c\big/\bar{H}_{1/3}\right]^{-0.4} \\[2mm] & C = \left[\Gamma(1+1/\alpha')\right]^{\alpha'} \end{array}\right\} \qquad (1.207)$$

However, the applicability of Eqs. (1.206) and (1.207) have not been fully investigated.

1.3.4 Long-term statistics
   The design waves (probability waves), which give the external forces for the design of coastal and offshore structures, are decided by means of statistical treatment of extraordinary waves under storm conditions. The accumulation of such wave data, however, is not large enough to deal with the maximum wave heights measured in one year. We therefore utilize the partial duration series applying extreme statistics analysis. In this analysis, use is made of the maximum wave height $(H_{1/3})_{peak}$ among the significant wave heights, each of which corresponds to the wave record due to one typhoon or one low pressure.

(1) Probability of non-exceedance of extreme wave heights

Gringorten (1963) and Petruaskas and Aagaard (1970) obtained the probability with which wave heights do not exceed the threshold H_m, assuming that the wave heights are independent of each other

$$P(H < H_m) = 1 - \frac{m - \alpha}{N + \beta} \tag{1.208}$$

where H_m denotes the m-th largest value among the extreme wave heights of N. Although we sometimes let $\alpha = 0$ and $\beta = 1$ for convenience in calculation, it is recommended using the values shown in Table 1.6 to avoid the bias introduced by letting $\alpha = 0$ and $\beta = 1$. Table 1.6 is given by using the distribution functions of extreme values shown below in Eqs. (1.209) and (1.210).

Table 1.6 Values of α and β in Eq. (1.208)

Distribution function	α	β
Double exponential distribution	0.44	0.12
Weibull distribution (k = 0.75)	0.54	0.64
(k = 0.85)	0.51	0.59
(k = 1.00)	0.48	0.53
(k = 1.10)	0.46	0.50
(k = 1.25)	0.44	0.47
(k = 1.50)	0.42	0.42
(k = 2.00)	0.39	0.37

(2) Distribution functions of extreme wave heights (Japan Society of Civil Engineers 1985; Chakrabarti 1985)

The Gumbel distribution and the Weibull distribution are commonly used as distribution functions for extreme values of wave heights. The distribution functions P, the mean values $\mu[X]$, and the variances $\sigma^2[X]$ of these are given as follows:

Gumbel distribution:

$$\left. \begin{array}{l} P(H \leq X) = \exp\left[-\exp\left(-\frac{X - B}{A} \right) \right] \\ \mu[X] = B + \gamma A \quad \sigma^2[X] = \left(\pi^2/6 \right) A^2 \\ \gamma = \text{Euler's constant} \end{array} \right\} \tag{1.209}$$

Weibull distribution:

$$\left. \begin{array}{l} P(H \leq X) = 1 - \exp\left[-\left(\frac{X - B}{A} \right)^K \right] \\ \mu[X] = B + A\Gamma\left(1 + 1/K \right) \\ \sigma^2[X] = A^2\left[\Gamma(1 + 2/K) - \Gamma^2(1 + 1/K) \right] \end{array} \right\} \tag{1.210}$$

where $\Gamma(\ )$ is the Gamma function, A is the scale parameter, K is the shape parameter, B is the minimum value of X, and X denotes the wave height we are concerned with. Kobune (1990) showed a table providing the values of A, B and K in the Weibull distribution function for the maximum significant wave height measured in one year on the coast of Japan. He also showed the correlation coefficient R between the distribution of field data and the theoretical distribution.

(3) Return period of extreme wave heights
    The return period of extreme wave heights is obtained by

$$R_p = \frac{K}{N} \frac{1}{1 - P(H \le X)} \tag{1.211}$$

where R_p denotes the return period in one year, K is the effective duration of wave data in one year, and N is the number of extreme wave heights in the period of K years.
    To calculate the probability wave height X of R_p years, i.e., the extreme value of X corresponding to the return period R_p, we first calculate the non-exceedance probability $P(H \le X)$ from Eq. (1.211) and then determine the wave height having the non-exceedance probability $P(H \le X)$ from Eq. (1.209) or Eq. (1.210).
    On the other hand, the statistics for extreme values of wave periods have not been investigated thoroughly. This is probably because such statistics are considered to be less important than those for wave heights. The wave period corresponding to the probability wave height of R_p years is obtained by making use of the joint distribution diagram between the wave heights and the corresponding wave periods, on the basis of the same wave data as used for the statistics of extreme wave heights. In the case available wave data being scarce, we are often required to correct the predicted extreme values to minimize the deviation from those of the real distribution functions, even if we adopt the most suitable distribution function.

References

Akai, S. and M. Mizuguchi (1988): Joint distribution of wave height, frequency and direction of multi-directional sea waves, Proc. 35th Japanese Conf. on Coastal Eng., JSCE, pp.143-147. (in Japanese)

Battjes, J.A. (1978): Surf similarity, Proc. 18th Int. Conf. on Coastal Eng., ASCE, pp.466-480.

Berkhoff, J.C.W. (1972): Computation of combined refraction-diffraction, Proc. 13th Int. Conf. on Coastal Eng., ASCE, pp.1972.

Berkhoff, J.C.W., N. Booy and A.C. Radder (1982): Verification of numerical wave propagation model for simple harmonic linear water waves, Coastal Eng., Vol.6, pp.255-279.

Bretherton, F.P. (1969): Wave trains in inhomogeneous moving media, Proc. Roy. Soc. London, A302, pp.529-554.

Bretschneider, C.L. (1954): Generation of wind waves over shallow bottom, U.S. Army Corps of Eng., Beach Erosion Board Tech. Memo., No.51.

Bretschneider, C.L. (1959): Wave variability and wave spectra for wind generated waves, U.S. Army Corps of Eng., Beach Erosion Board Tech. Memo., No.118.

Carry, C. (1953): Partial clapotis, La Houille Blanche, Vol.8, pp.482-494.

Chakrabarti, S.K. (1987): Hydrodynamics of Offshore Structure, Springer-Verlag, 440p.

Chappelear, J.E. (1961): Direct numerical calculation of nonlinear ocean waves, J. Geophys. Res. Vol.66, No.2, pp.501-508.

Cokelet, E.D. (1977): Steep gravity waves in water of arbitrary uniform depth, Phil. Trans. Roy. Soc. London, Vol.286, No.1335, pp.183-230.

Dean R.G. (1965): Stream function representation of nonlinear ocean waves, J. Geophys. Res., Vol.70, pp.4561-4572.

Donald, J.W. and D.H. Perigrine (1984): Steep unsteady water waves -An efficient computational scheme, Proc. 19th Int. Conf. on Coastal Eng., ASCE, pp.955-967.

Elmore, W.C. and M.A. Heald (1969): Physics of Waves, Dover Pub. Inc., pp.309-322.

Ewing, J. A. (1973): Mean length of run of high waves, J. Geophys. Res., Vol.78, No.12, pp.1993-1936.

Funke, E. R. and E.P.D. Mansard (1980): On the synthesis of realistic sea states, Proc. 17th Int. Conf. on Coastal Eng., ASCE, pp.2974-2991.

Galvin, C.J. (1968): Breaker type classification on three laboratory beaches, J. Geophys. Res., Vol.73, pp.175-200.

Gerristen, F. (1981): Wave attenuation and wave set-up on a coral reef, Look Labo. Tech. Rept., Univ. of Hawaii, No.48.

Goda, Y. and Y. Abe (1968): Apparent coefficient of partial reflection of finite amplitude waves, Rept. Port and Harbour Res. Inst., Vol.7, No.3, pp.1-58.

Goda, Y. and K. Nagai (1974): Investigation of the statistical properties of sea waves with field and simulation data, Rept. Port and Harbour Res. Inst., Vol.13, No.1, pp.3-37. (in Japanese)

Goda, Y. and Y. Suzuki (1975): Computation of refraction diffraction of sea waves with Mitsuyasu's directional spectrum, Tech. Note of Port and Harbour Res. Inst., No.230, 45p. (in Japanese)

Goda, Y. (1976): On wave groups, Proc. BOSS '76, pp.115-128.

Goda, Y. (1978): The observed joint distribution of periods and heights of sea waves, Proc. 16th Int. Conf. on Coastal Eng., ASCE, pp.227-246.

Goda, Y. (1985): Random Seas and Design of Maritime Structures, Univ. of Tokyo Press, 323p.

Gringorten, I.I. (1963): A plotting rule for extreme probability paper, J. Geophys. Res., Vol.68, No.3, pp.813-814.

Houston J.R. (1981): Combined refraction and diffraction of short waves using the finite element method, Appl. Ocean Res., Vol.3, No.4, pp.163-170.

Isobe, M. (1987): Theoretical study on wave-by-wave analysis for multi-directional irregular waves, Proc. 34th Japanese Conf. on Coastal Eng., pp.111-115. (in Japanese)

Iversen, H.W. (1952): Waves and breakers in shoaling water, Proc. 3rd. Int. Conf. on Coastal Eng., ASCE, pp.1-12.

Iwagaki, Y. (1987): New Coastal Engineering, Morikita-Shuppan, p.54. (in Japanese)

Iwata, K. and H. Kiyono (1985): Breaking of standing two-component composite and irregular waves, Coastal Eng. in Japan, JSCE, Vol.28, pp.71-87.

Iwata, K. and S. Itoh (1986): Length of runs of just breaking and broken waves in irregular wave train on gentle slopes, Proc. 20th Int. Conf. on Coastal Eng., ASCE, pp.1210-1224.

Iwata, K. and T. Tomita (1991): Fifth-order theory of partial clapotis in shallow water depth, Memoirs of the Faculty of Eng., Nagoya Univ., Vol.43, pp.225-257.

Japan Society of Civil Engineers (1985): Wave height estimation and long term statistics, in Manual of Hydraulic Engineering, JSCE, pp.485-495. (in Japanese)

Kimura, A. (1980): Statistical properties of random wave groups, Proc. 17th Int. Conf. on Coastal Eng., ASCE, pp.2955-2973.

Kimura, A., A. Seyama and T. Yamada (1981): Statistical properties of the short-term overtopping discharge, Proc. of 28th Japanese Conf. on Coastal Eng., JSCE, pp.335-338. (in Japanese)

Kishi, T. (1959): The possible highest gravity waves in shallow waters, Coastal Eng. in Japan, JSCE, Vol.2, pp.9-16.

Kobayashi, N., A.K. Otta and I. Roy (1987): Wave reflection and run-up on rough slopes, J. Waterway, Port, Coastal and Ocean Div., ASCE, Vol.113, No.WW3, pp.282-298.

Kobune, K. (1990): Observation method of waves along Japanese coast and appearance wave characteristics, Tech. Note of Port and Harbour Res. Inst., No.668. (in Japanese)

Koyama, H. and K. Iwata (1988): Estimation of water particle velocities of shallow water waves by a modified transfer function, Proc. 20th Int. Conf. on Coastal Eng., ASCE, Vol.1, pp.425-436.

Korteweg, D.J. and G. de Vries (1895): On the change in the form of long waves advancing in a rectangular channel and on a new type of long stationary wave, Phil. Mag., Vol.39, pp.422-443.

Kuwayama, S. and N. Hogben (1984): The estimation of persistence statics from cumulative probabilities of wave height, Rept. No.R183, NMI Ltd., 72p.

Kwon, J.G., H. Ishimoto, T. Sawaragi and I. Deguchi (1988): Joint distribution of wave height, period and direction, Proc. 35th Japanese Conf. on Coastal Eng., JSCE, pp.148-152. (in Japanese)

Laiton, E.V. (1960): The second approximation to cnoidal and solitary waves, J. Fluid Mech., Vol.9, pp.430-444.

Lee, T.T. and K.P. Black (1978): The energy spectra of surf waves on a coral reef, Proc. 16th Int. Conf. on Coastal Eng., ASCE, pp.588-608.

Longuet-Higgins, M.S. (1952): On the statistics of the heights of sea waves, J. Mar. Res., Vol.11, No.3, pp.245-266.

Longuet-Higgins, M.S. (1975a): Integral properties of periodic gravity waves of finite amplitude, Proc. Roy. Soc. London, A342, pp.157-174.

Longuet-Higgins, M.S. (1975b): On the joint distribution of the periods and amplitudes of sea waves, J. Geophys. Res., Vol.80, No.18, pp.2688-2693.

Longuet-Higgins M. S. and R.W. Stewart (1960): The change in amplitude of short gravity waves on steady non-uniform currents, J. Fluid Mech, Vol.10, pp.529-549.

Longuet-Higgins, M. S. and Cokelet, E. D. (1976): The deformation of steep surface waves on water I -A numerical method of computation, Proc. R. Soc. Lond. A., Vol.350, pp.1-26.

Madsen, P.A., R. Murray and O.R. Sφrensen (1991): A new form of the Boussinesq equations with improved linear dispersion characteristics, Coastal Eng., Vol.15, pp.371-388.

Mase, H., H. Doi and Y. Iwagaki (1983): Effect of wave grouping on characteristics of irregular wave run-up, Proc. 30th Japanese Conf. on Coastal Eng., JSCE, pp.114-118. (in Japanese)

Mei, C.C. (1978): Numerical methods in water-wave diffraction and radiation, Ann. Rev. Fluid Mech., Vol.10, pp.393-416.

Mei, C.C. (1983): The Applied Dynamics of Ocean Surface Waves, John Wily & Sons, 740p.

Miche, A. (1944): Mouvements ondulatories de la mer en profendeur constante ou decroissante, Forme limit de la houle lors de som déferlement: Application aux digues maritimes, Ann. Ponts et Chausees, Tome 114.

Michell, J.H (1983): The highest waves in water, Phil. Mag. (5), Vol.36, pp.430-437.

Mitsuyasu, H. et al. (1975): Observation of the directional spectrum of ocean waves using a cloverleaf buoy, J. Phys. Oceanogr., Vol.5, No.4, pp.750-760.

Nishimura, H., K. Maruyama and H. Hirakuchi (1983): Wave field analysis by finite difference method, Proc. 30th Japanese Conf. on Coastal Eng., JSCE, pp.123-127. (in Japanese)

Panchang, V.G., B.Cushman-Roisin and B.R. Pearce (1988): Combined refraction-diffraction of short gravity waves in large coastal regions, Coastal Eng., Vol.12, pp.113-156.

Patric, D.A. and R.L. Wiegel (1955): Amphibian tractors in the surf, Proc. 1st Conf. on Ship and Waves, pp.397-422.

Penny, W. G. and A.T. Price (1952): Finite periodic stationary gravity waves in a perfect fluid, Phil. Trans., Roy. Soc. London, A244, pp.254-284.

Petruaskas, C and P.M. Aagaard (1970): Extrapolation of historical storm data for estimating design wave heights, Prept. 2nd Offshore Tech. Conf., No.1190, pp.I-409-428.

Phillips, O.M. (1977): The Dynamics of the Upper Ocean, 2nd ed., Camb. Univ. Press, 336p.

Pierson, W.J., G. Neuman and R.W. James (1955): Practical method for observing and forecasting ocean waves by means of wave spectra and statistics, H.O. Pub. 603, U.S. Navy Hydrographic Office.

Radder A.C. (1979): On the parabolic equation method for water-waves propagation, J.Fluid Mech., Vol.95, pp.159-176.

Sakai, T., T. Mizutani, H. Tanaka and Y. Toda (1986): Vortex formation in plunging breaker, Proc.20th Ocean Eng. Conf., ASCE, pp.711-723.

Sawaragi, T. and K. Iwata (1974): On wave deformation after breaking, Proc. 14th Int. Conf. on Coastal Eng., ASCE, pp.481-498.

Sawaragi, T., C.R. Ryu and M. Kusumi (1983): Destruction mechanism and design of rubble mound structure by irregular waves, Coastal Eng. in Japan, JSCE, Vol.28, pp.173-190.

Schwartz, L.W. (1974): Computer extension and analytical computation of Stokes' expansion for gravity waves, J. Fluid Mech, Vol.62, pp.553-578.

Skjelbreia, L. (1958): Stokes' third order approximation, Tables of function, Council on Wave Res., the Engineering Foundation, 337p.

Skjelbreia, L. and J. Hendrickson (1960): Fifth order gravity waves theory, Proc. 7th Int. Conf. on Coastal Eng., ASCE, pp.184-196.

Smith, R. and T. Sprinks (1975): Scattering of surface waves by a cnoiical island, J. Fluid Mech., Vol.72, Part 2, pp.373-384.

Stoker, J.J. (1948): The formation of breakers and bores, The theory of nonlinear wave propagation in shallow water and open channels, Comm. Pure Appl. Math., Vol.1.

Stokes, G.G. (1880): On the theory of oscillatory waves, Mathematical Physics Papers, Camb. Univ. Press, Vol.1.

Tadjibaksh, I. and J.B. Keller (1960): Standing surface waves of finite amplitude, J. Fluid Mech., Vol.8, pp.442-451.

Teung, R.W. (1982): Numerical method in free-surface flows, Ann. Rev. Fluid Mech., Vol.14, pp.395-442.

Tsay, T.K. and P.L.F. Liu (1982): Numerical solution of water-wave refraction and diffraction problems in the parabolic approximation, Appl. Ocean Res., Vol.5, No.1, pp.30-37.

Tsuchiya, Y., T. Yasuda and Y. Takeyama (1981): Soliton spectrum theory without interaction, Proc. 28th Japanese Conf. on Coastal Eng., JSCE, pp.89-93. (in Japanese)

Whitham, G.B. (1962): Mass, momentum and energy flux in water waves, J. Fluid Mech., Vol.12, pp.135-147.

Wiegel, R.L. (1964): Oceanographical Engineering, Prentice Hall, 523p.

Yamada, H. (1957): On the highest solitary wave, Rept. Res. Inst. Appl. Mech. Kyushu Univ., 5, pp.53-67.

Yeung, R.W. (1982): Numerical method in free-surface flows, Ann. Rev. Fluid Mech., Vol. 14, pp.395-442.

Chapter 2   Wave Interactions with Structures and Hydrodynamic Forces

2.1 Introduction

2.1.1 Classification of marine structures

Various kinds of structures are utilized in coastal and harbor regions. For instance, we can immediately recall massive structures, such as a breakwaters, detached breakwaters, sea dikes, piers and so on. On the other hand, as more recently developed marine structures, we can easily recall fixed or floating platforms that have been used offshore for exploring and developing underwater natural resources, especially undermined oil in the sea floor. There is another kind of marine structure which is used for fisheries and aquacultural development, such as an artificial reef and a floating cage.

With respect to coastal and harbor structures, numerous comprehensive studies have been done on wave loading and wave deformation around these structures. Voluminous engineering literature about those works has already been published (e.g., Goda 1977).

The topics of hydrodynamics of offshore and marine structures are comparatively new. Only for a circular cylindrical body, a number of studies, especially concerning the diffraction wave force originally analyzed by MacCamy and Fuchs (1954) and the experimental works based on the Morison equation, have been conducted. However, there is only limited literature regarding wave interactions with more general offshore and marine structures of various shapes and types. In this chapter, after having classified briefly the offshore structures into the following three categories, hydrodynamic interaction between waves and the structures is discussed.

① Fixed large body, ② Fixed small body and ③ Floating body

First, remarking on the difference between large and small bodies from hydrodynamic aspects, it can be stated shortly that whether the influence of a structure on waves reaches a much wider region or not. Therefore, for a large body, due to the generation of distinctive scattered waves by the structure, the disturbance propagates for a much wider area far from the body. On the contrary, for a small body, which is characterized by the generation of separated flows in the neighborhood of the body, the influence of a body is bounded to a comparatively narrow area.

Isaacson (1979) has presented a comprehensive figure describing the generation mechanism of wave force on a circular cylindrical body, as seen in Fig. 2.1. In the figure, the dominant cause of wave force generation is specified as a function of the diffraction parameter, D/L (D: diameter of the cylinder, L:wavelength), and the Keulegan-Carpenter number, KC. The diffraction parameter is known as an important dimensionless variable relating to the intensity of scattered waves. KC is also known as an important parameter that is closely correlated with the wake development behind a cylinder and is defined by U_mT/D (U_m: velocity amplitude, T:wave period). According to this figure, it is seen that, for larger D/L, effect of wave scattering on the wave loading becomes more important. Also, for higher KC, the effect of the flow separation and the resultant vortex formation becomes more evident. Isaacson pointed out that the critical value of D/L dividing large and small body regimes is about 0.2 because KC becomes 2 at the most for the range of $D/L>0.2$ due to wave breaking. Under such a condition of KC, it is well known that the flow separation effect may be ignored in wave force calculation. However, it is noticed that the criterion described above is mainly for a rounded body, especially for a circular
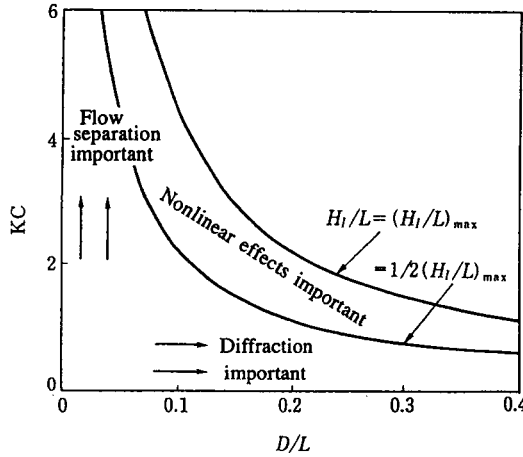
Fig. 2.1   Classification of wave force regimes (Isaacson 1979)

cylindrical body. For an angular body like a rectangular cylinder or plate, flow separation inevitably occurs and this resultant effect might not be negligible. Research on this subject must be continued in the future.

At present, anyhow, D/L=0.2 is used as a rough estimate of the critical boundary dividing the two regimes, large and small bodies, from the hydrodynamic aspect.

On the other hand, in the case of a floating body, there appears another hydrodynamic force due to body motion in addition to the wave forces exerted on the body under the fixed condition. The generation mechanism of hydrodynamic forces due to body motion can also be classified briefly into two regimes in the same way as the case of a fixed body. For a large floating body, the effect of radiation waves due to body motion becomes more significant for estimating the dynamic response.

There is another type of structure that has the features of both large and small bodies, like a permeable breakwater and an artificial fish reef. Hence, each member of the structure has small enough dimensions compared to the wavelength. However, because the spacing between members of the structure is comparatively small and also the whole dimension of the structure is a significant order of the wavelength, both effects of the wave scattering by the whole body and the flow separation around each member should be simultaneously accounted for. For such a structure, we have to deal with both wave scattering by the structure and wave energy dissipation caused by the flow separation for a wave force and wave diffraction calculation. In this chapter, in order to be able to treat such a hybrid type structure, a method of numerical modeling of the vortex flow around a bluff body and also an analytical treatment of the wave transmission and reflection by permeable structures are presented in different sections. Finally, a basic principle of the wave impact force on the structure, which is known as a very powerful wave load, is also described.

2.1.2 Hydrodynamic force and surface stress

As described in Fig. 2.1, a generation mechanism of wave loads on offshore structures is dependent upon the relative dimension of the structure to wavelength and also KC. In order to estimate the hydrodynamic forces on the structure, we have to know the relation between fluid forces and surface stresses.

In Fig. 2.2, distribution of the pressure p and shearing stress τ on the submerged surface of the body is schematically shown, where a two-dimensional flow is assumed for simplicity.
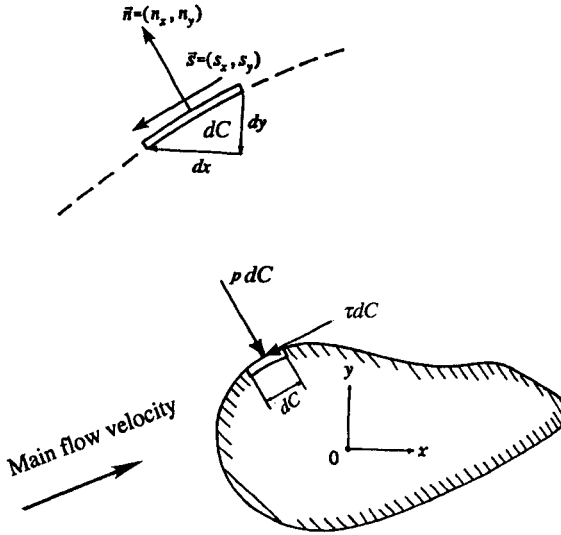
Fig. 2.2 Hydrodynamic forces and surface stresses

The fluid force and moment vectors per unit length of the body, $\mathrm{d}\vec{F}$ and $\mathrm{d}\vec{M}_z$ respectively, can be calculated by the simple integration of p and τ such as

$$\mathrm{d}\vec{F} = \int_C \left(-p\vec{n} + \tau\vec{s} \right)\mathrm{d}C \tag{2.1}$$

$$\mathrm{d}\vec{M}_z = \int_C \vec{r}_c \times \left(-p\vec{n} + \tau\vec{s} \right)\mathrm{d}C \tag{2.2}$$

where, C is a sectional curve of the body, $\vec{n}$ is a unit outward normal vector on C, and $\vec{s}$ is a unit tangential vector positive in a counterclockwise direction along C, $\vec{r}_c$ is a position vector extending from the origin to the submerged surface. A rotational vector $\mathrm{d}\vec{M}_z$ is assumed to be a moment about the z-axis that passes through the origin in an upright direction. Unit tangential and normal vectors can be expressed by the line element $\mathrm{d}C$ and its components $(\mathrm{d}x, \mathrm{d}y)$

$$\vec{s} = \left(s_x, s_y \right) = \left(\mathrm{d}x / \mathrm{d}C, \mathrm{d}y / \mathrm{d}C \right) \tag{2.3}$$

$$\vec{n} = \left(n_x, n_y \right) = \left(\mathrm{d}y / \mathrm{d}C, -\mathrm{d}x / \mathrm{d}C \right) \tag{2.4}$$

Using the middle expression of Eqs. (2.3) and (2.4), Eq. (2.1) can be rewritten for each directional component, dF_x and dF_y

$$dF_x = -\int_C pn_x dC + \int_C \tau s_x dC \tag{2.5}$$

$$dF_y = -\int_C pn_y + \int_C \tau s_y dC \tag{2.6}$$

In principle, fluid forces and moments can be obtained as the resultant vectors of local element force vectors, $-p\vec{n}$ and $\tau\vec{s}$, on the submerged surface.

For the practical design of offshore structures, it is well known that the contribution of pressure forces to wave loading is much larger than that of shearing forces because the shape of the body is hydrodynamically bluff and also the order of the Reynolds number ($=U_m D/\nu$, ν is the kinematic viscosity) may be greater than about 10^5. Sawaragi et al. (1979) reported that the ratio of the shearing force to the pressure force for a circular cylinder is less than about 5% in the range of an intermediate Reynolds number, 10^3-10^4.

In the following section, for the reason described above, it is assumed that wave loads on the structure can be given by the pressure force alone.

2.2 Boundary-Value Problems on Wave Interaction with Body

2.2.1 Governing equations and boundary conditions
(1) Formulation of the problem for a fixed body
It is presumed as an analytical model that an arbitrary three-dimensional body is placed in the wave field of constant depth h where monochromatic wave trains are propagating in the prescribed definite direction θ, and interacting with the body. It is also assumed that the fluid is incompressible and inviscid and its motion is irrotational. Under these assumptions, we can define a velocity potential, and then the problem determining fluid motion in the wave field is equivalent to seeking the velocity potential instead. A governing equation and boundary conditions for the velocity potential Φ around the fixed body, as shown in Fig. 2.3, are already prescribed in Chapter 1 and given by Eqs. (1.7), (1.21), and (1.24), respectively.

The velocity potential Φ around the body can be given by the summation of the incident wave potential Φ_I and the scattered wave potential Φ_S by the body.

$$\Phi = \Phi_I + \Phi_S \tag{2.7}$$

Φ must satisfy the kinematic boundary condition on the submerged surface S_B of a fixed body, that is a no-flux condition

$$\partial \Phi / \partial n = 0 \quad : \text{on } S_B \tag{2.8}$$

where, $\partial/\partial n$ is a normal derivative on S_B, and can be expressed as a function of a unit normal vector $\vec{n} = (n_x, n_y, n_z)$ which is defined as positive for outward normal from the body surface into the fluid.
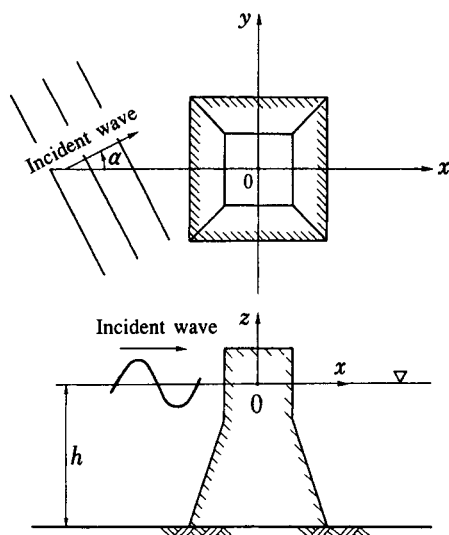
Fig. 2.3 Analytical model and definition sketch: the case of a fixed body

$$\frac{\partial}{\partial n} = \frac{\partial}{\partial x} n_x + \frac{\partial}{\partial y} n_y + \frac{\partial}{\partial z} n_z \tag{2.9}$$

If the body is made of elastic or flexible material, and is allowed to change its geometrical shape, additional boundary conditions are necessary in order to describe the equilibrium condition of forces acting on the body surface, which is a dynamic boundary condition. Details of this condition will be given in the later section, and at present we assume that the body is sufficiently rigid and no deformation can be seen.

Besides the no-flux condition on the submerged surface, Φ_S must satisfy another boundary condition that is termed the radiation condition originally introduced by Sommerfeld.

This condition mathematically assures the uniqueness of the solution and physically means that scattered waves must be outgoing and in a progressive mode in the far field from the body.

Linearized diffraction problems: The governing equations and boundary conditions described above can be used not only for small amplitude waves but also for finite amplitude waves. Here, for simplicity, it is assumed that nonlinear boundary conditions on the free surface can be approximated by the linearized ones and also the time dependency of Φ can be expressed by a simple harmonic motion with an angular frequency ω ($=T/2\pi$, T:wave period). Under these simplifications, the governing equation and boundary conditions can be summarized as

Governing equation:

$$\frac{\partial^2 \Phi}{\partial x^2} + \frac{\partial^2 \Phi}{\partial y^2} + \frac{\partial^2 \Phi}{\partial z^2} = 0 \tag{2.10}$$

Free surface boundary condition:

$$\eta = -\left(\frac{1}{g}\right)\frac{\partial \Phi}{\partial t}\bigg|_{z=0} \tag{2.11a}$$

$$\frac{\partial \eta}{\partial t} = \frac{\partial \Phi}{\partial z}\bigg|_{z=0} \tag{2.11b}$$

or combine these

$$\frac{\partial \Phi}{\partial z} = -\left(\frac{1}{g}\right)\frac{\partial^2 \Phi}{\partial t^2}\bigg|_{z=0} \tag{2.12}$$

Impermeable condition on the sea bed:

$$\frac{\partial \Phi}{\partial z}\bigg|_{z=-h} = 0 \tag{2.13}$$

where, Φ and η are the linearized velocity potential and its corresponding water surface elevation, respectively, and g is gravitational acceleration.

Φ also satisfies the kinematic boundary condition on the body surface and the radiation condition.

$$\frac{\partial \Phi}{\partial n} = \frac{\partial \Phi_I}{\partial n} + \frac{\partial \Phi_S}{\partial n} = 0 \quad : \text{on } S_B \tag{2.14}$$

$$\lim_{r \to \infty} \sqrt{r}\left(\frac{\partial \Phi_S}{\partial r} - ik\,\Phi_S\right) = 0 \tag{2.15}$$

in which r is a radial coordinate whose origin is located in the body, $i = \sqrt{-1}$ and k is a progressive mode wave number.

By using the latter condition, we can discard the inadequate solution included in the general solution of the governing equation for wave interactions with the body under consideration.

In the latter equation, the physical meaning of a multiplication of $\sqrt{r}$ is for compensating the decrease in wave amplitude due to the divergent nature of the scattered waves in circular form, which is proportional to $1/\sqrt{r}$ far from the body.

First, assuming a harmonic motion of waves, the time dependency of Φ_I and Φ_S is expressed as

$$\left(\Phi_I,\ \Phi_S\right) = \text{Real}\left[\left(\phi_I, \phi_S\right)\exp(-i\sigma t)\right] \tag{2.16}$$

where, Real[ ] is designated as taking a real part. ϕ_I and ϕ_S are complex amplitudes of incident and scattered waves, respectively. In the following, for simplifying notations, the expression of Real[ ] is omitted.

Using such a notation, the velocity potential of incoming waves with an incident angle α, as shown in Fig. 2.3, is represented as

$$
\begin{aligned}
\Phi_I(x, y, z, t)) &= \left[-\frac{igH_I}{2\sigma} \frac{\cosh k(h+z)}{\cosh kh} e^{i(kx\cos\alpha + ky\sin\alpha)} \right] \exp(-i\sigma t) \\
&= \phi_I(x, y, z)\exp(-i\sigma t)
\end{aligned}
\tag{2.17}
$$

where, H_I is the incident wave height.

Noting that Φ_I and Φ_S satisfy independently Eqs. (2.10)-(2.13), the governing equation and boundary conditions in terms of ϕ_S can be deduced by referring to Eqs. (2.10)-(2.15),

$$
\frac{\partial^2 \phi_S}{\partial x^2} + \frac{\partial^2 \phi_S}{\partial y^2} + \frac{\partial^2 \phi_S}{\partial z^2} = 0
\tag{2.18}
$$

$$
\frac{\partial \phi_S}{\partial z} = \frac{\sigma^2}{g}\phi_S \bigg|_{z=0}
\tag{2.19}
$$

$$
\frac{\partial \phi_S}{\partial z} = \frac{\sigma^2}{g}\phi_S \bigg|_{z=0}
\tag{2.20}
$$

$$
\frac{\partial \phi_I}{\partial n} + \frac{\partial \phi_S}{\partial n} = 0 \quad : \text{on } S_B
\tag{2.21}
$$

$$
\lim_{r \to \infty} \sqrt{r} \left(\frac{\partial \phi_S}{\partial r} - ik\phi_S \right) = 0
\tag{2.22}
$$

These equations are a set of governing equations and boundary conditions for a linearized wave boundary-value problem around a fixed body.

(2) Extension to a floating body

Next try to consider the more general case, in which the body is floating on the water surface and supported by some mooring lines as shown in Fig. 2.4.

However, the body is still rigid and there is no deformation with the body itself. In the same way as a fixed body case, if it is possible to use the potential flow theory, the velocity potentials of disturbed waves caused by the existence of a floating body and its motion have to satisfy Eqs. (1.23), (1.24), and (1.27). Total velocity potential around the floating body can be given by a superposition of the incident wave potential Φ_I and the disturbed wave potential Φ_B.

$$
\Phi = \Phi_I + \Phi_B
\tag{2.23}
$$
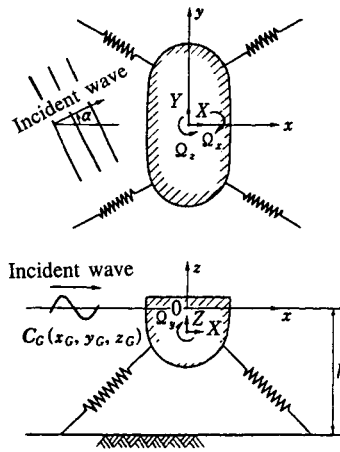
Fig. 2.4 Analytical model and definition sketch: the case of a floating body

Φ_B satisfies the same conditions for Φ_S, i.e., the kinematic boundary condition on the submerged surface and the radiation condition.

At first, try to derive the kinematic boundary condition on the submerged surface. At time $t=t$, it is assumed that the specific submerged surface is S_B and its surface function can be given by $z=f(x,y)$. Taking a total derivative of this surface function with time, the kinematic boundary condition can be derived

$$\left(\frac{\partial \Phi}{\partial x}\right)\left(\frac{\partial f}{\partial x}\right)+\left(\frac{\partial \Phi}{\partial y}\right)\left(\frac{\partial f}{\partial y}\right)+\frac{\partial f}{\partial t}=\frac{\partial \Phi}{\partial z} \quad : \text{on } S_B \qquad (2.24)$$

This surface changes with time and the variation directly corresponds to the motion of the floating body. Therefore, in order to determine the kinematics of the submerged surface, it is further required to describe the balance of forces acting on the body, including inertial forces and restoring forces due to mooring lines etc. In order to derive the equation of dynamics of the floating body, dynamic properties of the body, which determine natural modes and their characteristic frequencies, are necessary. In the most simple case of a three-dimensional rigid body, the motion consists of 6 different modes which are 3 translational and 3 rotational modes, i.e., translational motions are sway, heave and surge modes, and rotational motions are roll, pitch and yaw modes, respectively. Therefore, dynamic boundary conditions on the submerged surface can be expressed by the equations of motion for these 6 modes. Exciting force terms of these equations can be obtained by the Bernoulli equation, Eq. (1.22), after substituting $\Phi (= \Phi_I + \Phi_S)$ into this equation.

Linearized boundary-value problems for a floating body: Assuming that the small amplitude wave theory can be used for describing scattered and radiated waves by a floating body, the governing equation and boundary conditions, except for the kinematic condition on the submerged surface, are the same as those of a diffraction problem, i.e., Eqs. (2.10)-(2.12).

On the other hand, kinematic and dynamic boundary conditions on the submerged surface of the body can be derived at the equilibrium position of the body, after assuming small amplitude oscillations of the body. Such a derivation has already been given by John (1949).

At first, in the usual way of a perturbation method, we expand the submerged surface $z=f(x,y;t)$ of a floating body into a perturbation series around its equilibrium position $z=f_0(x,y)$

$$f(x, y, t) = f_0(x, y) + \sum_{n=1}^{\infty} \varepsilon^n f_n(x, y, t)$$

(2.25)

where, ε is a perturbation parameter.

Substituting both expansions of Φ and f of Eq. (2.25) into Eq. (2.24), and then taking only terms proportional to the order of ε,

$$\left(\frac{\partial \Phi_1}{\partial x}\right)\left(\frac{\partial f_0}{\partial x}\right) + \left(\frac{\partial \Phi_1}{\partial y}\right)\left(\frac{\partial f_0}{\partial y}\right) + \frac{\partial f_1}{\partial t} = \frac{\partial \Phi_1}{\partial z} \qquad : \text{on } z = f_0(x, y)$$

(2.26)

where Φ_1 is the velocity potential of the first order of ε. And $\partial f_1/\partial t$ included in Eq. (2.26) may be given by referring to the motion of the center of gravity of a floating body as following:

$$\begin{aligned}
\frac{\partial f_1}{\partial t} = & -\frac{\partial f_0}{\partial x}\left\{\frac{\partial X}{\partial t} + \frac{\partial \Omega_y}{\partial t}(z - z_G) - \frac{\partial \Omega_z}{\partial t}(y - y_G)\right\} \\
& -\frac{\partial f_0}{\partial y}\left\{\frac{\partial Y}{\partial t} + \frac{\partial \Omega_z}{\partial t}(x - x_G) - \frac{\partial \Omega_x}{\partial t}(z - z_G)\right\} \\
& +\frac{\partial Z}{\partial t} + \frac{\partial \Omega_x}{\partial t}(y - y_G) - \frac{\partial \Omega_y}{\partial t}(x - x_G)
\end{aligned}$$

(2.27)

Here, X, Y, and Z are translational mode responses of a floating body in the x, y, and z directions, respectively, and Ω_x, Ω_y, and Ω_z are rotational mode responses around the axes that pass through the center of gravity and are parallel to the x, y and z axes, respectively. (x_G, y_G, z_G) is the center of gravity of a floating body.

It is noted in Eq. (2.27) that only terms proportional to the order of ε is adopted, after expanding each mode response into the perturbation series.

Substituting Eq. (2.27) into Eq. (2.26), and also referring to the following relation based on three-dimensional geometry,

$$\vec{n} = \left(\frac{\partial f_0}{\partial x}, \frac{\partial f_0}{\partial y}, -1\right) \bigg/ \sqrt{1 + \left(\frac{\partial f_0}{\partial x}\right)^2 + \left(\frac{\partial f_0}{\partial y}\right)^2}$$

(2.28)

The linearized kinematic boundary condition on the submerged surface can be obtained after some manipulation

$$\begin{aligned}
\frac{\partial \Phi_1}{\partial n} = & \left(\frac{\partial X}{\partial t}, \frac{\partial Y}{\partial t}, \frac{\partial Z}{\partial t}\right)(n_x, n_y, n_z) \\
& + \left(\frac{\partial \Omega_x}{\partial t}, \frac{\partial \Omega_z}{\partial t}, \frac{\partial \Omega_z}{\partial t}\right)(\vec{R}_G \times \vec{n}) \qquad : \text{on } z = f_0(x, y)
\end{aligned}$$

(2.29)

where, $\vec{R}_G$ is the position vector directed from the center of gravity to the submerged surface.

Now, noting that the left hand side of Eq. (2.29) contains only the normal derivative of a linear order potential and also this condition is held at the equilibrium position of the floating body, that means at the fixed position, the kinematic condition for a fixed body surface should be included in Eq. (2.29). Therefore, subtracting Eq. (2.14) from Eq. (2.29), we can derive the kinematic boundary condition in terms of only the velocity potential caused by a body motion

$$
\begin{aligned}
\frac{\partial}{\partial n}\left(\Phi_B - \Phi_S\right) &= \frac{\partial \Phi_R}{\partial n} \\
&= \left(\frac{\partial X}{\partial t}, \frac{\partial Y}{\partial t}, \frac{\partial Z}{\partial t}\right)(n_x, n_y, n_z) \\
&+ \left(\frac{\partial \Omega_x}{\partial t}, \frac{\partial \Omega_y}{\partial t}, \frac{\partial \Omega_z}{\partial t}\right)\left(\vec{R}_G \times \vec{n}\right) \quad : \text{on } z = f_0(x, y)
\end{aligned}
\tag{2.30}
$$

where, Φ_R is the difference between Φ_B and Φ_S, which represents a velocity potential caused by a body motion. In the terminology, such a potential is called a radiated wave potential.

Consequently, the velocity potential around the oscillating floating body consists of three different potentials, i.e.,

$$
\Phi = \Phi_I + \Phi_S + \Phi_R
\tag{2.31}
$$

In the above, the notation expressing the first order component of the perturbation series, "1", has already been omitted for simplification.

Substituting Eq. (2.31) into Eqs. (2.10) to (2.12) and then subtracting the corresponding governing equation and boundary conditions to Φ_I and Φ_S from these equations, a set of governing equation and boundary conditions for Φ_R can be obtained in the following:

$$
\frac{\partial^2 \Phi_R}{\partial x^2} + \frac{\partial^2 \Phi_R}{\partial y^2} + \frac{\partial^2 \Phi_R}{\partial z^2} = 0
\tag{2.32}
$$

$$
\frac{\partial \Phi_R}{\partial z} = -\left(\frac{1}{g}\right)\left.\frac{\partial^2 \Phi_R}{\partial t^2}\right|_{z=0}
\tag{2.33}
$$

$$
\left.\frac{\partial \Phi_R}{\partial z}\right|_{z=-h} = 0
\tag{2.34}
$$

Φ_R also satisfies the kinematic boundary condition given by Eq. (2.30). With respect to the dynamic boundary condition, we can derive it by considering the dynamic equilibrium of a floating body on which various forces are acting, such as exciting wave forces, mass inertia forces, hydrostatic restoring forces, mooring line forces and so on. This dynamic

equilibrium condition is finally reduced to a set of equations of motion for a floating body. In addition to the above boundary conditions, it is further required for Φ_R to satisfy the radiation condition having the same form of Eq. (2.15).

As described above, under the assumption of the linearization, the wave boundary-value problem around a floating body can be decomposed into two independent problems, i.e., a diffraction problem and a radiation problem.

It is noticed that the principle of linear superposition can be used to obtain Φ_R because it satisfies the linear boundary value problem. Therefore, we can further decompose Φ_R into independent potentials associated with corresponding independent dynamic modes. Hence Φ_R can be expressed by a linear summation of element potentials $\Phi_{Rj}(j=1\sim6)$ caused by the harmonic motion with unit amplitude velocity in each dynamic mode.

$$
\begin{aligned}
\Phi_R = \phi_{R1}\left(\frac{\partial X}{\partial t}\right) + \phi_{R2}\left(\frac{\partial Y}{\partial t}\right) + \phi_{R3}\left(\frac{\partial Z}{\partial t}\right) \\
+ \phi_{R4}\left(\frac{\partial \Omega_x}{\partial t}\right) + \phi_{R5}\left(\frac{\partial \Omega_y}{\partial t}\right) + \phi_{R6}\left(\frac{\partial \Omega_z}{\partial t}\right)
\end{aligned}
\tag{2.35}
$$

2.2.2 Possible analytical solution

In this section, one of the available analytical solutions for linearized wave boundary-value problems is introduced. The well known result is based on the diffraction theory by MacCamy and Fuchs (1954). It is noted here that analytical solutions are available only for comparatively simple shaped bodies, such as a vertical circular cylinder, elliptical cylinder and so on.

(1) Scattered wave potential

The analytical model used here is specified in Fig. 2.5.
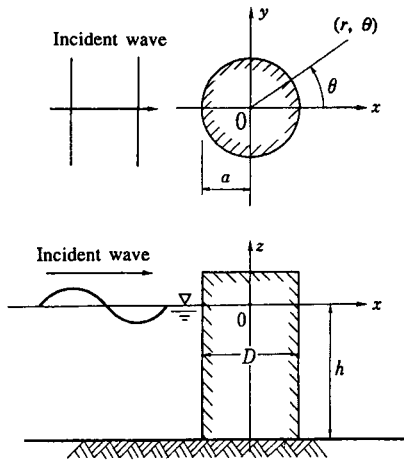
Fig. 2.5 Definition sketch for a vertical circular cylinder

A vertical circular cylinder of radius a is fixed on the sea floor with constant water depth h. It is assumed that waves are incident along the x axis from its negative to positive direction, and also the small amplitude wave theory can be used. In this case, a velocity potential of the incident wave train can be given by Eq. (2.17), but setting an incident wave angle α to 0.

The scattered wave potential by the cylinder Φ_s is obtained as a solution which satisfies the governing equation and boundary conditions of Eqs. (2.10) - (2.15). Assuming a simple harmonic solution of an angular frequency ω as shown by Eq. (2.15), the governing equation for a complex amplitude of the scattered wave potential ϕ_s can be written by the use of a cylindrical coordinate system (r, θ, z)

$$\frac{1}{r}\frac{\partial}{\partial r}\left(r\frac{\partial \phi_s}{\partial r}\right)+\frac{1}{r^2}\frac{\partial^2 \phi_s}{\partial \theta^2}+\frac{\partial^2 \phi_s}{\partial z^2}=0 \tag{2.36}$$

In order to solve Eq. (2.36) based on a separation of variables, we may assume the solution like the following form:

$$\phi_s(r, \theta, z)=\varphi(r, \theta)\mathit{\Pi}(z) \tag{2.37}$$

Substituting this into Eq. (2.36) and then doing some manipulations, we can obtain the following two sets of differential equations:

$$\frac{d^2\mathit{\Pi}}{dz^2}-C\mathit{\Pi}=0 \tag{2.38}$$

$$\frac{\partial^2 \varphi}{\partial r^2}+\frac{1}{r}\frac{\partial \varphi}{\partial r}+\frac{1}{r^2}\frac{\partial^2 \varphi}{\partial \theta^2}+C\varphi=0 \tag{2.39}$$

where, $\mathit{\Pi}$ is a function of z only, φ is a function of polar coordinates (r, θ), and C is a constant and not dependent upon (r, θ, z).

At first setting $C = k^2$ (k = real) and then solving Eq. (2.38) with the prescribed boundary conditions, Eqs. (2.19) and (2.20), the function $\mathit{\Pi}(z)$ can be determined

$$\mathit{\Pi}(z)=A_0\frac{\cosh k(h+z)}{\cosh kh} \tag{2.40}$$

where, A_0 is an arbitrary constant and k is the wave number of progressive mode waves, which satisfies the following dispersion relation:

$$\sigma^2 = g k \tanh kh \tag{2.41}$$

On the other hand, noting that φ is a function of (r, θ) and symmetrical about the x-z plane, we may expand it as a Fourier cosine series

$$\varphi(r, \theta) = \sum_{m=0}^{\infty} R_m(r) \cos(m\theta) \tag{2.42}$$

where, R_m is a function of only r and a Fourier coefficient of mode m.

Substituting Eq. (2.42) into Eq. (2.39), the ordinary equation for R_m is obtained

$$\frac{d^2 R_m}{dr^2} + \frac{1}{r} \frac{dR_m}{dr} + \left(k^2 - \frac{m^2}{r^2} \right) R_m = 0 \quad : (m = 0, 1, 2, \cdots \cdots) \tag{2.43}$$

This ordinary differential equation is known as the Bessel equation of order m with parameter k (e.g., Wylie 1966). The general solution of this equation is given by

$$R_m(r) = C_m H_m^{(1)}(kr) + D_m H_m^{(2)}(kr) \tag{2.44}$$

where, C_m and D_m are integral constants, $H_m^{(1)}$ and $H_m^{(2)}$ are the first and second kind of Hankel functions, respectively.

By using the radiation condition, Eq. (2.22), we can discard the term proportional to $H_m^{(2)}$ of Eq. (2.44) and then the solution is

$$\phi_S(r, \theta, z) = -\frac{igH_I}{2\sigma} \frac{\cosh k(h+z)}{\cosh kh} \sum_{m=0}^{\infty} C_m^* H_m^{(1)}(kr) \tag{2.45}$$

where, C_m^* is a newly defined constant which relates to both A_0 and C_m.

C_m^* can be determined by using the kinematic boundary condition on the submerged surface of the vertical cylinder and may be given by

$$C_m^* = -(2 - \delta_{m0}) \frac{i^m J_m'(ka)}{H_m^{(1)'}(ka)} \tag{2.46}$$

where, J_m is the first kind of Bessel function of order m, and δ_{m0} is the Kronecker delta and has the following property

$$\delta_{ij} = \begin{cases} 1 & : i = j \\ 0 & : i \neq j \end{cases}$$

and upper prime means the derivative.

The final form of the total velocity potential around the vertical cylinder can be derived as

$$\phi(r, \theta, z, t) = \left\{ \sum_{m=0}^{\infty} \phi_m(r) \cos(m\theta) \right\} \frac{\cosh k(h+z)}{\cosh kh} \exp(-i\sigma t) \tag{2.47}$$

where, ϕ_m is the amplitude of the velocity potential corresponding to the Fourier mode m and is given by

$$\phi_m(r) = i^m (2 - \delta_{m0}) \left\{ J_m(kr) - \frac{J_m'(ka)}{H_m^{(1)'}(ka)} H_m^{(1)}(kr) \right\} \tag{2.48}$$

(2) Wave forces and wave height distributions

Wave pressure p on the submerged surface of the cylinder can be calculated by inserting of Eq. (2.47) into the Bernoulli equation (ref. to Eq. (1.31)).

$$p\big|_{r=a} = \frac{\rho g H_I}{\pi ka} \frac{\cosh k(h+z)}{\cosh kh} \left\{ \sum_{m=0}^{\infty} \frac{i^{m+1}(2 - \delta_{m0})}{H_m^{(1)'}(ka)} \cos(m\theta) \right\} \tag{2.49}$$

where, ρ is the fluid density. On the derivation process of Eq. (2.49), the following relation with Bessel functions is used.

$$J_m(x) H_m^{(1)'}(x) - J_m'(x) H_m^{(1)}(x) = \frac{2i}{\pi x}$$

In Eq. (2.49), an infinite summation with respect to Fourier mode m appears. However, for practical calculation, approximation accounting only to the finite series summation must be used. In such an approximation, it is usual to set an adequate error criteria of convergence, e.g., 2 or 3%, and then to carry out the summation of the series until the convergence criteria is satisfied.

Although the wave pressure calculation has some uncertainty with the convergence, there is no ambiguity with the wave force calculation. For the wave force calculation, we can take advantage of the orthogonality property of trigonometric functions that are included in Eq. (2.49) and the force equation, Eq. (2.5). Using such an orthogonality property, the horizontal wave force on the vertical cylinder F_x can be obtained with certainty

$$F_x = \frac{2\rho g H_I \tanh kh}{k^2 H_1^{(1)'}(ka)} \exp(-i\sigma t) \tag{2.50}$$

and also the overturning moment about the sea bed M_y is given by

$$M_y = \frac{2\rho g H_I (kh \tanh kh + \operatorname{sech} kh - 1)}{k3 H_1^{(1)'}(ka)} \exp(-i\sigma t) \tag{2.51}$$

On the other hand, wave elevation around the vertical cylinder η can be obtained through the use of a dynamic boundary condition, Eq. (2.11a).

$$\eta(r, \theta, t) = \frac{H_I}{2}\left[\sum_{m=0}^{\infty} i^m (2-\delta_{m0})\left\{J_m(kr) - \frac{J_m^{'}(ka)}{H_m^{(1)'}(ka)} H_m^{(1)}(kr)\right\}\right.$$
$$\left. \times \cos(m\theta)\right]\exp(-i\sigma t) \qquad (2.52)$$

For the practical calculation of η, we have to reside to the same technique as that of the wave pressure calculation for the convergence problem.

One of the typical calculation results of the horizontal wave force is shown in Fig. 2.6, in which the ratio of a diameter D to the water depth h is fixed to 1.0.
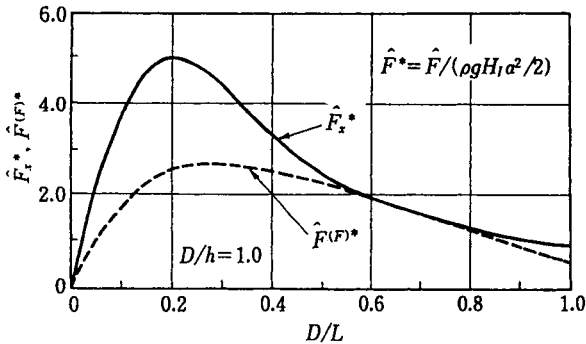
Fig. 2.6 Calculation results of wave forces on a vertical circular cylinder by the diffraction theory

In the figure, the so-called Froude-Krylov force $\hat{F}^{(F)}$, that is obtained by ignoring the wave scattering effect by the cylinder, is also plotted. From this figure, it can be seen that the nondimensionalized horizontal wave force $\hat{F}_x^*$ by the use of an incident wave amplitude($=H_I/2$) shows a peak at $D/L \approx 0.2$, which is consistent to the critical value of D/L between large and small bodies. It is also seen that the horizontal wave force cannot be altered by the Froude-Krylov force $\hat{F}^{(F)}$ except in the range of $0.6 \leq D/L \leq 0.8$. Therefore, for the practical estimation of the wave force on a vertical circular cylinder, it is necessary to account for the wave scattering by the cylinder.

In Fig. 2.7, the effective inertia coefficient $\hat{C}_M$ of the vertical cylinder corresponding to the result of Fig. 2.6 is shown.

Effective inertia coefficients can be obtained by applying only the inertia force equation of the Morison formula to the calculated wave forces. However, in the calculation, phase relationships between incident waves and wave forces are ignored. In the frame work of this expression, the horizontal wave force on the vertical cylinder can be represented
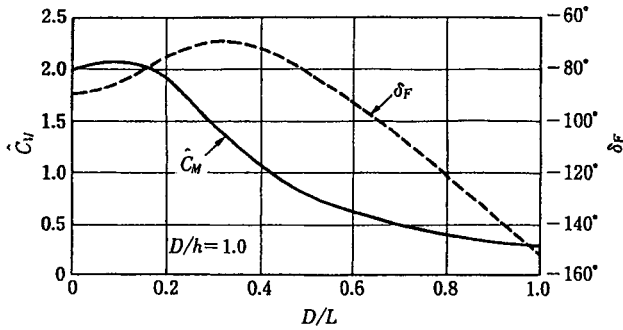
Fig. 2.7 Effective inertia coefficients and phase lags of the wave force on a vertical circular cylinder

$$F_x = \hat{C}_M \rho \left(\frac{\pi D^2}{4} \right) \int_{-h}^{0} \left(\frac{\partial u}{\partial t} \right)_{max} dz \, \cos(\sigma t - \delta_F) \tag{2.53}$$

where, $(\partial u/\partial t)_{max}$ is the amplitude of the local acceleration of water particles in the x direction at the center of the cylinder by incident waves, δ_F is the phase lag of the wave force from the incident wave.

From this figure, it is seen that the effective inertia coefficient $\hat{C}_M$ decreases for larger D/L and becomes 0.3 at $D/L \approx 1$, which is about 1/7 of the inertia coefficient of the small cylinder $\hat{C}_M \approx 2.0$. Therefore if the $\hat{C}_M$ value of 2.0, which is adequate for a small cylinder, is used for the wave force calculation of a large circular cylinder, such an estimation is much greater than the real wave load and results in a very uneconomical design.

As described above, the wave force estimation based on the wave diffraction theory gives us an economical design of large offshore structures and it has a characteristic of intensifying the importance of spatial variation of the wave field around the body for the wave load estimation.

2.3 Numerical Analysis on the Wave Boundary-Value Problems

As partly described in the preceding section, analytical solutions are available only for bodies having comparatively simple geometry, such as a vertical circular cylinder and an elliptical cylinder. In this section, basic theory of the numerical analysis on wave boundary-value problems, which can be applied to various shaped large bodies by computers, is introduced.

Available numerical procedures until recently may be largely classified into two groups. One is to deal with the entire fluid domain directly and to seek an unknown velocity potential on each element of the fluid domain from the boundary conditions. Another one is to deal with the boundary values on the surrounding surface of the fluid domain, including the normal derivative of the velocity potential. After having obtained both the velocity potential and its normal derivative, the velocity potential in the fluid domain can be calculated from these boundary values. In the latter procedure, we cannot directly obtain the unknown velocity potential in the fluid domain. The well-known procedure belonging to the former group is the finite element method, which is familiar and frequently used in

the field of structural mechanics. On the other hand, numerical methods of the latter group are generally called the boundary integral equation method (BIEM), because a basic equation is deduced from an integral equation for the surrounding surface of the fluid domain and the submerged surface of the body. There are several variations with the latter procedure, such as a method based on Green's formula and its modified version, e.g., Green's function method.

In this section, the latter procedure is mainly described, which is often preferred by coastal and ocean engineers, because in the latter procedure the number of dimensions of the framework can be reduced by one compared to the former procedure. For instance, we can solve the three-dimensional problems by a two-dimensional equation and the two-dimensional problems by a one-dimensional equation. Therefore it may be possible to solve the problem much more efficiently than the former procedure.

2.3.1 Application of Green's formula

Here, a more general three-dimensional flow is treated. When the governing equation is the Laplace equation, such as a potential flow around a three-dimensional body, Green's second formula becomes a powerful tool for the analysis

$$
\iint_S \left\{ \psi_1 \left(\frac{\partial \psi_2}{\partial \overline{n}} \right) - \psi_2 \left(\frac{\partial \psi_1}{\partial \overline{n}} \right) \right\} dS \\
= \iiint_V \left(\psi_1 \nabla^2 \psi_2 - \psi_2 \nabla^2 \psi_1 \right) dV
$$

(2.54)

where ψ_1 and ψ_2 are assumed to be continuous functions of (x, y, z) in the fluid domain V and on its surrounding surface S. Also the first and second derivatives of these functions are also continuous on the same domain. And $\partial / \partial \overline{n}$ specifies a normal derivative in the outward direction on the surface S. This equation can be derived from the Gauss divergence theorem that is well known in the field of hydrodynamics.

Now, consider a fluid domain V_F enclosed by the outer surface S_O and bounded by the body surface S_B fixed in the domain, as shown in Fig. 2.8.
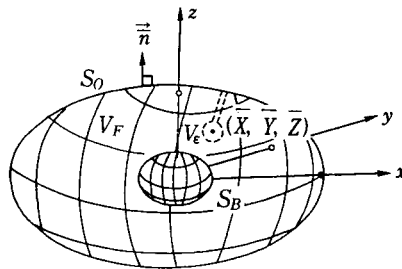

Fig. 2.8 Analytical model used for derivation of Green's formula

Suppose that we wish to analyze the potential flow around the body. We can set the unknown velocity potential Φ as ψ_1 and also a three-dimensional source function with unit strength Φ_W as ψ_2 in Eq. (2.54). Here, a three-dimensional source function Φ_W is given by

$$\Phi_W\left(x, y, z\,;\,\overline{X}, \overline{Y}, \overline{Z}\right) = -\frac{1}{4\pi R_S} \tag{2.55}$$

In this equation, (x, y, z) is the coordinate of a field point, $(\overline{X}, \overline{Y}, \overline{Z})$ is the source point and R_S is the distance between the two points denoted by

$$R_S = \sqrt{\left(x - \overline{X}\right)^2 + \left(y - \overline{Y}\right)^2 + \left(z - \overline{Z}\right)^2}$$

If we use the above setting, Eq. (2.54) can be transformed into the following equations due to the reasons described later:

(i) When the source point is inside V_F:

$$\iint_{S_o + S_B} \left\{ \Phi\left(\frac{\partial \Phi_W}{\partial \overline{n}}\right) - \Phi_W\left(\frac{\partial \Phi}{\partial \overline{n}}\right) \right\}\, dS(x, y, z) = \Phi(\overline{X}, \overline{Y}, \overline{Z}) \tag{2.56a}$$

(ii) When the source point is on S_F or S_O:

$$P.V. \iint_{S_o + S_B} \left\{ \Phi\left(\frac{\partial \Phi_W}{\partial \overline{n}}\right) - \Phi_W\left(\frac{\partial \Phi}{\partial \overline{n}}\right) \right\}\, dS(x, y, z) = \frac{\Phi(\overline{X}, \overline{Y}, \overline{Z})}{2} \tag{2.56b}$$

(iii) When the source point is outside V_F:

$$\iint_{S_o + S_B} \left\{ \Phi\left(\frac{\partial \Phi_W}{\partial \overline{n}}\right) - \Phi_W\left(\frac{\partial \Phi}{\partial \overline{n}}\right) \right\}\, dS(x, y, z) = 0 \tag{2.56c}$$

where, $P.V.$ denotes the Cauchy principal integration.

The reason Eq. (2.54) is divided into three cases is that the source function Φ_W has a singular nature when the source point approaches the field point, i.e., Φ_W diverges.

Let us consider the case of Eq. (2.56a), where the source point is included in the domain V_F. Then, Φ_W diverges under the condition of $(x, y, z) = (\overline{X}, \overline{Y}, \overline{Z})$ and Eq. (2.54) is not valid because Φ_W is not continuous. In order to avoid this difficulty, the new fluid domain V_F' in which the singular point is excluded from V_F by a small sphere V_ε is used instead of V_F. For this new domain, Eq. (2.54) can be applied, but the surface integral about the small sphere V_ε must be newly added. Therefore, we get

$$\iint_{S_o + S_B + S_\varepsilon} \left\{ \Phi\left(\frac{\partial \Phi_W}{\partial \overline{n}}\right) - \Phi_W\left(\frac{\partial \Phi}{\partial \overline{n}}\right) \right\}\, dS(x, y, z) = 0 \tag{2.57}$$

where, S_ε is the enclosed surface of V_ε.

Noting that $\partial/\partial\overline{n}$ on S_ε is equal to $-\partial/\partial R_S$, we can carry out the surface integration about S_ε in the following way

$$
\iint_{S_\varepsilon} \left\{ \Phi\left(\frac{\partial \Phi_w}{\partial \overline{n}}\right) - \Phi_w\left(\frac{\partial \Phi}{\partial \overline{n}}\right)\right\} dS(x, y, z)
$$

$$
= \iint_{S_\varepsilon} \left\{\left(\frac{-1}{4\pi R_S^2}\right)\Phi - \left(\frac{1}{4\pi R_S}\right)\left(\frac{\partial \Phi}{\partial R_S}\right)\right\} dS(x, y, z) \tag{2.58}
$$

$$
= -\Phi(\overline{X}, \overline{Y}, \overline{Z})
$$

In which, however, the process taking limitation $V_\varepsilon \to 0$ is considered after the integration.

By taking this result into account, Eq. (2.56a) is finally obtained.

For the second case, in which the source point is placed on the enclosed surface, Eq. (2.56b) is derived in the same manner as of Eq. (2.56a) after excluding the source point from V_F, but in this case by a semi-sphere. Therefore, the result of surface integration becomes one half of Eq. (2.58) and the final form results in Eq. (2.56b).

The physical aspect of Eq. (2.56) is quite interesting and significant. According to these equations, the potential flow can be obtained by the distribution of sources and dipoles (normal derivative of a source function) with adequate strength on both the surrounding surface and the body surface. Therefore once the strength of the source and dipole distributions has been determined, we can easily calculate the inside flow field. This point is advantageous to the direct domain analysis, which needs to treat the whole fluid domain simultaneously.

In the following, using Eq. (2.56), one typical example of analysis on the potential flow about an arbitrary three-dimensional body is shown.

(1) In the case of a three-dimensional flow

Unidirectional flow along the x-axis is assumed as a main flow about a three-dimensional fixed body. The velocity potential of this main flow Φ_I can be given by

$$
\Phi_I = Ux \tag{2.59}
$$

where, U is the main flow velocity.

An unknown potential Φ_S, which arises from the interaction between the main flow and the body, can be obtained by using Eq. (2.56). First, we shall define the fluid domain V_F bounded outside by a large sphere whose radius is large enough to enclose the fixed body and bounded inside by the body surface. Substituting Φ_S into Φ in Eq. (2.56b), and also noting the no-flux condition on the body surface, we may get

$$
P.V. \iint_{S_o} \left\{ \Phi\left(\frac{\partial \Phi_w}{\partial \overline{n}}\right) - \Phi_w\left(\frac{\partial \Phi_S}{\partial \overline{n}}\right)\right\} dS(x, y, z)
$$

$$
+ P.V. \iint_{S_B} \left\{ \Phi_S\left(\frac{\partial \Phi_w}{\partial \overline{n}}\right) + \Phi_w\left(\frac{\partial \Phi_I}{\partial \overline{n}}\right)\right\} dS(x, y, z) \tag{2.60}
$$

$$
= \frac{\Phi_S(\overline{X}, \overline{Y}, \overline{Z})}{2} \qquad : (\overline{X}, \overline{Y}, \overline{Z}) \quad \text{on } S_B, S_O
$$

As the radius of an outer sphere can be expanded without loss of generosity, we can adopt the far field value for the normal derivative of Φ_S on the virtual sphere surface, i.e., $\partial \Phi_S / \partial \overline{n} = 0$. Also, noting that $\partial \Phi_W / \partial \overline{n}$ diminishes on the outer sphere, Eq. (2.60) becomes

$$\frac{\Phi_S(\overline{X}, \overline{Y}, \overline{Z})}{2} - P.V. \iint_{S_B} \Phi_S \frac{\partial \Phi_W}{\partial \overline{n}} dS(x, y, z)$$
$$= \iint_{S_B} \Phi_W \frac{\partial \Phi_I}{\partial \overline{n}} dS(x, y, z) \qquad : (\overline{X}, \overline{Y}, \overline{Z}) \quad \text{on } S_B \tag{2.61}$$

In this equation, only the unknown potential Φ_S on the body surface is included. In an analogous manner, in Eq. (2.56a), the integral surface $(S_O + S_B)$ can be changed to S_B.

Eq. (2.60) is an integral equation in which the unknown potential Φ_S appears on the left-hand side and the known potential Φ_I on the right-hand side. In general, this equation is solved numerically after adopting adequate discretization techniques. For instance, decomposing the body surface S_B into small panels ΔS and then assuming that the strength of sources and potentials is constant on the small facet, we can derive the discretized equation of Eq. (2.61) as

$$\sum_{j=1}^{N} \alpha_{ij} \frac{\partial \Phi_{Sj}}{\partial t} = \frac{\partial \gamma_i}{\partial t} \quad : (i = 1, 2, 3, \cdots, N) \tag{2.62}$$

where, N is the total number of panels. α_{ij} and γ_i are defined by the following equations:

$$\alpha_{ij} = \frac{1}{2} \delta_{ij} - \iint_{\Delta S_i} \frac{1}{4\pi R_{Si}^2} \frac{\partial R_{Si}}{\partial \overline{n}} dS(x, y, z) \tag{2.63}$$

$$\gamma_i = \sum_{i=1}^{N} \iint_{\Delta S_i} \left(\frac{1}{4\pi R_{Si}^2} \right) \frac{\partial \Phi_I}{\partial \overline{n}} dS(x, y, z) \tag{2.64}$$

In the above equations, R_{Si} is given by

$$R_{Si} = \sqrt{\left(x - \overline{X}_i\right)^2 + \left(y - \overline{Y}_i\right)^2 + \left(z - \overline{Z}_i\right)^2}$$

Eq. (2.62) is a simultaneous equation of order N. Solving this equation, unknown potential Φ_S can be determined. After substituting this value of Φ_S into Eq. (2.56a), any velocity potentials inside the fluid domain can be obtained. But, in this case, the modification described above must be done with Eq. (2.56a). Also the velocity field in the fluid domain can be calculated by the equation that is derived after taking a derivative of Eq. (2.56a) with respect to $\overline{X}, \overline{Y}, \overline{Z}$ respectively. However, it is noticed that the velocity distribution on the body surface cannot be obtained by this equation. Other alternative method, e.g., taking a spatial derivative numerically from each surface value of potential, must be used.

On the other hand, a time derivative of the velocity potential, which is often required to calculate the unsteady fluid forces on the body, can be obtained by solving the following equation.

$$\sum_{j=1}^{N} \alpha_{ij} \Phi_{sj} = \gamma_i \ : \ (i = 1, 2, 3, \cdots, N) \tag{2.65}$$

This equation is derived from Eq. (2.62) by taking a time derivative.

There are several notices to carry out the numerical analysis by using the above techniques. The most noticeable point is how to deal with the singular functions, e.g., inverse functions included in α_{ij}. Such a numerical treatment has already been clarified by Hess and Smith (1964). For details, please refer to the paper.

(2) In the case of a two-dimensional flow

Green's formula for two-dimensional problems is given by only reducing the order of integration by one in Eq. (2.69), e.g., a surface integral is changed to a line integral and so on. A two-dimensional source function is used for Φ_W instead of a three-dimensional one. This two-dimensional source function is expressed by

$$\Phi_W \left(x, y ; \overline{X}, \overline{Y} \right) = \frac{1}{2\pi} \log (R_H) \tag{2.66}$$

where, (x, y) is a field point, $(\overline{X}, \overline{Y})$ is a source point and R_H is the distance between the two points and is given by

$$R_H = \sqrt{\left(x - \overline{X} \right)^2 + \left(y - \overline{Y} \right)^2} \tag{2.67}$$

Ijima et al. (1976) have developed the numerical procedure for water wave problems about both fixed and floating bodies based on the two-dimensional Green's formula. Liu et al. (1982) have also specified a numerical procedure for the water wave diffraction about a thin walled-body, using a dipole function instead of a source function.

2.3.2 Source distribution method

Applying Green's function to Green's formula, various extensions of numerical analysis may be possible. One of these extensions is a source distribution method.

A theoretical background of this method was given by Lamb (1964). In the following, a brief of this method is introduced.

(1) Derivation of the method of analysis

First, assuming that the inside of the body is also a subsidiary fluid domain in addition to V_F in the preceding example. We shall denote the velocity potential of this subsidiary fluid domain as $\overline{\Phi}$. Applying Green's formula to the inner fluid domain and also assuming the source point is located outside the body, we may get

$$\iint_{S_B} \left\{ \overline{\Phi} \left(\frac{\partial G}{\partial n} \right) - G \left(\frac{\partial \overline{\Phi}}{\partial n} \right) \right\} dS \ (x, y, z) = 0 \tag{2.68}$$

where, G is Green's function of the outer fluid domain and $\partial / \partial n$ is a normal derivative in the outward direction from the body surface and has an opposite positive direction to $\partial / \partial \overline{n}$ of Eq. (2.56).

Next, designating the velocity potential in the outer fluid domain as Φ and assuming the source point is located outside the body, the resulting Green's formula becomes Eq. (2.56a). But the integration surface should be replaced with S_B and also Φ_W with G. Subtracting this equation from Eq. (2.67) and noting that the positive direction of $\partial/\partial n$ and $\partial/\partial \bar{n}$ is opposite, we may deduce the following equation.

$$\Phi\left(\bar{X}, \bar{Y}, \bar{Z}\right) = \iint_{S_B} \left\{ \left(\bar{\Phi} - \Phi\right)\frac{\partial G}{\partial n} - G\left(\frac{\partial \bar{\Phi}}{\partial n} - \frac{\partial \Phi}{\partial n}\right) \right\} dS\,(x,y,z) \tag{2.69}$$

If we set the boundary condition on the body surface that $\bar{\Phi}$ is equal to Φ, and also define f_D given by the following equation:

$$f_D(x,y,z) = \frac{\partial \Phi}{\partial n} - \frac{\partial \bar{\Phi}}{\partial n} \tag{2.70}$$

the basic equation of the source distribution method is finally obtained.

$$\Phi\left(\bar{X}, \bar{Y}, \bar{Z}\right) = \iint_{S_B} f_D(x,y,z) G\left(\bar{X},\bar{Y},\bar{Z};x,y,z\right) dS\,(x,y,z) \tag{2.71}$$

In this equation, the velocity potential is expressed by only the distribution of G, i.e., a source function. And f_D corresponds to a strength of the source. Therefore, from the physical aspect, this method is much more understandable than the method of Green's formula, in which distributions of a source and dipole should be considered.

In general, another form of Eq. (2.71), in which the roles of a field point and a source point are interchanged, is usually used.

$$\Phi(x,y,z) = \iint_{S_B} f_D\left(\bar{X}, \bar{Y}, \bar{Z}\right) G\left(x,y,z ; \bar{X}, \bar{Y}, \bar{Z}\right) dS\,(\bar{X}, \bar{Y}, \bar{Z}) \tag{2.72}$$

The above interchange is possible due to the fact that Green's function has a reciprocity nature. In the last equation, (x, y, z) and $(\bar{X}, \bar{Y}, \bar{Z})$ corresponds to a field point and a source point, respectively and their definitions coincide to the former ones.

On the other hand, another different method of analysis is derived from Eq. (2.69). It is also based upon the distribution of singularities, but using a dipole or double source instead of a single source. A basic equation of this method can be obtained by setting $\partial \bar{\Phi}/\partial n = \partial \bar{\Phi}/\partial n$ on the body surface in Eq. (2.69). This method is effective especially for the potential flow problem about a thin-walled body.

(2) Example of a three-dimensional flow problem

Here, the same three-dimensional problem with the former example is considered. For this problem, the velocity potential Φ_S caused by the interaction between the unidirectional flow and a fixed body can be expressed by using Eq. (2.72) as follows:

$$\Phi_S(x,y,z) = \iint_{S_B} f_D\left(\bar{X}, \bar{Y}, \bar{Z}\right) G\left(x,y,z ; \bar{X}, \bar{Y}, \bar{Z}\right) dS\,(\bar{X}, \bar{Y}, \bar{Z}) \tag{2.73}$$

In the equation, the source strength f_D is unknown and has to be determined at first. The Green's function for this problem is a three-dimensional source function in an unbounded fluid, which has the same form as Φ_W given by Eq. (2.55).

The source strength f_D can be determined by the no-flux condition on the submerged surface of the body. Hence, inserting Eq. (2.73) into Eq. (2.8), we can obtain

$$
\iint_{S_B} f_D(\overline{X}, \overline{Y}, \overline{Z}) \frac{\partial G(x,y,z\,;\overline{X},\overline{Y},\overline{Z})}{\partial n(x,y,z)}\, dS(\overline{X}, \overline{Y}, \overline{Z})
$$
$$
= -\frac{\partial \Phi_I(x,y,z)}{\partial n(x,y,z)} \qquad :(x,y,z)\ \text{on}\ S_B
$$

(2.74)

This equation can be solved numerically after discretizing the body surface into a number of small facets in the same way as described in the preceding section. Once the source strength f_D has been determined, Φ_S can be obtained by Eq. (2.73) and the velocity field around the body is calculated by the equation derived after taking a spatial derivative of Eq. (2.73). In contrast to the method based on Green's formula, it is advantageous that the velocity distribution on the body surface can be calculated directly by the source distribution method.

On the other hand, in the case of a time dependent flow, the pressure force due to the fluid acceleration can be obtained by the equation derived after taking a time derivative of Eq. (2.73). Also the time derivative of source strength df_D/dt can be obtained by solving the simultaneous equation that is deduced after taking a time derivative of Eq. (2.74).

2.4 Analysis for Large Bodies

Here, we would like to introduce the numerical procedure for calculating wave loads on large bodies as well as the resultant effects of the body on the wave field, for which the wave diffraction phenomenon is important. The method applied here is the wave source distribution method described in the later part of the preceding section.

2.4.1 Wave diffraction around fixed bodies
(1) Three-dimensional analysis by the wave source distribution method

Available numerical procedures for the three-dimensional analysis of the water wave problems about large bodies can be classified briefly into the following four categories, depending upon the degree of restrictions to some definite configurations of the body.

Analysis based on ① the three-dimensional Green's function for an arbitrary body, ② the plane-symmetric Green's function for a body with plane symmetry, ③ the axisymmetric Green's function for a body with vertical axisymmetry and ④ the vertical line source Green's function for a vertical and surface piercing cylinder.

The method ① is the most general technique, but it also requires the heaviest power of computer, e.g., larger memory capacity and longer CPU time. By using an up-to-date computer, it still may not be enough to carry out the computations based on the method ①, especially for large and complicated marine structures. In order to resolve the difficulty, a more efficient algorithm such as in methods ② to ④ has been developed by taking advantage of the body geometry.

(a) Three-dimensional analysis for an arbitrary body: Let us consider the analytical model shown in Fig. 2.3, in which an arbitrary body is fixed in the wave field of constant water

depth h and struck by plane waves. We assume that the linear wave theory can be used to express the wave interaction with the body.

In this case, the incident wave potential Φ_I is given by Eq. (2.17). According to the source distribution method introduced in **2.3**, the complex amplitude of a scattered wave potential ϕ_S can be given by Eq. (2.73). In order to use this equation, it is necessary to find Green's function for the three-dimensional wave field, which satisfies the governing equation Eq. (2.18) and the boundary conditions from Eqs. (2.19) to (2.22), except for the no-flux condition on the submerged surface Eq. (2.21).

Such a Green's function G has already been obtained by John (1949). The series form of G is expressed as

$$G\left(x, y, z ; \overline{X}, \overline{Y}, \overline{Z}\right) = \frac{i}{2} \frac{\left(k^2 - k_0^2\right)}{\left\{\left(k^2 - k_0^2\right)h + k_0\right\}} \cosh k(h + z) \cosh k(h + \overline{Z})$$

$$\times H_0^{(1)}(kR_H) \tag{2.75}$$

$$+ \sum_{n=1}^{\infty} \frac{1}{\pi} \frac{\left(k_n^2 + k_0^2\right)}{\left\{\left(k_n^2 + k_0^2\right)h - k_0\right\}} \cos k_n(h + z) \cos k_n\left(h + \overline{Z}\right) K_0\left(k_n R_H\right)$$

where, k_0 is σ^2/g, K_0 is the modified Bessel function of the second kind with order 0, k_n is the evanescent mode wave number and R_H is the horizontal distance between the field point (x, y, z) in the wave field and the source point (X, Y, Z) on S_B. The evanescent mode wave number k_n is given by solving the following characteristics equation:

$$\frac{\sigma^2 h}{g} + k_n h \tan k_n h = 0 \quad : (n = 1, 2, 3, \cdots) \tag{2.76}$$

The first term of Eq. (2.75) specifies the progressive mode wave component that propagates in a circular form to the outward direction. On the other hand, the second term corresponds to the evanescent mode wave component that dampens rapidly with the distance from the body. Therefore, the first term is important in the wave field far from the body.

Another expression of G is the integral form, which is conveniently used for the deepwater condition. Such an expression is given by (e.g., Wehausen and Laitone 1960),

$$G\left(x, y, z ; \overline{X}, \overline{Y}, \overline{Z}\right) = \frac{1}{4\pi R_S} + \frac{1}{4\pi \hat{R}_S}$$

$$+ P.V. \int_0^{\infty} \frac{1}{2\pi} \frac{(\zeta + k_0)\exp(-k_0 h)\cosh \zeta(h + z)\cosh \zeta\left(h + \overline{Z}\right)}{\zeta \sinh \zeta h - k_0 \cosh \zeta h} J_0(\zeta R_H) d\zeta \tag{2.77}$$

$$+ \frac{i}{2} \frac{\left(k^2 - k_0^2\right)\cosh k(h + z)\cosh k(h + \overline{Z})}{\left\{\left(k^2 - k_0^2\right)h + k_0\right\}} J_0(kR_H)$$

where, R_S and $\hat{R}_S$ indicate the distances relating to the two points, the field point (x, y, z) and the source point (X, Y, Z). Definitions of these distances are as follows

$$R_S = \sqrt{\left(x - \overline{X}\right)^2 + \left(y - \overline{Y}\right)^2 + \left(z - \overline{Z}\right)^2}$$

$$\hat{R}_S = \sqrt{\left(x - \overline{X}\right)^2 + \left(y - \overline{Y}\right)^2 + \left(z + \overline{Z} + 2h\right)^2}$$

As seen in Eq. (2.74), the basic three-dimensional source function for an unbounded fluid domain is included. Remaining terms except this basic source function express the influence of various boundary conditions from the sea bed, free surface and far field.

(b) Practical evaluation of f_S: f_S can be obtained by Eq. (2.73), after having substituted the three-dimensional wave source Green's function of Eq. (2.75) or (2.77) into G in Eq. (2.73). In which, the source strength function f_D can be determined by the use of the impermeable condition on the submerged surface of a body, i.e., Eq. (2.74).

For the practical computations, the above equations are discretized based on the various numerical algorithms. The most simple one is the method based on the mid-point approximation. In this approximation, the submerged surface of a body is usually partitioned into small facets of a quadrangle or triangle. Then, assuming the source strength is constant on the small facet, the mid point of the facet is used as a representative point in the numerical computations.

Adopting such a discretization technique, Eq. (2.73) can be rewritten

$$\phi_S\left(x_i, y_i, z_i\right) = \sum_{j=1}^{N} f_D\left(\overline{X}_j, \overline{Y}_j, \overline{Z}_j\right) g_{ij} \tag{2.78}$$

where, g_{ij} is defined by

$$G_{ij} = \iint_{\Delta S_j} G\left(x_i, y_i, z_i ; \overline{X}, \overline{Y}, \overline{Z}\right) dS\left(\overline{X}, \overline{Y}, \overline{Z}\right) \tag{2.79}$$

The source strength function f_D can be obtained by solving the discretized form of Eq. (2.74), which is expressed

$$\sum_{j=1}^{N} f_D\left(\overline{X}_j, \overline{Y}_j, \overline{Z}_j\right) \alpha_{ij} = -\frac{\partial \phi_I\left(x_i, y_i, z_i\right)}{\partial n\left(x_i, y_i, z_i\right)} \tag{2.80}$$
$$: \left(x_i, y_i, z_i\right) \text{ on } S_B \ (i = 1 \sim N)$$

where, α_{ij} is defined by

$$\alpha_{ij} = \iint_{\Delta S_j} \frac{\partial G\left(x_i, y_i, z_i ; \overline{X}, \overline{Y}, \overline{Z}\right)}{\partial n\left(x_i, y_i, z_i\right)} dS\left(\overline{X}, \overline{Y}, \overline{Z}\right) \tag{2.81}$$

In order to carry out the numerical computations based on the above equations, since singular functions such as inverse functions, logarithmic functions and so on are included in α_{ij} and g_{ij}, special numerical treatments are necessary especially for the singular conditions.

Hogben et al. (1974) and Garrison et al. (1978) have derived the numerical algorithm including the treatment of such singular functions in α_{ij} and g_{ij}. They used both the series and integral forms of G in order to avoid the difficulties arisen from the numerical treatment of singular functions.

Recently, a new algorithm based on only the series form of G was developed by Nakamura (1990) for the shallow water condition. It is much simpler than the method based on both the series and integral forms of G. The central idea of the new algorithm is how to explicitly take out the singular functions included in G and its normal derivative $\partial G/\partial n$. We briefly describe the algorithm in the following.

First, in order to take out singular functions included in G, let us try to calculate the summation of the infinite series that appears on the second term of Eq. (2.75). Suppose that the rigorous result of the summation is specified by G_E and the n-th term of the series is by $(G_E)_n$. Then, noting that, for a sufficiently large integer n, k_n can be approximated by

$$K_n \cong \frac{n\pi}{n}$$

$(G_E)_n$ can be expressed as $(G_{EA})_n$ in the following:

$$(G_{EA})_n = \left(\frac{1}{\pi h}\right)\cos\left\{\frac{n\pi}{h}(h+z)\right\}\cos\left\{\frac{n\pi}{h}(h+\overline{Z})\right\}K_0\left(\frac{n\pi R_H}{h}\right) \tag{2.82}$$

Summation of the infinite series $(G_{EA})_n$ can be obtained analytically (Gradshten and Ryzhik 1980) and is given by

$$G_{EA} = G_{ES} + G_{ER} \tag{2.83}$$

$$G_{ES} = \frac{1}{2\pi h}\left\{\gamma_0 + \log\left(\frac{R_H}{4h}\right)\right\} + \frac{1}{4\pi R_S} + \begin{bmatrix} \dfrac{1}{4\pi \hat{R}_S} \\ \dfrac{1}{4\pi \hat{R}_{SP}} \end{bmatrix} \tag{2.84}$$

$$G_{ER} = \frac{1}{4\pi h}\sum_{l=1}^{\infty}\left[\frac{1}{\sqrt{(R_H/h)^2 + \{2l+(z-\overline{Z})/h\}^2}} \right.$$
$$\left. + \frac{1}{\sqrt{(R_H/h)^2 + \{2l-(z-\overline{Z})/h\}^2}} - \frac{1}{l}\right] \tag{2.85}$$

$$+\frac{1}{4\pi h}\left[\begin{array}{l}\sum_{l=1}^{\infty}\left[\dfrac{1}{\sqrt{(R_H/h)^2+\{2l-(z+\bar{Z}+2h)/h\}^2}}\right.\\\left.+\dfrac{1}{\sqrt{(R_H/h)^2+\{2l+(z+\bar{Z}+2h)/h\}^2}}-\dfrac{1}{l}\right]\\\sum_{l=1}^{\infty}\left[\dfrac{1}{\sqrt{(R_H/h)^2+\{2l-(z+\bar{Z})/h\}^2}}\right.\\\left.+\dfrac{1}{\sqrt{(R_H/h)^2+\{2l+(z+\bar{Z})/h\}^2}}-\dfrac{1}{l}\right]\end{array}\right] \qquad (2.85)$$

where, γ_0 is the Euler's constant and $\hat{R}_{SP}$ is defined by

$$\hat{R}_{SP}=\sqrt{(x-\bar{X})^2+(y-\bar{Y})^2+(z+\bar{Z})^2}$$

Upper and lower alternatives in Eqs. (2.84) and (2.85) correspond to the case for $\hat{R}<\hat{R}_{SP}$ and $\hat{R}>\hat{R}_{SP}$, respectively. Although the infinite series expressions are contained in G_{ER} of Eq. (2.85) in a similar manner to G_E of Eq. (2.82), the contained two sets of the series clearly show the well behavior even near the singular conditions, i.e., $(x,y,z)\to(\bar{X},\bar{Y},\bar{Z})$ and so on. Therefore, we can say that the diverging nature of the series in Eq. (2.82) near the singular conditions is improved in Eq. (2.85).

From these equations, it can be seen that several singular functions, such as a basic three-dimensional source function, a basic two-dimensional source function and so on, are contained in the evanescent mode component of G, i.e., G_E. It is also seen that, due to the singular nature of the wave source Green's function, the original infinite series contained in Eq. (2.75) diverges near the singular conditions.

Finally, we can derive the improved equation for calculating G_E near the singular conditions through the use of Eq. (2.83) as follows:

$$G_E=\sum_{n=1}^{N_A}(G_E)_n-\sum_{n=1}^{N_A}(G_{EA})_n+G_{EA} \qquad (2.86)$$

where, N_A is the minimum integer on which k_n can be approximated by $n\pi/h$.
The surface integration of the singular functions included in G can be carried out by the procedure referred to in **2.3**, such as a method by Hess and Smith (1964).

(c) Wave forces on a body: Wave pressure p on the submerged surface of a body can be calculated by the linearized Bernoulli equation, after having obtained Φ_S through the use of the above equations. By use of the numerical scheme for the wave source distribution method, the wave pressure is expressed as follows:

$$p(x_i, y_i, z_i) = i\rho\sigma\left\{\phi_I(x_i, y_i, z_i) + \sum_{j=1}^{N} f_D(\overline{X}_j, \overline{Y}_j, \overline{Z}_j)g_{ij}\right\}$$
$$\times \exp(-i\sigma t) - \rho g z_i \qquad :(x_i, y_i, z_i) \text{ on } S_B \tag{2.87}$$

Wave forces on the body and the corresponding overturning moments about a centroid of the body can be calculated by carrying out a surface integration of the wave pressure over the submerged surface S_B

$$\vec{F} = -\sum_{i=1}^{N} p(x_i, y_i, z_i)\, \vec{n}\,(x_i, y_i, z_i)\Delta S_i \tag{2.88}$$

$$\vec{M} = -\sum_{i=1}^{N} p(x_i, y_i, z_i)\left\{\vec{R}_G(x_i, y_i, z_i) \times \vec{n}(x_i, y_i, z_i)\right\}\Delta S_i \tag{2.89}$$

In Fig. 2.9, typical computed results of the horizontal wave force on a square and submerged cylinder in the wave propagation direction are shown.
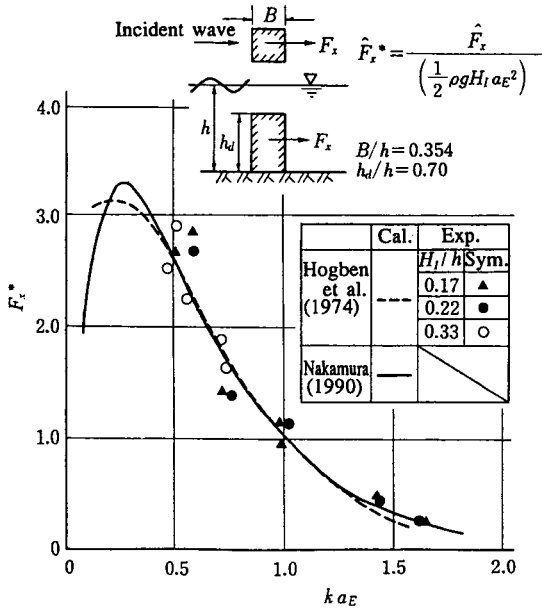

Fig. 2.9 Horizontal wave forces on a submerged cylinder of square section ($h_d/h = 0.7$); comparisons between the experimental result by Hogben et al. (1974) and the computation results by Hogben et al. (1974) and Nakamura (1981)

Experimental and computed results by Hogben et al. are also plotted. This figure shows the relation between the dimensionless wave force defined by the equation written in the figure and the dimensionless wave number ka_E. In the figure, a_E is an equivalent radius of the circular cylinder that has the same cross sectional area as the square cylinder. It is noted that Hogben's computation result is obtained by the numerical algorithm using both the series and integral forms of Green's function.

From the figure, it is seen that the wave force can be predicted by the wave source Green function method. The reason for the difference between the two computed results in the lower range of ka_E is not clear. It was reported by Nakamura that the numerical algorithm based on the series form of Green's function is superior to the one based on both the forms of Green's function, e.g., the necessary CPU time being reduced by a half.

(d) Wave height distribution around a body: Water wave elevations around a body can be calculated by inserting the linear summation of Φ_I and Φ_S into Φ of Eq. (2.11a). The dimensionless wave height ratio K_D divided by the incident wave height is given by using the above equation for the wave elevation

$$
K_D(x_i, y_i) = \Bigg| \exp\left\{i\left(k\, x_i \cos \alpha + k\, y_i \sin \alpha\right)\right\}
$$
$$
+ \frac{2i\sigma}{gH_I} \sum_{j=1}^{N} f_D\left(\overline{X}_j, \overline{Y}_j, \overline{Z}_j\right) g_{ij} \Bigg|_{z=0}
$$

(2.90)

(e) Another efficient algorithm taking advantage of the body geometry: As mentioned before, there are three alternatives to the full three-dimensional analysis described in the above, i.e., i) the plane-symmetric Green's function method for a body with vertical plane symmetry, ii) the axisymmetric Green's function method for a body with vertical axisymmetry and iii) the vertical line source Green's function method for a vertical and surface piercing cylinder. Main ideas for the efficient algorithm are to take advantage of the functional form of the source strength function $f_D(X,Y,Z)$. We shall introduce the brief features of these methods.

A method for a plane-symmetric body: This method was derived by Nakamura and Ono (1988). For a vertical plane-symmetric body, f_D can be decomposed into two parts, i.e., symmetric and anti-symmetric components for the two points Q and Q' which have a plane-symmetric relation with each other, as shown in Fig. 2.10. Hence,

$$
f_D(Q) = f_D^S(Q) + f_D^A(Q)
$$
$$
f_D(Q') = f_D^S(Q') + f_D^A(Q')
$$
$$
= f_D^S(Q) - f_D^A(Q)
$$

(2.91)

where, f_D^S and f_D^A are the symmetric and anti-symmetric components of f_D, respectively.

For the special case under which wave trains are incident to the body from the direction parallel to the symmetric plane, we can intuitively set $f_D^A = 0$. Therefore it is only necessary to solve for f_D^S, which can be determined by considering only a half part of the body surface. This analogy can be extended to the more general case of arbitrarily directional wave trains. For this case, both the two components of f_D may not be 0. In the

analogous manner to f_D, the scattered wave potential ϕ_S and the three-dimensional Green's function G can also be decomposed into two components, i.e., symmetric and anti-symmetric ones. For instance, the plane-symmetric Green's function G^S and the anti-symmetric one G^A are defined by

$$
\begin{aligned}
G^S\left(x,y,z;\overline{X},\overline{Y},\overline{Z}\right) &= G\left(x,y,z;\overline{X},\overline{Y},\overline{Z}\right) + G\left(x,y,z;-\overline{X},\overline{Y},\overline{Z}\right) \\
G^A\left(x,y,z;\overline{X},\overline{Y},\overline{Z}\right) &= G\left(x,y,z;\overline{X},\overline{Y},\overline{Z}\right) - G\left(x,y,z;-\overline{X},\overline{Y},\overline{Z}\right)
\end{aligned}
\tag{2.92}
$$
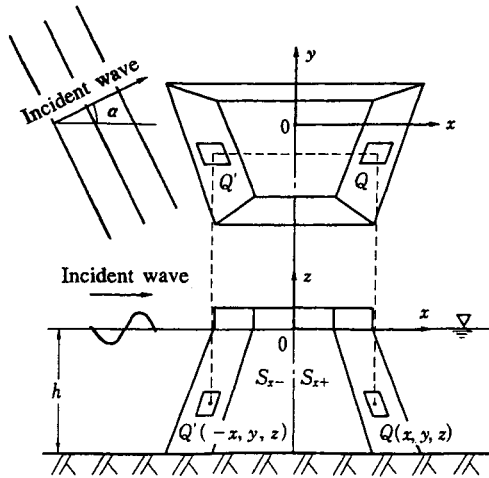
Fig.2.10 Analytical model of a plane–symmetric body and definition sketch

By the use of these components of f_D and G, the symmetric and anti-symmetric components of the scattered wave potential, $\phi_S{}^S$ and $\phi_S{}^A$, respectively, can be expressed as follows:

$$
\begin{aligned}
\phi_S^S(x,y,z) &= \iint_{S_{x+}} f_D^S\left(\overline{X},\overline{Y},\overline{Z}\right) G^S\left(x,y,z;\overline{X},\overline{Y},\overline{Z}\right) dS\left(\overline{X},\overline{Y},\overline{Z}\right) \\
\phi_S^A(x,y,z) &= \iint_{S_{x+}} f_D^A\left(\overline{X},\overline{Y},\overline{Z}\right) G^A\left(x,y,z;\overline{X},\overline{Y},\overline{Z}\right) dS\left(\overline{X},\overline{Y},\overline{Z}\right)
\end{aligned}
\tag{2.93}
$$

It is noted that the range of integration is only for a positive half plane of the x-axis, S_{x+}, which is specified in Fig. 2.10.

For a body with double symmetries about intersecting two vertical planes, we can easily extend the above analogy. In this case, the range of surface integration is reduced to a quarter of the submerged surface. Also the number of ranks of matrix equations for solving unknown variables corresponding to f_D is reduced to a quarter.

A method for an axisymmetric body: For an axisymmetric body about the vertical axis as shown in Fig. 2.11, the cylindrical coordinate system is much more convenient to develop every equation.
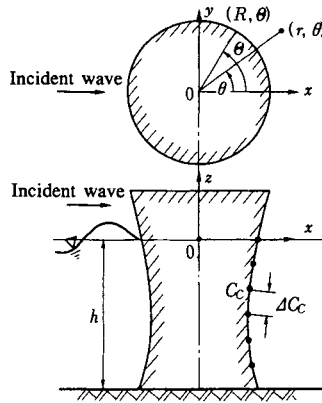
Fig. 2.11 Analytical model of an axisymmetric body and definition sketch

Thus, at first, f_D is interpreted as a function of (R,Θ,Z) whose framework is defined in Fig. 2.11. Since the body is axisymmetric and also the incident wave is unidirectional, we can expand $f_D(R,\Theta,Z)$ to the Fourier cosine series

$$f_D\left(R,\Theta,\overline{Z}\right) = \sum_{m=0}^{\infty} f_{Dm}\left(R,\overline{Z}\right)\cos\left(m\Theta\right) \tag{2.94}$$

where, f_{Dm} is the Fourier amplitude of the m-th cosine mode.

It is also possible to expand the three-dimensional Green's function G to the Fourier series (Black 1975, Fenton 1978),

$$\begin{aligned} G\left(r,\theta,z;R,\Theta,\overline{Z}\right) &= \sum_{m=0}^{\infty} \hat{G}_m\left(r,z;R,\overline{Z}\right)\cos\left\{m(\theta-\Theta)\right\} \\ &= \sum_{m=0}^{\infty}\left(\hat{G}_{m0} + \sum_{n=1}^{\infty}\hat{G}_{mn}\right)\cos\left\{m(\theta-\Theta)\right\} \end{aligned} \tag{2.95}$$

where, $\hat{G}_{m0}$ is the Fourier amplitude of the m-th cosine mode for the progressive mode component of G and $\hat{G}_{m0}$ is the Fourier amplitude of the m-th cosine mode for the evanescent mode component of G.

Noting the relation $dS(X,Y,Z) = Rd\Theta dC$ (dC is a line segment on the revolving curve as shown in Fig. 2.11) and also using the above relations, the basic equation of the source distribution method, Eq. (2.73), can be integrated analytically with respect to Θ. The final form of the equation becomes

$$\phi_S\left(r,\theta,z\right) = \sum_{m=0}^{\infty}\left[\int_{C_C} \pi R\, f_{dm}\left(R,\overline{Z}\right)\hat{G}_m\left(r,z,R,\overline{Z}\right)dC\left(R,\overline{Z}\right)\right]\cos\left(m\theta\right) \tag{2.96}$$

Here, the definition of $\hat{G}_m$ was given in Eq. (2.95). We can see that Eq. (2.96) consists of an infinite number of the one-dimensional integral equations. For wave force calculations, however, it can be shown that only the constant and first modes of f_{Dm} are required due to the orthogonality conditions described in **2.2.2**.

Therefore, only for the purpose of the wave force calculations on an axisymmetric body, we can effectively reduce the computation effort by the use of the axisymmetric Green's function method.

Hudspeth et al. (1980) and Isaacson (1981) extended the method to the radiation problems for the floating body dynamics. In the case of radiation problems, hydrodynamic force coefficients for an axisymmetric floating body, such as added mass coefficients and radiation damping coefficients, can also be obtained very efficiently by the use of the above algorithm.

A method for a vertical and surface-piercing cylinder: Isaacson (1978) developed a very efficient algorithm for the diffraction problem about a vertical and surface-piercing cylinder of an arbitrary section as seen in Fig. 2.12.
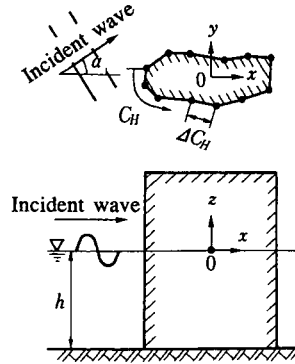

Fig. 2.12 Analytical model of a surface–piercing cylinder and definition sketch

For such a vertical cylinder, we can assume the source strength function f_D has the same function form as that of the incident wave potential in the vertical direction

$$f_D(\overline{X}, \overline{Y}, \overline{Z}) = \hat{f}_D(\overline{X}, \overline{Y}) \frac{\cosh\{k(h + \overline{Z})\}}{\cosh(kh)} \tag{2.97}$$

where, $\hat{f}_D$ is the source strength at the still water level. Substituting this equation into Eq. (2.72) with use of the three-dimensional Green's function of Eq. (2.75), and then integrating it with respect to Z, the final equation for this method is derived

$$\phi_S(x, y, z) = \int_{C_H} \hat{f}_D(\overline{X}, \overline{Y}) \hat{G}(\overline{X}, \overline{Y}; x, y) \, dC(\overline{X}, \overline{Y}) \frac{\cosh\{k(h + z)\}}{\cosh(kh)} \tag{2.98}$$

where, C_H is the cross-sectional curve of the cylindrical body in the horizontal plane and $\hat{G}$ is the vertical line source Green's function, which is defined by

$$\hat{G}(x, y; \overline{X}, \overline{Y}) = iH_0\left(k\sqrt{\left\{(x - \overline{X})^2 + (y - \overline{Y})^2\right\}}\right)\Big/4 \qquad (2.99)$$

In Eq. (2.99), there is no contribution from the evanescent mode term that is originally included in the three-dimensional Green's function. Because the evanescent mode term disappears due to the orthogonality nature of the eigenfunctions contained in Green's function.

As seen in Eq. (2.98), we can solve the diffraction problems about a three-dimensional cylindrical body by a line integral equation. Therefore it is possible to reduce the computation effort by a great deal as compared to the full three-dimensional Green's function method.

(2) Two-dimensional analysis by the wave source distribution method

Here, we will introduce the two-dimensional analysis for a horizontal cylinder with an infinite length in the y-axis direction as shown in Fig. 2.13. In this case, the problem can be treated in a framework of the vertical plane. Such a two-dimensional analysis has often been applied to the three-dimensional water wave problems about a comparatively slender body as an approximation, because the experimental model tests as well as the numerical calculations can be easily carried out as compared to the full three-dimensional method. There are several variations with the two-dimensional analysis as mentioned in the previous sections. Recently, the analysis was extended to the case of obliquely incident waves (Nakamura and Morita 1988). In the following, the more general procedure that is able to deal with the case of obliquely incident waves is described.

In Fig. 2.13, analytical model is shown. It is assumed that the horizontal cylinder with an infinite length is fixed in the wave field of constant water depth h and is interacted with the obliquely incident waves.
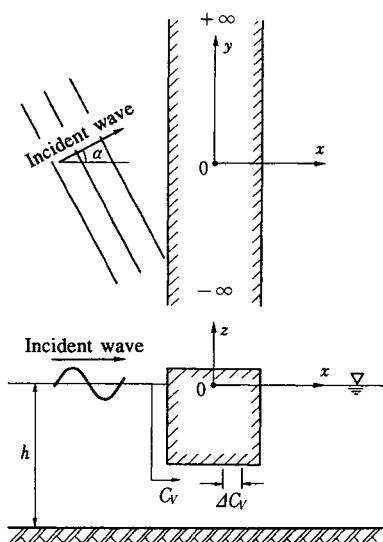

Fig. 2.13 Analytical model of a two-dimensional body and definition sketch.

In this case, noting that vertical cross section of the cylinder does not change in the y-axis direction, the complex amplitude of the scattered wave potential ϕ_S can be expressed as

$$\phi_s(x,y,z) = \Lambda_s(x,z)\exp(ik_yy) \tag{2.100}$$

where, Λ_S is the amplitude of ϕ_S in the y-axis direction and k_y is equal to $k\sin\alpha$.

Substituting Eq. (2.100) into the three-dimensional Laplace equation, the governing equation for Λ_S can be reduced to

$$\frac{\partial^2 \Lambda_S}{\partial x^2} + \frac{\partial^2 \Lambda_S}{\partial z^2} - k_y^2 \Lambda_S = 0 \tag{2.101}$$

It is necessary for Λ_S to satisfy the same boundary conditions as ϕ_S on the free surface and sea bed, i.e., Eqs. (2.18) and (2.19). The kinematic boundary condition on the submerged surface can be derived from Eq. (2.20) and is given by

$$\frac{\partial \Lambda_S}{\partial n} = -\frac{\partial \Lambda_S}{\partial n} \qquad : \text{on } C_V \tag{2.102}$$

where, Λ_I is the complex amplitude of ϕ_I in the y-axis direction and is given by Eq. (2.16) after having set $y=0$, and C_V is a cross section of the cylinder in the vertical plane.

On the other hand, the radiation condition Eq. (2.15) must be modified to the two-dimensional counterpart. Noting that wave number component in the x-axis direction is k_x, the radiation condition for this case can be expressed

$$\lim_{x\to\pm\infty}\left\{\frac{\partial \Lambda_S}{\partial x} - (\pm)ik_x\Lambda_S\right\} = 0 \tag{2.103}$$

As described above, the wave boundary-value problem for the horizontal cylinder in oblique waves can be treated as a two-dimensional problem in the vertical plane at $y=0$. For the special case of $\alpha=0$, i.e., for normal incident waves, a number of studies have been carried out up to now.

(a) Green's function: Green's function for the above wave boundary-value problem was derived by Nakamura and Morita (1988) and is given by

$$\begin{aligned}
G(x,z;\overline{X},\overline{Z};\alpha) = &-\frac{i}{k_x}\frac{\left(k^2-k_0^2\right)}{\left(k^2-k_0^2\right)h+k_0}\cosh k(h+z)\\
&\times \cosh k(h+\overline{Z})\exp\left(ik_x|x-\overline{X}|\right)\\
&-\sum_{n=1}^{\infty}\frac{1}{\mu_n}\frac{\left(k_n^2+k_0^2\right)}{\left(k_n^2+k_0^2\right)h-k_0}\cos k_n(h+z)\\
&\times \cos k_n(h+\overline{Z})\exp\left(-\mu_n|x-\overline{X}|\right)
\end{aligned} \tag{2.104}$$

where, μ_n is the evanescent mode wave number in this wave field and is defined by

$$\mu_n = \sqrt{k_n^2 + k_y^2} \tag{2.105}$$

The first and second terms in Eq. (2.104) specify the progressive mode and evanescent mode components, respectively. When $\alpha=0$, Eq. (2.104) is coincident with the two-dimensional Green's function in the normal incident waves derived by John (1950). Therefore, we can say that Green's function of Eq. (2.104) is a much more general one. Another form of Green's function, i.e., the integral form, is also known (Kim 1969), but limited to the normal incident wave condition.

(b) Evaluation of Λ_S by the source distribution method: By use of Green's function, Λ_S can be expressed as

$$\Lambda_S(x,z) = \int_{C_v} f_D(\overline{X}, \overline{Z}) G(x, z; \overline{X}, \overline{Z}; \alpha) \, dC(\overline{X}, \overline{Z}) \tag{2.106}$$

where, f_D is the source strength function on the sectional curve C_v. f_D can be determined by the boundary condition on the submerged surface, i.e., Eq. (2.102), which is rewritten as follows:

$$\int_{C_v} f_D(\overline{X}, \overline{Z}) \frac{\partial G(x, z; \overline{X}, \overline{Z}; \alpha)}{\partial n(x, z)} \, dC(\overline{X}, \overline{Z}) = -\frac{\partial \Lambda_I(x, z)}{\partial n(x, z)} \quad : (x, z) \text{ on } C_v \tag{2.107}$$

(c) Singularities included in Green's function: For practical computations, in the same way as the three-dimensional Green's function method, the treatment of singular functions included in the two-dimensional Green's function is important. In the following, we will briefly describe the singular nature of the two-dimensional Green's function.

At first, in order to take out the singular functions included in G, we will try to analytically obtain the summation of the infinite series included in the second term of Eq. (2.104). Suppose that this infinite series summation is denoted by G_E and also the m-th term of the series is G_{En}. Noting that, for sufficiently large n, k_n and μ_n are approximated by

$$k_n \cong \frac{n\pi}{h}, \quad \mu \cong \frac{n\pi}{h}$$

The approximation form of G_{En} may be expressed by the following G_{An}:

$$G_{An} = -\left(\frac{1}{2n\pi}\right)\left[\cos\left\{\frac{n\pi(z-\overline{Z})}{h}\right\} + \cos\left\{\frac{n\pi(z+\overline{Z}+2h)}{h}\right\}\right]$$
$$\times \exp\left(-n\pi\left|x-\overline{X}\right|/h\right) \tag{2.108}$$

It is possible to obtain analytically the infinite series summation of G_{An}, which is given by

$$
\begin{aligned}
G_{An} = \sum_{n=1}^{\infty} G_{An} \\
= \left[\log\left\{ 1 - 2\exp\left(\frac{-\pi|x-\overline{X}|}{h}\right)\cos\left(\frac{\pi|z-\overline{Z}|}{h}\right) + \exp\left(\frac{-2\pi|x-\overline{X}|}{h}\right)\right\} \right. \\
\left. + \log\left\{ 1 - 2\exp\left(\frac{-\pi|x-\overline{X}|}{h}\right)\cos\left(\frac{\pi|z-\overline{Z}|}{h}\right) + \exp\left(\frac{-2\pi|x-\overline{X}|}{h}\right)\right\} \right] \Big/ 4\pi
\end{aligned}
$$

$$(2.109)$$

As seen in this equation, there are logarithmic singular functions in G_A. Therefore, when the field point (x,z) approaches the source point $(\overline{X},\overline{Z})$, the series G_{En} shows the tendency of divergence. In other words, we cannot approximate the infinite series summation with the finite one under such a singular condition.

In order to improve the diverging nature of the series, we can use the above-mentioned results. Hence, the infinite series summation G_E may be approximately evaluated by

$$
G_E \cong \sum_{n=1}^{N_A} G_{En} - \sum_{n=1}^{N_A} G_{An} + G_A \tag{2.110}
$$

where, N_A is the minimum number n on which k_n and μ_n are reasonably approximated by $n\pi/h$.

(d) Wave forces and moments: Wave pressure at the cross section $y = y$ is obtained by use of the linearized Bernoulli equation, after having calculated the total wave potential consisting of the incident and scattered wave potentials. Hence,

$$
p\big|_{y=y} = \left\{ i\rho\sigma(\Lambda_I + \Lambda_S)\exp(ik_y y)\right\} e^{-i\sigma t} - \rho g z \tag{2.111}
$$

The local wave force vector on a unit length of the cylinder at $y=y$, $d\overline{F}(y) = (dF_x, dF_z)$, is given by carrying out the pressure integration along the sectional curve C_V

$$
\begin{Bmatrix} dF_x \\ dF_z \end{Bmatrix} = \left[-\int_{C_V} p\big|_{y=0} \begin{Bmatrix} n_x \\ n_z \end{Bmatrix} dC \right] \exp(ik_y y) \tag{2.112}
$$

In the same manner, the local moment in the vertical plane caused by the wave pressure about the point (x_G, z_G), $d\overline{M}_y$, is also given by

$$
dM_y = \left[-\int_{C_V} p\big|_{y=0} \left\{ (z-z_G)n_x - (x-x_G)n_z \right\} dC \right] \exp(ik_y y) \tag{2.113}
$$

On the other hand, if we assume that the cylinder has a finite length l_B in the y-axis direction, the total wave force and moment can be expressed as

$$\begin{Bmatrix} F_x \\ F_z \\ M_y \end{Bmatrix} = \begin{Bmatrix} dF_x \\ dF_z \\ dM_y \end{Bmatrix} \Bigg|_{y=0} l_B \gamma_R \tag{2.114}$$

where, γ_R is the wave force reduction factor compared to the case of uniform distribution of local wave forces along the y-axis, which is defined by

$$\gamma_R = \frac{\sin\left(k_y l_B/2\right)}{k_y l_B/2} \tag{2.115}$$

In Fig. 2.14, variation of γ_R with $l_B \sin\alpha/L$ is plotted.
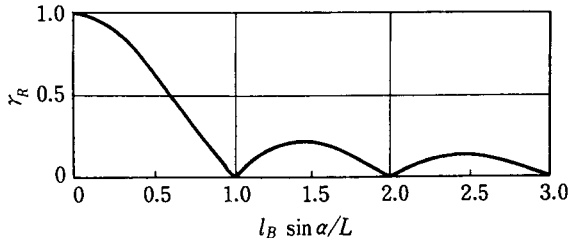
Fig. 2.14 Reduction factor γ_R of wave forces on a finite length of the cylindrical body in obliquely incident waves

From this figure, we can see that the total wave forces decrease by increasing the incident wave angle α. Especially, under the condition on which the value of $l_B\sin\alpha/L$ approaches a whole number, the total wave forces diminish. This reduction is directly caused by the phase difference of wave forces along the cylinder axis.

In Fig. 2.15, variation of the local wave force on a rectangular cylinder with the incident wave angle α is shown.

In the figure, wave number is fixed for the two different values. From this figure, it can be seen that the local wave force also decreases by increasing the incident wave angle α. Furthermore, the dimensionless horizontal wave force becomes smaller for longer waves. From these figures, it is clear that the total wave force on a finite length of the cylinder decreases with increasing the incident wave angle α due to both reduction effects.
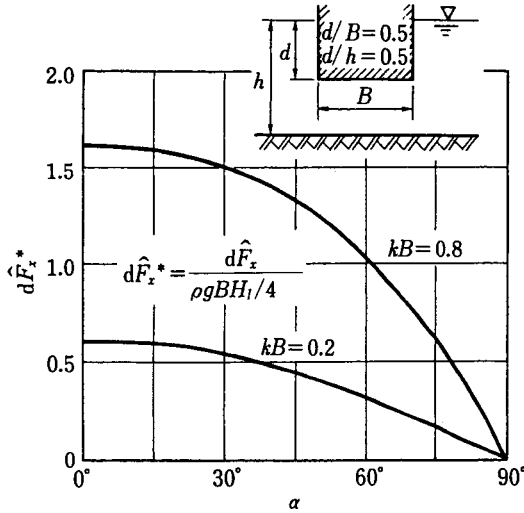
Fig. 2.15 Variation of the wave forces on a rectangular cylinder per unit length with the incident angle of wave

(e) Wave transmissions and reflections: Wave height distributions about the cylinder can be calculated by Eq. (2.11a). When we use the dimensionless wave height ratio K_D normalized by the incident wave height H_I, it is given by

$$K_D(x,y) = \left| (2\sigma/g) \{ \Lambda_I(x,z=0) + \Lambda_S(x,z=0) \} \right| / H_I \qquad (2.116)$$

From this equation, even in the obliquely incident waves, wave height distributions change only in the normal direction of the cylinder axis. However, on the reflection side of the cylinder, intersected wave field consisting of incident and reflected wave trains is formed and the resultant wave pattern becomes short crested.

Wave reflection and transmission coefficients, K_R and K_T, are defined by the wave height ratios of the reflected wave height H_R and transmitted wave height H_T to the incident wave height H_I, respectively. Hence,

$$K_R = \frac{H_R}{H_I} = \left| \frac{\Lambda_S(x,z=0)}{\Lambda_I(x,z=0)} \right|_{x \to -\infty} \qquad (2.117)$$

$$K_T = \frac{H_T}{H_I} = \left| \frac{\Lambda_I(x,z=0)\,\Lambda_S(x,z=0)}{\Lambda_I(x,z=0)} \right|_{x \to +\infty} \qquad (2.118)$$

In Fig. 2.16, one of the computed results on K_T is shown for a rectangular cylinder as mentioned before.
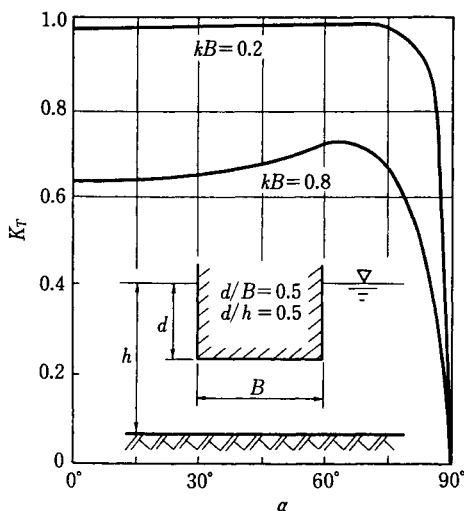
Fig. 2.16 Variation of the wave transmission and relection coefficients about a rectangular cylinder with the incident angle of wave.

In the figure, variation of K_T with the incident wave angle α is plotted for the two different values of kB. From this figure, it is seen that K_T is almost constant for the range $0°<\alpha<75°$, but over this range it decreases drastically.

2.4.2 Floating body dynamics in waves

(1) Motions of a three-dimensional floating body

The representative of floating bodies in the ocean and ship motions have already been studied in detail in the field of ship building. Their studies are summarized in the strip method which has sufficient accuracy in practice (Korvin-Kroukovsky 1955, Salvesen et al. 1970).

In ship hydrodynamics, as described in **2.2**, the phenomenon of floating body motions in waves is divided into the radiation problem where the body seems to move in still water and the diffraction problem where the body seems to be fixed and receive wave forces. This method gives us the relation between the added mass and own mass, frequency-dependency of added mass and damping coefficient and it is also effective in dealing with nonlinear mooring ship problems.

Concerning the dynamics of floating body in waves, many studies have been carried out since the analytical method with Green's function represented as the basic theory of the floating body motion in the finite water depth by John (1949, 1950).

In case of a slender body, the strip method (Korvin-Kroukovsky 1955, Salvesen et al., 1970) which transform the three-dimensional problem to two-dimensional one is devised. It will be described later.

In this section, the numerical calculation method for an arbitrary shaped floating body moored in the finite depth h by the elastic lines, as seen in Fig. 2.4, is described.

We assume that the body is moving harmonically in six degrees of freedom as follows:

$$X = \hat{X}e^{-i\sigma t} = X_1(\text{sway}), \quad Y = \hat{Y}e^{-i\sigma t} = X_2(\text{surge}), \quad Z = \hat{Z}e^{-i\sigma t} = X_3(\text{heave}),$$

$$\Omega_x = \hat{\Omega}_x e^{-i\sigma t} = X_4(\text{pitch}), \quad \Omega_y = \hat{\Omega}_y e^{-i\sigma t} = X_5(\text{roll}), \quad \Omega_z = \hat{\Omega}_z e^{-i\sigma t} = X_6(\text{yaw})$$

$$(2.119)$$

Relatedly, for the simplicity of expression, we define the vector which has six components consisting of translation vector $\bar{X}(X, Y, Z)$ and rotation vector $\bar{\Omega}(\Omega_x, \Omega_y, \Omega_z)$ and express these component of the vector with the subscript $1 \sim 6$ as follows:

$$X = \left(X, Y, Z, \Omega_x, \Omega_y, \Omega_z \right)$$
$$= \left(X_1, X_2, X_3, X_4, X_5, X_6 \right)$$

$$(2.120)$$

(a) Hydrostatic Stability: At first, let's see the generation mechanism of the righting moment $F^{(S)}_{55}$ due to static pressure when the floating body is rolling. Figure 2.17 shows the center of gravity C_G, the metacenter M_C and the centers of buoyancy C_B at upright and C'_B at small rotation.
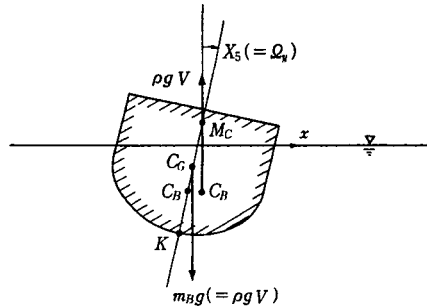
Fig. 2.17 Righting moments in the vertical plane of a floating body and definition sketch

The gravity force $m_B g$ (m_B = mass of the floating body) applies to C_G and the buoyancy force $\rho g V$ (V = displacement of the floating body) to C'_B. These two forces are out of line, so they make the righting moment $F^{(S)}_{55}$ as shown in Eq. (2.121) (Bhattacharyya 1978).

$$F^{(S)}_{55} = m_B g \, \overline{GM} \sin X_5$$
$$\cong m_B g \, \overline{GM} \sin X_5$$

$$(2.121)$$

where, the distance $\overline{GM}$ from the center of gravity to the metacenter is termed the metacentric height. Now let the keel position be K, then $\overline{GM}$ is given by

$$\overline{GM} = \overline{KB} + \overline{BM} - \overline{KG} \tag{2.122}$$

Using the transverse second moment of area $I_y^{(2)}$ and displacement V, $\overline{BM}$ is calculated by

$$\overline{BM} = \frac{I_y^{(2)}}{V} \tag{2.123}$$

In the same manner, letting the longitudinal metacentric height be $\overline{GM_L}$, the righting moment of pitch is given by

$$F_{44}^{(S)} \cong m_B \, g \, \overline{GM}_L \sin X_4 \tag{2.124}$$

Furthermore, the restoring force in heave $F^{(S)}{}_{33}$ is given by

$$F_{33}^{(S)} \cong pg \, A_W X_3 \tag{2.125}$$

where A_W is the area of the water plane.

As the center of rotation does not coincide with the center of floatation in general, the hydrostatic restoring forces in heave, pitch and roll are coupled mutually. They are discussed in detail in the literature (Bhattacharyya 1978).

(b) The restoring forces by mooring line: We pay attention to one of the mooring lines and use $\bar{a}_p$ and $\bar{b}_p$ for the position vectors of mooring points at floating body and sea bottom, respectively. Then, considering the geometrical relation, extension Δl of the mooring line due to the slip motion is derived

$$\Delta l = \left(\bar{b}_p - \bar{a}_p \right) \cdot \left(\bar{X} - \bar{R}_{Ga} \times \bar{\Omega} \right) \big/ l \tag{2.126}$$

where, l is the length of mooring line, $\hat{R}_{Ga}$ is the position vector drawn from C_G to the mooring point of floating body. And the restoring force $f^{(M)}$ for the above expansion is obtained by

$$f^{(M)} = K^{(M)} \Delta l \tag{2.127}$$

where, $K^{(M)}$ = linearized spring constant of the mooring line and it can be obtained by the catenary theory.

The above-mentioned restoring forces are applied to the mooring point of the body. And resolving the force vectors and composing the forces in each direction of motion, then the restoring forces or moments due to mooring line displacement are obtained. We define $F^{(M)}$ as the vector which are composed of three restoring forces and three restoring moments.

(c) Velocity potentials of waves around floating body and hydrodynamic forces: The velocity potentials of waves around the oscillating body can be divided into three kinds of potentials from the standpoint of the sources. Moreover, the velocity potential Φ_R of

radiated waves is separated into $\phi_{Rm}(m=1\sim6)$ of each motion mode. As the calculation method for the velocity potential Φ_S of diffracted waves is already described in **2.4**, the calculation method for Φ_R is explained. For the simplicity, we define the vector ϕ_R which has the six components $\phi_{Rm}(m=1\sim6)$. Using this expression, Eq. (2.35) is rewritten by

$$\Phi_R = \phi_R \cdot \dot{X} \tag{2.128}$$

Substituting Φ_R into the kinematic boundary condition Eq. (2.30) and decomposing it into each component of motion, the following equation is deduced.

$$\frac{\partial \Phi_R}{\partial n} = \begin{pmatrix} \vec{n} \\ \vdots \\ \vec{R}_G \times \vec{n} \end{pmatrix} = \begin{pmatrix} \xi_1 \\ \vdots \\ \xi_6 \end{pmatrix} = \boldsymbol{\xi} \tag{2.129}$$

In the same manner as Φ_S, $\phi_{Rm}(m=1\sim6)$ can be described by Eq. (2.72), which is the basic equation of the three-dimensional source distribution method. Here, the source strength $f_{Rm}(m=1\sim6)$ for each mode is treated as the unknown function. Substituting the expression into Eq. (2.129), Eq. (2.130) of settling the source strength $f_{Rm}(m=1\sim6)$ is derived as follows:

$$\sum_{j=1}^{N} f_R\left(\overline{X}_j, \overline{Y}_j, \overline{Z}_j\right) \alpha_{ij} = \boldsymbol{\xi}\left(x_i, y_i, z_i\right), \qquad (i=1, 2, ..., N) \tag{2.130}$$

where f_R is the vector defined by

$$f_R = \left(f_{R1}, f_{R2}, \cdots, f_{R6}\right) \tag{2.131}$$

Once we obtain the source strength of each mode from Eq. (2.130), by substituting them into Eq. (2.72), the velocity potential $\phi_{Rm}(m=1\sim6)$ of a sinusoidally oscillating body with unit velocity amplitude can be evaluated.

Calculating the pressures by using Φ_R and integrating them over the wetted surface of the floating body, the hydrodynamic force due to the body motion can be obtained. In this stage, however, oscillating velocities of the body have not been determined yet, leaving them unknown, and the expression of the applying hydrodynamic forces can merely be derived. Solving the equations of body motion with the above derived expression of hydrodynamic forces, the oscillatory velocities are determined at last.

When we consider the above and obtain the hydrodynamic forces, they can be represented as follows:

$$F^{(R)} = \left(F_1^{(R)}, F_2^{(R)}, \cdots, F_6^{(R)}\right) \tag{2.132}$$

where,

$$F_l^{(R)} = -\sum_{m=1}^{6} \left(M_{lm}^{(A)} \ddot{X}_m + N_{lm}^{(D)} \dot{X}_m\right) \quad (l=1, 2, ..., 6) \tag{2.133}$$

and $M_{lm}^{(A)}$, $N_{lm}^{(D)}$ are the quantities given by

$$\begin{Bmatrix} M_{lm}^{(A)} \\ N_{lm}^{(D)} \end{Bmatrix} = \rho \int_{S_B} \begin{Bmatrix} \text{Real}[\phi_{Rm}] \\ \text{Imag}[\sigma \phi_{Rm}] \end{Bmatrix} \xi_l \, dS \tag{2.134}$$

Here, $M_{lm}^{(A)}$ is the added mass, and $N_{lm}^{(D)}$ is the radiation damping coefficient. The latter is named after the reason that this term reduces the motions in proportion to the oscillating velocity and it closely related to the radiated waves. As shown in Eq. (2.133), the motion in the mode m induces the hydrodynamic forces not only in mode m, but also in other modes. It is very interesting when we compare this relation with Newton's second law.

In the field of ship building, the above mentioned hydrodynamic force generated by the motions of floating body is called the radiation force. Also the wave force applied to the fixed body as introduced in **2.4** is called the wave exciting force in general. Furthermore, the wave exciting force is further separated into the Froude-Krylov force and the diffraction force caused by the scattered waves. Hereafter, following the custom of naval architecture, we use these terms.

Referring to the method of wave force calculation described in **2.4**, the Froude-Krylov force $F^{(F)}$ and the diffraction force $F^{(D)}$ in vector expression can be deduced as follows:

$$F^{(F)} = -i\rho\sigma \int_{S_B} \Phi_I \, \xi \, dS \tag{2.135}$$

$$F^{(D)} = -i\rho\sigma \int_{S_B} \Phi_S \, \xi \, dS \tag{2.136}$$

As shown in the above, the diffraction force is obtained by the use of Φ_s. But using the next Haskind relation (Korvin-Kroukovsky 1955, Salvesen et al. 1970), it can also be obtained by ϕ_I and ϕ_{Rm}. Applying ϕ_s and ϕ_R to Green's theorem and considering their radiation conditions at infinity, the following equation can be obtained.

$$\int_{S_B} \left(\phi_S \frac{\partial \phi_R}{\partial n} - \phi_R \frac{\partial \phi_S}{\partial n} \right) dS = 0 \tag{2.137}$$

Substituting them into Eq. (2.190) and using Eq. (2.7), $F^{(D)}$ is given by

$$F^{(D)} = i\rho\sigma \int_{S_B} \frac{\partial \phi_I}{\partial n} \phi_R \, dS \tag{2.138}$$

(d) Equation of motion of the floating body: Considering the inertial force and many other forces obtained in the above, next equation is derived under the balance of the forces.

$$\begin{array}{cccccc} F^{(I)} & + & F^{(S)} & + & F^{(M)} & = & F^{(F)} + F^{(D)} + F^{(R)} \\ \text{(inertia)} & & \text{(damping)} & & \text{(restoring)} & & \text{(hydrodynamic forces)} \end{array} \tag{2.139}$$

Since $F^{(R)}$ contains the oscillating velocity and acceleration as shown in Eq. (2.133), transposing them to the left side, then, they can be combined to $F^{(I)}$. After this operation, Eq. (2.139) can be rewritten in the comprehensive matrix form.

$$\sum_{m=1}^{6}\left\{\left(M_{lm}^{(B)}+M_{lm}^{(A)}\right)\ddot{X}_m+N_{lm}^{(D)}\dot{X}_m+K_{lm}X_m\right\}=F_l^{(E)} \quad (l=1,2,\ldots,6) \qquad (2.140)$$

where $M_{lm}^{(B)}$ is the mass matrix, K_{lm} is the spring constant matrix containing the hydrostatic and mooring line's restoring forces, and $F_l^{(E)}$ is the wave-exciting force in l mode.

The oscillating displacement of the floating body X_m is obtained by solving Eq. (2.140) and substituting them into Eq. (2.128), the radiation potential Φ_R is determined lastly.

(e) Wave height distribution around body: Substituting the sum of the velocity potentials Φ_I, Φ_S and Φ_R into Eq. (2.11a), then the water surface elevation η around the floating body can be obtained. The ratio K_D of the wave height around the body to the incident wave height is given by

$$K_D=\left|\left(\Phi_I+\Phi_S+\sum_{m=1}^{6}\phi_{Rm}\dot{X}_m\right)\Big/\Phi_I\right|_{z=0} \qquad (2.141)$$

(2) Strip theory for three-dimensional floating body motions (Korvin-Kroukovsky 1955, Salvesen et al. 1970)

Here, the body is assumed to be slender like a ship. Then the strip method is useful, where the three-dimensional problem is transformed into the two-dimensional one. In the case of a three-dimensional oscillation, there exists surge ($m=2$), pitch ($m=4$) and yaw ($m=6$) which are not in a two-dimensional one. However, we look at the motions of a strip shown in Fig. 2.18, pitch and yaw are similar to two-dimensional heave and sway, respectively.
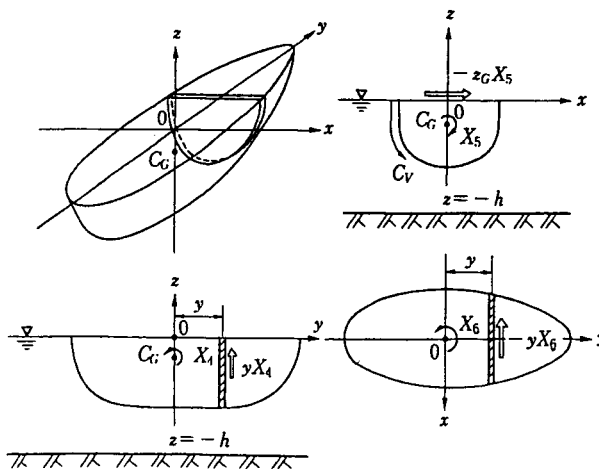
Fig. 2.18 Ship motions at a strip of slender floating body

Surge does not have any similarity to other motions, so the hydrodynamic force for surge is approximated independently. For this reason, the strip method is sometimes called the method with five degrees of freedom.

Based on the above background, analyzing the two-dimensional problem at first, next the hydrodynamic forces for pitch and yaw are given according to the two-dimensional ones. And, at last the hydrodynamic force for surge is also described.

(a) Radiation force: We consider the radiation problem when the floating body of infinite length with a strip shown in Fig. 2.18 is oscillating in still water of depth h. The radiation potential and the kinematic boundary condition can be derived by referring to the above three dimensional cases

$$\Phi_R = \phi_{R1}\dot{X}_1 + \phi_{R3}\dot{X}_3 + \phi_{R5}\dot{X}_5 \tag{2.142}$$

$$\frac{\partial \phi_{R1}}{\partial n} = \xi_1, \frac{\partial \phi_{R3}}{\partial n} = \xi_3, \frac{\partial \phi_{R5}}{\partial n} = \xi_5 \tag{2.143}$$

Green's functions in the vertical two-dimensional wave field can be obtained as the special case of Eq. (2.104) of $\alpha=0°$. When we use this Green's function, ϕ_{Rm} over the wetted surface of the body can be given by solving the simultaneous equations similar to Eq. (2.134). Once ϕ_{Rm} is obtained, the added mass $dM_{lm}^{(A)}$ and the damping coefficient $dN_{lm}^{(D)}$ are given in the same manner as the three-dimensional case

$$\left.\begin{array}{l} \mathrm{d}M_{lm}^{(A)} = -\rho \int_{C_V} \mathrm{Real}\left[\phi_{Rm}\right]\xi_l \, \mathrm{d}C \\[2mm] \mathrm{d}N_{lm}^{(D)} = -\rho\sigma \int_{C_V} \mathrm{Imag}\left[\phi_{Rm}\right]\xi_l \, \mathrm{d}C \end{array}\right\} \tag{2.144}$$

Here C_V shows the cross sectional wetted curve at $y=y$.

Now, we suppose the symmetric floating body with respect to the vertical surface of y-axis. In this case, the radiation potentials for sway and roll are anti-symmetric and that for heave is symmetric. Furthermore, ξ_1 and ξ_5 are anti-symmetric and ξ_3 is symmetric with respect to the y-axis. For the sake of these characteristics, the above integral results in the next relations

$$\mathrm{d}M_{13}^{(A)} = \mathrm{d}M_{53}^{(A)} = 0$$
$$\mathrm{d}N_{13}^{(D)} = \mathrm{d}N_{53}^{(D)} = 0 \tag{2.145}$$

These show the coupling of sway and roll and the non-coupling of heave with them. Moreover, yaw and sway, and pitch and heave are coupled with each other, so the motions of slender body symmetric with respect to the y-axis can be divided into three groups of i) sway and roll, ii) heave and pitch, and iii) surge.

Referring to Fig. 2.19, and assuming the representative position of the strip as $(x, z) = (0, 0)$, the horizontal velocity u_R and vertical velocity w_R at $(0, 0)$ are given by,

$$\left.\begin{array}{l} u_R = \dot{X}_1 - z_G\dot{X}_5 - y\dot{X}_6 \\[2mm] w_R = \dot{X}_3 + y\dot{X}_4 \end{array}\right\} \tag{2.146}$$

m=1, 5, Sway, Roll; Anti-Symmetric Radiation Waves
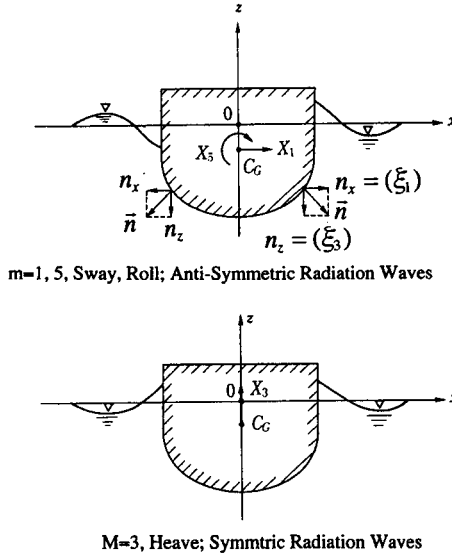

M=3, Heave; Symmtric Radiation Waves

Fig. 2.19 Symmetry and anti–symmetry of radiation waves and direction cosines

Then, three-dimensional Φ_R and the accompanied oscillatory pressure are approximated as follows:

$$
\left.
\begin{aligned}
\Phi_{R1} &= \phi_{R1}\, u_R, & p_{R1} &= i\rho\sigma\Phi_{R1} \\
\Phi_{R3} &= \phi_{R3}\, w_R, & p_{R3} &= i\rho\sigma\Phi_{R3} \\
\Phi_{R5} &= \phi_{R5}\, \dot{X}_R, & p_{R5} &= i\rho\sigma\Phi_{R5}
\end{aligned}
\right\}
\tag{2.147}
$$

So, using the relations of Eqs. (2.146) and (2.147), and integrating the pressure over the wetted curve, the radiation force acting on the cross section is obtained.

$$
\left.
\begin{aligned}
\mathrm{d}F_1^{(R)} &= -\int_{C_v} \left(p_{R1} + p_{R5}\right)\xi_1\,\mathrm{d}C \\
&= -\mathrm{d}M_{11}^{(A)}\dot{u}_R - \mathrm{d}N_{11}^{(D)}u_R - \mathrm{d}M_{15}^{(A)}\ddot{X}_5 - \mathrm{d}N_{15}^{(D)}\dot{X}_5 \\
\mathrm{d}F_3^{(R)} &= -\int_{C_v} p_{R3}\xi_3\,\mathrm{d}C = -\mathrm{d}M_{33}^{(A)}\dot{w}_R - \mathrm{d}N_{33}^{(D)}w_R \\
\mathrm{d}F_5^{(R)} &= -\int_{C_v} \left(p_{R1} + p_{R5}\right)\xi_5\,\mathrm{d}C \\
&= \mathrm{d}M_{51}^{(A)}\dot{u}_R - \mathrm{d}N_{51}^{(D)}u_R - \mathrm{d}M_{55}^{(A)}\ddot{X}_5 - \mathrm{d}N_{55}^{(D)}\dot{X}_5
\end{aligned}
\right\}
\tag{2.148}
$$

Furthermore, integrating them along the longitudinal direction, the three-dimensional radiation forces can be obtained.

$$F_1^{(R)} = \int_{l_B} dF_1^{(R)}, \quad F_2^{(R)} = -0.1 m_B \ddot{X}_2, \quad F_3^{(R)} = \int_{l_B} dF_3^{(R)} \left.\vphantom{\int}\right\}$$
$$F_4^{(R)} = \int_{l_B} y dF_3^{(R)}, \quad F_5^{(R)} = \int_{l_B} dF_5^{(R)}, \quad F_6^{(R)} = \int_{l_B} -y dF_1^{(R)} \left.\vphantom{\int}\right\}$$

$$(2.149)$$

where l_B is the length of a floating body, and the coefficient of added mass and the damping coefficient in surge are supposed to be 0.1 and 0, respectively.

(b) Wave-exiting force: Since, in the strip method, not only the beam waves but also oblique waves are the object, the velocity potential of incident waves is given by Eq. (2.17). In the wave-exciting force, the Froude-Krylov force is presented by Eq. (2.135). On the other hand, the diffraction force is almost given by the Haskind relation (2.137). According to the equation, the diffraction force acting on to a strip can be calculated by

$$dF_l^{(D)} = i\rho\sigma \int_{C_V} \left(\frac{\partial \Phi_I}{\partial n}\right) \phi_{Rl} dC$$
$$= i\rho\sigma \int_{C_V} \left(\frac{\partial \Phi_I}{\partial x}\xi_1 + \frac{\partial \Phi_I}{\partial z}\xi_3\right) \phi_{Rl} dC$$

$$(2.150)$$

Here, as $\partial\Phi_I/\partial x$ is mainly affected by the side wall of the floating body, it is approximated by the horizontal velocity at $x=0$, $z=-d/2$ and we may use u_I for this. For $\partial\Phi_I/\partial z$, since the bottom is only effective, we approximate it with the vertical velocity at $x=0$, $z=-S(y)/B$ where $S(y)$ is the cross sectional area at $y=y$, and we may use w_I for it. Moreover, using the Watanabe's approximation (Watanabe et al. 1958), Eq. (2.150) is rewritten as follows:

$$dF_l^{(D)} \cong i\rho\sigma \left(u_I \int_{C_V} \phi_{Rl}\xi_1 dC + w_I \int_{C_V} \phi_{Rl}\xi_3 dC \right)$$
$$= dM_{1l}^{(A)}\dot{u}_I + dN_{1l}^{(D)}u_I + dM_{3l}^{(A)}\dot{w}_I + dN_{3l}^{(D)}w_I$$

$$(2.151)$$

Substituting Eq. (2.145) into the above equation, the diffraction force applied to the strip can be approximated by

$$dF_1^{(D)} = dM_{11}^{(A)}\dot{u}_I + dN_{11}^{(D)}u_I \left.\vphantom{\int}\right\}$$
$$dF_3^{(D)} = dM_{33}^{(A)}\dot{w}_I + dN_{33}^{(D)}w_I \left.\vphantom{\int}\right\}$$
$$dF_5^{(D)} = dM_{15}^{(A)}\dot{u}_I + dN_{15}^{(D)}u_I \left.\vphantom{\int}\right\}$$

$$(2.152)$$

The relation of diffraction force between two- and three-dimensions is similar to Eq. (2.149) except for surge. The wave exiting force for surge may be approximated by the use of Froude-Krylov force.

$$F_2^{(D)} \cong -\int_{l_B} \rho g S(y) \frac{\partial \eta}{\partial y}\bigg|_{x=0} \gamma_c dy$$
$$\eta = -\frac{1}{g}\frac{\partial \Phi_I}{\partial t}, \quad \gamma_c = 0.73 + 0.6 z_G/d$$

$$(2.153)$$

Where γ_c is called the coefficient of effective wave slope.

(3) Drift force

When a floating body is moored and receives regular waves, the body shows not only the oscillatory motion, but also the slide motion to the forward direction of waves. The slide motion is caused by the steady drift force, which is given by considering the second order term of wave forces. The drift force in the infinite depth was given by Maruo (1960). In the following, using the same manner as Maruo, the drift force on the moored body in shallow water as shown in Fig. 2.20 is derived by the conservation law of momentum.
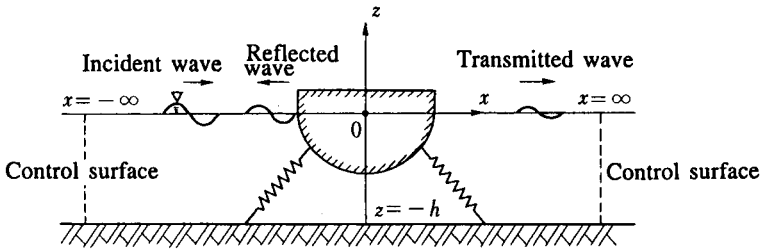
Fig. 2.20 Setting of control surface for obtaining drifting force

When we use H_I, H_R and H_T for the wave height of incident, reflected and transmitted waves, these corresponding velocity potentials Φ_I, Φ_R and Φ_T in the far field from the body are represented as follows:

$$
\left.
\begin{aligned}
\Phi_I &= \frac{igH_I}{2\sigma} \frac{\cosh k(h+z)}{\cosh kh} \exp\{i(kx - \sigma t)\} \\[2mm]
\Phi_R &= \frac{igH_R}{2\sigma} \frac{\cosh k(h+z)}{\cosh kh} \exp\{-i(kx + \sigma t - \tilde{\delta}_R)\} \\[2mm]
\Phi_T &= \frac{igH_T}{2\sigma} \frac{\cosh k(h+z)}{\cosh kh} \exp\{i(kx - \sigma t - \tilde{\delta}_T)\}
\end{aligned}
\right\}
\qquad (2.154)
$$

where, $\tilde{\delta}_R$ and $\tilde{\delta}_T$ are the phase lags of the reflected and transmitted waves from the incident wave, respectively.

If we set the control surfaces at $x=-\infty$ and $x=\infty$, the total velocity potentials at these positions can be denoted by $\Phi_{-\infty} = \Phi_I + \Phi_S$ and $\Phi_{\infty} = \Phi_T$. Using these relations and averaging the momentum difference between the both control surfaces over a wave period, the drift force F_D is given by

$$
\begin{aligned}
F_D &= \rho \int_{-h}^{\eta_{-\infty}} \overline{\left(\frac{\partial \Phi_{-\infty}}{\partial x}\right)^2} dz + - \int_{-h}^{\eta_{-\infty}} \overline{p}_{-\infty} dz - \rho \int_{-h}^{\eta_{\infty}} \overline{\left(\frac{\partial \Phi_{\infty}}{\partial x}\right)^2} dz \\[2mm]
&\quad - \int_{-h}^{\eta_{\infty}} \overline{p}_{-\infty} dz
\end{aligned}
\qquad (2.155)
$$

where, the pressure p is given by Bernoulli's equation (1.22). Substituting Eq. (2.154) into Eq. (2.155) and after having carried out some manipulations, the drift force is given by the simple relation as follows:

$$F_D = \frac{\rho g}{16}\left(1+\frac{2kh}{\sinh 2kh}\right)\left(H_I^2 + H_R^2 + H_T^2\right) \qquad (2.156)$$

Furthermore, substituting the conservation law of energy $H_I^2 = H_R^2 + H_T^2$ into the above, the drift force can be expressed by using only the reflected wave.

$$F_D = \frac{1}{8}\rho g\left(1+\frac{2kh}{\sinh 2kh}\right)H_R^2 \qquad (2.157)$$

The above equation coincides with Maruo's formula when $h=\infty$. Now writing K_R for the reflection coefficient, and defining the coefficient D_R of drift force by $F_D/(\rho g H_I/8)$, then,

$$D_R = \left(1+\frac{2kh}{\sinh 2kh}\right)K_R^2 \qquad (2.158)$$

This relation shows that the coefficient of drift force is proportional to the square of the reflection coefficient.

2.5 Wave Forces on Small Bodies

Up to the preceding sections, the method for estimating wave loads on large offshore structures has been discussed, focusing mainly on the wave diffraction and radiation phenomena by the structure. In this section, we will briefly describe the method of wave force calculation for a small body, for which the diffraction parameter D/L is small ($D/L<0.2$) and KC is comparatively large as shown in Fig. 2.1.

In this regime, the phenomena of flow separations and resultant vortex formations behind the body considerably affect the wave force. Therefore, it becomes important how to take such phenomena into consideration for the wave force calculation. Meanwhile, since the effect of wave diffraction and radiation by the body may be neglected in this regime, we can assume that there is little or no variation of unsteady fluid forces with D/L. This assumption is assured from Fig. 2.7 in which the effective inertia coefficient C_M for a vertical circular cylinder is almost constant in the range $D/L<0.2$ and is equal to the inertia coefficient in an oscillating fluid, i.e., $C_M=2.0$.

Until now, wave forces on a small body have been estimated by a semi-empirical formula because of its simplicity and convenience. For instance, wave forces on a vertical cylinder in the wave propagation direction, i.e., in-line forces, are usually calculated by the Morison equation. Further, the transverse forces or lift forces may be evaluated by the multi-component lift force equation proposed by Sawaragi et al. (1976).

In those semi-empirical formulas, however, hydrodynamic coefficients are included, which have to be determined experimentally or empirically. Thus, the selection of the hydrodynamic coefficients has been a controversial problem for a long time. In order to clarify the hydrodynamic features of these coefficients, many studies have been carried out especially for a vertical circular cylinder from both the experimental aspect (Sarpkaya

1975 (a), Garrison 1990) and the theoretical aspect (Stansby 1977, Sawaragi and Nakamura 1979). With such an accumulation of knowledge, characteristics of the hydrodynamic coefficients for a vertical circular cylinder have been gradually clarified (e.g., Sarpkaya and Isaacson 1981). Recently, the study for a sphere has been gradually advanced too (e.g., Iwata and Mizutani 1989). However, concerning other geometrical bodies, such as a rectangular cylinder, little comprehensive work has been done. Therefore, it is common to substitute the drag coefficients in a steady flow and the inertia coefficients in an idealized fluid to the wave force equation.

There is a completely different method from the previously described one to estimate wave forces on a small body, especially for a cylindrical body. This method is based on the numerical simulation results of the vortex flow about the body (Stansby 1977, Sawaragi and Nakamura 1979). The details of the method will be presented in a later section. Because the procedure can be used for estimating not only the hydrodynamic forces but also the flow features about the body, it may be widely applicable to other hydrodynamic problems. However, there are still some difficulties in the method, which should be solved in the future. For instance, it is difficult to model the influence of fluid viscosity on the vortex flow behind the body. In addition, this method requires a great amount of computation effort.

In this section, based on the Morison equation, we mainly introduce the method of wave force calculation on a cylindrical body. Furthermore, in the latter part of this section, proximity effects on the wave forces caused by placing the body near the boundary, such as a seabed and a water surface, are also described.

2.5.1 Wave forces on a cylindrical body

In-line forces on a vertical cylinder F_V are usually calculated by the Morison equation (Morison et al. 1950).

$$F_V = \int_{-h}^{\eta} \left\{ \frac{1}{2} C_D \rho D_P |u(z)| u(z) + C_M \rho A_P \frac{\partial u(z)}{\partial t} \right\} dz \qquad (2.159)$$

where, C_D is the drag coefficient, C_M is the inertia coefficient, D_P is the width of the cylinder projected on the normal plane to the wave propagation direction, A_P is the cross sectional area of the cylinder, $u(z)$ is the horizontal fluid velocity at elevation z, $\partial u(z)/\partial t$ is the horizontal fluid acceleration at elevation z, and η is the water surface elevation at the centroid of the cylinder.

If we assume the linear wave theory, the horizontal velocity u and the water elevation η can be expressed through the use of Eq. (2.17) as

$$u(z) = \text{Real} \left[\frac{\partial \Phi_I}{\partial x} \right]_{\alpha=0^\circ} \qquad : \text{at } (x,y) = (x_G, y_G) \qquad (2.160)$$

$$\eta = -\frac{1}{g} \text{Real} \left[\frac{\partial \Phi_I}{\partial t} \right]_{\alpha=0^\circ} \qquad : \text{at } (x,y,z) = (x_G, y_G, 0) \qquad (2.161)$$

The horizontal acceleration is obtained by taking the time derivative of Eq. (2.160). There are several assumptions for deriving the Morison equation, listed as follows:

i)   Wave scattering by the fixed cylinder can be negligible and there is no change in the incident waves after passing by the cylinder.
ii) Wave forces can be calculated by the linear summation of the drag and inertia forces.
iii) Drag forces on the cylinder under the wave motion can be approximated by the drag force equation for the body in a steady flow, which is proportional to the square to the velocity vector in the normal direction of the cylindrical axis.
iv) Inertia forces on the cylinder under the wave motion can be approximated by the unsteady force equation deduced from the unidirectional potential flow theory.

In short, considering that wave forces on a small body must be given as a summation of the unsteady force in the potential flow and the vortex-induced force, we can say that the drag force term in the Morison equation as described in iii) is used to approximately express the vortex-induced force.

According to the previous results, it has been known that drag and inertia coefficients are functions of both the Reynolds number ($Re = U_m D/v$; $v =$ kinematic viscosity) and KC number. Regarding these results on the hydrodynamic coefficients, please refer to other engineering literature (e.g., Sarpkaya and Isaacson 1981, Chakrabarti 1987).

Here, we will briefly describe the method of wave force calculation on an inclined cylinder (Chakrabarti 1975). In Fig. 2.21, the analytical model assumed here is shown, in which a circular cylinder with a diameter D is obliquely fixed in a plane wave field.
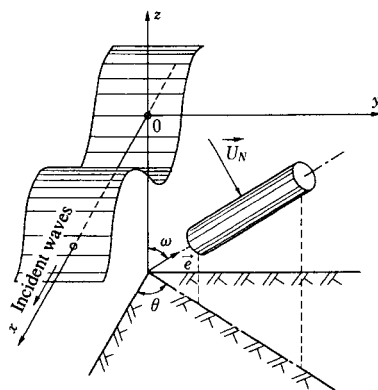
Fig. 2.21   Analytical model of an inclined tubular member and definition sketch

In this model, the wave induced velocity vector $\vec{V}_w$ is defined by

$$\vec{V}_w = (u, 0, w) \tag{2.162}$$

If we denote a unit vector in the axial direction of the cylinder as $\vec{e} = (e_x, e_y, e_z)$, it can be expressed by the use of the inclination angles θ and ω as follows:

$$(e_x, e_y, e_z) = (\sin \omega \cos\theta, \sin \omega \sin\theta, \cos\omega) \tag{2.163}$$

As specified previously, it is assumed in the Morison equation that there is no contribution from the axial velocity and acceleration to the wave force. Therefore, it is convenient to decompose the velocity vector into two different directions, i.e., axial direction and normal to it. The velocity component in the normal direction, $\vec{U}_N$, can be obtained by subtracting the axial velocity component from $\vec{V}_w$, i.e.,

$$\vec{U}_N = \vec{V}_w - \left(\vec{e}\cdot\vec{V}_w\right)\vec{e} \tag{2.164}$$

Through the use of $\vec{U}_N$ and its time derivative $\partial\vec{U}_N/\partial t$, we can specify the local wave force $\mathrm{d}\vec{F}_V$ on the inclined cylinder per unit length as follows:

$$\mathrm{d}\vec{F}_V = \frac{1}{2}C_D\rho D\left|\vec{U}_N\right|\vec{U}_N + C_M\rho\left(\frac{\pi D^2}{4}\right)\left(\frac{\partial\vec{U}_N}{\partial t}\right) \tag{2.165}$$

By decomposing the local wave force vector into the usual tri-axial components, we can obtain the x-, y- and z-axis components of force.

Equation (2.165) is the most general form of the Morison equation, which can be used for the complex offshore structure consisting of tubular members.

However, there are some difficulties to apply Eq. (2.165) to the other cylindrical members that have different sections from a circular one. Because the direction of the normal vector $\vec{U}_N$ is changing with time, i.e., rotating around the cylindrical axis, the projected area of the cylinder to the normal plane to the $\vec{U}_N$ changes with time too, and the hydrodynamic coefficients may vary with the $\vec{U}_N$ direction. Those problems should be solved in the future for the rational design of offshore structures.

On the other hand, it has become known that lift forces (or transverse forces) act on the cylinder in addition to the in-line forces simultaneously. In the previous studies, it was clarified that the lift force is generated by the asymmetrical vortex flow pattern behind the cylinder and has the same magnitude as the in-line force. In addition, as a distinctive feature, it has the predominant higher harmonic components compared to the in-line force (Sawaragi et al. 1976, Sarpkaya and Isaacson 1981). The frequency characteristics of the lift force will be partly introduced in Chapter 6.

2.5.2 Wave forces on a submerged sphere

The wave forces acting on a submerged sphere have been discussed experimentally by Iwata and Muzutani (1989). They reported that the wave force is closely related to the flow conditions around the sphere. The flow conditions around the sphere can be largely classified into two types; a rotating pattern and oscillating pattern. These patterns can be further classified into two types in connection with flow separation. Consequently, the flow condition can be classified into four types, such as the rotating pattern with and without flow separation and the oscillating pattern with and without flow separation. The rotating flow pattern appears under the condition that the vertical water particle motion is larger than half the horizontal one. Under such a condition, the horizontal and vertical wave forces can be evaluated with the Morison equation. On the other hand, the oscillating flow pattern appears when the vertical particle motion is less than one-third the horizontal one. The horizontal wave force can be estimated by the Morison equation under that condition as well. The Morison equation, however, becomes less accurate in evaluating the vertical

wave force because the lift force caused by the horizontal water particle motion dominates the vertical drag and inertia forces. Thus, it is very important to discuss the applicability of the Morison equation in advance.

The applicable range of the Morison equation to the estimation of wave forces on a submerged sphere was examined by Iwata and Mizutani (1989). The drag and inertia coefficients in the applicable range of the Morison equation are given graphically by them as shown in Figs. 2.22 through 2.25.
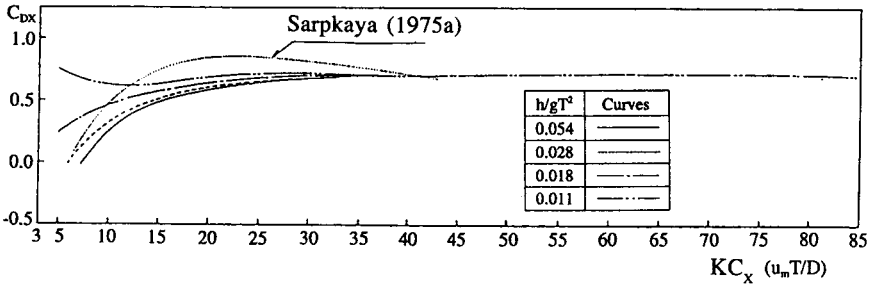

Fig. 2.22   Mean value of C_{Dx} versus KC_x
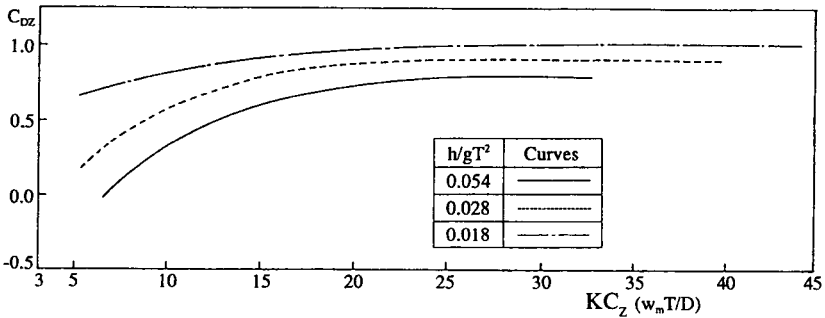
Fig. 2.23   Mean value of C_{Dz} versus KC_z

It is noted that the Morison equation is also inapplicable in estimating the vertical wave force in the case that the sphere is located near the bottom and free surface boundaries, since the bottom and free surface boundary proximities have a predominant effect on the wave force. A detailed discussion of the boundary proximity effect is described in the following section.

2.5.3 Boundary proximity effect on wave forces
(1) Horizontal circular cylinder

Flow around a structure located near a boundary is fluctuated by the existence of the boundary compared to the flow around a structure away from the boundary. Consequently, acting wave forces on it are also fluctuated. This proximity effect of the boundary is significant in designing structures, in particular undersea pipelines. Many reseraches have

been conducted on the proximity effect of the bottom boundary on the wave force being exerted on the horizontal circular cylinder located near the bottom boundary.
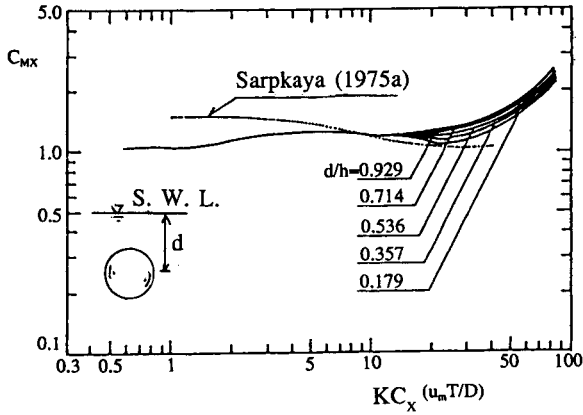
Fig. 2.24 Mean value of C_{Mx} versus KC_x
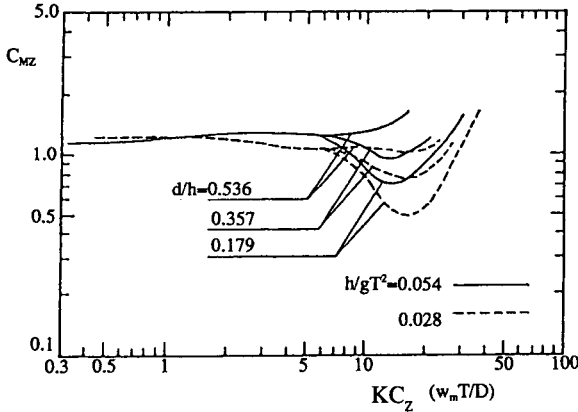
Fig. 2.25 Mean value of C_{Mz} versus KC_z

In evaluating the wave force acting on a horizontal circular cylinder with the Morison equation, the inertia and drag coefficients, C_D and C_M, are governed by the gap ratio $\hat{e}/D$ as well as the Re and KC numbers, where $\hat{e}$ is the gap between the cylinder and the bottom boundary. Yamamoto et al. (1974, 1976) discussed theoretically this gap effect and reported that C_M increases with decreasing $\hat{e}/D$ in the case that $\hat{e}/D$ is less than unity and it reaches 1.6 when $\hat{e}/D=0$. They confirmed these results through laboratory experiments. Sarpkaya (1977) investigated the wall proximity effect through detailed experiments using the U-tube and graphically showed C_D and C_M as functions of Re, KC and $\hat{e}/D$ as shown in Fig. 2.26.
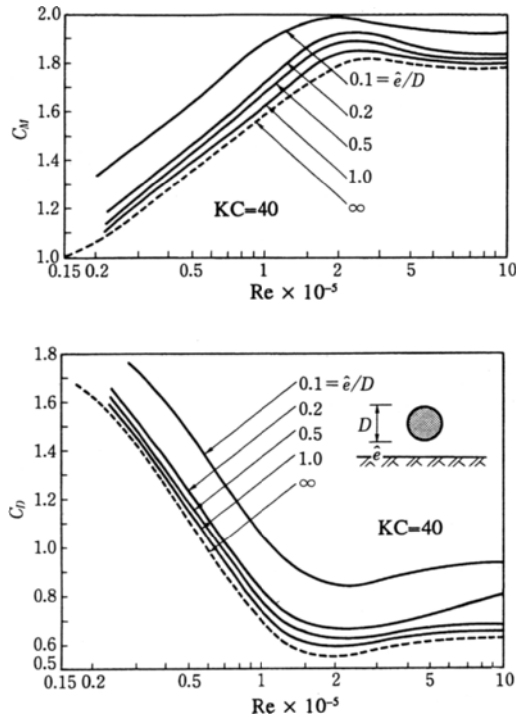
Fig. 2.26 Proximity effects of a sea bed boundary on C_M and C_D of a circular cylinder (Sarpkaya 1977)

The bottom boundary proximity affects not only the in-line force but also the lift force that arises from an asymmetric pressure distribution on the cylinder. Since the flow around the cylinder located near the boundary is fluctuated, the asymmetric pressure distribution on the cylinder causes the lift force even under the unseparated flow condition. Based on the potential theory (von Müller 1929), the lift force acts always downward on the cylinder when the cylinder does not attach to the boundary. But once the cylinder attaches to the boundary, the upward lift force acts on the cylinder. In this case, the lift coefficient becomes $\pi(\pi^2+3)/9 = 4.49$ (von Müller 1929). Sarpkaya (1977) discussed the proximity effect on the downward lift force and found that the effect of $\hat{e}/D$ on the upward lift force is different from that on the downward lift force. Shanker et al. (1988) reported that the second harmonic component of the lift force grows up under the flow condition that $5<KC<10$ through their laboratory experiments.

In the above discussion, the boundary proximity is due to the bottom boundary, like a sea bottom. It is confirmed that the free surface boundary proximity also affects the wave force. This effect has been discussed by Chakrabarti (1975) and Chaplin (1984) and revealed that the free surface proximity significantly affects the wave forces.

(2) Sphere
(a) Bottom boundary proximity: Iwata and Mizutani (1991) discussed the wave force acting on a submerged sphere and reported that the horizontal wave force can be evaluated by the Morison equation without a significant influence of the bottom boundary proximity.

The vertical wave force, however, has been revealed to be affected by the bottom boundary proximity and the Morison equation becomes less accurate in the estimation of it. Under the condition that d_B/D is less than 1.5, where d_B is the distance between the center of the sphere and the bottom boundary, the lift force caused by the asymmetric pressure distribution, which consists mainly of a steady downward component and a second harmonic component plays an important role on the vertical wave force. Iwata and Mizutani proposed the equation to estimate such a vertical wave force as follows:

$$F_z = \frac{1}{8} C_{Dz} \rho \pi D^2 w \sqrt{u^2 + w^2} + \frac{1}{6} C_{Mz} \rho \pi D^3 \frac{\partial w}{\partial t}$$
$$- \frac{1}{6} C_{L1} \rho \pi D^3 \alpha' \overline{u^2} - \frac{1}{6} C_{L2} \rho \pi D^3 \alpha' \left(u^2 - \overline{u^2} \right)$$

(2.166)

where, C_{DZ} and C_{MZ} are the drag and inertia coefficients in the z-axis direction, respectively. C_{L1} and C_{L2} are the lift coefficients corresponding to the steady and second harmonic components, respectively and α' is $9D^3/512d_B^4$. The upper bar in Eq. (2.166) indicates the time averaged value over one wave period. C_{L1} and C_{L2} are given experimentally by Iwata and Mizutani as shown in Fig. 2.27 as functions of h/gT^2 and d_B/D. Regarding the drag and inertia coefficients, they can be evaluated with the empirical formula by Iwata and Mizutani (1989), which was shown earlier in Figs. 2.23 and 2.25.
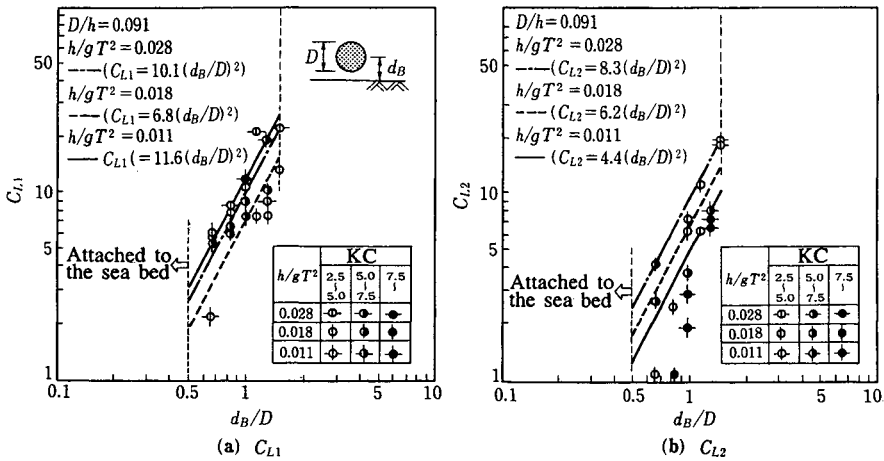
Fig. 2.27 Lift coefficients versus d_B/D

In the case that the flow separation takes place, the vertical wave force is governed by the vortex with complex behavior and its time variation becomes irregular. At the present stage, it is difficult to evaluate accurately such a wave force and further investigations are necessary.

(b) Free Surface Proximity Effect: Iwata and Mizutani (1991) discussed the free surface boundary effect on the wave force acting on a submerged sphere as well as the bottom boundary proximity. Their results show that the maximum vertical wave force is not affected by the free surface proximity. The time variation of it, however, is affected significantly because of the lift force with second harmonic frequency. Consequently, the Morison equation becomes useless. Iwata and Mizutani discussed the lift force and found that its amplitude is proportional to u^2 and $(d_F/D)^{-3}$, where d_F is the distance between the center of the sphere and the wave trough. These results are similar to the first approximation obtained by Kim (1978) for the sphere in the uniform flow field. They proposed the equation to evaluate the vertical wave force affected by the free surface proximity as follows:

$$F_z = \frac{1}{8} C_{Dz} \rho \pi D^2 w \sqrt{u^2 + w^2} + \frac{1}{6} C_{Mz} \rho \pi D^3 \frac{\partial w}{\partial t}$$
$$- \frac{1}{32} C_F \rho \pi D^2 u^2 \left(\frac{D}{\eta + d} \right)^3$$

(2.167)

where, C_F is the lift force caused by free surface proximity and is given in Fig. 2.28.
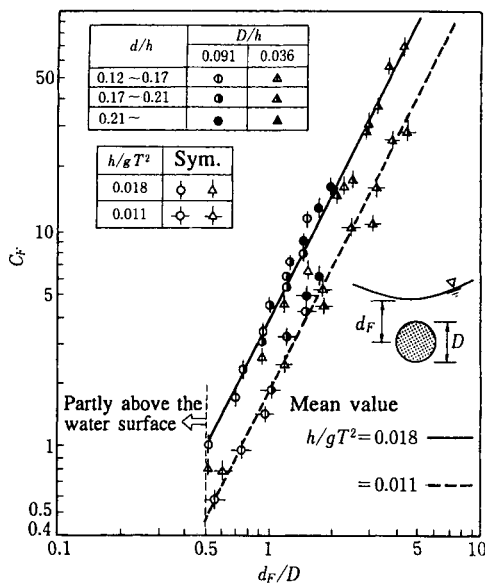
Fig. 2.28 C_F versus d_B/D

Regarding the drag and inertia coefficients, C_{Dz} amd C_{Mz}, they can be evaluated with Fig. 2.23 and 2.25, respectively.

2.6 Wave Transformation through Permeable Structures

2.6.1 Basic equation in permeable structure

When an incident wave encounters a permeable structure face, part of the wave is reflected back to the offshore-side, and some of the energy is lost to wave breaking and the remaining energy is transmitted to the structure interior. The wave inside the permeable structure decays as it propagates against the resistant force through the pores. In this section, wave propagation through hydraulically homogeneous porous materials is discussed. Although several theoretical models (e.g., Sollitt and Cross 1972, Madsen 1974) have been proposed to evaluate wave transformation, the model proposed by Sollitt and Cross (1972) is mainly employed here to discuss wave deformation.

x-, y-, and z- components of the discharge velocity $\vec{q} = (q_x, q_y, q_z)$ are related to those of the water particle velocity $\vec{u}_s = (u, v, w)$ with the use of a porosity λ of the materials,

$$q_x = \lambda u, \ q_y = \lambda v, \ q_z = \lambda w \tag{2.168}$$

Assumption of incompressibility of water yields the three-dimensional Eulerian continuity equation

$$\frac{\partial u}{\partial x} + \frac{\partial v}{\partial y} + \frac{\partial w}{\partial z} = 0 \tag{2.169}$$

where, x and y are the horizontal axes, x coincides with the wave propagation direction and z is the vertical axis taken positive upward with its origin on the still water level (see Fig. 2.29).
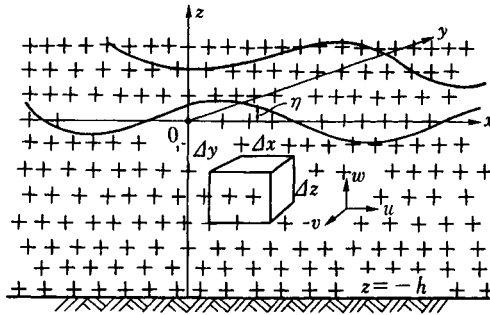
Fig. 2.29 Wave propagation in porous media and definition sketch

The equation of motion can be derived using the conservation law of momentum flux. The momentum balance within the control volume of $\Delta x \Delta y \Delta z$, Fig. 2.29, yields

$$\frac{\partial}{\partial t}\iiint \rho \vec{v}_s \, \mathrm{d}V + \iint \rho \vec{v}_s \left(\vec{v}_s \cdot \vec{\bar{n}}\right) \mathrm{d}S = \sum \vec{F} \tag{2.170}$$

Where, ρ is the density of water, $\vec{n}$ is the unit normal vector to control volume surface, and S and V are the closed surface and control volume bounded by S, respectively. The left-hand side of Eq. (2.170) represents time variation of the momentum within the control volume, the second term corresponds to the momentum flux from the control volume and the term on the right-hand side of Eq. (2.170) is the total force acting on the fluid within the control volume.

The total force acting on the unit mass $\sum \vec{f}_i$ is given with the sum of the pressure gradient and the resistive force to the fluid as follows:

$$\sum \vec{f} = -\frac{1}{\rho}\nabla(p+\rho gz) - \frac{v}{K_p}\lambda \vec{v}_S - \frac{C_f}{\sqrt{K_p}}\lambda^2 \vec{v}_S|\vec{v}_S| - \frac{(1-\lambda)}{\lambda}C_M\frac{D\vec{v}_S}{Dt} \qquad (2.171)$$

where, v is the kinematic viscosity, K_p is intrinsic permeability, C_f is the dimensionless turbulent resistance coefficient, and C_M is the inertia coefficient. The first term of the right-hand side of Eq. (2.171) is the pressure term, second and third terms are the linear and nonlinear drag forces with which solid materials act on the fluid, and the fourth term is the inertia force with which the solid material acts on the fluid.

Substitution of Eqs. (2.168), (2.169) and (2.171) into Eq. (2.170) and its rearrangement produces

$$S_M \frac{D\vec{v}_S}{Dt} = -\frac{1}{\rho}\nabla(p+\rho gz) - \frac{v}{K_p}\lambda \vec{v}_S - \frac{C_f}{\sqrt{K_p}}\lambda^2 \vec{v}_S|\vec{v}_S|$$

$$S_M = 1 + \{(1-\lambda)/\lambda\}C_M \qquad (2.172)$$

Equation (2.172) is nonlinear. Therefore, linearization is performed here to avoid complicated numerical calculation. Applying the Lorentz principle of equivalent work to the second and third terms of the right-hand side of Eq. (2.172) yields

$$\left. \begin{array}{l} \dfrac{v}{K_p}\lambda \vec{v}_S + \dfrac{C_f}{\sqrt{K_p}}\lambda^2 \vec{v}_S|\vec{v}_S| = \hat{f}_E \sigma \vec{v}_S \\[4mm] \hat{f}_E = \dfrac{1}{\sigma}\dfrac{\iiint dV \int_t^{t+T} \lambda^2 \left(v|\vec{v}_S|^2/K_p + C_f\lambda|\vec{v}_S|^3/\sqrt{K_p}\right)dt}{\iiint dV \int_t^{t+T} \lambda|\vec{v}_S|^2\, dt} \end{array} \right\} \qquad (2.173)$$

where, $\hat{f}_E$ is a nondimensional equivalent resistance coefficient and σ is the angular frequency. Substitution of Eq. (2.173) into Eq. (2.172) and neglecting the nonlinear acceleration term of $D\bar{u}_s/Dt$ produces.

$$S_M \frac{\partial \vec{v}_S}{\partial t} = -\frac{1}{\rho}\nabla(p+\rho gz) - \hat{f}_E \sigma \vec{v}_S \qquad (2.174)$$

Equation (2.174) is a linearized equation of motion. Accurate evaluation of wave kinematics inside the permeable structure depends on how accurately C_M and $\hat{f}_E$ are formulated.

2.6.2 Fluid force coefficient

A resistance formula of the Dupuit-Forchheimer type for one-dimensional steady flow is approximately employed to evaluate the resistance that the fluid receives from the granular materials such as stones and concrete blocks.

$$-\frac{1}{\rho}\nabla p = \vec{v}_s\left(b_1 + b_2\vec{v}_s\right) \tag{2.175}$$

The coefficients b_1 and b_2 are mainly related to the characteristics of solid materials and are usually determined by laboratory experiments. $b_1 = \nu/K_p$ and $b_2 = C_f/\sqrt{K_p}$ are adopted in the case of stones in Eq. (2.171) (Sollitt and Cross 1972). On the other hand, Engelund (1953) proposed different formulations.

The inertia coefficient C_M is, in general, unknown for random and densely packed materials. In the case that the dimension of porous space is almost equal to the material size, some or all of the fluid mass in the pores can be assumed to be an added mass (Kondo et al. 1972),

$$1 < C_M < \frac{1}{1-\lambda} \tag{2.176}$$

However, Eq. (2.176) has not yet been verified accurately.

2.6.3 Analysis by means of eigenfunction expansion method

A wave transformation problem in the case of a vertical permeable structure in a constant water depth of h, as shown in Fig. 2.30, is treated here.
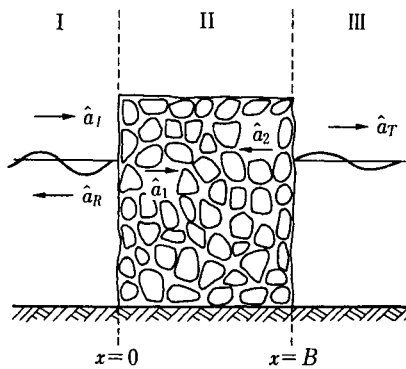
Fig. 2.30 Definition sketch and boundary setting about a permeable breakwater

Under the conditions that the wave is linear and its motion is irrotational, using the velocity potential Φ $(x, z; t)$ transforms Eq. (2.174) to

$$S_M \frac{\partial \Phi}{\partial t} + \frac{1}{\rho}(p + \rho g z) + \hat{f}_E \sigma \Phi = 0 \tag{2.177}$$

In addition, the wave period inside the porous structure is treated to be equal to the incident wave period and the velocity potential Φ $(x, z; t)$ is described as ϕ $(x, z) e^{-i\sigma t}$, in which $i = \sqrt{-1}$. The fluid region is devided into three parts in accordance with the structure shape, as shown in Fig. 2.30. Using Eqs. (2.11), (2.12), (2.169) and (2.177), the wave boundary-value problem in region II is described as follows:

$$\left.\begin{array}{ll} \text{Basic equation}: \dfrac{\partial^2 \Phi}{\partial x^2} + \dfrac{\partial^2 \Phi}{\partial z^2} = 0: & 0 \leq x \leq B \\[2mm] & -h \leq z \leq 0 \\[2mm] \text{Boundary conditions}: g\dfrac{\partial \Phi}{\partial z} + \sigma^2\left(i\hat{f}_E - S_M\right)\Phi = 0: & z = 0 \\[2mm] \dfrac{\partial \Phi}{\partial z} = 0: & z = -h \end{array}\right\} \tag{2.178}$$

Employing a separation of variables method, a two-dimensional general solution of velocity potential $\Phi^{(II)}$ in region II is derived as

$$\Phi^{(II)} = \sum_{n=1}^{\infty} \frac{-i\sigma}{k_n}\left\{\hat{a}_{1n}e^{iK_n x} + \hat{a}_{2n}e^{-iK_n(x-B)}\right\} \frac{\cosh K_n(h+z)}{\sinh K_n h} e^{-i\sigma t} \tag{2.179}$$

where, $\hat{a}_{1m}$ and $\hat{a}_{2m}$ are integral constants proportional to the wave amplitude in the porous structure, B is the width of the porous structure, and K_n is the wave number in the porous structure which satisfies the following relationship:

$$\sigma^2\left(S_M - i\hat{f}_E\right) = gK_n \tanh K_n h \quad (n = 1, 2, \cdots) \tag{2.180}$$

Since K_n is a complex number, $\Phi^{(II)}$ represents a damping progressive wave. Equation (2.180) in the case of $\hat{f}_E = 0$ and $C_M = 1$ is equal to the dispersion relationship (Eq. (2.41)) for the progressive mode wave with a small amplitude.

The incident and reflected waves exist in region I and the transmitted wave is included in region III. Using the velocity potential of the incident wave described in **2.2.1** and those of the evanescent mode waves in **2.4.1** the velocity potentials $\Phi^{(I)}$ and $\Phi^{(III)}$ are described as

Region I:

$$\Phi^{(I)} = \left[\frac{-i\sigma}{k} \left\{ \hat{a}_I e^{ikx} + \hat{a}_{R0} e^{-ikx} \right\} \frac{\cosh k(h+z)}{\cosh kh} \right.$$

$$\left. + \sum_{n=1}^{\infty} \frac{\sigma}{k_n} \hat{a}_{Rn} \frac{\cos k_n(h+z)}{\sin k_n h} e^{k_n x} \right] e^{-i\sigma t} \tag{2.181}$$

Region III:

$$\Phi^{(III)} = \left[\frac{-i\sigma}{k} \hat{a}_{T0} \frac{\cosh k(h+z)}{\sinh kh} e^{ik(x-B)} \right.$$

$$\left. + \sum_{n=1}^{\infty} \frac{\sigma}{k_n} \hat{a}_{Tn} \frac{\cos k_n(h+z)}{\sin k_n h} e^{-k_n(x-B)} \right] e^{-i\sigma t} \tag{2.182}$$

where, $\hat{a}_I$ is the incident wave amplitude, $\hat{a}_{R0}$ and $\hat{a}_{T0}$ are, respectively, the reflected and transmitted wave amplitudes, and $\hat{a}_{Rn}$ and $\hat{a}_{Tn}$ ($n = 1, 2, 3, ...$) are the amplitudes of the evanescent mode waves in regions I and III, respectively.

Equations (2.179), (2.181) and (2.182) contain $4n$ unknowns of $\hat{a}_{Rn}$, $\hat{a}_{1n}$, $\hat{a}_{2n}$ and $\hat{a}_{Tn}$ ($n = 1,2, ...$). Therefore, $4n$ additional boundary conditions are required to solve those unknowns. The appropriate boundary conditions are continuity of pressure and horizontal mass flux at $x = 0$ and $x = B$. The theory is evaluated using a given structure properties and five terms in the eigen series solution.

Figure 2.31 shows one example of comparison between theoretical values and experimental data, in which d_e is the representative length of material and C_M is assumed to be zero.

$h = B = 30.5\text{cm}$
$d_e \cong 2\text{cm}$
$0.75 < kh < 1.25$

	Exp.	Cal.
$K_R:$	o	- - - -
$K_T:$	•	——
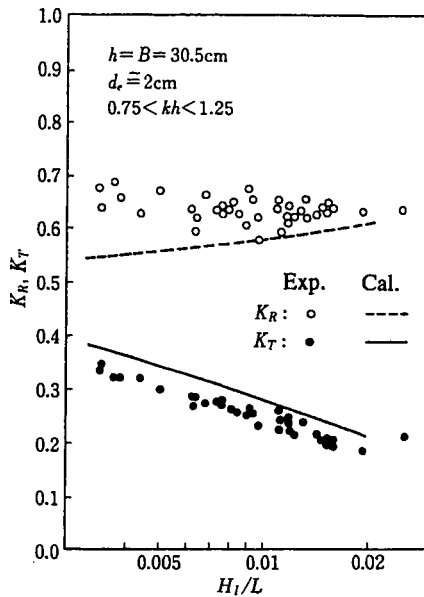
Fig. 2.31 Variations of K_R and K_T with H_I/L (Sollitt and Cross 1972)

The theoretical values correspond well, in general, to experimental data. However, the theory overestimates the transmission coefficient K_T $(=\hat{a}_{T0}/\hat{a}_I)$ and underestimates the reflection coefficient K_R $(=\hat{a}_{R0}/\hat{a}_I)$. This may be much improved by accurate evaluation of C_M. Therefore the accurate evaluation of C_M is one of the important problems left to future investigation.

Different theoretical methods have been developed. Madsen (1974) used a long wave theory. Ijima et al. (1974) employed Green's theorem, which can be extended to sloping permeable structures as well.

2.7 Vortex Flow and Fluid Force

2.7.1 Numerical modeling of a separated flow

The discrete vortex approximation has been suggested by a number of works as a powerful method for simulating the flow pattern around a bluff-based body with the separated flow as shown in Fig. 2.32 (a). This method approaches the separated shear layers by means of arrays of discrete vortices as shown in Fig. 2.32 (b).

(a) Separated flow

(b) Separted flow model
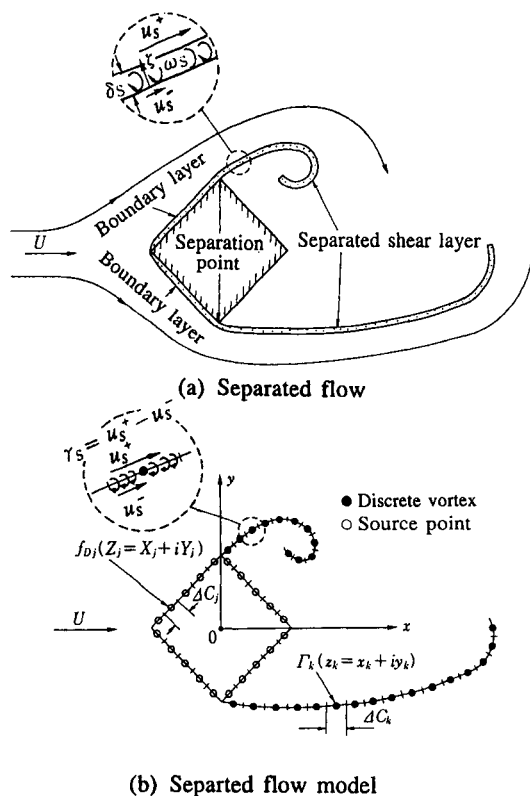
Fig. 2.32　Separated flow around a bluff-based body and its numerical modeling

Accordingly, the rolling-up behaviour of the shear layer behind body and the resultant complex vortex flow can be treated easily. The simulation model of the separated flow in the two-dimensional flow is described in here.

(1) Modeling of separated shear layers

The separated shear layer is formed due to the separation of the boundary layer generated on the surface of the body from the separation point (Fig. 2.32 (a)), and can be regarded as the continuous distributed vorticity sheet. In the discrete vortex approximation, the thickness of the separated shear layer is assumed to be very thin. Then, the shear layers are represented by a line as shown in Fig. 2.32 (b), the plane-distributions of vorticity along the shear layer are replaced by the line-distributions of the equivalent circulations to these vorticities. Since the surface integral of vorticity is equal to the circulation in the closed curve around it, the circulation per unit length can be given by

$$\int_0^{\delta_s} \omega_s \mathrm{d}\zeta = \gamma_s \tag{2.183}$$

where ω_s is the vorticity in the shear layer, δ_s is the shear layer thickness, ζ is a coordinate in the direction normal to the shear layer, γ_s is the circulation per the unit length along the shear layer. γ_s can be defined as the difference of velocities at the upper and lower positions of the shear layer ($u_s^+ - u_s^- : u_s^+$ and u_s^- being the respective velocities at the outskirts of the shear layer as shown in Fig. 2.32 (b)).

In the discrete vortex approximation, the separated shear layer is divided into the segments of the infinitely short line as shown in Fig. 2.32 (b), the discrete vortex with the circulation along the individual segment is located at the center of it. Consequently, the complex velocity potential W_v of flow which is induced by these approximated shear layers can be represented as a set of discrete vortices, and is given by

$$W_V(Z) = -\frac{i}{2\pi} \sum_{k=1}^{N_v} \left(\int_{\Delta C_\kappa} \gamma_s \mathrm{d}C \right) \log(z - z_k)$$

$$= -\frac{i}{2\pi} \sum_{k=1}^{N_v} \Gamma_k \log(z - z_k) \tag{2.184}$$

where, Γ_k is the circulation along the k-th line segment ΔC_k, $i = \sqrt{-1}$ and $z_k = x_k + iy_k$, which specifies the complex coordinate of a discrete vortex. The circulation with a counterclockwise direction is defined as positive. N_v is the total number of vortices and $z = x + iy$, which is the complex coordinate of the field point.

Since the discrete vortex approximation disregards the thickness of the shear layer and depends on the potential theory as represented in Eq. (2.184), the flow of a high Reynolds number is assumed in the strict sense. This is similar to the boundary layer theory which applies the viscous flow and the potential flow to the inner and the outer region of the thin layer on the surface of body respectively. Namely, the discrete vortex approximation assumes that the vorticity concentrates in a separated shear layer whose thickness is sufficiently thin. Furthermore, since the discrete vortex approximation mainly concerns with the interactions between the separated shear flow and the body as well as the main flow, it may be considered that this method is the analysis which deals with macroscopic features of the vortex flow patterns. Because of the simplification described above, this

approximation can reduce the computation efforts sharply in comparison with the manner which analyzes the Navier-Stokes equation directly. Consequently, this model has been used in calculations of the vortex flow patterns around various bodies and the fluid force acting on those.

(2) Complex velocity potential around a two-dimensional body

In the case where the flow separation does not occur, the velocity potential Φ of the flow around a two-dimensional body can be found using the manner described in **2.3**. The complex velocity potential which is defined by a pair of the velocity potential and the stream function is easily deduced by introducing the complex-number expression to the procedure in **2.3**.

On the other hand, when the flow separation occurs, the complex velocity potential W can be derived by summing the complex velocity potential W_v for the separated shear layer, the complex velocity potential W_v' which is necessary to maintain the boundary condition of zero flow across the body surface and the above described complex velocity potential for the flow without the separated flow.

The appropriate complex velocity potential for the flow with vortex around the body has been determined using two methods; the conformal mapping method which is used in the case of the simple flow like uniform flow, and the boundary integral equation method described in **2.3**. In the conformal mapping method (Clements 1973), the body is generally transformed to the circular or the flat plane in order to determine easily the appropriate complex velocity potential of the flow around the body. However, this method has a difficulty in the derivation of the mapping function, and accordingly this is not an entirely practical method. Therefore, the alternative methods based on the boundary integral equation method which have been efficiently used to formulate the boundary condition on the surface of any arbitrary body are described hereinafter. Regarding these alternative methods, in general there are two methods; the source distribution method focused on the velocity potential, and the vorticity distribution method (Lewis 1981) focused on the stream function. In the vorticity distribution method, the nonpermeable condition on the solid surface is satisfied by distributing the discrete vortices on the body surface. Since the vorticity distribution method deals with the stream function, this is easily applied to the vortex-in-cell method (Cholin 1973, Stansby and Dixon 1983) which approximates the separated shear layer by means of a square rotational core of the cell area. This is the advantage of this method. However, there is the drawback that the computation of the unsteady fluid force is complicated. The outline of the calculation method of the vortex flow based on these two methods is described below.

The appropriate complex velocity potential W for the flow around the two dimensional body with bluff edge as shown in Fig. 2.32 (b) is given by summing the complex velocity potential W_M for the main flow, W_V for the separated shear flow and W_B for the formulation of the boundary condition on the body surface.

$$W = W_M + W_V + W_B \tag{2.185}$$

W_B can be evaluated using the source distribution method described in **2.3.2**. When the body surface C is divided into N segments of length $\Delta C_j (j=1\text{-}N)$ as illustrated in Fig. 2.32 (b), W_B can be written as

$$W_B(z) = \frac{1}{2\pi} \sum_{j=1}^{N} \int_{\Delta C_j} f_{Dj} \log(z - Z_j) \mathrm{d}C \tag{2.186}$$

where, $Z_j = X_j + iY_j$, which specifies the source point on the surface C, and f_{Dj} is the strength of the source. f_{Dj} can be determined by the boundary condition of zero flow across the body surface as described in **2.3.2**.

Now, as shown in Fig. 2.32 (b), let's assume the uniform flow with velocity U in the x direction as the main flow, then the complex velocity potential W_M for the main flow is given by

$$W_M = UZ \tag{2.187}$$

On the other hand, in the case of the vorticity distribution method, the source points distributed on the body surface are replaced by the discrete vortices. Then, the complex velocity potential for the flow around the body is given by replacing W_B in Eq. (2.185) with the complex velocity potential W_{BV} for the discrete vortices which is expressed as follows:

$$W_{BV}(z) = -\frac{i}{2\pi} \sum_{j=1}^{N} \int_{\Delta C_j} \hat{\gamma}_j \log(z - Z_j) \, dC \tag{2.188}$$

where $\hat{\gamma}_j$ is the circulation of the discrete vortices distributed on the body surface. $\hat{\gamma}_j$ is determined by the boundary condition on the inner of the surface as introduced by Lewis (1981) (i.e., the induced velocity in the tangential direction on the surface becomes zero, because the body surface corresponds to the stream line).

(3) Kinematic equations and circulation of discrete vortices

Let u and v be the velocities in the x and y directions at any point of the fluid, then, the complex velocity $(u - iv)$ is given by dW/dz. The velocity of the discrete vortex is determined from the kinematic condition of the discrete vortices; a marked discrete vortex is affected only from the main flow, the other vortices and the source points on the body surface. Therefore, the velocity components u_k, v_k of the k-th vortex are expressed as

$$\frac{d\bar{z}_k}{dt} = u_k - iv_k$$
$$= \left[\frac{dW_M}{dz} + \frac{dW_B \text{ or } dW_{BV}}{dz} + \frac{dW_V}{dz} - \frac{i}{2\pi} \frac{\Gamma_k}{z - z_k} \right]\Bigg|_{z=z_k} \tag{2.189}$$
$$(k = 1, 2, 3, ..., N_V)$$

where $\bar{z}_k = x_k - iy_k$. Accordingly, the positions of discrete vortices at each time-step in calculations are determined by numerically solving this set of N_v ordinary differential equations through the Runge-Kutta method.

Regarding the presumptive method for determining the circulation Γ_k and the initial position of the nascent vortex which are consistent with the initial conditions at solving Eq. (2.189), there are various kinds of methods. The method which takes account of the Kutta condition (i.e., the velocity tangent to the body surface on the separation point becomes zero) is represented as the typical method (Sarpkaya 1976, Stansby 1977). For example, assuming that the initial position is located at a point detached outwardly from the separation point by the boundary layer thickness, the circulation of the nascent vortex is

determined through the Kutta condition. On the other hand, assuming that the circulation of the nascent vortex is given by Eq. (2.190) which is the equation for the vorticity flux of the boundary layer, the initial position of the nascent vortex is determined by means of the Kutta condition.

$$\partial \Gamma / \partial t \cong U_B^2 / 2 \tag{2.190}$$

where, U_B is the velocity at the outer edge of the boundary layer.

In the above method, however, there is drawback; the circulation of the nascent vortex critically depends on vertices in the neighbourhood of the separation point and the time interval Δt in the computation. Further, when a number of vortices are generated from the plural separation points, there is another drawback; the calculations of the Kutta condition are complicated very much. Therefore, because the discrete vortex approximation deals with the gross features of vortex patterns as described above, there is a simplified method (Sawaragi and Nakamura 1979) that the circulation of the nascent vortex is given by Eq. (2.190) and its position is fixed at the distance of the boundary layer thickness from the separation point.

In the case of the vorticity distribution method, the circulation of the nascent vortex is determined by using the Kelvin theorem concerning the constancy of circulation. Further, a method (Stansby et al. 1983) which takes the constancy of circulation into consideration has been proposed for determining the circulation of the discrete vortices distributed on the body surface.

There has been no established method for estimating the initial position and the circulation of the nascent vortex as described above. These problems require further investigation. Furthermore, it seems a more important subject in future investigations to clarify whether the discrete vortex approximation may be applied to simulate the detailed features of the vortex flow or the gross features of it. From the latter viewpoint, problems arisen in the real calculations are described hereunder.

(4) Considerations in numerical calculations

Since the rotational velocity of the vortex yields an infinite velocity at the center of the vortex as being evident from Eq. (2.184), some vortices induce extremely large velocities when they approach too close to each other, and an unreasonably large circulation of the nascent vortex is caused by the vortices in the vicinity of the separation point. These unreasonable phenomena have been avoided using the following method; the coalescence and cancellation of vortices, the application of the viscous vortex or the Rankine vortex model to the rotational velocity distribution of the vortex. Further, since the computation time exponentially increases in proportion to a number of vortices generated from the separation point, there are several ways to solve such a difficulty. For instance, one procedure is to replace the clusters of vortcies passed off farther downstream with a single vortex. Another is to account for the damping effect of the vortex due to the fluid viscosity and eliminate the sufficiently damped vortex. In the following, these techniques are introduced briefly.

(a) Coalescence and cancellation of vortices: When discrete vortices are close in nearer distance than that set up in the calculations, they are massed into an equivalent single vortex. Then, the circulation Γ' and the position z' of the equivalent vortex are given using the circulation Γ_m and the position z_m of the concentrated individual vortices as follows:

$$\Gamma' = \Sigma\Gamma_m$$

$$z' = \frac{\Sigma\Gamma_m z_m}{\Sigma\Gamma_m} \quad (\Sigma\Gamma_m \neq 0) \tag{2.191}$$

When $\Sigma\Gamma_m=0$ in Eq. (2.191), the concentrated vortices dissipate. The vortices which approach too close to the body can be handled in the same manner as the above described method, because of the presence of the image vortices in the body. Namely, the circulation of the equivalent vortex becomes zero, thereby the vortex is cancelled.

(b) Velocity induced by a vortex: In order to remove the singularity of an infinite velocity at the center of the vortex, the viscous vortex model which takes into account the damping effect of the vorticity due to the fluid viscosity is used in general. Then, the velocity induced by the discrete vortex is calculated by the following equation (Schaefer and Eskinazi 1959)

$$v_\theta = \frac{\Gamma_k}{2\pi r}\left\{1 - \exp\left(-\frac{r^2}{4\nu t^*}\right)\right\} \tag{2.192}$$

where v_θ is the velocity in the circumferential direction at the distance r $(= |z-z_k|)$ from the center of the vortex, ν is the kinematic viscosity, t^* is the elapsed time after the vortex is generated. In this model, the radius of vortex core, r_0, is given by

$$r_0 = 2.24\sqrt{\nu t^*}$$

Further, for other approximate modelings, $\Gamma_k/(2\pi r_0)$ (Kiya et al. 1982) or the induced velocity by the Rankine model, $\Gamma_k r/(2\pi r_0^2)$, may be adopted in the region of $r<r_0$ instead.

(c) Damping of circulation of vortex with time: As for the adequate approximations to the damping of circulation of the vortex with time in the calculations, there have been known the following methods. One is to use the viscous vortex model directly. Another is to adopt the experimentally observed result on the damping characteristics of the vortex. However, since the damping mechanism of the vortex has not been sufficiently clarified yet, it seems to be necessary that the investigation on the damping vortex model should be carried out under a precise theoretical background in the future.

2.7.2 Vortex formation and fluid force in steady flow

Focusing on vortex formation around the body in the steady flow, the calculated results of the flow pattern around it and the computation method of the fluid force acting on it are discussed in the following.

Figure 2.33 shows the calculations ($Re = UD/\nu = 1000$, D: cylinder diameter, ν = rinematic viscosity) for the Kármán vortex street formed behind the circular cylinder in the steady flow.

In this calculation, the separation points are fixed at $\pm 90°$ from the rear stagnation point, because the behaviour of separation point in the flow field with the vortex flow have not been sufficiently clarified yet. In these figures, the black and white circles denote the discrete vortex with the positive and the negative circulation, respectively. The arrays of discrete vortices shed from the separation points estimate the evolution of the separated shear layer, the rolling-up of these vortex sheets approximately simulates the large vortex clusters which are subsequently swept downstream. Figures (a) and (b) show the results

(a) Case without coalescence of vortices

(b) Case with coalescence of vortices
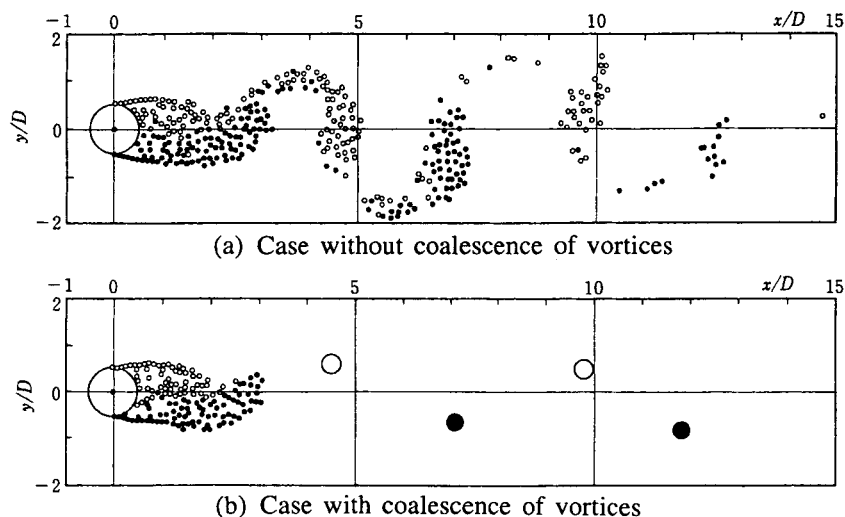
Fig. 2.33 Calculation of vortex formation behind a circular cylinder (Re = 1000)

with and without the coalescence of discrete vortices, respectively. It is found that the positions of vortices in each case equally simulate the concentrated vortices of the Kármán vortex street. In the case where the coalescence of the vortices has been carried out as shown in figure (b), the calculation is performed for four vortices combined and the vortices in the vicinity of the cylinder. Thereby, the computation time and the memory capacity of a computer can be drastically reduced in comparison with the case where the coalescence of vortices is not carried out. In these calculations, the discrete vortex model in which the circulation is exponentially decreased with time is adopted.

On the other hand, the fluid force exerted on the body can be estimated from the pressure distribution on the body which can be calculated from the unsteady Bernoulli equation, or from the generalized Blasius theorem directly. The general formulas for these methods of fluid force calculation are outlined below.

The surrounding pressure distribution p_T on the body surface is evaluated from the unsteady Bernoulli equation (i.e., Eq. (1.22) in Chapter 1) and is given using W of Eq. (2.185) as

$$p_T = -\rho \, \text{Real} \left[\frac{\partial W}{\partial t} \right] - \rho \left| \frac{dW}{dz} \right|^2 / 2 \quad \text{(on the surface)} \tag{2.193}$$

In Eq. (2.193), $\partial W_B/\partial t$ contained in the first term $\partial W/\partial t$ of the right-hand side can be given by differentiating Eq. (2.186) with respect to time t as

$$\frac{\partial W_B}{\partial t} = \frac{1}{2\pi} \sum_{j=1}^{N} \int_{\Delta C_j} \frac{\partial f_{Dj}}{\partial t} \log \left(z - Z_j \right) dC \tag{2.194}$$

where $\partial f_{Dj}/\partial t$ is the change of the strength of the source with time, which can be determined from the equation that is given by differentiating the nonpermeable boundary condition on

the body surface with respect to time. The differentiated equation is analyzed in the same manner as the method described in **2.3.1**. In addition, when the discrete vortex distribution method is used as a substitute for the source distribution method, the differentiated W_{BV} with respect to time cannot be easily analyzed. Therefore, in the numerical calculation, the values of W_{BV} at each time step are calculated, then, the differentiated values for W_{BV} are numerically evaluated from the finite difference of those.

The x and y components of the fluid force exerted on the body (F_x, F_y) are estimated by using p_T and the unit vector taken outward normal to the body $\bar{n}$ (n_x, n_y) as follows:

$$F_x = -\sum_{j=1}^{N} p_T n_x \Delta C_j, \quad F_y = -\sum_{j=1}^{N} p_T n_y \Delta C_j \tag{2.195}$$

On the other hand, if the generalized Blasius theorem is used, F_x and F_y are given by the following equation (Milne-Thomson 1960):

$$F_x - iF_y = \frac{i\rho}{2} \oint_{C'} \left(\frac{dW}{dz}\right)^2 dz + i\rho \frac{\partial}{\partial t} \oint_C \overline{W} \, d\overline{z} \tag{2.196}$$

where the over-bar ($^-$) denotes the conjugate complex, C' is any closed curve surrounding the body. In addition, it is assumed that there is no singularity of the integral in the region between the body and the closed curve C'. The advantage of the generalized Blasius theorem exists in the direct calculability of the fluid force through the Laurent theorem. However, since the pressure distribution around the body surface is not obtained, this theorem is not suitable to the investigation on the fluid force distribution around the body.

Figure 2.34 shows the calculated fluid forces F_x and F_y acting on the circular cylinder in the flow pattern as shown in Fig. 2.33, in which Ut/D is the normalized time.
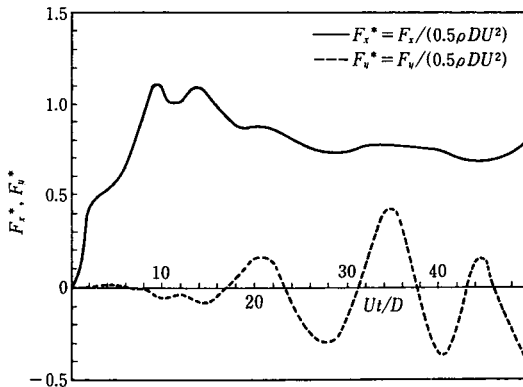
Fig. 2.34 Calculation result of fluid force acting on a circular cylinder (Re = 1000)

This calculation is the case where the discrete vortices are coalesced. It is found that in the region of $Ut/D \geq 20$, the fluid force F_x in the flow direction becomes constant with respect to time, and the alternating lift force F_y which is developed on the cylinder

transverse to the flow direction occurs remarkably. Therefore, it may be concluded that the calculation in this time region can simulate the steady state of the vortex formation around the cylinder.

In this figure, the normalized fluid forces F_x* and F_y* represent the drag coefficient C_D and the lift coefficient C_L respectively. F_x* is about 0.8 and this value is less than C_D=1.0 (in the case of Re=1000) obtained from numerous experiments. On the other hand, the Strouhal number (=$Df_v/U, f_v$: the frequency of the vortex shedding) can be determined from the fluctuation of F_y* with respect to time. The Strouhal number of this calculation is approximately 0.17, this value is less than 0.21 clarified in the previous experiments. The difference between the calculation and the experiment may be attributed to the initial angular position of the nascent vortex; in this calculation the two separation points of boundary layer on the circular cylinder are fixed at ±90° from the rear stagnation point, respectively. Hence, for a circular body where the separation point may move from one position to another with change of the flow, it seems that the characteristic of the behaviour of separation point must be taken into account in numerical simulation technique.

2.7.3 Vortex formation and fluid force in unsteady flow

In the case of an unsteady flow, the complex velocity potential can be obtained by replacing that of the main flow in Eq. (2.187) with that for the unsteady flow. The vortex formation and the fluid force can be numerically analyzed in the same manner as the method described in **2.7.1** and **2.7.2**.

In the case where the vortex formation around the two dimensional body in the vertical plane or the horizontal plane of wave field is dealt with, if the wave diffraction and radiation around the body can be ignored, a spatially uniform oscillatory flow may be used to approximate a main flow. On the other hand, if the structure is hydrodynamically large as described in **2.1**, it is necessary to clarify the complex velocity potential for the main flow by taking into account the wave deformation due to the structure, then the method described in **2.4** can be used as a powerful technique.

The expression for the discrete vortex in Eq. (2.184) is insufficient in the case where a two dimensional vortex formation in the vertical plane of wave field is treated. Then, it is necessary to formulate the boundary conditions on the bottom and the free surface in the wave field. The appropriate complex velocity potential of the discrete vortex in this case is given as the following equation by approximating the free surface with the fixed rigid surface:

$$W_V(z) = -\frac{i}{2\pi} \sum_{k=1}^{N_V} \Gamma_k \left[\log\left(e^{\hat{c}z_k} - e^{\hat{c}z}\right) - \log\left(e^{\hat{c}\bar{z}_k} - e^{\hat{c}z}\right) \right] \qquad (2.197)$$

where $\hat{c} = \pi/h$ (h: water depth), the origin of the complex coordinate (z=x+iy) is located at the free surface, the y axis is taken positive upward from the still water level and the x axis to the wave propagation direction.

In the case of a wave field and an oscillatory flow field, according to the reverse of the direction of main flow, the vortex generated in the previous half-period directly interacts with the vortex generated in the next half-period. In general, however, it is observed in experiments that the vortex generated in the 2 or 3 periods before gradually damps and vanishes with the elapsed time after being generated. Therefore, when the vortex formation in the wave field or the oscillatory flow field with the reverse of the flow direction is numerically simulated, the damping effect of the discrete vortex must be taken into account. Figure 2.35 (Nakamura 1992) shows the typical examples calculated by using the discrete vortex model in which the circulation exponentially decreases with time after generation.

Incident wave
⟹

x (cm)

(a) In case of no-damping with vortex circulation

Incident wave
⟹

(b) In case of damping vortex model
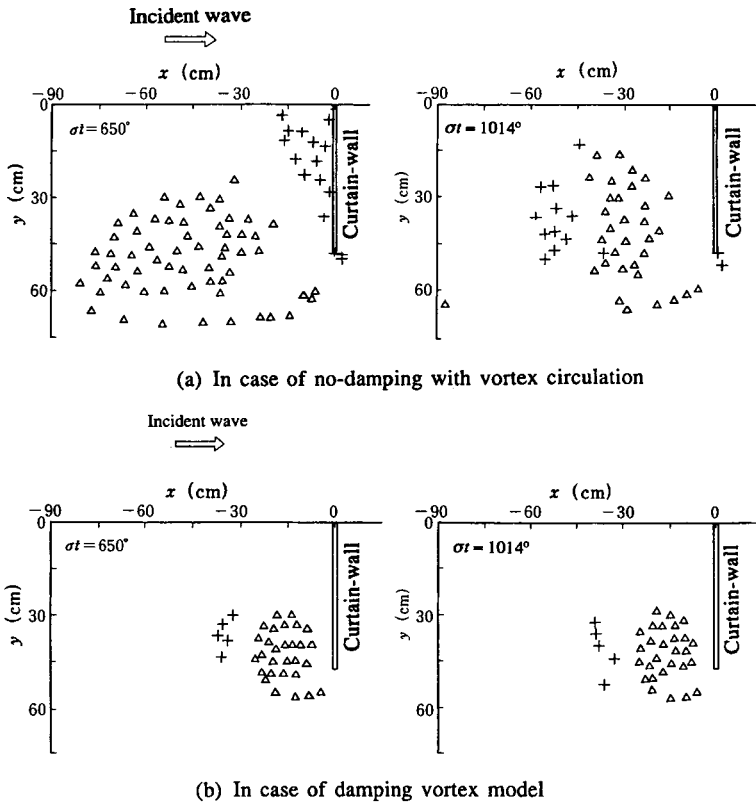
Fig. 2.35 Comparison of the vortex position plots at the two different time steps but corresponding wave phases (T is 2.35 sec, H_I is 15cm, draft of curtain-wall d is 47.5cm, and water depth h is 78cm)

These figures represent the distribution of the discrete vortices which approximate the behaviour of the separated shear layer around the curtain-wall breakwater, and show the comparison of the distribution of the discrete vortices before about one period (at $\sigma t = 650°$) with that after about one period (at $\sigma t = 1014°$). The symbols of + and Δ denote the position of vortices with the positive and the negative circulation, respectively. Figures (a) and (b) are the case without and with the damping of the vortex circulation, respectively. In the calculations taking the damping of the circulation into consideration (see figure (b)), the agreement of the respective distribution patterns of discrete vortices at $\sigma t = 650°$ and $\sigma t = 1014°$ is reasonably well, accordingly the vortex formation under steady state condition can be simulated. However, the calculations without the damping of the circulation are evidently different in the distribution pattern of the discrete vortices at the corresponding wave phase. Therefore, the damping of circulation of the discrete vortex becomes very important for simulation of the vortex formation under the wavy flow.

On the other hand, the fluid force acting on the body in the unsteady flow can be evaluated from the pressure distribution on the body surface or by using the generalized

Blasius theorem as described in **2.7.2**. However, it should be especially noted that the complex velocity potential of the main flow is defined as a function of time.

2.8 Generation of Wave Impact Load

There is another type of wave force acting on structures, which differs from the harmonically oscillating wave forces described up to the preceding section. The impact wave force is a representative one and is, in general, generated by breakers or breaking waves. Although the definition of the impact wave force has not been arrived at yet, the impact wave force is generally understood to have a spiked large value with a very short duration, compared to the incident wave period.

The impact wave force is understood to be basically generated when the front wave face collides parallel to the structure face. It has been pointed out that the impact wave force acting on circular cylinders and the impact uplift force on the floor slab of piers are typical examples of the impact wave force acting on a coastal and harbor structure.

The impact wave pressure caused by the breaking of the standing wave is attributed to a different mechanism, which remains a subject for the future. In this section, the fundamental principle of the generation mechanism of the impact wave force, which is caused by the normal collision of the wave from surface with a structure surface, is described.

One simple yet reliable model of wave collision with structures can be derived from the free fall analysis of an object to the still water surface. In constructing the model, compression of air entrapped in between the object and the still water surface is either neglected or taken into consideration according to the shape of the object. In the case of a sphere or a cylinder, the effect of compression of air to the impact wave force can be neglected. The contribution of air compression to the impact wave force is taken into consideration in the case of a flat plate.

When the contribution of compression of air entrapped in between the object and the still water surface to the impact fluid force is neglected, the object collides directly with the water and receives the impact fluid force at the instant that the water moves. This kind of impact fluid force can be expressed in terms of the added mass. That is, based on the conservation of momentum, the fluid force F can be expressed using the added mass of fluid $(M^{(A)})$ as follows:

$$F = \frac{d\left(M^{(A)} \cdot v\right)}{dt} = M^{(A)} \frac{dv}{dt} + v \frac{dM^{(A)}}{dt} \tag{2.198}$$

where, v is the falling velocity of the object and t is time. In the case of a fully submerged object, the 2nd term of the right hand side of Eq. (2.198) is neglected and the 1st term only defines the added mass force, since $(M^{(A)})$ is unchangeable with time. The added mass is a function of the shape of the object. Then, the added mass changes with time after collision of the object with water, since the submerged portion of the object changes with time. Thus, the 2nd term $v(dM^{(A)}/dt)$ is a specific term which appears only when the object collides with water and it is this term that presents the impact fluid force. Relatedly, since the added mass can be also evaluated using the velocity potential of fluid, the fluid force F can be directly evaluated by integrating the acting fluid pressure over the submerged surface of the object, once the velocity potential of the fluid after the collision of the object with water is determined.

On the other hand, in the case that the contribution of air entrapped in between the object

and the water surface to the fluid force cannot be neglected, the compression of air is more important than the motion of water. That is, the momentum of the object is transferred to air pressure by means of air compressibility, which generates the impact fluid force. The magnitude of the impact fluid force and its acting time caused by the air compressibility becomes relatively smaller and longer, respectively, compared to that caused by change of the added mass.

2.8.1 Impact force due to added mass change

In this section, the added mass and the impact fluid force in the cases of the free fall of a sphere, a circular cylinder and a triangular cylinder with a constant falling velocity of v into the still water are discussed. The exact evaluation of the added mass requires an exact evaluation of the velocity potential. Since the exact derivation of the velocity potential is difficult for arbitrarily shaped objects, the added mass is, in general, evaluated with approximation methods. The popular approximation method is the application of the known added mass of an object whose shape is very close to the object that is under consideration (Kármán 1922). Some representative methods are introduced here.

(1) Sphere (Fig. 2.36)
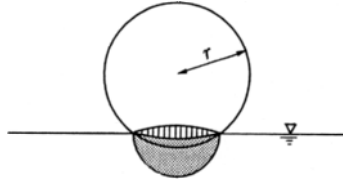
Fig. 2.36   Concept of added mass of sphere

The added mass $M^{(A)}$ in the case of the sphere is half the time of a disk that is fully submerged and placed normal to the flow direction. The diameter of the cross section of the sphere at the still water surface is equal to the diameter of the disk. The reason for employing the half value of the added mass of the disk is that the sphere is semi-submerged and one part is in the water and the rest is in the air. Employing two treatments, the added mass $M^{(A)}$ in the case of a sphere is

$$M^{(A)} = \frac{2}{3}\pi\rho r^3 \left(\frac{2t}{\tau} - \frac{t^2}{\tau^2} \right)^{3/2} \tag{2.199}$$

Applying Eq. (2.199) to the 2nd term of the right hand side of Eq. (2.198) yields the impact fluid force F as follows:

$$F = 2\pi\rho r^3 v^2 \left(\frac{2t}{\tau} - \frac{t^2}{\tau^2} \right) \left(1 - \frac{t}{\tau} \right) \tag{2.200}$$

where, τ is the duration of the impact force, τ is r/v, r is the radius of the sphere and t is the time from inception of the sphere collision with water. The detailed investigations

on the impact wave force were done by Trilling (1950) and Shiffman & Spencer (1945, 1947).

(2) Circular cylinder (Fig. 2.37)
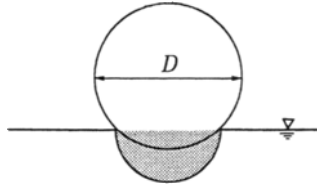
Fig. 2.37 Concept of added mass of circular cylinder

The added mass $M^{(A)}$ in the case of a circular cylinder is taken to be half of the added mass in the case of a motion produced by an infinitely long lamina of the breadth b moving "broadside on" in an infinite mass of fluid (Goda et al. 1966). The added mass $M^{(A)}$ per unit length and the impact fluid force per unit length F are

$$M^{(A)} = \frac{\pi}{8} \rho D^2 \left(2\frac{t}{\tau} - \frac{t^2}{\tau^2} \right)$$

$$F = \frac{\pi}{2} \rho v^2 D \left(1 - \frac{t}{\tau} \right) \tag{2.201}$$

$$\tau = \frac{D}{2v}$$

The concept of the added mass was first introduced into the impact fluid force of a circular cylinder by Kármán (1929). It is a remarkable feature in the case of the circular cylinder that the impact wave force becomes a maximum at the instant that the circular cylinder touches the water surface, i.e., $t = 0$. Besides this method, there are other treatments that deal with the impact wave force on a circular cylinder (Kaplan and Silbert 1976, Geers 1982 and Armand and Cointe 1986).

(3) Triangular cylinder (Fig. 2.38)
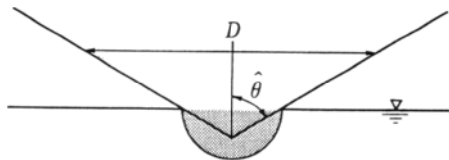
Fig. 2.38 Concept of added mass of triangular cylinder

The same method that is adopted in the case of the circular cylinder can be applied to the case of a triangular cylinder. The added mass $M^{(A)}$ per unit length and the impact fluid force F are given as follows:

$$M^{(A)} = \frac{\pi}{4}\rho D^2 \frac{t^2}{\tau^2}$$

(2.202)

$$F = \frac{\pi}{2}\rho v^2 D \tan \hat{\theta} \frac{t}{\tau}$$

(2.203)

$$\tau = \frac{D}{2v\tan\hat{\theta}}$$

(2.204)

where, $\hat{\theta}$ is half of the apex angle of the triangular cylinder as shown in Fig. 2.38.

Wager (1932) evaluated the pressure acting on the triangular cylinder that collides with the still water by means of approximation of the velocity potential, which is different from the method using the added mass. The velocity potential employed is derived for the steady flow past a flat plate with a breadth of $2b$ and applying the velocity potential Φ to the triangular cylinder as in Fig. 2.39 can evaluate the water surface rise around the apex of the triangular cylinder.
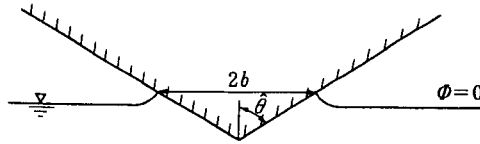
Fig. 2.39   Velocity potential used in the Wagner model

The velocity potential Φ and the pressure p estimated with Φ are given as

$$\Phi = -v\sqrt{b^2 - x^2}$$

(2.205)

$$p = \frac{1}{2}\rho v K(x, t)$$

(2.206)

$$K(x, t) = \frac{\pi \cos\hat{\theta}}{\sqrt{1-(x/b)^2}} - \frac{(x/b)^2}{1-(x/b)^2}$$

(2.207)

where, v is the falling velocity of the triangular cylinder and x is the breadth of the submerged part of the cylinder at the water surface at the instant time τ. The fluid pressure p changes according to time t and place x and the maximum fluid force p_{max} is given by

$$p_{max} = \frac{1}{2}\rho v^2 \left[\frac{\pi^2}{4}\cos^2\hat\theta + 1 \right] \qquad (2.208)$$

2.8.2 Impact force due to compression of air

Bagnold (1939) thought that the impact breaking wave force is produced by the compression of air that is captured between the curled wave front and the structure wall and he developed the following analyses. He dealt with the situation that the water mass with the moving velocity v collides with the air-chamber whose height is d, as shown in Fig. 2.40.
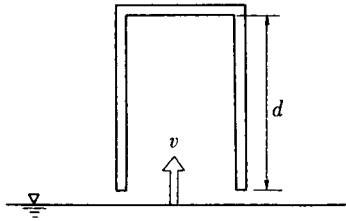
Fig. 2.40 Air compression model by Bagnold

When the water mass collides with an air-chamber, the air is entrapped in the air-chamber, and is compressed. Accordingly, the air pressure enlarges and then the water mass begins to lose its momentum. The air pressure becomes a maximum when the water mass loses its momentum, and then the air begins to be expanded. The relationship between the maximum air pressure p in the air-chamber and the atmospheric pressure p_0 is given by

$$B_g = \frac{2}{\gamma_a - 1}\left[\frac{p}{p_0}\right]^{1-\frac{1}{\gamma_a}} + 2\left[\frac{p}{p_0}\right]^{-\frac{1}{\gamma_a}} - \frac{2\gamma_a}{\gamma_a - 1} \qquad (2.209)$$

This equation is called the Bagnold equation and p_a is the absolute pressure with 0 at the vacuum, and γ_a is the specific heat ratio. B_g is the Bagnold parameter and is defined with

$$B_g = \frac{\rho K' v^2}{P_0 d} \qquad (2.210)$$

where, K' is an added mass thickness and is given by

$$K' = \frac{\pi b}{8} \qquad (2.211)$$

Further, b is the breadth of the air-chamber, and γ_a is the specific heat ratio that is equal to 1.4 with the adiabatic compression process. The adiabatic compression process can be widely applied to most of the physical phenomena that occurs in the field of coastal and

harbor engineering. Therefore $\gamma_a = 1.4$ is reasonable. Relatedly, when the isothermal compression process is applied instead of the adiabatic compression process, the pressure in the former process becomes smaller than that of the latter process. Therefore, the adiabatic compression process is on the safe side from an engineering standpoint.

There is a phenomenon of "pressure-caused air squash" that relates to the action of air. This phenomenon is usually understood to be that when air bubbles formed in the fluid are forced to be squashed, they generate a high magnitude of pressure. However, the air bubbles are in reality not squashed, but the volume of the air bubbles changes with time. The time oscillation of the volume of air bubbles becomes very large when the volume of air bubbles becomes a minimum. This results in the generation of an elastic wave. When the elastic wave is generated near the structure, it produces a high pressure on the structure. In addition, when the air bubbles are compressed very near the structure wall and the air bubbles are further deformed to become doughnut-shaped, the fluid jet that is called a "micro-jet" suddenly acts on the structure wall through the non-air center portion of the doughnut-shaped air bubbles. This fluid jet produces high pressure too. However, although the pressure caused by the "compressed squash phenomenon of air" ranges from 10MPa to 100MPa and shows a high value, its acting area is less than that of the air bubbles and its duration is of the order of 10^{-7}s. Therefore, it can be said that the force and the impulse acting on the structure caused by the "compressed squash phenomenon of air" can be neglected.

References

Armand, J.L. and R. Cointe (1986): Hydrodynamic impact analysis of a cylinder, Proc. 5th Offshore Mech. and Arctic Eng., ASME, Vol.2, pp.250-256.

Bagnold R.A. (1939): Interim report on wave pressure research, J. Inst. Civil Engineers, Vol.12, pp.210-226.

Black, J.L. (1975): Wave forces on vertical axisymmetric bodies, J. Fluid Mech., Vol.67, pp.369-376.

Chakrabarti, S.K. and D.C. Cotter (1975): Wave forces on cylinders near plane boundary (Discussion), J. Waterways, Harbors and Coastal Eng. Div., Proc. ASCE, Vol.101, No.WW3, pp.303-305.

Chakrabarti, S.K., W.A. Tam and A.L. Wolbert (1975): Wave forces on randomly oriented tube, Proc. Offshore Tech. Conf., Paper No.OTC2190.

Chakrabarti, S.K. (1987): Hydrodynamics of Offshore Structures, Springer-Verlag, 440p.

Chaplin, J.R. (1984): Nonlinear forces on a horizontal cylinder beneath waves, J. Fluid Mech., Vol.147, pp.449-464.

Cholin, A.J. (1973): Numerical Study of slightly viscous flow, J. Fluid Mech., Vol.57, pp.785-796.

Clements, R.R. (1973): An inviscid model of two-dimensional vortex shedding, J. Fluid Mech., Vol.57, pp.321-336.

Engelund, F. (1953): On the laminar and turbulent flows of ground water through homogeneous sand, Trans. of the Danish Academy of Technical Sciences, Vol.3, No.4.

Fenton, J.D. (1978): Wave forces on vertical bodies of revolution, J. Fluid Mech., Vol.85, pp.241-255.

Garrison, C.J. (1978): Hydrodynamic Loading of Large Offshore Structures - Three dimensional source distribution methods. In Numerical Methods in Offshore Engineering, (eds. O.C. Zienkiewicz, P. Lewis and K.G. Stagg), John Wiley, pp.97-140.

Geers, T.L. (1982): A boundary-element method for a slamming analysis, J. Ship Res., Vol.26, No.2, pp.117-124.

Goda, Y., S. Haranaka and M. Kitahara (1966): Study on impulsive breaking wave forces on piles, Rept. Port and Harbour Res. Inst., Vol.6, No.5, pp.1-30. (in Japanese)

Goda, Y. (1985): Random Seas and Design of Maritime Structures, Univ. of Tokyo Press, 323p.

Hess, J.L. and O.M.A. Smith (1964): Calculation non-lifting potential flow about arbitrary three-dimensional bodies, J. Ship Res., Vol.8, pp.22-44.

Hogben, N. and R.G. Standing (1974): Wave loads on large bodies, Proc. Int. Symp. on the Dynamics of Marine Vehicles and Structures in Waves, pp.258-277.

Hudspeth, R.T., T. Nakamura and J.W. Leonard (1980): Floating vessel response simulator by an axisymmetric Green's function, Ocean Eng. Program , Oregon State University.

Ijima, T., C.R. Chou and Y. Yumura (1974): Wave scattering by permeable and impermeable breakwater of arbitrary shape, Proc. 14th Int. Conf. on Coastal, ASCE, pp.1866-1905.

Ijima, T., C.R. Chou, and A. Yoshida (1976): Method of analysis for two-dimensional water wave problems, Proc. 15th Int. Conf. on Coastal, ASCE, pp.2717-2736.

Isaacson, M.Q. (1978): Vertical cylinders of arbitrary section in waves, J. Waterway, Port, Coastal and Ocean Div., Proc. ASCE, Vol.104, No.WW4, pp.309-324.

Isaacson, M.Q. (1979): Wave induced forces in the diffraction regime, in Mechanics of Wave-Induced Forces on Cylinders, (ed. T. L. Shaw), Pitman, pp.68-89.

Isaacson, M.Q. (1982): Fixed and floating axisymmetric structures in waves, J. Waterway, Port, Coastal and Ocean Div., Proc. ASCE, Vol.108, No.WW2, pp.180-199.

Iwata, K. and N. Mizutani (1989): Experimental study on wave force acting on a submerged sphere, Proc. 8th Int. Conf. on Offshore and Arctic Eng., pp.145-152.

Iwata, K. and N. Mizutani (1991): Proximity effects of bottom and free surface boundaries to wave forces acting on a submerged sphere, Proc. 1st Int. Offshore and Polar Eng. Conf., ISOPE, pp.164-171.

John, F. (1949): On the motions of floating bodies I, Comm. Pure Appl. Math., Vol.2, pp.13-57.

John, F. (1950): On the motions of floating bodies II, Comm. Pure Appl. Math., Vol.3, pp.45-101.

Kaplan, P. and M.N. Silbert (1976): Impact forces on platform horizontal members in the splash zone, Proc. Offshore Tech. Conf., Paper No.OTC 2498.

Kim, W.D. (1969): On a free floating ship in waves, J. Ship Res., Vol.10, pp.137-154.

Kim, W.D. (1978): Nonlinear free-surface effect on a submerged sphere, J. Hydronautics, Vol.3, No.1, pp.29-37, 1978.

Kiya M., K. Sasaki and M. Arie (1982): Discrete-vortex simulation of a turbulent separation bubble, J. Fluid Mech., Vol.120, pp.219-244.

Kondo, H. and S. Toma (1972): Reflection and transmission for porous structure, Proc. 13th Int. Conf. on Coastal, ASCE, pp.1847-1866.

Korvin-Kroukovsky, B.V. (1955): Investigation of ship motions in regular waves, TSNAME, Vol.63, pp.385-435.

Lamb, H. (1964): Hydrodynamics, 6th Edition, Cambridge Univ. Press, §58, pp.59-61.

Lewis, R.I. (1981): Surface vorticity modelling of separated flows from two-dimensional bluff bodies of arbitrary shape, J. Mech. Eng. Sci., Vol. 23, No.1, pp.1-12.

Liu, P. L-F. and M. Abbaspour (1982): Wave Scattering by a rigid thin wall barrier, J. Waterways, Port, Coastal and Ocean Div., Proc. ASCE, Vol.108, No.WW4, pp.479-491.

MacCamy, R.C. and R.A. Fuchs (1954): Wave forces on piles: A diffraction theory, U.S. Army Corps of Engineers, Beach Erosion Board, Tech. Memo., No.69.

Madsen, O.S. (1974): Wave transmission through porous structures, J. Waterways, Harbors and Coastal Eng. Div., Proc. ASCE, Vol.100, No.WW3, pp.169-188.

Maruo, H. (1960): The drift of a body floating on waves, J. Ship Res., Vol.4, No.3, pp.1-10.

Milne-Thomson, L.M. (1960): Theoretical Hydrodynamics, 5th edition, Macmillan, pp.253-256.

Morison, J.R., M.P. O'Brien, J.W. Johnson and S.A. Schaaf (1950): The forces exerted by surface waves on piles, Petroleum Trans., AIME, Vol.189, pp.149-157.

Nakamura, T. and M. Ono (1988): A practical analysis on the wave height distribution around a three-dimensional body with plane symmetries, Proc. Civil Eng. in the Ocean, Vol.4, pp.159-164. (in Japanese)

Nakamura, T. and S. Morita (1988): Wave diffraction by a permeable breakwater and wave force characteristics in obliquely incident waves, Proc. 35th Japanese Conf. on Coastal Eng., pp.547-551. (in Japanese)

Nakamura, T. (1990): A new evaluation method of three-dimensional wave source Green's function - Applicability to wave force calculation on large volume structures, Proc. Civil Eng. in the Ocean, Vol.6, pp.95-100. (in Japanese)

Nakamura, T. (1992): Numerical modeling of vortex formation around a large angular body in waves, Proc. 2nd Int. Offshore and Polar Eng. Conf., ISOPE, Vol.III, pp.217-224.

Rameswar Bhattacharyya (1978): Dynamics of Marine Vehicles, John Willy & Sons.

Salvesen, N., E.O. Tuck and O. Faltinsen (1970): Ship motions and sea load, TSNAME, Vol.78, pp.250-287.

Sarpkaya, T. and C.J. Garrison (1963): Vortex formation and resistance in unsteady flow, J. Appl. Mech., Vol.30, Series E, No.1, pp.16-24.

Sarpkaya, T. (1975a): Forces on cylinders and spheres in an oscillating fluid. J. Appl. Mech., Trans. ASME, Vol.42, pp.32-47.

Sarpkaya, T. (1975b): An inviscid model of two-dimensional vortex shedding for transient and asymptotically steady separated flow over an inclined plate, J. Fluid Mech., Vol.68, pp.109-128.

Sarpkaya, T. (1982): In-line and transverse forces on cylinders near a wall in oscillatory flow at high Reynolds numbers, Proc. Offshore Tech. Conf., Paper No.OTC2898.

Sarpkaya, T. and M.Q. Isaacson (1981): Mechanics of Wave Forces on Offshore Structures, Von Nostrand Reinhold, 615p.

Sawaragi, T., T. Nakamura and H. Kita (1976): Characteristics of lift forces on a circular cylinder in waves, Coastal Eng. in Japan, JSCE, Vol.19, pp.59-71.

Sawaragi, T. and T. Nakamura (1979): An analytical study of wave forces on a cylinder in oscillatory flow, Proc. Specialty Conf. on Coastal Structures' 79, ASCE, pp.154-173.

Schaefer, J.W. and S. Eskinazi (1959): An analysis of the vortex street generated in a viscous fluid, J. Fluid Mech., Vol.6, pp.241-260.

Shanker, N.J., H.F. Cheong and K. Subbiah (1988): Wave force coefficients for submarine pipelines, J. Waterways, Port, Coastal and Ocean Eng. Div., ASCE, Vol.114, No.4, pp.472-486.

Shiffman, M. and D.C. Spencer (1945): The force of impact on a sphere striking a water surface, AMG-NYU Nos. 105 and 133.

Shiffman, M. and D.C. Spencer (1947): The flow of an ideal incompressible fluid about a lens, Quart. Appl. Math., Vol. 5, pp.270-288.

Sollitt, C.K. and R.H. Cross (1972): Wave transmission through permeable breakwater, Proc. 13th Int. Conf. on Coastal, ASCE, pp.1827-1846.

Stansby, P.K. (1977): An inviscid model of vortex shedding from a circular cylinder in steady and oscillatory far flows, Proc. Inst. of Civil Eng., Vol.63, Part 2, pp.865-880.

Stansby, P.K. and A.G. Dixon (1983): Simulation of flows around cylinders by a Lagrangian vortex scheme, Appl. Ocean Res., Vol.5, No.3, pp.167-178.

Trilling, L. (1950): The impact of a body on a water surface at an arbitrary angle, J. Appl. Phys., Vol. 21, pp.161-170.

Von Muller, W. (1929): System von Doppelquellen in der Ebenen Stromung, insbesondere die Stromung um Zwei Dreiszylinder, Z. angew. Math. Mech. Band 9, pp.200-213.

Von Kármán Th.(1929): The impact of seaplanes floats during landing, NACA Tech. Mem., No.321.

Wagner, H. (1932): ber stop-und Heitvorg nge a der Oderfl che von Fl ssingkeiten, Z.angew Math. Meeh., Band. 12, pp.193-215.

Watanabe, K. (1958): Theoretical research on heave and pitch of ship, Tech. Rept. of Kyushu Univ., Vol.31, No.1, pp.26-30.

Wehausen, J.V. and E.V. Laitone (1960): Surface Waves, in Handbuch der Physik, ed. S. Flugge, Springer-Verlag, Vol.IX, pp.446-778.

Wylie, C.R. (1966): Advanced Engineering Mathematics, McGraw-Hill, 3rd ed., 937p.

Yamamoto, T. and J.H. Nath (1976): High Reynolds number oscillating flow by cylinders, Proc. 15th Int. Conf. on Coastal, ASCE, pp.2321-2340.

Yamamoto, T., J.H. Nath and L.S. Slotta (1974): Wave forces on cylinders near plane boundary, J. Waterways, Harbors and Coastal Eng. Div., Proc. ASCE, Vol.100, No.WW4, pp.345-359.

This Page Intentionally Left Blank

Chapter 3   Waves, Wave-Induced Currents and Sediment Transport

3.1 Introduction

One of the main purposes for studying waves and their resulting phenomena in a near-shore region is the prediction of beach deformations caused by sediment movement. There are various fluid motions in the near-shore region. Among them, water particle motion due to wave and wave-induced currents are the fluid motions most responsible for sediment movement. Waves approaching the shoreline cause secondary fluid motions such as wave setup, wave-induced currents and undertow that agitate the bottom sediment. Consequently, they transport sediment that results in beach deformation. The purpose of this chapter is to discuss the relation between waves, wave-induced currents and sediment movement.

Wave transformation in the shallow water region has already been mentioned in detail in Chapter 2. In this chapter, we refer to a bottom shear stress under waves and current, which becomes a direct force acting on the bottom sediment, and wave-induced currents, that transport sediment. Then, we discuss the mode and the mechanism of sediment transport in the near-shore region and a procedure to estimate the sediment transport rate.

3.2 Fluid Motion and Bottom Shear Stress in Wave-current Coexisting System

3.2.1 Resistance law in wave (or oscillatory flow) field

A boundary layer and a bottom shear stress have been investigated by many people who have an interest in wave energy dissipation and sediment movement. We can classify their procedures for investigations into the following three categories:
1) Direct measurement of near bottom water particle velocity to investigate the flow structure in the boundary layer and resistance law,
2) Direct measurement of bottom shear stress to formulate resistance law,
3) Analysis of the boundary layer equation to determine the fluid motion and the boundary shear stress.

Direct velocity measurement in the vicinity of the boundary layer was first carried out by Kalkanis (1957) by using a Pitot tube on a smooth oscillating plate. Jonsson (1963) measured velocity distribution on a fixed roughness by using a propeller-type velocity-meter. Horikawa and Watanabe (1968) developed a hydrogen bubble method to measure velocity near the bottom. Recently, more precise and detailed measurements of velocity have been conducted by virtue of hot-film and laser-Doppler anemometers.

Among these researches, Jonsson (1963) proposed the resistance law by applying logarithmic distribution to velocity and using a measured water particle velocity on the rough bottom. He expressed the amplitude of the bottom shear stress τ by Eq. (3.1) where a friction factor f_w is given by Eq. (3.2)

$$\hat{\tau} = (1/2)\rho f_w \hat{u}_{bp}{}^2 \qquad (3.1)$$

$$\frac{1}{4\sqrt{f_w}} + \log\left(\frac{1}{4\sqrt{f_w}}\right) = -0.08 + \log\left(\frac{a_b}{k_s}\right) \tag{3.2}$$

where $\hat{u}_{bp}$ is the amplitude of water particle velocity at the bottom, a_b is the water particle excursion at the bottom and k_s is the equivalent roughness. The water particle excursion a_b is defined in Eq. (3.3) by using the angular frequency σ through a linear wave theory

$$a_b = \hat{u}_{bp}/\sigma, \ \ \sigma = 2\pi/T \tag{3.3}$$

Although the bottom shear stress expressed by Eq. (3.1) can not express a phase (time) variation and the phase difference between the water particle velocity and the bottom shear stress, it has often been used to investigate and explain various phenomena such as sediment movement and wave attenuation in the shallow water region. The expression of the friction factor can not be determined analytically, because Eq. (3.2) is a transcendence equation. Swart (1974) proposed the following approximate expression of Eq. (3.2) that is valid in the region of $1 < a_b/k_s < 3000$:

$$f_w = \exp\left\{-5.977 + 5.213\left(a_b/k_s\right)^{-0.194}\right\} \tag{3.4}$$

On the other hand, the friction factor corresponding to the maximum shear stress in a laminar flow is given by Eq. (3.5) by solving a laminar boundary layer equation analytically.

$$f_w = 5.01 R_{et}^{-1/2} \tag{3.5}$$

here, R_{et} is the Reynolds number defined by using the kinematic viscosity ν as follows:

$$R_{et} = \hat{u}_{bp}^{\ 2} T \Big/ \nu \tag{3.6}$$

Most of the direct measurements of bottom shear stress were carried out by using a shear plate. Riedel et al. (1973) measured the bottom shear stress in the extensive range from the laminar to the rough turbulent flow conditions in the oscillatory flow tunnel. Kamphuis (1975) related the friction factor to a_b/k_s in rough turbulent conditions by the following equation based on the measured bottom shear stress that is varied in the region of $a_b/k_s < 100$

$$f_w = 0.4\left(a_b/k_s\right)^{-0.75} \tag{3.7}$$

Many efforts have been made to close and solve the turbulent boundary layer equation just like a turbulent closure problem. Kajiura (1964, 1968) is the first person who analyzed

the turbulent boundary layer based on a 0-equation model. In his analysis Reynolds stress was expressed by using a Boussinesq type expression with a kinematic eddy viscosity. He assumed that flow in the boundary layer continued to be turbulent throughout one wave period and proposed a three-layer model for the kinematic eddy viscosity.

Johns (1968) and Noda (1969) conducted analysis of the boundary layer equation supposing the kinematic eddy viscosity.

According to the increase of our information about the flow in the boundary layer brought about by the development of the flow measuring apparatus, we became aware of the defect in the analysis based on the 0-equation model. A typical problem is to use a constant kinematic eddy viscosity without depending on a phase. To improve this point at issue, a so-called one- or two-equation model has been applied to the analysis of the boundary layer flow. In these models one or two auxiliary equation(s), transport equation(s) of turbulent energy and/or kinematic eddy viscosity is/are used. These approaches were originally developed to analyze steady turbulent flow. Therefore, we have to reconstruct the auxiliary equations on the basis of detailed experimental results to apply them to the flow inside wave boundary layer that is non-isotropic and have a large pressure gradient.

As for the bottom shear stress in the wave-current coexisting system the first formulation was carried out in an establishing process of a theory of wave-induced current (Bowen 1969, Longuet-Higgins 1970 and so on). The expression of time averaged bottom shear stress for a few waves that become a resistance force against a driving force expressed as a spatial gradient of radiation stress was proposed. Many researches have been carried out after them in various ways.

The expressions of time averaged bottom shear stress proposed by Jonsson et al. (1974), Liu and Darlymple (1976), Sawaragi et al. (1978) and Nishimura (1982) tried to apply conventional resistance laws of waves and currents to the time averaged bottom shear stress under the wave-current coexisting field. The common point at issues of these approach are how to evaluate the friction factor and how to take into account the time variation of the bottom shear stress.

Research that tries to evaluate a bottom shear stress, by solving a bottom boundary layer equation of wave-current coexisting system.

On the other hand, Bijker (1966), Grant and Madsen (1979), Tanaka and Shuto (1981) and Asano and Iwagaki (1983) applied the 0-equation model to analyze the near bottom velocity and boundary shear stress assuming proper distribution of the kinematic eddy viscosity. In such an approach, it is slightly difficult to get a solution to the boundary layer equation under the wave-current coexisting system, because the vertical gradients of water particle velocities due to waves and current are greatly different each other.

In the following, I will derive the boundary layer equation in the wave-current coexisting system and discuss the effect of the current on the wave boundary layer. I will also refer to the resistance law under the wave-current coexisting field.

3.2.2 Boundary layer equation of wave and current coexisting system
For simplicity, we consider that waves and current are in the same vertical plane as shown in Fig. 3.1 where waves propagate in the positive x-direction and a z-axis is taken upward from the bottom.

The momentum equations in x- and z-directions and a pressure gradient in the boundary layer are expressed as follows:
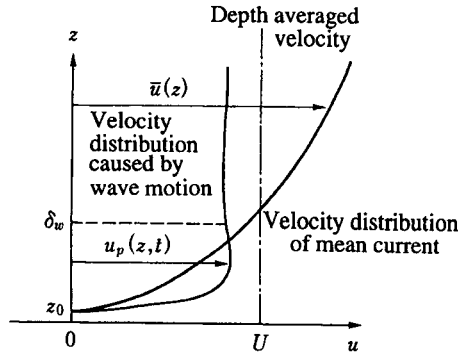
Fig. 3.1 Coordinate system

$$\frac{\partial u}{\partial t} + u\frac{\partial u}{\partial x} + w\frac{\partial u}{\partial z} = -\frac{1}{\rho}\frac{\partial p}{\partial x} + \nu\nabla^2 u \tag{3.8}$$

$$\frac{\partial w}{\partial t} + u\frac{\partial w}{\partial x} + w\frac{\partial w}{\partial z} = -g - \frac{1}{\rho}\frac{\partial p}{\partial z} + \nu\nabla^2 w$$

$$-\frac{1}{\rho}\frac{\partial p}{\partial x} = \frac{\partial u_b}{\partial t} + u_b\frac{\partial u_b}{\partial x} \tag{3.9}$$

where, u_b is the water particle velocity just outside of the boundary layer due to waves (i.e., a potential velocity at the bottom), u and w are the water particle velocities in the boundary layer and p is the pressure in and outside the boundary layer. The equation of continuity is given by the next equation.

$$\frac{\partial u}{\partial x} + \frac{\partial w}{\partial z} = 0 \tag{3.10}$$

The boundary conditions are given at the bottom or at $z = z_0$ and at the outer edge of the boundary layer $z = \delta$ as follows:

$$u = w = 0 \quad at \ \ z = 0 \ or \ z_0 \tag{3.11}$$

$$u = u_b \ and \ w = w_b \ at \ \ z = \infty \ or \ \delta \tag{3.12}$$

where z_0 is the height of the roughness element and δ is the thickness of the boundary layer.

Here, we decompose the variables in Eqs. (3.8) - (3.12) into steady, wave and turbulent components and express each component by using an over bar ($^{\sim}$), subscript p and '. Substituting these components into Eqs. (3.8) and (3.9) and taking a time average, we can derive the following boundary layer equations for the steady component:

$$\frac{\partial}{\partial x}\left(\overline{u}^2 + \overline{u_p^2} + \overline{u'^2}\right) + \frac{\partial}{\partial z}\left(\overline{u_p w_p} + \overline{u'w'}\right) = -\frac{1}{\rho}\frac{\partial \overline{p}}{\partial x} + v\frac{\partial^2 \overline{u}}{\partial z^2} \tag{3.13}$$

$$-\frac{1}{\rho}\frac{\partial \overline{p}}{\partial x} = \frac{\partial}{\partial x}\left(\overline{u_b^2} + \overline{u_{bp}^2}\right) \tag{3.14}$$

We further assume that all time averaged quantities are uniform in the x-direction and introduce a kinematic eddy viscosity ε_{cz} defined by Eq. (3.15)

$$\varepsilon_{cz} = -\left(\overline{u_p w_p} + \overline{u'w'}\right)\Big/(\partial \overline{u}/\partial z) + v \tag{3.15}$$

Then we can obtain the boundary layer equation for the steady current as follows:

$$\frac{\partial}{\partial z}\left(\varepsilon_{cz}\frac{\partial \overline{u}}{\partial z}\right) = 0 \tag{3.16}$$

When we take a phase average after the substitution of three components into Eqs. (3.8) and (3.9), the following equations concerning the wave component are obtained:

$$\frac{\partial}{\partial t}\left(\overline{u} + u_p\right) + \left(\overline{u} + u_p\right)\frac{\partial}{\partial x}\left(\overline{u} + u_p\right) + w_p\frac{\partial}{\partial z}\left(\overline{u} + u_p\right)$$
$$= -\frac{1}{\rho}\frac{\partial}{\partial x}\left(\overline{p} + p_p\right) + v\frac{\partial^2}{\partial z^2}\left(\overline{u} + u_p\right) - \frac{\partial}{\partial x}\langle u'^2\rangle - \frac{\partial}{\partial z}\langle u'w'\rangle \tag{3.17}$$

$$-\frac{1}{\rho}\frac{\partial}{\partial x}\left(\overline{p} + p_p\right) = \frac{\partial}{\partial t}\left(\overline{u}_b + u_{bp}\right) + \left(\overline{u}_b + u_{bp}\right)\frac{\partial}{\partial x}\left(\overline{u}_b + u_{bp}\right) \tag{3.18}$$

$$\frac{\partial}{\partial x}\left(\overline{u} + u_p\right) + \frac{\partial}{\partial z}w_p = 0 \tag{3.19}$$

where, $< >$ means the phase averaged quantity.
By subtracting Eq. (3.13) from Eq. (3.17) and Eq. (3.14) from Eq. (3.18) and using the relation of Eq. (3.19), the boundary layer equations for the wave component are derived as follows:

$$\frac{\partial u_p}{\partial t} + \left(\overline{u} + u_p\right)\frac{\partial u_p}{\partial x} + w_p\frac{\partial}{\partial z}\left(\overline{u} + u_p\right) = -\frac{1}{\rho}\frac{\partial p_p}{\partial x} + v\frac{\partial^2 u_p}{\partial z^2} - \frac{\partial}{\partial z}\left(\langle u'w'\rangle - \overline{u_p w_p} - \overline{u'w'}\right) \tag{3.20}$$

$$-\frac{1}{\rho}\frac{\partial p_p}{\partial x} = \frac{\partial u_{bp}}{\partial t} + \left(\overline{u}_b + u_{bp}\right)\frac{\partial u_{bp}}{\partial x} \qquad (3.21)$$

Here, we assume that $\overline{u}, \overline{u_p^2}, \overline{u'^2}$ and $<u'^2>$ are uniform in the x-direction. We further apply a linear wave theory and assume that $|u_p|>>|w_p|$ and the existence of the kinematic eddy viscosity ε_{wz} defined by

$$\varepsilon_{wz} = -\left(\langle u'\,w'\rangle - \overline{u_p w_p} - \overline{u'\,w'}\right)\Big/\left(\partial u_p/\partial z\right) + v \qquad (3.22)$$

Then we finally obtain the following boundary layer equation for a wave component:

$$\frac{\partial u_p}{\partial t} + \overline{u}\frac{\partial u_p}{\partial x} = -\frac{1}{\rho}\frac{\partial p_p}{\partial x} + \frac{\partial}{\partial z}\left(\varepsilon_{wz}\frac{\partial u_p}{\partial z}\right) \qquad (3.23)$$

$$-\frac{1}{\rho}\frac{\partial p_p}{\partial x} = \frac{\partial u_{bp}}{\partial t} + \overline{u}_b\frac{\partial u_{bp}}{\partial x} \qquad (3.24)$$

The influence of the mean flow on the wave boundary layer in Eq. (3.23) appears in the 2nd term of the left hand side of Eq. (3.23) explicitly and in the kinematic eddy viscosity implicitly. Asano and Iwagaki (1983) investigated the effect of the advection term (2nd term) on the wave boundary layer numerically and reported that it was negligible in the usual shallow water region. If we omit the advection term in Eqs. (3.23) and (3.24), the mean flow does not affect the wave boundary layer explicitly. The effect of the wave component is not also included in the boundary layer equation of the mean flow (Eq. 3.16).

Therefore, in the boundary layer under the coexisting fluid motion of current and linear waves, they interact indirectly through the Reynolds stress $(\overline{u'w'}, \overline{u_p w_p})$ in the kinematic eddy viscosity that is defined by Eqs. (3.15) and (3.22).

When we apply a Prandtl-type expression to the kinematic eddy viscosity in the boundary layer for the steady current, a logarithmic distribution for the steady current is obtained. When we neglect the advection terms in Eqs. (3.23) and (3.24), they become the same equations that Kajiura (1966) used in the analysis of the turbulent boundary layer. Grand and Madsen (1979), Tanaka and Shuto (1981) and Asano and Iwagaki (1983) also used the same fundamental equation to analyze the bottom boundary layer under the wave-current coexisting field.

3.2.3 The bottom shear stress in wave and current coexisting field

To derive the resistance law in the wave and current coexisting field, we have to solve the boundary layer equation by giving the proper kinematic eddy viscosity and thickness of the boundary layer. Among these, it is confirmed empirically that the kinematic eddy viscosity ε_{wz} and the thickness of the boundary layer δ change with the phase (e.g., Sato et al. 1986 and Tanaka 1985). We can also imagine from the definition of Eq. (3.22) that the value of ε_{wz} depends on the phase. We have to analyze the boundary layer equations based on the higher closure problem to know the detailed dependency of the kinematic viscosity on the phase.

We can define the thickness of the boundary layer from the definition of a displacement or a momentum thickness if we know the velocity profile. However, when we solve the

boundary layer equation as an unknown boundary value problem to determine the thickness on the boundary layer and the bottom shear stress and compared them with the results obtained by assuming a constant thickness of the boundary layer. He reported that there was not any significant difference between them.

Here, we judge that we can discuss the characteristic of the bottom shear stress based on the results obtained by assuming a constant kinematic eddy viscosity and boundary layer thickness as the first order approximation. Referring to the former analytical approach, we will derive the resistance law under the wave-current coexisting field by solving the current and the wave boundary layer equations, Eqs. (3.16) and (3.23) without taking into account of the advection term by the steady current.

Generally the flow condition inside the boundary layer is classified into a laminar flow, a smooth turbulent and also rough turbulent flows with different resistance laws used individually. For the wave and current coexisting flow, there may exist some combinations of these conditions for waves and current. The existence of turbulence in the fluid motion due to waves or current causes Reynolds stress which affects both wave and current boundary layers through the kinematic eddy viscosity defined by Eqs. (3.15) and (3.22). Therefore, in the wave and current coexisting flow, both wave and current boundary layers must be either laminar or turbulent.

(1) Solution in laminar flow

First of all, we derive the solution to the boundary layer equations in the laminar flow. Tanaka et al. (1984) derived the distribution of steady current by applying the two-dimensional Poiseuille flow. Here, we will obtain the resistance law based on the mean velocity formula in an open channel flow.

According to Eqs. (3.16) and (3.23) and the definition of the kinematic eddy viscosity, Eqs. (3.15) and (3.22), there is no room for the interaction between waves and current to take place when there is not any turbulence. In such a condition, we can express the mean velocity of steady current U by using the bottom slope S, the hydraulic radius R and friction factor f_c as follows:

$$U = \sqrt{2g/f_c}\sqrt{RS} \tag{3.25}$$

From the Moody diagram, the friction factor of the laminar steady current is approximated by Eq. (3.26).

$$f_c = 15/(4R_{ec}) \tag{3.26}$$

where, R_{ec} is the Reynolds number ($= UR/\nu$).

The bottom shear stress τ_c due to the steady current of the mean velocity U is then expressed by using the molecular viscosity of the fluid μ as follows:

$$\tau_c = \frac{15}{8}\mu\frac{U}{R} \tag{3.27}$$

On the other hand, the velocity distribution of the laminar wave boundary layer $u_p(z,t)$ and the bottom shear stress $\tau_w(t)$ are calculated from Eq. (3.23) in the following form:

$$u_p(z,t) = \hat{u}_{bp}\{\cos \sigma t - \exp(-\zeta z)\cos(\sigma t - \zeta z)\} \tag{3.28}$$

$$\tau_w(t) = \mu \frac{\partial u_p}{\partial z}\bigg|_{z=0} = \sqrt{2}\,\mu\zeta\hat{u}_{bp}\cos\left(\sigma t + \frac{\pi}{4}\right) \tag{3.29}$$

where, u_{bp} is the amplitude of the water particle velocity due to waves just outside of the boundary layer and $\zeta = (\sigma/(2\nu))^{1/2}$.

From these results, we can derive the bottom shear stress $\tau_{cw}(t)$ in the wave and current coexisting laminar flow field as follows:

$$\tau_{cw}(t) = \tau_c + \tau_w(t) = \frac{15}{8}\mu\frac{U}{R} + \sqrt{2}\,\mu\zeta\hat{u}_{bp}\cos\left(\sigma t + \frac{\pi}{4}\right) \tag{3.30}$$

The nondimensional friction velocity $u_{cw}*/u_{bp}$ is calculated from Eq. (3.30).

$$\left(\frac{u_{cw}*}{\hat{u}_{bp}}\right)^2 = \frac{15}{8}\left(\frac{h\hat{u}_{bp}}{\nu}\right)^{-1}\left(\frac{U}{\hat{u}_{bp}}\right) + \sqrt{2}\left(\frac{\hat{u}_{bp}}{\nu\zeta}\right)^{-1}\cos\left(\sigma t + \frac{\pi}{4}\right) \tag{3.31}$$

Table 3.1 Expression of kinematic eddy viscosity and boundary layer thickness

	ε_{wz}	ε_{cz}	$\varepsilon_{cw}\,\partial u/\partial z$	δ_w
Kajiura (1968)	$ku_{wo}^{*}\delta_0,\ z \geq \delta_0$ $ku_{wo}^{*}z,\ \delta_0 > z \geq \delta_L$ $\nu,\ \delta_L \geq z$			
Grant and Madsen (1979)	$ku_c^{*}z,\ z \geq \delta_w$ $ku_{cw}^{*}z,\ z_0 < z < \delta_w$	$ku_c^{*}z,\ z \geq \delta_w$ $ku_{cw}^{*}z,\ z_0 < z < \delta_w$	u_c^{*2} u_c^{*2}	$\delta_w = 2l \sim 4l$ $l = ku_{cw}^{*}/\sigma$
Tanaka and Shuto (1984)	$ku_{cw}^{*}\delta_w,\ z \geq \delta_w$ $ku_{cw}^{*}z,\ z_0 < z < \delta_w$	$ku_c^{*}\delta_w,\ z \geq \delta_w$ $ku_{cw}^{*}z,\ z_0 < z < \delta_w$	$u_c^{*2}(1 - z/h)$ u_c^{*2}	Displacement thickness
Asano and Iwagaki (1983)	$ku_c^{*}z,\ z \geq \delta_w$ $ku_{cw}^{*}z,\ z_0 < z < \delta_w$	$ku_c^{*}z,\ z \geq \delta_w$ $ku_{cw}^{*}z,\ z_0 < z < \delta_w$	u_c^{*2} u_{cw}^{*2}	Unknown (unknown boundary value problem)

u_c*: the friction velocity due to steady current, $u_{wo}*$: the maximum shear velocity due to waves, $u_{cw}*$: the maximum shear velocities due to waves and current, δ_w: the thickness of the wave boundary layer, δ_L and δ_0: thicknesses of the laminar sublayer and the inner layer defined by Kajiura (1964) z_0: height of roughness element, κ: Karman constant.

(2) Solution in rough turbulent flow

To solve turbulent boundary layer equations, Eqs. (3.16) and (3.23), we have to estimate the kinematic eddy viscosity for steady current and waves ε_{cz}, ε_{wz} and the thickness of the boundary layer δ. Some examples of the proposed expression for these values are listed in Table 3.1 with the notation used in the expressions.

We can easily imagine that the Reynolds stress originated in the turbulence of wave motion dominates in the region of wave boundary layer ($z<\delta_w$) and turbulence due to steady current dominates outside the wave boundary layer. We assume here that the turbulence of steady current outside the wave boundary layer has little influence on the wave motion and analyze the boundary layer equations by applying the expressions of the kinematic eddy viscosity after Grant et al. (1979) in the following forms:

$$\left. \begin{array}{l} \text{In the region of } z \geq \delta_w: \qquad \varepsilon_{cz} = \kappa u_c^* z, \varepsilon_{wz} = 0 \\[4mm] \text{In the region of } z_0 \leq z \leq \delta_w: \quad \varepsilon_{cz} = \varepsilon_{wz} = \kappa u_{cw}^* z \end{array} \right\} \qquad (3.32)$$

By introducing these kinematic eddy viscosities into Eq. (3.16), we obtain the vertical distribution of the steady current $u(z)$:

$$\left. \begin{array}{l} u(z) = \dfrac{u_c^{*2}}{\kappa u_{cw}^*} \ln\left(\dfrac{z}{z_0}\right) \quad : z_0 \leq z < \delta_w \\[5mm] u(\delta_w) = \dfrac{u_c^{*2}}{\kappa u_{cw}^*} \ln\left(\dfrac{\delta_w}{z_0}\right): \ z = \delta_w \\[5mm] u(z) = \dfrac{u_c^*}{\kappa}\left(\dfrac{z}{\delta_w}\right) \qquad : \delta_w < z \end{array} \right\} \qquad (3.33)$$

The depth-averaged velocity U is calculated by integrating Eq. (3.33) between $z = z_0$.

$$U = \dfrac{1}{h - z_0}\dfrac{1}{\kappa}\left(\dfrac{u_c^{*2}}{u_{cw}^*}\alpha_1 + u_c^*\alpha_2\right)$$

$$\alpha_1 = h\ln(\delta_w/z_0) - \delta_w + z_0 \qquad\qquad (3.34)$$

$$\alpha_2 = h\ln(h/\delta_w) - h + \delta_w$$

From these relations, the time-averaged bottom shear stress and the nondimensional friction velocity are expressed as follows:

$$\tau_c = \rho u_c^{*2} = \frac{\rho u_{cw}^{*2}}{2} \left\{ \left(\frac{\alpha_2}{\alpha_1} \right)^2 + 2\kappa \left(\frac{U}{u_{cw}^*} \right) \frac{h - z_0}{\alpha_1} \right.$$

$$\left. - \frac{\alpha_2}{\alpha_1} \sqrt{ \left(\frac{\alpha_2}{\alpha_1} \right)^2 + 4\kappa \left(\frac{U}{u_{cw}^*} \right) \frac{h - z_0}{\alpha_1} } \right\} \tag{3.35}$$

$$\frac{u_c^*}{\hat{u}_{bp}} = \frac{1}{2} \left\{ -\left(\frac{\alpha_2}{\alpha_1} \right)\left(\frac{u_{cw}^*}{\hat{u}_{bp}} \right) + \sqrt{ \left(\frac{\alpha_2}{\alpha_1} \right)^2 \left(\frac{u_{cw}^*}{\hat{u}_{bp}} \right)^2 + 4\kappa \left(\frac{U}{\hat{u}_{bp}} \right)\left(\frac{u_{cw}^*}{\hat{u}_{bp}} \right) \frac{h - z_0}{\alpha_1} } \right\} \tag{3.36}$$

To obtain the velocity distribution of the wave component, we eliminate the pressure gradient in Eq. (3.23) using Eq. (3.34). Then we get the following equation to be solved with respect to $u_p(z,t)$:

$$\frac{\partial}{\partial t}\left(u_p - u_{bp} \right) = \frac{\partial}{\partial z}\left(\varepsilon_{wz} \frac{\partial u_p}{\partial z} \right) \tag{3.37}$$

The solution to Eq. (3.37) under the boundary conditions at $z = z_0$ ($u_p = 0$) and $z = \delta_w$ ($u_p = \hat{u}_{bp}\cos(\sigma t)$) is given as follows:

$$u_p(z,t) = \text{Real}\left[\left(1 - \frac{\mathbf{ker}q + i\mathbf{kei}q}{\mathbf{ker}q_0 + i\mathbf{kei}q_0} \right) \hat{u}_{bp}\exp(i\sigma t) \right] = \hat{u}_{bp}\left(R_{up}^2 + I_{up}^2 \right)^{\frac{1}{2}}\cos(\sigma t + \psi) \tag{3.38}$$

where, $q = 2\{z/(ku_{cw}^*/\sigma)\}^{1/2}$, $q_0 = 2\{z_0/(ku_{cw}^*/\sigma)\}^{1/2}$,

$$R_{up} = 1 - \frac{\mathbf{ker}q\,\mathbf{ker}q_0 + \mathbf{kei}q\,\mathbf{kei}q_0}{\left(\mathbf{ker}q_0\right)^2 + \left(\mathbf{kei}q_0\right)^2} \quad , \quad I_{up} = \frac{\mathbf{ker}q\,\mathbf{kei}q_0 + \mathbf{kei}q\,\mathbf{ker}q_0}{\left(\mathbf{ker}q_0\right)^2 + \left(\mathbf{kei}q_0\right)^2}$$

$$\psi = \tan^{-1}\left(I_{up}/R_{up} \right)$$

and **ker** and **kei** are the real and imaginary parts of the modified Bessel Functions of the 2nd kind and Real{ } signifies the real part of the quantity in { }.

The bottom shear stress due to wave motion $\tau_w(t)$ is calculated from Eq. (3.38) as follows:

$$\tau_w(t) = \rho \varepsilon_{wz}\left(\partial u_p / \partial z \right)\big|_{z=z_0}$$

$$= \rho \hat{u}_{bp}\sqrt{\kappa \sigma z_0 u_{cw}^*}\left(R_{up}'^2 + I_{up}'^2 \right)^{1/2}\cos(\sigma t - \psi') \tag{3.39}$$

where,

$$R_{up}' = 1 - \frac{\mathbf{ker}'q_0\mathbf{ker}q_0 + \mathbf{kei}'q_0\mathbf{kei}q_0}{\left(\mathbf{ker}q_0\right)^2 + \left(\mathbf{kei}q_0\right)^2} \quad , \quad I_{up}' = \frac{\mathbf{ker}'q_0\mathbf{kei}q_0 + \mathbf{kei}'q_0\mathbf{ker}q_0}{\left(\mathbf{ker}q_0\right)^2 + \left(\mathbf{kei}q_0\right)^2}$$

$$\psi' = \tan^{-1}(I_{up}'/R_{up}')$$

and **ker'** and **kei'** are the derivatives of **ker** and **kei**, respectively.
Using these results, we can obtain the bottom shear stress $\tau_{cw}(t)$ and the maximum shear velocity u_{cw}^* under the wave and current that are expressed by Eqs. (3.40) and (3.41).

$$\begin{aligned}
\tau_{cw}(t) &= \tau_c + \tau_w(t) \\
&= \rho u_c^{*2} + \rho\hat{u}_{bp}\sqrt{\kappa\sigma z_0 u_{cw}^*}\left(R_{up}'^2 + I_{up}'^2\right)^{1/2}\cos(\sigma t - \psi')
\end{aligned} \tag{3.40}$$

$$\left(\frac{u_{cw}^*}{\hat{u}_{bp}}\right)^2 = \left(\frac{u_{cw}^*}{\hat{u}_{bp}}\right)^2 + \sqrt{\kappa\left(\frac{z_0}{a_b}\right)\left(\frac{u_{cw}^*}{\hat{u}_{bp}}\right)}\left(R_{up}'^2 + I_{up}'^2\right)^{1/2} \tag{3.41}$$

Equation (3.41) is the relation between the depth averaged steady current velocity U, angular frequency σ, the amplitude of water particle velocity due to waves at the bottom u_{bp}, the height of the roughness element z_0, the shear velocity due to steady current u_c^* and the maximum shear stress due to waves and current u_{cw}^*. We have to carry out iterative calculation to determine the values of u_c^* and u_{cw}^* based on Eqs. (3.35) and (3.41) with the expression of the kinematic eddy viscosity (Eq. (3.32)).

(3) Solution of smooth turbulent flow
We assume here that the expression of kinematic eddy viscosity (Eq. (3.32)) is applicable to the smooth turbulent boundary layer higher than the laminar sublayer (Kajiura 1966). Then, the results obtained for the case of the rough turbulent boundary layer (Eqs. (3.38-3.41)) can be used by replacing the height of the roughness element $z0$ by a function of the thickness of laminar sublayer δ_L as shown by Eq. (3.42).

$$\delta_L = 11.6\,\nu/u_{cw}^* \tag{3.42}$$

$$z_0 = \delta_L/105$$

3.2.4 Increase of bottom shear stress in the presence of steady current
We can discuss the effect of steady current on the bottom shear stress based on Eqs. (3.30) and (3.31) in the laminar case and Eqs. (3.40) and (3.41) in the turbulent case. In the laminar case, the parameters that affect the bottom shear stress caused by waves and current are $U/\hat{u}_{bp}$, ζh and $\hat{u}_{bp}/(\zeta\nu)$ or $\hat{u}_{bp}^2 T/\nu$ and the bottom shear stress under waves and current is expressed by a simple summation of the bottom shear stresses due to waves and current. There is not any interaction between the bottom shear stresses caused by waves and current. In the turbulent case, the following three parameters are predominant: $U/\hat{u}_{bp}$,

a_b/z_0 and z_0/h or a_b/h. Among these, $\hat{u}_{bp}/(\zeta v)$ and a_b/z_0 give a direct influence on the bottom shear stress caused by waves and ζh and z_0/h have very much to do with the bottom shear stress due to the steady current.

In the following, effect of the steady current on the amplitude of the shear velocity due to waves u_w^* and the maximum shear velocity due to waves and current u_{cw}^* in a turbulent boundary layer is examined. There is no interaction between waves and current in the laminar boundary layer (Eq. (3.30)).

Figure 3.2 illustrates the relation between u_w^* and $U/\hat{u}_{bp}$ calculated from Eq. (3.39) with the relation between u_{cw}^* and $U/\hat{u}_{bp}$ calculated from Eq. (3.41) in the case of $a_b/z_0 = 1000$. The vertical axis is normalized by the shear velocity due to waves without any current u_{w0}^* ($U/\hat{u}_{bp} = 0$). As can be seen from the figure, both values of u_w^*/u_{w0}^* and u_{cw}^*/u_{w0}^* increase linearly from unity with the increase in the value of $U/\hat{u}_{bp}$. When the depth becomes relatively shallow, i.e., h/a_b becomes smaller, the shear velocity becomes more sensitive to the increase in the velocity of steady current.
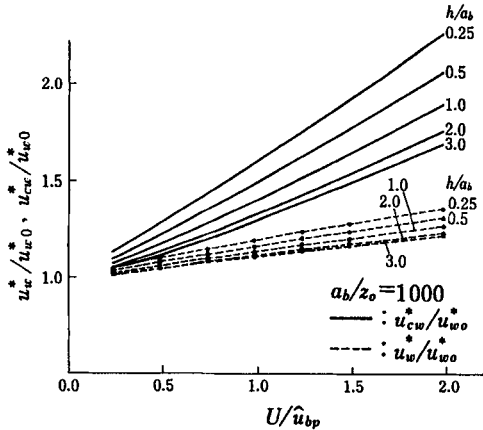
Fig. 3.2 Increase in bottom shear stress with current

The results shown in Fig. 3.2 are those in the case of $a_b/z_0 = 1000$. The value of a_b/z_0 does not have any significant effect on the bottom shear stress under waves and current coexisting field because it has very related to the wave boundary layer and has nothing to do with the current boundary layer (see Eq. (3.36)).

3.2.5 Resistance law in waves and current coexisting field

According to the method derived in the former section, we have to determine the shear velocity under waves and current through the iterative calculation and it is not a practical way. Here, an approximate relation to explicitly determine the maximum and the time-averaged bottom shear stresses τ_{cw} and τ_c is introduced by using the friction factor.

There are three conventional ways to take the effect of the steady current into account in the expression of the bottom shear stress due purely to waves (Eq. (3.1)). One way is to modify the friction factor f_w defined in the wave field to the friction factor f_{cw} in the wave and current coexisting field still using water particle velocity due to waves $\hat{u}_{bp}$ (e.g., Grant

and Madsen 1979, Tanaka and Shuto 1981 etc.). The second one is to use the wave and current combined water particle velocity $u_{comb.}$ instead of $\hat{u}_{bp}$ still using the wave friction factor f_w (e.g., Sawaragi et al. 1978a and Nishimura 1982). The last one is to estimate the bottom shear stresses due to waves and current independently and sum them vectorally (e.g., Jonsson et al. 1974).

Sawaragi et al. (1978a) measured cross-shore and longshore components of the bottom shear stress on a uniformly sloping model beach where the uniform longshore current was generated by obliquely incident waves. Based on the measured results, they reported that the contribution of the longshore current to the bottom shear stress was relatively smaller then that of the wave motion when the bottom shear stress was evaluated from Eq. (3.1) by using the resultant velocity $u_{comb.}$ of the vertically averaged longshore current velocity $V(x)$ and the water particle velocity due to waves $\hat{u}_{bp}$.

In other words, we can express the cross-shore and the longshore components of the resultant velocity u_{bx} and u_{by} as Eq. (3.43) in the place where the uniform longshore current is generated in the longshore direction with the coordinate system shown in Fig. 3.3.

$$u_{bx} = \hat{u}_{bp} \cos \theta \cos \sigma t, \quad u_{by} = \hat{u}_{bp} \sin \theta \cos \sigma t + V \tag{3.43}$$
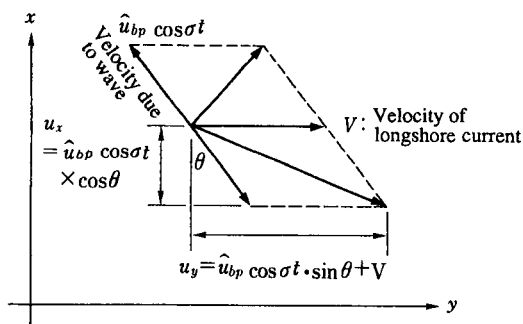
Fig. 3.3 Resultant velocity due to waves and current

When we express the maximum bottom shear stress τ_{cwm} in the form of $\rho f u_{comb.}^2/2$ by using the maximum resultant velocity $u_{comb.}$, the cross-shore and the longshore components of τ_{cwm} are given as follows:

$$\tau_x = \tau_{cwm} \hat{u}_{bp} \cos \theta / u_m, \quad \tau_y = \tau_{cwm} \left(\hat{u}_{bp} \sin \theta + V \right) / u_m \tag{3.44}$$

The direction of this maximum bottom shear stress becomes

$$\tau_y / \tau_x = \tan \theta + \left(V / \hat{u}_{bp} \right) \sec \theta \tag{3.45}$$

When there is not any steady current, i.e., $V = 0$, the value τ_y/τ_x is the tangent of the wave direction and Eq. (3.45) is rewritten as

$$\frac{V}{\hat{u}_{bp}} = \cos\theta \left\{ \frac{\tau_y}{\tau_x} - \left(\frac{\tau_y}{\tau_x} \right)_0 \right\}$$

(3.46)

where $(\tau_y/\tau_x)_0$ means the value where there is no current.

Figure 3.4 shows the relations between $V/\hat{u}_{bp}$ and the value of the right hand side of Eq. (4.46), i.e., $\cos\theta\{\tau_y/\tau_x-(\tau_y/\tau_x)_0\}$ based on the measurement by Sawaragi and Deguchi (1978b). From the figure, it is found that the relation between $V/\hat{u}_{bp}$ and $\cos\theta\{\tau_y/\tau_x-(\tau_y/\tau_x)_0\}$ is given by Eq. (3.47) rather than Eq. (3.46).

$$\frac{V}{\hat{u}_{bp}} = 0.5\cos\theta \left\{ \frac{\tau_y}{\tau_x} - \left(\frac{\tau_y}{\tau_x} \right)_0 \right\}$$

(3.47)
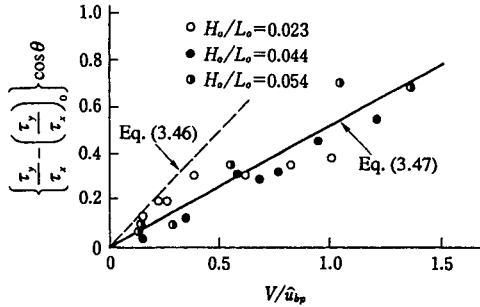
Fig. 3.4 Relation between longshore current and bottom shear stress

This means that it is necessary to reduce the depth-averaged velocity of the steady current when we evaluate the bottom shear stress due to waves and current by using the resultant velocity.

On the other hand, Grant and Madsen (1979) and Tanaka and Shuto (1981) defined a new friction factor f_{cw} to estimate the maximum bottom shear stress due to waves and current from the relation $\tau_{cwm} = \rho f_{cw} \hat{u}_{bp}^2/2$ based on their analytical solution of the boundary layer equations. Equation (3.48) is the approximate expression for the modified friction factor f_{cw} in the rough turbulent boundary layer by Tanaka and Shuto (1981).

$$\frac{f_{cw}}{2} = \frac{\kappa}{\ln(h/z_0)-1} \frac{U}{\hat{u}_{bp}} + \frac{\kappa}{\pi} \left[0.25 + 0.101 \left\{ \ln\left(\frac{\sigma z_0}{\hat{u}_{bp}} \right) \right. \right.$$
$$\left. \left. + \frac{1}{2}\ln f_{cw} + 2.42 \right\}^2 \right]^{-1/2}$$

(3.48)

However, in the case where waves and current are not in the same vertical plane and they cross at an arbitrary angle, it seems convenient to evaluate the maximum bottom shear stress using the resultant velocity of waves and current so that we can easily determine the direction of the maximum shear stress. Here, the parameter $P(\leq 1)$ is introduced to reduce the effect of the vertically averaged mean current according to the experimental results of

Sawaragi and Deguchi (1978b) and the dependency of the P-value on various wave and current parameters are examined.

We assume first that the maximum shear stress τ_{cwm} and the amplitude of the shear stress due to waves τ_{w0m} are expressed by using the friction factor defined by Jonsson (1963) as follows:

$$\tau_{cwm} = \rho f_w \left(\hat{u}_{bp} + PU \right)^2 \big/ 2 = \rho u_{cw}^{*2} \qquad (3.49)$$

$$\tau_{w0m} = \rho f_w \, \hat{u}_{bp}^{\,2} \big/ 2 = \rho u_{w0}^{*2} \qquad (3.50)$$

Eliminating f_w from Eqs. (3.49) and (3.50), we have the following expression for P:

$$P = \frac{\hat{u}_{bp}}{U} \left(\frac{u_{cw}^{*}}{u_{w0}^{*}} - 1 \right) \qquad (3.51)$$

In the laminar case, τ_{cwm} and τ_{w0m} are obtained from Eqs. (3.30) and (3.29) and Eq. (3.51) becomes

$$P = \frac{\hat{u}_{bp}}{U} \left[\left\{ 1 + \frac{15}{8\sqrt{2}} \frac{1}{\zeta h} \left(\frac{U}{\hat{u}_{bp}} \right) \right\}^{1/2} - 1 \right] \qquad (3.52)$$

In this case, P is a function of $\hat{u}_{bp}/U$ and ζh.
In the same way, in the turbulent case, we have the following expression for P:

$$P = \frac{\hat{u}_{bp}}{U} \left[\left\{ 1 + \frac{u_c^{*2}}{\hat{u}_{bp} \sqrt{\kappa \sigma z_0 u_{cw}^{*}} \left(R_{up}'^{2} + I_{up}'^{2} \right)^{1/2}} \right\}^{1/2} - 1 \right] \qquad (3.53)$$

This equation shows that P in the turbulent case is a function of a_b/z_0, $\hat{u}_{bp}/U$ and h/z_0 (or h/a_b).

We can easily calculate the value of P in the laminar case because there is not any interaction between waves and current in the boundary layer. Figure 3.5 illustrates the dependency of the P-value in the rough turbulent cases where $U/\hat{u}_{bp} = 0.5$ (Fig. (a)) and 1.0 (Fig. (b)) calculated based on Eq. (3.53). We can see from these figures that the value of P becomes large with increases in a_b/z_0 and with the decrease in h/a_b. However, the P-value does not significantly depend on the value of $U/\hat{u}_{bp}$.

Based on the calculation of Eq. (3.53), some examples of which are shown in Fig. 3.5, the value of P is expressed approximately by the function of a_b/z_0, h/a_b and $U/\hat{u}_{bp}$ as follows:
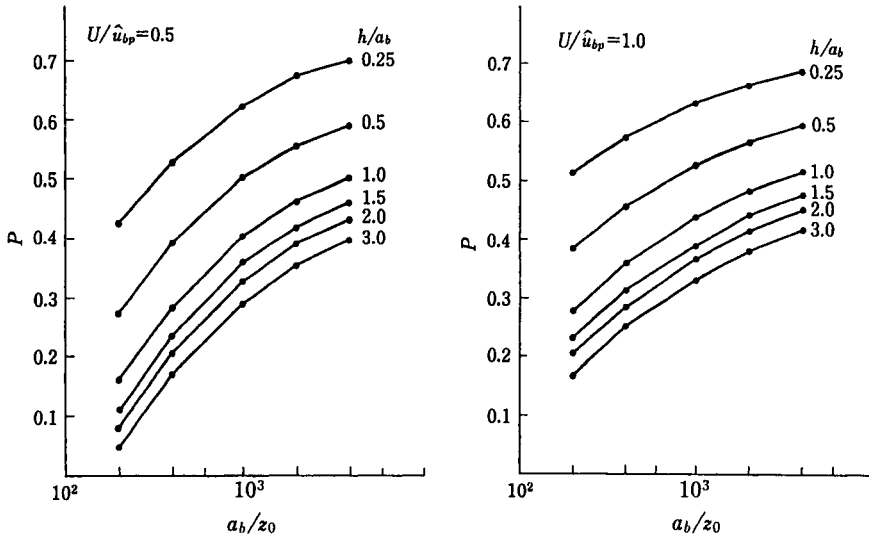
Fig. 3.5 P-value as a function of a_b/z_0 ((a): $U/\hat{u}_{bp} = 0.5$, (b): $U/\hat{u}_{bp} = 1.0$)

$$P = \left[\left\{\log(a_b/z_0) - b\right\}/a\right]^{1/c}$$

$$a = -18.2(U/\hat{u}_{bp})^{-0.194} + 29.8$$

$$b = 0.167/(U/\hat{u}_{bp}) + 1.8$$
(3.54)

$$c = r(h/a_b)^{-n} + s$$

here, $n = 0.685 - 0.305\ (U/\hat{u}_{bp})$ and r and s are a function of $U/\hat{u}_{bp}$ listed in Table 3.2 provided that the value of a_b/z_0 is in the range of $2*10^2$-$4*10^3$ and $U/\hat{u}_{bp}$ is less than 3.0.

Table 3.2 Values of r and s

	$U/\hat{u}_{bp} < 0.52$	$0.52 \le U/\hat{u}_{bp} < 1.5$	$1.5 \le U/\hat{u}_{bp} < 3$
γ	$1.52(U/\hat{u}_{bp}) + 0.910$	$6.22(U/\hat{u}_{bp}) - 1.54$	$14.0(U/\hat{u}_{bp}) - 13.2$
s	$-0.704(U/\hat{u}_{bp}) + 1.47$	$-5.41 \le U/\hat{u}_{bp} < -3.91$	$-13.4(U/\hat{u}_{bp}) + 15.9$

Finally, the procedure to estimate the time-averaged bottom shear stress in the case where waves and current cross at arbitrary angles is shown in the coordinate system shown in Fig. 3.6. Here, again the interaction between waves and current is taken into account through the kinematic eddy viscosity in the turbulent case. When we assume that the kinematic eddy viscosity in the case where waves and current cross at arbitrary angles can

be expressed in the same form as they are in the same vertical plane, the bottom shear stress due to waves and current τ_{cw} is evaluated as the resultant of the shear stresses due to current and waves τ_c and τ_w. From the definition illustrated in Fig. 3.6, the components of the resultant bottom shear stress in the cross-shore and the longshore directions τ_x and τ_y become

$$\tau_x = \tau_c \cos \theta_c + \tau_w \cos \theta_w$$
$$= \rho u_c^{*2} \cos \theta_c + \rho u_w^{*2} \cos \theta_w \qquad (3.55)$$

$$\tau_y = \tau_c \sin \theta_c + \tau_w \sin \theta_w$$
$$= \rho u_c^{*2} \sin \theta_c + \rho u_w^{*2} \sin \theta_w \qquad (3.56)$$

where τ_c and τ_w in the laminar and the turbulent cases are given by Eqs. (3.27) and (2.39) and Eqs. (3.35) and (3.39), respectively.
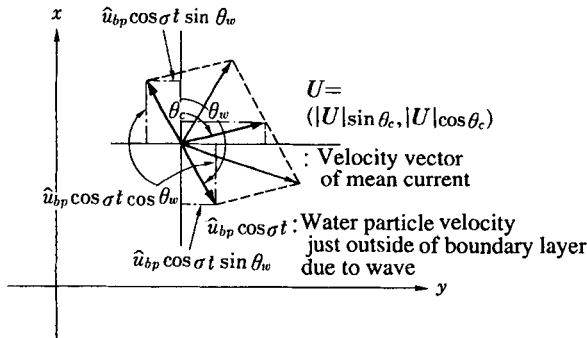
Fig. 3.6 Resultant velocity due to waves and current

From Eqs. (3.55) and (3.56), it is found that the cross-shore and the longshore components of the time-averaged resultant bottom shear stress are expressed as follows:

$$\overline{\tau}_x = \tau_c \cos \theta_c = \rho u_c^{*2} \cos \theta_c$$
$$\overline{\tau}_y = \tau_c \sin \theta_c = \rho u_c^{*2} \sin \theta_c \qquad (3.57)$$

3.3 Sediment Movement and Beach Deformation

3.3.1 Relation between sediment movement and beach deformation

Here, the mechanism of the topographic change caused by sediment movement in a shallow water region is explained. We usually use the following equation of continuity of sediment concentration C in the coordinate system shown in Fig. 3.7.

$$\frac{\partial C}{\partial t}+\frac{\partial u_s C}{\partial x}+\frac{\partial v_s C}{\partial y}+\frac{\partial w_s C}{\partial z}=0$$

(3.58)

where $V_s = (u_s, v_s, w_s)$ is the vector of migration speed of sediment in the direction of x-, y- and z-axes.
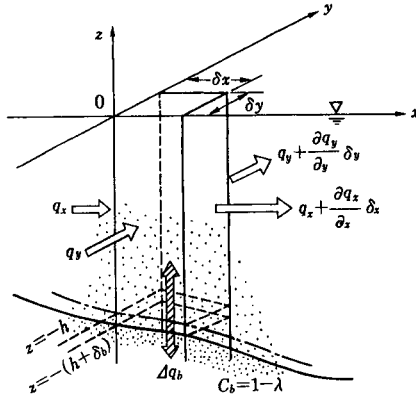
Fig. 3.7 Definition sketch of continuity of sediment transport

We are going to examine the relation between sediment movement and topographic change based on the sediment budget in a vertical water column on a unit area on the bottom shown in Fig. 3.7 by integrating Eq. (3.58) between $\eta \geq z > -h$ (suspended load layer), $-h \geq z > -(h+\delta_b)$ (bed load layer) and $z \leq -(h+\delta_b)$ (non-movement layer).
In a suspended load layer, $\eta \geq z > -h$:

$$\frac{\partial}{\partial t}\int_{-h+}^{\eta}Cdz+\frac{\partial}{\partial x}\int_{-h+}^{\eta}Cu_s dz+\frac{\partial}{\partial y}\int_{-h+}^{\eta}Cv_s dz=\Delta q_s$$

(3.59)

In a bed load layer, $\eta \geq z > -h$:

$$\frac{\partial}{\partial t}\int_{-h_{bd}}^{-h-}Cdz+\frac{\partial}{\partial x}\int_{-h_{bd}}^{-h-}Cu_s dz+\frac{\partial}{\partial y}\int_{-h_{bd}}^{-h-}Cv_s dz=-\Delta q_s +\Delta q_b$$

(3.60)

In a sand layer of no motion, $z \leq -(h+\delta_b)$:

$$\frac{\partial}{\partial t}\int_{-\infty}^{-h_{bd}}Cdz=-\Delta q_b$$

(3.61)

where

$$\Delta q_s = C_{-h} \left\{ \frac{\partial h}{\partial t} + u_{s,-h} \frac{\partial h}{\partial x} + v_{s,-h} \frac{\partial h}{\partial y} \right\} + \left[C w_s \right]_{-h}$$

$$\Delta q_b = C_{-h_{bd}} \left\{ \frac{\partial h_{bd}}{\partial t} + u_{s,-h_{bd}} \frac{\partial h_{bd}}{\partial x} + v_{s,-h_{bd}} \frac{\partial h_{bd}}{\partial y} \right\} + \left[C w_s \right]_{-h_{bd}}$$

(3.62)

Δq_s and Δq_b are the exchange rates of sediment between the bed load and suspended load layers and bed load and non-movement layers, respectively. The notations $-h_+$ and $-h_-$ in the integral mean the limits of approaching $z = -h$ from the positive and the negative direction of the z-axis.

The left hand side of Eq. (3.61) shows the time change of total sand volume included into the non-movement sand layer. We can express the time change of the lowermost location of the bed load layer $z = -h_{bd} = -(h+\delta_b)$ by using the mean sediment concentration in the non-movement layer C_b as follows:

$$\frac{\partial (h + \delta_b)}{\partial t} = \frac{1}{C_b} \Delta q_b$$

(3.63)

Generally, the thickness of the bed load layer δ_b is sufficiently small when compared with the water depth h. Then Eq. (3.63) is rewritten using the void ration of the non-movement layer $\lambda (= 1 - C_b)$ in the following form:

$$\frac{\partial h}{\partial t} = \frac{1}{1 - \lambda} \Delta q_b$$

(3.64)

On the other hand, we can derive the following expression for Δq_b by using Eqs. (3.59) and (3.60):

$$\Delta q_b = \frac{\partial}{\partial t} \int_{-h+}^{\eta} C \, dz + \left(\frac{\partial}{\partial x} \int_{-h+}^{\eta} C u_s \, dz + \frac{\partial}{\partial y} \int_{-h+}^{\eta} C v_s \, dz \right)$$
$$+ \frac{\partial}{\partial t} \int_{-h_{bd}}^{-h^-} C \, dz + \left(\frac{\partial}{\partial x} \int_{-h_{bd}}^{-h^-} C u_s \, dz + \frac{\partial}{\partial y} \int_{-h_{bd}}^{-h^-} C v_s \, dz \right)$$

(3.65)

The 2nd and 4th terms in the right hand side of Eq. (3.65) are the spatial gradients of suspended load flux and bed load flux, respectively and the 1st and 3rd terms are the time change of the sediment volumes in the suspended and bed load layer, respectively.

Beach deformation and change in water depth that become objects of our research from a viewpoint of engineering includes various time scales. Beach deformation caused by a moving low pressure system accompanied by high waves will continue for a few days or a few week. Topographic change brought about by the longshore sediment transport will usually continue for more than a few years. However, these time scales are sufficiently longer than the period of incident waves and the topographic change that takes place within one wave period is generally disregarded. Therefore, we usually discuss the topographic change based on the time-averaged form of Eq. (3.65) over at least a few wave periods and the expression of $-h_\pm$ is replaced by $-h$ in Eq. (3.65).

The cross-shore and the longshore sediment flux in Eq. (3.65) are called the cross-shore and the longshore sediment transport rates q_x and q_y are expressed as follows:

$$q_x = q_{sx} + q_{bx} = \overline{\int_{-h}^{\eta} Cu_s dz} + \overline{\int_{-(h+\delta_b)}^{-h} Cu_s dz}$$

(3.66)

$$q_y = q_{sy} + q_{by} = \overline{\int_{-h}^{\eta} Cv_s dz} + \overline{\int_{-(h+\delta_b)}^{-h} Cv_s dz}$$

where, $^-$ means the time-averaged value and subscripts s and b show that the quantities with these subscripts concern the suspended load and bed load.

Here, we consider the topographic change in the case where the concentration of suspended sediment is in a steady state so that we can neglect the 1st and 3rd terms in Eq. (3.65). Such conditions appear in the following states:

In the case where external forces such as waves and current in the objective range do not show any rapid temporal change, and in the case where sand supply to the objective range such as sand discharge from the river and so on is constant.

Then Eqs. (3.64) and (3.65) are rewritten into Eqs. (3.67) and we can estimate the topographic change provided that the longshore and the cross-shore sediment transport rates are given

$$\frac{\partial h}{\partial t} = \frac{1}{1-\lambda} \overline{\Delta q_b}$$

(3.67)

$$\overline{\Delta q_b} = \frac{\partial q_x}{\partial x} + \frac{\partial q_y}{\partial y}$$

Furthermore, if there are not any significant spatial gradients of fluid motion and bottom topography, a vertical distribution of suspended sediment concentration is in an equilibrium state. Various formulations and modeling have already been carried out to evaluate the longshore and the cross-shore sediment transport rates in such conditions and we will refer to them in **3.4**.

On the other hand, change in the water depth in the case where the vertical distribution of suspended sediment concentration is not in an equilibrium or steady state, we are not able to calculate topographic change from the usual sediment transport rate in the equilibrium state. These conditions may take place in the cases where the spatial gradient of water depth or the temporal change in wave field are large. In such cases we have to estimate Δq_s given by Eq. (3.62) to calculate topographic change. This procedure will be explained in detail in **3.6**.

3.3.2 Modeling of beach deformation and procedure for predicting beach deformation
(1) Objective beach deformations and their time scale

As was mentioned in the former section, change in the water depth caused by successive attacks of constant waves is expressed by Eq. (3.67). We will examine the characteristics of topographic changes brought about by the cross-shore and the longshore sediment transports based on Eq. (3.67). A definition sketch is shown in Fig. 3.8.
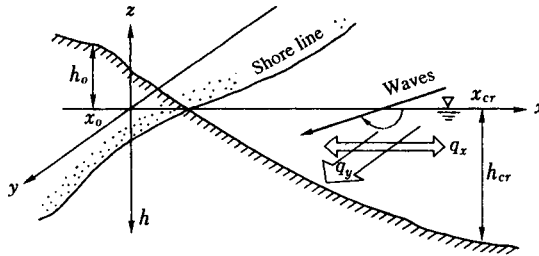
Fig. 3.8 Definition sketch of coordinate system

To investigate the topographic change caused by the longshore sediment transport, we integrate Eq. (3.67) in the cross-shore direction between $x = x_0$ and $x = x_{cr}$ where x_0 and x_{cr} are the landward and the seaward limits of the topographic change whose depths correspond to h_0 and h_{cr}. The integration of Eq. (3.67) using the Leibnitz relation leads to the following equation:

$$\left\{ \frac{\partial}{\partial t} \int_{x_0}^{x_{cr}} h dx - h_{cr} \frac{\partial x_{cr}}{\partial t} + h_0 \frac{\partial x_0}{\partial t} \right\} (1 - \lambda)$$

$$= \left(q_{x,x_{cr}} - q_{x,x_0} \right) + \frac{\partial}{\partial y} \int_{x_0}^{x_{cr}} q_y dx - q_{y,x_{cr}} \frac{\partial x_{cr}}{\partial y} + q_{y,x_0} \frac{\partial x_0}{\partial y}$$

In the equation, the cross-shore sediment transport at $x = x_0$ and $x = x_{cr}$ in the ( ) of the right hand side is zero because there is not any significant sediment movement in the region of $x < x_0$ and $x > x_{cr}$. When we define the beach sectional area A and the total longshore sediment transport Q_y by Eq. (6.68), we can finally obtain the following relation between A and Q_y:

$$A = \int_{x_0}^{x_{cr}} h dx, \ Q_y = \int_{x_0}^{x_{cr}} q_y dx \tag{3.68}$$

$$\frac{\partial A}{\partial t} = h_{cr} \frac{\partial x_{cr}}{\partial t} - h_0 \frac{\partial x_0}{\partial t} + \frac{\partial Q_y}{\partial y} \left(\frac{1}{1 - \lambda} \right) \tag{3.69}$$

Equation (3.69) shows that the temporal change in the beach sectional area A is caused by the longshore gradient of the total longshore sediment transport rate Q_y and the temporal variation of the region where the significant sediment transport takes place. The cross-shore sediment transport has nothing to do with the change in the sectional area.

On the other hand, any longshore sediment transport does not take place in a movable bed experiment on a sloping beach in a two-dimensional wave tank. In such a case, we can discuss the topographic change based on Eq. (3.70).

$$\frac{\partial h}{\partial t} = \frac{1}{1 - \lambda} \frac{\partial q_x}{\partial x} \tag{3.70}$$

When we integrate Eq. (3.70) in the same way as we did in Eq. (3.67), Eq. (3.70) becomes as follows:

$$\frac{\partial}{\partial t}\int_{x_0}^{x_{cr}} h dx = 0$$

This means that the cross-shore sediment transport causes changes in the cross-shore profile of the beach without any change in the sectional area.

A deformation pattern of the cross-shore profile of the beach caused by the cross-shore sediment transport is usually classified into the four patterns as illustrated in Fig. 3.9 (Sunamura and Horikawa 1974, Sawaragi and Deguchi 1980, Shimizu et al. 1985). Full lines in the figures are the illustration of the deformations of the cross-shore profile and broken lines are the rough illustrations of the distribution of the cross-shore sediment transport rate estimated based on Eq. (3.70).
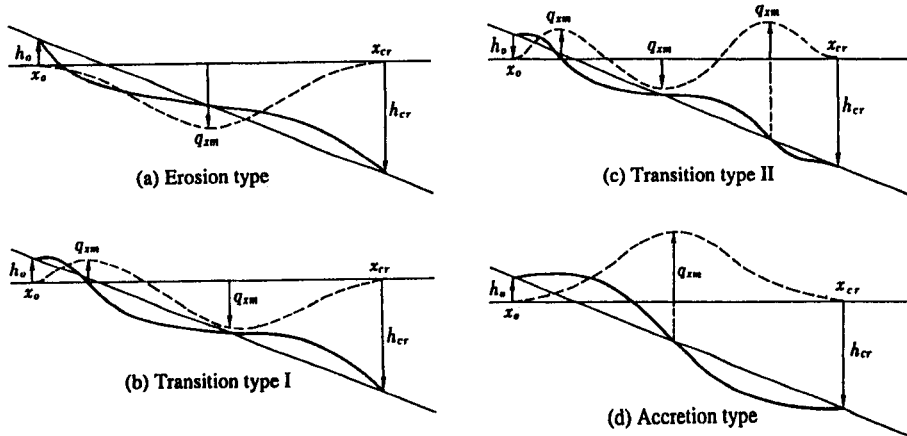
Fig. 3.9 Changes in beach section caused by cross-shore sediment transport

Figure (a) is the deformation of erosion type caused by the net offshore sediment movement through the whole section. Figure (d) is an accretion type deformation caused by the net onshore sediment movement through the whole section. In the topographic changes shown in Figs. (b) and (c), both net onshore and net offshore sediment movements took place at the same time.

The upper figures of Figs. 3.10 and 3.11 show examples of topographic changes of erosion and accretion type beach deformations measured in the two-dimensional experiments. Figure (b) is the cross-shore distribution calculated from Eq. (3.70) by using the change in measured water depth shown in Fig. (a).
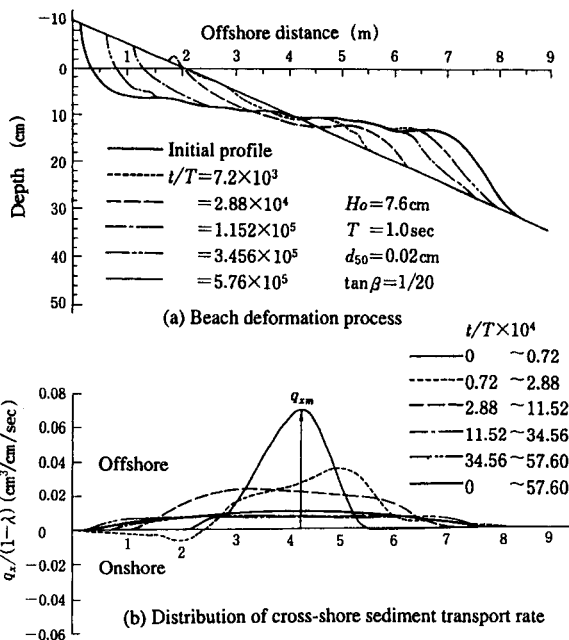
Fig. 3.10 Erosion type beach deformation process and cross-shore sediment transport rate
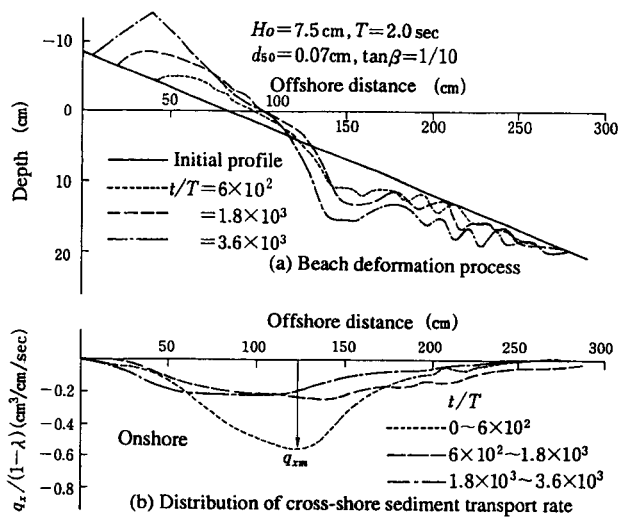
Fig. 3.11 Accretion type beach deformation process and cross-shore sediment transport rate

As we can see from these two examples, the cross-shore sediment transport rate decreases with the increase of elapsed time and beach profile reaches to the equilibrium. The time change of the natural phenomena that will reach an equilibrium state is generally expressed by the exponential function. We suppose here that the time variation of the maximum cross-shore sediment transport rate q_{xm} decreases in the following manner:

$$q_{xm}(t) = q_{x0} \exp(-A_t t/T)$$

(3.71)

where, q_{x0} is the initial maximum cross-shore sediment transport rate at $t/T = 0$ and A_t is the attenuation rate of q_{x0}.

We calculated the time variation of the maximum cross-shore sediment transport rate based on the existing experimental results reported by many researchers and evaluated the value of A_t. Figure 3.12 shows the relation between calculated A_t and the value of $N_s (= H_0/(T\sigma'gd_{50})^{1/2})$. The parameter N_s is a kind of Shields number indicating the deformability of the whole beach where H_0 and T are the equivalent deepwater wave height and period, σ' is the submerged specific gravity and d_{50} is the median grain size.
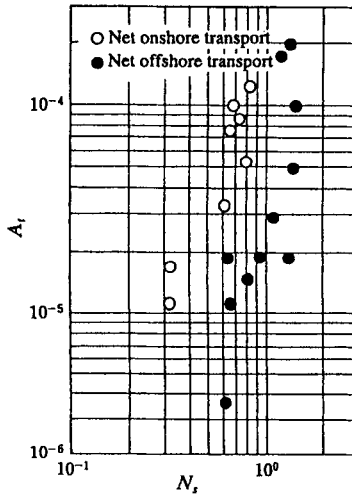
Fig. 3.12 Attenuation rate of cross-shore sediment transport rate

The value of A_t increases from $2.5 * 10^{-6}$ to $2.0 * 10^{-4}$ with the increase in the value of N_s in the range of $0.3 < N_s < 1.3$. The decrease of the cross-shore sediment transport in the accretion type is faster than that in the erosion type beach deformation which means that the accretion type beach deformation reaches an equilibrium state faster than the erosion type beach deformation does.

Beach profiles in the field are usually almost in an equilibrium state after the continuous attack of nearly constant waves of a certain period and little net cross-shore sediment transport occurs. A significant cross-shore sediment transport takes place only when the characteristics of incident waves change largely and beach profile approaches the new equilibrium condition corresponding to the new wave characteristics.

In the laboratory case of $A_t = 10^{-5} - 10^{-4}$, it will take $t/T = 3*10^4 - 3*10^5$ for the cross-shore sediment transport rate to decrease 80% of its initial value. If we can apply the attenuation

coefficient shown in Fig. 3.12 to the beach deformation in the field of the same value of A, under the incidence of waves of period about 5s, it will take a few days for the beach deformation to reach an almost equilibrium state.

On the other hand, the beach deformation caused by the longshore sediment transport whose transporting agency is the longshore current continues even if an incident wave characteristics do not change. As a result, large-scale erosion (shoreline retreat) and accretion (shoreline advancement) takes place in an extensive range for a long period. Therefore, the time scale of the prediction of beach deformation due to the longshore sediment transport becomes a wide range from a few days to several years.

There are of course topographic changes due to both longshore and cross-shore sediment transport in the field. We have to fully investigate the predominant mode and direction of sediment transport in the objective beach deformation to be predicted. The general method regarding this point is to utilize the so-called empirical eigenfunction analysis of the measured topographic change (Winant et al. 1975). Hashimoto and Uda (1979) extracted the patterns of topographic changes caused by cross-shore and longshore sediment transport by expanding the deviation of the measured water depth from the time averaged water depth at Ajigaura Coast to cross-shore and time functions using the empirical eigenfunction analysis method. Sawaragi and Deguchi (1982) and Deguchi and Sawaragi (1986) expanded the deviation of the measured water depth from the averaged water depth into cross-shore and longshore function by the empirical eigenfunction method and discussed the function of groins to trap longshore sediment transport in the laboratory and characteristics of topographic change took place around the submerged breakwater in the field.

(2) Prediction model of beach (sectional) deformation due to cross-shore sediment transport

Deformation process of a beach profile due to cross-shore sediment transport is essentially an unsteady and non-equilibrium process. When we discuss a deformation process, we have to know the history of the objective coast, that is, what kinds of waves created the beach profile?

A change in water depth of such beach deformation is unable to be predicted by using the cross-shore sediment transport rate in an equilibrium state formulated in various ways. To predict deformation of beach profile due to cross-shore sediment transport, we must incorporate a nonequilibrium nature and unsteadiness of the beach process. We have to at least take into account the time variation of the cross-shore sediment transport rate in the beach deformation process.

A direct result of this time variation of the cross-shore sediment transport rate in the beach deformation process is that the onshore and the offshore sediment transport rates in one wave cycle approach the same value and the time averaged (net) sediment transport rate becomes zero. The mechanism of this process may be explained as follows:
a) Interaction between the change in water depth, wave transformation and the mean flow such as undertow that originates in wave motions on a sloping beach,
b) Asymmetricity of the resistance force of bed material on the sloping bottom the beach deformation process.

In the existing numerical model for the prediction of beach deformation caused by cross-shore sediment transport, the dependency of the cross-shore sediment transport rate on time is usually taken into account through the dependency of the critical shear velocity on the local bottom slope (Deguchi and Sawaragi 1988) or the dependency of the cross-shore sediment transport rate on the local bottom slope (Watanebe et al. 1986 and Nishimura and Sunamura 1986). However, we cannot yet evaluate these mechanisms quantitatively.

On the other hand, the deformation of a beach profile caused by the cross-shore sediment transport usually reaches the equilibrium profile under the condition of the same wave incidence. Some attempts have been made to formulate this equilibrium beach profile without using the equation of continuity of sediment transport. Eagleson et al. (1963) proposed a procedure to determine the equilibrium beach profile by introducing a null-point theory. They calculated the migration speed of bed materials on the sloping beach based on the equation of the motion of a single particle and defined the zero-net motion of the particle where the gravity effect on the particle is in balance with the time averaged drag force due to the mass transport velocity.

Bowen (1980) derived another concept of the equilibrium beach profile determined from his cross-shore sediment transport rate based on the power model. In his concept, the time averaged cross-shore sediment transport rate becomes zero on the equilibrium beach.

These beach profiles are effective only in the region where the fluid motion due to waves and wave-induced steady current can be predicted accurately. Generally, they cannot apply in the breaker zone including the swash zone.

Swart (1974) carried out a number of two-dimension movable bed experiments concerning the deformation of beach profile. He formulated the equilibrium beach profile and the rate of cross-shore sediment transport throughout the whole active beach based on the results as functions of the incident wave height, period, bed materials and so on. However, his model was not derived from the consideration of kinematics and dynamics of sediment movement and includes various empirical constants with dimensions.

(3) Prediction model of a plane beach deformation
(a) Prediction of the change in the location of a contour line caused by longshore sediment transport
i) Model based on One (Single)-line theory

The first modeling of the beach deformation caused by longshore sediment transport was carried out based on Eq. (3.69) by Pernard et al. (1956). If there is a strong relation between the change in the sectional area surrounded by the bottom and the water surface in a plane perpendicular to the shoreline (ΔA) and corresponding change in the location of the shoreline or any contour line (Δl), we can express ΔA as:

$$\Delta A = \alpha \Delta l \tag{3.72}$$

Equation (3.69) is written in the following form when we can neglect the time variation of the value α.

$$\frac{\partial l}{\partial t} = \frac{1}{1-\lambda} \frac{1}{\alpha} \frac{\partial Q_y}{\partial y} \tag{3.73}$$

In Eq. (3.73), the whole topographic change caused by the longshore gradient of the longshore sediment transport rate is represented by the change in the location of the shore line (or contour line). A prediction of beach deformation by this model is usually called the prediction based on the one (single)-line theory. The total longshore sediment transport rate in Eq. (3.73) is usually expressed by the Savage-type equation and Eq. (3.73) is transformed into a diffusion type equation by assuming the small wave breaking angle, a small curvature of shoreline and a small displacement of shoreline to obtain the shoreline profile analytically. Bakker (1968) developed this model and analyzed the shoreline

deformations around groins, river mouth and so on. The detailed commentaries for the one-line theory are given by Komar (1976), Hashimoto (1981) and so on.

Recently, prior to the construction of large coastal structures, we are obligated to predict the influence of them on the surrounding coast as part of the environmental assessment. Their long-term influences on the surrounding shoreline are usually predicted by the one-line theory. We also utilize the one-line theory to determine the proper plane arrangement for the shore protection works. Because the objective shorelines of these are usually arbitrary shapes and the boundary conditions are also complicated, it is difficult to calculate the change of the shoreline analytically. Accordingly, the calculations are carried out numerically by giving the longshore distribution of the total longshore sediment transport rate in Eq. (3.73).

Anyway, there still remain the following problems:

a) The physical meaning and quantitative evaluation of the value α in Eq. (3.73);
b) Assumptions of a small incident angle of breaking waves and a small curvature of the shoreline that result in the small deformation of the shoreline; and
c) Neglection of the change in the beach profile caused by the cross-shore sediment transport rate.

As for the second point at issue, Rea and Komar (1972) as well as Uda (1982) proposed the modified one-line theory that can cope with the arbitrary shoreline configuration whose radius of curvature is larger than the width of the breaker zone to the required degree.

Bakker et al. (1970) modified the one-line theory to solve the last problem where the location of two contour lines are predicted by taking into account the cross-shore sediment transport between the contours. The model is called the two-line theory and is expanded to the multi-line theory by Perline and Dean (1983). Figure 3.13 shows the outline of the two-line theory.
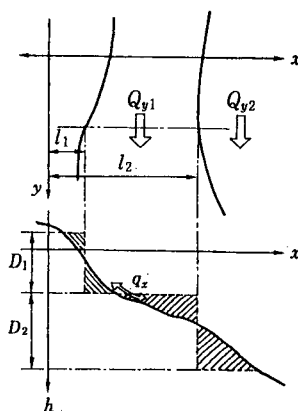
Fig. 3.13 Definition sketch of two-line theory

In the coordinate system shown in Fig. 3.13, time changes of the positions of two contour lines l_1 and l_2 are expressed by the following equations according to the two-line model.

$$\frac{\partial l_1}{\partial t} = \frac{1}{D_1(1-\lambda)}\frac{\partial Q_{y1}}{\partial y} + q_x$$

$$\frac{\partial l_2}{\partial t} = \frac{1}{D_2(1-\lambda)}\frac{\partial Q_{y2}}{\partial y} - q_x$$

(3.74)

where q_x is the cross-shore sediment transport rate across the contour line of the depth D_1. However, the estimation method of the cross-shore sediment transport rate is not established. Furthermore, any contour line must be a single-value function of the cross-shore distance.

In the following, the first point at issue is discussed in detail.

ii) Physical meaning and determination of α in the one-line theory

The value of α in Eq. (3.73) is usually explained as the representative height of the topographic change or the vertical scale for the topographic change that is equivalent to h_{cr}-h_0 in Fig. 3.9. On the other hand, from Eq. (3.72), the value of α is defined as

$$\alpha = \Delta A/\Delta l$$

(3.75)

According to this definition, the value of α depends on the depth of the contour line. Figure 3.14 illustrates the example of the dependency of α on the depth of the contour line. Open, closed and semi-closed circles are the relation between the change in the sectional area ΔA shown in Fig. 3.15 and the changes in the locations of the contour lines whose depths are 0cm (shoreline), $l_{0.0}$, -2.5cm (landward of the shore line), $l_{-2.5}$ and 5cm, $l_{5.0}$, respectively.
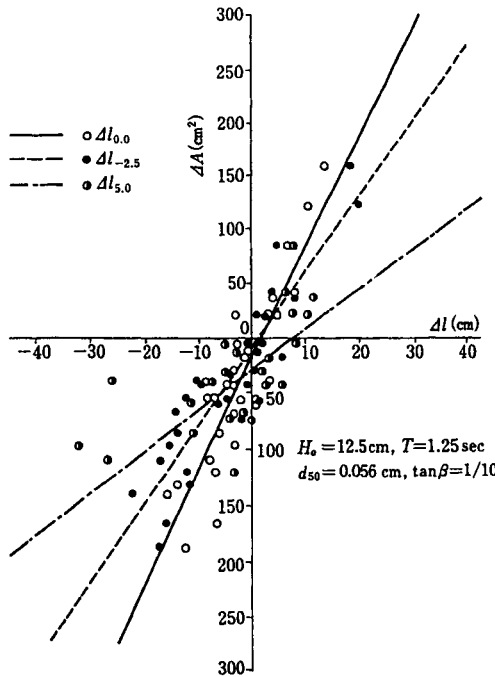
Fig. 3.14 Relation between change in sectional area and shift of shoreline location

$H_o = 12.5\,\text{cm}$, $T = 1.25\,\text{sec}$
$d_{50} = 0.056\,\text{cm}$, $\tan\beta = 1/10$

Accretion (▨) Erosion (☐)

$-\Delta h$ (cm)		Δh (cm)	
-4	$3.5\sim$	4	$3.5\sim$
-3	$2.5\sim3.5$	3	$2.5\sim3.5$
-2	$1.5\sim2.5$	2	$1.5\sim2.5$
-1	$0.5\sim1.5$	1	$0.5\sim1.5$
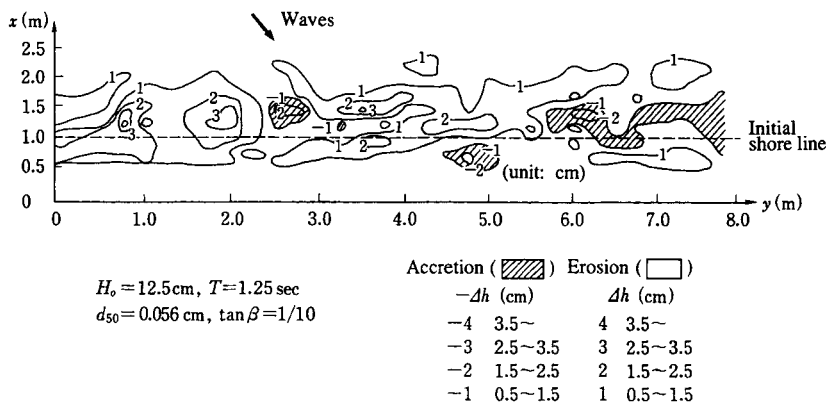
Fig. 3.15 Example of three-dimensional topographic change in wave basin

The result illustrated in Fig. 3.15 is obtained in the experiment on the 1/10 model beach in the wave basin. The experimental conditions are illustrated in the figure. Each change in the location of the contour line has a high correlation to the change in the sectional area. However, the value corresponding to each contour line is clearly different.

The change in the water depth Δh_y caused by the longshore sediment transport $q_y(x,y)$ during Δt is expressed by the following equation:

$$\Delta h_y / \Delta t = \left\{1/(1-\lambda)\right\} \Delta q_y(x,y)/\Delta y \tag{3.76}$$

We assume that the cross-shore distribution of the longshore sediment transport rate is expressed by the distribution function $f(x)$ and the strength $q_{y0}(y)$ as follows:

$$q_y(x,y) = q_{y0}(y)f(x) \tag{3.77}$$

The value of Δh_y becomes

$$\Delta h_y(x) = \frac{1}{1-\lambda}\frac{\Delta t}{\Delta y}\Delta q_{y0}f(x) \propto f(x) \tag{3.78}$$

While, it is natural to assume that the change in water depth Δh_{yk} at $x = x_k$ whose depth is h_k and the displacement of the contour line Δl_k at the depth $h = h_k$ are proportional (see Fig. 3.16).
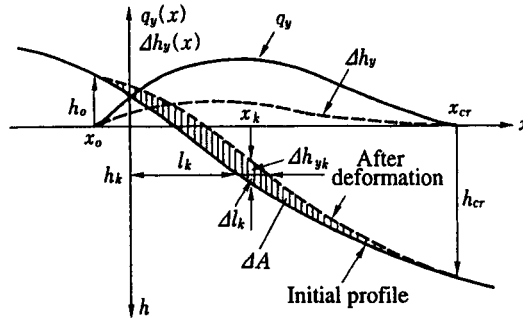
Fig. 3.16 Definition sketch of topographic change caused by local longshore sediment transport

Then

$$\alpha_h = \frac{\Delta A}{\Delta l_k} \propto \frac{\Delta A}{\Delta h_{yk}} \propto \frac{\Delta A}{f(x)} \tag{3.79}$$

This means that the inverse of α_h is proportional to the distribution function $f(x)$.

Figure 3.17 shows the cross-shore distributions of the inverse of α_h, i.e., $1/\alpha_h$, the cross-shore eigenfunction $e_1(x)$ corresponding to the maximum eigenvalue obtained from the empirical eigenfunction analysis of the topographic change shown in Fig. 3.15. In the figure, the local longshore sediment transport rate $q_y(x)$ evaluated by the flux model that will be mentioned later is also shown.
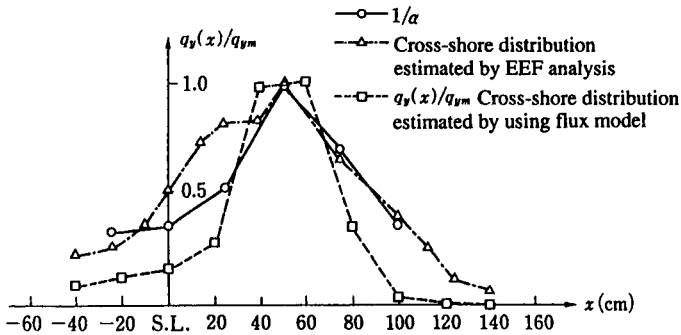
Fig. 3.17 Cross-shore distribution of local longshore sediment transport rate

All of them are normalized by their maximum value. Both distributions of $e_1(x)$ and $1/\alpha$ roughly coincide with the distribution of the local longshore sediment transport rate estimated from the flux model. This implies that we can use both values of $e_1(x)$ and $1/\alpha$ to estimate the cross-shore distribution of the local longshore sediment transport rate. Saito

et al. (1985) carried out the prediction of topographic change including the deformation of beach profile that came from the cross-shore distribution of the local longshore sediment transport rate estimated by using the value of $1/\alpha_h$.

However, in many cases, there is not enough data of the bottom profile to determine the value of α accurately. In such cases, α is usually determined as a sum of the critical water depth for sediment movement h_{cr} (e.g., Hallermeier 1983 and Sato and Tanaka 1965) and the run-up height on the beach h_0 (e.g., Savage 1959). These two values depend on the characteristics of incident waves. Therefore, we have to carefully determine the representative wave during the objective period for the prediction of shoreline deformation that will be used for evaluation of the value of α and the total longshore sediment transport rate. We have to examine the reproductivity of the typical topographic change of the objective beach through the calibration of the model.

iii) Representative wave in prediction of shoreline deformation based on one-line theory

Different representative waves should be used in the prediction of shoreline deformation according to the purpose and the objective period of the prediction. If we know the beach deformation including the seasonal change of the coast where there is an obvious seasonal change in the characteristics of the incident wave such as on the Japanese coast, we have to determine more than two representative waves for each season.

In principle, one-line theory is able to apply to the prediction of shoreline deformation irrespective of the duration of prediction provided that there is a clear relation between ΔA and Δl. However, there is a possibility for the cross-shore sediment transport to take place when the characteristics of an incident wave change significantly, which will result in the deformation of the beach profile. Furthermore, the shoreline deformation predicted by the one-line theory is not linear to the change in the wave direction and there is hysteresis in the shoreline deformation to the wave characteristics, especially to the wave direction. Therefore, the shoreline deformation predicted by using many representative waves does not always reproduce the actual shoreline deformation accurately.

iv) Other problems in the prediction of shoreline deformation by the one-line theory

One of the most remarkable feature of the one-line theory is to predict the change in the shoreline using only the longshore gradient of the total longshore sediment transport rate. The total longshore sediment transport rate on a natural beach is usually evaluated from wave height, water depth (or group velocity) and incident angle at wave breaking point like a Savage-type formula. Therefore, we can not apply such a formula to evaluate the total longshore sediment transport rate around the structure constructed within the surf zone, such as the short groin, the offshore detached breakwater and the sea dikes. The most popular way to cope with these situation is to use the trap rate of the longshore sediment transport rate based on the cross-shore distribution of the local longshore sediment transport rate. When we estimate the trap rate of the longshore sediment transport rate of the structure from the cross-shore distribution of the longshore sediment transport rate on a natural beach, there is a possibility for a large error to occur because the wave-induced current around the structure that becomes a sediment transporting flow is usually different from that on the natural beach. We should determine the magnitude of the total longshore sediment transport rate by integrating the cross-shore distribution of the local longshore sediment transport rate that is calculated properly. In Chapter 5, these procedures will be mentioned in detail. A full detail of the numerical procedure for solving Eq. (3.73) is given by Maruyama (1988).

(b) Direct prediction of change in water depth

The change in water depth is generally expressed by using the gradient of the horizontal local sediment transport rate as Eq. (3.64). Furthermore, Eq. (3.64) is rewritten as Eq. (3.67) when the time-averaged sediment concentration is in a steady state. All the proposed numerical models for directly predicting topographic change are based on these two equations.

i) Numerical model for predicting topographic change using local sediment transport rate in equilibrium state:

In this model the change in water depth is calculated from Eq. (3.67) using the local longshore and cross-shore sediment transport rates in an equilibrium state that have been formulated in various ways and will be mentioned in a later section. The spatial gradient of the bottom topography is assumed to be small and the time-averaged vertical distribution of sediment concentration is also assumed to be in a steady and equilibrium state.

Yamaguchi and Nishioka (1983) calculated topographic changes that took place around the groin and the offshore detached breakwater using the local sediment transport rate formulated based on the flux model (Eq. (3.97)). Sawaragi et al. (1985) also conducted numerical simulation of the topographic change around various coastal structures in the field using the local longshore sediment transport rate based on the flux model (Eq. (3.98)).

Watanabe et al. (1986) performed calculations of the bottom topography around the offshore detached breakwater using the local longshore sediment transport rate formulated based on the power model where the sediment transport caused by both waves and wave-induced current are taken into account. The net sediment transport rate caused by waves decreases in the beach deformation process. They cope with this effect by using the following equation of continuity of sediment transport:

$$\frac{\partial h}{\partial t} = \frac{1}{1-\lambda}\left\{\frac{\partial}{\partial x}\left(q_x + \gamma_s|q_x|\frac{\partial h}{\partial x}\right) + \frac{\partial}{\partial y}\left(q_y + \gamma_s|q_y|\frac{\partial h}{\partial y}\right)\right\} \qquad (3.80)$$

here, γ_s is the empirical constant of a positive value.

ii) Numerical model for the prediction of topographic change using vertical sediment flux as a solution to the advection-diffusion equation

The vertical distributions of suspended sediment concentration around the navigation channel where the water depth changes abruptly, a river mouth with the discharged sediment and so on are often in the non-equilibrium state where the upward and the downward sediment flux are not in balance. Furthermore, even on a natural beach we have to take into account the non-equilibrium property of sediment concentration in the transporting and settling process of suspended sediment near the wave breaking point. To cope with such a non-equilibrium property of sediment movement, we have to evaluate the vertical sediment flux at the bottom by solving the advection-diffusion equation.

Sawaragi et al. (1985) and Deguchi and Sawaragi (1988) evaluated the vertical sediment flux at the bottom Δq_s (Eq. (3.82)) by solving the advection-dispersion equation of vertically and temporally averaged sediment concentration $\hat{c}$ (Eq. (3.82)) to simulate topographic change around the river mouth with discharged sediment.

$$\hat{C}(x,y,t) = \overline{\int_{-h}^{\eta} C(x,y,z,t)dz} \Big/ (h + \overline{\eta}) \tag{3.81}$$

$$\left.\begin{array}{l} \dfrac{\partial \hat{C}}{\partial t} + \dfrac{\partial \hat{C}u_s}{\partial x} + \dfrac{\partial \hat{C}v_s}{\partial y} = \dfrac{\partial}{\partial x}\left(\varepsilon_{sx}\dfrac{\partial \hat{C}}{\partial x}\right) + \dfrac{\partial}{\partial y}\left(\varepsilon_{sy}\dfrac{\partial \hat{C}}{\partial y}\right) + \Delta q_s \\[4mm] \Delta q_s = -\left\{(1-r)C_0 W_f\left(1 - u^*/W_f\right) + \hat{C}W_f\right\}\Big/(h + \overline{\eta}) \end{array}\right\} \tag{3.82}$$

where C_0 is the reference concentration and W_f is the settling velocity of the sediment in still water and ε_{sx} and ε_{sy} are the horizontal dispersion coefficients of suspended sediment in x and y directions that are expressed by using the depth averaged mean velocity U, V and the water depth h as follows:

$$\left(\varepsilon_{sx}, \varepsilon_{sy}\right) = \left(0.15Uh, \ 0.15Vh\right) \tag{3.83}$$

The first and the second terms in { } of the right hand side of the expression of Δq_s are the up-ward and down-ward flux, respectively.

According to Eq. (3.81), the settling flux is apt to be underestimated because of the use of the vertically averaged sediment concentration. To avoid this point at issue, Irie et al. (1985) proposed the 3-layer model where the sediment concentration is evaluated after being vertically divided into three layers. Although some formulations of the vertical profile of non-equilibrium suspended sediment have also been carried out, they are still far from the universal one.

We have to solve a three-dimensional advection-diffusion equation with respect to suspended sediment concentration as a function of both horizontal and vertical locations to strictly take the non-equilibrium property of suspended sediment into account. However, it requires much CPU-time and computer capacity to obtain the numerical solution to the three-dimensional advection-diffusion equation. Nadaoka et al. (1988) proposed a procedure to solve the three-dimensional advection-diffusion equation by assuming an exponential vertical distribution of suspended sediment concentration. They carried out numerical calculation of the topographic change by both their method and the existing model using the local sediment transport rate in equilibrium state and pointed out the importance of the non-equilibrium property of sediment transport.

Komatsu et al. (1984) and Kanayama et al. (1988) conducted a detailed analysis about the highly accurate numerical procedure (a sprit operator approach) for solving the three-dimensional advection-diffusion equation. Sawaragi et al. (1990) applied this approach to the numerical simulation of the shoaling process of a navigation channel.

In the above mentioned evaluation of the non-equilibrium property of suspended sediment, some problems such as the estimation of the diffusion coefficient and reference concentration are left unsolved. The effect of the non-equilibrium behavior of a bed load should also be investigated in detail in the future.

Table 3.3 shows the summary of the numerical model for predicting topographic change together with the sediment transport rate and quantities that have to be given for the actual prediction.

Table 3.3 Sediment transport rate and hydraulic quantities required in the prediction model

Objective topographic change	Required sediment transport rate	Required hydraulic quantities	
Deformation of beach profile	$q_x(x,t)$	$H(x,t), h(x,t), u(x,z,t),...$	
Shoreline change	$Q_y(y,t)$	$h_b(y,t), \theta_b(y,t), H_b(y,t)$	One-line theory
Shoreline change+deformation of beach profile	$q_y(x,y,t)$	$H(x,y,t), \theta(x,y,t), U(x,y,t), V(x,y,t), \eta(x,y,t),$	Modified one-line theory
	$\Delta Q_{yi}, (i=1, N)$ $q_{xi}, (i-1, N-1)$	$h_b(y,t), \theta_b(y,t), H_b(y,t)$ $H(x,y,t), \eta(x,y,t),...$	Mutlti-line theory
Topographic change caused by local sediment transport due to mean current	$q_x(x,y,t), q_y(x,y,t)$	$H(x,y,t), \theta(x,y,t), h(x,y,t), U(x,y,t), V(x,y,t)$	
Topographic change caused by local sediment transport due to waves and mean current	$q_x(x,y,t), q_y(x,y,t)$	$H(x,y,t), \theta(x,y,t), h(x,y,t), U(x,y,t), V(x,y,t)$	

3.4 Formulation of Sediment Transport Rate

3.4.1 Modes of sediment movement and their appearance region

Here, the mode of sediment movement that may take place in each region of the beach profile is explained and then the formulation of sediment transport rate is reviewed. The mode of sediment movement in the coast is usually divided into bed load, suspended load and sheet flow. Figure 3.18 shows these modes of sediment movement caused by wave on each section of the beach profile schematically.
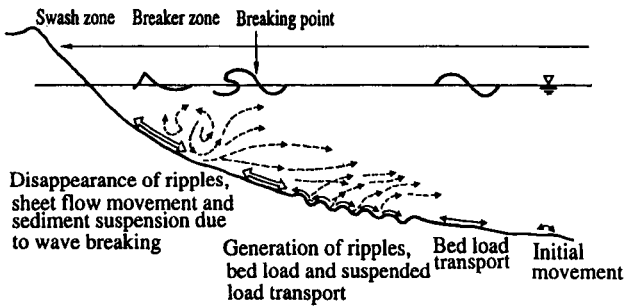
Fig. 3.18 Sediment movement and mode of sediment transport on beach

(1) Critical condition for sediment movement

The water particle velocity at the bottom due to waves increases as water depth becomes shallow. The bottom shear stress also increases simultaneously. When a resisting force of the sand particle on the bottom becomes smaller than a wave force on it, the sand begins

to move. The depth of this point on the beach is called a critical depth for sediment movement and the critical velocity is defined as the water particle velocity at this critical depth.

Various critical depths and a critical velocity for sediment movement are defined by many researchers from various points of views. Among them the following critical depths are representatives:
1) Critical depth for the movement of projected sand on the bottom (initial movement),
2) Critical depth for the entire surface sand particle to move,
3) Critical depth where surface sand is moved toward the wave direction,
4) Critical depth of perfect movement where evident changes in water depth occur.
These critical conditions for sediment movement become shallow from 1) to 4).

There are two methods to analyze the critical condition for initial sediment movement theoretically (Tsuchiya 1986). One is the static analysis method and another is the dynamic analysis method. In the static analysis, the critical condition is determined from the balance between the resisting force of projected sand on the bottom and the wave force on it or the balance of the resisting shear of the bed surface and bottom shear stress due to waves. Anyway, some problems are left to be solved concerning the depth to decide the wave force acting on the particle and evaluation of the effective shear stress that is directly exerted on the bottom.

Various empirical but practical formulas have also been proposed in addition to these theoretical analyses. The representative of them applies a critical condition in a uni-directional flow by using the Shields number ψ that indicates the ratio between the static resistance force of sand on the bottom and the drag force due to waves acting on it.

$$\psi = u^{*2}\Big/\big\{(\rho_s/\rho - 1)gd_{50}\big\}$$

(3.85)

where u^* is the shear velocity, ρ_s is the density of bed material and d_{50} is the mean grain size.

Madsen and Grant (1976) reanalyzed the existing experimental results concerning the critical condition for the sediment movement. Figure 3.19 shows the result. The vertical axis of the figure is the critical Shields number and the horizontal axis is the sediment Reynolds number whose representative velocity is $\{(\rho_s/\sigma-1)gd_{50}\}^{1/2}$. The critical condition for sediment movement in uni-directional flow is shown by a full line and the experimental results are shown by vertical sticks the length of which indicates the variance. Although the experimental critical values are slightly larger than those of the uni-directional flow, they are expressed by the two parameters shown in Fig. 3.19.

On the other hand, Tsuchiya (1986) proposed the following critical condition for sediment movement by using the parameter $D^*(= \{(\sigma_s/\sigma-1)g/\nu^2\}^{1/2}d_{50}\})$ introduced by Iwagaki based on the results of experiments and dynamic analysis.

$$\psi_c = \begin{cases} 0.2 & :D_* \le 1 \\ 0.2D_*^{-2/3} & :1 < D_* \le 20 \\ 0.01D_*^{1/2} & :20 < D_* \le 125 \\ 0.05 & :125 < D_* \end{cases}$$

(3.86)
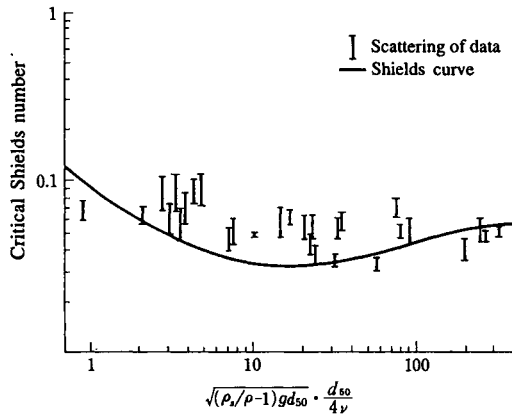
Fig. 3.19   Critical Shields number as a function of Reynolds number

(2) Modes of sediment movement and their appearance region

When a shearing force larger than the critical condition for sediment movement acts on the sea bed a sediment movement of traction mode (bed load transport) takes place. This mode of sediment movement occurs within a thickness of a few diameters of the grain size at the maximum. As the shear stress increases further, sand ripples are formed on the bed. Suspended sediment occurs by the advection of the trapped sediment in the vortex formed periodically around the sand ripple. In the shallow water region where incident waves break, a great deal of sediment is brought into suspension by the turbulence caused by breaking waves. Breaking waves of the plunging type suspend more sediment than breaking waves of the spilling type do.

On the rippled bed, bed load sediment becomes a boundary condition of the suspended sediment and diffusion plays an important role. On the other hand, sediment near the wave breaking point is directly lifted up by the turbulent fluid motion and advection plays an important role. Accordingly, at some time, a time averaged concentration of suspended sediment in the upper layer becomes larger than that in the lower layer (Kana 1977 and Deguchi and Sawaragi 1984).

When the bottom shear stress increases beyond a certain limit, ripples disappear and the so-called sheet flow in which sediment in high concentration is transported within a thin layer appears. Because a great deal of sand particles are transported in the thin layer in this range, fluid turbulence near the bottom is repressed and any systematic turbulence, such as the vortex on the ripple does not occur there. Accordingly, any obvious suspension of sediment does not occur in the upper region. The momentum for keeping sediment in motion is transferred by the violent collision between sand grains. A detailed explanation of sediment transport in the sheet flow is given by Sawamoto (1985) and Shibayama (1988).

In the swash zone, fluid motion becomes entirely different from that in the shallow water region and sand movement also differs from the other part on the beach. Ogawa and Shuto (1982) and Sunamura (1984) investigated sediment transport in such a region through field measurements and two-dimensional experiments.

The critical conditions for the occurrence of suspension or sheet flow have been investigated based on the experimental results. It is said that suspension begins to appear

when the value of $u*/W_f$ is greater than 1.0-1.2 (Engelund 1965 and Sawaragi and Deguchi 1978(b)) and sheet flow appears when the value of the Shields number is greater than 0.4-1.5 (Nielsen 1979, Shibayama and Horikawa 1982 and Sakakiyama et al. 1984). The critical condition for the appearance of the sheet flow varies widely depending on the researchers. We have to carry out a detailed survey for these values through field measurements.

3.4.2 Modeling of sediment transport

The sediment transport rate has been formulated in various ways. Some of them are derived through the modeling of the transport process and others are formulated purely empirically. The model uses in the formulation of the sediment transport rate are roughly classified into a power model, a stochastic model and a flux model.

(1) Power model

Bagnold (1956) carried out detailed experiments and a theoretical analysis regarding the characteristic of shear resistance of sand particles and their motions in a uni-directional flow. He proposed the following expression for the rate of sediment transport considering that a part of fluid energy lost by the bottom friction D_{loss} is used to transport bottom material.

$$i = e D_{loss} / u_s \tag{3.87}$$

where i is the immersed weight sediment transport rate, e is the transport efficiency and u_s is the transporting velocity. This model is very simple and clear. If we are able to precisely estimate the efficiency and dissipation rate of fluid energy, we can apply this model to both suspended and bed load sediment transport. As will be mentioned afterward, many sediment transport rate formulas have been proposed on the basis of this model.

(2) Stochastic model

Einstein (1950) expressed the transport rate of a bed load in the uni-directional flow by using the probability of transition from rest to move of bed material (pick-up rate) and the step length that is also a probabilistic variable. This model is effective to estimate the sediment transport rate of the bed load where only the sediment on the surface layer moves.

(3) Flux model

As shown by Eq. (3.66), the sediment transport rate should be expressed as flux. The volumetric sediment transport rate q is expressed as the product of the sediment concentration C and transporting velocity u_s as follows:

$$q = C u_s \tag{3.88}$$

This is the most universal expression for the evaluation of the sediment transport rate, provided that we can estimate the concentration and the transporting velocity of sediment including the bed load precisely.

The flux model is effective when the suspended sediment transport is predominant and the power model is effective to express the bed load sediment transport. However, both models include an empirical constant that should be decided based on experiments or field

measurements. We have to determine the values of these constants by considering the kinematics of the sediment transport phenomena.

Recently many researchers have been carrying out analyses on the motion of sand grains near the bottom from this viewpoint. For example, Kobayashi (1982), Hino et al. (1982) and Kawata (1989) analyzed the motion of sand grain(s) on the bottom. Deguchi and Sawaragi (1984) and Nadaoka and Yagi (1990) calculated the motion of the bed layer assuming that the sand layer is a Newtonian fluid with a hypothetical viscosity. Asano (1990) analyzed and calculated the motions of fluid and sediment in it by using a two-phase flow theory.

The local sediment transport rate that we have to evaluate for the prediction of the topographic change as shown in Table 3.3 consists of two parts. One is the purely wave induced sediment transport and the other is the sediment transport by the mean current. The deformation of a beach profile took place in a two-dimensional wave tank is caused by the former type of sediment transport. A large part of the so-called cross-shore sediment transport belongs to this category. The longshore sediment transport transported by the longshore current and the offshore sediment transport due to the rip current are the representatives of latter. Katori (1988) gave a detailed commentary on the existing formulas for evaluating the sediment transport rate.

In the following, the results of the previous studies concerning the evaluation of the sediment transport rate are reviewed. As was mentioned before, the wave-induced cross-shore sediment transport, e.g., the sediment transport on the sloping beach in the two-dimensional wave tank decreases in the beach deformation process. Therefore, in the following review of the cross-shore sediment transport, some results obtained on the horizontal bottom are shown. As for the longshore sediment transport, the representative results obtained under the steady and equilibrium condition are reviewed.

3.4.3 Cross-shore sediment transport rate

The most widely referred sediment transport rate formula for the cross-shore sediment transport rate averaged over a half wave period q_x is the one proposed by Madsen and Grant (1976). They proposed the following expression for q_x based on the existing experimental results:

$$q_x / \left(W_f d_{50} \right) = 12.5 \psi^3 \tag{3.89}$$

This expression gives an average sediment transport rate for a wide range of a Shields number ($0.04 < \psi < 0.6$).

Sawamoto (1985) showed that the following equation gives a more precise estimation of the value of q_x including sheet flow:

$$
\begin{aligned}
q_x &= 2.2 \left(u^* / W_f \right)^3 \\
&= 2.2 \left[W_f / \left\{ (\rho_s / \rho - 1) g d_{50} \right\} \right]^{-3} \psi^{1.5}
\end{aligned}
\tag{3.90}
$$

Watanabe et al. (1980) proposed the net cross-shore sediment transport formula on the sloping beach based on the power model. Equation (3.91) is the proposed formulation by Watanabe et al.

$$q_{net} = \alpha' \left(\psi - \psi_c \right) \psi^{0.5} \tag{3.91}$$

where ψ_c is the critical Shields number for sediment movement and α' is the empirical constant. According to Watanabe et al., the value of α' is 7 in the region of $0.08 < \psi < 0.5$ and Kajima et al. obtained the value of 3 for α' in the region of $0.2 < \psi < 1.3$ using a two-dimensional model beach experiment in a large wave tank. However, as has already been mentioned, the net sediment transport rate evaluated from Eq. (3.91) depends on a wave running time.

Bowen (1980) expressed the suspended and bed load sediment transport rate as a function of time in the following way on the basis of the power model:

$$i_{sx} = e_s C_d \rho |u| u^3 / \left(W_f - u \tan \beta \right) \tag{3.92}$$

$$i_{bx} = e_b C_d \rho u^3 / \left(\tan \phi - u \tan \beta / |u| \right) \tag{3.93}$$

where i_{sx} and i_{bx} are the immersed weight suspended and bed load sediment transport rate, ε_s and ε_b are the transport efficiencies of suspended and bed load, C_d is the drag coefficient, $\tan \beta$ is the bottom slope and ϕ is the angle of repose of the bed material.

He investigated the effects of mean current, water particle velocity due to subharmonic wave motion and the velocity of the turbulent component in wave motion on the net sediment transport rate based on Eqs. (3.92) and (3.93).

Kawata (1990) solved an equation of motion of a sand particle on the sloping bottom and derived the net sediment transport rate in equilibrium state by applying the conservation of momentum of sand grains. He obtained the expression for evaluating sediment transport on a sloping beach.

3.4.4 Longshore sediment transport rate

Various formulas for estimating the longshore sediment transport rate have been proposed. Many of them are based on the power model or the flux model.

(1) Longshore sediment transport rate based on the power model

Komar (1977) proposed the following expression for the local longshore sediment transport rate using the bottom shear stress under waves and current derived by Bijker:

$$q_y = \alpha_1 \left(C_f V^2 + 0.5 f_w \hat{u}_{bp}^{\,2} \right) \tag{3.94}$$

where C_f and f_w are the friction factors due to mean current (longshore current) of the velocity V and waves and α_1 is the constant. The value of constant α_1 is determined by equating the integrated value of Eq. (3.94) in the cross-shore direction and the total longshore sediment transport rate calculated from the formula proposed by Komar and Inman (1970) that will be mentioned later.

Walton and Chiu (1979) applied the power model of Bagnold to the longshore sediment transport rates and derived the following expression for the suspended and bed load transport rate:

$$q_{by} = \frac{e_b \sin 2\theta_b}{2\tan\phi} \hat{V}^2 \hat{X}^{1/2} \left\{ \frac{25\pi}{16} \frac{\gamma(1-K)\tan\beta}{f_w} \right\} \frac{P_l}{x_b} \frac{1}{(\rho_s - \rho)g(1-\lambda)}$$

$$q_{sy} = \frac{e_s \sqrt{gD_b}\cos\theta_b}{W_f} \hat{V}\hat{X}^{3/2} \left\{ \frac{25\pi}{16} \frac{\gamma(1-K)\tan\beta}{f_w} \right\} \frac{P_l}{x_b} \frac{1}{(\rho_s - \rho)g(1-\lambda)} \qquad (3.95)$$

where $\hat{V} (= V/V_b)$ is the nondimensional velocity of longshore current normalized by the longshore current velocity at the breaking point without the lateral mixing V_b, $X (= x/x_b)$ is the nondimensional distance from the mean shoreline normalized by the width of breaker zone x_b, K is the quantity concerning the gradient of the mean water depth and P_l is the breaking wave energy flux in the longshore direction. The values of V_b, K and P_l are expressed as

$$\left. \begin{array}{l} V_b = (5\pi/16)(\gamma/f_w)(1-K)\tan\beta\sin 2\theta_b \\[2mm] K = \gamma^2 \left(3 - 2\sin^2\theta_b\right) \big/ \left\{ 8 + \gamma^2\left(3 - 2\sin^2\theta_b\right) \right\} \\[2mm] P_l = (\rho g/16)H_b{}^2 \sqrt{gD_b} \sin 2\theta_b \end{array} \right\} \qquad (3.96)$$

where γ_b is the ratio of wave height and water depth at the breaking point, D_b is the total water depth at the wave breaking point and θ_b is the breaking wave angle.

Watanabe et al. (1980) derived the sediment transport rate formula by using the effective shear force that is defined by the excess shear stress due to waves and current from the critical shear stress based on the power model. The following expression is the longshore component of the sediment transport rate:

$$q_y = \alpha_2 F_c V \qquad \text{: transport rate by mean current}$$

$$qy = \alpha_3 F_w u^* \sin\theta \qquad \text{: transport rate by wave orbital motion} \qquad (3.97)$$

where $F_c = A(f_w V^2 + u^{*2} - u^*{}_{cr}{}^2)/g$, $u^{*2} = f_w \hat{u}_{bp}{}^2$, α_2 and α_3 are the empirical constants($= 1$ and -5), $u^*{}_{cr}$ is the critical shear velocity $F_w = (u^{*2} - u^*{}_{cr}{}^2)(1+\alpha'|r|)/g$, α' is the empirical constant and r is the local second derivative of the beach profile.

(2) Longshore sediment transport rate based on flux model

Tsuchiya and Yasuda (1978) expressed the local longshore sediment transport rate using the time and depth averaged sediment concentration C and the longshore current velocity.

$$q_y = CVD$$

$$C = 0.2(\rho_s/\rho)(1 - \psi_c/\psi) \qquad (3.98)$$

where ψ_c is the critical Shields number and D is the total depth.

The author et al. proposed formulas to estimate the local longshore sediment transport rate by the bed load and suspended load separately based on the flux model. The migration speed of the bed load was estimated by solving the motion of the bed load layer (Deguchi and Sawaragi 1984) and the concentration of the bed load was determined from the bed load transport rate proposed by Sleath (1978). Concentration of suspended sediment was determined using the reference concentration C_0 and diffusion coefficient K_z obtained from the experiments.

$$\left.\begin{array}{l} q_{by} = 47\pi\sigma d_{50}^2 (\psi_m - \psi_c)^{3/2} (V/\hat{u}_{bp}) \\ q_{sy} = \int CVdz \end{array}\right\}$$

$$= \begin{cases} C_0(K_z/W_f)V & : \text{outside breaker zone} \\ C_0 \min\{K_z/W_f, D\}V & : \text{in breaker zone} \end{cases}$$

$$(3.99)$$

where ψ_m is the Shields number defined as $(f_w/2)F_b/\{(\sigma_s/\sigma-1)gd_{50}\}$ and $\min\{\ ,\ \}$ means the minimum value of the quantities in $\{\ \}$. The value of F_b, the diffusion coefficient and the reference concentration are given by the following equations:

$$F_b = \hat{u}_{bp}^2/2 + (2/\pi)\hat{u}_{bp}V\sin\theta + V^2/4 \qquad (3.100)$$

$$K_z/W_f = 0.021\exp\left\{0.5(f_w F_b^2/2)^{1/2}\right\} \quad : cgs\ unit \qquad (3.101)$$

$$C_0 = 0.347\left\{\frac{0.688\hat{u}_{bp}^2}{1.13(\rho_s/\rho-1)gW_fT}\right\} \qquad (3.102)$$

(3) Other formulation

Bijker (1971) proposed the following local longshore sediment transport rate for bed load and suspended load based on his own formulation of the bottom shear stress due to waves and current:

$$q_{by} = 5d_{50}g^{1/2}\frac{V}{C_e}\exp\left[\frac{-0.27(\rho_s/\rho-1)gd_{50}}{\mu_c\tau_{cu}\left\{1+(\xi a_b/V)^2\right\}}\right] \quad : MKS\ unit \qquad (3.103)$$

$$q_{sy} = 1.83q_{by}\left\{I_1\log(33D/k_s) + I_2\right\}$$

where C_e is the Chezy coefficient ($= 18\log(12R/k_s)$, R:hydraulic radius), $\xi = C_e(f_w/2g)$, $\tau_{cu} = \rho g(V/C_e)^2$ and $\mu_c = \{\log(12R/k_s)/\log(12R/3d_{90})\}^{3/2}$. I_1 and I_2 that appear in the expression of suspended sediment transport rate are given by the following integration:

$$I_1 = \frac{0.216(k_s/D)^{z^*-1}}{(1-k_s/D)^{z^*}} \int_{k_s/D}^1 \left(\frac{1-y}{y}\right)^{z^*} \mathrm{d}y$$

$$I_2 = \frac{0.216(k_s/D)^{z^*-1}}{(1-k_s/D)^{z^*}} \int_{k_s/D}^1 \left(\frac{1-y}{y}\right)^{z^*} \log y\, \mathrm{d}y$$

$$Z^* = W_f \Big/ \left[\kappa\sqrt{\rho g}\,(V/C_e)\left\{1+\left(\xi\hat{u}_{bp}\right)^2 \big/ 2\right\}^{1/2} \right]$$

(4) Total longshore sediment transport rate

Total longshore sediment transport rate should be calculated by integrating the local longshore sediment transport rate in the cross-shore direction. To do so, we have to estimate many hydraulic quantities for the estimation of local longshore sediment transport rate. We are not always required to evaluate the local longshore sediment transport rate when we carry out the prediction of topographic change that will take place for a long time. In such cases, it is usually sufficient to evaluate the total longshore sediment transport rate as a function of less variables. A great number of formulations of the total longshore sediment transport rate have been proposed. Among them, two representative formulas are introduced here.

Komar et al. (1970) measured longshore sediment transport rate by using tracers at two coasts of different characteristics. Based on the measured results, they proposed the following formula for evaluating the volumetric total longshore sediment transport rate Q_y:

$$Q_y = 0.77 P_l \Big/ \left\{ (\rho_s/\rho - 1)g(1-\lambda) \right\} \tag{3.104}$$

In their original formulation, Q_y is expressed as the immersed transport rate I_y. Equation (3.104) is rewritten using the relation $I_y = Q_y\{(\sigma_s/\sigma-1)g(1-\lambda)\}$. A value 0.77 in Eq. (3.104) is a nondimensional empirical constant and P_l is given by Eq. (3.96).

The empirical formula that has been used for a long time is as follows:

$$Q_y = a_3 P_l \tag{3.105}$$

The value of constant α_3 varies from place to place.

Iwagaki and Sawaragi (1962) applied the Kalinsk-Brown type formula in the uni-directional flow to the longshore sediment transport rate and proposed the following expression:

$$Q_y = 31.7g^{1/2}\left\{\frac{1}{16(\rho_s/\rho-1)}\right\}^{3/2} d_{50}^{-1/2}\left(\tan\beta\sin 2\theta_b\right)^{4/3}$$

$$* \cos\theta_b \frac{1}{(2\pi)^{2/3}}\left(\frac{H_0}{L_0}\right)^{2/3}\left(\frac{L_b H_b^2}{L_0}\right)^{3/2} \quad : \text{MKS unit} \tag{3.106}$$

where L_0 is the wavelength in deepwater and L_b is the wavelength at the wave breaking point.

A characteristic of this expression is that the effect of the bottom slope, sediment size and characteristics of the incident wave on the total longshore sediment transport rate are taken into account.

It is worthwhile to compare the evaluated results from the various formula listed above under the same conditions. Figure 3.20 illustrates the example of such a comparison. The total longshore sediment transport rate shown in Fig. 3.20 was calculated on the long straight beach of the uniform slope ($\tan\beta = 1/10$-$1/50$) under the conditions of deepwater wave height 1m, deepwater wave steepness 0.01-0.08 and incident wave angle 10°-40°. The mean size of the bed material is also changed between 0.01cm-0.5cm.
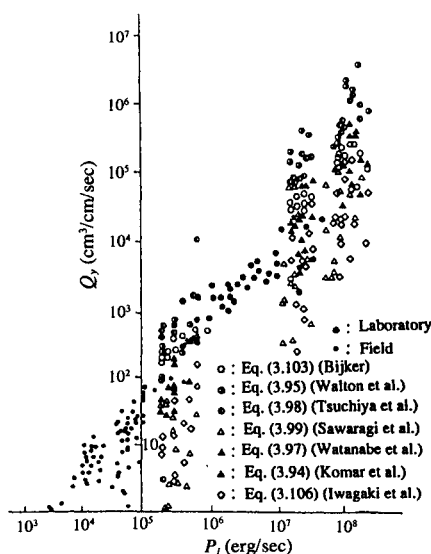
Fig. 3.20 Comparison of calculated total longshore sediment transport rate

Wave transformation on the beach was simulated numerically by solving the difference equation of conservation of wave energy at the grid point. The wave-induced current (longshore current) was also obtained numerically by solving the time and depth averaged momentum and mass flux conservation using the ADI method. In the numerical simulations, wave transformation and wave-induced current were calculated iteractively to take the interaction into account. The details of the procedure will be mentioned in the following section.

In Fig. 3.20, the total longshore sediment transport rate Q_y, except for the values of Q_y of Eqs. (3.104) and (3.106), is evaluated by integrating the local longshore sediment transport rate in the cross-shore direction. A horizontal axis of the figure is a value of P_l calculated from Eq. (3.96). The difference between the maximum and the minimum estimations for the same value of P_l is quite large. Therefore, when we apply the various formulas listed above, sufficient attention must be paid as to the applicability condition of each formula.

3.4.5 Reference concentration as a boundary condition for suspended sediment

Here, the reference concentration of suspended sediment that is required to determine the vertical sediment flux in the prediction of topographic change under non-equilibrium conditions and to fix the vertical profile of time averaged suspended sediment concentration is explained. Extensive research has already been carried out concerning the reference concentration of suspended sediment and some expressions for estimating the reference concentration have already been proposed.

Fredsøe (1985) expressed the reference concentration at the bottom (at the crest level on the rippled bottom) as a function of the Shields number on the basis of the experimental results. The proposed relation between the reference concentration C_0 and the Shields number is shown by a solid line in Fig. 3.21.
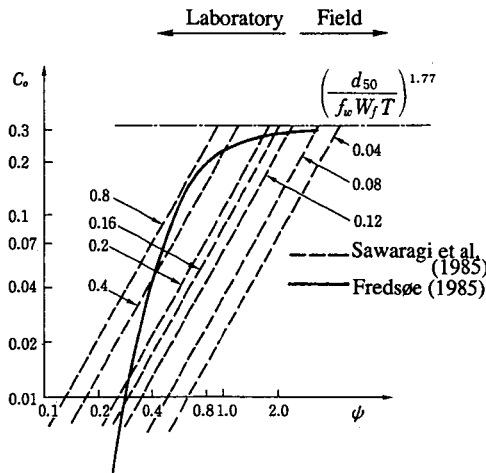
Fig. 3.21   Relation between reference concentration and Shields number

Sawaragi et al. (1985) also proposed an expression for the reference concentration at the same reference level as defined by Fredsoe in the form of Eq. (3.102). We can rewrite Eq. (3.102) using the Shields number in the following form:

$$C_0 = 0.49 \psi^{1.77} \left\{ d_{50} / \left(W_f T f_w \right) \right\}^{1.77}$$

$$(3.107)$$

Values of C_0 for various values of $\{d_{50}/(W_f T f_w)\}$ are also shown by broken lines in Fig. 3.21.

According to the expression of Fredsøe, the value of C_0 is uniquely determined by the Shields number. However, the expression of Sawaragi et al. indicates that the reference concentration depends on the Shields number and the value of $\{d_{50}/(W_f T f_w)\}$. In the field, the size of bottom material is relatively small and the period of incident waves is long. Therefore, the value of the latter parameter becomes small compared with that in the laboratories. It is generally recognized that the suspended sediment concentration in the field is somewhat smaller than that measured in the laboratory. The expression of Sawaragi et al. coincides well with this recognition.

Skafel and Krishnappan (1984) also proposed Eq. (3.108) based on the assumption that the thickness of the bed load layer is 3 times larger than the mean grain size and their expression for the bed load transport rate q_b.

$$C_0 = q_b / \left(3 d_{50} \hat{u}_{bp}\right) = 3.33 \psi^2 \left(f_w / 2\right)^{1/2} \tag{3.108}$$

3.5 Prediction of Wave Transformation and Wave-induced Current

Various information is required in the prediction of beach deformation depending on the type of prediction model. We can predict changes in the shoreline position from the longshore distribution of the total longshore sediment transport rate that is evaluated from the wave conditions at the wave breaking point. We can also calculate the change in water depth from the gradient of local sediment transport rate or the vertical sediment flux at the bottom for predicting nonequilibrium suspended sediment flux. To evaluate these quantities, we have to know the local condition of waves and mean currents such as wave-induced currents, tidal currents and so on.

Required quantities for each prediction model were listed in Table 3.3. In this section some representative numerical procedures for predicting wave transformation and wave-induced currents are reviewed.

3.5.1 Prediction of wave transformation

Wave transformation is usually calculated based on the concept of conservation of wave energy (wave action) or momentum.

(1) Wave transformation based on conservation of wave energy (or wave action)

As was already shown in Chapter 1, when we neglect the mass transport due to waves, wave energy conservation is expressed as follows:

$$\frac{\partial E}{\partial t} + \frac{\partial \{E(c_g \cos\theta + U)\}}{\partial x} + \frac{\partial \{E(c_g \sin\theta + V)\}}{\partial y}$$
$$+ S_{xx} \frac{\partial U}{\partial x} + S_{xy} \frac{\partial V}{\partial x} + S_{yl} \frac{\partial U}{\partial y} + S_{yy} \frac{\partial V}{\partial y} = -D_i \tag{3.109}$$

where $E = \rho g H^2 / 8$, θ is the wave direction, c_g is the group velocity, D_i is the energy dissipation rate, S_{xx}, S_{xy}, S_{yx}, S_{yy} are the radiation stress and $U = (U, V)$ is the depth averaged mean current velocity vector.

A wave number vector $k(= k\cos\theta, k\sin\theta)$ and the wave direction θ are evaluated from the conservation of wave number and the irrotational condition of the wave number

$$\frac{\partial k}{\partial t} + \nabla(\sigma(k) + k \cdot U) = 0 \tag{3.110}$$

$$\nabla \times k = 0 \tag{3.111}$$

In the steady state, Eq. (3.110) is rewritten as

$$\sigma_0 = \sigma + k_x U + k_y V, \quad \sigma^2 = gk \tanh kh \tag{3.112}$$

where $\sigma_0 (= 2\pi/T)$ is the angular frequency in still water.

On the other hand, the conservation of wave action E/σ is expressed as follows (Bretherton 1969).

$$\frac{\partial}{\partial t}(E/\sigma) + \nabla\left\{(U + c_g)(E/\sigma)\right\} = 0 \tag{3.113}$$

There are two numerical procedures for evaluating wave transformation from these equations. One is the so-called wave ray method where Eq. (3.109) (or Eq. (3.113)) is solved along the characteristic curve (wave ray) determined by the following equation:

$$\frac{dX}{dt} = Cg \cos\theta + U, \quad \frac{dY}{dt} = Cg \sin\theta + V \tag{3.114}$$

The wave direction θ and the wave number k (group velocity c_g) are evaluated from Eqs. (3.111) and (3.112). In another method, Eq. (3.109) (or Eq. (3.113)) is solved on grid points that cover the whole objective region to avoid the problem caused by ray crossing.

We often use a breaker index proposed by Goda (1975) to determine the wave breaking point. Various formulations have been proposed for estimating the energy dissipation rate. Some of them are listed in Table 3.4.

Table 3.4 Example of expression of energy dissipation rate

	Expression of dissipation	Model
Battjes (1979)	$\dfrac{B}{4\gamma_0^3}\dfrac{\rho g H^2 \sqrt{gD}}{L}\left(\dfrac{H}{D}\right)^4$ $\gamma_b = 0.7 + 5\tan\beta$	Bore model, D: total depth ($= h + \overline{\eta}$), $\gamma_b = H_b/D_b$, B: constant. Iwagaki et al. (1981) proposed the empirical expression for the value of B.
Mizuguchi et al. (1978)	$\dfrac{\rho g H^2}{8} 4k^2 \nu_{eb}\left\{\dfrac{1}{\gamma_b}\left(\dfrac{H}{D} - \gamma_r\right)\right\}^{1/2}$ $\nu_{eb} = \dfrac{5g\tan\beta_b}{8\kappa_b\sigma\sqrt{1 - \gamma_r/\gamma_b\left(1 + 3r_b^2/2\right)}}$	Eddy viscosity model, ν_{eb}: eddy viscosity, γ_r: ratio of wave height to depth in reformation region, β_b and k_b: bottom slope and wave number at breaking point.
Izumiya et al. (1983)	$\beta_0\left(M_*^2 - M_{*s}^2\right)^{1/2}\dfrac{E^{3/2}}{\rho^{1/2}D^{3/2}}\left(\dfrac{2c_g}{c} - 1\right)^{1/2}$ $M_*^2 = \left(c_g/c\right)\left\{E/\left(\rho g D^2\right)\right\}$	Turbulent model, M_s^*: value of M^* in the reformation region, β_0: constant,
Sawaragi et al. (1984)	$0.18F\rho^{-1/2}D^{-3/2}E^{3/2}$ $F = 5.3 - 3.3\xi_0 - 0.07/\tan\beta$	Turbulent model, ξ_0: surf similarity parameter, $\tan\beta > 1/60$

These procedures were originally developed for predicting wave transformation due to shoaling and refraction. We can predict wave transformation in a wide region economically by the wave ray method. However, we cannot calculate wave transformation including the effect of wave diffraction. Some attempts have been done to modify these procedures for predicting wave transformation including wave diffraction (e.g., Southgate 1982).

(2) Prediction of wave transformation based on conservation of momentum
    – time-dependent mild-slope equation –
As was shown in Chapter 1, numerical procedures for predicting wave transformation including shoaling, refraction and diffraction have also been developing based on the conservation of mass and momentum flux the fundamental equation of which is referred to as an unsteady mild slope equation. This procedure possesses the same accuracy as a mild slop equation of Berkoff (1972) and the same applicability to the arbitrary boundary as the numerical wave analysis method proposed by Ito and Tanimoto (1971). The fundamental equations of the unsteady mild slope equation expanded to the wave and current coexisting field are of the following form (Ohnaka et al. 1988):

$$\frac{\partial Q}{\partial t} + \sigma c^2 \nabla \left(\frac{\eta}{\sigma_0} \right) - f_d Q = 0 \tag{3.115}$$

$$a(\partial \eta / \partial t) + \nabla (U \eta) + \nabla \cdot (n Q) = 0$$
$$a = 1 + (\sigma_0 / \sigma)(n - 1) \tag{3.116}$$

where Q is the vector of flow rate per unit width, $n = c_g / c$ and f_d is the coefficient concerning the momentum dissipation due to wave breaking expressed as follows:

$$f_d = \alpha_d \tanh \beta \left\{ (g/h)(|Q|/Q_r - 1) \right\}^{1/2} \quad :\text{within the breaker zone of } |Q|/Q_r > 1$$

$$f_d = 0 \quad : \text{outside the breaker zone and within the breaker zone of } |Q|/Q_r < 1 \tag{3.117}$$

where Q_r ($= \gamma_d (gh^3)^{1/2}$) is the critical flow rate per unit width in the reforming region, α_d and γ_d are the nondimensional coefficients of about 2.5 and 0.25.

3.5.2 Calculation of wave-induced current
Wave-induced current is usually calculated based on the time and depth averaged equations of mass and momentum flux as shown in Chapter 1. These equations are the following forms:

$$\frac{\partial \overline{\eta}}{\partial t} + \frac{\partial U(h + \overline{\eta})}{\partial x} + \frac{\partial V(h + \overline{\eta})}{\partial x} = 0 \tag{3.118}$$

$$\frac{\partial U}{\partial t} + U \frac{\partial U}{\partial x} + V \frac{\partial U}{\partial y} = -g \frac{\partial \overline{\eta}}{\partial x} - \frac{1}{\rho(h + \overline{\eta})} \left(\frac{\partial S_{xx}}{\partial x} + \frac{\partial S_{xy}}{\partial y} + \overline{\tau}_x \right) + R_x \tag{3.119}$$

$$\frac{\partial V}{\partial t} + U\frac{\partial V}{\partial x} + V\frac{\partial V}{\partial y} = -g\frac{\partial \overline{\eta}}{\partial y} - \frac{1}{\rho(h+\overline{\eta})}\left(\frac{\partial S_{yx}}{\partial x} + \frac{\partial S_{yy}}{\partial y} + \overline{\tau}_y\right) + R_y \tag{3.120}$$

where (τ_x, τ_y) and (R_x, R_y) are the time averaged bottom shear stresses and lateral mixing terms in x and y directions.

Under the steady condition of oblique wave incidence on a long straight beach with parallel contours, the time derivatives and gradient in the longshore direction disappears and consequently the cross-shore mean current becomes 0. In such a condition, $g\partial\overline{\eta}/\partial x$ and $\partial S_{xx}/\partial x/\{\rho(h+\overline{\eta})\}$ are in balance in the cross-shore direction and $\partial S_{yx}/\partial x/\{\rho(h+\overline{\eta})\}$, $\tau_y/\{\rho(h+\overline{\eta})\}$ and $R_y/\{\rho(h+\overline{\eta})\}$ are in balance in the longshore direction.

Wave-induced current as a sediment transport flow is predicted by solving Eqs. (3.118)-(3.120) numerically. An ADI method is usually applied for solving these equations in a time domain. To find the numerical solution of steady state wave-induced current, an implicit scheme, that has the great advantage of stability and convergence, is usually used. In these calculations, it is not practicable to evaluate the time averaged bottom shear stress in the strict sense according to the method mentioned in **3.2**. Approximate expressions of the time averaged bottom shear stress with a friction factor, mean current velocity and water particle velocity due to waves (e.g., Longuet-Higgins 1970) are usually used in the calculation of wave-induced current in a wide region.

Various expressions of the lateral mixing term have also been proposed. Most of them are diffusion type expressions and some of them are listed in Table 3.5.

Table 3.5 Various expressions of lateral mixing terms and a lateral mixing coefficient

	Expression of lateral mixing terms	Lateral mixing coefficient	Remarks
Bowen (1969)	$R_y = \varepsilon d^2V/dx^2$	$\varepsilon = $ const.	
Longuet-Higgins (1970)	$R_y\rho h = \dfrac{d}{dx}\left(\rho\varepsilon h\dfrac{dV}{dx}\right)$	$\varepsilon = Nx\sqrt{gh}$	$0 < N < 0.016$
Thornton (1970)	$R_y = \dfrac{d}{dx}\left(\dfrac{H^2}{8\pi^2}\dfrac{gT}{h}\cos^2\theta\dfrac{dV}{dx}\right)$	$\varepsilon = \dfrac{H^2}{8\pi^2}\dfrac{gT}{h}\cos^2\theta$	θ : Wave direction
James (1974)	$R_y\rho h = \dfrac{d}{dx}\left(\rho h\varepsilon\dfrac{dV}{dx}\right)$	$\varepsilon = \begin{cases} N\sqrt{gh}\ h/\tan\beta \\ \qquad : 0 < h \le h_b \\ N\sqrt{gh}\ h_b^{\,2}/(h\tan\beta) \\ \qquad : h_b < h \end{cases}$	$\tan\beta$: Bottom slope
Jonsson et al. (1974)	$R_y\rho h = \dfrac{d}{dx}\left(\rho h\varepsilon\dfrac{dV}{dx}\right)$	$\varepsilon = \dfrac{4}{T}a_b^{\,2}\cos^2\theta$	a_b : Water particle excursion at bottom
Battjes (1975)	$R_y\rho h = \dfrac{d}{dx}\left(\rho h\varepsilon\dfrac{dV}{dx}\right)$	$\varepsilon = M\left(5\pi^2/16\right)^{1/3}$ $\times(\tan\beta)^{4/3}x\sqrt{gh}$	M : const, $\gamma = H/(h+\overline{\eta})$
Kim et al. (1986)	$R_y = \begin{cases} \varepsilon d^2V/dx^2 \\ \qquad : 0 < h < h_b \\ 0 \\ \qquad : h_b < h \end{cases}$	$\varepsilon = AF^{1/3}\gamma S^* x\sqrt{gD}$ $F = 5.3 - 3.3\xi_0 - 0.07/\tan\beta$ $S^* = (-0.413\xi_0 + 0.98)\times\tan\beta$	A: constant, S*: modified bottom slope where the mean water level is taken into account, $\tan\beta > 1/60$

3.6 Prediction of Topographic Change Caused by Non-equilibrium Suspended Sediment Transport

In this section, two examples of the prediction of topographic change caused by non-equilibrium suspended sediment transport are shown. One is the deposition pattern of discharged sediment along a coast from a river and the other is the topographic change around a navigation channel. In such cases, topographic change takes place according to the non-uniformity of sediment transport which is brought about by the abrupt changes in current velocity and wave characteristics due to the geometry. Especially, when suspended sediment is included, the non-equilibrium state of suspended sediment has to be analyzed accurately.

(1) Numerical simulation for predicting deposition pattern of discharged sediment from a river mouth

Deguchi and Sawaragi (1988) proposed the numerical procedure for predicting the deposition pattern of discharged sediment and examined the applicability of the procedure using the experimental results that will be shown in **5.8** (Figs. 5.31 and 5.32). They assumed that discharged sediment is composed of wash load and bed material load in an equilibrium state that was expressed by the local sediment transport rate proposed by Rijin (1985). Then, the deposition of discharged sediment takes place by the spatial gradient of the local sediment transport rate and settling of wash load ΔQ_s and the rate of topographic change is expressed as follows:

$$\frac{\partial h}{\partial t} = \frac{1}{1-\lambda}\left(\frac{\partial q_x}{\partial x} + \frac{\partial q_y}{\partial y} + \Delta Q_s\right) \tag{3.121}$$

The value of ΔQ_s is estimated by using the fall velocity W_f and the depth averaged concentration C in the following way:

$$\Delta Q_s = -W_f C \tag{3.122}$$

The value of C is calculated by solving the following depth and time averaged advection-dispersion equation (Eq. (3.82)):

$$\frac{\partial C}{\partial t} + U\frac{\partial C}{\partial x} + V\frac{\partial C}{\partial y} = \varepsilon_{sx}\frac{\partial^2 C}{\partial x^2} + \varepsilon_{sy}\frac{\partial^2 C}{\partial y^2} \tag{3.123}$$

A boundary condition of Eq. (3.123) is given by the concentration at the upstream end of the calculation region C_{or}. The depth averaged velocity (U, V) of discharged flow is obtained by solving fundamental equations for the wave-induced current mentioned in **3.5.2** (Eqs. (3.118 - 3.120)) with the boundary condition given at the upstream side of the river numerically. Figure 3.22 illustrates an example of the calculated flow pattern around the model river mouth shown in the same figure.
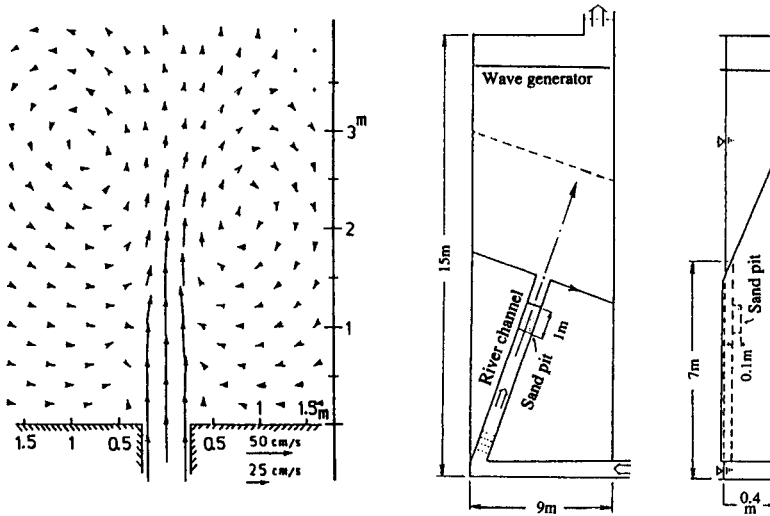
Fig. 3.22 Calculated flow pattern around a model river mouth

Figure 3.23 shows the comparison of measured and calculated deposition patterns of discharged sediment in the case of fine sand (d_{50} = 0.015cm). Figures (a) and (b) are the measured and calculated deposition patterns. Figure(c) is the calculated deposition pattern caused by the wash load and bed load. Fig. (d) is the calculated topographic change caused by a suspended load.
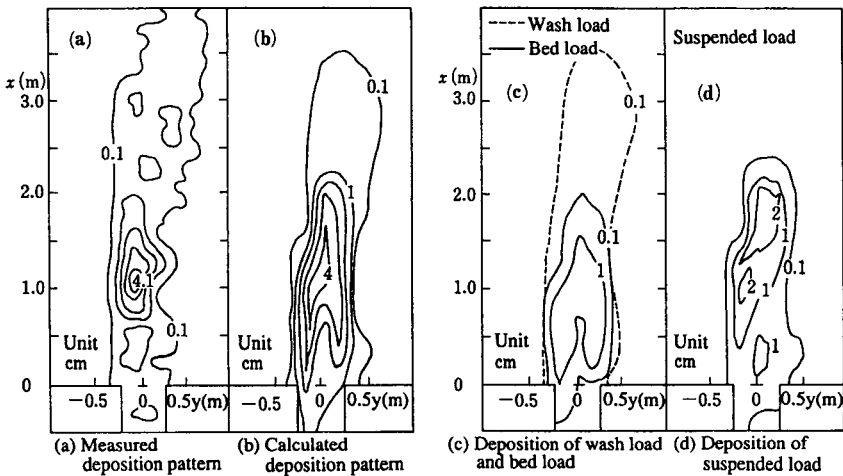
Fig. 3.23 Comparison of measured and calculated deposition patterns of discharged sediment ((a): measured deposition pattern, (b): calculated deposition pattern, (c): calculated deposition pattern caused by a wash load and bed load, (d): calculated deposition pattern caused by a suspended load)

On the other hand, Fig. 3.24 illustrates the comparisons of measured and calculated topographic change along the center line of the river in the case of fine sand (d_{50} = 0.015cm, Fig. (a)) and coarse sand (d_{50} = 0.035cm, Fig. (b)).
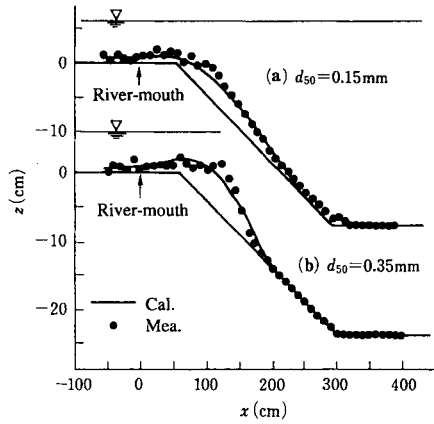
Fig. 3.24 Comparison of measured and calculated topographic change along the center line of the river ((a): fine sand, (b): coarse sand)

From these figures, it is judged that the proposed numerical procedure can reproduce the measured deposition pattern fairly well.

(2) Topographic change around a navigation channel
The shoaling process of the channel caused by waves and currents is discussed in a two-dimensional problem where waves and currents cross the channel at a right angle. In such a case, vertical distribution of nonequilibrium suspended sediment concentration plays an important role in the topographic change. Sawaragi et al. (1991) proposed the numerical procedure for predicting topographic change where the two-dimensional advection-diffusion equation is solved to estimate settling flux of suspended sediment accurately by applying a split operator approach.
Vertical sediment flux that causes topographic change around the channel is schematically illustrated in Fig. 3.25 and the change in water depth is expressed by Eq. (3.124) in the coordinate system shown in Fig. 3.25.
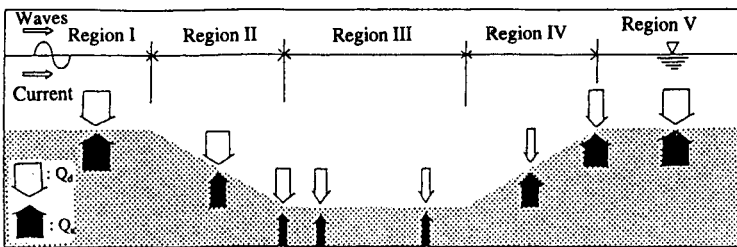
Fig. 3.25 Coordinate system and vertical sediment flux around the channel

$$\frac{\partial h}{\partial t} = \frac{1}{(1-\lambda)} \Delta Q = \frac{1}{(1-\lambda)}(Q_u - Q_d)$$

(3.124)

where Q_u and Q_d are the upward and downward sediment flux at the bottom and are estimated from the suspended sediment concentration in nonequilibrium state $C(x,z)$. The nonequilibrium suspended sediment concentration is estimated by solving the following two-dimensional advection-diffusion equation with the split-operator approach:

$$\frac{\partial C}{\partial t} + u\frac{\partial C}{\partial x} + w\frac{\partial C}{\partial z} = K_x\frac{\partial^2 C}{\partial x^2} + K_z\frac{\partial^2 C}{\partial z^2}$$

(3.125)

where K_x and K_z are the diffusion coefficient.

The proposed numerical procedure consists of the following three parts:

1) Calculation of flow fields; A time averaged current velocity is calculated based on the usual time and depth averaged equations of wave-induced currents. Driving forces of the currents are the gravity (slope of mean water surface) and radiation stresses. Wave height distribution is calculated from the equation of energy conservation in a steady state. These two groups of equations are calculated iteratively until the current velocity, mean water displacement and wave height reach the steady state.

2) Calculation of sediment flux; Flux of suspended sediment is estimated from the concentration of suspended sediment obtained numerically by the above-mentioned procedure. In the calculation of concentration, the vertical distribution of the mean current is estimated from the vertically averaged mean current velocity by assuming a logarithmic distribution. The rate of bed load sediment transport is calculated from the modified Rijn formula which was originally proposed for the prediction of the rate of bed load in the unidirectional flow.

3) The rate of topographic change; The topographic change is evaluated from the spatial gradient of the bed load and the difference between upward and downward fluxes of suspended sediment.

The applicability of these procedures were verified through two-dimensional movable bed experiments with the bed material of d_{50} = 0.012cm. Experimental conditions were as follows: the mean current velocity U and the depth at the channel approach were 19.4cm/s and 20cm respectively; the height and period of incident waves were 8cm and 1.4s respectively; and the depth, the width and the side slope of the channel were 30cm, 2m and 1/5. It is confirmed that the measured concentration of suspended sediment along the channel section can be predicted well by the proposed procedure.

Figure 3.26 is the comparison of measured and calculated topographic changes of the channel section. "SOA" shown by a broken line in the figure is the result of the present numerical model. The result shown in Fig. 3.26 is obtained by using the depth and time averaged suspended sediment concentration (a solution to Eq. (3.82)) instead of the local concentration (Eq. (3.125)). The result illustrated by Fig. 3.26 is obtained by using the local sediment transport rate in an equilibrium state where the vertical distribution of suspended sediment concentration is estimated by solving the so-called vertical one-dimensional diffusion equation in a steady and equilibrium state.

We can judge that the measured topographic change is most closely simulated by the procedure using the split operator approach.
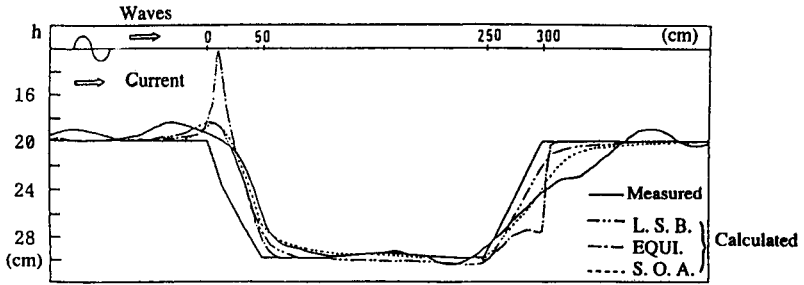
Fig. 3.26 Comparison of measured and calculated topographic change in water depth around the channel

References

Asano, T. and Y. Iwagaki (1984): Bottom turbulent boundary layer in wave-current co-existing systems, Proc. 19th Int. Conf. on Coastal, ASCE, pp.2397-2413.

Asano, T. (1990): Two-phase flow model on oscillatory sheet-flow, Proc. 22nd Int. Conf. on Coastal, ASCE, pp.2372-2384.

Bagnold, R.A. (1956): The flow of cohesionless grains in fluids, Proc. Roy. Soc. Series A, 964, Vol.249, pp.235-297.

Bakker, W.T. (1968): The dynamics of a coast with groyne system, Proc. 11th Int. Conf. on Coastal, ASCE, pp.492-517.

Bakker, W.T., E.H.J. Klein Breteler and A. Roose (1970): The dynamics of a coast with groin system, Proc. 12th Int. Conf. on Coastal, ASCE, pp.1001-1020.

Battjes, J.A.(1975): A note on modeling of turbulence in the surf zone, Proc. Sympo. Modeling Technique, pp.1050-1064.

Battjes, J.A. and J.P.F.M. Janssen(1979): Energy loss and set-up due to breaking of random waves, Proc. 16th Int. Conf. on Coastal, ASCE, pp.569-587.

Berkoff, C. W., (1972): Computation of combined refraction-diffraction, Proc. 13rd Int. Conf. on Coastal, ASCE., pp.471-490.

Bijker, E.W. (1966): The increase of bed shear stress in a current due to wave motion, Proc. 10th Int. Conf. on Coastal, ASCE, pp.746-765.

Bijker, E.W. (1971): Longshore transport computation, J. Waterway, Harbor and Coastal Eng., ASCE, Vol.97, No.WW4, pp.687-701.

Bowen, A.J. (1969): The generation of longshore currents on a plane beach, J. Marine Res., Vol.27., pp.206-215.

Bowen, A.J. (1980): Simple models of nearshore sedimentation -beach profiles and longshore bars, The Coastline of Canada (ed. by MaCann), Geol. Survey of Canada, pp.1-11.

Bretherton, F. P., (1969): Wave trains in inhomogeneous moving media, Proc. Roy. Soc. London, Ser. A, Vol.302, pp.529-554.

Deguchi, I, and T. Sawaragi (1984): Calculation of on-offshore sediment transport rate on the basis of flux concept, Proc. 19th Int. Conf. on Coastal, ASCE, pp.1325-1341.

Deguchi, I. and T. Sawaragi (1986): Beach fill at two coasts of different configurations, Proc. 21st Int. Conf. on Coastal, ASCE, pp. 1030-1046.

Deguchi, I. and T. Sawaragi (1988): Effects of coastal structure on deposition of discharged sediment around river mouth, Proc. 21st Int. Conf. on Coastal, ASCE, pp. 1573-1587.

Eagleson, P.S., B. Glenne and J.A. Dracup (1963): Equilibrium characteristics of sand beaches, J. Hydraulic Div., Proc. ASCE, Paper No.3387, pp.35-57.

Einstein, H.A. (1950): The bed load function for sediment transport in open channel flow, U.S. Dept. of Agriculture, Soc. Tech., Bull. No.1026, 78p.

Engelund, F. (1965): Turbulent energy and suspended load, Coastal Eng. Lab., Tech. Univ. of Denmark, Rept. No. 10.

Fredsøe, J., O.H. Anderson and S. Silberg (1985): Distribution of suspended sediment in large waves, J. Waterway, Port, Coastal and Ocean Eng. Div., ASCE, Vol.111, No.6, pp.1041-1059.

Grant, W.D. and O.S. Madsen (1979): Combined wave and current interaction with a rough bottom, J. Geophys. Res., Vol.81, pp.1797-1808.

Goda, Y. (1975): Irregular wave deformation in the surf zone, Coastal Eng. in Japan, JSCE, Vol.18, pp.13-26.

Hallermeier, R.J. (1983): Sand transport limits in the shoreline numerical model, Proc. Coastal Structures '83, ASCE, pp.703-716.

Hashimoto, H. and T. Uta (1979): Analysis of beach profile changes at Ajigaura by empirical eigenfunction, Coastal Eng. in Japan, JSCE, Vol.22, pp.47-57.

Hashimoto, H. (1981): Numerical simulation of beach deformation, Lecture Note of the 17th Summer Seminar on Hydraulics, Committee on Hydraulics, JSCE, pp.B8-1-B8-12. (in Japanese)

Hino, M., T. Yamashita and S. Yoneyama (1982): Study on sand particle motion on plane horizontal and sloping bottoms by water waves, Coastal Eng. in Japan, JSCE, Vol.25, pp.65-74.

Horikawa, K. and A. Watanabe (1968): Laboratory study on an oscillatory boundary layer flow, Coastal Eng. in Japan, JSCE, Vol.11, pp.13-28.

Irie, I., Y. Kuriyama and M. Tagawa, (1985): Prediction of sea bottom topography by combining physical model and numerical model, Proc. 32nd. Japanese Int. Conf. on Coastal, JSCE, pp.345-349. (in Japanese)

Ito, K. and K. Tanimoto, (1971): Numerical wave analysis method and its application - waves around coastal structure-, Proc. 18th Japanese Int. Conf. on Coastal, JSCE., pp.67-70. (in Japanese)

Iwagaki, Y. and T. Sawaragi (1962): A new method for estimation of the rate of littoral sand drift, Coastal Eng. in Japan, JSCE, Vol.5, pp.67-79.

Iwagaki, Y., H. Mase and T. Tanaka(1981): Modeling for irregular wave transformation in surf zone, Proc. 28th Japanese Int. Conf. on Coastal, JSCE, pp.104-108. (in Japanese)

Izumiya T. and K. Horikawa (1984): Wave energy equation applicable in and outside the surf zone, Coastal Eng. in Japan, JSCE, Vol.27, pp.119-137.

James, I.D. (1974): A non-linear theory of longshore current, Estuarine and Coastal Marine Science, Vol.2, pp.207-234.

Johns, B. (1968): The damping of waves in shallow water by energy dissipation in a turbulent boundary layer, Tellus, Vol.XX.

Jonsson I.G. (1963): Mearsurement in the turbulent wave boundary layer, Proc. 10th Cong. IAHR, pp.85-92.

Jonsson I.G., O. Skovgaad and T.S. Jacobsen (1974): Computation of longshore currents, Proc. 14th Int. Conf. on Coastal, ASCE, pp.699-714.

Kajiura. K. (1964): On the bottom friction in an oscillatory current, Bull. Earthquake Res. Inst., Univ. of Tokyo, Vol.42, pp.147-174.

Kajiura, K. (1968): A model of the bottom boundary layer in water waves, Bull. Earthquake Res. Inst., Univ. of Tokyo, Vol. 46, pp.75-123.

Kalkanis, G. (1957): Turbulent flow near an oscillating wall, Univ. of California, Inst. of Eng. Res., Ser. No.72, Issue No.3.

Kamphuis, J.W. (1975): Friction factor under oscillatory waves, J. Waterways, Harbors and Coastal Eng. Div., Proc. ASCE, Vol.101, No.WW3, pp.135-144.

Kana, T., K. (1977): Suspended sediment transport at Price Inlet, S.C., Proc. Coastal Sediment '77, ASCE, pp.366-382.

Kanayama, S., T. Shimizu and H. Kondo (1988): High accurate numerical procedure for solving advection-diffusion equation, Proc., 35th Japanese Int. Conf. on Coastal, JSCE, pp.287-291. (in Japanese)

Katori, H. (1988): Sediment transport rate, in Nearshore Dynamics and Coastal Processes, (ed. by Horikawa, K.), Univ. of Tokyo Press, pp.194-217.

Kawata, Y. (1989): Law of cross-shore sediment transport on a sloping beach, Proc. Coastal Eng., JSCE, Vol.36. pp.289-293. (in Japanese)

Kim, K.H., T. Sawaragi and I. Deguchi (1986): Lateral mixing and wave direction in the wave-current interaction region, Proc. 20th Int. Conf. on Coastal, ASCE, pp.366-379.

Kobayashi, N. (1982): Sediment transport on gentle slope due to waves, J. Waterways, Harbors and Coastal Eng. Div., Proc. ASCE, Vol.108, No.WW3, pp.254-271.

Komar, P. D. and D.L. Inman (1970): Longshore sand transpor on beaches, J. Geophys. Res., Vol.75, No.30, pp.5914-5927.

Komar, P.D. (1976): Beach Process and Sedimentation, Prentice-Hall, 429p.

Komatsu, T., N. Nakashiki and K. Ohgushi (1984): Numerical calculation of contaminant advection-diffusion in rivers and coastlines, Proc. 31st Japanese Int. Conf. on Coastal, JSCE, pp.635-639. (in Japanese)

Liu, P.L.F. and R.A. Darlymple (1976): Bottom frictional stresses and longshore currents due to waves with large angles of incidence, J. Marine Res., Vol.36, No.2, pp.357-375.

Longuet-Higgins, M.S.(1970): Longshore current generated by obliquely incident sea waves, 1 and 2, J. Geophys. Res., Vol.75. pp.6778-6789 and pp.6790-6801.

Madsen, O.S. and W.D. Grant (1976): Quantitative description of sediment transport by waves, Proc. 15th Int. Conf. on Coastal, ASCE, pp.1093-1112.

Maruyama, K. (1988): Numerical calculation method, in Nearshore Dynamics and Coastal Processes, (ed. by Horikawa, K.), Univ. of Tokyo Press, pp.336-344.

Mizuguchi, Y., K. Tsujioka and K. Horikawa (1978): On wave height transformation in the surf zone, Proc. 25th Japanese Int. Conf. on Coastal, JSCE, pp.155-159. (in Japanese)

Nadaoka, K., H. Kamata and H. Yagi (1988): A simple calculation model of nonequalibrium three-dimensional suspended sediment concentration, Proc. 35th Japanese Int. Conf. on Coastal, JSCE, pp.322-326. (in Japanese)

Nadaoka, K. and H. Yagi (1990): Shingle-phase fluid modeling of sheet-flow toward the developement of 'numerical movile bed', Proc. 22nd Int. Conf. on Coastal, ASCE, pp.2346-2359.

Nielsen, P. (1979): Some basic concept of wave sediment transport, Series Paper, No.20, Tech. Univ. of Denmark, 160p.

Nishimura H. (1982): Numerical simulation of wave-indiced circulation, Proc. 29th Japanese Int. Conf. on Coastal, JSCE, pp.333-337. (in Japanese)

Nishimura, H. and T. Sunamura (1986): Numerical simulation of beach profile changes, Proc. 20th Int. Conf. on Coastal, ASCE, pp. 1444-1455.

Noda, H. (1969): Development of turbulent boundary layer in waves, Proc.15th Japanese Conf on Coastal Eng., JSCE, pp.23-27. (in Japanese)

Ogawa, Y. and N. Shuto (1982): On the dynamic of the swash zone, Proc. 28th Japanese Int. Conf. on Coastal, JSCE, pp. 212-216. (in Japanese)

Ohnaka, S., A. Watanabe and M. Isobe (1988): Numerical modeling of wave deformation with a current, Proc. 21st Int. Conf. on Coastal, ASCE, pp.393-407.

Pernard-Considere, R. (1956): Essai de theorie de l'evolution des formes de vivage en plages de sable et de gralets, IV eme Journees de l'Hydraulique, Les Energries de la Mer, Question III, Rept., No.1, pp.289-298.

Perlin, M. and R.G. Dean (1983): A numerical model to simulate sediment transport in the vicinity of coastal structures, U.S. Army Corps of Engnrs., CERC, Miscel. Rept., No.83-10, 199p.

Rae, C.C. and P.D. Komar (1972): Computer simulation models of beach shoreline configuration, J. Sed. Pet., Vol.45, No.4, pp.866-872.

Reidel H.P., J.W. Kamphuis and A. Brebner (1973): Measurement of bed shear stresses under waves, Proc. 13th Int. Conf. on Coastal, ASCE, pp.587-603.

Rijjn, L.C. (1985): Sediment transport , Delft Hydraulic Labo., Publication No.334.

Sakakiyama, T., N. Shimizu, R. Kajima, S. Saito and K. Maruyama (1984): Ripples generated by prototype waves in the large wave flume, Proc. 31st Japanese Int. Conf. on Coastal, JSCE, pp.381-385. (in Japanese)

Saito, H., T. Uda, M. Tsunata, Z. Sawada and S. Hayashi (1985): Beach erosion of Ogawarako Beach and its prediction, Proc. 32nd Japanese Int. Conf. on Coastal, JSCE, pp.380-384. (in Japanese)

Sato, S. and N. Tanaka (1965): Sediment movement due to waves on a horizontal bed, Proc. 9th Japanese Int. Conf. on Coastal, JSCE, pp. 95-100. (in Japanese)

Sato, S., K. Uehara and A. Watanabe (1986): Numerical simulation of the oscillatory boundary layer flow over ripples by a k-ε turbulent model, Coastal Eng. in Japan, JSCE, Vol.29, pp.65-78.

Savage, R.P. (1959): Wave run-up on roughened and permeable slopes, Trans. ASCE, Vol.124, pp.852-870.

Sawamoto, M. (1985): Mechanism of sediment transport due to wave action, Lecture note of the 21st Summer Seminar on Hydraulics, Course B, Committee on Hydraulics, JSCE, pp.B-8-1-B-8-17. (in Japanese)

Sawaragi, T., I. Deguchi and T. Taruno (1978a): Study on bottom shear stress under waves and longshore current, Proc. 25th Japanese Int. Conf. on Coastal, JSCE, ppl.42-45. (in Japanese)

Sawaragi, T. and I. Deguchi (1978b): Distribution of sand transport rate across a surf zone, Proc. 16th Int. Conf. on Coastal, ASCE, pp.1596-1613.

Sawaragi, T. and I. Deguchi, (1980): On-offshore sediment transport rate in the surf zone, Proc. 17th Int. Conf. on Coastal, ASCE, pp.1195-1214.

Sawaragi, T. and I. Deguchi (1982): Function of groin to trap sediment transported in longshore direction, Proc. 29th Japanese Int. Conf. on Coastal, JSCE, pp.250-254. (in Japanese)

Sawaragi, T., J.S. Lee and I. Deguchi (1984): Study on numerical model for predicting wave-induced current and topographic change around river mouth, Proc. 31st Japanese Int. Conf. on Coastal, JSCE, pp.411-415. (in Japanese)

Sawaragi, T., I. Deguchi and K.H. Kim (1984): Energy loss and wave set-up due to breaking waves, Tech. Rept. Osaka Univ., Vol.34, No.1779, pp.329-338.

Sawaragi, T., J.S. Lee and I. Deguchi (1985): A new model for a prediction of beach deformation around a river mouth, Proc., Int. Sympo. on Ocean Space Utilization '85, pp.29-236.

Sawaragi, T., I. Deguchi, M. Ono and K.S. Bae (1990): Numerical simulation for predicting shoaling process of navigation channel, Int. Sympo. on Natural Dissaster Reduction and Civil Eng., JSCE, pp.117-126.

Shibayama, T. and K. Horikawa (1982): Sediment transport and beach transformation, Proc. 18th Int. Conf. on Coastal, ASCE, pp.1439-1458.

Shibayama, T. (1988): Mechanism of Sediment Transport, in Nearshore Dynamics and Coastal Processes (ed. by K. Horikawa), Univ. of Tokyo Press, pp.167-193.

Shimizu, T., S. Saito, M. Maruyama, H. Hasegawa and Y. Kajima (1985): Modeling of cross-shore sediment transport rate distribution based on large flume experiments, Central Research Inst. Electric Power Industry, Civil Eng. Lab., Rept. No.384028, 60p. (in Japanese)

Skafel, M.G. and B.G, Krishnappan (1984): Suspended sediment distribution in wave field, J. Waterway, Port, Coastal and Ocean Eng. Div., ASCE, Vol.110, No.2, pp.215-230.

Sleath, J.F.A (1978): Measurement of bed load in oscillatory flow, J. Waterway, Port, Coastal and Ocean Div., Proc. ASCE, Vol.104, No.WW4, pp.291-307.

Southgate, H. N., (1985): A harbor ray method of wave refraction-diffraction, J. Waterway, Port, Coastal and Ocean Eng. Div., Proc. ASCE, Vol.111, No.1, pp.29-44.

Sunamura, T. and K. Horikawa (1974): Two-dimensional beach transformation due to waves, Proc. 14th Int. Conf. on Coastal, ASCE, pp.920-938.

Sumanura, T. (1984): Onshore-offshore sediment transport rate in the swash zone of laboratory beaches, Coastal Eng. in Japan, JSCE, Vol. 27, pp.205-212.

Swart, D.H. (1974): Offshore sediment transport and equilibrium beach profiles, Delft Univ. Tech. Diss., Delft Hydr. Lab., Publ. No. 131, 244p.

Tanaka, H. and N. Shuto (1981): Friction coefficient for a wave-current co-existion system, Coastal Eng. in Japan, JSCE, Vol.24, pp.105-128.

Tanaka, H. and N. Shuto (1984): Friction law and flow regimes under waves and current motions, J. Hydraulic Res., IAHR, Vol.22, pp.245-261.

Tanaka, H. (1985): Study on turbulence and boundary shear under waves and current, Proc. 32nd Japanese Int. Conf. on Coastal, JSCE, pp.31-35. (in Japanese)

Thornton, E.B. (1970): Variation of longshore current across the surf zone, Proc. 12nd Int. Conf. on Coastal, ASCE, pp.291-308.

Tsuchiya, Y., and T. Yasuda (1978): A mathematical model of beach change, Proc. 25th Japanese Conf. on Coastal Eng., JSCE, pp.189-193. (in Japanese)

Tsuchiya, Y., (1986): Lecture note of the 22nd Summer Seminar on Hydraulics, Committee on Hydraulics, JSCE, pp.B-4-1-B-4-22. (in Japanese)

Uda, T. (1982): An application of a shoreline change model to the prediction of change of a spit in a river mouth, Proc. JSCE, No.322, pp.77-88. (in Japanese)

Walton, J.L. and T.Y. Chiu (1979): Littoral sand transport on beaches, Rept. No.UFL/COEL/TR-041, Univ. of Florida, Gainsvill, 345p.

Watanabe, A. (1980): Numerical models of nearshore currents and beach deformation, Coastal Eng. in Japan, JSCE, Vol.25, pp.147-162.

Watanabe, A., Y. Riho and K. Horikawa (1980): Beach profile and on-offshore sediment transport, Proc. 17th Int. Conf. on Coastal, ASCE, pp.1106-1121.

Watanabe, A., M. Maruyama, T. Shimizu and T. Sakakiyama (1986): Numerical prediction model of three-dimensional beach deformation around a structure, Coastal Eng. in Japan, JSCE, Vol.29, pp.19-39.

Winant, C.D., L.D. Inman and C.E. Nordstorm (1975): Description of seasonal beach changes using empirical eigenfunction, J. Geophys. Res., Vol.8, No.15, pp.1979-1986.

Yamaguchi, M. and Y. Nishioka (1984): Numerical simulation on the change of bottom topography by the presence of coastal structures, Proc. 19th Int. Conf. on Coastal, ASCE, pp.1732-1748.

Chapter 4   Structures for Wave Control

4.1 Wave Control Mechanism

The water surface profile of a progressive monochromatic wave is generally described

$$\eta = \frac{1}{2}H\cos\left\{(k\cos\theta)x + (k\sin\theta)y - \sigma t + \varepsilon\right\} \tag{4.1}$$

in which, η is the water surface profile, H is the wave height, k $(=2\pi/L)$ is the wave number, L is the wavelength, θ is the wave direction, σ $(=2\pi/T)$ is the angular frequency, T is the wave period, ε is the phase lag, t is the time, x and y are horizontal axes perpendicular to each other. k and σ satisfy the dispersion relationship (Eq. 1.33).

Since the water surface profile comprises the four physical quantities (1) wave height, (2) wave direction, (3) wave period, and (4) phase lag, wave control implies controlling these four basic physical quantities. Hitherto, we have optimized the use of such physical phenomena as (1) refraction, (2) diffraction, (3) reflection, (4) shoaling and breaking, and (5) friction and large-scale vortex formation and shedding in order to control waves from an engineering viewpoint. At present, we have reached a stage of being able to control the wave height, wave direction and wave phase to some degree. However, wave period control has yet to be achieved. This is one of the important problems facing us in the future.

Coastal engineers have chiefly devoted themselves to investigating and developing coastal and offshore structures from the viewpoint of "how to efficiently attenuate the incident wave height". Very recently, however, owing to the increased social concern regarding the utilization of clean ocean energy, multi-purpose utilization of controlled sea areas, and the increasing need for marine recreational activities, new policies on "how to effectively utilize sea waves" and "how to converge waves to some specific location and break them" have been stressed.

4.1.1 Wave control by wave energy dissipation

Since wave energy is proportional to the square of the wave height, wave height can be attenuated by converting wave energy into another type of energy. Some parts of wave energy can be transformed into heat and sound energy through the viscosity of water and air using the mechanisms of friction, vortex formation and shedding around structures, jet mixing and wave breaking. Maximum energy decay is achieved by wave breaking. Utilizing these mechanisms, we have succeeded in decaying the height of an incoming wave.

Most coastal and harbor structures are furnished with a wave energy dissipation function. It is well known that large-scale vortex formation and shedding around the leading wall edge of a curtain-type breakwater, jet mixing with the pipe-type breakwater, friction and wave breaking with the sloping rubble-mounted breakwater, and friction and permeability of the submerged breakwater with a wide crown all play an important part in attenuating incoming waves vis-á-vis their respective breakwater types.

4.1.2 Wave control by phase interaction

Waves can be controlled by utilizing the phase lag among the incident, reflected, and transmitted waves. Valembois (1953) first attempted to decay waves using the "resonance" phenomenon. Valembois (1955) attempted to decay a transmitted wave height to zero by arranging a resonant basin in a wave propagating channel, as shown in Fig. 4.1. The resonant basin had a width and depth of $L/2$ and $L/4$, respectively, and these dimensions were determined in order that the reflected wave at the resonant basin should be 180° out of phase against the incident wave phase, resulting in no waves being transmitted due to phase interaction.
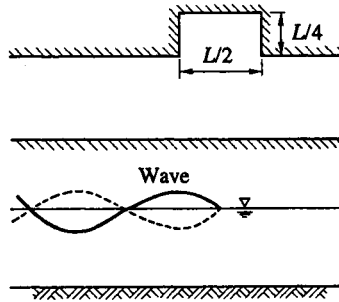
Fig. 4.1 Wave control method by arranging a resonant basin

In the case of a structure with multi-reflection sources, reflected waves caused by the multi-reflection sources, in general, have mutually different phase lags and propagate in a uniform direction. Assuming that two linear monochromatic waves η_1 and η_2 with the same wave period propagate in the same direction and the linear super-imposition principle is applied, the combined profile η_c of the two waves is given by

$$\eta_c = \eta_1 + \eta_2 = \frac{1}{2}H_1 \cos(kx - \sigma t + \varepsilon_1) + \frac{1}{2}H_2 \cos(kx - \sigma t + \varepsilon_2) \qquad (4.2)$$

When the two waves are in phase $(\varepsilon_1 = \varepsilon_2)$

$$\eta_c = \frac{1}{2}(H_1 + H_2)\cos(kx - \sigma t + \varepsilon_1) \qquad (4.3)$$

On the other hand, when the phases are shifted 180° $(\varepsilon_1 - \varepsilon_2 = \pi)$

$$\eta_c = \frac{1}{2}(H_1 - H_2)\cos(kx - \sigma t + \varepsilon_1) \qquad (4.4)$$

Figure 4.2 clearly shows that η_c in the case of "in phase $(\varepsilon_1 = \varepsilon_2)$" is larger than in the case of "π out of phase $(\varepsilon_1 - \varepsilon_2 = \pi)$" (Ippen 1966). This would suggest that the wave height can be attenuated by devising a structure in such a way as to generate two progressive waves whose phase lag is π. The low reflection quaywall with air-chambers (Sawaragi et al. 1973) and the multi-slotted wall-type structure are cited as typical wave energy-dissipating structures utilizing phase interaction.

4.1.3 Wave control by reflection

Wave direction and height can be controlled by utilizing wave reflection. The control of the propagation direction of sea waves is based on the same principle as for ray reflection. When a wave advances toward a structure with angle θ to the normal structure surface, as shown in Fig. 4.3, the wave is reflected back with the same angle θ. Therefore, utilizing this principle, the wave propagation direction can be changed by varying the angle of the structure's front face against the incident wave angle θ.
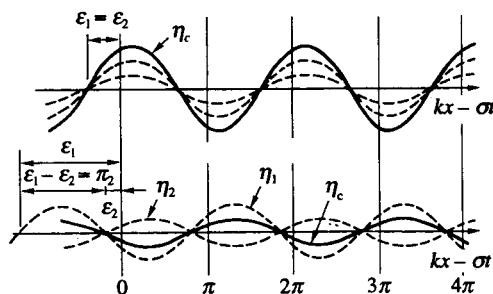
Fig. 4.2 Linear super-imposed profile of the two progressive waves with the same period
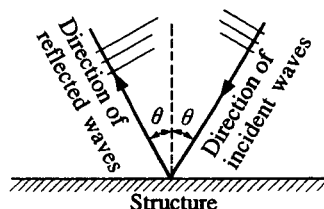
Fig. 4.3 Direction of reflected waves

The wave height can be controlled by changing the reflection coefficient K_R (=reflected wave height/incident wave height) of the structure. Wave height control of a partially standing wave and transmitted wave through porous structures has usually been done by adjusting the reflection coefficient K_R of the structures. The reflection coefficient K_R is generally dominated by surface slope, roughness and porosity, and geometrical slope of the structure as well as by the still water depth and incident wave conditions. An outline of the reflection coefficient K_R for various structures is given in Table 4.1 (Goda 1985).

Table 4.1 Reflection coefficients for various structures

Type of Structure	Reflection Coefficient
Vertical wall with crown above water	0.7~1.0
Vertical wall with submerged crown	0.5~0.7
Slope of rubble stones (slope of 1 on 2 to 3)	0.3~0.6
Slope of energy dissipating concrete blocks	0.3~0.5
Vertical structure of energy dissipating type	0.3~0.8
Natural beach	0.05~0.2

4.1.4 Wave control by wave direction change

The wave direction and wave height can be controlled by utilizing the principles of the wave refraction and diffraction phenomena. A wave obliquely advancing to the current or depth contour has the nature of changing its propagation direction, following the "refraction principle".

It is well known within linear wave theory that when a wave propagates obliquely to the coast with parallel depth contour, the wave experiences refraction. When the wave with an incident angle θ_1 at the depth h_1 encounters a change of water depth, its propagation direction is changed from θ_1 to θ_2 at the depth h_2, based on the Snell law, as shown in Fig. 4.4. θ_1 and θ_2 satisfy

$$\frac{\sin\theta_1}{c_1} = \frac{\sin\theta_2}{c_2}$$

(4.5)

in which c_1 and c_2 are the wave celerities at depths h_1 and h_2, respectively.
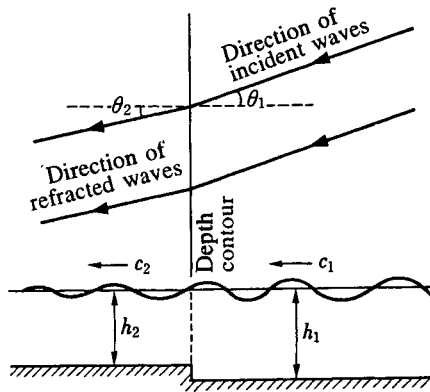
Fig. 4.4 Direction of refracted waves

The wave height is also controlled by wave refraction, since the wave height increases in sea areas where the wave ray converges and decreases in areas where the wave ray diverges. However it should be noted that the structure should be submerged and its representative length should be at least several times the length of the incoming wave, in order to make the best use of the refraction phenomenon. Hitherto a semi-spherical shoal and a curved shoal have been investigated from the viewpoint of utilizing wave power. Very recently, research and development of technology using a submerged sloping plate type breakwater has become an exciting topic in relation to new waterfront development.

Wave direction and wave height can also be controlled by utilizing the wave diffraction phenomenon. It is well known that waves propagate to the shadow area behind an island or a long breakwater, like a ray, following the Huygen principle. The diffracted wave propagates in all directions like a concentric circle, and the magnitude of the wave direction change and wave height decay in the shadow area becomes remarkable. The offshore breakwater, successfully employed as a countermeasure against beach erosion, the shape of which is a tombolo, owes its function to wave diffraction.

The diffracted wave height decays with wave propagation. The wave height distribution of the diffracted wave around the structure is theoretically calculated using the potential theories (Penny et al. 1952), (Putnam et al. 1948). They require, however, complicated numerical calculation, since the potential theories include the Fresnel integral. To avoid this complicated calculation, the diffraction diagrams are well prepared, enabling easy estimation of the diffracted wave height.

The finite amplitude wave usually generates the wave-induced current. The wave-induced current is also closely connected with the wave propagation direction, and therefore the velocity and the flow direction of the wave-induced current can be controlled by control of wave direction. Since a wave-induced current is closely connected to sediment transport, convection and diffusion of materials, marine products and ecological systems, and wave direction control technology would have a high possibility of being able to develop a "mezzo-scale engineering" that systemizes marine physics, chemistry and biology.

4.1.5 Wave control by frequency change

Shorter period waves can be easily controlled, since they are more easily refracted, diffracted, reflected and broken, compared to longer period waves. In addition, wave energy dissipation, due to vortex and turbulence, is inversely proportional to the wave period. Therefore, technology converting longer period waves into shorter period waves is extremely useful for wave control.

Sawaragi and Iwata (1976) revealed that the incident monochromatic wave is broken into many high frequency component waves by wave breaking as shown in Fig. 4.5. However, as seen in Fig. 4.5, the fundamental frequency component before wave breaking is still the dominant component even after wave breaking. This would show that the wave period is not shortened by wave breaking. The resonant interaction (MacGoldrick et al. 1966), which is the third order wave-wave interaction among different period waves, is revealed to generate a shorter period free wave. However, even in this case, fundamental frequency waves are still predominant, and the resonant interaction cannot be utilized to shorten the incident wave period.

Thus, it seems impossible to technologically control the wave period to our will even with the help of modern science. In other words, developing the technology to convert longer period waves into shorter period waves is an important task challenging modern science. Research and development of a new super-technology is required to over come the difficulty of changing wave period.
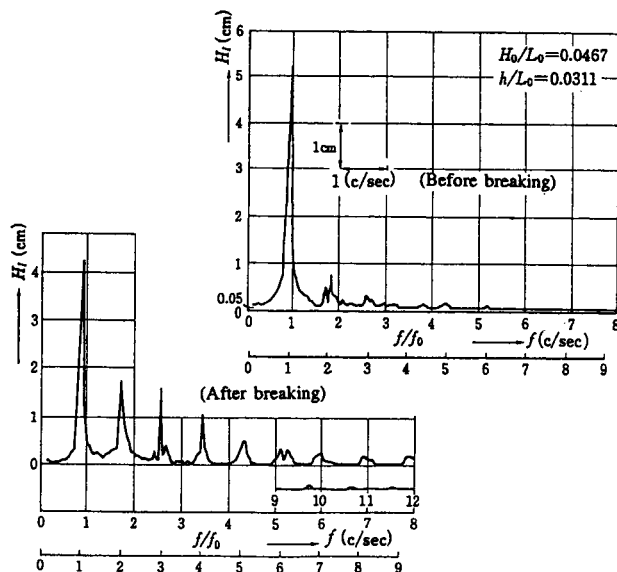
Fig. 4.5 Wave height spectrum before and after breaking

4.2 Rubble Mound Breakwaters

Rubble mound breakwaters, the most common coastal structure from the past, have been constructed to protect harbors and beaches from strong waves. The oldest type of rubble mound breakwaters consisted only of sloped layers of stone, however, recently breakwaters have been covered with concrete blocks. Rubble mound breakwaters have the advantage of being economical and easy to construct under severe wave conditions. They also show a smaller wave reflection than the vertical type breakwaters and require less maintenance.

4.2.1 Wave controlling function of rubble mound breakwaters
(1) Rubble mound breakwaters with a uniform slope
As mentioned in 4.1.1, the wave controlling function of rubble mound breakwaters depends on energy dissipation by wave breaking and friction on the rough mound. Reflection and transmission of the breaking or nonbreaking wave by the rubble mound breakwater have been experimentally investigated by many researchers. The general theory of wave transformation around a permeable structure in a nonbreaking state is described in **2.7**.
Losada and Gimenez-Curto (1981) proposed the following empirical formula for the reflection coefficient of a permeable structure with a uniform slope in regular waves

$$K_R = 1.35 \, [1\text{-}\exp(-0.071\xi)] \tag{4.6}$$

Here ξ is the surf similarity parameter defined as $\tan\alpha \, / \sqrt{H/L_o}$, in which α denotes the slope angle of the rubble mound. The empirical formula for wave run-up R_u on a uniform permeable slope in regular waves is proposed by Aherns and McCarney (1975):

$$R_u = \frac{1.13\xi}{1+0.506\xi} \tag{4.7}$$

For wave run-down R_d, Losada and Gimenez-Curto (1981) also proposed the empirical formula

$$R_d = -6.22[1\text{-}\exp(-0.0398\xi)] \tag{4.8}$$

On the other hand, Kobayashi and Wurjanto (1990) proposed a numerical model for wave run-up, run-down and reflection due to regular and irregular waves on a rough permeable slope.

(2) Rubble mound breakwaters of a composite slope
After high waves attack themselves to a rubble mound breakwater, the rubble mound breakwater tends to finally show a S-shaped equilibrium profile in its section as indicated by the solid line in Fig. 4.6, which suggests that we can make use of this characteristic and design a rubble mound breakwater that has an initial section with such a composite slope. Ryu and Sawaragi (1986) studied wave reflection and run-up through model tests and theoretical considerations.
Figure 4.7 shows the comparison of the reflection coefficient K_R between the uniform and the composite slope for regular waves. The reflection coefficients of the composite slope are half to a quarter of those of the uniform slope and they are strongly dependent on the length l_B of the horizontal part of the slope. To explain this low-reflection effect of the composite slope, we here develop a theory based on a simple summation of repeatedly

reflected waves on the berm of a composite slope. It is similar to that of a perforated quaywall with an air chamber as described in **4.4**. A schematic diagram of the incident and of the repeatedly reflected waves is shown in Fig. 4.8.
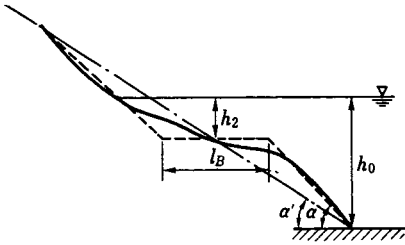
Fig. 4.6 Stable profile of a rubble mound structure
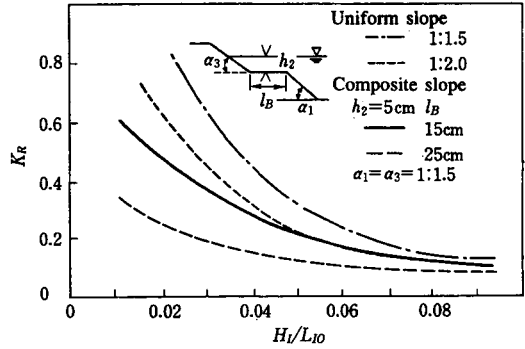
Fig. 4.7 Comparison of the reflection coefficient between the uniform and the composite slope for regular waves

The surface dispalcements $\eta(x,t)$ of the incident and reflected waves indicated by ①, ②, and ③ in Fig. 4.8 are expressed as

$$\eta_{①}(x,t) = \frac{H_I}{2}\cos(\sigma t - kx) \tag{4.9}$$

$$\eta_{②}(x,t) = \frac{H_I}{2}K_{R1}\cos(\sigma t + kx + \varepsilon_{R1}) \tag{4.10}$$

$$\eta_{③}(x,t) = \frac{H_I}{2}K^2{}_{T1}K_{R2}\bar{\alpha}^2\cos(\sigma t + kx + 4\pi l_B/L + 2\varepsilon_{T1} + \varepsilon_{R2}) \tag{4.11}$$
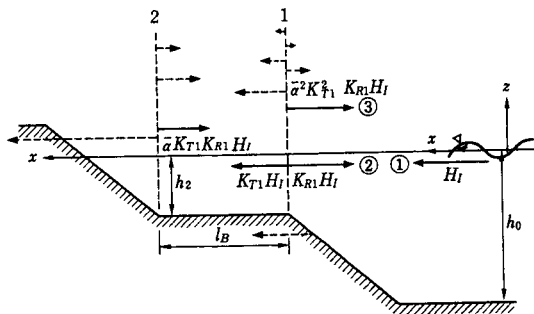
Fig. 4.8 Schematic diagram of the incident and reflected waves

Here K_{R1} and K_{T1} are the reflection and transmission coefficients, respectively, at boundary 1, K_{R2} is the reflection coefficient at boundary 2, $\bar{\alpha}$ is the energy dissipation rate on the berm, ε_{R1} and ε_{T1} are the phase lags between the reflected and the transmitted waves, respectively, at boundary 1, and ε_{R2} is the phase lag due to reflection at boundary 2.

The distribution of nondimensional surface evaluation $2\eta_c(x,t)/H_I$ is then obtained by summing up the Eqs. (4.11), (4.12), and (4.13) as

$$\frac{2\eta_c(x,t)}{H_I}=A\cos\sigma t-B\sin\sigma t=\sqrt{A^2+B^2}\,\cos(\sigma t+\varepsilon^*) \tag{4.12}$$

Here

$$\left.\begin{aligned} A &=\cos kx+K_{R1}\cos(kx+\varepsilon_{R1})+K^2{}_{T1}K_{R2}\bar{\alpha}^2\cos(kx+4\pi l_B/L+2\varepsilon_{T1}+\varepsilon_{R2})\\ B &=\sin kx+K_{R1}\sin(kx+\varepsilon_{R1})+K^2{}_{T1}K_{R2}\bar{\alpha}^2\sin(kx+4\pi l_B/L+2\varepsilon_{T1}+\varepsilon_{R2})\\ \varepsilon^* &=\tan^{-1}\frac{B}{A} \end{aligned}\right\} \tag{4.13}$$

Figure 4.9 shows the comparison between predicted and experimental results of the wave height distribution. In the numerical calculation, experimental results of the reflection and transmission coefficients of a submerged breakwater with an infinite width were used as K_{R1} and K_{T1} in Eq. (4.13). For K_{R2}, we used the reflection coefficient of a uniformed slope. The phase lags and the energy dissipation in Eq. (4.12) were ignored in the calculation. Calculated and experimental results show fairly good agreement, and the small difference between them may be ascribed to the ignored phase lag terms and to energy dissipation. It is very interesting that the berm of a composite slope has a similar wave absorbing function as an air chamber of a perforated quaywall. When we design the optimal composite slope for the reduction of wave reflection, the main factors to be considered are the reflection and the transmission at boundary 1, which may be the function of the depth and width of the berm.
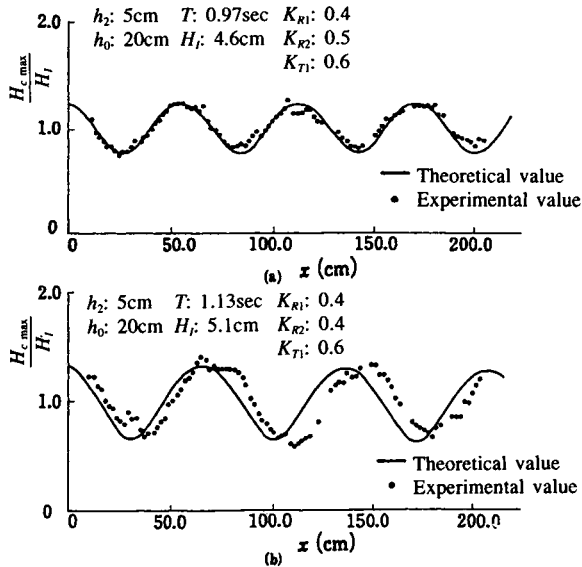
Fig. 4.9 Comparison between predicted and experimental results of the wave height distribution for the composite slope
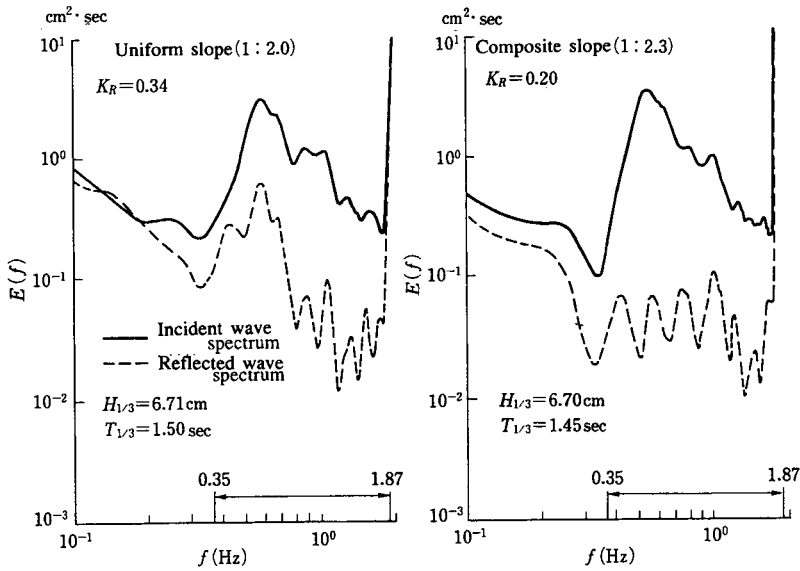
Fig. 4.10 Reflected wave characteristics for irregular waves on uniform and composite slopes

Theoretical considerations suggest the optimal berm length to be $l_B/L_o \approx 0.2$ to minimize the reflection of the composite slope. Figure 4.10 shows examples of incident and reflected wave spectra for irregular waves on the uniform and composite slopes, where the equivalent slope is defined by the Saville method for the composite slope. Also seen in these figures, reflection coefficients of the composite slope are smaller than those of the uniform slope.

4.2.2 Destruction mechanism of rubble mound breakwaters

Rubble mound breakwaters have been designed using empirical formulas such as the Hudson formula

$$W = \frac{1}{K_D \cot \alpha} \frac{H_I^3 \rho_s}{(\rho_s / \rho - 1)^3} \qquad (4.14)$$

where W is the weight of the rubble stone, ρ_s the density of the rubble stone, ρ the density of the sea water, α the seaward slope angle of the rubble mound, H_I the incident wave height, and K_D the stability coefficient.

Recently, however, these formulas have been reconsidered by taking the following effects into account:

(i) Interaction effect of successive waves on the slope

(ii) Effect of the spectrum shape and grouping characteristics of incoming waves.

(1) Definition of failure ratio

Definition of the failure ratio is very important in discussing stability of the rubble mound breakwaters. The failure ratio has been defined as

$$D'_{a1}(\%) = \frac{\text{number of stones moved from their former position}}{\text{total number of stones}} \times 100 \qquad (4.15)$$

or

$$D'_{a2}(\%) = \frac{\text{number of stones moved from their former position in the reference section}}{\text{total number of stones}} \times 100$$

$$(4.16)$$

In these definitions, the number of stones is usually counted over the region between *S.W.L.* $\pm H$ or *S.W.L.* $\pm 2H$ on the slope. To express the degree of failure more accurately, Ryu et al. (1986) proposed a new definition for the failure ratio D_a

$$D_a(\%) = (A'_o / A_o) \times 100 \qquad (4.17)$$

where A'_0 is the destroyed volume of the cover layer or revetment and A_0 is the destroyed volume of the cover layer when the destruction reaches the core layer as shown in Fig. 4.11.
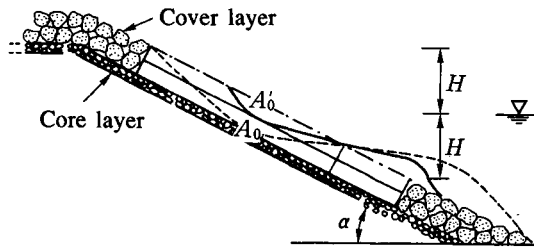
Fig. 4.11   Definition of the failure ratio

A 100% failure therefore means that the failure line penetrates the core layer. D'_{a1} and D'_{a2} are related to D_a as

$$\left.\begin{array}{l} D'_{a1} = 0.2 D_a \\ (D'_{a2})_i = 0.5 D_a \quad \text{for the region of } S.W.L \pm H \\ (D'_{a2})_j = 0.4 D_a \quad \text{for the region of } S.W.L. \pm 2H \end{array}\right\} \qquad (4.18)$$

The allowable failure ratio in D_a has yet to be clarified. 10% damage in D_a means 2% damage in D'_{a1} and 20% corresponds to 4%. Since the allowable critical failure ratio in D'_{a1} is recognized to be 2% to 4%, the allowable critical ratio in D_a is roughly estimated to be 10% to 20%. On the other hand, the failure ratio S used in Holland (1987) is defined as

$$S = \frac{A'_0}{a'^2_0} \qquad (4.19)$$

where $a_0'^3 = W/\rho_s$, A_0' is the area of the cross section where rubble stones have moved, as shown in Fig. 4.11, a_0' is a representative diameter of a stone, W is the weight of a stone in air, and ρ_s is the density of the stone. The failure ratio defined by Eq. (4.19) implies that the number of cubic stones as S with the side length of a_0' are moved over the width of a_0'. The condition under which S takes the value between 1 and 3 is referred to as a no damage condition.

(2) Resonance on a slope

Bruun et al. (1976) pointed out that the wave resonance phenomenon occurring on the slope of a rubble mound has a significant influence on its destruction. The resonance is defined as "the situation that occurs when run-down is in a low position and collapsing-plunging wave breaking takes place simultaneously and repeatedly at or close to the location." When the resonance occurs on the slope, the maximum water particle velocity on the slope, u_{max}, increases rapidly as shown in Fig. 4.12, where g is the acceleration of gravity, H_I the incident wave height, ξ the surf similarity parameter ($= \tan\alpha/\sqrt{H_I/L_0}$), α slope angle and L_0 wavelength in deepwater. Such a large velocity on the slope causes a large drag force on the stones.

As shown in Fig. 4.12, the water particle velocity on the slope is expressed as a function of the surf similarity parameter and the resonance occurs in the region $2<\xi<3$. This fact, which is not considered in the Hudson formula, suggests that the effect of the wave period must be taken into account in a design formula for rubble mound breakwaters. Figure 4.13 is an example that indicates the critical state of destruction for several failure ratios in the ξ-N_s plane. N_s is the stability number of rubble stones defined as

$$N_s = \frac{\rho_s^{1/3} H_D}{\rho_s/\rho - 1} W^{1/3} = (K_D \cot\alpha)^{1/3} \tag{4.20}$$

where H_D is the design wave height, ρ density of water and K_D the constant in the Hudson formula, Eq. (4.14). In Fig. (4.13), the lowest value of N_s for the same failure ratio lies in the region of resonance occurrence, $2<\xi<3$. Since N_s still depends on the slope angle and the friction factor between rubble stones, Ryu et al. (1986) proposed an alternate stability number N_s'

$$N_s' = N_s \tan\alpha/\tan\phi \tag{4.21}$$

where $\tan\phi$ is the angle of repose of the rubble stones.

(3) Critical destruction state for irregular waves

When designing rubble mound break waters using conventional design formulas, the selection of a statistical design wave height for irregular waves is one of the most important and difficult problems. Design engineers are often puzzled about which representative wave height should be used as the design wave height, $H_{1/3}$ or $H_{1/10}$. Figure 4.14 shows the correlation between the failure ratio D_a and the stability number N_s in the case of a 1:2 mound slope, where N_{sR} denotes the minimum N_s in the experiments for regular waves, and $N_{s1/3}$ and $N_{s1/10}$ indicate N_s calculated by using $H_{1/3}$ and $H_{1/10}$, respectively.
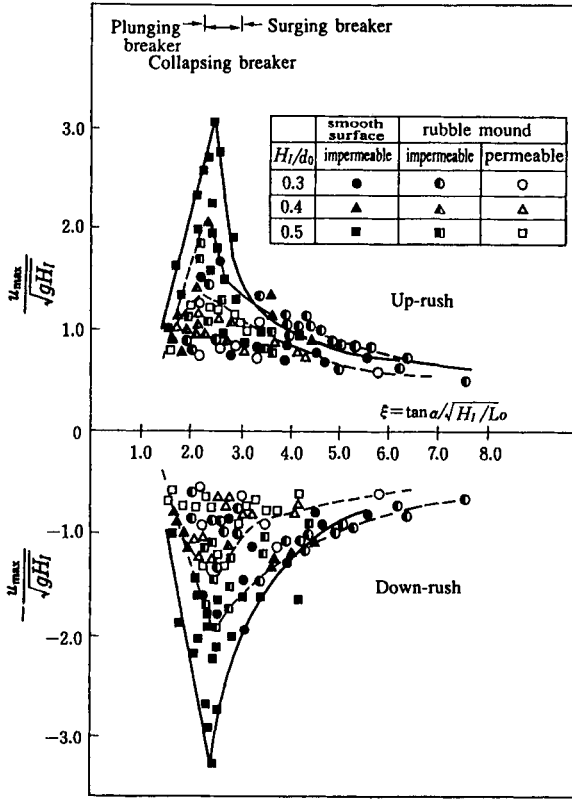
Fig. 4.12 Changes of the maximum water velocity on a slope with resonance
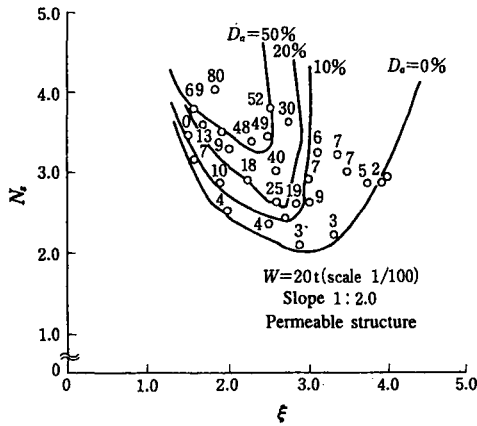
Fig. 4.13 Change of the stability numbers for rubble stones with resonance
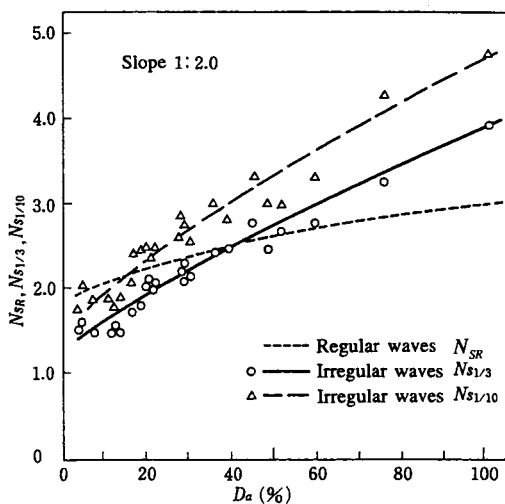
Fig. 4.14 Correlation between D_a and N_s for a 1:2 mound slope

Judging from this figure, the following problems can be pointed out, if $H_{1/3}$ is used as the design wave height for irregular waves:

(i) In the region $D_a < 40\%$, the rubble mound would be more unstable if we apply the results obtained for regular waves to irregular wave conditions.

(ii) In the region $D_a > 40\%$, the weight of the rubble stone would be overestimated if we apply the results for regular waves to irregular wave conditions.

Looking at the destruction process on rubble mound breakwaters in irregular waves, we notice that the rubble stones are moved by successive high waves instead of by a single high wave. The importance of such an interaction among successive high waves was mentioned above as a resonance. The properties of wave grouping should therefore be considered in a design formula for irregular waves.

(4) Influence of the wave action duration time on the destruction of rubble mound breakwaters

The effect of the wave action duration time has been investigated by various researchers. Van der Meer and Pilarczyk (1984) proposed the following equation for irregular waves:

$$S(N)/S(5000)=1.3[1-\exp(-3.10^{-4}N)]\approx 0.014\sqrt{N} \qquad (4.22)$$

where $S(N)$ is the failure ratio and N is the number of waves. They pointed out that the equilibrium state of a rubble mound deformation is established after the action of 5000 waves.

4.2.3 New design formula for rubble mound breakwaters

(1) New design formula

As shown in Fig. 4.13, the stability of rubble mound breakwaters strongly depends on the surf similarity parameters ξ. A run of irregular waves may also influence destruction,

as was mentioned in **4.2.2** (3). Furthermore, destruction occurs under the conditions where the wave height is larger than the critical wave height H_c, and may be effected by the run-sum of wave energy. In order to consider these factors, the following various definitions of run-length and run-sum are used in constructing a new design formula:

(i)   Conventional concept for a run of high waves

(ii) Run of ξ^* that satisfies the resonance condition $(2< \xi^* <3)$

(iii) Conditional run of ξ^* under the condition that the incident wave height H_I is larger than the   critical wave height H_c

(iv) Run of ξ_0^* that corresponds to the breaking condition on the steep slopes $(1.5<\xi_0^*<2.5)$

(v)   Conditional run of ξ_0^* under the condition $H_c<H_I$

Here, $\xi_0^*=\xi/\xi_0$, $\xi=\tan\alpha/\sqrt{H_I/L_0}$, $\xi_0=2.65\,\tan\alpha$ (breaking condition) and α is the angle of the slope. We here define the mean run-sum E_{sum} as the mean energy-sum of an irregular wave train

$$E_{\text{sum}} = \frac{\sum_{j=1}^{\infty}\frac{1}{8}\rho g\left(\sum_{i=1}^{\infty}H_{ij}^2 N_j\right)}{\sum_{j=1}^{\infty}N_j} \tag{4.23}$$

where N_j is the run number of the run length j $(j=1,2,...)$ (see **1.3.2**) and H_i denotes the i-th wave height in a run of run-length j. The relation between the mean run sum and the mean run length $\bar{j}$ was investigated by experiments for the various definitions of run, and the following relation was obtained by Ryu et al. (1986).

$$\frac{E_{\text{sum}}\,j\left(\xi_0^*\big|_{H_{1/3}}\right)}{\frac{1}{8}\rho g H^2_{1/3}}=1.78\,\overline{j\left(\xi_0^*\big|_{H_{1/3}}\right)}-0.44 \tag{4.24}$$

E_{sum} in Eq. (4.24) and the mean run length j are closely related to the spectrum peakedness parameter Q_p regardless of the value of $\tan\alpha$. From the experimental results, these relationships are expressed as follows:

$$E_{\text{sum}}j(\xi_0^*\big|_{H_{1/3}})=\rho g H^2_{1/3}(0.04Q_p+0.13)\quad\text{for }H_c=H_{1/3} \tag{4.25}$$

$$\overline{j(\xi_0^*\big|_{H_{1/3}})}=\frac{3}{16}Q_p+0.81 \tag{4.26}$$

$$Q_p=\frac{2}{m_0}\int_0^\infty f E^2(f)\,df \tag{4.27}$$

Here f denotes frequency, $E(f)$ is energy spectrum density, and m_0 is the 0th order moment of the spectrum defined as $\int_0^\infty E(f)df$. The relation between the failure ratio D_a and E_{sum} is obtained through experiments

$$D_a = 153.8 \left[\frac{E_{\text{sum}} j\left(\xi_0^* \big|_{H_{1/3}}\right)}{\rho_s g l_a^2} \frac{\tan\alpha}{\tan\phi} \right] - 30.1 \quad \text{for uniform slope}$$

$$D_a = 136.4 \left[\frac{E_{\text{sum}} j\left(\xi_0^* \big|_{H_{1/3}}\right)}{\rho_s g l_a^2} \frac{\tan\alpha'}{\tan\phi} \right] - 36.3 \quad \text{for composite slope}$$

$$(4.28)$$

Here l_a is a representative diameter of rubble stones, ϕ is the repose angle of rubble stones in water, α' is the equivalent slope angle for the composite slope estimated by the Saville method, and ρ_s is the density of rubble stones. If the rubble stones are spherical, the weight of a rubble stone W is expressed as

$$W = \rho_s g l_a^3.$$

Using Eqs. (4.24) - (4.28), the weight of a rubble stone W is expressed as follows:

$$W = \left[\frac{\rho g (6.15 Q_p + 20.0)}{(\rho_s g)^{1/3}(D_a + 30.1)} \frac{\tan\alpha}{\tan\phi} \right]^{3/2} H_{1/3}^3 \quad \text{for uniform slope} \qquad (4.29)$$

$$W = \left[\frac{\rho g (5.46 Q_p + 17.73)}{(\rho_s g)^{1/3}(D_a + 36.3)} \frac{\tan\alpha'}{\tan\phi} \right]^{3/2} H_{1/3}^3 \quad \text{for composite slope} \qquad (4.30)$$

Equation (4.30) is obtained for the composite slope under the condition that the length of the horizontal part l_B in Fig. 4.6 is equal to $L_p/4$ and the water depth of the horizontal part h_2 is in the region of $0.4 H_{1/3} < h_2 < 0.7 H_{1/3}$ where L_p is the wavelength corresponding to the peak frequency of the wave spectrum.

The relation between W and Q_p calculated from Eqs. (4.29) and (4.30) is shown in Fig. 4.15. The weight of a rubble stone depends not only on the wave height but also on the peakedness of the wave spectrum. Furthermore, we should notice that the composite slope is more than the uniformed slope. If we let $E(f)$ in Eq. (4.27) be the Bretschneider type spectrum, Q_p becomes 2.0. According to field observations in Japan, Q_p shows nearly 2.0 for the ordinary wave condition in the off shore region, whereas it shows 1.0 to 1.5 near the breaking point. Thus the estimation of Q_p at the construction site is important for designing rubble mound breakwaters.

(2) Comparison of the new design formula with the Hudson formula

Figure 4.16 shows the comparison of the weight of a rubble stone calculated from both the new design formula and the Hudson formula. Predicted results using the new formula give the relation between W and D_a in the case where Q_p=2.5, $H_{1/3}$ = 7 m and the slope of the rubble mound is 1:2.3. Calculated results using the Hudson formula are also plotted as a function of D_a, since the value of K_D in Eq. (4.14) is supposed to vary with D_a. It is obvious from this figure that the Hudson formula predicts a smaller weight for a rubble stone than the proposed formula, which means that the rubble mound breakwater designed using the Hudson formula may not be stable under this wave condition. However, since the

Hudson formula is usually used with $D_a = 0$, the estimation using the new formula with D_a = 20% gives a similar stone weight as that derived from the Hudson formula. The failure ratio for the practical design must therefore be discussed further. Figure 4.16 also suggests that the composite section be useful to reduce the weight of the rubble stone.
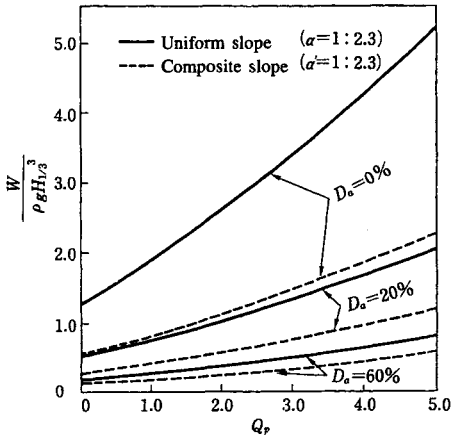
Fig. 4.15 Relation between W and Q_p for various values of D_a
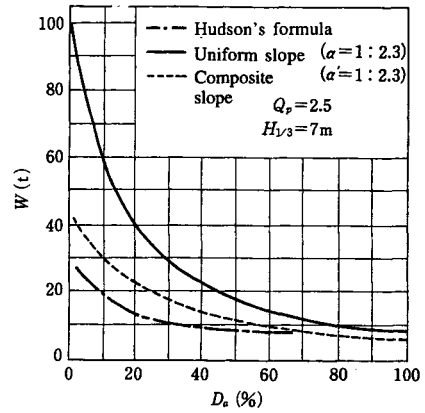
Fig. 4.16 Comparison between the new design formula and the Hudson formula

The percolation effect of the filter layer under the revetment was discussed by various researchers regarding the stability of rubble mound breakwaters. They reported that rubble mound breakwaters became more stable when the filter layer is constructed of a homogeneous material. Furthermore, the research of the stability of rubble mound breakwaters is being advanced making use of the probabilistic design for the construction of structures (Nielsen et al. 1983; Le Mehaute et al. 1985; Van der Meer et al. 1987). However, the destruction mechanism must first be fully investigated to apply a reliability design to rubble mound breakwaters, since the reliability design requires a certain destruction standard function for a structure.

4.3 Composite Breakwaters

As construction of breakwaters extends into deepwater, the breakwaters must become larger to withstand probable high waves, which means that the rubble mound breakwaters mentioned in **4.2** require a huge amount of large rubble stones. Composite breakwaters, which consist of a rubble mound foundation and an upright section such as a concrete caisson placed on the foundation, can reduce the size and the number of rubble stones and have the advantages of both the vertical and the rubble mound breakwaters. Since the end of the 19th century, this type of breakwater has been commonly used along the coast of Japan for geological reasons.

4.3.1 Wave pressure formulas for the composite breakwaters
Wave pressure formulas for the vertical breakwater have been proposed by many researchers such as Sainflou, Minikin and Hiroi. These are classified as formulas for breaking waves and for non-breaking waves, and it is pointed out that the wave pressure

abruptly changes at the boundary point of the two pressure formula categories. Furthermore, in an actual random wave condition we cannot determine if the waves are in a breaking or non-breaking state because an irregular wave train has various combinations of wave height and period. Therefore, a universal formula covering both breaking and non-breaking wave pressures must be established for the practical design.

Goda (1974) proposed a new wave pressure formula for the composite breakwater resolving the above mentioned problems through a large number of hydraulic model tests. The Goda formula assumes that the trapezoidal pressure distribution as shown in Fig. 4.17 and the representative pressures are given as

$$p_1 = \frac{1}{2}(1 + \cos\theta)(\beta_1 + \beta_2 \cos^2\theta)\rho g H_{max} \tag{4.31}$$

$$p_2 = \frac{p_1}{\cosh 2\pi h/L} \tag{4.32}$$

$$p_3 = \beta_3 p_1 \tag{4.33}$$
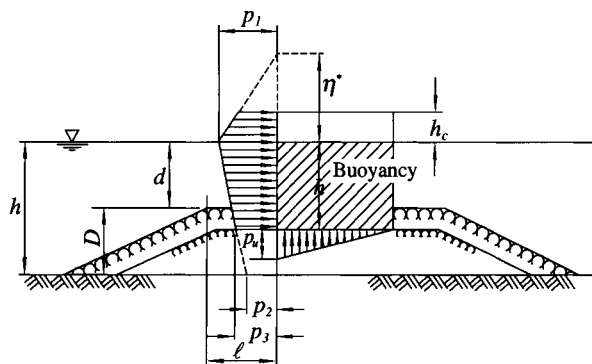
Fig. 4.17 Distribution of wave pressure on an upright section of a vertical breakwater (after Goda 1974)

in which

$$
\left.
\begin{aligned}
\beta_1 &= 0.6 + \frac{1}{2}\left[\frac{4\pi h/L}{\sinh 4\pi h/L}\right]^2 \\
\beta_2 &= \min\left\{\frac{h_0 - d}{3h_0}\left(\frac{H_{max}}{d}\right)^2, \frac{2d}{H_{max}}\right\} \\
\beta_3 &= 1 - \frac{h'}{h}\left[1 - \frac{1}{\cosh 2\pi h/L}\right]
\end{aligned}
\right\} \tag{4.34}
$$

where min $\{a,b\}$ gives the smaller of a or b, and h_0 is the water depth at the location a distance $5H_{1/3}$ seaward of the breakwater. As shown in these equations, this formula takes into account the effect of the angle of wave incidence θ, the angle between the normal line to a breakwater and the wave direction. In Fig. 4.17, h is the water depth in front of the breakwater, d the depth above the rubble mound, D the height of the rubble mound, l the distance between the foot of the mound and the front upright section, and h' the height from the design water level to the bottom of the upright section. The elevation to which the wave pressure, η^*, is given as

$$\eta^* = 0.75(1 + \cos\theta)H_{max} \tag{4.35}$$

As shown in Eqs. (4.31) - (4.35), the highest wave height H_{max} is used as a design wave height. H_{max} is estimated either by the relation $H_{max} = 1.8H_{1/3}$ in the region outside the surf zone or by the following equations within the surf zone:

$$H_{max} = \begin{cases} 1.8K_s(H_{1/3})_0' & \text{for } h/L_0 \geq 0.2 \\ \min\left\{\left(\beta_0^*(H_{1/3})_0' + \beta_1^* h\right), \beta_{max}^*(H_{1/3})_0', 1.8K_s(H_{1/3})_0'\right\} & \text{for } h/L_0 < 0.2 \end{cases} \tag{4.36}$$

in which

$$\left. \begin{aligned} \beta_0^* &= 0.052\left\{(H_{1/3})_0'/L_0\right\}^{-0.38} \exp\left[20\tan^{1.5}\beta\right] \\ \beta_1^* &= 0.63\exp[3.8\tan\beta] \\ \beta_{max}^* &= \max\left[1.65, 0.53\left\{(H_{1/3})_0'/L_0\right\}^{-0.29} \exp(2.4\tan\beta)\right] \end{aligned} \right\} \tag{4.37}$$

where H_{max} is estimated at the location a distance $5H_{1/3}$ seaward of the surf zone. $(H_{1/3})_0'$ the equivalent deepwater significant wave height, K_s the shoaling coefficient, β the slope angle between the sea bottom and the horizontal plane and max $\{a,b,c\}$ indicates the largest among a, b and c. $(H_{1/3})_0'$ is a hypothetical wave height that may have undergone reflection, diffraction and is given by

$$(H_{1/3})_0' = K_d K_R (H_{1/3})_0 \tag{4.38}$$

where K_R and K_d denote the coefficients of irregular wave refraction and diffraction, respectively. L_0 in Eq. (4.37) is the deepwater wavelength corresponding to the significant wave period $T_{1/3}$.

4.3.2 Effect of the rubble mound foundation

Using the rubble mound foundation gives the following advantages in constructing vertical breakwaters:
(i)   easy construction on an uneven sea bottom
(ii) decreasing the incident wave height to the upright section by virtue of the wave breaking on the mound.

(iii) protecting the foot of the breakwater from scouring

In the following section, the second item mentioned above will be discussed further.

(1) Attenuation of the reflected coefficient

Observing the wave height distribution in front of a composite breakwater, attenuation of the wave height and phase lag between incident and reflected waves are indicated. Figure 4.18 shows the influence of the mound height D and the mound length l on the reflection coefficient of the composite breakwater K_R (Sawaragi et al. (1986)). This figure shows that the effect of D/h on the attenuation of K_R is remarkable especially in the region $D/h \geq 2/4$, where the reflection coefficient approaches to that of a rubble mound breakwater, 0.2. On the other hand, the effect of l/L is not as much as that of D/h, but the effect of l/L is also clear in the region $D/h \geq 2/4$.
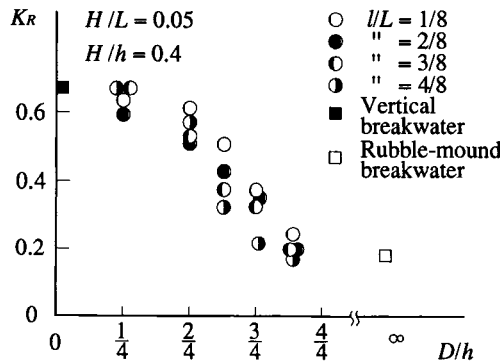
Fig. 4.18 Effect of D/h on the attenuation of K_R

In the case of non-breaking waves, the wave profile of standing waves in front of the composite breakwater is calculated by a similar method to that used for the rubble mound breakwater by using Eq. (4.12). In the calculation, the reflection coefficient K_{R2} and the transmission coefficient K_{T2} of the upright section can be assumed to be 1 and 0 respectively, and the phase lags due to reflection and transmission, ε_{R2} and ε_{T2}, may be 0. For K_{R1} and K_{T1} in Eq. (4.12), as mentioned in **4.2.1**, we can use the experimental results for a submerged breakwater with a semi-infinite crown width or the theoretical solution for the wave transformation over the discontinuous bottom profile based on the potential theory. On the other hand, ε_{R1} can be estimated by calculating the travelling time Δt of the incident and reflected waves over the mound width

$$
\left.
\begin{aligned}
\Delta t &= \left\{ 2 \times \frac{1}{s} \times (h-d) \middle/ 2 \right\} \middle/ c \\
\varepsilon_{R1} &= 2\pi \Delta t / T
\end{aligned}
\right\}
\tag{4.39}
$$

Here s is the slope of the mound foundation. The phase lag due to transmission ε_{T1} can be assumed to be 0. Furthermore, the estimation of the damping coefficient due to percolation can be referred to in **4.4**.

(2) Stability of the rubble mound foundation

The weight of a rubble stone from the mound foundation is often estimated through the experimental results of Brebner and Donnely (1962). Japanese harbor engineers have also used the following formula based on many field observations.

$$
\left.\begin{aligned}
W &= W_0 \times 5^{-d/H} \\
W_0 &= 0.08 H^3
\end{aligned}\right\}
\tag{4.40}
$$

4.4 Submerged Breakwaters with a Wide Crown Width (Artificial Reef)

In Japan, offshore detached breakwaters have been widely used to provide protection against natural disasters such as beach erosion, wave overtopping and so on, since they effectively reduce and absorb incident wave energy. The powerful effects of detached breakwaters on wave transformation, especially the effect of diffraction greatly affects the surrounding coast. It has also been pointed out that the breakwaters reduce the exchange of sea water behind them and that they often detract from the natural coastal landscape.

Recently, with the increasing concern for the preservation of coastal environments and easier access to the shoreline and with demands for improved waterfront, new forms of coastal protection works have been devised. To cope with these demands, detached breakwaters are being replaced by submerged breakwaters, which are often referred to as artificial reefs.

The reasons why submerged breakwaters were not widely used before are as follows: 1) the crown width of the breakwater must be wide enough to reduce incident wave height significantly, which makes the breakwaters more expensive, 2) the efficiency of the breakwater to reduce wave height in the region of a large tidal range depends on the tidal level because the function of the breakwater is limited by the crown height, and 3) the submerged breakwaters themselves become an obstacle for small vessels, such as fishing boats.

The submerged breakwaters mentioned above are usually constructed to reduce incident wave energy so that they can control sediment movement in a shallow water region. There are two kinds of energy displacement mechanisms that attenuate wave height. First, energy is dissipated when waves break due to an abrupt change in the water depth when they meet the submerged breakwaters. Secondly, energy dissipation takes place on the surface of and in the permeable layer of the submerged breakwater.

The rate of the second energy dissipation is estimated by applying the Darcy non-linear unsteady law for fluid motion in the permeable layer. In the following, an analytical expression for the attenuation of wave height is derived based on a wave theory for the permeable layer (Deguchi et al. 1988). The applicability of the procedures is also discussed through experiments.

4.4.1 Wave attenuation on a permeable layer
(1) Unsteady fluid in a permeable layer

Fluid motion in a permeable layer of the large permeability K_p, whose dimension is (length)^2 and void ratio λ, is expressed as follows:

$$
\left(\frac{1}{\lambda} + \frac{1-\lambda}{\lambda} C_m\right) \frac{\partial u_d}{\partial t} = -\frac{1}{\rho} \nabla P_d - \frac{\nu}{K_p} u_d - \frac{\alpha C_f}{\sqrt{K_p}} u_d^{\,2}
\tag{4.41}
$$

where u_d is the macroscopic velocity, C_m is the added mass coefficient of the rubble stones, ∇P_d is the pressure gradient in the permeable layer, C_f is the turbulent drag coefficient in a steady flow, ρ and v are the density and kinematic viscosity of the fluid, and α is the coefficient that indicates the difference of the turbulent drag coefficients between steady and unsteady flows. The values of K_p, C_m, C_f, and α are determined by conducting permeability tests under steady and unsteady conditions.

Equation (4.41) contains a nonlinear term. In the analysis of wave motion on and through the permeable layer, Eq. (4.41) is usually linearized by using the Lorentz law of equivalent work in the following form (Sollitt et al., 1972):

$$S_M \frac{\partial u_d}{\partial t} = -\frac{1}{\rho} \nabla P_d - \frac{v}{K_{pe}} u_d \qquad (4.42)$$

where $S_M=(1+(1-\lambda)C_m)/\lambda$ and K_{pe} is the equivalent linear permeability.

Another procedure to linearize Eq. (4.41) is to use an equivalent linear drag coefficient f (Deguchi, et al., 1988), which is defined as

$$f\sigma = \frac{v}{K_p} + \frac{\alpha C_f}{\sqrt{K_p}} u_d \qquad (4.43)$$

where σ is the angular frequency ($=2\pi/T$). The value of f can be determined from the permeability test by applying the law of equivalent work.

Deguchi et al. (1988) obtained the following empirical expression for f from the unsteady permeability tests for the crashed stones of the mean diameters $D=1.3$cm and 3.3cm:

$$f = \left(K_{pe}\,\sigma/v\right)^{-1} = \left[10.5 + 50.0\left(a_\delta/d_{50}\right)\right]R_d^{-1/2} \qquad (4.44)$$

where a_δ/d_{50} is the KC number ($=|u_d|/\sigma d_{50}$), a_δ is the excursion length of the water particle, d_{50} is the diameter of rubble stone, R_d is the Reynolds number ($|u_d|d_{50}/v$) and $|u_d|$ is the amplitude of the water particle velocity in the permeable layer.

By introducing Eq. (4.43), Eq (4.41) is written as

$$S_M \frac{\partial u_d}{\partial t} = -\frac{1}{\rho} \nabla P_d - f\sigma u_d \qquad (4.45)$$

Eq. (4.42) or Eq. (4.45) becomes a fundamental equation for the fluid motion in the permeable layer.

(2) Governing equation for waves on the permeable layer

Deguchi et al. (1988) have already derived a nonlinear wave theory which corresponds to the Stokes 2nd order waves on the permeable layer. Here, only the first order wave

theory is introduced with respect the coordinate system shown in Fig. 4.19 where h is the depth at the permeable layer, d_a is the thickness of the permeable layer and η is the surface displacement.
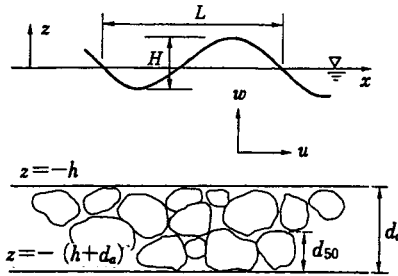
Fig. 4.19 Co-ordinate system

Fluid motion on the permeable layer is fundamentally irrotational and is expressed by the Laplace equation.

$$\nabla^2 \phi = 0 \tag{4.46}$$

Water particle velocities u, w, and pressure on the permeable layer p are expressed using ϕ as follows:

$$u = \partial \phi / \partial x, \partial \phi / \partial z \tag{4.47}$$

$$p / \rho = -\partial \phi / \partial t + gz \tag{4.48}$$

Fluid motion in the permeable layer is expressed by the linearized non-linear, unsteady Darcy law and an equation of continuity in the following forms:

$$\left. \begin{array}{l} S_M \dfrac{\partial u_d}{\partial t} = -\dfrac{1}{\rho} \dfrac{\partial P_d}{\partial x} - \dfrac{\nu}{K_{pe}} u_d \\[3mm] S_M \dfrac{\partial w_d}{\partial t} = -\dfrac{1}{\rho} \dfrac{\partial P_d}{\partial z} - \dfrac{\nu}{K_{pe}} w_d \end{array} \right\} \tag{4.49}$$

$$\frac{\partial u_d}{\partial x} + \frac{\partial w_d}{\partial z} = 0 \tag{4.50}$$

Fluid motion in the permeable layer is also assumed to be irrotational. Therefore, the water particle velocity in the permeable layer is expressed as follows:

$$u_d = \frac{\sigma K_{pe}}{v} \frac{\partial \phi_d}{\partial x} \quad \text{and} \quad w_d = \frac{\sigma K_{pe}}{v} \frac{\partial \phi_d}{\partial z}$$

(4.51)

Substituting Eq. (4.51) with Eqs. (4.49) and (4.50), the following fundamental equation for water particle motion in the permeable layer is obtained.

$$\nabla^2 \phi = 0$$

(4.52)

$$\frac{P_d}{\rho} = -\sigma \phi - S_M \frac{\sigma K_{pe}}{v} \frac{\partial \phi}{\partial t}$$

(4.53)

These equations are solved analytically under the boundary conditions at the free water surface, $z = \eta \ (= 0)$, on the surface of the permeable layer, $z = -h$, and at the bottom, $z = -(h + d_a)$. These conditions are expressed as follows:

On the free water surface, $z = \eta$ (as far as the linear wave theory is concerned, these conditions are applied at $z = 0$):

$$\frac{\partial \phi}{\partial z} = \frac{\partial \eta}{\partial t} \quad : \text{kinematic condition}$$

(4.54)

$$\eta = -g \frac{\partial \phi}{\partial t} \quad : \text{dynamic condition}$$

(4.55)

Here g is the acceleration of gravity.
On the surface of the permeable layer, $z = -h$:

$$P = P_d \qquad\qquad\qquad : \text{continuity of pressure}$$

(4.56)

$$u = u_d, w = w_d/\lambda \qquad\quad : \text{continuity of velocity}$$

(4.57)

$$\frac{\partial u}{\partial z} = \frac{1}{\lambda} \frac{\partial u_d}{\partial z}, \frac{\partial w}{\partial z} = \frac{1}{\lambda} \frac{\partial w_d}{\partial z} \quad : \text{continuity of velocity gradient}$$

(4.58)

At the bottom, $z = -(h+d_a)$:

$$w_d = 0$$

(4.59)

(3) Waves on the permeable layer
When the surface displacement is given by the sinusoidal function with an amplitude expressed by Eq. (4.60), the velocity potential ϕ is given by Eq. (4.61).

$$\eta = a \mathrm{Real}\left[\exp\left\{i\left(k^*x - \sigma t\right)\right\}\right] \tag{4.60}$$

$$
\begin{aligned}
\phi &= \frac{ga}{\sigma}\mathrm{Real}\left[i\left\{\cosh k^*z - \frac{1}{k^*}\sinh k^*z\right\}\exp\left\{i\left(k^*z - \sigma t\right)\right\}\right] : z = -h \\
&= \frac{ga}{\sigma}\mathrm{Real}\left[\left\{\frac{i}{i + \gamma S_M}\cosh k^*(h+z)\left(\cosh k^*h + \frac{1}{k^*}\sinh k^*h\right)\right.\right. \\
&\quad \left.\left. -\frac{1}{\gamma}\sinh k^*(h+z)\left(\sinh k^*h + \frac{1}{k^*}\cosh k^*h\right)\right\}\exp\left\{i\left(k^*x - \sigma t\right)\right\}\right] : -h \geq z \geq -(h + d_a)
\end{aligned}
\tag{4.61}
$$

where Real [ ] means a real part in a complex quantity in [ ], $i = \sqrt{-1}$, a is the amplitude of the incident wave and γ is the nondimensional permeability ($=K_{pe}\,\sigma/v$). The complex wave number k^* satisfies the following dispersion relation:

$$\sigma^2 = gk^* \frac{(\gamma S_M + i)\sinh k^*h\cosh k^*d_a + \gamma\cosh k^*h\sinh k^*d_a}{(\gamma S_M + i)\cosh k^*h\cosh k^*d_a + \gamma\sinh k^*h\sinh k^*d_a} \tag{4.62}$$

4.4.2 Effects of the permeable layer on wave attenuation

Let α and β be the real and imaginary parts of k^*, then waves on the permeable layer are expressed by

$$\eta = a\mathrm{Real}\left[\exp\left\{i(\alpha + \beta i)x - \sigma t\right\}\right] = a\exp(-\beta x)\cos(\alpha x - \sigma t) \tag{4.63}$$

This means that the non-negative imaginary part β of the wave number k^* becomes a wave attenuation factor. The following quantities will affect the wave attenuation factor; density of the fluid ρ, kinematic viscosity of the fluid v, gravity acceleration g, amplitude of incident waves a, wave period T, depth of the permeable layer h, thickness of the permeable layer d_a, mean diameter and density of the rubble stone from the permeable layer d_{50}, and ρ_s, and the void ratio of the permeable layer λ. Here, the equivalent linear permeability k_p (or equivalent linear drag coefficient f) instead of d_{50} and ρ_s are used to express the properties of the permeable layer. The value of β is expressed by the following nondimensional parameter using dimensional analysis

$$\beta = f\left(\sigma^2 a/g,\ \sigma^2 h/g,\ d_a/(h + d_a),\ \gamma\left(= k_{pe}\,\sigma/v\right)\text{ or } f,\ \lambda\right)$$

If one will evaluate wave attenuation based on Eq. (4.41) by applying the Lorentz law of equivalent work, the turbulent drag coefficient C_f must be added. Among these 6 variables, the value α has nothing to do with the property of the permeable layer and the void ratio is almost constant.

Figures 4.20 and 4.21 illustrate how the values of $\sigma^2 h/g$, $d_a/(h+d_a)$ and γ affect the nondimensional wave attenuation rate $\beta'(=\beta/(g/\sigma^2))$ calculated from Eq. (4.41) in the cases of C_f=0.0, 0.1 and 0.2.
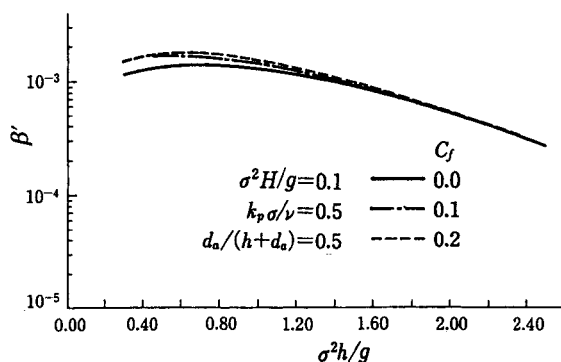
Fig. 4.20 Relation between β' and $\sigma^2 h/g$
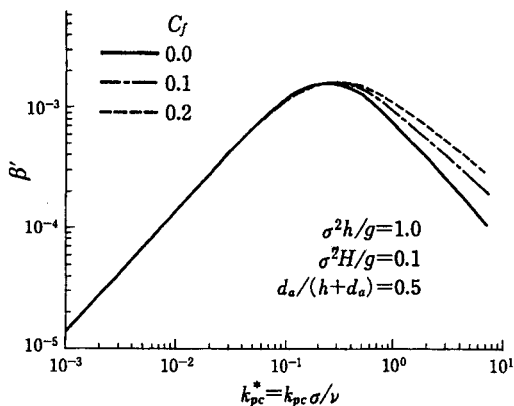
Fig. 4.21 Relation between β' and γ

From these figures, it is found that the value of β' is less influenced by C_f. The value of $d_a/(d_a + h)$ has little influence on β' in the region of $0.8 < d_a/(d_a + h)$. It is also seen that the value β' becomes the maximum at a certain value of γ implying that there exists the optimum value of permeability to attenuate wave height effectively.

4.4.3 Wave controlling function of submerged breakwaters

(1) Calculation of wave transformation through a submerged breakwater based on energy conservation

In this section, wave theory on the permeable layer derived in **4.4.2** is applied to the calculation of wave transformation through the submerged breakwater. Some numerical
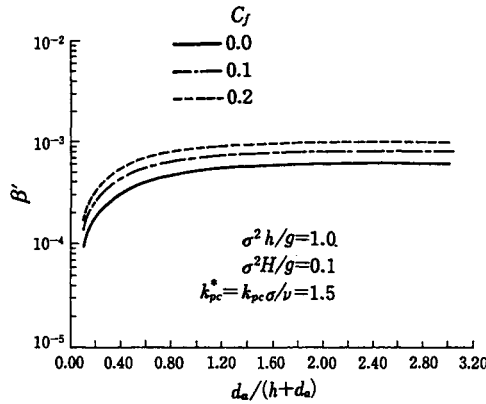
Fig. 4.22 Relation between β' and d_a/h

procedures for predicting wave transformation using the unsteady mild slope equations which have been proposed (by Izumiya et al. 1989 and others). In this section, a numerical procedure is proposed based on an equation of energy conservation to effectively predict wave field around the submerged breakwater, where the effects of wave shoaling, refraction and breaking are taken into account. The wave energy loss on the submerged breakwater is estimated from the wave attenuation rate on the permeable layer which is derived in the previous section.

Wave energy loss caused by the permeability of the submerged breakwater and a boundary friction per unit length and unit time, D_p and D_f are expressed as follows:

$$D_p = -\frac{1}{T}\int_0^T \left(wp\right)_{z=-h} dt \tag{4.64}$$

$$D_f = \frac{2}{T}\int_0^{T/2} \tau_0 u_{z=-h} dt \tag{4.65}$$

where w is the vertical water particle velocity and τ_0 is the boundary shear stress on the surface of the submerged breakwater which is roughly estimated from the Jonsson's expression.

Substituting w and p calculated from the velocity potential Eq. (4.48), D_p becomes

$$D_p = \rho g H^2 c_g \beta / 4 \tag{4.66}$$

where c_g is the group velocity. When the horizontal water particle velocity on the submerged breakwater u is approximated by that of a linear wave at the bottom of the same depth as the crown depth, D_f is expressed using a friction factor f_w as follows:

$$D_f = \frac{2}{3}\pi^2 \rho f_w \left(\frac{H}{T\sinh kh}\right)^3 \tag{4.67}$$

The total energy loss for incident waves D is the sum of this energy loss. Furthermore, when the incident waves break on the submerged breakwater, energy loss by wave breaking D_b must be added to D. Using this expression of energy loss, the equation of energy conservation in a steady state is expressed as

$$\frac{\partial}{\partial x}E(c_g\cos\theta+U)+\frac{\partial}{\partial y}E(c_g\sin\theta+V)+S_{xx}\frac{\partial U}{\partial x}+S_{xy}\left(\frac{\partial V}{\partial x}+\frac{\partial U}{\partial y}\right)+S_{yy}\frac{\partial V}{\partial y}=-D \quad (4.68)$$

where S_{xx}, S_{xy}, and S_{yy} are the radiation stresses expressed by Eq. (1.73), (U,V) are the depth averaged mean current velocities in x and y directions, and θ is the angle of wave incidence.

(2) Critical depth on the submerged breakwater for wave breaking

Figure 4.23 shows the critical condition for the occurrence of the forced wave breaking on the submerged breakwater plotted by using experimental results. The vertical axis is the non-dimensional crown depth of the submerged breakwater R/H_I and the horizontal axis is the nondimensional depth at the foot of the submerged breakwater h/L_I. The steepness of the experimental waves ranged from 0.004 to 0.051 and the ratio for the crown depth and height of the submerged breakwater R/d_a ranged between 0.55 and 0.7. The forced wave breaking took place in the region of $R/H_I < 1.6$ regardless of the values for the steepness and for R/d_a.

(3) Two-dimensional wave transformation on a permeable layer and submerged breakwater

Figure 4.24 illustrates the calculated wave height distribution on the permeable layer from Eq. (4.68) together with the measured wave height in the experiment. The incident
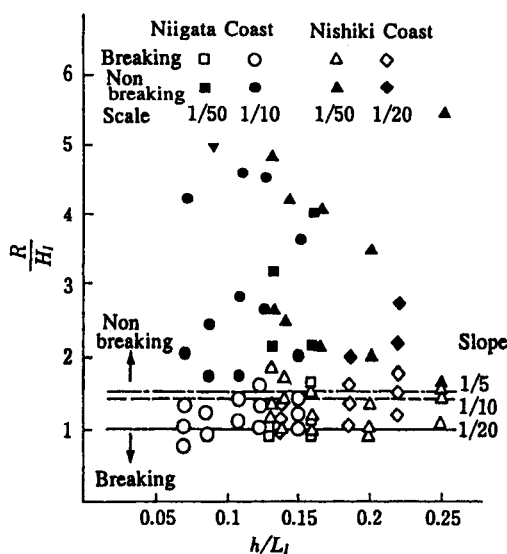
Fig. 4.23 Critical condition on the submerged breakwater for wave breaking
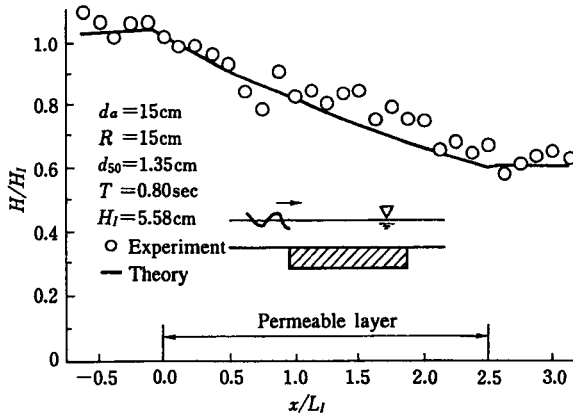
Fig. 4.24 Effect of wave attenuation due to the permeable layer

wave height decreased by approximately 60% on the permeable layer with the length $2.5L_I$ in the experiment, where L_I is the incident wavelength and the calculated wave height coincides well with the measured wave height.

Figures 4.25 and 4.26 show the comparisons of measured wave height and calculated wave height with and without the boundary shear stress on the submerged breakwaters. Incident waves did not break in the case of Fig. 4.25 and forced wave breaking took place on the submerged breakwater in the case of Fig. 4.26. The energy loss after wave breaking in the case of Fig. 4.26 was evaluated by the expression proposed by Sawaragi et al. (1989) (see **1.2.6**). It was found through these figures that wave transformation through submerged breakwaters can be predicted by Eq. (4.68) as a whole even in the case where the forced wave breaking takes place on the breakwater.
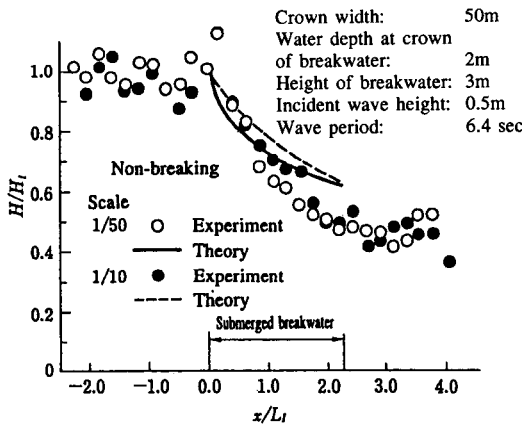
Fig. 4.25 Wave height attenuation on the submerged breakwater (in the case of non-breaking)
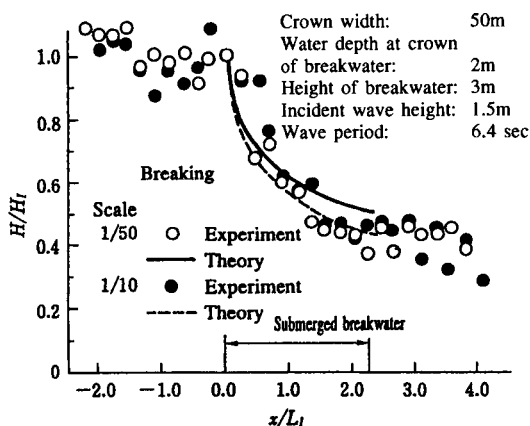
Fig. 4.26 Wave height attenuation on the submerged breakwater (in the case of breaking)

Next the effect of a submerged breakwater on wave shoaling, refraction, breaking in a shallow water region and the resulting wave set-up and wave-induced current are discussed. As mentioned in **4.3.2**, wavelength changes on the permeable layer and as a result, wave refraction takes place.

In Fig. 4.27, cross-shore distribution of wave height and mean water level on the natural beach without the submerged breakwater are also shown. Wave height on the submerged breakwater decreased significantly and mean water level on the submerged breakwater corresponds to the distribution of wave height. Although wave height decreased significantly on the submerged breakwater when compared with that of the natural beach, wave set-up at the shoreline for both cases became almost the same.

4.4.4 Reduction of wave overtopping by the use of an artificial reef

To cope with wave overtopping from existing seawalls and sea dikes, various kinds of wave energy dissipating structures such as an offshore detached breakwater, wave energy absorbing blocks and so on have been constructed. The highest priority has been given to the wave energy dissipating function of these structures and utilizing the natural coastal view has been left out of the considerations. Recently, the artificial reef has been widely used as a multi-purpose coastal structure for controlling incident wave energy and coastal erosion and for utilizing coastal zones to their best advantage. It is needless to say that the artificial reef serves the function of reducing wave overtopping from the existing seawalls and sea dikes.

In this section, the effect of the artificial reef, which consists of the submerged breakwater and an artificial nourishment on the shoreward side, to reduce wave overtopping from the existing seawalls and sea dikes, is discussed. However, in this section, the effect of the permeability of the artificial reef is not taken into account. Therefore, the wave controlling function of the artificial reef comes only from the forced breaking of incident waves.

(1) Effect of the artificial reef on wave overtopping

The wave overtopping rate from the seawalls and sea dikes on uniformly sloping beaches has been studied by many researchers under various conditions. Most of these results are
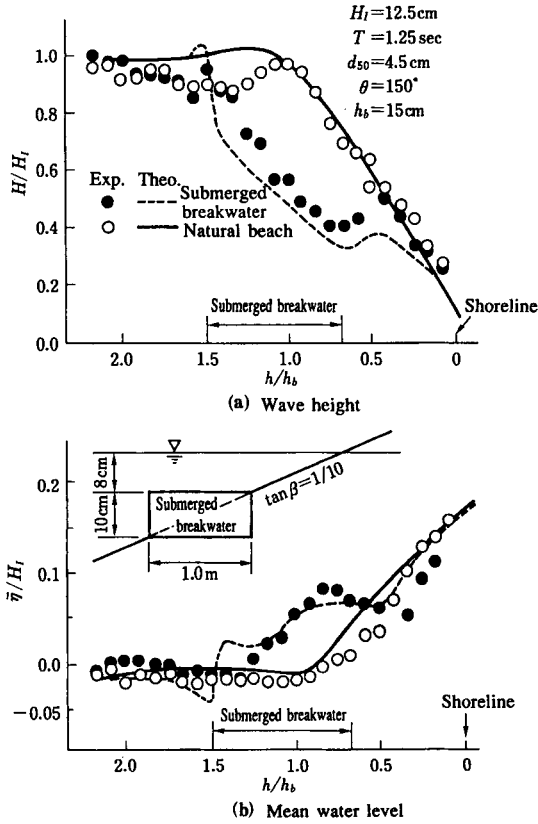
Fig. 4.27 Cross-shore distribution of wave height and mean water level on the submerged breakwater

analysed using wave conditions in deepwater regions. A crest elevation of a surface displacement and the crown height of the seawall are also measured from the still water (for example, Goda (1985) and CERC (1984)). Therefore, the effect of the artificial reef cannot be discussed based on their results because incident waves in front of the seawalls are greatly changed by the reefs.

Let q be the wave overtopping rate from the seawall shown in Fig. 4.28. The non-dimensional wave overtopping rate $q^*(= q/(\sqrt{gL_i}\,H_i))$ is expressed by the following expression through dimensional analysis:

$$q^* = f\left(\frac{H_c}{H_i}, \frac{H_I}{h_i}, \frac{H_I}{L_I}, i, \alpha, f_s\right) \tag{4.69}$$

where H_I and L_I are the incident wave height and wavelength in front of the seawall, h_i and H_c are the depths at the foot of seawalls and the crown height of the seawalls measured from the mean water level, i is the slope of the artificial reef in front of the seawalls, α

is the slope of the seawall and f_s is the parameter indicating the condition at the location of the seawall.
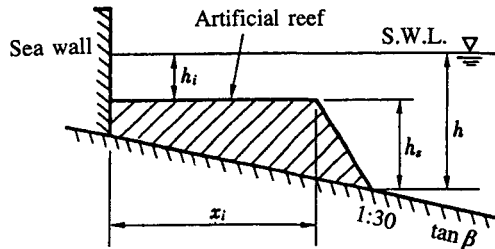
Fig. 4.28 Sketch of the artificial reef

Figure 4.29 illustrates reanalyzed results of the existing data of the wave overtopping from seawalls on natural beaches without artificial reefs, based on Eq. (4.69). In the cases where the values of H_I, h_i and H_c in Eq. (4.69) were not given, these values were estimated using the procedure for predicting two-dimensional wave transformation and mean water level which is introduced in Chapter 1. In this figure, the wave overtopping rate from the seawalls with the artificial reefs are also indicated using a different symbol.

It was discovered that the wave overtopping rate from the seawalls within the breaker zone q_b^* is larger than that from the seawalls outside the breaker zone q_c^*, where clapotis was formed in front of the seawall regardless of the steepness of the incident waves. All incident waves in front of the seawall with the artificial reef q_r^* were less than that in the breaker zone.

Figure 4.30 shows the effect of the distance from the breaking point to the seawall x_i measured positive shoreward from the breaking point on the wave overtopping rate in the breaker region (Sawaragi et al., (1988)). The values for x_i in the case of the wave overtopping rate from the seawall with the artificial reef correspond to the length of the reef because incident waves break just at the offshore edge of the reef. Mean wave overtopping rates in the clapotis region are indicated in the figure for comparison. In the region of $x_i/L_b < 0.4$ the value of q_r^* is almost the same as that of q_b^*. The value of q_r^* becomes less than that of q_b^* as the value of x_i/L_b increases from 0.4 which means that the length of the artificial reef must be longer than $0.4L_b$.

(2) Evaluation of the wave overtopping rate

To predict the wave overtopping rate from the seawall with the artificial reef, a weir model is applied. The weir model was originally developed by Kikkawa et al. (1967) to calculate the wave overtopping rate in the clapotis region based on the weir discharge in the unidirectional flow. The wave overtopping rate q is evaluated from the following equation by the weir model:

$$q = \frac{4\sqrt{2g}}{3} m K^{3/2} H_I^{3/2} \int_{t_1/T}^{t_2/T} \left\{ F(t/T) - \frac{H_c}{KH_I} \right\}^{3/2} d(t/T) \tag{4.70}$$
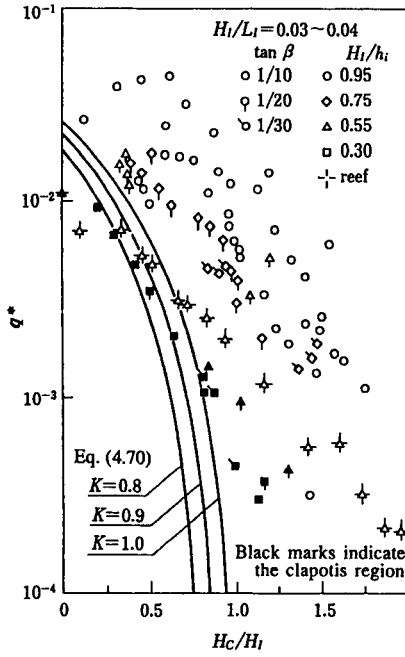
Fig. 4.29 Relation between the non-dimensional wave overtopping rate and H_c/H_I
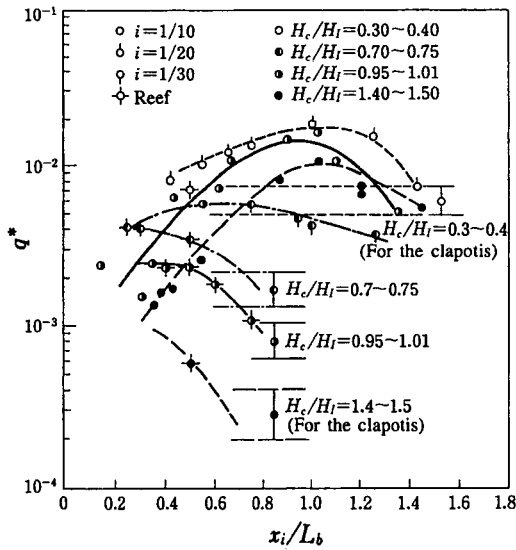
Fig. 4.30 Effect of the length of the artificial reef on the wave overtopping rate

where m is the discharge coefficient, $K=\eta_{max}/H_I$, $F(t/T)$ is the nondimensional time variation of the surface displacement in front of the seawall defined by $F(t/T) = \eta(t)/\eta_{max}$ and η_{max} is the maximum surface displacement. The time when the surface displacement becomes H_c within one wave period is expressed by t_1 and t_2 ($t_1 < t_2$). Here the value of m is assumed to be 0.5 by Kikkawa et al. (1967). If we can find a universal expression for the value of K and $F(t/T)$, we can estimate the wave overtopping rate based on Eq. (4.70) provided that the incident wave height and the mean water level in front of the seawall are given.

In Fig. 4.29, the nondimensional wave overtopping rate calculated from Eq. (4.70) is shown for three different values of K. In the calculation, $F(t/T)$ is assumed to be sinusoidal. It seems that q^*, in the region where H_c/H_I is small, corresponds to the small value of K and q^*, in the region where H_c/H_I is large, corresponds to the large value of K.

Figure 4.31 illustrates the dependency of K on H_c/H_I (Sawaragi et al., (1988)). The values of K in the figure are calculated from Eq. (4.70) by giving the measured wave overtopping rate and other parameters which are necessary to determine the wave overtopping rate assuming that $F(t/T)$ is expressed by the sinusoidal function. The value of K in the clapotis region is uniquely determined by H_c/H_I and does not depend on the steepness of incident waves. The value of K in the breaker region also increases with the increase of H_d/H_I and indicates little dependency on H_I/L_I. However, some scatter comes from the difference in the position of the seawall within the breaker zone. The value of K, in the region where x_i/L_b is greater than 0.5, indicates less scatter.
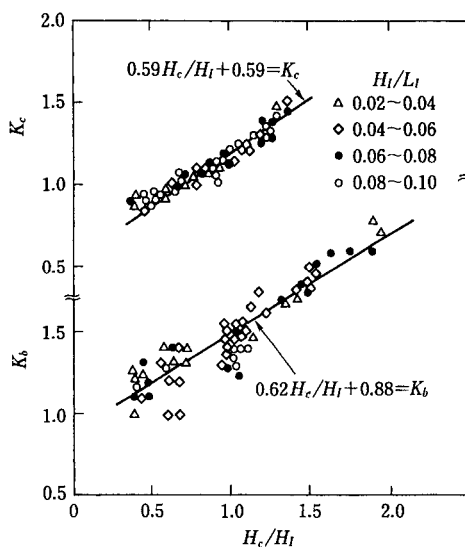
Fig. 4.31   Relation between K and H_c/H_I

From these results, the following two expressions are derived for the clapotis region K_c and the breaker region of $x_i/L_b > 0.5$ K_b (Sawaragi et al. 1988)

$$K_c = 0.59 H_c/H_I + 0.59 \quad : x_i/L_b < 0$$
$$K_b = 0.62 H_c/H_I + 0.88 \quad : x_i/L_b < 0.5$$

(4.71)

In the region of $0 < x_i/L_b < 0.5$, K_b can be determined by linear interpolation.

Figure 4.32 shows the comparison of the measured and the calculated wave overtopping rate from the vertical seawall on the artificial reef (Sawaragi et al. 1988). Calculations were carried out by using Eqs. (4.70) and (4.71) and experiments were conducted on the uniformly sloping beach with the slope 1/30.

4.5 Low Reflection Structures

4.5.1 Low reflection structures and the wave-dissipating principle

The structure with a low reflection coefficient which has the function of energy dissipation or absorption by means of its porosity, roughness or other specific mechanism is generally referred to as a low reflection structure. This structural type is classified into two groups: (1) permeable structures permitting the wave energy transmission and (2) impermeable structures permitting no wave energy transmission behind the structure. There is no rigorous upper value for the reflection coefficient which defines the low reflection structure. Generally, a structure whose reflection coefficient is less than 0.5 - 0.4 is usually called a low reflection structure.
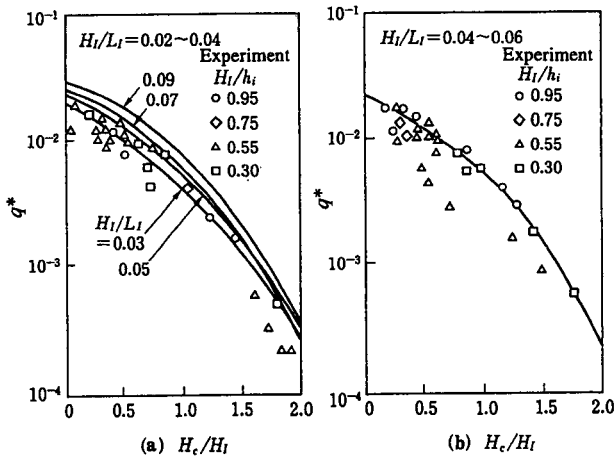
Fig. 4.32 Comparison of measured and calculated wave overtopping rate for the artificial reef

The low reflection structure has several wave-absorbing functions as described in **4.1**. Phase-interaction, friction, large-scale turbulence, jet mixing, and wave breaking are the main factors used to dissipate the wave energy. The rubble mound breakwater is a typical example of the permeable structure with a low reflection coefficient and the vertical wave-absorbing is one example of the permeable of the impermeable structure with a low reflection coefficient. The rubble mound structure has been described in **4.2**, and some important permeable structures are described in **4.5 - 4.7**. In this section, an impermeable structure with a low reflection coefficient is described.

4.5.2 Vertical seawall with wave-absorbing air-chamber

This kind of vertical seawall or dike has a high wave energy dissipating function, and its great merit lies in that its body mass is less than that of the sloping dike. The perforated-type caisson dike proposed by Jarlan (1961) is an outstanding upright wave-absorbing structure and was first constructed at Commo Port in Canada in 1964. The slit-type caisson dike was constructed at the Oinao fishery harbor and the table-type block dike was constructed at the Kagoshima New Port in Japan. Since then, research and development of vertical wave absorbing dikes and quaywalls have been conducted and a large number of dikes of this kind and quaywalls have been constructed throughout Japan.

So far, wave energy dissipating efficiency and wave reflection of vertical dikes having a wave-dissipating air-chamber have been investigated theoretically and experimentally. Theoretical models have been developed by Sawaragi and Iwata (1973, 1978, 1979), and Kondo (1977). In this section, the theoretical model proposed by Sawaragi and Iwata is described.

The incident wave H_I, the reflection coefficient K_{Rj}, the transmission coefficient K_{Tj}, the phase lags ε_I, ε_{Rj}, ε_{Tj}, and the wave attenuation coefficient $\bar{\alpha}$ are expressed using complex variables

$$\left.\begin{array}{l} H_I = \hat{H}_I \exp\left(i\varepsilon_I\right) \\[4pt] K_{Rj} = \hat{K}_{Rj} \exp\left(i\varepsilon_{Rj}\right) \\[4pt] K_{Tj} = \hat{K}_{Tj} \exp\left(i\varepsilon_{Tj}\right) \\[4pt] \bar{\alpha} = \alpha_p \exp\left(-2\pi x_i/L\right),\ \alpha_p = \exp\left(-A_n x/L\right) \end{array}\right\} \tag{4.72}$$

in which $\wedge$ indicates the amplitude, x is the horizontal distance taken positive onshore with its origin on the offshore face of the structure, A_n is the wave damping coefficient, L is the incident wavelength, ε is the phase lag, $i = \sqrt{-1}$. The subscripts I, R, and T represent the quantity regarding the incident, reflected and transmitted waves, respectively. Exp $(-2\pi ix/L)$ included in $\bar{\alpha}$ corresponds to the phase lag against the initial phase of the incident wave at $x=0$.

The vertical dike with two wave-absorbing air-chambers, as shown in Fig. 4.33, is discussed here. The incident wave H_I is assumed to repeatedly reflect and transmit between the first perforated wall and the impermeable wall as indicated in Fig. 4.33. Summing up linearly all the waves produced by an infinite repetition of reflection and transmission, the reflection coefficient K_R and the nondimensional wave height R_H^*/H_I are given as follows with the help of Eq. (4.72).

$$K_R^* = \left| K_{R3} + \bar{\alpha}_1^2 K_{R2} K_{T3} \left(\frac{1}{1 - \bar{\alpha}_1^2 K_{R2} K_{R3}} \right) + \left\{ \bar{\alpha}_1^2 \bar{\alpha}_2^2 K_{R1} K_{T2}^2 K_{T3}^2 \right. \right.$$

$$\times \left(\frac{1}{1 - \bar{\alpha}_2^2 K_{R1} K_{R2}} \right) \left(\frac{1}{1 - \bar{\alpha}_1^2 K_{R2} K_{R3}} \right)^2 \tag{4.73}$$

$$\times \left. \left. \left[\frac{1}{1 - \bar{\alpha}_1^2 \bar{\alpha}_2^2 K_{R1} K_{R3} K_{T2}^2} \left(\frac{1}{1 - \bar{\alpha}_2^2 K_{R1} K_{R2}} \right) \left(\frac{1}{1 - \bar{\alpha}_1^2 K_{R2} K_{R3}} \right) \right] \right\} \right|$$

$$\frac{R_H^*}{H_I} = \left| \bar{\alpha}_1 \bar{\alpha}_2 K_{T2} K_{T3} (1+K_{R1}) \left(\frac{1}{1-\bar{\alpha}_1^2 K_{R2} K_{R3}} \right) \left(\frac{1}{1-\bar{\alpha}_2^2 K_{R1} K_{R2}} \right) \right.$$

$$\left. \times \left[\frac{1}{1-\bar{\alpha}_1^2 \bar{\alpha}_2^2 K_{R1} K_{R3} K_{T2}^2 \left(\dfrac{1}{1-\bar{\alpha}_1^2 K_{R2} K_{R3}} \right) \left(\dfrac{1}{1-\bar{\alpha}_2^2 K_{R1} K_{R2}} \right)} \right] \right| \tag{4.74}$$

In Eqs. (4.73) and (4.74), the subscripts j=1, 2 and 3 with regard to K_{Rj} and K_{Tj} show, respectively, the quantity at the impermeable wall, and at the onshore and offshore perforated walls, and the subscripts $p = 1$ and 2 regarding α_p indicate the quantity between the two perforated walls and between the impermeable and onshore perforated walls.

The first term on the right-hand side of Eq. (4.73) is the reflection from the offshore perforated wall, the second term shows the reflection from the two perforated walls.

K_R^* and R_H^*/H_I, in the case of a Jarlan-type dike with one air-chamber, are easily derived with the help of $\hat{K}_{T2} = 1.0$, $\hat{K}_{R2} = 0$, $\varepsilon_{T2} = \varepsilon_{R2} = 0$ and by ignoring α_2,

$$K_R^* = \left| K_{R3} + \frac{\bar{\alpha}_1^2 K_{R1} K_{T3}^2}{1-\bar{\alpha}_1^2 K_{R1} K_{R3}} \right| \tag{4.75}$$

$$\frac{R_H^*}{H_I} = \left| \bar{\alpha}_1 K_{T3}(1+K_{R1}) \left(\frac{1}{1-\bar{\alpha}_1^2 K_{R1} K_{R3}} \right) \right| \tag{4.76}$$
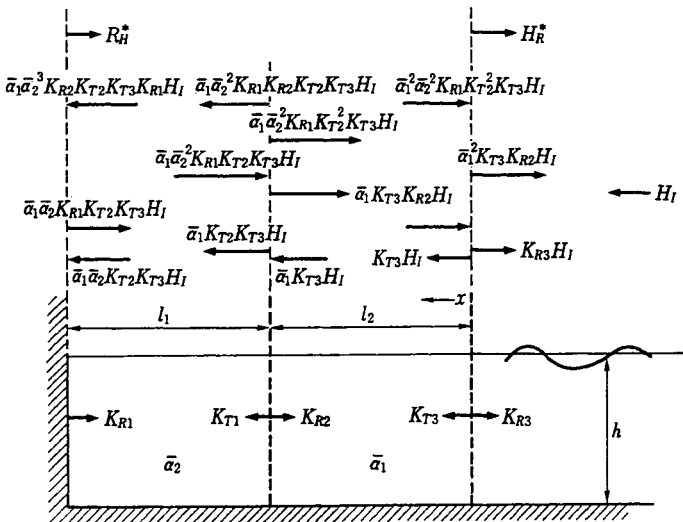
Fig. 4.33 Sketch of the vertical dike with two wave absorbing air-chambers

In the case of a Jarlan-type dike with a thin perforated wall which permits no phase lag among the incident, reflected and transmitted waves, K_R^* becomes minimum at $l/L=1/4$ and becomes maximum at $l/L=1/2$. The reflection coefficient of the vertical dike with two air-chambers is, in general, smaller than that of a Jarlan-type dike (Sawaragi et al., 1979) with a wider range of the non-dimensional incident wavelength l/L.

Sawaragi and Iwata (1978) showed that their theoretical values are in strong agreement with experimental values. An example of this is shown in Fig. 4.34. Sawaragi and Iwata (1979) also revealed that the wave energy-dissipation of the Jarlan-type dike for irregular waves can be accurately estimated with the significant wave.

Recently, a curved slit breakwater, as shown in Fig. 4.35, has been designed and it has been pointed out that this type of breakwater has a higher wave dissipation function than other types used in laboratory experiments, as shown in Fig. 4.35 (Tanimoto et al. 1987).

The doubly-placed perforated and cylindrical breakwater has been constructed in this field very recently. Thus, construction of new types of wave energy-dissipating breakwaters and dikes has been encouraged, from the viewpoint of seascaping, sea water exchange, and ecological systems. However it should be noted that the breakwaters or dikes with air-chambers have one weak point in that the high wave-dissipating function is limited to some specific frequency range. This has continuously encouraged the development of a new type of breakwater or dike with air-chambers, whose wave-dissipation function is high for a wider range of the wave period.
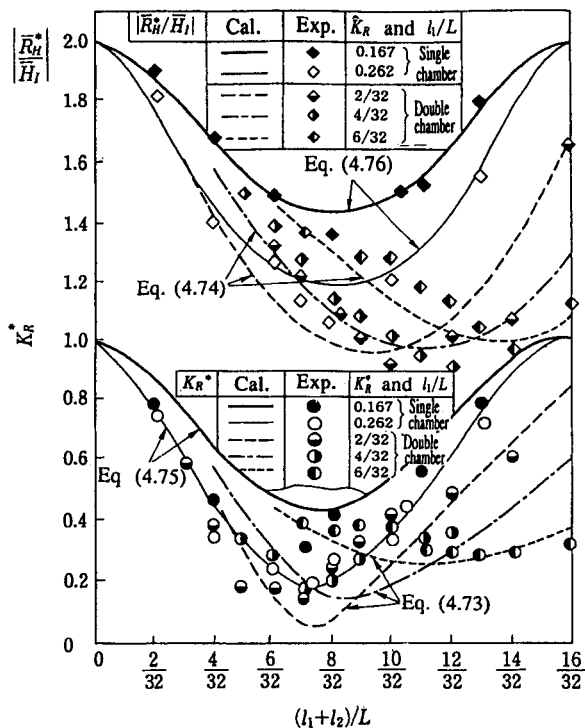
Fig. 4.34 Comparison between the experimental results and theoritical values for the absorbing dike with and air-chamber

The vertical wave absorbing dike or quaywall constructed with specially designed concrete blocks has been placed in a small harbor and an inner gulf area. The wave energy dissipating function of this type of structure is inferior to that of the vertical structure with air-chambers, although the former's crown width is shorter than the latter's one. Thus, research and development of vertical structures with a wave-dissipating function are still being carried out, and some will be introduced in **7.5.3**.

In developing the wave-dissipating structures, they must be equipped with the following functions: (1) high wave-dissipation function for a wider range of wave period, (2) good seascaping, (3) simple maintenance accommodating a future rise in the sea level, (4) better harmony with the ecological system, and (5) high ability to exchange sea water. In order to attain the above mentioned functions, new technological devices to encourage rapid wave energy dissipation and a flexible structure as a floating body will be required.
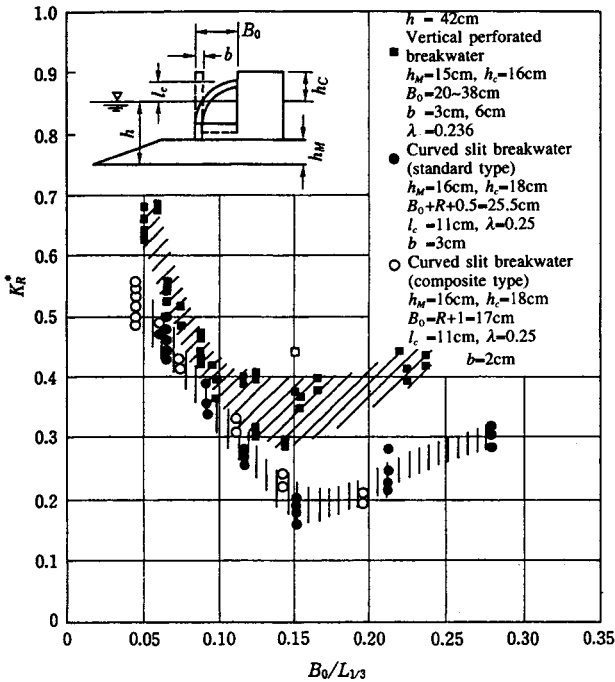
Fig. 4.35   Reflection characteristics of a curved slit breakwater (after Tanimoto et al. 1987)

4.6 Curtain-wall Type Breakwater

A curtain-wall type breakwater has a cross section that intercepts fluid motion near the free surface with a vertically supported wall, as shown in Fig. 4.36. However, it allows the fluid to move through the gap between the lower end of the wall and the ocean bottom. A major function of this breakwater, which reduces the transmitted wave height, is to reflect incident waves offshore by means of the wall. Some of the wave energy may be dissipated by the flow separation near the lower edge of the wall.
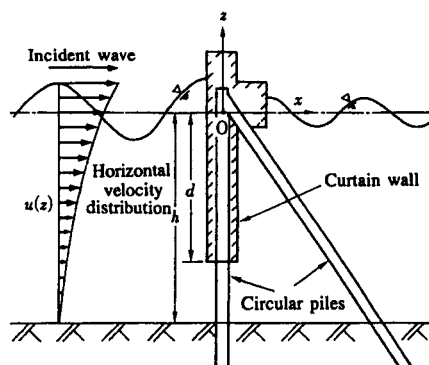
Fig. 4.36 Sketch of a curtain-wall type breakwater

A curtain-wall type breakwater has several advantages compared to conventional gravity-type breakwaters. For instance, it is possible to intercept only incoming waves without stopping steady currents, which is sometimes preferable near a river mouth and in a tidal region. In addition, it can be economically constructed on comparatively soft ground because the weight of the breakwater is light and can usually be supported by piles.

On the other hand, effectiveness of the curtain-wall type breakwater is limited only to comparatively short waves. For long waves, the fluid motion under the curtain wall cannot be neglected because it significantly contributes to wave energy transmission. Therefore the construction of curtain-wall type breakwaters has been limited to inlets or bay areas where wave conditions are comparatively mild.

It has been known that the function of a curtain-wall type breakwater is heavily dependent upon the ratio of the draft of a curtain wall d to wavelength L. Therefore, selection of the draft depth of the curtain wall is very important for practical design.

In the last two decades, numerous studies have been done in order to clarify the wave transmission and reflection characteristics of the curtain-wall type breakwater and also the hydrodynamic forces on this type of breakwater. Haskind (1959) and Ursell (1974) have derived an analytical solution for the transmission and reflection coefficients of a vertically supported thin plate extending from the water surface into deepwater. Because of the difficulty of extending the solution to intermediate and shallow water conditions, Wiegel (1960) proposed the semi-empirical solution for the transmission coefficient of a vertically supported plate placed in intermediate and shallow water based on the theory of wave energy flux, usually called the "power transmission theory" (PTT).

Morihira et al. (1964) conducted a series of model experiments in order to clarify the wave transmission and wave force characteristics of the curtain-wall type breakwater, and also proposed a method for estimating the wave force on the breakwater, which is partly based on the Sainflou formula. On the other hand, Liu et al. (1982) and Nakamura et al. (1983, 1984) have developed numerical approaches that can accomodate wave boundary-value problems around a thin-walled body such as a curtain-wall type breakwater, based on the integral equation method shown in Chapter 2. Although their methods are similar in principle, there are nevertheless some differences between the two. For example, Liu et al. used a double source, while Nakamura et al., on the other hand, used a wave source using Green's function based on a single source. They have shown numerical results on the transmission and reflection coefficients and also the wave forces on a plate placed in

intermediate and shallow water regions. Nakamura (1992) has also analyzed the effect of separated flow from the lower edge of the plate on the wave transmission and wave forces by the use of the combined wave diffraction and discrete vortex model.

In this section, referring mainly to the theoretical results based on the wave boundary-value analysis, wave transmission and reflection characteristics and hydrodynamic forces of the curtain-wall type breakwater are briefly discussed.

4.6.1 Wave transmission and reflection by a curtain-wall type breakwater

In the following, a curtain-wall type breakwater is idealized as a single vertical plate without support piles, as shown in Fig. 4.36. Also the length of the breakwater in the longshore direction is assumed to be infinite; i.e. a two-dimensional model in a vertical plane.

Transmission and reflection coefficients of such an idealized curtain-wall type breakwater, designated as K_T and K_R, respectively, can be obtained by the two-dimensional wave source Green's function, which has already been presented in Chapter 2. Considering a much more general case where wave trains are obliquely incident to the breakwater with an inclination angle θ measured from the normal direction of the breakwater line, K_T and K_R can be calculated by Eqs. (2.118) and (2.117) respectively. The complex amplitude of the scattered wave potential ϕ_s is given by Eq. (2.100) through the use of A_s defined by Eq. (2.106).

(1) In the case of normal incident waves

Typical experimental and computed results of the transmission and reflection coefficients, K_T and K_R, are shown in Figs. 4.37 (a)–(c). In each figure, variations of K_T and K_R with respect to the ratio of the draft to the equivalent deepwater wavelength d/L_0 are specified under the conditions of the constant ratio of draft to depth and the ratio of the incident wave height to depth. In addition, the transmission coefficient by the power transmission theory, denoted as PTT, is shown in these figures.

From these figures, it is apparent that K_T decreases as d/L_0 increases, i.e.; K_R has an inverse relation to K_T for shorter waves. Also the variation of K_T and K_R with d/L_0 becomes milder in cases of deeper draft, i.e. for larger d/h. This trend is much more apparent in Fig. 4.38, in which the variation of K_T with d/h for different d/L_0 is specified. From this figure, it is seen that K_T is mainly dependent upon d/L_0 under the condition $d/h<0.8$.

If we set the criterion for the effective reduction of a transmitted wave height as $K_T<$ 50%, it is recommended for practical design that the draft "d" should be deeper than about 15% of the equivalent deepwater wavelength L_0, provided that the condition of $d/h<0.8$ is satisfied.

As seen in Fig. 4.37, the transmission and reflection coefficients may be practically estimated by numerical analysis based on the potential flow theory. However for a larger wave height and deeper draft conditions, the difference between the experimental and computed results becomes larger because the effect of flow separation near the lower edge of the wall might be important. The transmission coefficients given by the power transmission theory are consistent with the experimental results especially in the range of a small d/L_0, where the wave reflection from the wall can be practically neglected. It is noted that the power transmission theory cannot predict the reflection coefficient and wave forces on the wall.

Liu et al. (1982) have examined theoretically the effect of the inclination angle of the curtain wall in a vertical plane on K_T and K_R, in addition to the case of a vertical wall, by numerical analysis based on the double source method. They pointed out that under identical definite wave conditions, the inclined curtain wall is more effective than the vertical one.

(2) In the case of obliquely incident waves

In Fig. 4.39, a typical example regarding the effect of incident wave angle θ on K_T and K_R is given, where θ is defined as the subtended angle from the normal direction of the breakwater axis to the incident wave direction. In the figure, the conditions of d/L_o and d/h are fixed, in other words, a fixed wave period and draft depth for the curtain. The computed result is obtained by the numerical analysis shown in Chapter 2.

From the figure, it is seen that K_T increases with θ, also K_R shows an inverse trend to that of K_T. For different conditions of d/L_0, Nakamura et al. also examined the variation of K_T and K_R with θ, and concluded that the effect of the wave angle on K_T and K_R is not very significant in the range of $\theta < 40°$, and therefore the values of K_T and K_R in that range can be approximately given by the result of the normal incident wave.

(a) $d/h=0.353, H/h=0.064$

(b) $d/h=0.353, H/h=0.128$

(c) $d/h=0.609, H/h=0.064$
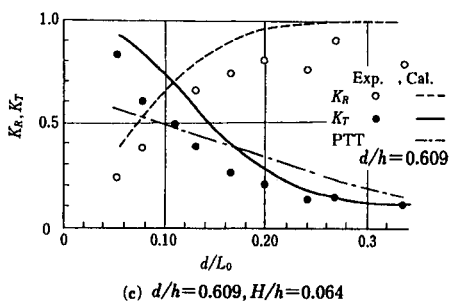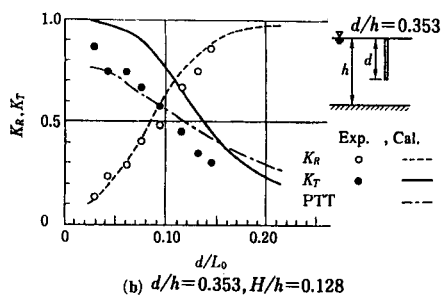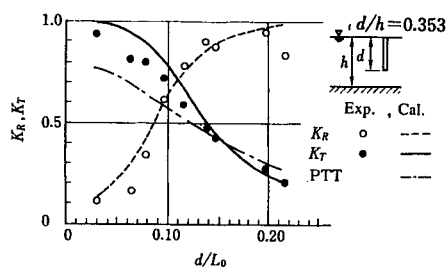
Fig. 4.37 Wave transmission and reflection coefficients of the curtain-walled breakwater
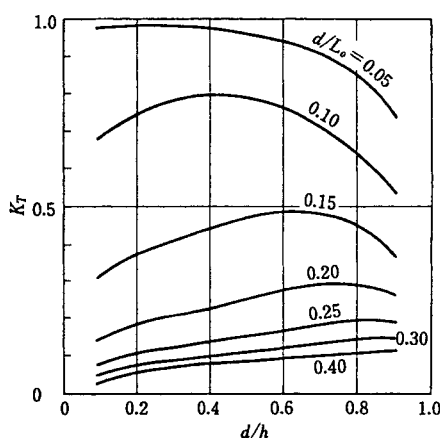
Fig. 4.38 Variation of the transmission coefficient with d/h
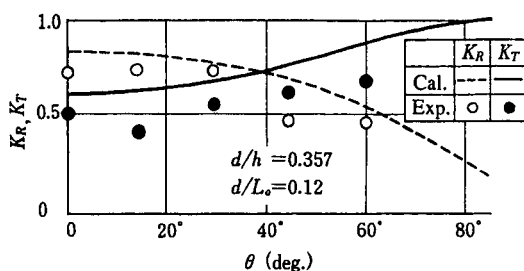
Fig. 4.39 Variation of the reflection and transmission coefficients with incident wave angle

(3) In the case of double rowed curtain walls

As mentioned above, the effectiveness of the curtain-wall type breakwater is limited to the range of comparatively short waves. In order to improve the function of a breakwater, especially for long waves, doubly arranged curtain-wall type breakwaters may be used instead of the single curtain-wall type by Stiassnie et al. (1981), and Nakamura et al. (1985). The doubly arranged curtain-walls may cause more wave reflection from the breakwater to offshore and also effect the wave resonance between the two walls, where incident wave energy is partly trapped and finally dissipated by the flow separation near the lower edge of the wall. Nakamura et al. (1985) reported that the amount of energy dissipation from the double-wall, due to the flow separation, becomes almost double compared to that of the single wall. They also pointed out that numerical analysis based on the potential flow theory cannot be used to predict the wave transmission coefficient of the double curtain-walls because of the predominant flow separation effect. In this case they suggested that a modified analysis, in which the water region between the two walls is assumed to be dead water, i.e., replaced with the rigid body, can be used to give a reasonable estimation of the transmission coefficient.

4.6.2 Wave forces on the curtain-wall type breakwater

In Figs. 4.40 (a)–(c), horizontal wave forces on the curtain-wall per unit length of the transverse direction, $d\hat{F}_x$, are specified, in which both the experimental results and computed results by Green's function based on the potential flow theory are plotted. The numerical method adopted here has already been described in Chapter 2. In these figures, a dimensionless wave force defined as the following is shown.

$$d\hat{F}_x^* = d\hat{F}_x / (\rho g H d / 2)$$

With respect to the experimental results, positive and negative peak wave forces are distinguished in the figure by adding the sign $\pm$, in which the $+$ refers to a peak wave force acting in the direction of wave propagation.

From these figures, it can be seen that the measured wave forces are roughly less than the computed figures for almost all ranges of d/L_0 regardless of the depth of the draft. However, it is noted that in the case of larger wave height and longer wavelength conditions, the measured wave force may become greater than the computed one. The main reason for this might be due to the increasing effect of flow separation from the edge of the curtain-wall.

On the other hand, focusing on the magnitude of $d\hat{F}_x^*$, which is equivalent to the transfer coefficient from the wave height to the peak wave force for the definite wave period, we can see the maximum value of $d\hat{F}_x^*$ always appears at the same condition of d/L_0 without being relevant to the draft condition, $d/L_0 = 0.12$. This fact means that the maximum horizontal wave force is not necessarily caused by the design wave, which is usually represented by the significant or maximum wave based on the wave statistics. Because the design wave would have the same wave condition with the possible maximum wave height, which often has a comparatively longer wave period and wavelength. Consequently, the ratio, d/L_0, for the design wave becomes comparatively small and the corresponding transfer coefficient, $d\hat{F}_x^*$, may be small according to the above results. Therefore when we estimate wave forces on the curtain-wall type breakwater based on the design wave concept, it is noticed that there may be some possibility of not predicting the possible maximum wave forces. In order to avoid this ambiguity, it is necessary to check the variation of the wave force transfer coefficient, $d\hat{F}_x^*$, with the wave period as a preliminary design step.

Nakamura (1992) has also examined the overturning moment and wave pressure distribution on the curtain-wall type breakwater and confirmed that a trend similar to the horizontal wave force described above is observed. They also reported that the normal incidence condition of the incoming wave is more critical for wave force calculation than any other incident angle of waves.
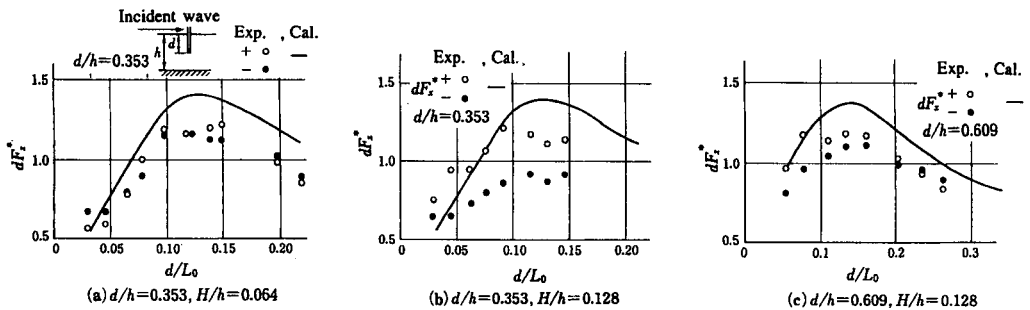
Fig. 4.40 Horizontal wave forces on the curtain-walled breakwater

4.7 Floating Breakwater

A floating breakwater is one type of structure used for wave control. The wooden floating breakwater constructed at Plymouth Port in England in 1811 appears to be the first such breakwater of the modern era. Since then, research and development of the floating breakwater have been mainly conducted in European countries such as England, France and the Soviet Union. It is well known that Bombardon floating breakwaters, with unit dimensions of length 60m, width 7.5m and height 7.5m, were placed over a distance of 1.6km along the Normandy coast during World War II. In Japan, the first floating breakwater was placed in Aomori Port in 1930, to test its resistiveness against waves and the wave dissipation function.

A floating breakwater is moored to prevent free movement under wave action, which differs from fixed-type breakwaters. The floating breakwater has the following advantages:
(i)   The floating breakwater can prevent sea water pollution, since it has a high sea water exchange function.
(ii) The construction cost of the floating breakwater becomes cheaper than the fixed-type breakwater as the water depth of the construction site becomes deeper.
(iii) The floating breakwater can be easily placed on soft ground without soil improvement.
(iv) The placement location of the floating breakwater can be easily changed.
(v)   The floating breakwater can be used for many purposes.
(vi) The construction period in the field is much shorter compared to the fixed-type breakwater
(vii) The floating body, mooring lines and anchors are usually manufactured in a factory, which assures a high level of maintenance, management and reliability.
  The disadvantages of the floating breakwater are as follows:
(i)   Several technological devices are required to attain the designed wave dissipation.
(ii) The mooring line and anchorage are apt to be broken by the wave action.

(iii) If the mooring line breaks, the body freely floats, which poses a danger to ships, coastal and offshore structures.

(iv) Field repairs of a damaged floating structure are more difficult than for a fixed-type structure.

Due to the above mentioned disadvantages, at present, the floating breakwater has been mainly constructed for limited purposes such as a simple portable breakwater, aquacultural facilities and as a floating wharf for yachts and ships.

4.7.1 Types of floating breakwaters and the principle of wave dissipation

The structure of a floating breakwater is, in general, skilfully designed to be equipped with some wave-dissipation mechanisms such as reflection, wave breaking, friction, vortex formation and shedding, jet mixing and resonance. From the view point of wave dissipation mechanisms, the structural types of floating breakwaters can be classified into (a) reflection-type structures, (b) reflection and wave breaking-type structures and (c) friction-type structures.

(a) Reflection-type structures

This type of structure reflects some of the incident wave energy to the offshore side and decays the transmitted wave. A typical example is the pontoon-type breakwater, which will be discussed later.

(b) Reflection and wave breaking-type structure

This structure encourages wave breaking and attenuates both the reflected and transmitted waves. The barrier-type floating breakwater and the pontoon-barrier-type floating breakwater are typical examples of this type.

(c) Friction-type structure

Incident wave energy is attenuated by friction and the transmitted wave decays according to the magnitude of energy loss through the breakwater. The mattress-type and sheet-type floating breakwaters are examples of this kind of structure.

On the other hand, from the point of view of structural flexibility, the floating breakwater can be classified into flexible-type and rigid-type structures. The flexible-type breakwater changes its shape according to the wave action. On the contrary, the rigid-type breakwater does not change its shape under wave action. Sheet-type, membrane type and mattress-type floating breakwaters and floating breakwaters with revolving joints are examples of flexible-type structures. The main mechanism of wave dissipation of these flexible-type breakwaters exhibit is friction and it is because of this basic characteristic that the transmitted wave height decreases exponentially as the crown width of the breakwater increases. The hydraulic properties of the membrane-type structure, which belongs to the flexible-type breakwater, will be described in **4.8**. The rigid-type floating breakwater is discussed in detail in the following section.

4.7.2 Transmission coefficient of the rigid-type floating breakwater

The rigid-type floating breakwater is not deformed by wave action and is largely classified into the pontoon-type, barrier-type, and pontoon-barrier-type floating breakwaters.

The pontoon-type floating breakwater is basically a reflection-type structure, and attenuates the transmitted wave height mainly by reflection. The rectangular-, trapezoidal-, and circular-shaped floating breakwaters are popular. The barrier-type floating breakwater has the reflection-wave breaking-structure and the transmitted wave is decayed by

reflection, resonance and wave breaking. The perforated caisson-type, the vertical two-wall-type and the horizontal two-plate type floating breakwaters are popular barrier-type floating breakwaters. The pontoon-barrier-type floating breakwater comprises pontoon-type and barrier-type structures.

The characteristics of the transmission coefficient of the rigid-type floating breakwater differ from those of the flexible-type. The transmission coefficient in the case of the rigid-type floating breakwater becomes alternatively maximum and minimum. One example is shown in Fig. 4.42. Thus, the rigid-type floating breakwater can sufficiently attenuate the transmitted wave height to match the design value even when its crown width is much shorter than the flexible-type. Thus, if the disadvantages of the rigid-type breakwater can be overcome, it can possibly be used as a long-life structure in the same way as a fixed-type breakwater.

The transmission coefficient varies according to the geometrical shape of the structure, mooring system, wave conditions and still water depth. The transmission coefficient of the non-breaking regular wave in the case of the pontoon-type and barrier-type breakwaters can be numerically evaluated by means of a boundary element method, the eigenfunction expansion method, etc., which have been discussed in Chapter 2.

In addition, sea waves are irregular and therefore field engineers require knowledge of the transmission coefficient for irregular sea waves. Laboratory experiments by Yamamoto (1981), have revealed that the transmission coefficient for irregular waves can be accurately evaluated by using the results of the regular waves, as long as the incident wave does not break.

4.7.3 Floating breakwaters with a pressurized air-chamber

The basic equations for motions of a floating breakwater whose cross-section is rectangular or circular, and the resulting wave deformation are introduced in detail in **2.5**. Therefore, in this section, the floating breakwater utilizing pressurized air, which has recently received much attention, will be discussed here. This floating structure is of the barrier-type and its major advantage is that the control of its natural frequency is facilitated simply by adjusting the air pressure in the air-chamber.

The analytical situation for a tauntly moored semi-submerged structure with a pressured air chamber is shown in Fig. 4.41. The structure is a rectangular body anchored to the seafloor, having an outer width $2l_2$, inner width $2l_1$, draft q_1h, initial pressurized air depth $d + q_2h$ and a center of gravity $G(0, \bar{z}_0)$. In the theoretical model, the following assumptions are taken into account; (1) the fluid is incompressible, (2) the wave motion is irrotational, (3) the linear theory is valid, (4) the floating body displays a small harmonic motion, and (5) the Hook law is obeyed regarding the mooring lines.

The fluid field is vertically divided into five regions in accordance with the sectional shape of the structure. Region I includes the incident and reflected waves, while the transmitted wave is in region V.

(1) Displacement of the floating body
   The dynamic motions are given by

$$X = \hat{X}_e e^{i\sigma t}, \quad Z - \bar{z}_0 = \hat{Z}_e e^{i\sigma t} \text{ and } \Omega = \hat{\Omega}_e e^{i\sigma t} \tag{4.77}$$

in which X, Z and Ω are the x- and z- directional and the rotational displacements, respectively, where Ω is positive counter-clockwise. $\hat{X}_e$, $\hat{Z}_e$, and $\hat{\Omega}_e$ are the complex amplitudes of the swaying, heaving, and rolling motions, respectively, at the center of
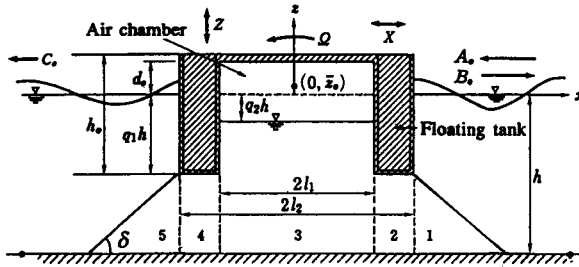
Fig. 4.41 Cross section of the floating breakwater with a pressurized air-chamber

gravity. σ is the angular frequency, $i = \sqrt{1}$, t is time, x is the horizontal axis taken negative in the direction of incident wave propagation and z is the vertical axis taken upwardly positive with its origin on the still water level.

(2) General solution for the velocity potential

The general solutions for the velocity potentials $\Phi_j(x,z,t) = \phi_j e^{i\sigma t}(j = 1\text{-}5)$ which satisfy the Laplace equation and boundary conditions in the fluid region are given as follows:

$$\Phi_1 = \left[\left\{ A_0 e^{ik(x-l_2)} + B_0 e^{-ik(x-l_2)} \right\} \frac{\cosh k_n(h+z)}{\cosh k_n h} \right.$$
$$\left. + \sum_{n=1}^{\infty} B_n e^{-k_n(x-l_2)} \frac{\cosh k_n(h+z)}{\cosh k_n h} \right] e^{i\sigma t}$$

$$\Phi_2 = \left[C_0 x + D_0 + \sum_{n=1}^{\infty} \left\{ C_s \sinh \frac{s\pi x}{(1-q_1)h} \right. \right.$$
$$\left. + D_s \cosh \frac{s\pi x}{(1-q_1)h} \right\} \cos \frac{s\pi(h+z)}{(1-q_1)h}$$
$$+ \frac{i\sigma \hat{Z}}{(1-q_1)h} \left\{ -\frac{1}{2}x^2 + \frac{(h+z)^2}{2} - \frac{(1-q_1)^2 h^2}{6} \right\}$$
$$\left. + \frac{i\sigma \hat{\Omega} x}{(1-q_1)h} \left\{ -\frac{x^2}{6} + \frac{(h+z)^2}{2} - \frac{(1-q_1)^2 h^2}{6} \right\} e^{i\sigma t} \right] \tag{4.78}$$

$$\Phi_3 = \left[\left\{ E_0 e^{ik'x} + F_0 e^{-ik'x} \right\} \frac{\cosh k'(h+z)}{\cosh k'h} \right.$$
$$\left. + \sum_{m=1}^{\infty} \left(E_m e^{k_m'x} + F_m e^{-k_m'x} \right) \frac{\cosh k_m'(h+z)}{\cosh k_m'h} + \frac{p_0}{\rho\sigma} i \right] e^{i\sigma t}$$

$$\Phi_4 = \left[G_0 x + H_0 + \sum_{s=1}^{\infty} \left\{ G_s \sinh \frac{s\pi x}{(1-q_1)h} + H_s \cosh \frac{s\pi x}{(1-q_1)h} \right\} \times \right.$$
$$\cos \frac{s\pi(h+z)}{(1-q_1)h} + \frac{i\sigma \hat{Z}}{(1-q_1)h} \left\{ -\frac{x^2}{2} + \frac{(h+z)^2}{2} - \frac{(1-q_1)^2 h^2}{6} \right\}$$

$$+\frac{i\sigma\hat{\Omega}x}{(1-q_1)h}\left\{-\frac{x^2}{6}+\frac{(h+z)^2}{2}-\frac{(1-q_1)^2h^2}{6}\right\}\Bigg]e^{i\sigma t}$$

<div align="right">(4.78)
cont.</div>

$$\Phi_5=\left[J_0 e^{ik(x+\ell_2)}\frac{\cosh k(h+z)}{\cosh kh}+\sum_{n=1}^{\infty}J_n e^{kn(x+\ell_2)}\frac{\cosh k_n(h+z)}{\cosh k_n h}\right]e^{i\sigma t}$$

in which h is the still water depth, ρ is the fluid density, p_0 is the amplitude of the air pressure in the chamber, A_0, B_0, C_0, D_0, E_0, F_0, G_0, H_0, J_0, B_n, J_n, E_m, F_m, C_s, D_s, G_s, and H_s (m, n, $s =1$, 2,... ∞) are complex coefficients, and k, k', k_n and k'_m are the eigenvalues determined from

$$\frac{\sigma^2}{g}=k\tanh kh=k'\tanh k'(1-q_2)h$$

$$=-k_n\tan k_n h=-k'_m\tan k'_m(1-q_2)h$$

<div align="right">(4.79)</div>

(3) Air compressed model

Assuming the adiabatic process of an ideal gas, the amplitude of the air pressure fluctuation p_0 in Φ_3 is given as a function of the heave motion of the floating structure and the mean water level in the air-chamber is defined by

$$p_0=-\gamma\bar{p}_0(\hat{\Omega}_e-\eta_0)V_0\quad\gamma=1.4$$

<div align="right">(4.80)</div>

where V_0 is the initial air volume, and η_0 is the amplitude of the mean water level fluctuation and is defined by

$$\eta_0=\frac{1}{2l_1}\int_{-l_1}^{l_1}\left\{-i\frac{\sigma}{g}(Ee^{ik'x}+Fe^{-ik'x})\frac{\cosh k'(1-q_2)h}{\cosh k'h}\right\}dx$$

<div align="right">(4.81)</div>

(4) Equation of motion for a floating structure

The motion of the structure is expressed as

$$M\frac{\partial^2 X}{\partial t^2}=-\int_s i\rho\sigma\phi_j e^{i\sigma t}n_x ds-2K_{xx}X-2K_{x\theta}\Omega\quad\text{(swaying motion)}$$

$$M\frac{\partial^2 Z}{\partial t^2}=-\int_s i\rho\sigma\phi_j e^{i\sigma t}n_x ds-2K_{zz}Z\quad\text{(heaving motion)}$$

$$I\frac{\partial^2\Omega}{\partial t^2}=-\int_s i\rho\sigma\phi_j e^{i\sigma t}\left\{Xn_z-(Z-\bar{z}_0)n_x\right\}ds-2K_{\theta x}X$$

$$-2K_{\theta\theta}\Omega+M_V+M_{GM}\quad\text{(rolling motion)}$$

<div align="right">(4.82)</div>

in which M and I are the mass and the inertia moments of a floating structure, n_x and n_z are the directional cosines to the x- and z- axis, K_{pq} is the q-component of the resistance force of the mooring lines due to motion in direction p, M_V is the moment of the viscous damping force, M_{GM} is the restoring moment and S denotes the surface area of the floating structure. Expressions for K_{pq}, M_{GM} and M_V are given as

$$K_{xx} = K\cos^2\delta, \; K_{x\theta} = K_{\theta x} = K\cos^2\delta\left\{(q_1 h + \bar{z}_o) - l_2\tan\delta\right\}$$

$$K_{zz} = K\sin^2\delta, \; K_{\theta\theta} = K\cos^2\delta\left\{(q_1 h + \bar{z}_0) - l_2\tan\delta\right\}^2$$

(4.83)

$$M_{GM} = -Mg\overline{GM}\,\hat{\Omega}$$

$$= -pg\theta_0\left[\frac{2}{3}(l_2^3 - l_1^3) - (l_2 - l_1)(q_1 h)^2 - l_1(q_2 h)^2 - \frac{M\bar{z}_0}{\rho}\right.$$

$$\left. + \frac{2F_0\cos\delta}{\rho g}\left\{l_2 + (q_1 h + \bar{z}_0)\tan\delta\right\}\left(\frac{\sqrt{(q_1 h + \bar{z}_0)^2 + l_2^2}}{L_s} + 1\right)\right]$$

(4.84)

$$M_V = -V_s\frac{\partial\Omega}{\partial t} = -2(\beta_E - \beta_T)\frac{2\pi}{T_d}(1 + \Delta I)\frac{\partial\Omega}{\partial t}$$

where K is the spring constant of the mooring line, δ is the angle between the bottom and the mooring line, $\overline{GM}$ is the metacentric height, L_s is the length of the mooring line, V_s is the viscous resistance coefficient in the rolling motion, F_0 is the initial tensile force of the mooring line, β_T is the damping modulus due to wave-making resistance and β_E is the damping modulus in the free rolling of the floating structure. $\beta_T - \beta_E$ represents the damping modulus due to eddy generation, T_d is the damping period of the free rolling and ΔI is the added inertia moment.

The complex coefficients of the velocity potentials and the amplitudes of the motions of the structure can be solved with help of the conditions that the water pressure and the horizontal velocity should be continuous at the interface between the adjacent two fluid regions and between the fluid and the structure, with a given complex coefficient of incident wave A_0,

$$A_0 = iage^{ik_1 l_1}/\sigma$$

(4.85)

in which a is the incident wave amplitude.

The transmission coefficient K_T calculated with the proposed theory is shown to be in strong agreement with the experimental values, as shown Fig. 4.42. In theoretical calculations, the evanescent modes up to $n = m = s = 10$ were taken into account. The motion of the structure and the tensile force of the mooring line are also in strong agreement with calculations and hydraulic experiments. The dynamic behaviours of this floating structure and the resulting wave deformation under both a semi-submerged state with a catenary mooring system and under a fully submerged state with a taunt mooring system have been investigated by Iwata et al. (1990) and Kim et al. (1992).

As previously stated, the floating breakwater is not as popular as the fixed type breakwater. In order to establish the floating breakwater as a reliable and popular structure, the following investigations have to be conducted:

(i) Accurate evaluation of the breaking wave force and the snap tensile force of the mooring line.

(ii) Elucidation of a mechanism for fatigue failure of the mooring line by repeat loading, and development of technology as a countermeasure against fatigue failure.

(iii) Development of new technologies that reduce the shock tensile force acting on the mooring line.

(iv) Accurate evaluation of the pulling resistance force of the anchorage, and development of new anchoring works, to counter destruction by wave action.

(v) Elucidation of mechanisms for mooring line corrosion, and development of new mooring line materials highly resistant against corrosion as well as fatigue.

(vi) Establishment of an accurate analytical method for the dynamic response of a floating structure and its resulting wave deformation which considers foundation-structure-wave interaction.

The subject (iii) above will be discussed in detail in **8.4.5**.
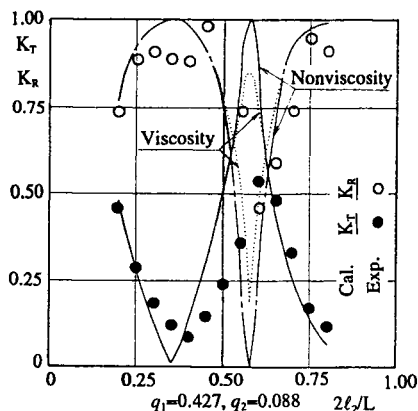
Fig. 4.42 Transmission and reflection coefficients of the floating breakwater with a pressurized air-chamber

4.8 Membrane Structures

"Membrane structure" is a general term referring to a structure that mainly consists of a membrane made of a synthetic fiber or rubber, etc. Oil boom and silt curtains shown in **6.4** are examples of membrane structures in practical use and serving a specific function in the sea. However, we do not know of any membrane structures yet devised for controlling waves. The idea of using membranes to control waves originated a long time ago: floating a sheet on a sea surface is one example of this primitive idea. Recently, some new types of membrane structures that actively utilize wave-induced motions have been proposed.

When we require membrane structures to have such functions as dissipating or reflecting wave energy as utilized in ordinary structures such as breakwaters, membrane structures show less effect than rigid structures since the flexibility of the membrane makes them easily deformed and affected by wave motion. However, we can easily fabricate a large structure by using membranes, which enable us to control waves in a wide region. If we intend to make use of membrane motions, we can take advantage of the multi-mode motions of the membrane and possibly widen the effective frequency range for wave attenuation, which can improve the effectiveness on irregular waves. In general, however, the more effectively structures can reduce wave height, the larger the wave forces acting on the structure will be, and thus stability sometimes becomes a problem for flexible structures such as membrane structures. We must therefore pay special attention to the similarity between models and prototypes when investigating the stability of the flexible structures by performing physical experiments.

Although possibilities exist for membrane structures to become new types of structures for wave attenuation in the future, we have to solve many problems in order to put them into practical use. In the following section, we will first show how membrane structures reduce wave height and then we will introduce some membrane structures that have been previously mentioned.

4.8.1 Wave attenuation mechanism for membrane structures
(1) Wave energy dissipation on the membrane

Suppose a sheet of a membrane is extended over several times the wavelength on a water surface. If the moment of the membrane does not completely follow the water particle motion due to waves, the friction between the membrane and the water surface causes energy dissipation. This energy dissipation mechanism is similar to that of bottom friction, and wave transformation can be described by the following energy conservation equation:

$$\frac{d}{dx}\left(c_g E\right) = -E_f \tag{4.86}$$

where the direction of the x-axis coincides with that of the wave propagation and c_g, E and E_f denote the group velocity, time averaged wave energy per unit length, and energy dissipating ratio; i.e., energy dissipating per unit length and unit time due to friction. If we can express the dissipating energy ratio as $E_f = mE$, where m is constant, Eq (4.86) can be integrated into an equation which indicates that the wave height exponentially decreases with wave propagation. Estimation of E_f, however, is not straightforward because it may be difficult to estimate the friction coefficient and relative velocity between the membrane and water.

Friction is not the only factor involved in the dissipation of wave energy. Some other methods have been proposed to dissipate the wave energy more effectively (Jones 1971). For example, turbulent energy dissipation can be increased by pleating the membrane, or viscous energy dissipation due to fluid motion can be utilized by filling an impermeable membrane with high a viscosity fluid and floating it on the water surface.

(2) Wave attenuation by making use of radiated waves due to membrane motion

The wave attenuation method that makes use of radiation waves due to the structure's motion is one of the methods that utilize phase interaction between waves (see **4.1.2**). Let us consider a wave field as a combination of diffraction and radiation wave fields. If the radiation waves generated by the structure's motion have almost the same propagation direction and amplitude as those of diffraction waves and if these waves are out of phase, the wave height of the combination waves becomes very small. As mentioned in **4.7**, one of the most important wave attenuation mechanisms of a floating breakwater is this phase interaction effect. In order to make this interaction strong, high radiation waves must be generated by large motions of the structure. However, the rigid floating breakwater has only 6 modes of motion, therefore the frequencies at which generated wave heights become large, i.e., effective frequencies, are at most only 6, even if high waves are generated at the natural frequencies for every mode of motion. On the other hand, membrane structures have an infinite number of modes of motion, which suggests the possibility of having many effective frequencies.

In order to investigate the magnitude of radiation waves due to membrane motions with several modes, let us take a two-dimensional wave maker as a simple example. The solution for radiation waves generated by the wave maker is analytically obtained from the linear wave maker theory. Assuming that the movement of the wave maker is expressed as $X = \hat{X}(z)\,e^{-i\sigma t}$ as shown in Fig. 4.43, the amplitude of radiation waves "a" is given by

$$a = \frac{4k\sinh kh}{\sinh 2kh + 2kh}\left|\int_{-h}^{0} \hat{X}(z)\cosh k(z+h)dz\right| \tag{4.87}$$

As shown in Fig. 4.44, we now choose the forms of $\hat{X}(z)$ the seven types of motion: (A) piston type: $\hat{X}(z)=l_d$, (B) flap type: $\hat{X}(z) = l_d(\frac{z}{h}+1)$, (C) cosine function type: $\hat{X}(z) = l_d\cos(\frac{(2n-1)\pi}{2} \frac{z}{h})$ ($n=1, 2, 3, 4, 5$). The ratio of the wave amplitude "a" to the amplitude of the wave maker stroke at a free surface, l_d, is a function of the product of the wave number k and the water depth h. Figure 4.45 shows the relation between a/l_d and kh. As clearly seen in this figure, the amplitudes of generated waves due to the motion with the higher modes of the cosine function ($n=2, 3, 4, 5$) are much smaller than those for other modes of motion. For sufficiently large kh, however, the amplitude becomes large, so that the higher mode motion may be effective only for large kh.
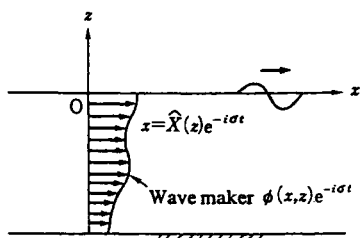
Fig. 4.43 A flexible wave maker
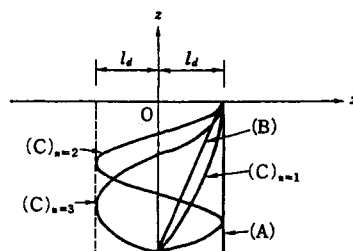
Fig. 4.44 Oscillation modes of the wave maker
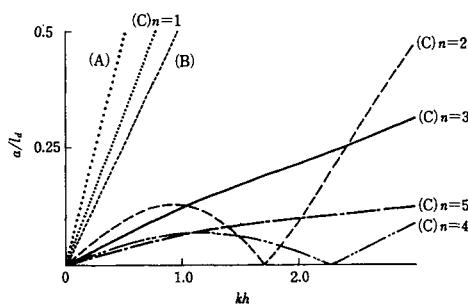
Fig. 4.45 Wave amplitude to stroke amplitude ratios

In Fig. 4.45 we should notice that there is a particular kh at which no radiation waves are generated for even numbers of n. The no wave condition is expressed as

$$kh \sinh kh = \frac{(2n-1)\pi}{2} \quad (n=2,4,6,\cdots) \tag{4.88}$$

This fact indicates that if waves propagate from the region of the negative x in Fig 4.43 and a vertical membrane located at $x = 0$ moves in the way that generates no radiation waves under the condition of Eq. (4.88), we cannot see any transmitted waves in the region of a positive x.

Sawaragi et al. (1989) calculated wave reflection and transmission by a submerged vertical membrane lifted by floats shown in Fig. 4.46. The linear wave maker theory is used in their calculation, assuming that displacement of the membrane is very small. Fig 4.47 shows the reflection coefficient K_R against buoyancy of the float B_u for three different wave frequencies σ, where γ_w and γ are the densities of the membrane in water and in air, respectively, A_{tt} represents the damping coefficient due to membrane motion, and R denotes the distance between the top of the membrane and the still water surface. As seen in this figure, for a certain wave frequency, there exists a particular buoyancy that makes $K_R = 1$, i.e., there is no wave transmission. At this particular buoyancy the membrane oscillates in a mode similar to $(C)_{n=1}$ in Fig. 4.44 and in a different phase from the wave motion. Both wave forces acting on the float and wave transformation by the float are neglected in this calculation, and the float becomes so large that these factors cannot be neglected so that we give it the buoyancy that realizes no transmission. Actually, experimental results did not show such a large reflection coefficient as shown in Fig. 4.47. Thus, this attempt was not successful but implies the possibility of controlling waves by utilizing the motion of the membrane.
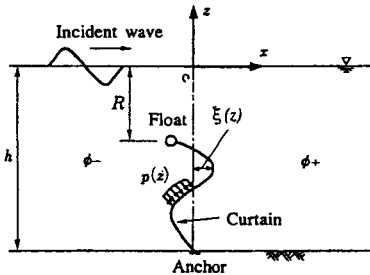
Fig. 4.46 Sketch of a submerged membrane lifted by floats
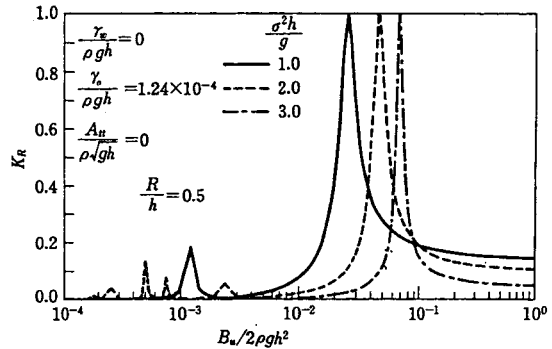
Fig. 4.47 Reflection coefficient versus buoyancy of the float

4.8.2 Some membrane structures for wave attenuation

(1) Sheet breakwaters

Weigel (1962) investigated wave transmission through a sheet floating on a water surface in model tests. According to his experiments, where the length of the sheet is varied, the sheet must be five to ten times as long as the wavelength in order to make the transmission coefficient, (transmitted wave amplitude)/(incident wave amplitude), less than 0.5. Kato (1969) carried out experiments under several different mooring conditions, where it was shown that a sheet with the length of only two times the wavelength can sufficiently reduce transmitted wave amplitudes by improving the mooring system. This is because the sheet motion is controlled by the mooring system and then generates turbulence such as wave breaking. Watarai (1987) carried out experiments on a submerged sheet horizontally supported by poles, and reported that this sheet showed equivalent efficiently or sometimes higher efficiently than a fixed horizontal plate because of the radiation waves due to the sheet motion.

Many other types of sheet breakwaters have been proposed and tested in experiments (Jones 1971). In general, the shorter the wavelength, the more effectively sheet breakwaters can reduce wave height, thus, sheet breakwaters are suitable for attenuating short periodic waves. We should, however, remember that the similarity between models and prototypes must be considered further when applying these sheet breakwaters to an actual sea site.

(2) The submerged air balloon breakwater

Ijima et al. (1985) devised a pair of submerged balloons filled with air and connected by a duct as shown in Fig. 4.48 (a). The wave attenuation mechanism of this device is such that the balloons periodically deform, as shown by the solid and broken lines in Fig. 4.48 (b), in correspondence to wave forms with the some types of lines. The radiation waves due to this oscillatory deformation become out of phase with incident waves in the onshore side, which can reduce the amplitude of transmitted waves. In order to generate the radiation waves effectively, the balloons should be placed at intervals of about half a wavelength. In addition to the phase interaction effect, energy dissipation caused by air flow in the duct also contributes to wave attenuation.

(a)   (b)
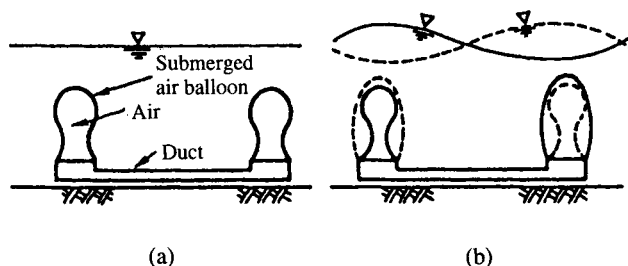
Fig. 4.48   Submerged air balloon breakwater
(after Ijima et al. 1985)

Ijima et al. (1986) have investigated the effect of a submerged air balloon breakwater through model tests and numerical calculations. In order to put the above-mentioned balloons into practical use, where the irregularity of waves should be considered, they put a group of balloons protected by cylinders on a horizontal plate anchored to the bottom as shown in Fig. 4.49. Figure 4.50 shows an example of the transmission coefficient K_T obtained by the experiments for the submerged air balloon breakwater.

The closed and open circles represent the cases with and without the horizontal plate, respectively. The balloons with cylinders are effective in the region where B/L (B: length of the row of balloons, L: wavelength) is large, while the transmission coefficients are almost constant for the cases with the plate. In this figure, we can see that the wave attenuation mechanism of the breakwater becomes different from that of a simple pair of balloons mentioned above, and the turbulence caused by the horizontal plate may influence the wave transformation. The submerged air balloon breakwater is considered to be a breakwater against low waves such as a tentative breakwater for a maritime construction project or as a breakwater for marine product facilities, and field tests have already been performed.
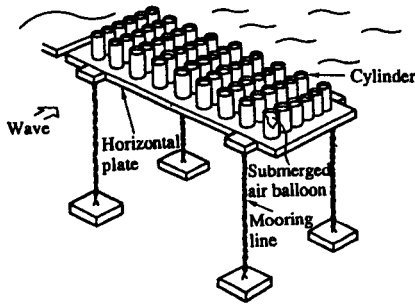
Fig. 4.49 Submerged balloons with cylinders and horizontal plates
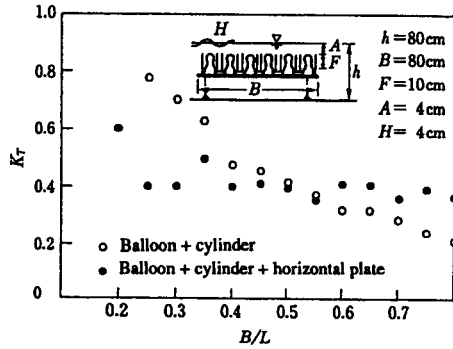
Fig. 4.50 Transmission coefficients for submerged balloon breakwater (after Ijima et al. 1986)

(3) The flexible mound

Tanaka et al. (1990) proposed a rubber-made submerged breakwater filled with water to a slightly higher pressure than the surrounding water as shown in Fig. 4.51, and named it a "flexible mound". Figure 4.52 shows transmission and reflection coefficients for the flexible mound, K_T and K_R, respectively, compared with those for a rigid submerged breakwater with the same shape, where Δp denotes additional pressure of the enclosed water. In flexible mound cases, the transmission coefficients show smaller values than those for the rigid breakwater in all the tested ranges of B/L, while the reflection coefficients become much larger. Other characteristics of the transformation by the flexible mound different from those of the rigid breakwater are such that the ratio of the water depth at the top of the mound to the incident wave height, R/H_I – which is the most important factor for rigid submerged breakwaters – hardly influences the wave transformation, and also that the transmission coefficients show smaller values even for the large water depth at the top of the mound, for example $K_T = 0.5$ for $R/h = 0.5$. It is considered that these differences exist because the main wave attenuation mechanism of the flexible mound is the phase interaction between radiation waves due to the motions of the mound and diffraction waves that correspond to the transmitted waves over the rigid breakwater.

Oyama et al. (1989) explained the wave attenuation mechanism through numerical analyses by using linear and nonlinear potential theories, which clearly show the effect of radiation waves in reducing transmitted wave amplitudes. Their numerical simulations also show wave attenuation in a wide wave frequency range because of the multi-mode motion of the flexible mound. The flexible mound thus has practical potential if some problems such as anchoring are solved.
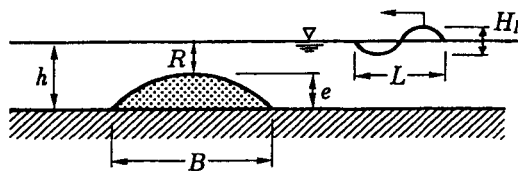
Fig. 4.51   Sketch of the flexible mound
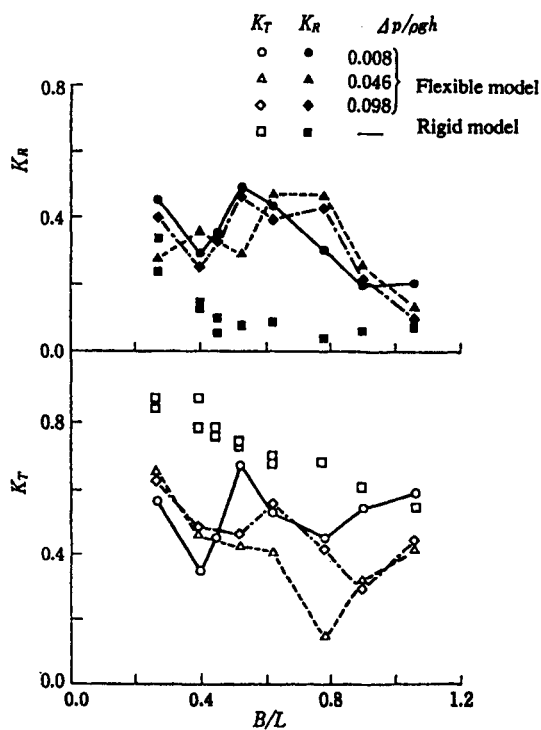
Fig. 4.52   Reflection and transmission coeffcients for flexible mound
($R/h = 0.24 - 0.26$, $R/H_I = 0.83 - 1.08$) (after Tanaka et al. 1990)

References

Ahrens, J.P. and B.L. Mccartney (1975): Wave period effect on the stability of riprap, Proc. Civil Eng. in the Ocean/III, ASCE, 2, pp.1019-1034.

Breber, A. and D. Donnely (1962): Laboratory study of rubble foundation for vertical breakwaters, Proc. 8th Int. Conf. on Coastal, ASCE, 1962.

Bruun, P. and A.R. Günbak (1976): Hydraulic and friction parameters affecting the stability of rubble mounds, Proc. PIANC Bull.24, pp.33-46.

Coastal Engineering Research Center (1984): Shore Protection Manual, Vol. II.

Deguchi, I., T. Sawaragi and K. Shiratani, (1988): Applicability of non-linear unsteady Darcy's law to the waves on permeable layer, Proc. 35 Japanese Conf. on Coastal Eng., JSCE, pp.487-491. (In Japanese)

Goda, Y. (1974): A new method of wave pressure calculation for the design of composite breakwater, Proc. 14th Int. Conf. on Coastal, ASCE, pp.1702-1720.

Goda, Y., (1985): Random Seas and Design of Maritime Structures, Univ. of Tokyo Press, pp.114-116.

Haskind, M.D. (1959): Radiation and diffraction by a flat plate floating vertically, Prikl. Mat. Mekh., Vol.23, pp.372-382.

Ijima, T., T. Uwatoko and Y. Ushifusa (1985): Wave interception by sea-balloon breakwater, Memoirs of the Faculty of Eng., Kyushu Univ., Vol.45, No.4, pp.357-392.

Ijima, T., T. Uwatoko and Y. Ushifusa (1986): Experiments on the improvement of wave interception effect of sea-balloon breakwater, Memoirs of the Faculty of Eng., Kyushu Univ., Vol.46, No.2, pp.193-206.

Ippen, A.T. (1966): Estuary and Coastline Hydrodynamics, McGraw-Hill, 744p.

Iwata, K. and D. Kim (1990): Dynamic behaviour of submerged tension-moored floating structure with pressurized air-chamber and wave transformation, Proc. PACOMS '90, ISOPE, Vol.II, pp.287-294.

Izumiya, T. and M. Endo, (1989): Analysis of wave field around submerged breakwater and permeable structure, Proc. 36th. Japanese Conf. on Coastal Eng., JSCE, pp.638-642. (in Japanese)

Jarlan, G.E. (1961): A perforated vertical wall breakwater, Dock & Harbor Authority, Vol. XIII, No. 486, April, pp.394-398.

Jarlan, G.E. (1965): The application of acoustic theory to the reflection properties of coastal engineering structures, Quaterly Bull., No.1965(1), NRC of Canada, pp.23-63.

Jones, D.B. (1971): Transportable breakwaters — A survey of concepts, Tech. Rept., Naval Civil Engineering Laboratory, U.S. Army Corps of Eng.

Kikkwawa, H., H. Shiijai and F. Kohno, (1967): Fundamental study on wave overtopping on seawalls, Coastal Eng. in Japan, JSCE, Vol.3, pp.53-62.

Kim, D. and K. Iwata (1992); Dynamic behaviour of tautly moored semi-submerged structure with pressurized air-chamber and resulting wave transformation, Coastal Eng. in Japan, JSCE, Vol.34, No.2, pp.223-242.

Kobayashi, N. and A. Wurjanto (1990): Numerical model for waves on rough permeable slopes, J. Coastal Res., Special Issue, No.7, pp.149-166.

Kobayashi, N. and A. Wurjanto (1990): Irregular waves on rough permeable slopes, J. Coastal Res., Special Issue, No.7, pp.167-184.

Kondo, H. (1977): Analysis of breakwaters having two porous walls, Coastal Structures '79, ASCE, Vol.1, pp.962-977.

Le Mehauté, B. and S. Wang (1985): Wave statistical uncertaintities and design of breakwater, J. Waterway, Port, Coastal and Ocean Eng., ASCE, Vol.111, No. 5, pp.921-938.

Liu, P. L-F and M. Abbaspour(1982): Wave scattering by a rigid thin barrier, J. Waterway, Port, Coastal and Ocean Div., Proc. ASCE, Vol.108, No.WW4, pp.479-490.

Losada, M.A. andd L.A. Gimenez-Curto (1981): Flow characteristics on rough, permeable slopes under wave action, Coastal Eng., 4, pp.187-206.

Morihira, M., S. Kakizaki and Y. Goda (1964): Experimental investigation of a curtain-wall breakwater, Rep. Port and Harbour Res. Inst., Vol.3, No.1.

Nakamura, T. (1983): Numerical analysis on wave boundary-value problem around a thin-walled body of arbitrary section, Proc. 30th Japanese Conference. on Coastal Eng., pp.410-414. (in Japanese)

Nakamura, T. (1984): Wave transmission and reflection characteristics of a curtain walled breakwater and wave loading on it, Proc. 31st Japanese Conference. on Coastal Eng., JSCE, pp.512-516. (in Japanese)

Nakamura, T. and S. Morita (1985): Wave attenuation method by the use of wave resonance between double-row of curtain-walls, Proc. 32nd Japanese Conference. on Coastal Eng., JSCE, pp.525-529. (in Japanese)

Nakamura, T. (1992): Numerical modeling of vortex formation around a large angular body in waves, Proc. 2nd Int. Offshore and Polar Eng. Conf., ISOPE, Vol.III, pp.217-224.

Nielsen, S.R.K. and H.F. Burcharth (1983): Stochastic design of rubble mound breakwaters, Proc. 11th IFIP Conf. on Symp. Modeling and Optimization.

Oyama, T., M. Tanaka, T. Kiyokawa, T. Uda and Y. Murai (1989): Transmission and reflection characteristics of waves over a submerged flexible mound, Coastal Eng. in Japan, JCSE, Vol. 32, No.1, pp.53-68.

Penny, W.G. and A.T. Price (1952): The diffraction theory of sea waves by breakwaters. Phil. Trans., Roy. Soc. London. A244, pp.236-253.

Pilarczyk, K.W. (1987): Sea defences, Dutch guidelines on dike protection, Report, W.B.No.87110, Dutch Ministry of Transport and Public Works Road and Hydraulic Eng. Department.

Putman. J.A. and R.S. Arthur (1948): Diffraction water waves by breakwaters. Trans. Amer. Geophys. Union, Vol.29, No.4, pp.481-490.

Ryu, C.R. and T. Sawaragi (1986a): A new design method of rubble mound structures, Proc. 20th Int. Conf. on Coastal, ASCE, pp.2188-2202.

Ryu, C.R. and T. Sawaragi (1986b): Wave control function and design principles of composite rubble mound structures, Coastal Eng. in Japan, JSCE, Vol.29, pp.227-240.

Sawaragi, T. and K. Iwata (1973a): On wave deformation due to permeable structures, Coastal Eng. in Japan, JSCE, Vol.16, pp.107-122.

Sawaragi, T. and K. Iwata (1973b): Some considerations on hydraulic properties of perforated-type vertrical quaywalls,. Proc. JSCE, No. 220, pp.53-63. (in Japanese)

Sawaragi, T. and K. Iwata (1976): Wave spectrum of breaking waves, Proc. 15th Int. Conf. on Coastal, ASCE, pp.580-594.

Sawaragi, T. and K. Iwata (1978): Wave attenuation of a vertical breakwaater with two air-chambers, Coastal Eng. in Japan, JSCE, Vol.21, pp.63-74.

Sawaragi, T. and K. Iwata (1979): Irregular wave attenuation due to a vertical breakwater with air-chamber, Coastal Structures '79, ASCE, Vol.1, pp.29-47.

Sawaragi, T., I. Deguchi and G. Hong (1986): Effect of rubble mound foundations of composite type breakwater on reductuion of reflection, Proc. 5th Cong. APD, IAHR, pp.361-378.

Sawaragi, T., I. Deguchi and S.K. Park, (1988): Reduction of wave overtopping rate by the use of artificial reef, Proc. 21st Int. Conf. on Coastal, ASCE, pp.335-349.

Sawaragi, T., Y. Okahara and I. Deguchi, (1989): Study on reduction of wave energy by submerged breakwater with wide crown width and its scale effect, Proc. 36th Japanese Conf. on Coastal Eng., JSCE, pp.633-637. (in Japanese)

Sawaragi, T., S. Aoki and H. Liu (1989): Wave deformation and forces on a submerged silt curtain, Proc. 30th Japanese Conf. on Coastal Eng., JSCE Vol.36, pp.559-563. (in Japanese)

Sollitt, C.K. and R.H. Cross (1972): Wave reflection and transmission at permeable breakwaters, Rept. Ralph Person's Lab., MIT, No. 147.

Stiassnie, M., Y. Agnon and E. Naheer (1981): Scattering of water waves by a system of vertical floating plates, Proc. Int. Symp. on Hydrodynamics in Ocean Eng., pp.1111-1132.

Tanaka, M., T. Oyama, T. Kiyokawa, T. Uda and A. Omata (1990): Wave control by flexible underwater mound, Proc. Offshore Tech. Conf., OTC 6405, pp.551-558.

Tanimoto, K., K. Shimozako, and K, Miyazaki (1987): Irregular wave forces acting on dual cylindrical-type structure for wave control, Proc. 34th Japanese Conf. on Coastal Eng., JSCE, pp.571-575. (in Japanese)

Ursell, F. (1974): The effect of a fixed vertical barrier on surface waves in deepwater, Proc. Camb. Phil. Soc., Vol.43, pp.372-382.

Valembois, J. (1953): Etude de l'action d'ouvrages resonants sur lu propagation de la houle, Minnesota International Hydraulic Convention.

Valembois, J. et C. Birard (1955): Les ouvrages resonants et heur application a la protection des ports, Proc. 5th Conference on Coastal Eng., ASCE, p.637.

Van der Meer, J.W. and K.W. Pilarczyk (1984): Stability of rubble mound slopes under random wave attack, Proc. 19th Int. Conf. on Coastal, ASCE, Vol.III, pp.2620-2634.

Van der Meer, J.W. and K.W. Pilarczyk (1987): Stability of breakwater armour layers deterministic and probabilistic design, Delft Hyd. Lab., Pub. No.378, 34p.

Watarai, H., Y. Ohashi and S. Nagasaki (1987): Wave dissipating structure of new type using piles and flexible textile sheet, Proc. 34th Japanese Conf. on Coastal Eng., JSCE, pp.502-506. (in Japanese)

Wiegel R.L. (1960): Transmission of wave past a rigid vertical thin barrier, J. Waterways and Harbors Div., Proc. ASCE, Vol. 86, No.WW1, pp.1-12.

Wiegel, R.L. (1962): Oceanographical Engineering, Chapter VI, Effect of structures on waves, pp.137-141.

Yamamoto, T. (1981): Moored floating breakwater response to regular and irregular waves, Appl. Ocean Res., Vol.3, No.1, pp.27-36.

Chapter 5   Structure for Controlling Sediment Movement

5.1 Basic Concept and Structure for Controlling Sediment Movement

Up until now, many devices have been concentrated to control and also to prevent various phenomena such as beach erosion, blockage of river mouths, shoaling of harbors and navigation channels caused by sediment movement. Deformations of bottom topography in coastal areas have various time and spatial scales. There are also topographic changes on a global scale that may continue for a century. Deformation of ripples on the bottom may be the smallest scale.

The time scale of topographic changes, e.g., beach erosion, is classified into the following from the engineering point of view:

(1) Beach erosion that continues for at least several years; a decrease in the sand supply from rivers, and the artificial destruction of the natural balance of sediment movement in coastal areas due to the construction of structure, bring about such beach erosion where longshore sediment transport plays an important role. Erosion of this type usually occurs on a large scale.

(2) Beach erosion that continues for only a week or so; an attack of high waves generated by a low pressure system to the almost equilibrium beach causes beach erosion. Sediment movement in a cross-shore direction, especially a sediment movement offshore, plays an important role.

There are various modes of sediment movement such as a bed load, suspended load and sheet flow. Therefore, when we try to reduce beach erosion, we have to know the mode and direction of sediment transport that causes erosion. In this chapter, our basic concept for controlling sediment movement and beach deformation is explained. Then the function of structures that have been used for controlling sediment transport and beach deformation are reviewed briefly. Finally, the hydraulic and beach erosion controlling function of some representative structures are discussed based on the results of recent research.

5.1.1 Basic concept for controlling sediment movement and existing structures used for erosion control

The beach deformations to be controlled are the erosion type and accretion type. Schematic examples of these are shown in Fig. 5.1. Beach deformations of the erosion type are caused by an imbalance of longshore sediment transport in the longshore direction brought about by a decrease of discharged sediment from the source, due to the artificial destruction of sediment transport brought about by the construction of coastal structures etc. When extremely high waves attack the beach that nearly in an equilibrium state, net offshore sediment transport will also cause beach erosion. At this time, eroded sediment in the shallow water region usually deposited offshore and decreases the water depth there. At the toe of coastal structures, such as sea walls and breakwaters, local scouring may occur by a return flow or mass transport velocity in front of them.

On the other hand, a topographic change of the accretion type to be controlled are the blockage of river mouths, the shoaling of navigation channels and harbors and so on. Because such beach deformations become obstacles for our social and economic activities various structure have been constructed to reduce and control them. Recently, various coastal structures have also been constructed not only from the viewpoint of disaster prevention but also from the viewpoint of effective utilization of the seashore.
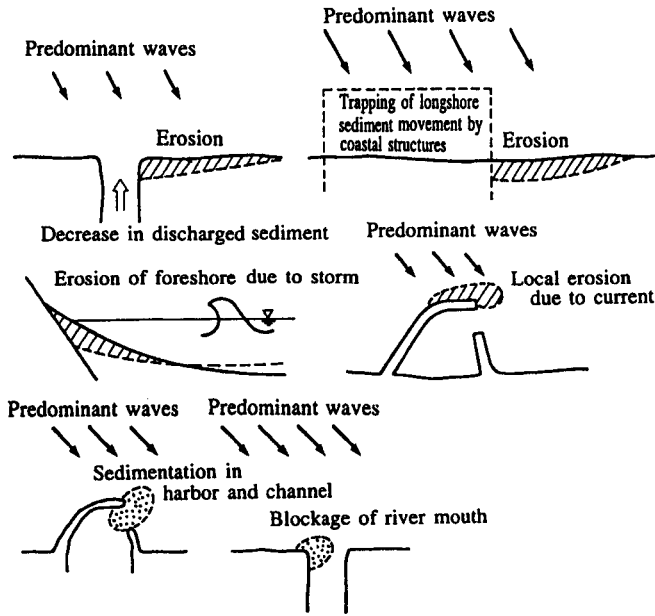
Fig. 5.1 Topographic change to be controlled

In Table 5.1, existing coastal structures that have been constructed in coastal areas are listed together with their hydraulic function and function to control sediment movement. Other structures such as "L-shape" or "T-shape" jetties, which exhibit the characteristics of both jetties and offshore detached breakwaters have also been used. The artificial reef in Table 5.1 includes submerged breakwaters with a wide crown width and a perched beach-type artificial beach.

5.1.2 Procedure for determining beach deformation controlling works

The procedure to determine which method should be adopted from various works, some examples of which are listed in Table 5.1, has not established yet. Figure 5.2 is the general procedure for determining the work to control beach deformation.

(i) Past and present characteristics of beach deformation and sediment movement of the objective beach:

First of all, we have to analyze the cause of beach deformation and the predominant sediment movement (direction and mode) to be controlled on the basis of sounding data, bed material characteristics, river run-off, and weather and sea conditions of the objective beach. We also have to fix various input conditions, such as characteristics of beach and incoming waves, that will be used in the assessment of the effect of the structures on the surrounding coast.

(ii) Selection of various methods:

Based on the analysis carried out in (i), some candidates are chosen from various types of structures. To do so, functions of structures to control fluid motion and sediment movement have to be fully investigated.

Table 5.1 Hydraulic function of various coastal structures

Structures	Hydraulic function	Function to control sediment movement	
Groins	Spur dike for longshore current	Direct trapping of longshore current	Saw-tooth shape shoreline
Offshore detached breakwaters	Reduction and control of wave height and direction by diffraction	Control of longshore and cross-shore sediment transport	Concabo-convex shoreline, obstacle to natural coastal view
Headland	Control of wave height and direction by diffraction and reflaction	Re-distribution of incident wave energy evenly	
Artificial beach	Reduction of wave energy by breaking and energy loss in permeable layer	Control of longshore and cross-shore sediment transport	
Sea dike	Control of land ward limit of wave penetration	Prevention of shoreline to retreat, control of longshore sediment transport	Local scouring, loss of foreshore due to return flow or reflected waves

(iii) Evaluation of the effects of the candidates on the surrounding coast:
At this stage, we have to evaluate the effects of each candidate and assess the influence of them on the surrounding coast. This is usually done by numerical simulation (numerical model) or by hydraulic model experiments (physical model). The detail of the numerical model has already been described in Chapter 3. Although many studies of this kind have been conducted, unsolved problems still remain, especially in the movable bed experiments, related to the similitude law and reproducibility of the phenomena in the field in the laboratory. Furthermore, we cannot always predict fluid motion close to the structures with sufficient accuracy by the numerical method. Hybrid method (for example, Irie and Kuriyama, 1985) where topographic change is predicted numerically by using waves and current fields obtained in the hydraulic experiments might be an effective tool.
(iv) Other evaluations and (v) Determination of evaluation criteria:
The cost of construction, view, durable years, water quality environment, and relation to fishing industry are raised in these items. However, the standard evaluation criteria are not established. They are determined case-by-case.
Here a general procedure to determine the beach deformation controlling work is explained. Whichever procedure we use to determine the proper structure, it is needless to say that we have to quantitatively evaluate the effect and the influence of them. In the following, functions of representative structures (offshore detached breakwaters, groins, artificial reefs, gentle slope seadikes and beach nourishment) to control fluid motion (waves and current) and the resulting sediment transport are reviewed.

(i) Investigation of present state and
characteristics of past topographic
changes and sediment movement

(ii) Selection of countermeasures

(v) Determination of standard criteria

(iii) Assessment for the effect of shore protection
and effect on surrounding coast

(iv) Assessment for other issues

Optimum

Construction
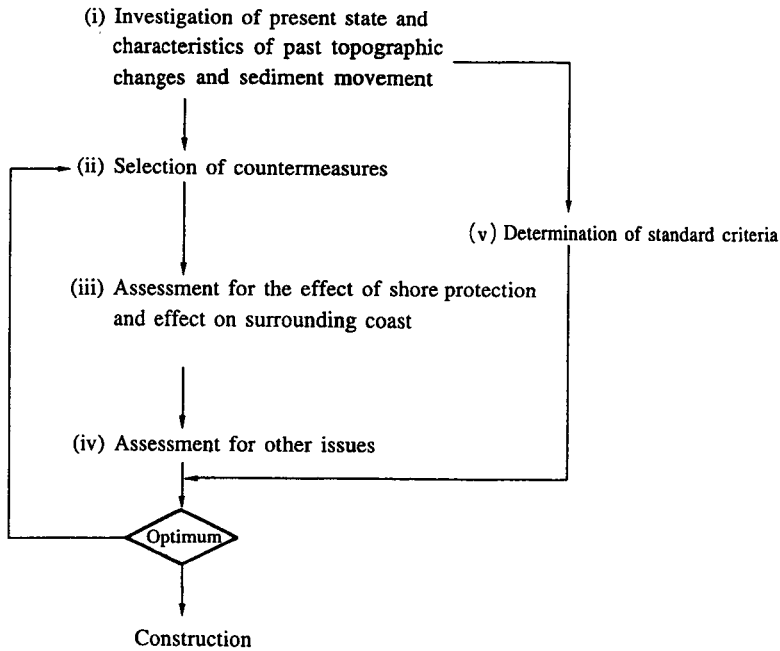
Fig. 5.2 Flow chart for determining countermeasures

5.2 Beach Deformation Control by Offshore Detached Breakwaters

5.2.1 Dimensions of existing offshore detached breakwaters and occurrence limit of salient and tombolo

Offshore detached breakwaters have been constructed as coastal disaster prevention works all over Japan. The reason for this is that they have an effective function to reduce wave energy and trap sediment shoreward of them and that their construction and maintenance are also not so difficult. Tong shaped topographic features called salient and tombolo are usually formed along the shoreline shoreward of them. Many studies have been carried out about the wave transformation and topographic change around offshore detached breakwaters.

Offshore detached breakwaters control waves mainly by diffracting waves. We can predict the wave-height distribution around offshore detached breakwaters caused purely by diffraction including the effect of an opening between them (see Chapter 2). Offshore detached breakwaters in the field are usually constructed on the coasts that have a certain bottom slope. Waves diffracted by an offshore detached breakwater experience various changes in water depth such as shoaling, refraction and breaking. We can also predict such wave transformation by using the so-called unsteady mild slope equations (see Chapter 1). However, all existing offshore detached breakwaters were not always constructed after investigating their wave controlling functions by such a method.

Figure 5.3 shows the relation between the water depth at the toe at HWL. h_i, the offshore distance from the shoreline x_{off} and the length l of the offshore detached breakwaters that were constructed along various coasts of Japan for the purpose of controlling beach erosion. Where they were constructed as a group, average values are shown.
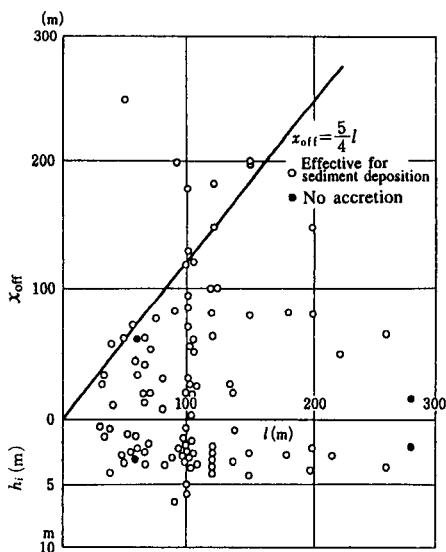
Fig. 5.3 Length and locations of existing offshore detached breakwaters

The length and offshore distance of the offshore detached breakwaters range between 30m to 320m and 10m to 370m. The toe depth at HWL. of more than 90% of the breakwaters is shallower than 5m. The crown height of the breakwater is usually higher than the HWL. by one half of the design wave height.

The opening width B when they were executed with a group is distributed widely between 6m to 100m. Figure 5.4 shows the relation between the non-dimensional opening width B/l and the non-dimensional offshore distance x_{off}/l. Most groups of offshore detached breakwaters were constructed in the range of $x_{off}/l < 1.0$ and $x_{off}/l > B/l$. Only one case is reported where there is no significant effect to reduce erosion that is illustrated by a closed circle in the figure.
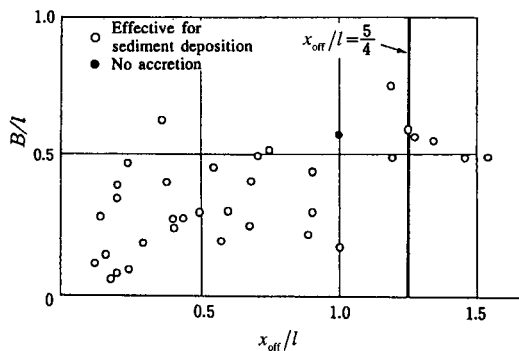
Fig. 5.4 Opening width and location of existing offshore detached breakwaters

It is needless to say that we must discuss the effect of the offshore detached breakwater on deposition of sediment with respect to incident wave characteristics. Savage (1954) examined the occurrence limit of salient and tombolo behind the offshore detached breakwater through simplified movable bed experiments in the case where the length of the breakwater was equal to the length of incident waves L_o. The results showed that a salient occurred in the region of $x_{off}/L_o<5/4$, in other words, $x_{off}/l<5/4$. However, according to the experimental results of Shinohara and Tsubaki (1966) salient was generated even in the case of $x_{off}/L_o=2.0$ ($x_{off}/l=1.76$) when $l/L_o=1.13$. Furthermore, Figs. 5.3 and 5.4 show that existing offshore detached breakwaters whose dimensions and locations are beyond the limit of Savage have enough function to reduce beach erosion.

This means that we cannot discuss the occurrence limit of salient and the effect of offshore detached breakwaters based on the experimental results under limited conditions. In the following, the function of offshore detached breakwaters to control sediment transport around them are discussed from the view point of external forces of sediment transport such as waves, and wave-induced current around them.

5.2.2 Function of offshore detached breakwater to control wave and wave-induced current

The function of offshore detached breakwaters to control incident waves depends largely on their diffraction effect. Wave deformation caused by diffraction becomes a function of the distance from the body of the breakwater. In shoreward region of the offshore detached breakwater executed on a sloping beach, diffracted waves refract, shoal and break and finally loose their energy on the sloping beach. For controlling wave-induced current and sediment movement, it becomes very important to know how the offshore detached breakwater affects the waves in the surf zone.

Figure 5.5 is an example of the experimental result showing the effect of the length and the location of an offshore detached breakwater on the wave height distribution along the shoreline at $x/x_b=0.28$, where x_b is the width of the breaker zone (Sawaragi and Deguchi, 1990). Figures (a), (b) and (c) correspond to the cases of the location of the breakwater of $x_{off}/x_b=0.57$, 0.86 and 1.70, respectively. The vertical axis of each figure is the wave height measured along the line of $x/x_b=0.28$ normalized by the measured wave height H_n at the same point on a natural beach without breakwaters. The values of $\tan\beta$, H_o, T and θ are the beach slope, the equivalent deepwater wave height, period and angle of wave incidence at deepwater.

As is naturally expected, wave attenuation is large when the location of the breakwater is close to the measuring line ($x/x_b=0.28$). When the breakwater was constructed in the surf zone, the maximum wave attenuation rate in two cases of $l/L_o\geq0.75$ are almost the same but the maximum wave attenuation rate in the case of $l/L_o=0.5$ is smaller than other longer cases (Figs. 5.5 (a) and (b)). The interaction of diffracted waves from both ends of the breakwater causes this difference. As the distance between the line $x/x_b=0.28$ and the breakwater increases, that is, in the case where the breakwater was constructed outside the breaker zone, the longshore distribution of wave height approaches uniform due also to the interaction of diffracted waves from both ends of the breakwater (Fig. 5.5 (c)).

As for the effect of the interaction of two breakwaters, wave height distribution in the shoreward side of the breakwater is almost the same as that behind the single breakwater up to $x/x_b=0.67$. However, the wave height distribution along the line of $x/x_b=0.33$ no longer coincides with that behind the single breakwater.

It is well known that wave-induced current behind the breakwater caused by normal incident waves is characterized by the formation of a pair of circulation cells. It is also shown that such wave-induced current patterns can be reproduced by numerical simulation (e.g., Sawaragi et al., 1981 and Ohnaka et al., 1988).

However, under conditions of oblique wave incidence, longshore current flowed behind the breakwater smoothly. Figure 5.6 shows the flow patterns of wave-induced current around breakwaters of various lengths. Arrows in the figures are the velocity vectors obtained by tracing floats in the experiments. Although wave heights decrease to a great extent behind the breakwater, these wave fields have little influence on the longshore current behind the breakwater.
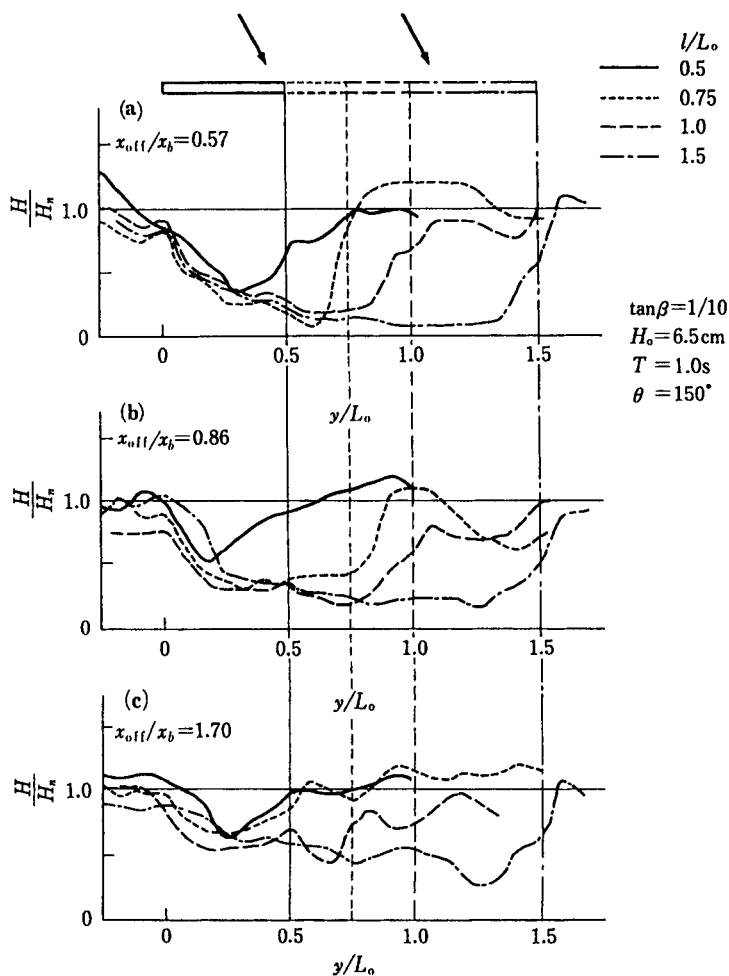
Fig. 5.5 Wave height distribution behind offshore detached breakwaters ((a):x_{off}/x_b=0.57,(b):x_{off}/x_b=0.86,(c):x_{off}/x_b=1.70)
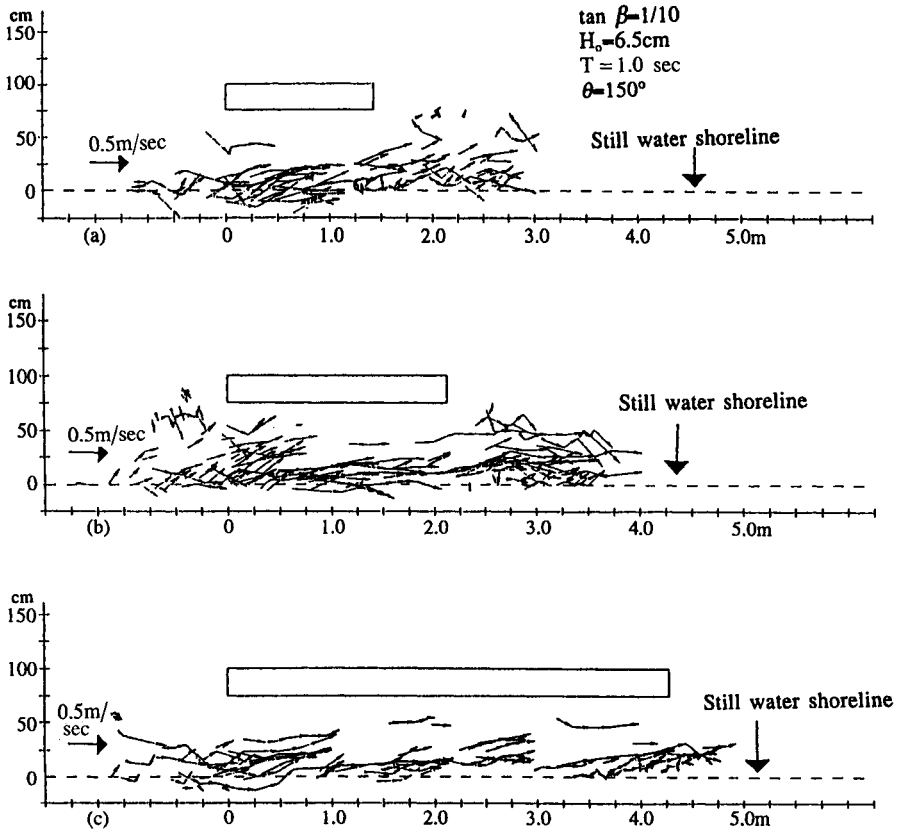
Fig. 5.6 Flow pattern of wave-induced current (x_{off}/x_b=0.86)
((a):l/L_o=0.5, (b):l/L_o=0.75, (c):l/L_o=1.5)

5.2.3 Longshore sediment transport and topographic change around the offshore detached breakwater

Shoreward of the offshore detached breakwater, under the condition of an almost normal wave incidence, diffracted waves and a pair of wave-induced circulation cells generate tongue shaped sand bars called salient and tombolo. The probability of occurrence of net offshore sediment movement decreases behind the offshore detached breakwater because of the wave attenuation. It is also pointed out that they exhibit a function to trap suspended sediment transported from the offshore of the breakwater.

On the other hand, an offshore detached breakwater constructed on a sloping beach where longshore sediment transport is established by obliquely incident waves traps a larger amount of sediment than in the case of normal wave incidence. In such a case, salient becomes easy to form. As a result, sand supply at the down stream side of the breakwater decreases significantly and erosion occurs there.

Figure 5.7 shows three examples of the topographic changes that took place around the breakwaters 1hr after wave generation measured in the movable beach model experiment

with the mean diameter bed material d_{50}=0.05cm. Figures 5.7 (a) and (b) are the cases of a single breakwater constructed inside and outside of the breaker zone. Figure 5.7 (c) is the case of a pair of breakwaters constructed outside the breaker zone.
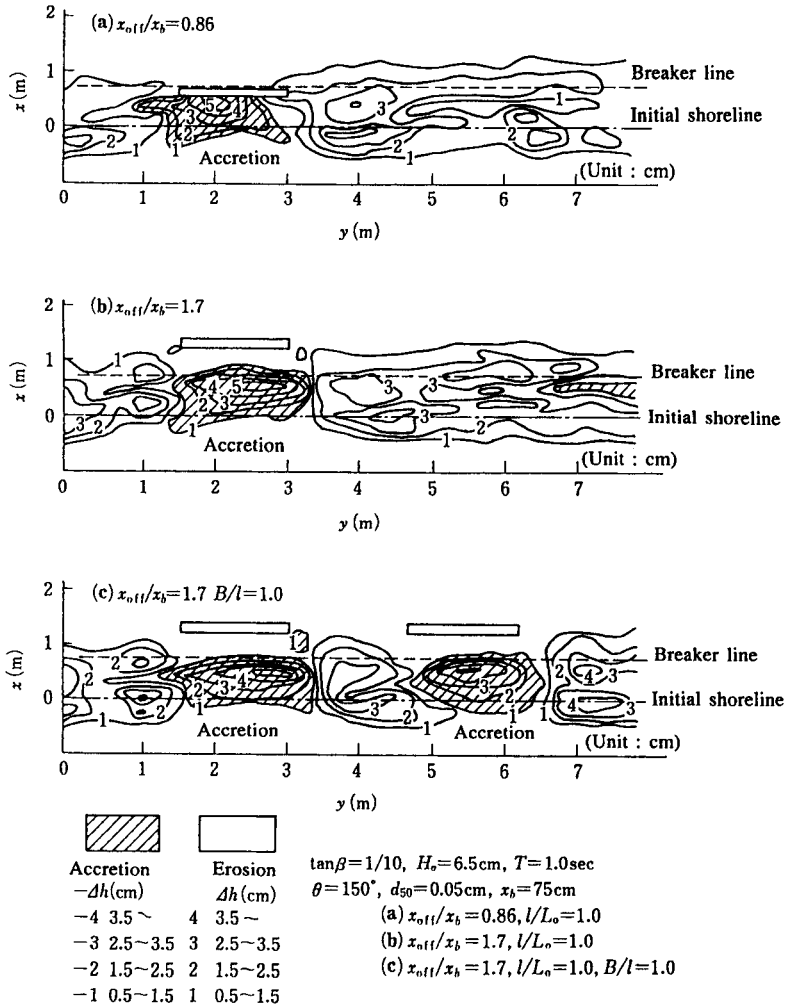
Fig. 5.7 Topographic change around breakwater (l/L_o=1.0)
((a):x_{off}/x_b=0.86, (b):x_{off}/x_b=1.7 and (c):x_{off}/x_b=1.7, B/l=1.0)

In the figure, accreted regions are shown by the hatched area. A significant deposition took place behind the breakwater in every case. To discuss the function of the offshore detached breakwater of controlling sediment transport, it is necessary to examine where did the deposited sand come from; i.e., from the upstream side, downstream side or from

offshore region. The authors investigated this point by analyzing the topographic change $\Delta h(x,y)$ at a measuring grid point (x,y) in two different ways. One was to examine the distribution of the total longshore sediment transport rate $Q_{ye}(y)$ and the other was using empirical eigenfunction analysis.

(1) Function of the offshore detached breakwater to trap sediment with respect to the total longshore sediment transport rate

The total longshore sediment transport rate is calculated using measured change in the water depth $\Delta h(x,y)$ during the time interval Δt in the following equation:

$$\Delta A(j)\big/\Delta t = \left\{Q_{ye}(j+1)-Q_{ye}(j)\right\}\big/\Delta y\big/(1-\lambda) \tag{5.1}$$

$$\Delta A(j) = \int \Delta h(x,j\Delta y)\,dx$$

where j is the number of the measuring line set at the distance of Δy in the longshore direction, λ is the void ratio of the bed material.

Solid lines with closed circles in Fig. 5.8 shows some examples of calculated longshore distribution of the total longshore sediment transport rate $Q_{ye}(y)$ from Eq. (5.1) using topographic change took place during $t/T=0$ and 1800.
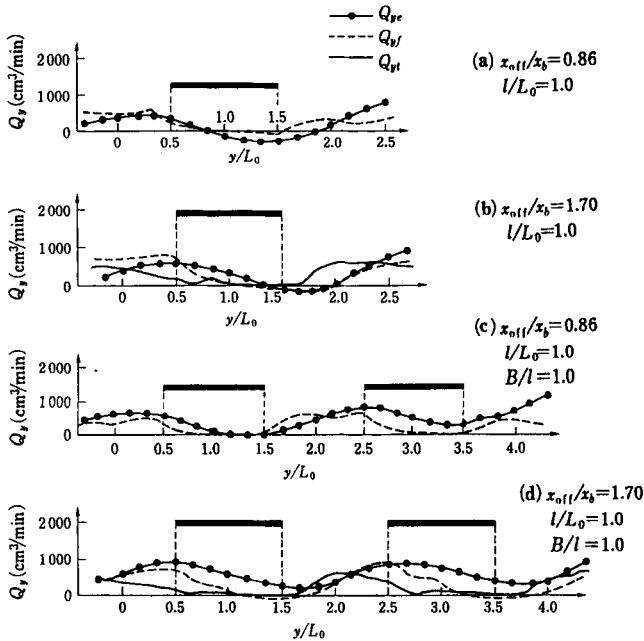
Fig. 5.8 Total longshore sediment transport rate around breakwater
$((a):x_{off}/x_b=0.86, (b):x_{off}/x_b=1.7, (c):x_{off}/x_b=0.86, B/l=1.0, (d):x_{off}/x_b=1.7, B/l=1.0)$

When a single breakwater was constructed within the breaker zone, the value of Q_{ye} becomes negative in the lee-side of the breakwater which means that sediment was transported in the opposite direction of the longshore current in this region (Fig. (a)). On the other hand, when a pair of breakwaters was constructed, although the value of Q_{ye} almost approaches zero, no significant negative value of Q_{ye} appears regardless of its position (Figs. (c) and (d)). This means that most of the sediment transported from the upstream side is trapped behind the breakwater.

(2) Function of the offshore detached breakwater evaluated from empirical eigenfunction
In this section, the pattern of sediment movement and function of trapping sediment of an offshore detached breakwater are investigated based on the cross-shore and the longshore eigenfunction of the measured topographic changes around the breakwaters.

Figures 5.9 illustrates examples of the longshore and cross-shore eigenfunctions of the maximum eigenvalue ($e_1(x)$ and $c_1(y)$). The ratio of the maximum eigenvalue to the trace is more than 60%.
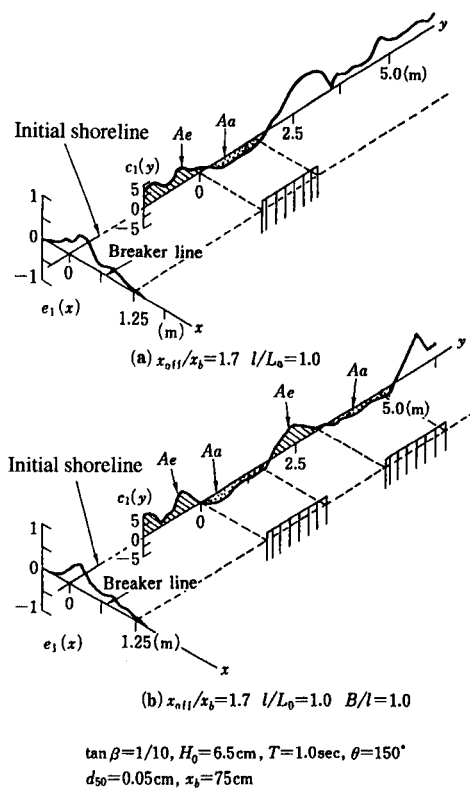
Fig. 5.9 Cross-shore and long-shore eigenfunction corresponding to the largest eigenvalue ($x_{off}/x_b=1.7$) ((a):$l/L_o=1.0$, (b):$l/L_o=1.0$, $B/l=1.0$)

Figure (a) is the case where the single breakwater was set at $x_{off}/x_b=1.7$. Figure (b) is the result of the case where a pair of breakwaters was constructed at the same location. As can be seen from these figures, $e_1(x)$ is positive throughout the whole region and $c_1(y)$ indicates both positive and negative values along the longshore direction. Especially, behind the breakwater, the value of $c_1(y)$ is negative. Therefore, it can be judged that the pattern of the topographic change represented by the product $c_1(y)*e_1(x)$ was caused by the longshore sediment transport. Therefore, we can evaluate the eroded and deposited volume caused by the longshore sediment transport from the longshore distribution of the longshore eigenfunction $c_1(y)$; that is, the ratio of the volume of deposited sediment behind the breakwater and the volume of eroded sediment in the upstream side of the breakwater is estimated by the ratio of the area of hatched region A_e and the area of dotted region A_a. If A_a is greater than A_e, more sediment transported from the upstream side of the breakwater was deposited behind the breakwater. This means that the sediment in the downstream side of the breakwater was transported in the opposite direction of longshore current by the diffracted waves. If A_a is smaller than A_e, a part of the sediment transported from the upstream side of the breakwater in the longshore direction was transported to the lee-side behind the breakwater.

Figure 5.10 shows the ratio of A_a/A_e of all the cases carried out in the experiments. Open circles are the cases of a single breakwater and the breakwater of the up-stream side. Closed circles are the results of the leeward breakwater.
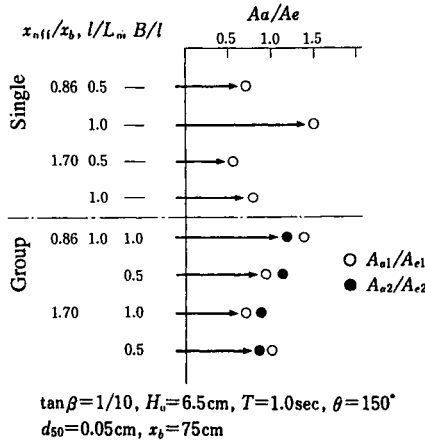
Fig. 5.10 Ratio of A_a/A_e

In the case of $x_{off}/x_b=0.86$ and $l/L_o=1.0$, the ratio of A_a/A_e becomes almost 1.5. In this case, the sediment in both the upstream-side and lee-side of the breakwater was transported behind the breakwater and settled there. The same conclusion has already been derived from the analysis of the distribution of Q_{ye} (see Fig. 5.8).

When the length of the breakwater is 1/2 of the incident wavelength, 50 to 60% of the amount of the sediment transported in the longshore direction is trapped behind the breakwater and the rest flows leeward behind the breakwater. Furthermore, a group of breakwaters has a high efficiency to trap sediment behind them when compared with the single breakwater of the same dimensions regardless of the opening width.

5.2.4 Estimation of total longshore sediment transport rate around offshore detached breakwater

As explained in the foregoing sections, a beach deformation in the shore side of the offshore detached breakwater is mainly caused by littoral sand drift. There also exists a strong correlation between a change in the sectional area ΔA and the shift of the location of shoreline Δl . A correlation coefficient is larger than 0.8 regardless of the location and length of the breakwaters. Accordingly, the so-called one-line theory (see **3.3.2**) can be applied for estimating the shoreline configuration around the offshore detached breakwater if we can predict the longshore distribution of the total longshore sediment transport rate Q_y.

The value of Q_y is usually estimated by using the wave characteristics at breaking point and the direction of the longshore sediment transport is uniquely determined by the wave breaking angle. However, there is possibility that the direction of longshore sediment transport shoreward of the offshore detached breakwater under the oblique wave incidence where strong wave-induce current is generated, an example of which is shown in Figure 5.6, does not coincide with the wave breaking angle.

Furthermore, the longshore sediment transport rate cannot be calculated from the wave characteristics at the breaking point when the breakwater is constructed within the breaker zone. In such cases, the value of Q_y must be determined through the integration of the cross-shore distribution of the local longshore sediment transport rate that will be estimated by using the wave field and wave-induced current around the breakwater.

The wave field around the breakwater is estimated by solving the unsteady mild slope equations where the effect of momentum dissipation due to wave breaking is included numerically (Eqs. (3.114) and (3.115)). Wave-induced current around the breakwater is also calculated by using a depth and time averaged fundamental equation of a wave-induced current (Eqs. (3.117) to (3.119)) by applying the ADI method.

The local longshore sediment transport rate $q_y(x,y)$ is then evaluated by using wave characteristics, and the wave-induced current velocity at an arbitrary location by the proper method that has been mentioned in Chapter 3 (**3.4.4**). Finally, the total longshore sediment transport rate $Q_y(y)$ is finally obtained by integrating $q_y(x,y)$ in the cross-shore direction.

A longshore distribution of the total longshore sediment transport rate Q_{yf} where the local longshore sediment transport is evaluated from a flux model (Eq. (3.99)) is shown in Fig. 5.8. The wave field was calculated at a homogeneous grid point set at a distance of Δs=2.5cm and a time step Δt=0.01s. Wave-induced current was calculated at a homogeneous grid point of Δs=20cm and a time step Δt=0.05s.

The total longshore sediment transport rate Q_{yt} evaluated from the Savage-type expression (Eq. (3.105) where α_3=1.0) by using wave characteristics at the breaking point is also shown by solid lines in Fig. 5.8. In the case where a breakwater was constructed outside the breaker zone (Figs. (b) and (d)) the total longshore sediment transport rate estimated from the measured topographic change Q_{ye} gives a closer value to Q_{yf} than Q_{yt} does. This means that the total longshore sediment transport rate around the breakwater predicted by using wave characteristics at breaking point has less accuracy than that obtained from integrating the local longshore sediment transport rate even when the breakwater was constructed outside the breaker zone.

When the breakwater was constructed in the surf zone (Figs. (a) and (c)), the rough figure of the longshore distribution of Q_{ye} is reproduced by Q_{yf}. However, it required a great deal of computation time to obtain the value of Q_{yf}.

5.3 Control of Beach Deformation Using Groin

5.3.1 Characteristic function of groins

A groin and a training jetty are the structures that are constructed along a coast usually sticking out from the normal direction of the shoreline to fix the shoreline by controlling longshore sediment transport. We have been utilizing such structures to prevent coastal regions including river mouths from both erosion and accretion of sand. In this section, the hydraulic function of the groin is discussed. The detail of the training jetty is referred to in **5.8**.

Groins are usually constructed as a group and they have a longer history than the offshore detached breakwater does. Many studies have been carried out about the function of groin for controlling waves, current and sediment transport. Recently, a group of groins are also constructed to control longshore movement of replenished sand through a sand-by-passing system.

A fundamental methodology of reducing and controlling beach erosion by using a group of groins is as follows: A retreat of the shoreline is caused by the longshore gradient of the total longshore sediment transport. We can control the movement of the longshore sediment transport by constructing a group of groins so that the longshore gradient of the total longshore sediment transport may become small. We can also enclose a part of the beach by constructing a pair of groins from the surrounding beach to make a pocket beach where the longshore sediment transport rate is closed.

However, the groin does not have the function to control sediment movement in the cross-shore direction. A T-type groin and a L-type groin are also constructed for controlling the cross-shore sediment transport.

The trap rate of the longshore sediment transport rate of a groin is a function of the dimensions and plane arrangement of groins (length of the groin, spacing and so on) and the characteristic of incident wave and the beach (bottom slope, bed material and so on). It is needless to say that the trap rate increases with the increasing length of the groins. When the length of a groin is short, the groin may lose its function to trap sediment.

According to research conducted by Toyoshima (1972) the lengths of 60% of the groins are in the range of 10-30m in Japan. Many of them are reported to have enough function to reduce beach erosion. Some researchers have pointed out through the experiments that the effective length l and the spacing B of a groin to trap longshore sediment transport are $(0.4\text{-}0.6)x_b$ and $(1\text{-}3)l$, respectively (Nagai et al., 1955 and Shimano et al., 1956). On the other hand, procedures to determine the plane arrangement of the groins have also been proposed based on the final shape of the shoreline (Bruun, 1952) or the trap rate of the each groin in a group (Ishihara et al., 1963). In this section, the procedure for determining the longshore sediment trap rate of the groin is discussed based on the hydraulic function of a groin.

5.3.2 Hydraulic function of groins

The main hydraulic function of groins is to control the longshore current. They have little influence of the incident waves, especially on normally incident waves. In the upstream coast of the groins constructed on the beach where longshore current develops, it does not exert a significant influence on the current. In the case where the length of a groin is shorter than the width of the breaker zone, the longshore current is accelerated when it passes the edge of the groin. When the length of the groin is longer than the width of the breaker zone, no significant flow in the longshore direction passes through the top of the groin. Anyway, strong offshore current develops along the upstream side of the groin in both cases. However, the groin gives a strong influence on the wide leeward coast.

Figure 5.11 illustrates the flow patterns obtained by float-tracing around a pair of groins of the length l that is a half of the width of the breaker zone $x_b/2$ in laboratory experiments. The spacing B of the groins of each figure is $B/l=2$ and 3, respectively. The length of the arrow corresponds to the vector of advection speed of the tracer within 1s.

(a) $l/x_b=0.5, B/l=2.0$

(b) $l/x_b=0.5, B/l=3.0$

$\tan\beta=1/10, H_0=6.5\text{cm}, T=1.0\text{sec}, \theta=150°$
$H_b=7.7\text{cm}, x_b=75\text{cm}$
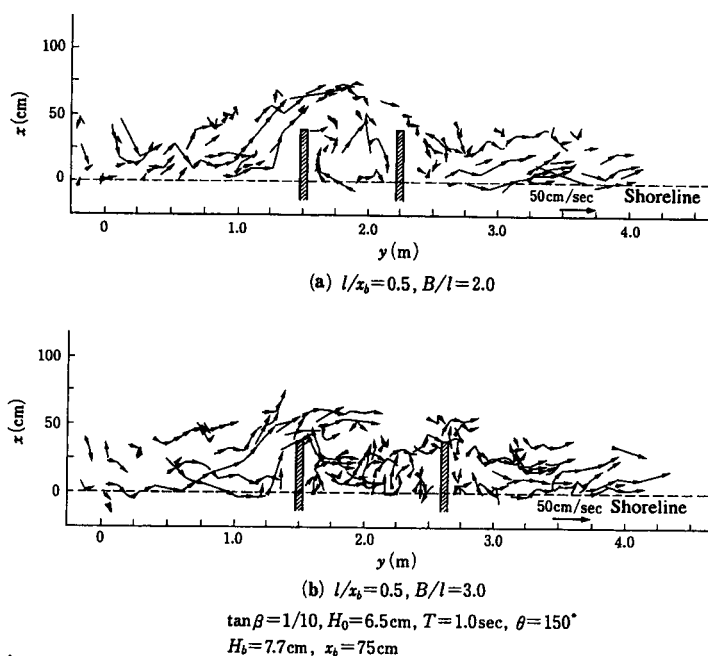
Fig. 5.11 Wave-induced current around groins
((a):$l/x_b=0.5$, $B/l=2.0$, (b):$l/x_b=0.5$,$B/l=3.0$)

In the case of narrow spacing (Fig. 5.11 (a)), a clear circulation cell is generated between the groins. On the other hand, although the flow between the groins becomes slightly complex and the flow velocity decreases, there is no significant circulation and tracers flow downward in the case of wider spacing (Fig. 5.11 (b)).

We have to discuss the effect of the interaction of groins with respect to the direction of incident waves. But we can judge from the experimental results, examples of which are shown in Fig. 5.11, that when the distance of the groins B is shorter than $2l$, a strong interaction will take place and when the value of B is greater than $3l$, the interaction becomes less significant.

The quantity that governs the cross-shore scale of the longshore current is the width of the breaker zone. The length of the wavelength as well as the wave height and the bottom slope are the quantities that determine the width and the cross-shore profile of the longshore current. However, it does not have a direct influence on the with of the breaker zone and the length of the incident waves have little influence on the above-mentioned interaction of the groins.

5.3.3 Longshore sediment transport and topographic change around groins

The function of the groin set at the beach where the longshore sediment transport develops is to trap a part of the sediment transported in the longshore direction to settle it in the upstream side of the groins. The rest of the sand is transported through the groins downward. When the length of the groin is long enough to trap the whole longshore sediment transport, severe erosion takes place in the downstream side of the groin. The groin reduces its function to trap sediment after the amount of deposited sand in the upstream side of it exceeds its capacity.

Figure 5.12 shows such an example. In the figure, the measured topographic change took place around the groin of the relative length measured from the still water shoreline l/x_b = 0.5 in the laboratory experiment. Figures 5.12 (a) and (b) are the results of the topographic changes during $(0 - 900)Ts$. and $(900 - 3600)Ts$ after wave generation, respectively.
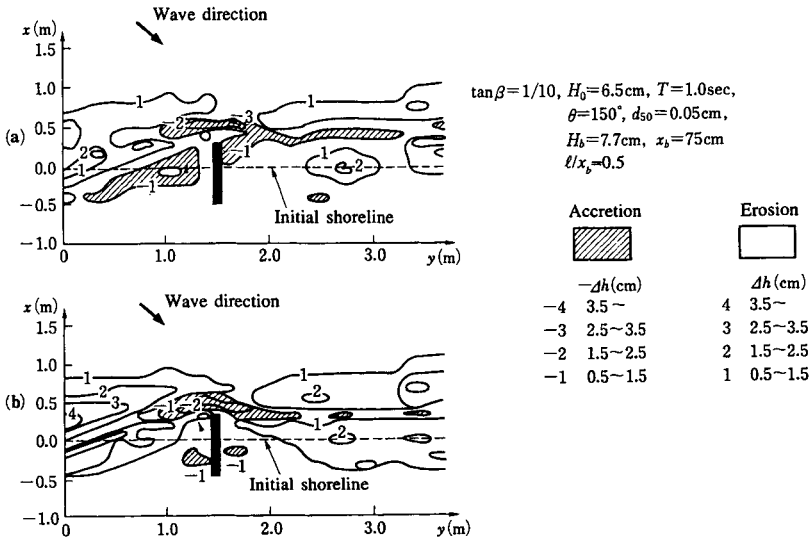
Fig. 5.12 Topographic change around a single groin
($(a):t/T$=0-900, $(b):t/T$=900-3600)
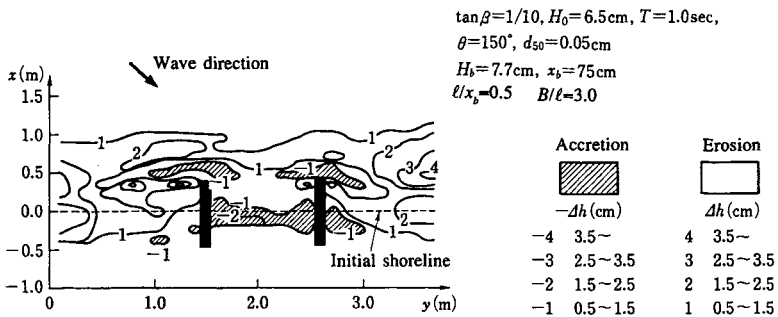
Fig. 5.13 Topographic change around a pair of groins (t/T=900-3600)

We can see from Fig. (a) that accretion takes place in the upstream side of the groin and some sediment is transported through the top of the groin. While, Fig. (b) shows that the groin does not have any function to trap sediment anymore at this stage of the beach deformation process. Figure 5.13 is the topographic change measured around the pair of groins of the same dimension as shown in Fig. 5.12 which took place during the same period as shown in Fig. 5.12 (b). This result implies that groins constructed as a group still have a function to settle sediment between them after a single groin lost its function.

5.3.4 Trap rate of longshore sediment transport

To predict beach deformation around the groin using the one-line theory, we have to give the trap rate of the longshore sediment transport of the groin. In this section, the procedure to determine the trap rate of the longshore sediment transport is discussed based on the existing studies.

The longshore sediment transport occurs in the region between the run-up point of incident waves and the critical water depth for sediment movement in the offshore. Therefore, when we discuss the function of the groin for trapping longshore sediment transport, we have to measure the length of the groin from the wave run-up point rather than from the still water shoreline. We define this length as the effective length le that is expressed by the sum of the wave run-up length x_r and the length of the groin measured from the still water shoreline l.

Sawaragi et al., (1982) carried out experimental studies regarding the trap rate of the longshore sediment transport of the groin. They defined the trap rate T_r of the groins of various effective lengths in the following way:

$$T_r = \left\{ Q_{ye}\left(j_g\right) - Q_{ye}\left(j_g + 1\right)\right\} \Big/ Q_{ye}\left(j_g\right) \tag{5.2}$$

where $Q_{ye}(j_g)$ and $Q_{ye}(j_g+1)$ are the total longshore sediment transport rate calculated from Eq. (5.1) using the measured topographic change and (j_g, j_g+1) are the cross-shore measuring lines just upstream and downstream sides of the groins. Figure 5.14 is the topographic change that took place around the groin of the non-dimensional length $l_e*=1$ during (0 to 240)Ts after wave generation where the non-dimensional effective length is defined by Eq. (5.3).

$$l_e^* = l_e \Big/ \left(x_r + x_b\right) \tag{5.3}$$

Figure 5.14 (b) is the longshore distributions of the total longshore sediment transport rate at various stages of topographic change shown in Fig. 5.14 (a) calculated from Eq. (5.1).
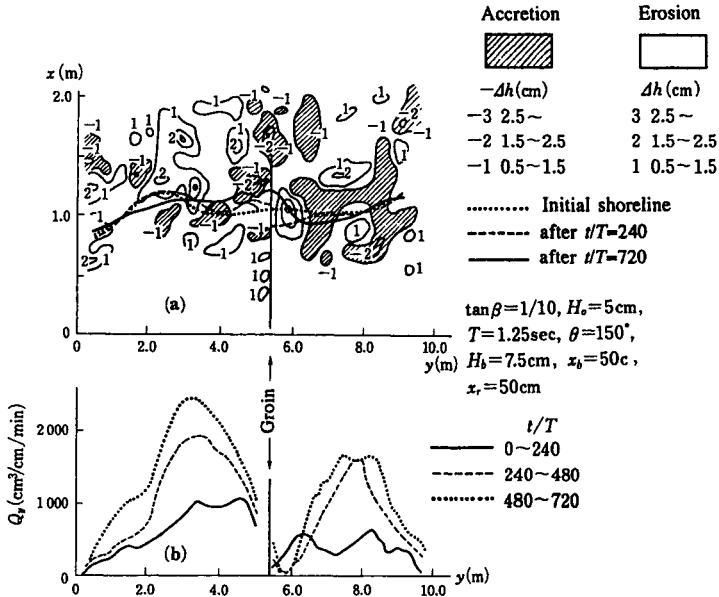
Fig. 5.14 Topographic change and total longshore sediment transport rate around groin

The trap rate of the groin T_r estimated from Eq. (5.2) using the longshore distribution of the total longshore sediment transport rate as shown in Fig. 5.14 is illustrated in Fig. 5.15.
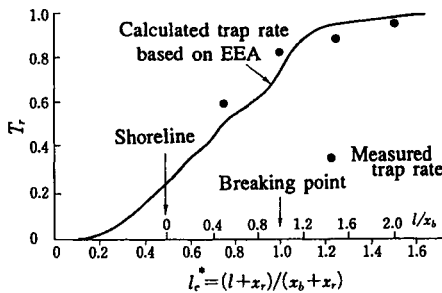
Fig. 5.15 Trap rate of longshore sediment transport rate of groin

Two scales are shown on the horizontal axis. One is the non-dimensional length of the groin l/x_b and the other is the non-dimensional effective length of the groin l_e^*/x_b. The result shown in Fig. 5.15 indicates that the trap rate T_r does not increases linearly with the increase in the length of the groin. When the groin covers the whole breaker zone, it traps about 80% of the total longshore sediment transport rate and the trap rate increases a little beyond that region.

A solid line in the figure is the cumulative longshore sediment transport rate calculated by integrating the local longshore sediment transport rate between the land ward limit of the sediment transport and the location of the offshore end of the groin. The local longshore sediment transport rate is estimated from the cross-shore distribution of the cross-shore eigenfunction. The integrated value corresponds to the longshore sediment transport rate in the shaded region of the groin. The calculated trap rate from Eq. (5.2) roughly coincides with the solid line implying that the trap rate is estimated by integrating the local longshore sediment transport rate over the length of the groin.

As was already shown in Fig. 5.14, the total longshore sediment transport rate around the groin changes with the increase in the wave running time. Therefore, the trap rate also changes according to the changes in the longshore sediment transport. Even under such a condition, we can evaluate the trap rate by assuming that the effective length is a function of the wave running time.

A comparatively high correlation (a correlation coefficient in the range of 0.5 to 0.6) exists between the change in the cross-shore sectional area and the shift of the shoreline location. However, the correlation coefficient is lower than that in the topographic change around the offshore detached breakwater. This difference comes from the fact that the trapped sediment in the upstream side of the groin does not always contribute to the advance of the shoreline due to the strong offshore current there.

5.4 Control of Beach Deformation by Submerged Breakwater and Artificial Reef

5.4.1 Definition of an artificial reef

Recently, the number of coasts where artificial reefs are constructed is increasing. The object of the construction is the reduction of coastal disasters and the effective utilization of the coastal area by reproducing the function of the natural reef in the south sea artificially. At present, there are two different shapes of an artificial reef. One is the submerged breakwater with a wide crown width that is already mentioned in **4.3** and the other is the so-called perched beach-type artificial reef.

The artificial beach of a perched beach-type usually consists of the submerged offshore breakwater and sand replenishment at the shoreward of it as schematically shown in Fig. 5.16. In this system, the width of the breaker zone becomes wider than that of the native beach and the potential for preventing disaster increases.
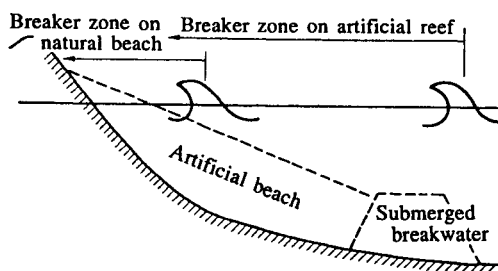
Fig. 5.16 Definiction of perched beach type artificial beach

The submerged breakwater in the perched beach-type artificial reef is required to be able to reduce the energy of high incident waves that may become dangerous to the beach behind it and to keep replenished sand.

The effect of the submerged breakwater on the two-dimensional beach deformation has been examined by Tanaka (1976) through movable bed experiments. Various investigations about the effect of the submerged breakwater on the cross-shore sediment transport and two-dimensional beach deformation have also been carried out before the construction of the submerged breakwaters in the field. However, the two-dimensional beach deformation of artificially nourished beach of the perched beach-type artificial reef seems to be different from that of the natural beach.

Here, we investigate the sediment movement in the cross-shore direction on an artificially nourished beach based on two-dimensional experiments. The movement of replenished sand on an artificial beach is also examined through three-dimensional model beach experiments.

5.4.2 Two-dimensional beach deformation of artificial reef of perched beach-type and its control by submerged breakwater

The problem that is technically comprehended in the perched beach-type artificial reef is the loss of replenished sand of the artificial reef in the offshore direction. In this section, the influence of the toe depth h, the height of the reef h_s and the width B of the submerged breakwater on the deformation of the artificially nourished beach are examined based on the two-dimensional experiments (Sawaragi et al., 1988).

Figure 5.17 shows the experimental results of the two-dimensional beach deformations of the artificial reefs constructed by using sand of mean grain size d_{50}=0.03cm at various depths on the fixed beach of the slope 1/10. The slope of the artificial reef is 1/30 and the height of the reef h_s/h is 0.7. The condition of the experimental wave (H_0=13.1cm, T=1.1s) was determined so that the beach deformation of a natural beach with a slope of 1/10 became the erosion type and this wave broke at the offshore of the reef or at the offshore edge of the reef.

Figures 5.17 (a), (b) and (c) correspond to the cases of h/L_0=0.053, 0.085 and 0.111. In the case shown in Fig. 5.17 (a), the incident waves broke offshore of the reef. From these figures, we can find that the eroded region on the reef increases with the increase in the value of h_s/h. Such erosion is mainly caused by the fluid motion including strong turbulence associated with breaking waves. We can easily imagine that if the width of the submerged breakwater is larger than the length beyond which the turbulence due to breaking waves decreases, significant erosion does not occur on the reef.

In the figures, calculated distributions of the wave height and the ratio of the bottom shear velocity and the settling velocity of the bottom sediment $u*/W_f$ are also illustrated. Wave height was calculated by the method mentioned in **1.2** and the shear velocity was estimated by using the calculated wave height and the Jonsson expression of the bottom shear stress.

Figure 5.18 illustrates the relation between the minimum value of $u*/W_f$ of the place where significant erosion took place on the reef and the non-dimensional toe depth of the reef. The figure indicates that the height of the reef has little influence on the critical value of $u*/W_f$ corresponding to a limit of erosion. In the case where $h/L_0 \leq 0.7$, significant erosion took place in the region where $u*/W_f \geq 0.6$ and when h/L_0 is in the range of 0.8 to 0.85, erosion of the reef begun in the region where $u*/W_f \geq 0.5$.

(a) $(h/L_0=0.053, h_s/h=0.7)$

(b) $(h/L_0=0.085, h_s/h=0.7)$
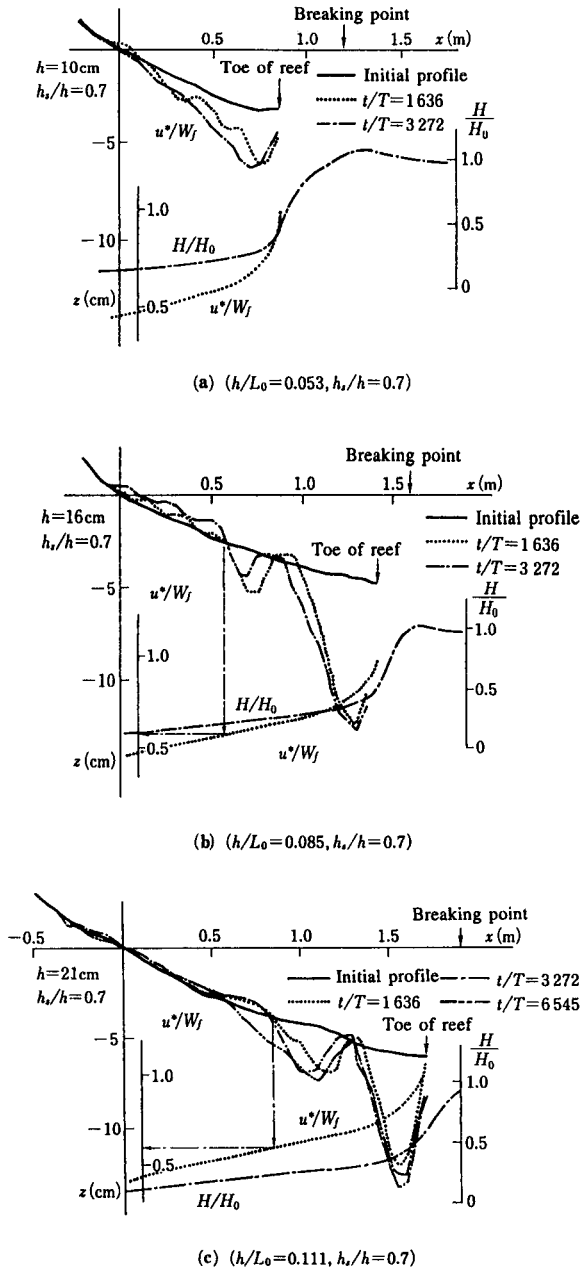
(c) $(h/L_0=0.111, h_s/h=0.7)$

Fig. 5.17 Deformation of perched beach-type artificial beach
((a):h/L_0=0.053, h_s/h=0.7, (b):h/L_0=0.085, h_s/h=0.7 and (c):h/L_0=0.111, h_s/h=0.7)
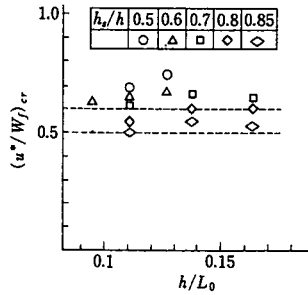
Fig. 5.18 Minimum value of $u*/W_f$ in eroded area on the beach

Figure 5.19 shows the two-dimensional beach deformations of the artificial reefs where the offshore part of the reef in the case of $h/L_0=0.111$, $h_s/h=0.55$ was covered with rubble stones. The relative length of the covered region B/x_e, where x_e is the length of the eroded region in the case of no cover stone, of Figs. 5.19 (a), (b), (c), (d), and (e) correspond to 0.0, 1.0, 0.75, 0.5 and 0.3 respectively. The results shown in Fig. 5.19 indicate that we can reduce the erosion on the reef by covering 3/4 of the expected eroded region in the case of no cover stone. In the following, the procedure for determining the width to effectively reduce the erosion on the reef is discussed.
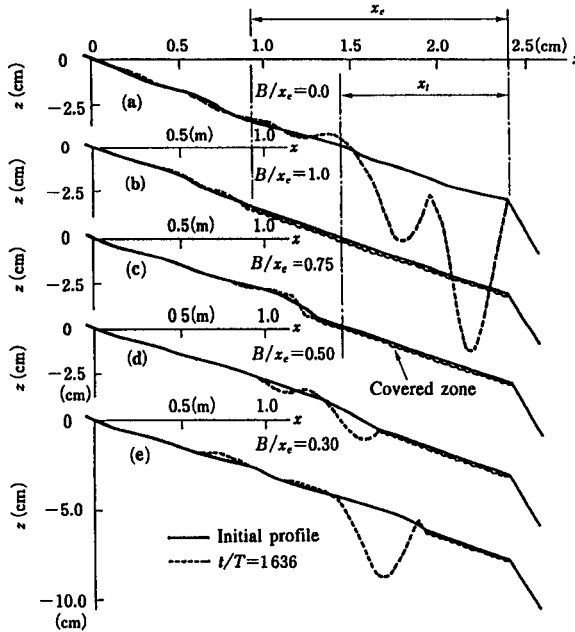
Fig. 5.19 Change in the eroded section of perched beach with various length of covered region ((a):B/x_e=0, (b):B/x_e=1.0, (c):B/x_e= 0.75, (d):B/x_e=0.5 and (e):B/x_e=0.3)

As mentioned before, the erosion on the artificial reef is mainly caused by the turbulent fluid motion due to breaking waves. Therefore, detailed information of the water-particle motion under breaking waves is required to discuss sediment movement in such a region. However, at present, there is no sufficient information of fluid motion associated with breaking waves to quantitatively discuss the sediment movement in the breaker zone.

Here, we apply the result of Galvin (1969) to estimate the distance where the turbulent energy generated by wave breaking continues. He defined the length of the breaker travel on a sloping beach x_t as the distance between the breaking point and the place where the splash touches the surface using the breaking wave height H_b and the bottom slope $\tan\beta$ as follows:

$$x_t = 2(4 - 9.52\tan\beta)H_b \qquad (5.4)$$

In Fig. 5.19, the value of x_t calculated from Eq. (5.4) using the measured breaking wave height and the bottom slope of the reef is also shown. It is found that when we cover the reef over the length of at least the same length as x_t, we can reduce the erosion on the reef to a significant extent.

5.4.3 Three-dimensional deformation of perched beach-type artificial reef

In this section, three-dimensional deformation of the perched beach-type artificial reef where the width of the submerged offshore breakwater is determined through the procedure mentioned in the former section is investigated through experiments.

Figure 5.20 illustrates the examples of topographic changes measured around artificial reef(s) of the slope 1/20 constructed on the model beach of the uniform slope of 1/10 took place during 2670Ts after wave generation. The median grain size of the model beach and artificial reef is 0.05cm. The non-dimensional toe depth and height of the of the submerged breakwater h/L_0, h_s/h are 0.059 and 0.55, respectively. The width of the submerged breakwater B is determined to be 40cm (B/L_0=0.14) from the procedure mentioned in the former section. The condition of the experimental wave is shown in the figure. The non-dimensional length of the reef l/L_0 in Fig. 5.20 (a) is 0.7 and Fig. 5.20 (b) is the result where two reefs of the non-dimensional length l/L_0=0.35 are set at the distance of 0.5*l.

Although incident waves broke at the offshore edge of the reef, any offshore sediment movement did not take place because of the incidence of the accretion type waves. In the case shown in Fig. 5.20 (a), any significant longshore transport of the sediment from the reef did not take place and the deposited sediment around the shoreline behind the reef remained even 2670Ts after wave generation. On the other hand, a large part of sediment is eroded from the upstream side reef and is transported downstream in Fig. (b). This means that we can keep replenished sand on the reef effectively by constructing a longer reef rather than by constructing a group of shorter reefs with an opening.

The correlation between the changes in the sectional area and the shift of the shoreline location around the artificial reef is not so high (less than 0.5) as measured around offshore detached breakwaters and groins. The relative importance of the maximum eigenvalue obtained from the empirical eigen function analysis is also low (40-50%). This reason is explained that at the early stage of the topographic change, the onshore sediment transport dominated on the reef until the bottom slope of the reef reached about 1/20 and then the longshore sediment transport became predominate.

These characteristics of the topographic change around the artificial reef found in the experiment are also observed around the artificial reef in the field (Deguchi and Sawaragi, 1986).

$\tan\beta=1/10$, $H_0=5\text{cm}$, $T=1.35\text{sec}$, $\theta=150°$
$d_{50}=0.05\text{cm}$, $l=2.0\text{m}$

Accretion ([///]) Erosion ([ ])

$-\Delta h$ (cm)		Δh (cm)	
−4	3.5~	4	3.5~
−3	2.5~3.5	3	2.5~3.5
−2	1.5~2.5	2	1.5~2.5
−1	0.5~1.5	1	0.5~1.5

(a) Single reef

$l=1.0\text{m}$, $B/l=0.5$

(b) Double reefs
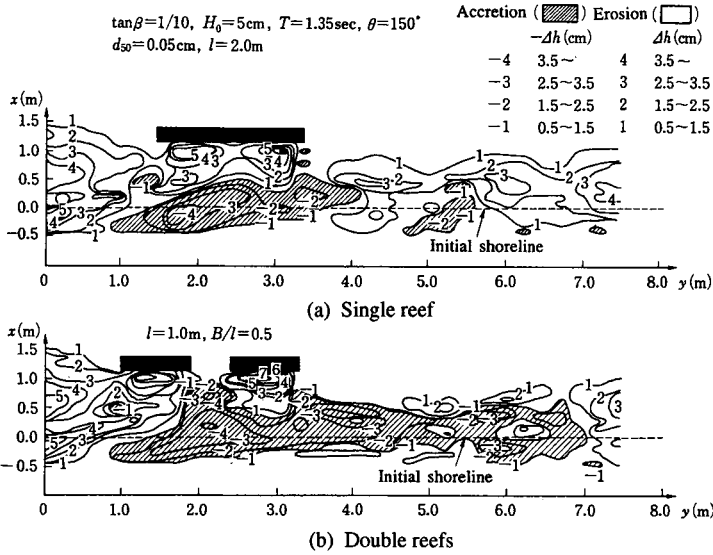
Fig. 5.20 Topographic changes around perched beach type artificial reef(s)

5.5 Control of Beach Deformation by Sea Dike of Gentle Slope

5.5.1 Influence of sea dike on beach deformation

A seawall and a sea dike have been constructed for the purpose of preventing waves from overtopping and inundation caused by a storm surge and a tsunami. They also have the function to prevent the shoreline from setback physically. Accordingly, they have demonstrated an effect to prevent beach erosion, especially cliff erosion.

Conventional sea dikes were classified into two groups according to slope: a nearly vertical sea wall with the slope $\tan\alpha$ steeper than 1 and the gentle slope sea dike with the slope $\tan\alpha$ smaller than 1. The goal to prevent inundation and wave overtopping is achieved by constructing seawalls and sea dikes of any slope. However, it is often reported that the foreshore in front of nearly vertical seawalls and sea dikes disappeared by the attack of high waves. Many were destroyed by sand drawing from the inner part of the sea dikes and seawalls. It is also reported that the disappeared foreshore recovered after the destruction of the seawalls and sea dikes.

The conceivable causes for the disappearance of the foreshore are as follows:
(i) The net offshore sediment transport caused by the high waves (change in the beach deformation process from accretion type to erosion type),
(ii) The local offshore sediment transport caused by the down-rush flow on the slope and the increase of the reflected waves from the sea dike, and
(iii) The increase in the longshore sediment transport in front of the sea walls due to the acceleration of the longshore current there.

In the field, these phenomena act together to cause the disappearance of the foreshore and local scouring at the toe of the sea dikes. Among them, we can control the two-dimensional local scouring and longshore current in front of the sea dike. According to numerous studies about the two-dimensional local scouring in front of the sea dike, the maximum scouring depth increases with the increases in the reflection from the sea dikes and the increases in the velocity of the down-rush flow on the slope. Both reflections from

the sea dike and the velocity of down-rush flow decrease with the decrease of the slope of the sea dike. Furthermore, the damaged foreshore due to high waves is more easily recovered in front of the gently sloping sea dike.

Toyoshima (1984) proposed a sea dike of gentle slope covered with blocks having permeability. This type of sea dike was tested for its effectiveness in the field and proved successful. Recently, the number of coasts protected by sea dikes of gentle slope are increasing in Japan.

5.5.2 Longshore current and longshore sediment transport in front of sea dike

When we predict shoreline change by the one-line theory or plan the plane arrangement of the sea dike, we have to know the effect of the sea dike on the longshore current and longshore sediment transport on the natural beach. In this section, the effect of sea dikes on the longshore current and resulting longshore sediment transport is discussed through experiments (Deguchi, 1984).

Figure 5.21 shows a cross-shore distribution of the longshore current velocity in front of vertical and gently sloping sea dikes measured in a wave basin by tracer tracing. The sea dikes were constructed on a uniformly sloping beach of $\tan\beta=1/10$ and the location of the toe of sea dikes x_i were on the still water shoreline and just half of the width of the breaker zone ($x_i/x_b=0.0$ and 0.5). The slope of the gentle slope sea dike $\tan\alpha$ was 1/2.7. The condition of the experimental waves and the cross-shore distribution of the longshore current measured on the natural beach are also shown in the figure.
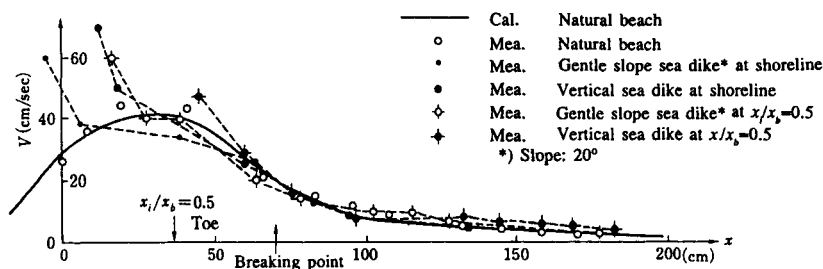
Fig. 5.21 Cross-shore distribution of longshore current in front of sea dikes

The velocity of longshore current in front of a sea dike is accelerated in the region of $0.1*L_0$ from the sea dike. The velocity becomes several times larger than that at the same location on a natural beach. Longshore currents occur especially in front of gently sloping sea dikes.

According to the experimental results concerning the wave field in front of a vertical sea dike (Sawaragi et al., 1986) constructed on the sloping beach, reflected waves from the sea dike have little influence on the wave breaking of incident waves when the sea dike is constructed in the region shallower than $x_i/x_b\leq0.5$. When the breakwater is set in the region deeper than $x_i/x_b\geq1.2$, wave breaking does not take place. Breaking of composite waves occurs and the characteristics of incident progressive waves are totally lost when it is constructed in the region of $0.5\leq x_i/x_b\leq1.0$. Even in the case of the oblique wave incidence, incident waves break in front of the sea dike at the same point as the natural beach when the sea dike is constructed in the region of $x_i/x_b\leq0.5$. Therefore, the acceleration of the longshore current may take place in the local area just close to the sea dikes.

Figure 5.22 shows the total longshore sediment transport rate Q_{yem} measured in front of the vertical and gentle slope sea dikes set on the uniformly sloping bottom of 1/10. The mean grain size is 0.03cm. The vertical axis is normalized by the total longshore sediment transport rate Q_{ye0} on the natural beach. Both values of Q_{yem} and Q_{ye0} are calculated from Eq. (5.1) using the topographic change measured in the accretion type and erosion type beach deformation processes. Wave heights at deepwater were 6cm (accretion type) and 12cm (erosion type) and the period was 1.28s.
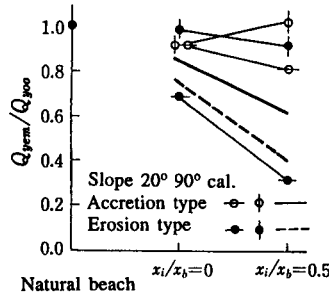
Fig. 5.22 Total longshore sediment transport rate in front of various sea dikes

From Fig. 5.22, it is found that more than 80% of the total longshore sediment transport on the natural beach occurs in front of the sea dikes except in the case of the gently sloped sea dike under the incidence of erosion type waves. The thick solid and broken lines in the figure are the calculated total longshore sediment transport rate by integrating the local longshore sediment transport rate (Eq. (3.99)) in front of the sea dikes assuming that the existence of the sea dike does not influence the local longshore sediment transport rate on the natural beach. The calculated longshore sediment transport rate does not coincide with the measured longshore sediment transport rate. This means that we have to take into account the effect of the acceleration of the longshore current and reflected waves in front of the sea dike to precisely evaluate the longshore sediment transport rate.

5.6 Artificial Beach Nourishment
In the former sections, various functions of coastal structures that have been used to control and reduce beach deformation have been discussed. However, the actual phenomena in the field such as beach erosion, filling-up of navigation channels and harbors and so on are not always controlled by these structures. Artificial sand replenishment in the eroded region and dredging of the deposited sand are effective and in some cases unique countermeasures against unexpected topographic change.

There are two kinds of beach nourishment: dynamic and static. In dynamic beach nourishment, sands are replenished temporally at the upstream side of the eroded region so that they are transported downstream to feed the eroded area. The so-called sand-bypass is representative method of dynamic beach nourishment. We have to carefully select the place for the temporal replenishment and a plane arrangement of structures to effectively catch the transported sediment in the eroded area. In static nourishment, the artificial beach is constructed by direct sand replenishment to reduce incident wave energy and to reduce coastal disasters such as wave overtopping and so on. In the latter nourishment, deformation of the artificial beach has to be minimized to keep its function of controlling incident wave energy. The artificial reef referred to in **5.4** is representative of static beach nourishment.

On the other hand, "beach" provides us with various opportunities for pleasure such as swimming, fishing, camping and so on. There are some artificial beaches constructed as a means of mitigation for the development of the coastal area.

The Ministry of Transport of Japan prepared a technology manual (Ministry of Transport, 1979) for constructing artificial beaches in this category. According to the manual, it is suggested that the height of the back shore defined in Fig. 5.23 should be higher than the run-up height of the incident waves of the return period of 0.4-0.5 years. The foreshore slope is also suggested to be a little steeper than the equilibrium slope for the incident waves. In the manual, empirical expressions for estimating the run-up height and the foreshore slope are given from the analysis of 12 existing artificial beaches in Japan as follows:

$$\left.\begin{array}{ll} R/H_0 = \left(52 H_0/L_0\right)^{-2.7} & H_0/L_0 \geq 0.013 \\ R/H_0 = \left(8.25 H_0/L_0\right)^{-0.461} & H_0/L_0 \leq 0.013 \end{array}\right\} \tag{5.5}$$

$$\left.\begin{array}{ll} \tan\beta = \left\{\left(d_{50}/H_0\right)/1.37\right\}^{0.158} & d_{50}/H_0 \geq 2.4\times10^{-4} \\ \tan\beta = \left(376.6 d_{50}/H_0\right)^{0.7856} & d_{50}/H_0 \leq 2.4\times10^{-4} \end{array}\right\} \tag{5.6}$$

Equations (5.5) and (5.6) are expressed using wave characteristics in deepwater. As mentioned in the former sections, various coastal structures have been constructed around artificial beaches to prevent replenished sand from being transported offshore. In such cases, characteristics of incident waves become different from those on a natural beach. We have to estimate wave characteristics in deepwater from the wave characteristics in the near shore region that are deformed by structures and are actually related to beach deformation by a proper procedure.

It is needless to say that a large deformation of an artificial beach of this kind also has to be controlled from the view point of maintenance and management.
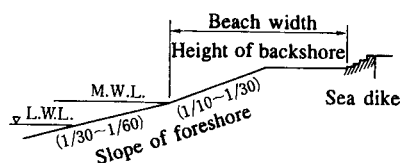
Fig. 5.23 Definition sketch of a section of artificial beach

5.7 Protection Works Against Shoaling in Harbors and Navigation Channels

5.7.1 Shoaling process in harbors and navigation channels

Sedimentation at a harbor entrance or inside a harbor prevents ships from navigating and sometimes spoils the harbor. Figure 5.24 shows an example of the topographic change around a harbor in Japan. Sedimentation at the harbor entrance due to sand transport

coming around the east breakwater can be seen in the figure ②, which finally blocked up the harbor with the shoreline being advanced because of the west breakwater as seen in the figures ③ and ④.
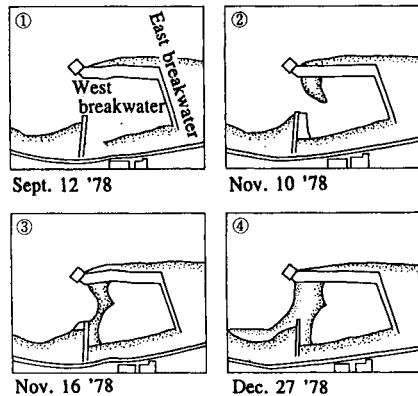
Fig. 5.24 Topographic change around Ichiburi Harbor in Japan

Shoaling in navigation channels in rivers or estuaries is also an important problem in Japan as well as in China and several countries in Southeast Asia. Such sedimentation is usually caused by fine sediments such as silt or silty sand carried by waves or currents. This kind of sedimentation is referred to as siltation and has recently been investigated as a new sedimentation problem. Shoaling due to siltation is rather difficult to predict because its behavior is different from that of sand in some phases of sedimentation such as suspension by current, interaction between waves and sediments, process of advection and deposition, and flocculation in a mixing region of salt and fresh water. In the following sections, we will separately discuss sedimentation on two types of coasts: sandy and silty.

5.7.2 Procedure of protection works against sedimentation in harbors on a sandy coast

(1) Sediment transport causing shoaling in harbors and navigation channels
Various kinds of sediment transport that may cause shoaling in harbors and navigation channels have been pointed out:
(i) Sediment transport entering through a harbor entrance
(ii) Sediment transport due to wave overtopping into a harbor
(iii) Sediment transport through rubble mound breakwaters
(iv) Entertainment of suspended sediment into the harbor by low frequency fluid motion such as harbor seiche
(v) Sand transport as wind-blown sand from neighboring beaches
Sediment transport (i) is the main cause in most harbors, but others have also been reported to be important causes in some harbors. The most important cause of shoaling in navigation channels has the similar mechanism to (i); sediments suspended by waves or currents in a shallow water region are carried and deposited in the channel where the current velocity is slower.

(2) Procedure of protection works

As for the protection works corresponding to cause (ii), construction of higher breakwaters is obviously effective. For cause (iii), it is effective to reduce the permeability of the rubble mound breakwaters by inserting impermeable core or sheet-piles inside the breakwaters or by covering the mounds with sheets. Wind-blown sand can be protected by planting grass on the neighboring beach or by constructing windbreaks. However, effective countermeasures against cause (i) have not been well established and protection works have sometimes been done by trial and error. Here, we first show the necessary basic surveys to establish countermeasures against cause (i) and then discuss the procedure of protection works.

a. Oceanographic survey

The main driving force in sediment transport into a harbor may be waves and thus we should first investigate the statistics of wave heights, wave periods and wave directions by using wave data or by means of wave hind casting from wind data. Regarding cause (iv), we should also investigate the characteristics of long period waves in a harbor by field measurements or numerical simulations. Figure 5.25 shows the results of spectral analysis of the water surface elevation measured at points a and c in the harbor indicated in the figure, where a record over a period of 300s is used and the tidal deviation is eliminated from it. Long period components with a period between 25 and 30 minutes are clearly observed in the wave record.

b. Topography survey

The survey of topography around a harbor can be utilized in selecting a location or a type of structure for protection against littoral drift. We can sometimes stop littoral drift by constructing structures making use of the topography such as a cape or a rock reef.

c. Survey of nearshore currents

As mentioned in **3.4**, the littoral drift is strongly influenced by nearshore currents, especially by longshore current. Thus we should survey the actual condition of the nearshore currents and also predict the change of the currents due to the construction of structures.

d. Survey of littoral drift

The survey of littoral drift is classified into two kinds of surveys: transport pattern and transport rate surveys. We should first figure out the predominant transport pattern, suspended load or bed load, using the results of the investigation on the sediment transport pattern. The survey of the sediment transport rate provides the quantities of sediment in both forms of longshore and cross shore sediment transport. The change in such transport patterns and transport rates after the construction of structures should also be examined by numerical predictions.

e. Survey of topographic change

The sediment transport finally causes topographic change. We should therefore carry out the prediction of the seasonal topographic change before and after the construction of structures.

As stated above, it is necessary to examine the effect of structures using physical or numerical models in the planning countermeasures against shoaling. Both physical and numerical models however have their own problems. A similarity law has not been established in the physical model with movable beds and thus a quantitative estimation is
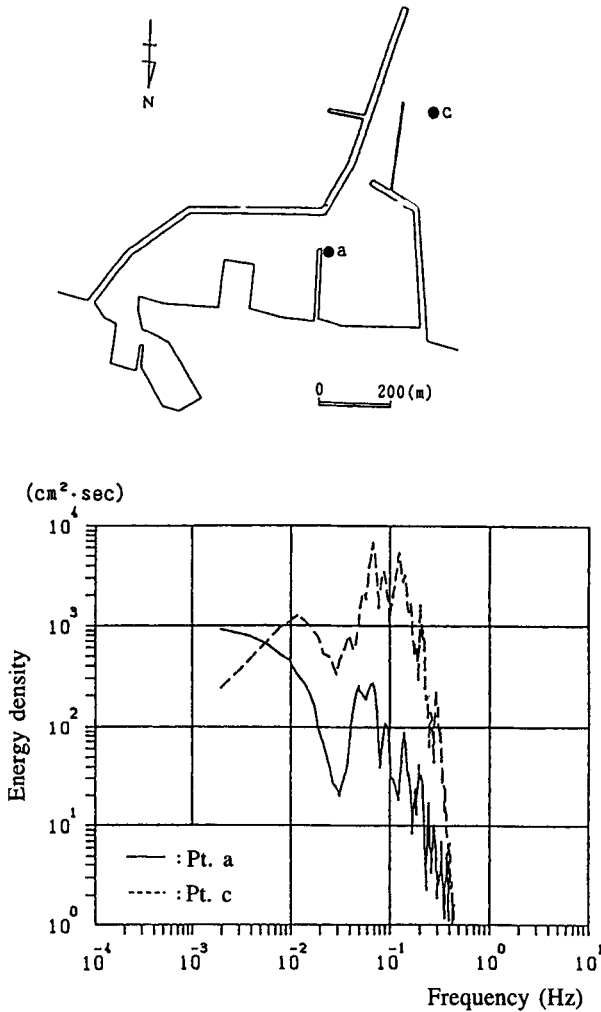
Fig. 5.25 Spectrum of water surface elevation measured around a harbor

rather difficult. In the numerical models, there are still some uncertainties in the calculation of wave transformation including wave breaking. The hybrid method, the method combining the physical and numerical methods, has recently been proposed and used to discuss the effect of shoaling protection structures. A representative flowchart of the hybrid method is shown in Fig. 5.26.

The quantities regarding the driving forces in sediment transport; e.g., current velocity, current direction, wave height, and wave direction are first measured in the physical model experiments, and then they are used as data in the numerical models. We have shown the details of the numerical models on sediment transport and associated topographic change in Chapter 3. Different countermeasures may be taken corresponding to the two representative sediment transport patterns, suspended load and bed load, and therefore the

amount of suspended and bed loads must be individually evaluated using the formulas for sediment transport rate shown in **3.4**.
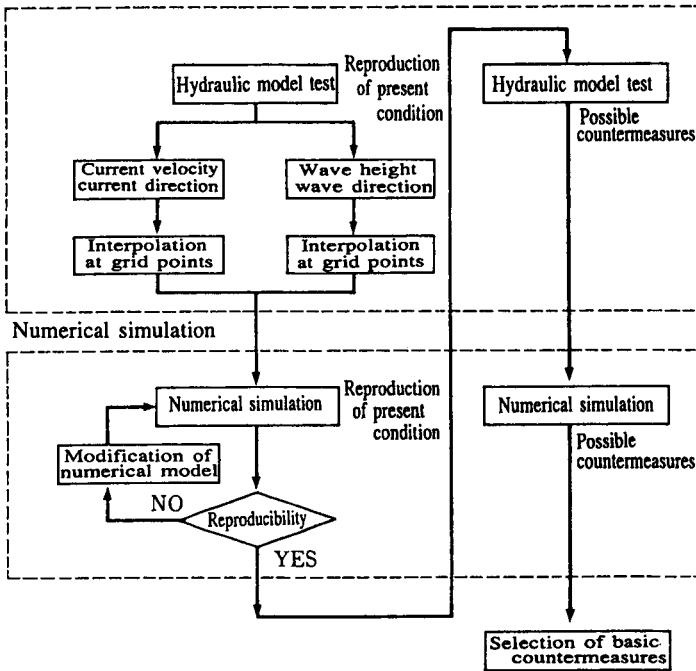
Fig. 5.26 Flow chart of hybrid method

5.7.3 Procedure of protection works against sedimentation in a harbor on a silty coast

As shown above, important problems regarding siltation may be the mechanism of sediment suspension, the process of advection and deposition, and the flocculation of fine particles. Here, we show methods to study these problems on the basis of Tsuruya's work (1990).

(1) Quantitative estimation of suspended sediments

We first need to estimate the shear stress due to wave-induced current or tidal current. This provides the amount of suspended sediments Q_s that will be used as a boundary condition in solving the equations of advection and diffusion. Partheniades (1965) shows the formula for Q_s:

$$Q_s = M\left(\frac{\tau_b}{\tau_c} - 1\right)$$

(5.7)

where M is a constant given as a function of material and water content of sediments, τ_b is the bottom shear stress , and τ_c denotes the critical shear stress of sediment suspension.

General expressions for M and τ_c have not been established. The value of τ_c is usually obtained by the experiments using real materials. As for the value of M, Van Leussen and Dronkers (1988) propose to use the values between 0.06 and 0.24 kg/m^2/min, whereas Tsuruya (1990) uses 1.2 kg/m^2/min in his calculation.

(2) Calculation of advection and diffusion

We can calculate the advection and diffusion of the sediments by first estimating the tidal and wave-induced currents and then by solving the advection-diffusion equation (see **3.6**). Since the sediment concentration varies in the vertical direction; a higher concentration near the bottom and lower near the water surface, the calculation should be carried out by dividing the water into multiple layers. In particular, such a subdivision is important for studying the effect of submerged breakwaters such as shoaling protection structures.

(3) Estimation of deposition and sedimentation

The amount of sedimentation D is generally expressed as a product of the setting velocity W_f and the sediment concentration at the bottom C_{bed}:

$$D = p_r W_f C_{bed} \tag{5.8}$$

where p_r denotes the probability that suspended sediment is deposited and this is expressed as $p_r = 1 - (\tau_b / \tau_d)$ using the critical shear stress τ_d against the deposition. Tsuruya (1990) however let p_r be 1 in his calculation.

The settling velocity W_f is usually given as a function of the Reynolds number with respect to the particle diameter (e.g., Rubey's table). However, fine particles sometimes form a flock that contains water. As the sediment concentration increases the frequency of collision between the particles increases and then the flocculation develops, which makes the setting velocity larger. However, if the concentration exceeds a certain critical value the setting velocity decreases due to the interaction between flocks and due to the dropping of pore water and associated ascending current. Figure 5.27 shows the relationship between the sediment concentration C and the settling velocity W_f.
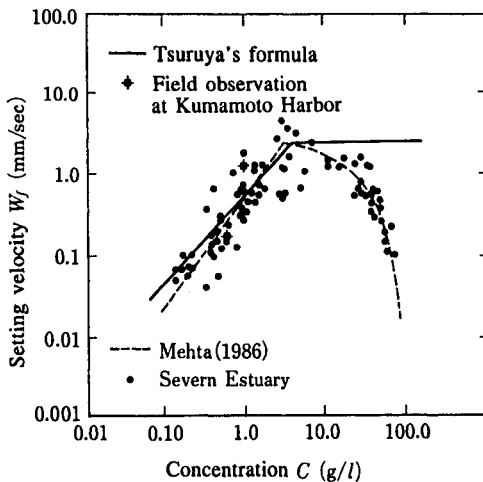
Fig. 5.27 Relationship between sediment concentration and settling velocity (after Tsuruya (1990))

(4) Sediment transport due to waves

We have mainly discussed the mechanism of sediment transport and deposition by tidal or wave-induced currents. Sediment transport associated with mass transport due to waves is another factor of the siltation, which can be recognized as a mud flow. The total amount of sedimentation can be estimated as the sum of currents and waves. According to Tsuruya's prediction for the navigation channel in Kumamoto harbor, the ratio of sedimentation volume due to currents is about 85% near the harbor entrance and 75% inside the harbor.

5.7.4 Examples of protection works against shoaling in harbors on a sandy coast

Construction of longer breakwaters has been the most popular countermeasure to protect harbors on a sandy coast from sedimentation through the harbor entrance, which is due to the fact that the driving force in sediment transport is smaller in deeper water. In the case that the suspended load transport is dominant, however, the extension of breakwaters is not always effective. Not only that, in the case of longshore sediment transport being dominant, the bed load transport coming into the harbor around a breakwater end sometimes increases because of the topographic change of the neighboring beach, which consequently makes the situation worse. Thus the protection works must be carefully designed considering the behavior of sediment transport.

(1) Bed load dominant case

Bed load transport is usually dominant on the coast that consists of larger size sediments relative to the incoming wave height. In such a case, as shown in Fig. 5.28, the construction of sand groins outside the harbor is often effective as well as the extension of breakwaters.
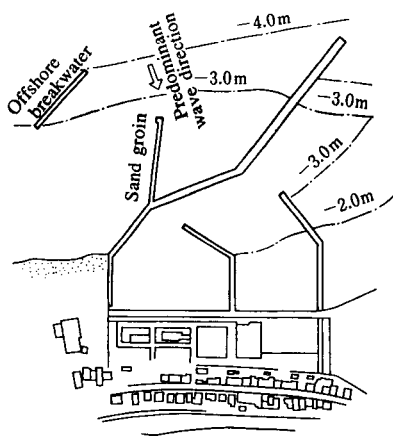
Fig. 5.28   Countermeasures at a harbor on a sandy coast

(2) Suspended load dominant case

Under storm conditions, the suspended load transport may be predominant around a harbor on a sandy coast facing the ocean. In such a case, the construction of offshore breakwaters, which interrupt the suspended load and deposit it outside the harbor, may be as effective as the extension of breakwaters (see Fig. 5.28).

If there is a cape or a rock reef near the harbor, it is also effective constructing a groin at such places to change the magnitudes and directions of currents and waves. Such a countermeasure was adopted at a harbor in Sri Lanka, where the sediment transport coming around a cape was significant.

As mentioned in **5.7.2** (2), the suspended load may be carried into a harbor by the current associated with a long period harbor oscillation. In this case, as taken at Gumizaki harbor in Fig. 5.29, it may be effective to decrease harbor oscillation by constructing slopes instead of existing quay walls or to change the natural period of harbor oscillation by changing the harbor configuration or dredging in the harbor.

Newly constructed part

Original quay wall

Slope
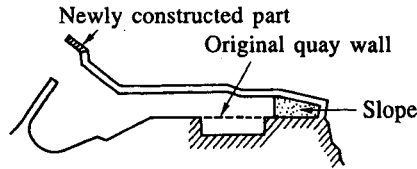
Fig. 5.29 Countermeasures at Gumizaki fish harbor

We have shown various countermeasures using coastal structures against shoaling in harbors. It is however difficult to completely interrupt sediment transport into a harbor by the structures. Maintenance dredging must therefore be taken into account and a dredging plan should be scheduled at the same time the construction plan is organized. We can estimate the amount of maintenance dredging by using the methods shown in **5.7.2** (2).

5.7.5 An example of protection works in a harbor on a silty coast

Siltation is one of the most difficult coastal problems and so too is the countermeasure against sedimentation due to siltation. Here we show the protection work being planned at Kumamoto harbor. As shown in Fig. 5.30, a set of submerged breakwaters on both sides of the navigation channel is considered. The submerged breakwaters are 1m high and 2000m long. According to Tsuruya's simulation results, the submerged breakwaters will be able to decrease the amount of sedimentation by up to 53% - 80% of that without the breakwaters, although the effect of the breakwaters varies over the location in the channel.

$H=1/1\,000$
$V=1/200$

1.5   1.5 -2.1m
-4.1m
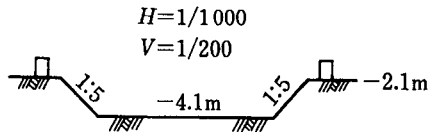
Fig. 5.30 Submerged breakwater as protection works against shoaling in navigation channel (Tsuruya et al., 1990)

5.8 Structure for Processing River Mouth

5.8.1 Classification of river mouth topographic features with respect to sediment movement

The flow field around a river mouth becomes extremely complicated due to various fluid motions such as discharged flow from a river, waves, wave-induced current and tidal

current of different densities. There are large rivers from which always flow more than tens of thousands of liters of water per hour. There also exist small rivers where there is usually no water. The hydrological regime of a river discharge also changes variously from place to place by the difference of the scale of the river. Furthermore, even in the same river, the flow field around the river mouth after the run-off of rainfall differs from that in the dry season. The density difference of fresh water and sea water mainly comes from a difference in the salt concentration and water temperature between both of them and exerts a significant influence on vertical structure of the flow around the river mouth.

On the other hand, fluid motions caused by waves and wave-induced current also give a great influence on the flow field and topographic features around river mouth. When a river flow enters the coastal region from the river mouth the velocity of the flow decreases, resulting in discharged sediment from upstream being deposited.

There are some numerical models for analyzing the behavior of discharged fresh water in a coastal region where the density difference between fresh water and coastal water are taken into account (e.g., Nakatsuji et al., 1992).

However, because the sediment transport phenomenon in the fluid motions of different densities becomes extremely complex, most of the existing experimental studies concerning the sediment transport around a river mouth were carried out without considering density difference. Here, the depositional pattern of the discharged sediment from a river mouth is discussed based on experimental results without taking into account the effect of the density difference because of the difficulty of the similitude of sediment movements in the river and in the coast.

From the point of view of fluid motion that controls the sectional area of a river mouth, river mouths are classified into the following three types:

(1) *River flow dominating type* : The discharge of the river of this type is large and the bottom slope is steep. The opening of the river mouth depends only on the discharge of the river.

(2) *Wave dominating type* : The river mouth of a river whose discharge is small and the tidal difference is not so large. The topography around the river mouth depends on the waves and wave-induced current.

(3) *Tidal current dominating type* : The section of the river mouth is maintained by the tidal current in the river mouth.

Numerous studies have been carried out concerning topographic change around a river mouth. According to these results, topographic change around a river mouth is classified as shown in Table 5.2 in terms of the relative magnitude of the discharged sediment from the river and the sediment movement in the coastal region, mode of sediment movement around the river mouth and so on.

When there is enough flow at a river mouth, as is the case in the river flow and tidal current dominating types, discharged sediment from the river is deposited in front of the river mouth to form a terrace of a half moon shape (Type I and II; Suga et al., 1986 and Deguchi and Sawaragi, 1988). If the depth at the river mouth decreases by the accretion of discharged sediment, the velocity of the discharged flow and bottom shear stress increase to transport deposited sediment into a deeper region. As a result, a terrace develops offshore. In such a case, there is interaction between the changes in water depth and discharged flow and a perfect blockage of the river mouth hardly occurs.

On the other hand, a river mouth of the wave dominating type is easily blocked when waves of the accretion type attack and a river mouth bar is formed (Type X and XI). Even in the case of the incidence of erosion type waves, continuity of longshore sediment transport is broken at the river mouth. There is a possibility for the occurrence of the blockage of a river mouth by the deposition of sediment caused by the discontinuity of

Table 5.2 Classification of river mouth topography
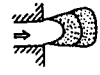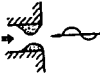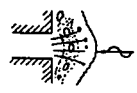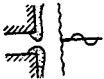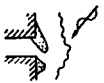
Type	Transport agency	Wave climate	Source	River discharge	Characteristic topography	Shape of sand bar	References
I	River flow	Calm	Bed load from river	Mean	Formation of river mouth bar		Ozsoy (1977) Butakov (1971)
II	River flow	Calm	Bed load and suspended load from river	Rich	Formation of delta and terrace		Ozsoy (1977) Butakov (1971) Suga et al. (1986) Deguchi et al. (1988)
III	River flow and waves	High waves and high tide	Discharged sediment from river and onshore sediment transport by waves	—	Formation of bar in river		—
IV	River flow and waves	Normal waves (normal inci- dence)	Bed load from rive and onshore sediment transport by waves	Mean	Discontinuous longshore bar		FitzGerald (1982)
V	River flow and waves	Normal waves (ob- liquely inci- dence)	Bed load from river and longshore sediment transport by waves	Mean	Asymmetrical bars with opening		Bruun (1978)
VI	River flow >waves	Normal waves (normal inci- dence)	Bed load and suspended load from river and onshore transport by waves	Rich	Formations of terrace and horn shape bar		Butakov (1971) FitzGerald (1982)
VII	River flow >waves	Normal waves (oblique inci- dence)	Bed and suspended load from river and longshore sediment transport	Rich	Formation of terrace and asymmetric bars		Bruun (1978)
VIII	Waves> river flow	High waves (normal inci- dence)	Offshore sediment transport	Low	Formation of longshore bar		—

Table 5.2 (continued)

Type	Transport agency	Wave climate	Source	River discharge	Characteristic topography	Shape of sand bar	References
IX	Waves> river flow	High waves (oblique inci- dence)	Longshore sediment transport	Low	Formation of longshore and river mouth bars		—
X	Waves> rive flow	Normal waves (normal inci- dence)	River mouth bar	Drough	Formation of river mouth bars		—
XI	Waves> river flow	Normal waves (oblique inci- dence)	Cross-shore and longshore sediment transport	Drough	Formation of asymmetric river mouth bars		—

longshore sediment transport (Type IX). When the waves propagate and break in the river, discharged sediment from the river cannot flow out of the river mouth. Discharged sediment is deposited in the river and reduces the area of the river mouth. (Type III).

As shown in Table 5.2, river mouth topographic features deeply depend on a characteristics of incident waves, existence of tide, river discharge and so on.

5.8.2 Conventional procedure of river mouth processing and its problem

A blockage of a river mouth deeply influences the drainage of flood water, navigation and the ecosystem. Although continuous observations have been carried out about the flashing mechanism of a river mouth bar at a few river mouths, a large part of the mechanism of sedimentation around a river mouth remains unsolved. A training jetty, a gate, a culvert and artificial dredging are popular countermeasure works against river mouth closure.

Training jetties are constructed to flow river water downward smoothly and to prevent sedimentation in the river mouth and the invasion of waves into the river. The length of jetties must be long enough to prevent sedimentation of littoral sand movement around the river mouth. However, such long jetties break the continuity of longshore sediment transport around them and bring about a secondary influence on the coast around them. They also increase the resistance of the river flow that may result in an increase in the water level of the river.

A culvert is usually constructed as a countermeasure against the closure of a small river with a design flood discharge smaller than 200m³/s and whose river mouth is located at the beach where a backshore develops. A culvert is effective at the river mouth where there is the possibility of sedimentation due to aeolian sand. A characteristic of this method is to utilize local scouring caused by waves and current at the opening of the culvert to prevent closure by sedimentation. However, the culvert may more or less bring discontinuity of longshore sediment transport.

A gate is also constructed at the river mouth of a small discharge. It also utilizes the local scouring caused by waves and current. We can also operate a gate to flash deposited sediment in front of it. However, artificial dredging is required when the amount of the deposited sediment becomes greater than the amount that can be flashed by the discharged flow from the gate.

As was mentioned above, the fluid motion around the river mouth shows a complicated aspect with the combined effects of river discharge, tidal current, waves and wave-induced current. A topographic change around a river mouth becomes more complicated than the fluid motion because one more independent variable, characteristics of the bed material, plays an important part in the phenomena. Therefore, it is generally impossible to determine the dimensions of countermeasure work against closure in a universal way. At present, the type and dimensions of countermeasures are decided by carrying out numerical or physical case studies or purely empirical knowledge.

Countermeasure works against river mouth closure have to possess the following functions:

(i)   to prevent and reduce sedimentation in the river and to preserve the river mouth cross-section for river discharge and

(ii) to prevent the invasion of waves into the river and to reduce wave set-up in the river. These demands come from the point of view of preventing flood disaster due to drainage failure. However, the beach erosion originating in a decrease of discharged sediment from a river becomes significant. Therefore, in terms of beach erosion control, it is desired that the following two conditions is satisfied:

(iii) not to disturb continuity of longshore sediment transport around the river mouth and

(iv) to redistribute discharged sediment from the river effectively to the surrounding coast to feed the beach.

These demands may be better satisfied by other coastal structures; e.g., by an offshore detached breakwater, than by the three types of countermeasure works mentioned above. In the following, we will discuss the functions of a training jetty and an offshore detached breakwater as countermeasure works for river mouth closure based on the experimental results.

5.8.3 Effect of countermeasure works on the river discharge and deposition pattern of discharged sediment.

It is not so difficult to prevent and reduce accretion of sediment around a river mouth through controlling the sediment movement around the river mouth by constructing countermeasure works such as a training jetty and an offshore detached breakwater. We have to be sure that such structures do not disturb the flow of sediment to the coast. However, when the discharged sediment is transported in the deeper region, it cannot be fed to the shoreline around the river mouth. In the dry season, when there is little river discharge, the river mouth has to keep its cross-section even under the attack of accretion type waves. From these points of view, the effect of waves and structures on the discharged flow and the deposition pattern of discharged sediment from a river is investigated based on experimental results.

Figures 5.31 and 5.32 show measured deposition patterns of coarse and fine sands discharged from the river in the experiments. The width and the depth of the river are 50cm and about 6.7cm respectively and the bottom slopes in the river and the coast are 1/100 and 1/20. Figure (a) is the result where there are no waves and Figs. (b) and (c) are the results where there are waves. The wave period in both cases is 1s. The mean discharged velocity at the river mouth is about 45cm/s. In the case of coarse sand (Fig. 5.31), discharged sediment is mainly transported as bed load. A large part of sediment is transported in suspension in the case of fine sand (Fig. 5.32).
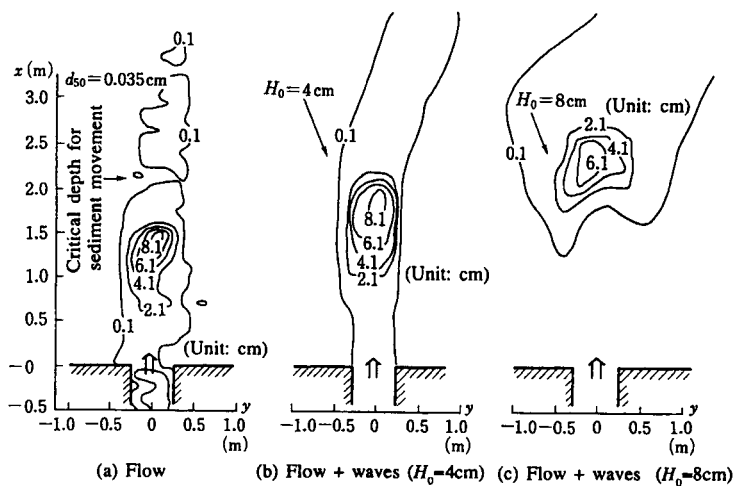
Fig. 5.31 Deposition pattern of discharged sediment from river mouth (d_{50}=0.035cm). ((a): without waves, (b): with waves of H_0=4cm, (c): with waves of H_0=8cm)
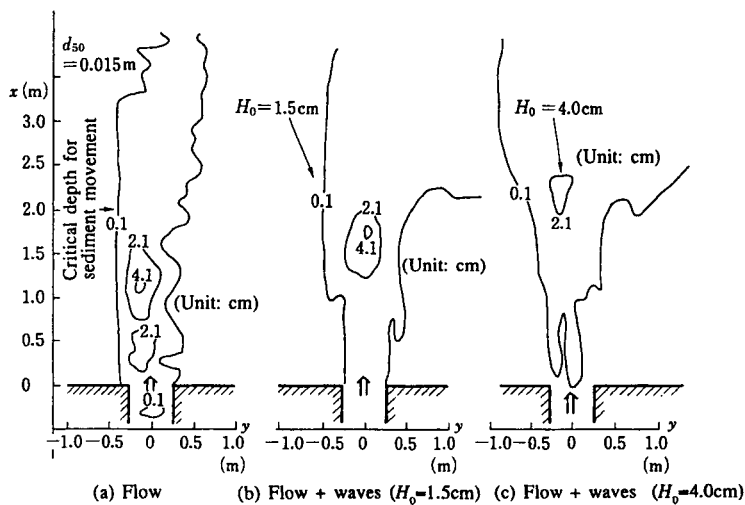
Fig. 5.32 Deposition pattern of discharged sediment from river mouth (d_{50}=0.015cm). ((a): without waves, (b): with waves of H_0=1.5cm, (c): with waves of H_0=4.0cm)

Predominant modes of sediment transport in the river and in the coast (by waves) in these experiments are listed in Table 5.3.

Table 5.3 Predominant mode of sediment transport

Figure No.	H_0 (cm)	d_{50} (cm)	in river (by current)	in coast (by waves)
Fig. 5.31 (b)	4	0.035	bed load	bed load
Fig. 5.31 (c)	8	0.035	bed load	suspension
Fig. 5.32 (b)	1.5	0.015	suspension	bed load
Fig. 5.32 (c)	4	0.015	suspension	suspension

When there are no waves, coarse sediment discharged from the river mouth is deposited in a comparatively narrow region without spreading in the longshore direction (Fig. 5.31 (a)). Fine sediment discharged from the river mouth is widely distributed in the downward direction but again it does not spread in the longshore direction (Fig. 5.32 (a)).

On the other hand, when there are waves, the deposited region moves offshore and discharged sediment spreads widely in the longshore direction. These tendencies increase as the wave height increases and the size of the bed material decreases (Figs. 5.31 (c) and 5.32 (c)).

In Fig. (a), the place where the velocity of the discharged flow in the centerline of the river decreases until the critical velocity for each sediment movement is reached is shown by an arrow. Most of the discharged sediment is deposited in the shallower region of this critical point when there are no waves. However, sediment discharged in waves spreads and settles beyond the critical point. This means that the bottom shear stress increases and critical water depth for sediment movement moves offshore when waves exist.

Figure 5.33 illustrates the influence of the waves on the mean water level (Fig. (a)) and velocity of discharged flow (Fig. (b)) along the center line of the river measured on the fixed bottom.
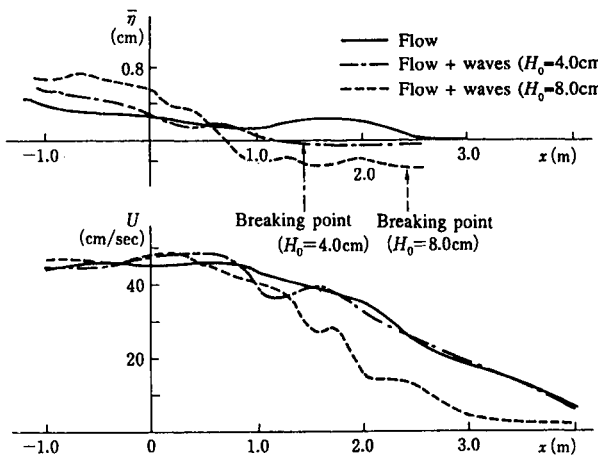
Fig. 5.33 Effect of waves on discharged flow and mean water level ((a): mean water level, (b): velocity of discharged flow)

Experimental conditions of these results are the same as those shown in Figs. 5.31 and 5.32. When the height of incident waves is large and they break offshore of the river mouth, the momentum of the discharged flow is weakened by the large gradient of radiation stress in the breaker zone. As a result, velocity of discharged flow decreases and a large wave set-up occurs that continues upstream of the river. In the case that the height of incident waves is 4cm, they break in the shallower region than waves of 8cm height do and they have little influence on the discharged flow and the mean water level.

From the viewpoint of maintaining the river mouth cross-section, an undesirable topographic change in the coastal region is the accretion type beach deformation associated with the net on-shore sediment transport caused by accretion type waves.

Figure 5.34 shows the influence of training jetties and offshore detached breakwaters on the deposition pattern of discharged sediment. The lengths of jetties and offshore detached breakwaters are 1m and the opening of the breakwater is the same as the river width (50cm). Other experimental conditions are the same as shown in Fig. 5.31 (a). It is found that the deposition pattern of the case of training jetties (Fig. 5.34 (a)) is almost the same as shown in Fig. (5.31 (a)). In the case where offshore detachments are constructed, a small portion of the discharged sediment is trapped shoreward region of the breakwaters (Fig. 5.34 (b)). However, the breakwaters have little influence on the deposition pattern near the river mouth.

(a) Training jetties   (b) Offshore detached breakwaters
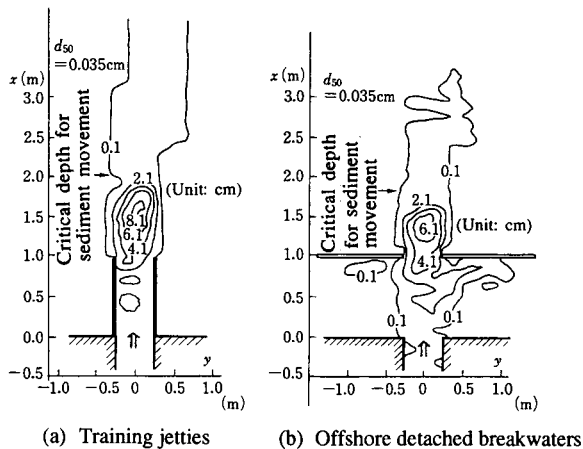
Fig. 5.34 Effect of training jetties and offshore detached breakwaters on the deposition pattern of discharged sediment from the river

Through these experiments, it is found that these structures have little influence on discharged flows in the coast and mean water level within the river. It is waves that break in front of the river mouth that exert a great influence on these quantities. It is also recognized that these structures do not have significant influence on the deposition pattern of discharged sediment in the presence of waves. Based on these results, properly arranged offshore detached breakwaters may become an alternative to training jetties.

References

Bruun, P. (1952): Measures against erosion at groins and jetties, Proc. 2nd Int. Conf. on Coastal Eng., ASCE, pp.137-164.

Bruun, P. (1978): Stability of Tidal Inlets, Elsevier, 506p.

Butakov, A.N. (1971): Study of developement and deformation of mouth bar, Proc. 14th Cong. IAHR, Paris.

Deguchi, I. (1984): Gentle slope sea dikes, Report of the Grant in Aid for Scientific Research, Ministry of Education, Science and Culture, Japanese Govt., No.A-59-1, pp.56-74. (in Japanese)

Deguchi, I. and T. Sawaragi (1986): Beach fill at two coast of different configurations, Proc. 20th Int. Conf. on Coastal Eng., ASCE, pp.1030-1046.

Deguchi, I. and T. Sawaragi (1988): Effects of structure on deposition of discharged sediment around river mouth, Proc. 21st Int. Conf. on Coastal Eng., ASCE, pp.1573-1587.

FitzGerald, D.M. (1982): Sedimentation by passing at mixed energy tidal inlets, Proc. 13th Coastal Eng. Conf., ASCE, pp.1094-1118.

FitzGerald, D.M. and S. Penland and D. Nummedal (1984): Numerical simulation processes along the east Friesian Island, West Germany, Proc. 14th Coastal Eng. Conf. ASCE, pp.3051-3066.

Galvin, C.J. (1969): Breaker travel and choice of gesign wave height, J. Waterways and Harbors Div., Proc. ASCE, Vol.95. No.WW2, pp.175-200.

Irie, K. and Y. Kuriyama (1985): Prediction of the rate of sedimentation in channels and basins by considering the deposition process due to convective more by bed materials. Rept. Port and Harbour Res. Inst., Vol.24, No.2, pp.157-204.

Ishihara, T. and T. Sawaragi (1963): Study on the stabilization of coastline by groins, Proc. 10th Japanese Conf. on Coastal Eng., JSCE, pp.156-161. (in Japanese)

Ministry of Transportation, Working Group on the development of construction technique of artificial beach (1979): Construction manual of artificial beach, 112p.

Nagai, S. (1955): Study on the groins at coast, Proc. 2nd Japanese Conf. on Coastal Eng., JSCE, pp.107-116. (in Japanese)

Nakatsuji, K., K. Muraoka and S. Aburatani (1992): Effects of tidal modulation on river plume spreading, Hydraulic and Environmental Modeling,.Estuarine and River waters, (ed. by R.A. Falconer. K. Shiono and R.G.S. Matthew), Ashugate, pp.229-309.

Ohnaka, S., A. Watanabe and M. Isobe (1988): Numerical modeling of wave deformation with curent, Proc. 21st Int. Conf. on Coastal Eng., ASCE, pp.393-407.

Ozsoy, E. (1977): Suspended sediment transport near tidal inlets, Proc. Coastal Sediment '77, ASCE, pp.914-926.

Partheniades, E. (1965): Erosion and deposition of cohesive soils, J. Hydraul. Div., Proc. ASCE, Vol.91, No. HY. 1, pp. 105-139.

Rijin, L.C. (1985): Sediment transport, Delft Hydraulic Labo., Publication No.334.

Savage, S.M. and M.G. Vincent (1954): Transport littoral formations de fleches de tombolos, Proc. 5th Int. Conf. on Coastal Eng., ASCE, pp.169-174.

Sawaragi, T., I. Deguchi and Y. Izumi (1981): Wave-induced current around offshore detached and submerged breakwaters, Proc. 28th Japanese Conf. on Coastal Eng., JSCE, pp.310-314. (in Japanese)

Sawaragi, T. and I. Deguchi (1982): Function of groin to trap longshore sediment transport, Proc. 29th Japanese Conf. on Coastal Eng. JSCE, pp.279-283. (in Japanese)

Sawaragi, T., I. Deguchi and G.P. Hong (1986): Effect of rubble mound foundation of composite type breakwater on reduction of reflection, Proc. 5th Cong. of APD, IAHR, pp.361-397.

Sawaragi, T., I. Deguchi and S.K. Park (1988): Experimental study on the function of submerged breakwater to control cross-shore sediment on artificially nourished beach, Coastal Eng. in Japan, JSCE, Vol.31, No.1, pp.121-130.

Sawaragi T. and I. Deguchi (1990): Function of detached breakwater to control longshore sediment transport, Proc. 22nd Int. Conf. on Coastal Eng., ASCE, pp.2603-2515.

Shimano, T. and H. Honma (1956): Experiments on effect of groins, Proc. 3rd Japanese Conf. on Coastal Eng., JSCE, pp.195-202. (in Japanese)

Shinohara, R. and T. Tsubaki (1966): Model study on the change of shoreline of sandy beach by the offshore breakwater, Proc. 10th Int. Conf. on Coastal Eng., ASCE, pp.550-563.

Simmons, H.S. and F.R. Brown (1969): Salinity effects on estuarine hydraulics and sedimentation, Proc. 13th Cong. IAHR, C-34, pp.311-325.

Suga, G. (1986): Study on countermeasures against intrusion of river mouth bar into rivers, Report of the Grant in Aid for Scientific Res., Ministry of Education, Science and Culture, Japanese Govt., 35p. (in Japanese)

Tanaka, N. (1976): Effect of submerged breakwater of wide crown width on wave attenuation and stabilization of the beach, Proc. 23rd Japanese Conf. on Coastal Eng., JSCE, pp.152-157. (in Japanese)

Toyoshima O. (1972): Coastal Engineering in the Field – Beach Erosion Control –, Morikita-Shuppan, 317p. (in Japanese)

Toyoshima, O. (1984): New type blocks for seawall slope protection, Proc. 19th Int. Conf. on Coastal Eng., ASCE, pp.2536-2545.

Tsuruya, H., K. Murakami and K. Irie (1990): Development of numerical calculation model for the countermeasure against harbor shoaling with a multi-level model, Rept. Port and Harbour Res. Inst., Vol.29, No.1, pp.3-51.

Van Leusser, W. and J. Dronkers (1988): Physical Process in Estuaries, Springer-Verlag, pp.1-18.

Chapter 6   Marine Structures for Ocean Space Utilization

6.1 Introduction

Marine structures discussed in this chapter are mainly for utilizing ocean space, not for providing a sheltered water area. Therefore, functions of marine structures differ somewhat from those for wave control described in Chapter 4. By using the term "ocean space utilization," we can quickly imagine an offshore development. Thus it is adequate to focus on offshore structures as the main subject of this chapter. There is another type of marine structure for ocean space utilization, such as a piled pier for berthing ships, an oil boom for preventing the spilt oil from spreading and so on. In this chapter, hydrodynamic aspects of these marine structures are presented, focusing on engineering design matters. Concerning an aqua-cultural structure, which should be classified as a marine structure, we would like to describe it later in Chapter 8, because it would be desirable to discuss it from not only engineering aspects but also ecological aspects.

6.2 Offshore Structures

6.2.1 Classification of the structures

Offshore structures for exploring and developing natural resources under the sea, especially undersea oil mines, can be largely classified into the three types as shown in Fig. 6.1; i.e.; a fixed gravity platform made of steel or concrete, a fixed jacket platform consisting of cylindrical members with a relatively small diameter and a floating platform with tensioned tethers (tension-leg platform).

(a) Gravity platform   (b) Fixed jacket platform   (c) Floating platform (tension leg platform)
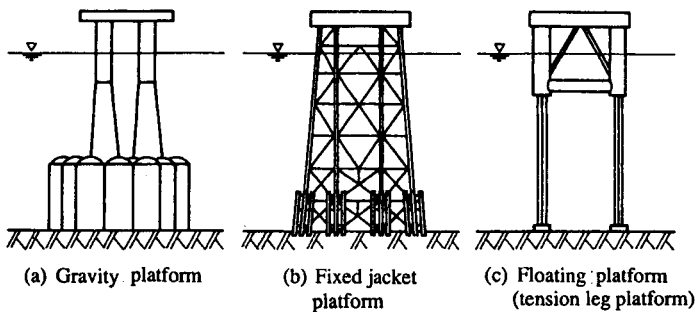
Fig. 6.1   Classification of offshore platforms

From the hydrodynamic point of view, these offshore structures have their own distinctive features. These features can be summarized as follows.

(1) Gravity platforms
This kind of structure usually has a significant fraction of the wavelength L in the horizontal dimension. Therefore, wave diffraction phenomena by the structure become

important to estimate the wave loads on it. In this category, effects of the separated flow around the body on wave loads may be neglected, especially for a rounded body like a circular cylinder. Consequently, we can use the potential flow theory to analyze the ambient flow about the body.

(2) Jacket platforms

A whole dimension of the structure reaches a significant fraction of the wavelength L. However, individual members of the structure are very small compared to the wavelength L. Since the effects of wave diffraction by the structure may be negligible here, we can approximate the local flow about each member as an oscillatory flow. The most important feature of the flow about the body is the generation of distinctive flow separations and resultant vortex formations. It is largely contributed by the fact that the excursion length of a water particle becomes large compared to the representative length of the structure. Therefore, we have to account for the effect of vortex flow on the wave force calculation, in addition to the unsteady fluid forces that can be estimated by the potential flow theory.

(3) Floating platforms

Additional fluid forces act on the floating structure due to motion in the fluid. For the estimation of hydrodynamic forces due to motion, the distinction between large and small bodies, similar to the case of fixed bodies, must be taken into consideration. For a body that is large compared to the wavelength L, generation of radiation waves caused by the body motion becomes distinctive. On the other hand, for the motion of the small body, fluid forces caused by the flow separation and resultant vortex formation must be considered in the fluid force calculation, where the generation of the radiation waves may be negligible.

As have been mentioned above, offshore structures can be largely classified by the use of the criteria: "whether or not the effect of a structure on the wave field reaches a far distance from the structure." For instance, for a large body, since scattered waves by the fixed body or radiated waves by the oscillating body become distinctive, these effects propagate far from the body. On the contrary, for a small body, flow separations and resultant vortex formations become predominant. However, these effects may remain in the vicinity of the body because of the little or weak propagating nature of the vortex flow in the wave field.

Analytical procedures for wave loading on the large body as well as wave diffraction and radiation about it have already been presented in **2.3** and **2.4**. A method of the wave boundary-value problem, mainly based on the potential flow theory, has been used.

For the small body, on the contrary, the Morison equation (Morison et al. 1950) is usually applied to estimate the wave load, which is a semi-empirical formula accounting for the fluid force caused by the flow separation and resultant vortex formation. In the Morison equation, it is assumed that the wave force can be given by the linear summation of the inertia force and the drag force. The drag force term is added to account for the vortex-induced force that is very hard to treat analytically. The Morison equation is very convenient to use because of its simplicity. However, there are still controversial problems in selecting the hydrodynamic coefficients included in the equation, i.e.; drag and inertia coefficients.

For a circular cylindrical pile, many studies have been carried out to examine the hydrodynamic features of these coefficients. It has been known that these coefficients have a close relation to the vortex flow pattern about a cylinder (Sawaragi et al. 1976; Sawaragi and Nakamura 1979; Sarpkaya and Isaacson 1981). Recently, various numerical simulation

methods of the vortex flow about the cylinder have been developed. In **2.7**, one of the simulation techniques based on the discrete vortex model has already been presented. In this section, practical calculation methods of the wave force on offshore structures are mainly discussed.

6.2.2 Gravity platforms

Wave forces on large offshore structures as shown in Fig. 6.1 (a) can be evaluated by the analysis described in **2.4**. In the analysis, the effect of wave diffraction by the structure is considered to have a major role in wave force calculation. If we adopt the Green's function method as a numerical procedure, which was introduced in **2.4**, the scattered wave potential ϕ_S can be obtained by Eq. (2.78) for an arbitrary three-dimensional body. Also, wave force vectors F (F_x, F_y, F_z) and overturning moment vectors M (M_x, M_y, M_z) on the body can be calculated by Eqs. (2.88) and (2.89), through the use of the wave pressure equation Eq. (2.87). In order to carry out the calculation described in the above, we have to deal with the discretized equations, after having divided the submerged surface of the body S_B into a finite number of small facets ΔS. First, we would like to examine the effect of the division number of facets on the accuracy of numerical calculation results.

(1) Discretization of a submerged surface

In Fig. 6.2, typical examples of the numerical error caused by the relative size of a facet to a wavelength, $\sqrt{\Delta S}/L$ (L=wavelength), are shown, where dimensionless horizontal wave forces $\hat{F}_x^*$ and overturning moments about the sea bed $\hat{M}_y^*$ on the vertical circular cylinder are plotted for various values of kD (k = wave number, D = diameter of the cylinder) as well as the corresponding relative size of a facet $\sqrt{\Delta S}/L$. ε is defined as the relative error of the numerical result to the analytical one, which is given by the diffraction theory by MacCamy and Fuchs.
The numerical procedure adopted here is the plane-symmetrical three-dimensional Green's function method described in **2.4.1**. At the top of the figure, a schematic view of the discretization of a quarter of the cylinder surface into facets is specified. From the figures, it is seen that the numerical error becomes less than 2 or 3% if we divide the submerged surface into facets so that its equivalent side length $\sqrt{\Delta S}$ is less than 10% of the wavelength. In the figures, we can see a tendency that ε increases again for the smaller value of $\sqrt{\Delta S}/L$. However, this is because the numerical solution is gradually approaching the analytical solution with some oscillation. Note that the calculation based on the smaller facets takes longer computational time, probably increasing by a rate proportional to the square of the number of facets. It may be advisable to use the facet whose equivalent side length $\sqrt{\Delta S}$ is about 10% of the wavelength L. Hogben et al. (1974) recommended the discretization of the submerged surface into facets so that its equivalent side length ($=\sqrt{\Delta S}$) is less than 1/8 of the wavelength. In the above, paying attention to only the parameter $\sqrt{\Delta S}/L$, the criterion on the discretization error has been discussed. However, for an angular body such as a rectangular cylinder, it is easily estimated that the fluid velocity near the edge is larger than the other flat part. Because of the large velocity gradient near the edge, the source strength varies drastically near the corner. Therefore, it may be necessary to use smaller facets near the corner. But, such a proof has not been given. This kind of examination must be carried out in the future, including the effect of the inevitable flow separation from the edge on the wave load.

(2) Calculation examples for a gravity platform

Here, the Condeep, which is under operation in the North Sea to produce the undersea oil, is taken as an example of the gravity platform. The model test for the Condeep has

(a) Partitioning a quarter of the cylindrical surface into facets
(30 facets)

(b) Horizontal wave forces $\left(\hat{F}_x^* = \hat{F}_x / \left(\rho g H_I D^2 / 8\right)\right)$
and their numerical errors

(c) Overturning moments about the sea bed
$\left(\hat{M}_y^* = \hat{M}_y / \left(\rho g H_I D^3 / 16\right)\right)$ and their numerical errors
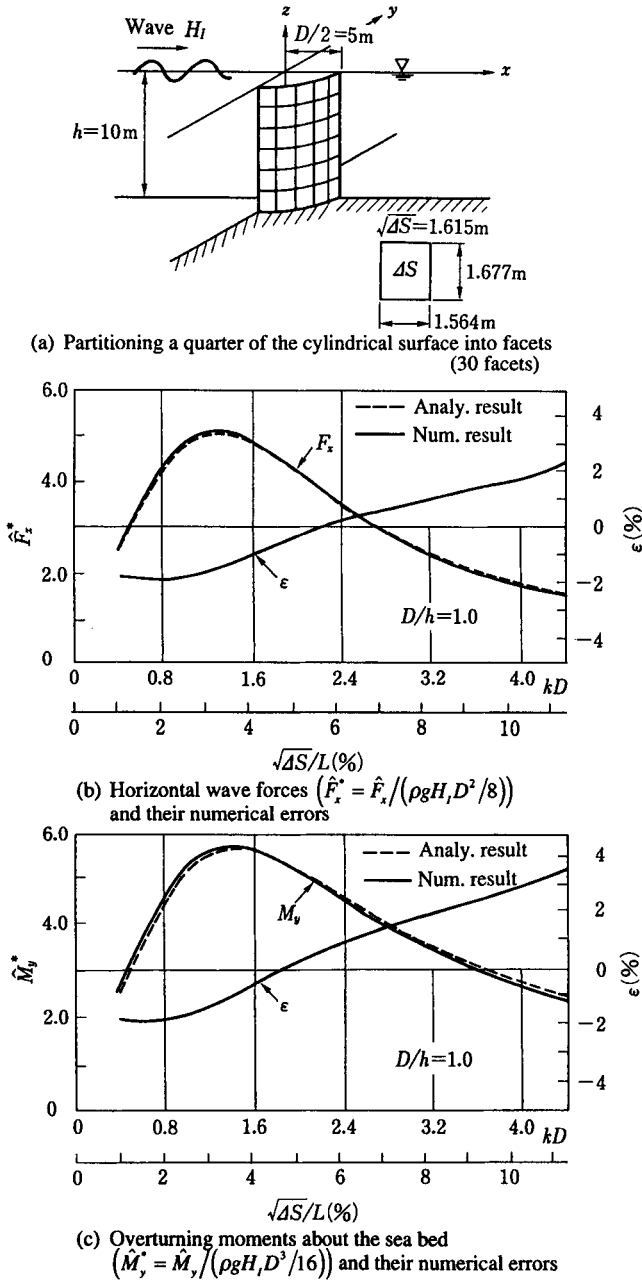
Fig. 6.2 Numerical errors of wave forces by portioning the submerged surface

already been carried out by Garrison et al. (1974). Figure 6.3 shows the brief dimensions of the Condeep, which has six cylindrical tanks on its base and three columns for supporting a platform.
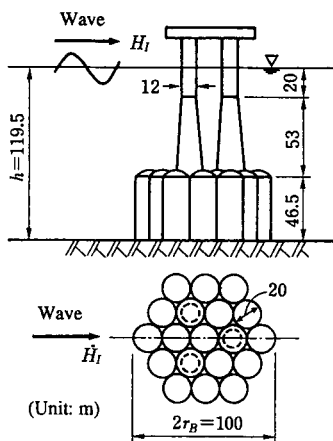
Fig. 6.3 Schematic view of the Condeep

The partitioning of the submerged surface of the structure into small panels used in the numerical calculation is given in Fig. 6.4. Only half of the structure is specified because it is symmetrical about a vertical plane as seen in Fig. 6.3.
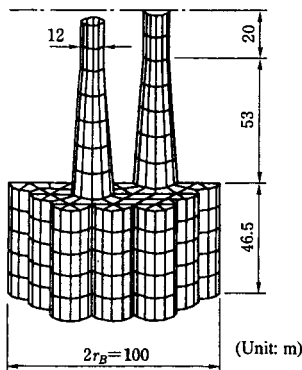
Fig. 6.4 Representation of a half of the submerged surface of the Condeep facets (Number of facets = 382)

The discretization criterion, $\sqrt{\Delta S}/L \leq 0.1$, is satisfied in the calculation for the wave conditions used. In Figs. 6.5 to 6.7, results of the horizontal wave force $\hat{F}_x$, vertical wave force $\hat{F}_z$ and overturning moment $\hat{M}_y$ by the plane-symmetrical Green's function method

are shown, respectively. These numerical results were given by Nakamura (1990). The model test results by Garrison et al. (1974) are also plotted for the comparison, where the incident wave height H_I is fixed at 20m on a prototype scale. Garrison et al. also conducted the numerical computation, but limited it to only the model test conditions. Such calculation results are also shown in the figures.
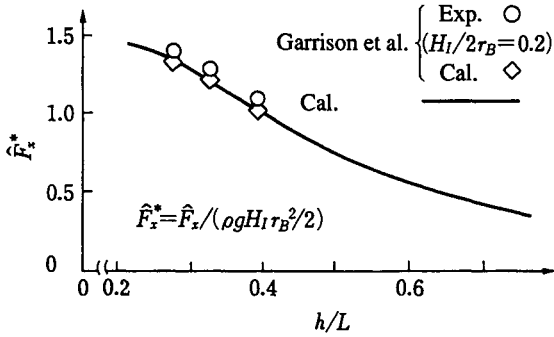
Fig. 6.5 Horizontal wave forces on the Condeep ($H_I/2r_B$=0.2)
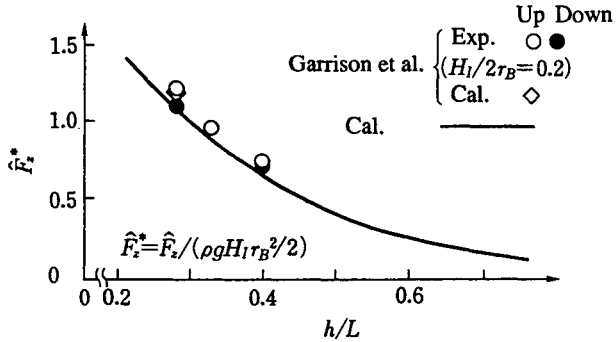
Fig. 6.6 Vertical wave forces on the Condeep ($H_I/2r_B$=0.2)
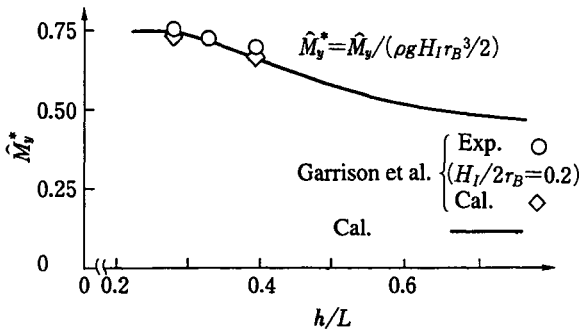
Fig. 6.7 Overturning moments about the sea bed on the Condeep ($H_I/2r_B$=0.2)

From these figures, we can see the tendency that the wave forces and overturning moment increase with decreasing h/L; i.e., for longer waves. It is also seen that the calculation results agree well with the model test results. It is noted that the calculation results by Garrison et al. were given by taking the three steps as follows. First, using the three-dimensional Green's function method, wave forces on the base structure were computed, where the existence of column structures was ignored. At the same time, the velocity distribution above the base structure was calculated. Second, applying the Morison equation with the substitution of the calculated fluid velocity above the base structure, wave forces on the column structures were calculated. Finally, a summation of the two wave forces was carried out to obtain the total wave force. It is seen that the calculated results obtained by the hybrid method described above agree well with those based on only the potential flow theory by Nakamura et al. The reason for the consistency is that the inertia force is predominant over the drag force for the columns. However, in order to use the hybrid method, it is noticed that we have to apply the ambient fluid velocity above the base structure to the Morison equation.

In Figs. 6.8 and 6.9, the nonlinearity effect caused by the difference in wave height on the wave loads $\hat{F}_x$ and $\hat{M}_y$ is examined.
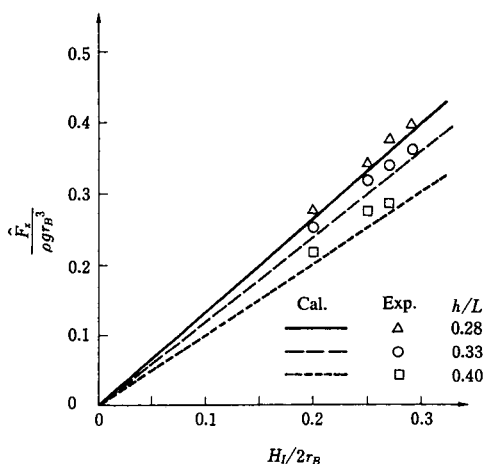
Fig. 6.8 Variation of horizontal wave forces on the Condeep with incident wave heights

According to the linear wave theory, the wave load is proportional to the incident wave height if the wave period is fixed. Therefore, we can check the nonlinearity effect on the wave loads by examining the linear relation between the wave height and wave load as shown in these figures. From the figures, we can see a linear relation between the wave height and wave loads for various conditions of the wave period; i.e., for different values of h/L. Therefore, it may be pointed out that the wave loads on the large body, especially like the Condeep that has a massive base structure near the sea bed, can be estimated by the linear diffraction theory.

The important aspect for a practical design, which we can suggest from the previous examination, is the fact that there is a significant variation in wave loads with the wave period. If we use the conventional design method; i.e., the deterministic design, a design
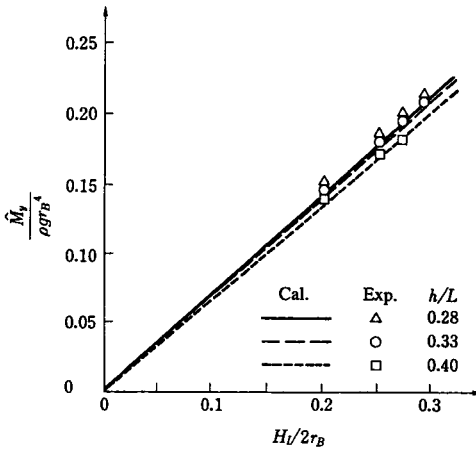
Fig. 6.9 Variation of overturning moments on the Condeep with incident wave heights

wave must be selected based on the wave forecasting or observations. In this occasion, it is very likely to select the wave condition with the possible maximum wave height as a design wave without paying special attention to the selection of the wave period. However, for the engineering design, the maximum wave load is necessary rather than the maximum wave height. In order to estimate the possible maximum wave loads on the structure, it is strongly recommended to take the following design process, especially for large structures. First, check the variation of the transfer coefficient from waves to wave loads with the wave period. The transfer coefficient is defined by the dimensionless wave load as shown in Figs. 6.5 to 6.7. Second, examine the possible band width of the wave period. If there is a significant variation in the transfer coefficient within the band, carry out the wave force calculation using every wave period condition with the corresponding wave height. Finally, choose the possible maximum wave load from these comparisons.

In Fig. 6.10, the effect of the incident angle of incoming waves on the wave loads for the Condeep is examined, where the absolute value of the horizontal wave force vector $|\hat{\tilde{F}}_H|$ is shown for various conditions of the wave period. From this figure, we can see that there is little effect of the incident angle on the horizontal wave force, since the Condeep is almost axisymmetrical about the vertical axis. However, for another offshore platform such as a rectangular-shaped platform, dependency of the wave force on the incident wave angle cannot be ignored and must be examined first in the practical design.

A critical condition for the sliding of a gravity platform in the horizontal direction can be estimated by

$$F_f > \left|\hat{\tilde{F}}_H\right| \tag{6.1}$$

where F_f is the bottom frictional force of the structure. If we define the weight of the structure in the water as B_w' and the vertical wave force $\tilde{F}_z$ at the time phase when F_H shows a maximum, F_f is given by

$$F_f = \mu\left(B_w' - \tilde{F}_z\right) \tag{6.2}$$
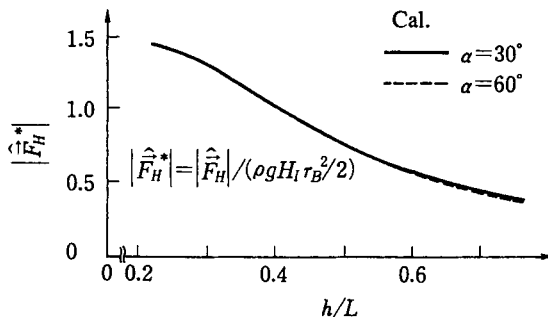
Fig. 6.10 Effect of the incident wave angle on the horizontal wave force vector

where μ is the frictional coefficient between the sea bed and the structure.

Also we can estimate a critical condition for the overturning of a gravity platform by considering the balance between the wave exciting moment M_F and the resisting moment M_R due to the weight around the rear toe of the structure

$$M_R > M_F \qquad (6.3)$$

6.2.3 Jacket platforms

In this section, an estimation method of wave forces on a fixed jacket platform is discussed. A jacket platform consists of comparatively slender members. Since the radius of the member is sufficiently small compared to the wavelength, the Morison equation is usually used to predict the wave force on the cylindrical member in the direction of the wave propagation. Recently, it has been known that transverse or lift forces act on the slender member in directions normal to the wave propagation directions (Sawaragi et al. 1976; Sarpkaya and Isaacson 1981) in addition to the in-line forces expressed by the Morison equation. In the following, taking both directional forces into consideration, the estimation method of the wave forces is described. A jacket platform consists of tubular members interconnecting with each other and has comparatively large column members from the sea floor to the upper platform. Wave forces on such tubular members with various inclinations can be calculated by the generalized Morison equation described in **2.6**. However, we have to add the effect of transverse forces to the in-line forces given by the Morison equation.

(1) In-line forces

In-line forces on tubular members of the jacket platform can be estimated by Eq. (2.165) in **2.5.1**. Let's derive the equation for the total in-line force on these members by taking an example of the jacket platform specified in Fig. 6.11. Here, we assume that incoming waves are incident to the jacket platform in the direction parallel to the x axis as shown in Fig. 6.11.

First, define the unit vector in the tubular axis direction of the member m as $\bar{e}_m$ (e_{mx}, e_{my}, e_{mz}) and also the coordinates of upper and lower nodes of this member as $Q''_m(x''_m, y''_m, z''_m)$ and $Q'_m(x'_m, y'_m, z'_m)$, respectively. Referring to Eq. (2.165), the in-line force vector on this member can be given by
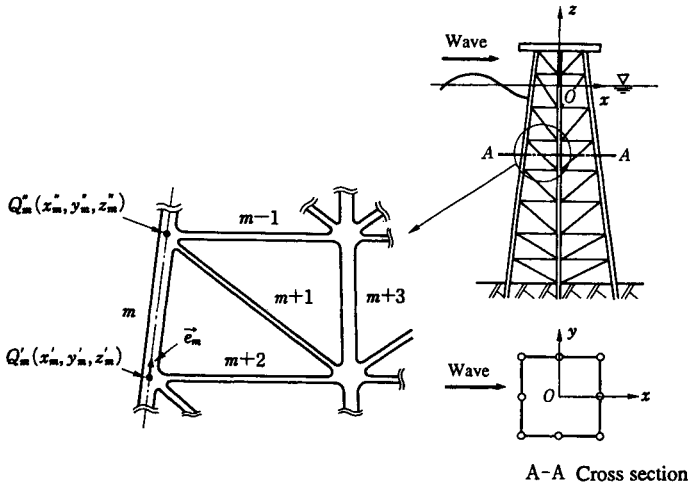
Fig. 6.11 Definition sketch of the tubular members of a jacket platform

$$\vec{F}_{Vm} = \int_{Q'_m}^{Q''_m} \left\{ \frac{1}{2} C_D \rho D_m \left| \vec{U}_{Nm} \right| \vec{U}_{Nm} + C_M \rho \frac{\pi D_m^2}{4} \frac{\partial \vec{U}_{Nm}}{\partial t} \right\} dC(x_m, y_m, z_m) \qquad (6.4)$$

where C_D is the drag coefficient, C_M is the inertia coefficient, D_m is the diameter of the member m, C is the line segment parallel to the tubular axis extending from point Q'_m to Q''_m, (x_m, y_m, z_m) is the coordinate along the line C, $\vec{U}_{Nm}$ is the fluid velocity in the normal direction to the tubular axis, and $\partial \vec{U}_{Nm}/\partial t$ is the fluid acceleration in the normal direction of the tubular axis. By referring to Eq. (2.164), we can express $\vec{U}_{Nm}$ in terms of the wave induced velocity (u_m, w_m) at the position (x_m, y_m, z_m) on C

$$\vec{U}_{Nm} = \left(U_{xm}, U_{ym}, U_{zm} \right) \qquad (6.5a)$$

$$\left. \begin{array}{l} U_{xm} = u_m(1 - e_{xm}^2) - w_m e_{xm} e_{zm} \\ U_{ym} = -u_m e_{xm} e_{ym} - w_m e_{ym} e_{zm} \\ U_{zm} = w_m(1 - e_{zm}^2) - u_m e_{xm} e_{zm} \end{array} \right\} \qquad (6.5b)$$

The wave induced velocity (u_m, w_m) can be obtained with the use of an adequate wave theory. For instance, if we use the linear wave theory, these velocity components are

$$u_m = \text{Real}\left[\partial(\Phi_I|_{\alpha=0})/\partial x \right]\Big|_{\substack{x=x_m \\ z=z_m}} = \frac{gkH_I}{2\sigma} \frac{\cosh k(h+z_m)}{\cosh kh} \cos(kx_m - \sigma t) \qquad (6.6a)$$

$$w_m = \text{Real}\left[\partial(\Phi_I|_{\alpha=0})/\partial z \right]\Big|_{\substack{x=x_m \\ z=z_m}} = \frac{gkH_I}{2\sigma} \frac{\sinh k(h+z_m)}{\cosh kh} \sin(kx_m - \sigma t) \qquad (6.6b)$$

where the term kx_m expresses the phase effect due to the location of the member. This phase effect is important for calculating the total wave force on the structure.

On the other hand, the moment $\bar{M}_{Vm}$ caused by the in-line force acting on the member m about the position (x_c, y_c, z_c) can be given as

$$\bar{M}_{Vm} = \int_{Q_m}^{Q_m''} \bar{r}_m \times d\bar{F}_{Vm} \tag{6.7}$$

where $\bar{r}_m$ is the position vector extending from the center of moment to the line segment dC along the member m:

$$\bar{r}_m = (x_m - x_c, y_m - y_c, z_m - z_c) \tag{6.8}$$

The total in-line force vector $\bar{F}_V$ and the total moment $\bar{M}_V$ around (x_c, y_c, z_c) can be obtained by summing up the local wave force $\bar{F}_{Vm}$ and moment $\bar{M}_{Vm}$ on each member, respectively:

$$\bar{F}_V = \sum_m \bar{F}_{Vm} \tag{6.9}$$

$$\bar{M}_V = \sum_m \bar{M}_{Vm} \tag{6.10}$$

Maximum values of the total in-line force and the total moment are usually estimated by the time-step analysis because of the complicated phase relations among the local wave forces.

Next, we briefly review the problem for the selection of hydrodynamic coefficients C_D and C_M included in the above equations. As described in **2.5**, a comparatively large number of studies have been carried out to examine the characteristic of these hydrodynamic coefficients, especially for a vertical circular cylinder. It has become known that C_D and C_M are functions of both the Reynolds number (Re) and the Keulegan-Carpenter number (KC) (Sawaragi and Nakamura 1979; Sarpkaya and Isaacson 1981; Chakrabarti 1987). However, for inclined cylinders, there has not been enough data to estimate the hydrodynamic coefficients. Chakrabarti et al. (1975) conducted a series of experiments with the in-line force on an inclined circular cylinder, but the range of Re is comparatively small. Also, the estimation of lift forces on an inclined cylinder has not been clarified.

Sarpkaya et al. (1982) proposed the approximate method for the estimation of force coefficients of the inclined cylinder based on the result of the vertical cylinder. The central idea of this method is to adopt the normal velocity to the cylinder axis $\bar{U}_{Nm}$ as the representative velocity, which is used to define Re and KC. The theoretical background of this method is in Eq. (6.4), in which an in-line force is represented to be proportional to the normal velocity and its corresponding acceleration. Thus we can use the results for the vertical cylinder to estimate the force coefficients for the inclined cylinder, simply after replacing the horizontal velocity with the normal velocity of the cylinder axis. Chakrabarti (1975) confirmed the validity of this method by the experiment. However, for a large angle of inclination of the cylinder, it is also known that this approximation is not always adequate (Garrison 1985). Anyhow, much more extensive work on the inclined cylinder must be done in the future for definite results.

Another problem concerning the wave force on cylindrical members is an interference effect among them. This problem is related to the proximity effect of a cylindrical member near the sea bed or the free surface, which was presented in **2.5.3**. Chakrabarti (1982) have examined the interference effect of both a row and a column of vertical circular cylinders on wave forces, varying the number of the cylinders and the spacing between the cylinders. According to these results, if the center to center distance between the cylinders is two or three times greater than the diameter of the cylinder, we can practically neglect the interference effect.

(2) Lift forces (transverse forces)

There are mainly two different methods to estimate a lift force on a vertical circular cylinder. One is to give only a peak value of the lift force. Another one is to evaluate the time variation of the lift force during one wave period, considering the time phase relation between the in-line force and the lift force. Sawaragi et al. (1976 and 1978) presented an empirical formula that belongs to the latter, considering the contribution from the higher harmonics of the lift force. According to their results, the lift force $(\bar{F}_L)_s$ on a vertical circular cylinder fixed in the wave field with water depth h is given by

$$\left(\bar{F}_L\right)_s = \left[\int_{-h}^{\eta} (\pm)\frac{1}{2}\left(C_L\right)_{rms}\rho D\{\hat{u}(z)\}^2 \sum_{n=1}^{4} P_L^*(n\sigma)\cos(n\sigma t - \delta_{Ln})dz\right]\vec{j} \qquad (6.11)$$

where $(C_L)_{rms}$ is the lift coefficient concerning to the RMS (root mean square) value of the peak lift forces. The sign $\pm$ accounts for the indefinite of positive direction of the lift force. Since the lift force shows an irregular nature even in the regular waves, such a statistical treatment is necessary. $P_L^*(n\sigma)$ is the dimensionless spectral density of the n-th higher harmonics of the lift force, δ_{Ln} is the phase lag of the n-th higher harmonics of the lift force from the water elevation at the center of the cylinder, $\hat{u}$ is the amplitude of the horizontal fluid velocity in the wave propagation direction, η is the water elevation at the center of the cylinder, $\vec{j}$ is the unit vector in the y-axis direction.

Properties of $(C_L)_{rms}, P_L^*(n\sigma)$ and δ_{Ln} are specified as a function of KC based on the experimental results by Sawaragi et al. (1978). Also, it was pointed out that the probability distribution of the peak lift forces is approximately like the Rayleigh distribution. Consequently, there is a definite relation between $(C_L)_{rms}$ and the 1/10 maximum significant lift coefficient $(C_L)_{1/10}$ as follows:

$$(C_L)_{rms} \approx (C_L)_{1/10}/1.8$$

In Fig. 6.12, as one of the typical results, $P_L^*(n\sigma)$ is shown as a function of $(KC)_r$, where $(KC)_r$ is the RMS value of KC along the vertical axis (z-axis) of the cylinder.

From the figure, it is seen that the lift force on the cylinder has several higher harmonic components and the ratio of the higher harmonics increases with KC. In the previous work (Sarpkaya 1976; Sawaragi and Nakamura 1980), it was also reported that the magnitude of the peak lift force reaches the same order of the in-line force at the condition $(KC)_r$ being about 10. Simultaneously, under such a condition, the second higher harmonic component of the lift force overwhelms the others as seen in the figure. From these facts, we can say that the lift force is very important when the dynamics of the structure due to wave actions are examined because the natural frequency of a fixed jacket platform is usually higher than the wave frequency encountered in the ocean.
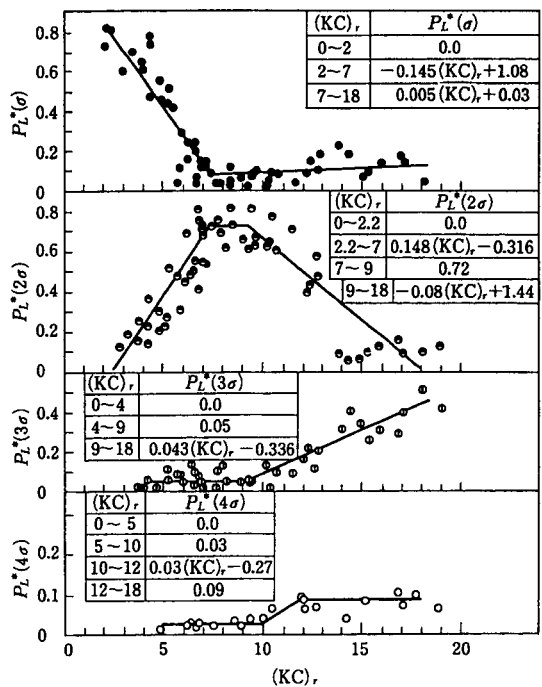
Fig. 6.12 Frequency characteristics of lift forces on a vertical circular cylinder

Now, let us try to evaluate the total lift force on the fixed jacket platform shown in Fig. 6.11, where it is assumed that the total lift force is given by considering the lift forces only on the principal members like the jacket columns because no definite result is available for lift forces on horizontal members and interconnecting members such as bracing. Taking the column member m in Fig. 6.11 as an example, we can evaluate the lift force on this member through the use of Eq. (6.11) by

$$\vec{F}_{Lm} = \int_{z_m'}^{z_m''} d\vec{F}_{Lm}$$

$$= \left[\int_{z_m'}^{z_m''} (\pm)\frac{1}{2}(C_L)_{1/10}\rho D|\hat{u}_m|^2 \sum_{n=1}^{4} P_L^*(n\sigma)\cos\{n(kx_m - \sigma t) + \delta_{Ln}\}dz \right]\vec{j} \tag{6.12}$$

where $(C_L)_{1/10}$ is used instead of $(C_L)_{rms}$ in order to evaluate the more critical value of the lift force for the practical design. Also, the moment $\vec{M}_{Lm}$ about the position (x_c, y_c, z_c) by F_{Lm} is given by

$$\vec{M}_{Lm} = \int_{z_m'}^{z_m''} \vec{r}_m \times d\vec{F}_{Lm} \tag{6.13}$$

It is noted that one of the signs ± should be used so that the total lift force on the structure shows the larger value. The validity of such a selection of the sign ± was confirmed experimentally by Sawaragi and Nakamura (1981). The total lift force on the structure $\vec{F}_L$ and the total moment $\vec{M}_L$ due to $\vec{F}_L$ about the position (x_c, y_c, z_c) are calculated by summing up local forces and moments, respectively:

$$\vec{F}_L = \sum_m \vec{F}_{Lm} \tag{6.14}$$

$$\vec{M}_L = \sum_m \vec{M}_{Lm} \tag{6.15}$$

Finally, the total wave force and moment can be obtained by combining both the effects of the in-line force and lift force on the structure:

$$\vec{F}_T = \vec{F}_V + \vec{F}_L \tag{6.16}$$

$$\vec{M}_T = \vec{M}_V + \vec{M}_L \tag{6.17}$$

Sawaragi and Nakamura (1981) confirmed the validity of the above equations that includes both the in-line and lift forces, performing the experiments on dynamic behavior of a four-pile supported platform in waves.

6.2.4 Dynamic response of offshore structures

In Fig. 6.13, the natural period of horizontal oscillation T_n of the various offshore structures, such as a fixed jacket platform, a tension leg platform (TLP) and so on, are specified with the wave conditions encountered in the real ocean (Leonard et al. 1990), where the wave condition is given by the use of the wave spectrum with the parameter of a significant wave height H_s.
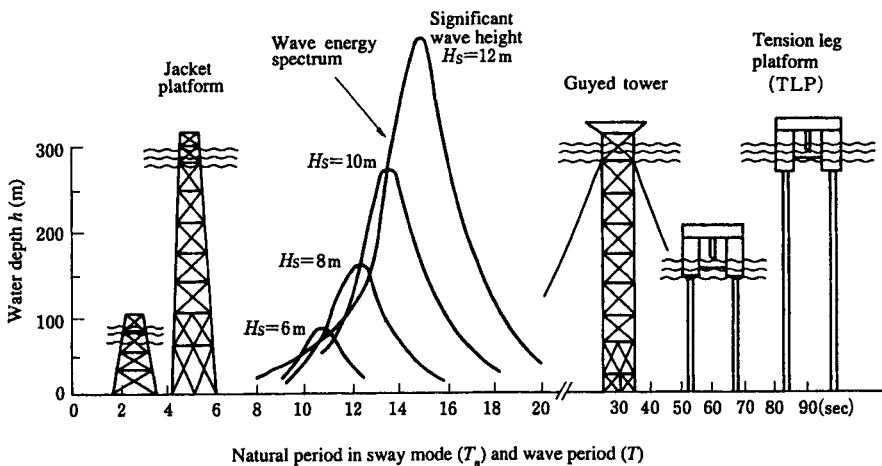
Fig. 6.13 The natural period of oscillation for various offshore platforms and the wave energy spectrum (Leonard et al. 1990)

It is seen from the figure that the natural period in the horizontal mode of a fixed jacket platform is less than the wave period corresponding to the peak frequency of the wave spectrum. On the contrary, the natural period of a TLP ranges far above the wave period of wind waves. If we use the same analogy with the seismic response of the land structure, i.e., a rigid structure and a flexible structure, the jacket platform is classified to the group of a rigid structure and a TLP is a flexible structure. However, for offshore structures, the assumption that the period of the wave exciting force is equal to the wave period is not always valid. This is because there is a generation of higher harmonic components due to the lift force as described above. Therefore, there is a great possibility that the resonant response appears by the lift force if the natural period of the structure ranges from 1/3 to 1/2 of the wave period.

Since a TLP can be classified to a flexible structure from the viewpoint of the horizontal motion, we have to account for the body motion in the engineering design. Concerning the motion of the large body like a TLP, a method of the analysis was given in 2.4, including a theoretical treatment of the wave boundary-value problem around the floating body. In this section, dynamic analysis of a multiple-pile supported platform is mainly discussed, where the pile diameter is sufficiently small compared to the wavelength, as with the tubular members of a jacket platform.

(1) Equations of motion for a small body

For a small body, although the effect of radiation waves due to the body motion can be neglected, we have to newly take the effect of flow separations and the resultant vortex motions into consideration. Considering the added mass force due to the body motion and the wave force by the Morison equation, we can derive the following dynamic equilibrium relation among various forces:

$$\underbrace{\mathbf{F}^{(I)}}_{Mass\,inertia\,force} + \underbrace{\mathbf{F}^{(S)} + \mathbf{F}^{(M)}}_{Restoring\,force} = \underbrace{\mathbf{F}^{(P)} + \mathbf{F}_S^{(A)} + \mathbf{F}_d^{(A)} + \mathbf{F}^{(DR)} + \mathbf{F}^{(L)}}_{Hydrodynamic\,force} \quad (6.18)$$

where $F^{(I)}$ is the mass inertia force, $F^{(S)}$ is the hydrostatic restoring force, $F^{(M)}$ is the restoring force by mooring lines or structural stiffness, $F^{(P)}$ is the force due to the pressure gradient in the wave field, $F_S^{(A)}$ is the added mass force proportional to the fluid acceleration, $F_d^{(A)}$ is the added mass force proportional to the body acceleration, $F^{(DR)}$ is the drag force proportional to the square of the relative velocity between the body and the fluid, and $F^{(L)}$ is the lift force. Under the assumption of small motions of the body, the terms $F^{(P)}$ and $F_S^{(A)}$ are combined and expressed as an inertia force term that is equivalent to the inertia force in the Morison equation. In general, a structural damping term is added to the above equation. As Eq. (6.18) is the most general equation of motion for a small body, we can apply it to both the floating body and the fixed body consisting of tubular members.

(2) Dynamic analysis of a pile supported platform

In order to derive the equation of motion by referring to Eq. (6.18), we have to further construct an analytical model for the real structure. For instance, we have to model a real structure to a spring-mass system according to dynamic similarity. Harleman et al. (1963) have presented the simple modeling of a pile supported platform in waves, as shown in Figs. 6.14 (a), where the platform is idealized as a vibration system with a single degree of freedom as seen in Fig. 6.14 (b).

(a) Structural model

(b) Equivalent spring-mass system
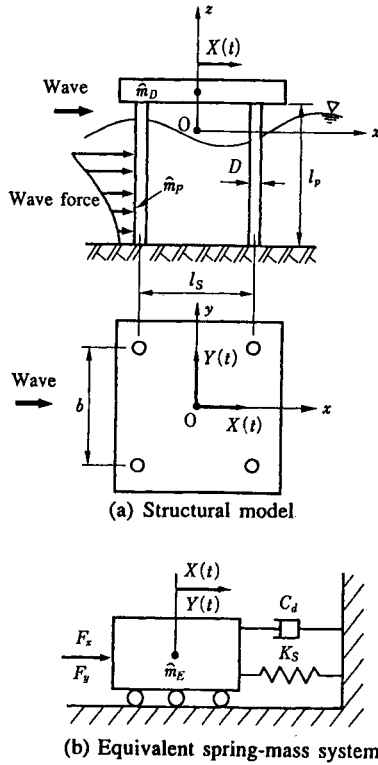
Fig. 6.14 A multi-pile supported platform and its equivalent spring-mass system

Sawaragi and Nakamura (1981) extended the model by Harleman et al. to a two dimensional model that is able to treat the displacements in both the in-line force direction and the lift force direction simultaneously. There are several other ways for modeling the pile supported structure to the vibration system, such as modeling to a system with multi-degrees of freedom. Here, we introduce the simplest modeling used by Harleman et al. (1963) and Sawaragi et al. (1983).

(a) Equivalent spring-mass system: According to the previous work (Harleman et al. 1963), the following relationships exist between the model structure and equivalent spring-mass system.
i) Equivalent mass $\hat{m}_E$

$$\hat{m}_E = m_D + m(13/35)\hat{m}_P \qquad (6.19)$$

in which, m_D is the mass of the deck , m_P is the mass of a support pile and m is the number of the support piles.

ii) Spring constant K_S

$$K_S = m(12EI / l_P^3)$$ (6.20)

in which, EI is the flexural rigidity of the support piles and l_P is the length of the support piles.
iii) Influence fraction f_l

$$f_l = 3\{(z+h)/l_P\}^2 - \{(z+h)/l_P\}^2$$ (6.21)

f_l is used as a transform coefficient which translates the wave force acting on the pile at elevation z into the equivalent exciting force acting on the deck. It is noted that the modeling described in the above is based on the assumption that both the weight and rigidity of the deck are sufficiently large compared to those of the support piles.

(b) Equation of motion: Using the above quantities and the force equations developed in the preceding section, the equation of motion for a four-pile supported platform can be expressed as follows.
i) Equation of motion in the X-direction (wave propagation direction)

$$\left(\hat{m}_E + M^{(A)}\right)\ddot{X} + C_d\dot{X} + K_S X = F_x$$ (6.22)

where, X is the displacement of the deck in the X-direction, C_d is the structural damping, $M^{(A)}$ is the added mass proportional to the oscillatory acceleration of the structure, F_x is the equivalent in-line force acting on the deck. $M^{(A)}$ is given by

$$M^{(A)} = \sum_m C_A \rho \frac{\pi D^2}{4} \int_{-h}^{\eta_m} f_l^2 \, dz$$ (6.23)

Here, η_m is the water surface elevation at the location of the support pile m, C_A is the added mass coefficient and expressed as $(C_M - 1)$ using the inertia coefficient C_M. Considering to $F^{(DR)}$ in Eq. (6.18), F_x may be expressed as

$$F_x = \sum_m \left\{ \frac{1}{2} C_D \rho D \int_{-h}^{\eta_m} (u_m - \dot{X}f_l)|u_m - \dot{X}f_l|f_l \, dz + C_M \rho \frac{\pi D^2}{4} \int_{-h}^{\eta_m} \frac{\partial u_m}{\partial t} f_l \, dz \right\}$$ (6.24)

where u_m and $\partial u_m/\partial t$ indicate the horizontal fluid velocity and acceleration, respectively, at the location of the support pile m. They are given by Eq. (6.6a).
ii) Equation of motion in the Y-direction (normal to the wave propagation direction)

$$\left(\hat{m}_E + M^{(A)}\right)\ddot{Y} + C_d\dot{Y} + K_S Y = F_y$$ (6.25)

Here, Y is the displacement in the Y-direction and F_y is the equivalent lift force acting on the deck. F_y is given by

$$F_y = \sum_m \left\{ F_{Lm} \Big|_{z_m'' = -h}^{z_m'' = \eta_m} - \frac{1}{2} C_D \rho D \int_{-h}^{\eta_m} (\dot{Y} f_l) \big| \dot{Y} f_l \big| f_l \, dz \right\} \tag{6.26}$$

In this equation, F_{Lm} is expressed by Eq. (6.12), where $(C_L)_{1/10}$ must be replaced by $(C_L)_{rms}$ because a steady state response is needed. The second term in Eq. (6.26) represents the contribution from the drag force due to the oscillation in the Y-direction.

(c) Results for a four-pile supported platform: Sawaragi and Nakamura (1981) carried out comprehensive work on the validity of the above estimation method of the dynamic displacements of the platform. In the experiment, the model structure shown in Fig. 6.15 was used. Dynamic properties of the model structure are summarized in Table 6.1, where C_c indicates the critical damping.
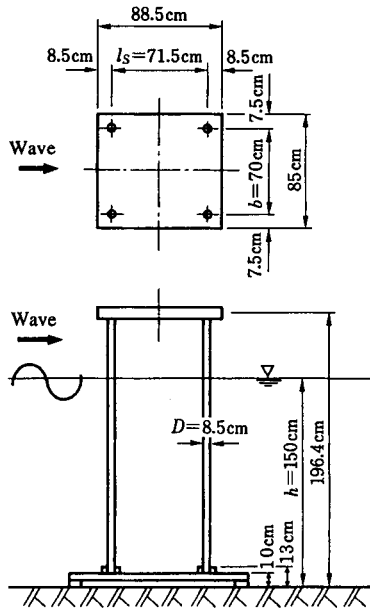
Fig. 6.15 Schematic diagram of the model platform (Sawaragi and Nakamura 1980)

In Fig. 6.16, the ratio of the Y-displacement to the X-displacement is shown as a function of T/T_n, where T_n is the natural period of oscillation of the platform. In the figure, a dotted line indicates the mean value of the measured results.

Table 6.1 Dynamic properties of the model platform for each mass of deck

Case	1		2		3	
$\hat{m}_D(g)$	17.62		18.64		27.82	
Mode	x	y	x	y	x	y
K_s (N/cm)	17.66	20.63	17.66	20.63	15.99	17.79
C_d/C_c	0.025	0.023	0.022	0.021	0.023	0.023
T_n (sec)	0.67	0.63	0.69	0.65	0.86	0.83
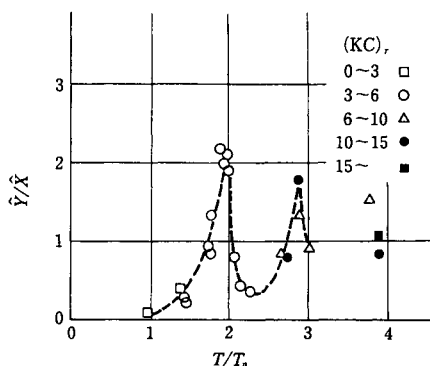
Fig. 6.16 Variation of the ratio of Y-displacement to X-displacement with T/T_n

It can be seen that the Y-displacement caused by the lift force predominates over the X-displacement by the in-line force when $T/T_n > 1.5$. Especially, when the T/T_n ratio approaches a whole number; i.e., 2, 3, or 4, the Y-displacement exceeds the X-displacement. This tendency is caused by the fact that the lift force has several higher harmonic components as shown in Fig. 6.12. It is clear that the lift force exerts a dominant influence on the structural motion when actual conditions are considered, under which the value of T/T_n is usually greater than 2 or 3.

Figures 6.17(a), (b) and (c) specify some typical calculated results (right-hand side of the figure) along with measured results (left-hand side of the figure), which correspond to the dynamic responses at $T/T_n = 1.75$, 1.94 and 2.85, respectively.

In each figure, the dynamic locus during a one wave cycle is shown. A spacing parameter l_S/L (l_S = center to center distance between adjacent piles in the wave propagation direction) is also specified in order to examine the phase effect of the local force of each pile on the total force. Concerning the calculated results, two different loci are plotted. One is obtained by taking the effect of the uncertainty on the sign $\pm$ in Eq. (6.12) into consideration; i.e., adopting the + or - sign on each pile in such a way that the larger possible lift force as a total occurs. This result is shown by a solid line. Another one is obtained by using only the + sign in Eq. (6.12) for each pile. This result is shown by a broken line. It can be seen that the former calculated results show good agreements with the measured results in their major features, i.e., in terms of the maximum resultant displacement and the geometrical configuration of the loci. These comparisons show that the equations described above can be effectively used to predict the dynamic behavior of a four-pile supported platform in response to both in-line and lift forces in waves.

Wave →

(Exp.) (Cal.)

(a) $T/T_n=1.75$ $T=1.18$sec $H_I=19.2$cm
$l_S/L=0.33$ $(KC)_r=3.8$

Wave →

(Exp.) (Cal.)

(b) $T/T_n=1.94$ $T=1.24$sec $H_I=21.1$cm
$l_S/L=0.30$ $(KC)_r=4.3$

Wave →

(Exp.) (Cal.)

(c) $T/T_n=2.85$ $T=1.82$sec $H_I=26.5$cm
$l_S/L=0.15$ $(KC)_r=8.7$
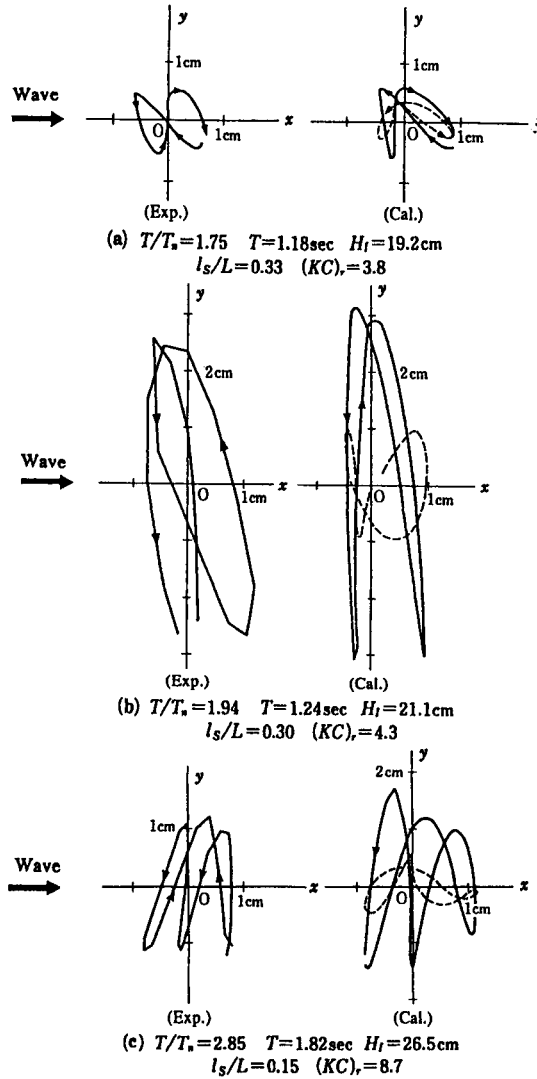
Fig. 6.17   Calculated dynamic loci versus measured dynamic loci of a four-pile supported platform during one wave cycle

Sawaragi and Nochino (1985) have developed a more sophisticated model than the one described above. They included the effect of torsional motions of a multi-pile supported platform about its vertical axis due to in-line and lift forces in the model. Nath et al. (1967) examined the spacing effect of the support piles on the dynamic behavior of a two-pile supported platform in the wave propagation direction. According to this result, the dynamic displacement caused by the in-line force can be effectively decreased by using the canceling effect of the in-line forces between the front and rear piles, in particular, under the spacing condition, $l_S/L=1/2,\ 3/2,\ 5/2, \cdots$.

In the above analysis, it is assumed that the wave forces on the oscillating piles are given by those on the rigidly fixed pile. Recently, however, it has become known that wave forces, especially lift forces, on the elastically supported piles are larger than those on rigidly fixed piles (e.g., Sarpkaya and Isaacson 1981). Also, the synchronization phenomenon between the dynamic oscillation and vortex shedding occurs when a pile is supported elastically. A detailed examination on these hydro-elastic phenomena must be carried out in the future.

6.3 Piled Pier Structures

Piled piers are usually constructed as one of the mooring facilities on soft ground and are classified into open-type wharfs and piers. An open-type wharf is, in general, defined as a piled pier whose longshore length is much larger than its on-offshore length. An open-type wharf is usually constructed in order to provide an apron space for the front part of a marine terminal and the front area of a vertical quay. On the other hand, a pier is the structure jutting out from land in the sea, the on-offshore length of which is much larger than the longshore length. A pier is usually utilized as one of the handling facilities on a shallow beach.

6.3.1 Open-type wharf

The significant wave force acting on an open-type wharf is the uplift force on the floor slab, which is generated by the standing wave formed in front of a vertical quay wall located behind the floor slab. As was already described in Chapter 2, the fluid force caused by the collision of the standing wave with the floor slab is impulsive and different from the ordinary wave force generated by a non-breaking wave. In this section, the characteristics of the impact uplift force acting on an open-type wharf located in front of a vertical quay wall under a normal wave incidence are discussed.

Figure 6.18 shows experimental results of variation of the dimensionless uplift pressure $p/\rho g H_I$ acting on the floor slab with x/L, in which x is the distance from the quay wall, ρ is the density of water, g is the gravitational acceleration, H_I is the incident wave height, L is the incident wavelength, p is the uplift pressure, d_c is the clearance between the floor slab and the still water surface, l is the on-offshore length of wharf, and h is the still water depth.
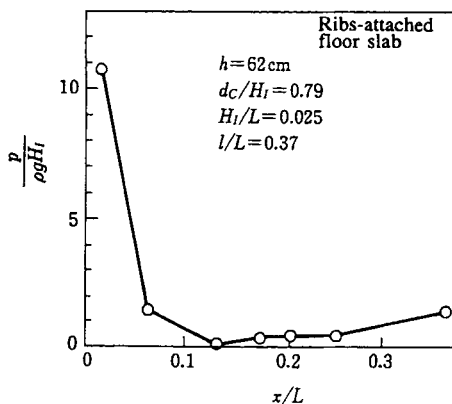
Fig. 6.18 Spatial distribution of uplift pressure

Ribs are attached to the back side of the floor slab of the experimental model, like the prototype wharf. The box formed by the ribs and slab is called a "rib-block". The experimental values of $p/\rho g H_l$ shown in Fig. 6.18 are the uplift pressures measured in the rib-block and it is seen that the maximum value of $p/\rho g H_l$ occurs at the loop of a standing wave in front of a vertical quay wall ($x/L\approx0$) and $p/\rho g H_l$ decreases as x/L increases.

Figure 6.19 shows one comparison of $p/\rho g H_l$ between a flat floor slab without ribs and the floor slab with ribs attached. $p/\rho g H_l$ in the case of the flat floor slab tends to increase as H_l increases and d_c decreases. On the other hand, in the case of the floor slab with ribs attached, $p/\rho g H_l$ becomes a maximum around $d_c/H_l\approx1$. Thus, the effect of ribs on the uplift pressure is significant.
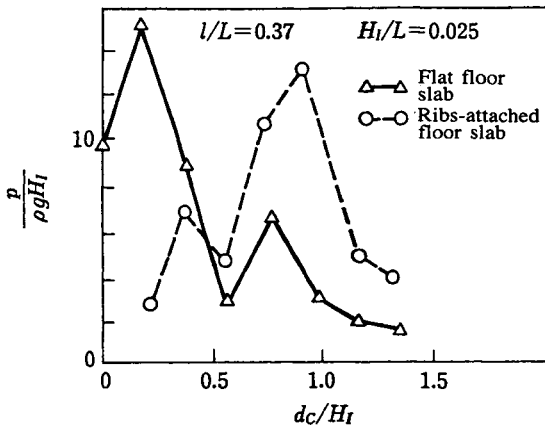
Fig. 6.19 Uplift pressure on flat floor slab and floor slab with ribs attached

The impact uplift pressure in the rib-block generated at the loop of a standing wave is revealed to be attributed to the combined action of the compression of air and the collision of water mass by experimental investigation of uplift pressure in the rib-block in front of a vertical quay wall (Sawaragi and Nochino 1987). Sawaragi and Nochino measured the uplift pressure and the colliding time of a water mass with the floor slab at several locations in the single rib-block shown in Fig. 6.20. In Fig. 6.20, R_h and R_b are the height and breadth of the rib, respectively and R_w is the length of the rib-block. Figure 6.21 shows one example of experimental results, in which t_i (i=1-3) is the colliding time of the water mass with the pressure gages 1, 2 and 3, respectively.

The pressures p_1, p_2 and p_3 were measured with the pressure gages 1, 2 and 3, respectively, and t_0 is the colliding time of the water mass with the offshore rib. Since the water surface of the standing wave is inclined offshore, as shown in Fig. 6.21, air in the rib-block is enclosed at $t=t_0$ and then compressed. Accordingly, all the measured pressures, p_1, p_2 and p_3 simultaneously present almost the same large magnitude of impact uplift pressure and the colliding times t_1, t_2 and t_3 of the water mass after the air-enclosure in the rib-block ($t = t_0$). Then, Sawaragi and Nochino (1987) concluded that the impact and large uplift force is generated by the compression of air in the rib-block. They further discussed the effect of the compression of the air mass on the pressure in the rib-block. They calculated a relationship between the variation of compressed air mass and the pressure variation in the rib-block and pointed out that the air must be leaked from the rib-block, otherwise the

impact force will be much larger than the measured one. The leakage of air from the rib-block was observed in their experiments to take place by means of a leakage of air bubbles formed in the rib-block passing through the bottom of the offshore rib, which is also confirmed by their numerical calculation. Thus, the leakage of air bubbles from the rib-block is understood to decrease the impact uplift force in the rib-block.
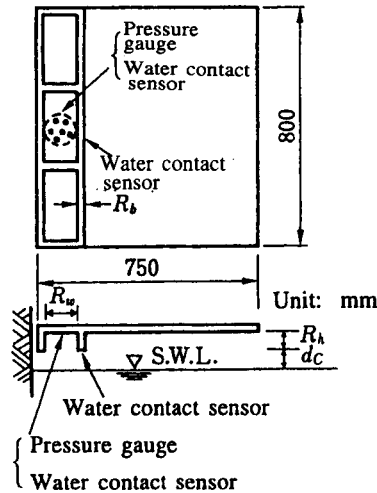
Fig. 6.20 Experimental setup of single rib-block
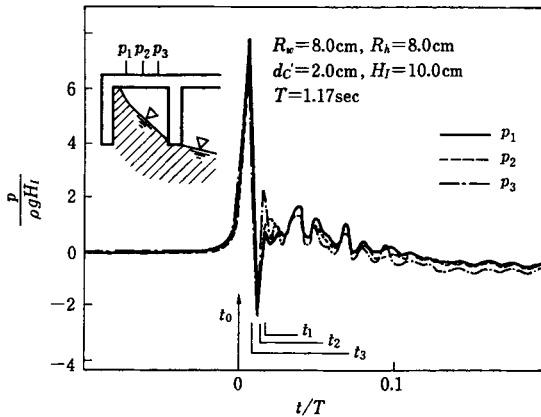
Fig. 6.21 Time histories of air-compression-type

Figure 6.22 shows the experimental results in the case where the water mass collides with pressure gages in the floor slab before air is completely trapped and compressed in the rib-block (t_1, t_2, $t_3 < t_0$).
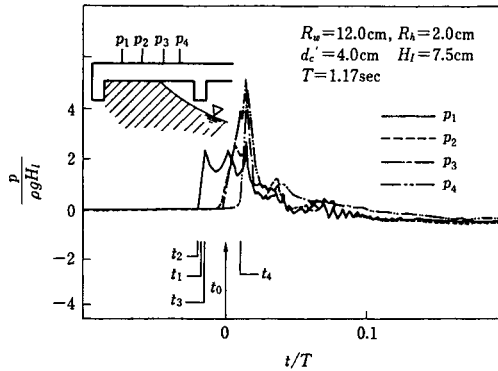
Fig. 6.22 Added-mass-type impact uplift pressure

It is clear in this case that the impact uplift pressure is produced not by the compression of air, but by the added mass which is described in **2.8.1**. Tanimoto et al. (1978) confirmed the propriety of Wagner theory, which is based on the added mass concept, in their investigation on the impact force acting on a flat floor slab. Sawaragi and Nochino (1987) also applied Wagner theory to evaluate the impact wave pressure acting on the floor slab with ribs attached. They calculated numerically the water surface profile in the rib-block by developing their theory which takes into account the air compression and the leakage of air as well. They showed good agreement between the theoretically estimated values and experimental ones.

Thus, as described above, the uplift force acting on the rib-attached floor slab of an open-type wharf is understood to be produced by a complex combined action of air-compression, air-leakage and the collision of water mass with the floor slab. Therefore, a reliable and practical formula to evaluate accurately the impact uplift force acting on an open-type wharf has not yet been established. Since the magnitude of the impact uplift force is generally several times the ordinary wave force, it should be noted that a strong and large uplift force would act on the floor slab when the incident wave height is more than 1m. In order to avoid the impact uplift force, taking d_c as a sufficient clearance between the floor slab and the still water level is recommended in designing an open-type wharf. It can be said from Fig. 6.19 that it is recommended for the clearance d_c to be more than 1.5 times the incident wave height H_I. In the case where sufficient clearance is not allowed, the following countermeasures are recommended: (i) separation of the floor slab from the vertical quay wall or (ii) placing a wave absorber in front of the vertical quay wall to decrease the standing wave height as low as possible. When the floor slab of the open-type wharf is separated from the vertical quay, bridging plates should be placed over the gap. The bridging plates are allowed to be destroyed by an extraordinary large uplift force and require constant maintenance. In the case where the impact uplift force is inevitably expected to act, the hydraulic model experiment under the adequate similitude law is recommend to fully evaluate the uplift force.

6.3.2 Pier

The wave force acting on piles is of great significance in the case of a pier. Since the pier juts out from land to the sea, the piles are located in a wide range which covers the offshore zone as well as the surf zone. The wave force acting on piles in the offshore zone

can be evaluated with the Morison equation introduced in **2.5**. The breaking wave force F_i has to be added to the wave force F_v calculated with the Morison equation in order to evaluate the wave force on piles located in the surf zone, especially near the breaking point. The breaking wave force F_i is an impact force described in Chapter 2 and has a different character from the Morison-type wave force F_v. In this section, characteristics of the breaking wave force exerted on a circular cylinder and its estimation method are discussed.

Goda et al. (1966) presented the following equation to evaluate the wave force F on the circular cylinder under a breaking wave action.

$$F = F_v + F_i \tag{6.27}$$

They proposed a wave profile model of a breaker as shown in Fig. 6.23 and they assumed that the vertical wave front $\lambda\eta_B$ produces the breaking wave force when it collides with the circular cylinder.
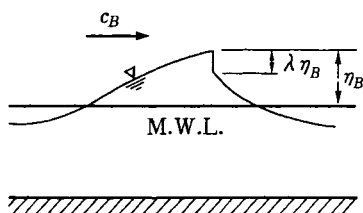
Fig. 6.23   Breaker profile model of Goda et al. (Goda et al. 1966)

They applied Eq. (2.201) to the breaking wave force, in which the falling velocity v is replaced by the wave celerity c_B and they proposed Eq. (6.28) as the maximum value of F_i

$$\left(F_i\right)_{max} = \frac{\pi}{2}\rho c_B^2 D\lambda\eta_B \tag{6.28}$$

Here, D is the diameter of the circular cylinder, η_B is the wave crest height of breaker from the mean water level (see Fig. 6.23), ρ is the density of fluid, and λ is the curling factor of breaker which is regarded to be constant. The important point is the accurate evaluation of λ, since λ controls the magnitude of breaking wave force on the cylinder. The value of λ has not yet been formulated in relation to incident wave characteristics and its formulation is still under investigation.

Figure 6.24 shows time histories of the local wave force on the unit length (1cm) of the circular cylinder measured at five different locations under a breaking wave action, in which z is the acting height of wave force from the still water level.

It is seen from Fig. 6.24 that the wave forces display a sudden rise followed by a gradual decrease, which is a typical feature of the impact force, and that the peak value and the acting time of the impact force change according to the relative acting height z/η_B. Although the time histories of the wave force are impulsive, the peak value does not occur at the instant the wave front touches the cylinder, different from the impact fluid force

exerted on a circular cylinder described in **2.8.1**. It is also seen from Fig. 6.24 that there is a rising time before the wave force reaches the peak value in the wave force - time curves. The wave front shape of a breaker is not always the same as the model of Goda et al. (1966) in Fig. 6.23, and the inclined wave front, instead of the vertical wave front, usually hits the cylinder. The reason for the rising time appearance can be explained well by taking the inclined wave front of a breaker into consideration (Sawaragi and Nochino 1982).
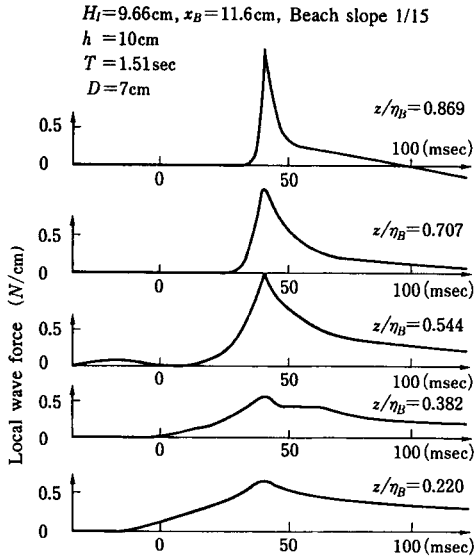
Fig. 6.24 Local force-time curve of breaking wave

Let us consider an inclined front of a breaker with angle θ_w passing through the cylinder at the velocity c_B as shown in Fig. 6.25.
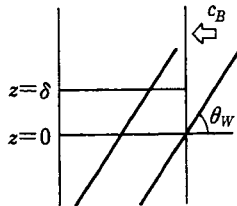
Fig. 6.25 Collision model of inclined wave-front with cylinder

The angle θ_w and the velocity c_B are assumed to be constant until the wave front passes through the cylinder with the diameter D. Consider the segment $[0, \delta]$ of the cylinder in the vertical direction z, and define the origin of time as the instant when the inclined wave

front collides with the cylinder front at $z = 0$. Then, the colliding time t of the wave front with the cylinder front at any location z is given by

$$t = \frac{z}{c_B}\cot\theta_w \qquad (6.29)$$

When the theory of Goda et al. (1966) is applied to the small segment dz in the vertical direction, the impact wave force dF_i on the small segment $[z, z+dz]$ is written as

$$dF_i = \frac{\pi}{2}\rho c_B^2 D\left[1 - \frac{1}{\tau}\left(t - \frac{z}{c_B}\cot\theta_w\right)\right]\varepsilon_i dz \qquad (6.30)$$

in which

$$\varepsilon_t = \begin{cases} 1 & : \quad (z/c_B)\cot\theta_w < t < (z/c_B)\cot\theta_w + \tau \\ 0 & : \quad t < (z/c_B)\cot\theta_w \quad \text{or} \quad t > (z/c_B)\cot\theta_w + \tau \end{cases} \qquad (6.31)$$

τ in Eqs. (6.30) and (6.31) is given by $\tau = D/2v$. Employing the following nondimensional forms:

$$F^* = F/(\pi\rho c_B{}^2 D\delta/2) \qquad (6.32)$$

$$t^* = t/\tau \qquad (6.33)$$

and utilizing Eqs. (6.30), (6.31) and (6.32), F^* acting on the small segment δ of the vertical circular cylinder is given as follows:

$$F^* = \int_0^1 \left(1 - t^* + z^*/\beta\right)\varepsilon_i^* dz^* \qquad (6.34)$$

where

$$z^* = z/\delta \qquad (6.35)$$

$$\beta = (c_B\tau/\delta)\tan\theta_w \qquad (6.36)$$

$$\varepsilon_t^* = \begin{cases} 1 & : \quad z^*/\beta < t^* < 1 + \left(z^*/\beta\right) \\ 0 & : \quad t^* < z^*/\beta \quad \text{or} \quad t^* > 1 + \left(z^*/\beta\right) \end{cases} \qquad (6.37)$$

The integrand in Eq. (6.34) is non-zero in the range of

$$z^*/\beta \leq t^* \leq 1 + (z^*/\beta) \qquad (6.38)$$

Thus the integration range of z^* is governed by β and z^*. Performing integration of Eq. (6.34) with the help of Eqs. (6.35) - (6.38) yields the following formulas in terms of β and t^*.

(i) In the case of $\beta \geq 1$

(a) $0 \leq t^* \leq 1/\beta$

$$F^* = \beta\left(t^* - \frac{1}{2}t^{*2}\right) \qquad (6.39a)$$

(b) $1/\beta \leq t^* \leq 1$

$$F^* = 1 - t^* + \frac{1}{2}\beta \qquad (6.39b)$$

(c) $1 \leq t^* \leq 1 + 1/\beta$

$$F^* = \frac{\beta}{2}\left(1 - t^* + \frac{1}{\beta}\right)^2 \qquad (6.39c)$$

(ii) In the case of $\beta \leq 1$

(a) $0 \leq t^* \leq 1$

$$F^* = \beta\left(t^* - \frac{1}{2}t^{*2}\right) \qquad (6.39d)$$

(b) $1 \leq t^* \leq 1/\beta$

$$F^* = \frac{\beta}{2} \qquad (6.39e)$$

(c) $1/\beta \leq t^* \leq 1 + 1/\beta$

$$F^* = \frac{\beta}{2}\left(1 - t^* + \frac{1}{\beta}\right)^2 \qquad (6.39f)$$

The dimensionless parameter β is a ratio of the slope of the wave front to a slope $\delta/(D/2)$, which is shown by the broken lines in Fig. 6.26. $\beta \geq 1$ implies that the slope of wave front is steeper than the slope $d/(D/2)$, and $\beta < 1$ corresponds to the gentler slope of wave front than $d/(D/2)$.

(a) $\beta > 1$ (b) $\beta < 1$
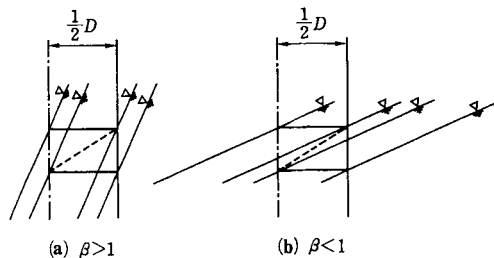
Fig. 6.26   Relationship between β and wave front slope

The schematic illustration of time histories of the impact breaking wave force, which are evaluated with Eqs. (6.39a) - (6.39f), is shown in Fig. 6.27.

(a) : $\beta > 1$ (b) : $\beta < 1$
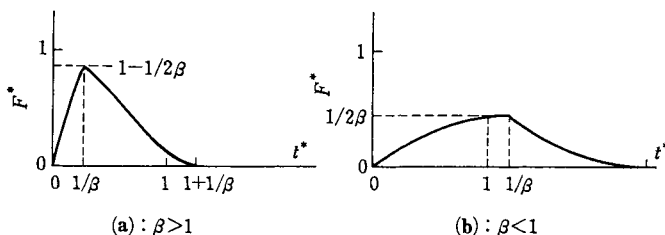
Fig. 6.27   Force-time curve by the theory of inclined wave front

$F^* = 1$ and $t^* = 1$ indicate respectively the nondimensional maximum force and acting time of the impact force proposed by Goda et al. (1966) (see Eqs. (6.32) and (6.33)). The maximum impact breaking wave force estimated with Eqs. (6.39a) - (6.39f) is $1 - (\beta/2)$ in the case of $\beta > 1$ and $\beta/2$ in the case $\beta < 1$, which are smaller than that evaluated with the theory of Goda et al. (1966).

Figure 6.28 shows several examples of the vertical distribution of the nondimensional maximum impact force F_p^*, in which F_p^* is the maximum value of F^* defined by Eq. (6.32), x_B is the distance measured from the breaking point to the offshore surface of the cylinder taken onshore positive. It is found from Fig. 6.28 that F_p^* becomes a maximum around $z/\eta_\beta \approx 0.6$ - 0.7 and that F_p^* becomes a minimum near the wave crest and near the still water level. Also, the distribution of the local breaking wave force is recognized to be significantly varied with the location of the cylinder and breaker types.

The integration of F_p^* over the domain from the still water level to the wave crest with the help of Eq. (6.32) and comparing with Eq. (6.28) yields the curling factor of breaker λ proposed by Goda et al. (1966) as follows:

$$\lambda = \frac{\int_0^\eta F_p \, dz}{\pi \rho c_B^2 D \eta_B / 2} \tag{6.40}$$

Figure 6.29 shows the relationship between the curling factor λ of the breaker and the relative distance x_B/L, in which ξ is the surf similarity parameter, and the spilling breaker occurs when $\xi < 0.3$ and the intermediate breaker and the plunging breaker occur, respectively, at $0.3 < \xi < 0.5$ and $\xi > 0.5$. The figure shows that the maximum valu of λ
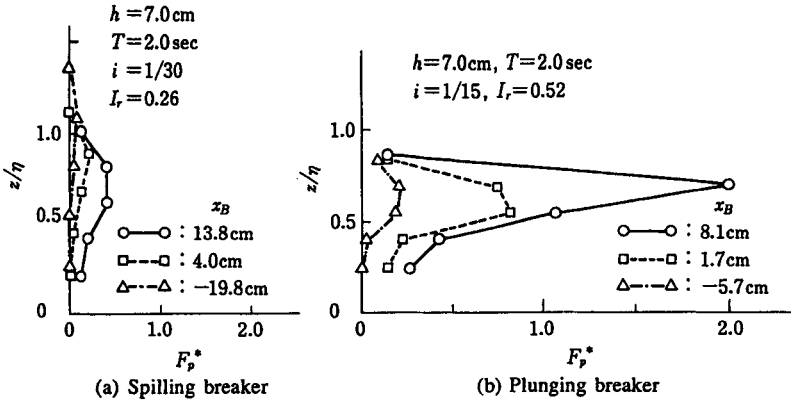
Fig. 6.28 Vertical distribution of peak values of F_p^*
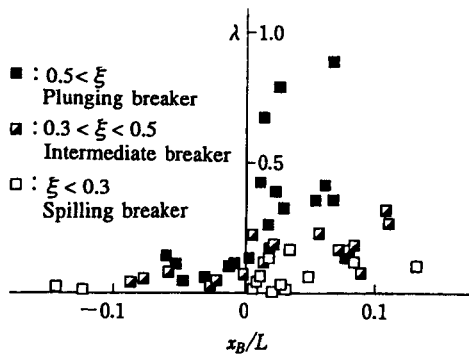
Fig. 6.29 Relation between λ and x_B/L

is possibly 0.9, although λ changes with x_B/L. The values of λ shown in Fig. 6.29 are experimental results with regular waves. On the other hand, ocean waves are irregular and their breaking points are wider than the those of regular waves, and therefore a change of λ with x_B/L may not be so significant from an engineering viewpoint. The relationship between λ and ξ is much more important (Tanimoto et al. 1986).

The breaking wave forces acting on the inclined circular cylinder has been investigated (Tanimoto et al. 1986; Sawaragi et al. 1989), since the inclined circular cylinders have been constructed as members of the piled piers. Figure 6.30 shows the relationship between λ

and ξ, in which θ is the inclined angle of the cylinder to the vertical line, and $\theta = 0°$ corresponds to the vertical cylinder. Since the surf similarity parameter ξ is determined for a given incident wave, the curling factor λ of the breaker is obtained from Fig. 6.30, and then the breaking wave force F_i acting on the inclined circular cylinder can be evaluated by means of substitution of known values of ξ and λ into Eq. (6.28).
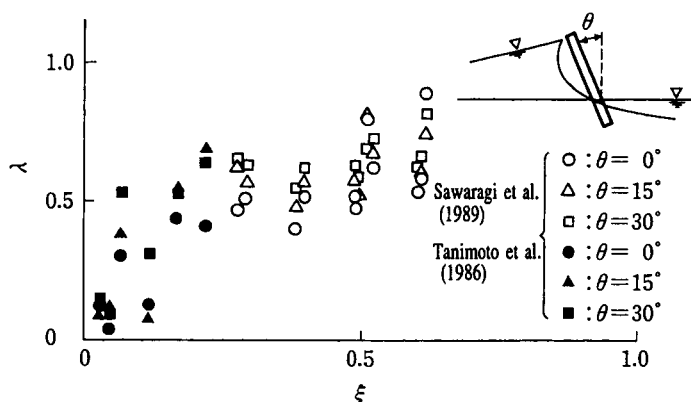
Fig. 6.30 Relationship between λ and ξ

6.4 Oil Booms and Silt Curtains

In **4.8**, we showed several types of membrane structures designed for attenuating wave height. Here, we first give outlines of oil booms and silt curtains that are both membrane structures in practical use for their specific functions, and then we consider the hydrodynamic forces acting on such flexible structures taking silt curtains as an example.

6.4.1 Oil booms

Oil booms are used to prevent spilt oil on a sea surface from diffusing into neighboring water and to collect it easily. In many countries, oil spills are one of the most serious types of pollution in the sea and are regulated by laws and acts. In Japan, oil booms are standardized in size by law as shown in Table 6.2, while many types of oil booms, which differ mainly in terms of floatation members, are used. The representative structure of an oil boom is shown in Fig. 6.31.

Table 6.2 Standard sizes of oil booms in Japan

Category	Main part		Connection part
	Freeboad height cm	Draft cm	Total height cm
Oil boom A	> 20	> 30	60
Oil boom B	> 30	> 40	80
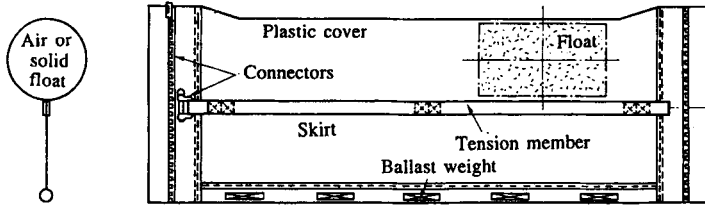
Fig. 6.31 Sructure of oil boom

Since the most important function of an oil boom is of course to prevent spilt oil from diffusing, it must be designed not to leak any oil. Leakage of oil is induced not only by natural forces such as winds, currents and waves but also by the towing of oil booms. There is extensive research available on the oil containment ability of oil booms. Ueda et al. (1985) show that, in a steady current, fluctuations on a boundary surface between oil and water gradually increase with time at the up-stream end of a slick and finally oil droplets split and slip away passing under the oil boom as shown in Fig. 6.32, when the Froude number F_r defined as

$$F_r = V / \sqrt{g(1 - \rho^*)} \sqrt{q_o} \tag{6.41}$$

becomes larger than 0.7 or 0.8, where V and q_o are the current velocity and the oil quantity per unit width, respectively, and ρ^* denotes the ratio of the oil density ρ_1 to the water density ρ, ρ_1/ρ.
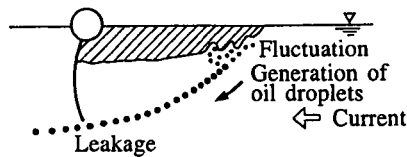
Fig. 6.32 Oil leakage due to current

As to the influence of the wave action on the oil containment ability, they report that the leakages both over and under the oil boom can be seen when the relative motion of the boom to the wave motion, i.e., the phase difference between these motions, becomes large, whereas the oil containment ability is rather improved by the coexistence of waves with currents when the boom oscillates completely in phase with the waves.

The external forces acting on oil booms produce tension in a tension cable and are transmitted to anchors or ships. When the oil boom is used under rough sea conditions, the safety of the cable against tearing by its own tension must be considered. Milgram (1971) and Nielsen (1980) studied theoretical behaviors of oil booms and hydrodynamic forces due to currents and waves. Cross and Hoult (1970) and Ueda et al. (1985) carried out the model tests in currents and obtained drag force coefficients.

6.4.2 Silt curtains

It is said that turbidity generated by maritime construction, such as reclamation or dredging, influences ecology in the neighboring sea and as a result adversely affects marine products. In contrast to oil contamination, however, there are as yet neither any legislation nor any environmental quality standards governing turbidity. When performing such construction, therefore, generation and diffusion of turbidity should be minimized as much as possible by improving construction methods and equipment. Furthermore, it is much better to extend silt curtains surrounding the construction site as shown in Fig. 6.33 and prevent the turbidity from spreading into the neighboring water when even a little turbidity diffusion may possibly cause a serious problem.
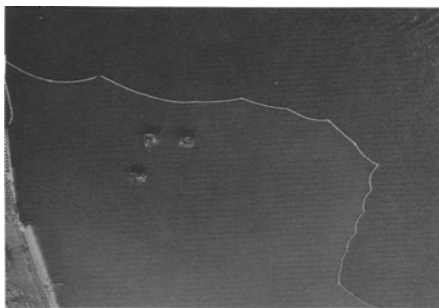
Fig. 6.33 Extension of silt curtains (by courtesy of Taiyo Kogyo Corporation)

In that there are no regulations governing turbidity, there are no standards for the design of silt curtains such as those for oil booms, so the silt curtains are usually designed in a manner similar to oil booms. The differences between silt curtains and oil booms are considered to be

(i)   The draft of a curtain is usually larger than that of an oil boom because turbidity is often distributed from the water surface to the sea bottom, while spilt oil initially stays near the surface.

(ii) Silt curtains are much more likely to be exposed to high waves than oil booms because they must always be extended during construction.

(iii) Since silt curtains are anchored to a sea bottom at close intervals so that they can be kept at the desired location, the restriction forces on the silt curtains are usually larger than those on oil booms.

Considering these differences in external forces, the safety of a silt curtain should be more carefully investigated than would be necessary for oil booms. Figures 6.34 (a) and (b) represent floating and submerged silt curtains, respectively, which are typical of those presently used in Japan. The floating silt curtain is similar to the oil boom shown in Fig. 6.31 and the submerged silt curtain is a canvas lifted up by floats from a sea bottom.

Silt curtains function not only to impound the turbid water but also to accelerate sedimentation by reducing current velocity or by changing current direction. Floating silt curtains are designed to settle suspended solids floating near the water surface by the deflection of currents down the curtain, and the submerged silt curtains are placed to block the horizontal spreading of turbidity generated near the bottom. We show here the results of the field experiments on turbidity diffusion carried out at the construction site of Kansai International Airport in Japan. In Fig. 6.35, we show the locations of floating and submerged silt curtains, in which sand was dropped from a barge into the water, and the three lines, A, B and C, under which the turbidity distribution was measured.

(a) Floating silt curtain   (b) Submerged silt curtain
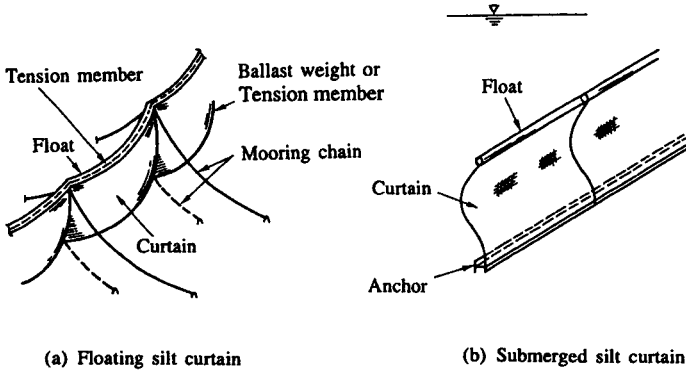
Fig. 6.34   Sketch of silt curtains
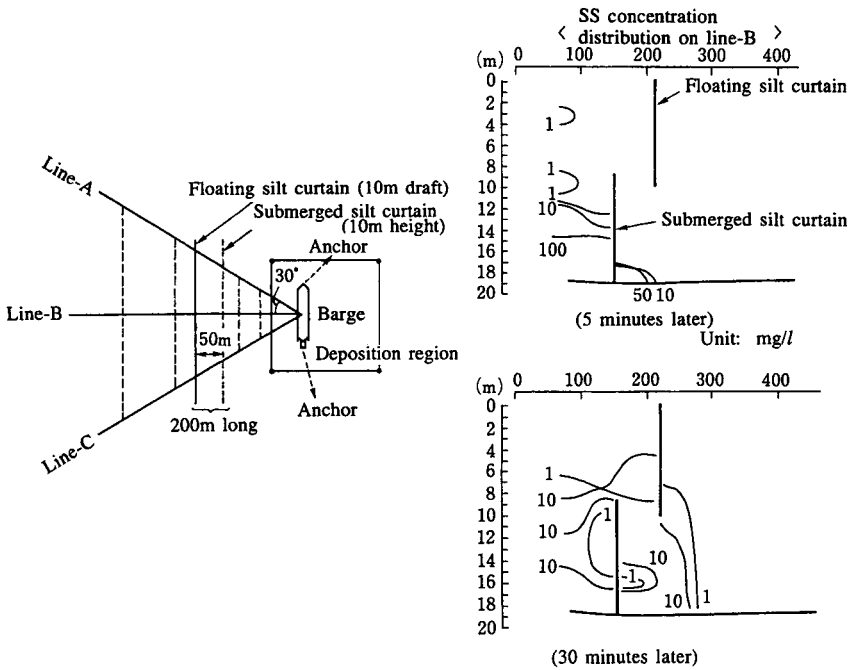
Fig. 6.35   Field measurement of turbidity near floating and submerged silt curtains

The two contour diagrams in the figure show the distributions of the concentration of suspended solids (SS) under line B, at five and thirty minutes after the dropping of sand. As shown in these figures, the turbidity impounded by the submerged curtain five minutes after the sand was dropped passed through the curtains in thirty minutes. Thus, although the diffusion of the turbidity cannot be completely blocked, rapid diffusion up to the water

surface is prevented by the curtains. Since only a few studies have been carried out on the function of silt curtains in preventing turbidity diffusion, further investigations are required in order to determine the most effective depth/height or disposition of the curtains.

6.4.3 Hydrodynamic forces acting on a membrane structure and deformation of the structure

(1) Relations between hydrodynamic forces and internal forces of a structure

In designing rigid fixed structures such as breakwaters, we first estimate the hydrodynamic forces acting on the structures and then consider the stability by calculating the total forces and the internal forces in the structural members. As for floating structures, however, since the hydrodynamic forces strongly depend on the motions of those structures, the hydrodynamic forces can be estimated only when the motions of the structures are known. On the other hand, since the motions of the floating structures are in turn determined by hydrodynamic forces, both the hydrodynamic forces and the motions of the structures must be determined at the same time by solving the equations of motion. Nevertheless, the internal forces in the members of the floating structures can still be calculated independently from the external forces in which the motions are taken into account.

For a flexible structure such as a membrane, which is not only shifted and rotated but also deformed by external forces, the hydrodynamic forces vary with the deformation of the structure as well as its motion as a rigid body. Since such deformation is determined by solving equilibrium equations between external forces on and internal forces in the structure, the internal forces in the structural members are also determined simultaneously with the hydrodynamic forces. Thus, for flexible structures, we must take into account the internal forces in the structure to estimate the hydrodynamic forces.

Now let us take an oil boom in a steady current as a simple example. As shown in Fig. 6.36 (a), if the oil boom is rigid and fixed at the water surface, the horizontal hydrodynamic force F due to the current with velocity V will be simply expressed as $F = 1/2 C_D \rho V^2 d$, where ρ and d are the density of water and the depth of the oil boom, respectively. For a flexible oil boom, however, the curtain canvas will be rolled up as shown in Fig. 6.36 (b) and the hydrodynamic force will be expressed as $F = 1/2 C_D \rho V^2 d'$, where d' is the effective depth of the oil boom shown in the figure.
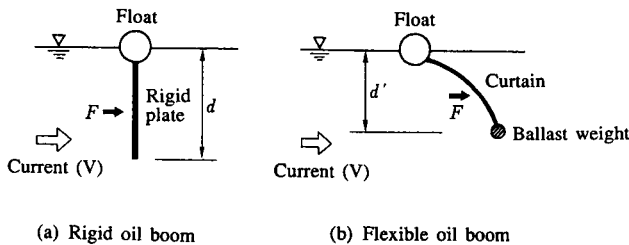
Fig. 6.36 Oil booms in a current

The effective depth d' is determined by how the oil boom deforms in the current, and the deformation is also determined by the hydrodynamic forces, the buoyancy of the float, the weight of the ballast, and the material characteristics of the canvas etc. The hydrodynamic forces acting on the flexible oil boom, therefore, strongly depend on the composition of the oil boom and the materials of the members.

Thus, in order to estimate the hydrodynamic forces acting on flexible structures, we must not leave the deformation of the structure out of consideration but pay careful attention to it, which indicates that we must make a model similar to its prototype not only in size but also showing the characteristics of the deformation. We must, therefore, carefully choose the materials of the model when estimating the hydrodynamic forces through physical experiments.

(2) Hydrodynamic forces due to currents and the deformation of a silt curtain

As mentioned above, since the hydrodynamic forces acting on flexible structures depend on the composition and materials of the structure, it is difficult to discuss them unless we take a particular structure as an example. Consequently, it is difficult to establish a general method for predicting the hydrodynamic forces acting on flexible structures. Here we consider the floating silt curtain shown in Fig. 6.34 (a) of which the tension cables are extended both at the top and at the bottom.

Figure 6.37 shows the external and internal forces relating to a portion of the curtain between the mooring chains.
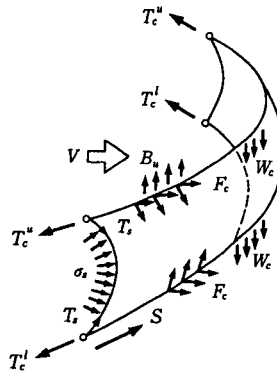
Fig. 6.37 External forces and tensions in a curtain

Hydrodynamic forces σ_s acting on the curtain canvas causes tension T_s in the canvas, and then the tensions in the upper and lower cables, T_c^u and T_c^l, are determined by T_s, the buoyancy B_u and the weight of the cable W_c. Therefore, providing that both the deformation of the curtain and the distribution of σ_s on the canvas are known, we can in principle calculate the tensions T_s and T_c.

Now let us derive an equation for calculating the tension of the cable T_c on some assumptions. We first assume that the vertical displacement of the cable is much smaller than the horizontal one and therefore T_c is determined by only the horizontal component of the tension of the canvas F_c. Furthermore, we assume that F_c perpendicularly acts on every portion of the cable, which indicates that T_c is constant everywhere in the cable. Suppose that a cable with the initial length l (the length of a stretched cable is denoted by l') is extended in a current with the velocity V as shown in Fig. 6.38, where B represents the extension width. The origin of the coordinate system is taken as the mid-point of the cable and the x and y axes are determined as shown in the figure.
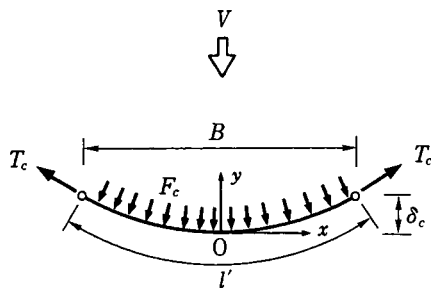
Fig. 3.38 Forces on tension cable and coordinate system

If we express the plan form of the cable as $y = f(x)$, we obtain the following equation from the equilibrium of the forces acting on a small segment of the cable in the normal direction:

$$F_c(x) = T_c \frac{f''(x)}{\left\{1 + f'(x)^2\right\}^{3/2}} \tag{6.42}$$

Additionally, the length of the stretched cable l' is given by

$$l' = \int_{-B/2}^{B/2} \sqrt{1 + f'(x)^2} \, dx \tag{6.43}$$

and T_c is expressed as

$$T_c = E_c A \left(\frac{l'}{l} - 1 \right) \tag{6.44}$$

by Hook's law, where $E_c A$ is the axial stiffness of the cable. Equations (6.42), (6.43) and (6,44) give the relations among T_c, $f(x)$ and $F_c(x)$.

Next, let us assume that $F_c(x)$ is expressed as

$$F_c(x) = \frac{1}{2} C_D \rho d V^2 \cos^2 \theta = \frac{1}{2} C_D \rho d V^2 \frac{1}{1 + f'(x)^2} \tag{6.45}$$

where θ is the angle between x-axis and the cable, C_D is the drag force coefficient, and d is the draft of the curtain. This equation indicates that F_c is a drag force described by the velocity component normal to the cable $V\cos\theta$. Substituting Eq. (6.45) into Eq. (6.42) and solving this equation, we have

$$f(x) = \frac{T_c}{\sigma_c} \left\{ \cosh\left(\frac{\sigma_c x}{T_c} \right) - 1 \right\} \tag{6.46}$$

where we let $\sigma_c = C_D \rho d V^2/2$. Substituting Eq. (6.46) into Eq. (6.43) and eliminating l' by using Eq. (6.44), we obtain

$$\frac{1}{2R_E} = \sinh\left(\frac{R_{gc}}{2\tau_c}\right) - \frac{1}{2\tau_c} \tag{6.47}$$

where $\tau_c = T_c/\sigma_c l$, $R_E = E_c A/\sigma_c l$ and $R_{gc} = B/l$. This equation was derived by Sawaragi et al. (1989) by modifying Milgram's equation (1971) to take the elasticity of a cable into account. Milgram referred to τ_c and R_{gc} as a tension parameter and a gap ratio, respectively.

In Fig. 6.39, the dependencies of the tension parameter τ_c, the deflection at the middle of the cable δ_c, and the y-component of the tension at the end of the cable V_c are plotted as functions of the gap ratio R_{gc} with R_E taken as a parameter.
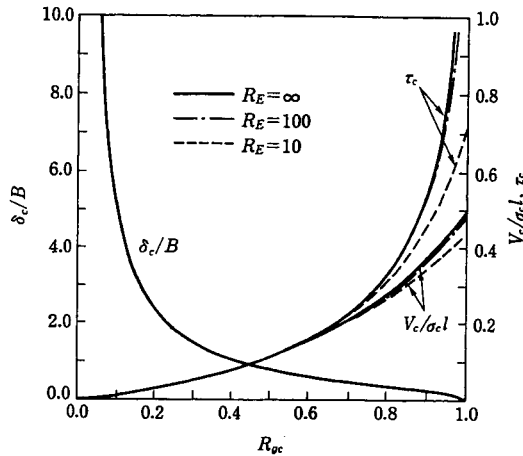
Fig. 6.39 Influence of gap ratio

The tension of the cable increases as the gap ratio increases, and the rate of increase becomes large as R_{gc} approaches 1.0; i.e., as the length of the curtain approaches the extension width. The influence of the elasticity of the cable appears only for small R_E and large R_{gc}.

Sawaragi et al. (1989) investigated the characteristics of the nondimensional tension C_T defined as $C_T = T_c/\frac{1}{2}\rho V^2 Bd$ through experiments where they changed the curtain length, curtain depth, water depth and current velocity. According to their results, C_T increases as the relative curtain depth d/h (h=water depth) increases and the influence of the gap ratio appears only in the region of small d/h.

(3) Wave-induced oscillations and wave forces

Here we show experimental results of the behavior of floating and submerged silt curtains in waves and the characteristics of wave-induced tension observed in a cable or canvas.

(a) The floating silt curtain

Figure 6.40 shows an example of the time history of tension in a cable of a floating curtain extended by both upper and lower cables, compared with that of water surface displacement.
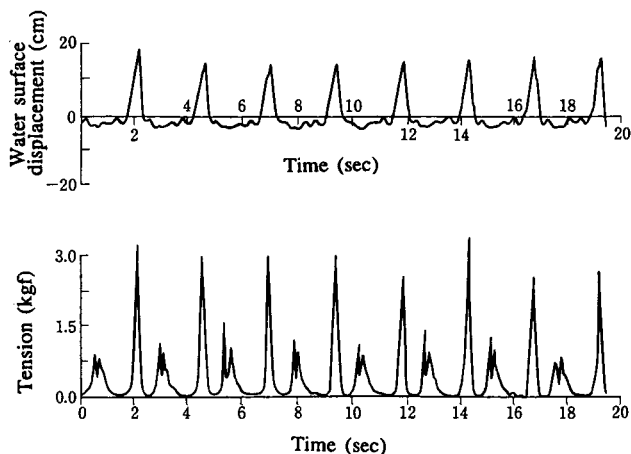
Fig. 6.40 Time histories of water surface displacement and tension in a cable

When the silt curtain is anchored slack in regular waves, it oscillates periodically in such a way that it is pushed forward and tightened up by waves in a half period of the motion and in turn is drawn back and tightened up again in the other half period. Large impulsive forces are observed in the tension cable at the moment when the curtain is tightened up. If the curtain is extended so slack that the curtain is not tightened up by waves, the forces become very small.

Sawaragi et al. (1992) proposed the parameter P_t that describes the limit of occurrence of such an impulsive tension as

$$P_t = \frac{e}{f} = \frac{H_I \coth kh}{\sqrt{l^2 - B^2}} \tag{6.48}$$

where H_I and k are the incident wave height and wave number, respectively. P_t is a ratio of the maximal horizontal displacement of a water particle at the surface e, to that of the middle point of the curtain f, shown in Fig. 6.41.

$$f = \frac{1}{2}\sqrt{l^2 - B^2}$$
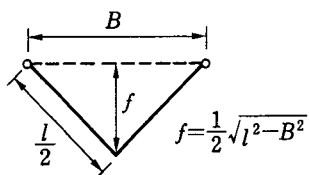
Fig. 6.41 Assumed deformation of a curtain

In Fig. 6.42, the maximal tension in the upper cable T^u_{max} is plotted against P_t, which shows that large tension tends to occur in the region of $P_t > 0.8$. According to the experimental results, however, the magnitude of the tension is not just the function of P_t but still depends on the curtain length and on the phase of the wave motion at the moment of tightening.
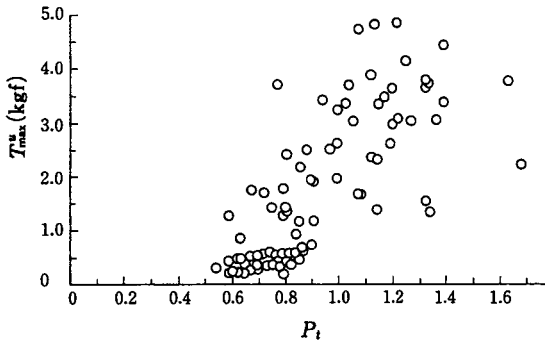
Fig. 6.42 Maximal tension versus P_t ($l = 57$cm, $B = 54$cm)

Sawaragi et al. (1992) investigated the impulsive tension through experiments in a steady current and proposed numerical models for the prediction of the impulsive tension based on the concept of added mass.

(b) The submerged silt curtain
Sawaragi et al. (1989) measured the tension in a canvas of a submerged silt curtain in the two-dimensional model tests where the water depth and curtain height were 1.13m and 0.47m, respectively. They show that the amplitudes of both horizontal and vertical components of the tension are proportional to the incident wave height H_I. Their nondimensional values are approximately expressed as

$$\left.\begin{array}{l} \dfrac{X_a}{\rho g d H_I} = \alpha_X \dfrac{\sinh kd}{2kd \cosh kh} \\[4mm] \dfrac{Y_a}{\rho g d H_I} = \alpha_Y \dfrac{\sinh kd}{2kd \cosh kh} \end{array}\right\} \tag{6.49}$$

where d is the curtain height, and α_X and α_Y are coefficients determined by fitting the curves expressed by these equations to the experimental results. Equation (6.49) indicates that X_a and Y_a are proportional to the integrated force of the hydrodynamic pressure from the bottom to the top of the curtain. Figure 6.43 is an example that shows the applicability of Eq. (6.49). It is also reported that the values of α_X and α_Y increase with the increase of the buoyancy of the float.

Aoki et al. (1994) calculated the tension in the submerged curtain by employing the same numerical method as mentioned in **4.8**. Figure 6.44 shows the comparison between experiments and computations, where R denotes the distance between the water surface and the top of the curtain, and C_o is the equivalent linear damping coefficient that represents structural damping due to membrane motions and hydraulic damping due to fluid viscosity.
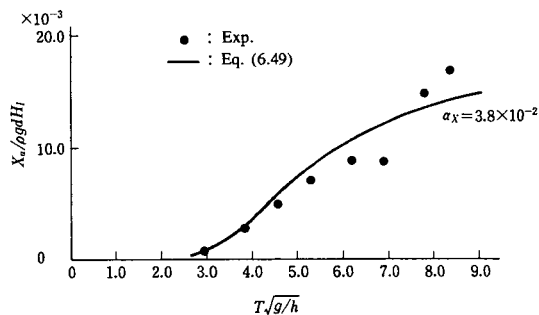
Fig. 6.43 Horizontal component of tension versus wave period
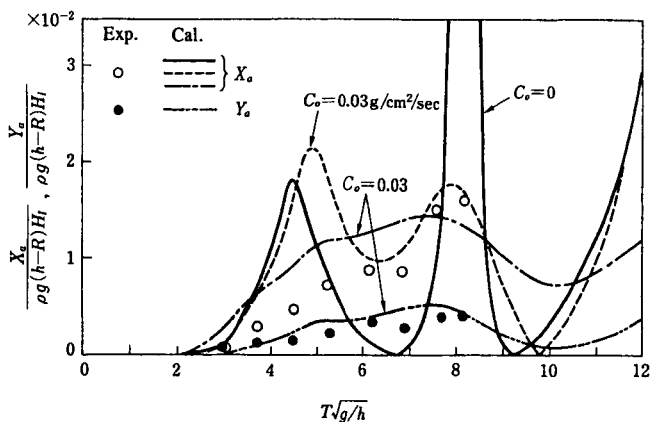
Fig. 6.44 Comparison of tension between experiments and computations

In this figure, the broken line corresponds to the case where the damping alone is considered, and the two dashed-and-dotted lines correspond to the cases where finite displacement of the curtain as well as the damping are taken into account in calculating the tension. As seen in the figure, both damping and finite displacement must be considered to apply the numerical method to the estimation of the tension.

References

Aoki, S., H. Liu and T. Sawaragi (1994): Wave transformation and wave forces on submerged vertical membrane, Proc. Int. Symp. on Waves - Physical and Numerical Modelling, Vol. III, Vancouver, pp.1287-1296.

Chakrabarti, S. K., W. A. Tam and A. L. Wolbert (1975): Wave forces on inclined tubes, Coastal Eng., Vol.1, pp.149-165.

Chakrabarti, S. K. (1982): Transverse forces on a vertical tube array in waves, J. Waterways, Port, Coastal and Ocean Div., Proc. ASCE, Vol.108, No.WW1, pp.1-15.

Chakrabarti, S. K. (1987) : Hydrodynamics of Offshore Structures, Springer-Verlag, pp.168-231.

Cross, R.H. and D.P. Hoult (1970): Oil booms in tidal currents, Proc. 12th Int. Conf. on Coastal, ASCE, pp.1745-1758.

Garrison, C. J., A. Torum, C. Iverson, S. Leviseth and C. C. Ebbesmeyer (1974): Wave forces on large volume structures - A comparison between theory and model tests, Proc. Offshore Tech. Conf., Paper No.OTC2137.

Garrison, C. J. (1985): Comments on the cross flow principle and Morison's equation, J. Waterways, Port, Coastal and Ocean Div., ASCE, Vol.111, No.6, pp.1075-1079.

Goda, Y., S. Haranaka and M. Kitahara (1966): Study on impulsive breaking wave forces on piles, Rept. Port and Harbor Res. Inst., Vol.6, No.5, pp.1-30. (in Japanese)

Harleman, D. R. F., W. C. Nolan and V. C. Honsinger (1963): Dynamic analysis of offshore structures, Proc. 8th Int. Conf. on Coastal, ASCE, pp.482-499.

Hogben, N. and R. G. Standing (1974): Wave loads on large bodies, Proc. Int. Symp. on the Dynamics of Marine Vehicles and Structures in Waves, pp.258-277.

Leonard, J. W., R. T. Hudspeth, F. D. Schaumburg, T. Mise, T. Mizusawa, H. Kotoguchi, M. Kubota, E. Funawatashi and T. Kuwayama (1990): Fundamental study on dynamic failure and design of offshore structures, Rep. to the Ministry of Education, Science and Culture of Japan, Grant No.62045040.

Milgram, J.H. (1971): Forces and motions of a flexible floating barrier, Jour. Hydronautics, Vol.5, No.2, pp.41-51.

Morison, J. R., M. P. O'Brien, J. W. Johnson and S. A. Schaaf (1950): The forces exerted by surface waves on piles, Petroleum Trans., AIME, Vol.189, pp.149-157.

Nakamura, T. (1990): A new evaluation method of three-dimensional wave source Green's function - Applicability to wave force calculation on large volume structures, Proc. Civil Eng. in the Ocean, Vol.6, pp.95-100. (in Japanese)

Nath, J. H. and D. R. F. Harleman (1967): The dynamics of fixed towers in deepwater random waves, Proc. Civil Eng. in the Ocean, ASCE, pp.99-122.

Nielsen, F.G.(1980): Loads and motion responses of offshore oil booms in waves, Proc. Int. Symp. on Ocean Eng. — Ship Handling, September, Gothenburg, Sweden, pp.11:1-11:23.

Sarpkaya, T. (1976): In-line and transverse forces on smooth and sand-roughened cylinders in oscillatory flow at high Reynolds numbers, Rep. No. NPS-69SL76062, Naval Postgraduate School.

Sarpkaya, T. and M. Q. Isaacson (1981): Mechanics of Wave Forces on Offshore Structures, Von Nostrand Reinhold, 651p.

Sarpkaya, T., T. S. Raines and D. O. Trytten (1982): Wave forces on inclined smooth and rough circular cylinders, Proc. Offshore Tech. Conf., Paper No.OTC4227.

Sawaragi, T., T. Nakamura and H. Kita (1976): Characteristics of lift forces on a circular pile in waves, Coastal Eng. in Japan, JSCE, Vol. 19, pp.59-71.

Sawaragi, T. and T. Nakamura (1978): Dynamic behavior of vertical cylinder due to wave forces, Proc. 16th Int. Conf. on Coastal, ASCE, pp.2378-2396.

Sawaragi, T. and T. Nakamura (1979): An analytical study of wave forces on a cylinder in oscillatory flow, Proc. the Specialty Conf. on Coastal Structures' 79, ASCE, pp.154-173.

Sawaragi, T. and T. Nakamura (1980): Characteristics of lift force on a circular pile in regular and irregular wave environment, Proc. 3rd Int. Symp. on Stochastic Hydraulics, IAHR, pp.715-723.

Sawaragi, T. and T. Nakamura (1981): Dynamic analysis of offshore platform response to in-line and lift force, Coastal Eng. in Japan, JSCE, Vol. 23, pp.159-177.

Sawaragi, T. and M. Nochino (1982): Experimental study on local wave forces acting on a circular cylinder, Proc. 29th Japanese Conf. on Coastal Eng., JSCE, pp.438-442. (In Japanese)

Sawaragi, T., M. Nochino and T. Iwahashi (1983): Total wave force and local impact breaking wave force on pile-supported structure in shallow water area, Proc. 30th Japanese Conf. on Coastal Eng., JSCE, pp.376-380. (in Japanese)

Sawaragi, T. and M. Nochino (1985): Two dimensional responses of fixed offshore platform in waves, Appl. Ocean Res., Vol.7, No.3, pp.140-151.

Sawaragi, T. and M. Nochino (1987): Study on the effect of air layer to characteristics of uplift force acting on the floor slab of the open-type wharf, Proc. JSCE, No.3811/II-7, pp.141-149. (in Japanese)

Sawaragi, T., S. Aoki and A. Yasui (1989): Tensions on silt curtains in currents and waves, Proc. 8th Int. Conf. Offshore Mech. and Arctic Eng., Vol.2, pp.13-21.

Sawaragi, T., M. Nochino and T. Nozaki (1989): Numerical investigation on impact breaking wave force acting on a circular cylinder, Proc. Coastal Engineering, JSCE, Vol.36, pp.714-718. (in Japanese)

Sawaragi, T., S. Aoki and H. Liu (1992): Wave-induced impulsive forces in tension cables of a floating silt curtain, Proc. 2nd Int. Offshore and Polar Eng. Conf., ISOPE, Vol.3, No.2, pp.243-265.

Tanimoto, K., S. Takahashi and Y. Izumida (1978): Study on uplift force acting on the horizontal floor slab, Rept. Port and Harbor Res. Inst., Vol.17, No.2, pp.3-47. (in Japanese)

Tanimoto, K., S. Takahashi, T. Kaneko, K. Shiota and K. Kogura (1986): Experimental study on impact force on a circular cylinder, Rept. Port and Harbour Res. Inst., Vol.25, No.2, pp.29-87. (in Japanese)

Ueda, K., Y. Ueta, H. Yamanouchi and K. Watanabe (1985): Prevention of escaping oil from mechanical barriers in the presence of water currents, Rep. Ship Res. Inst., Vol.22, No.5, pp.421-432. (in Japanese)

Chapter 7 Harbor Tranquility

7.1. Workable Limit of a Harbor

7.1.1 Harbor workability

Ship activities within a harbor consist of entering the harbor, mooring, and cargo handling. In cases where cargo handling is not possible, the shipping expenditure (as shown in Table 7.1) becomes a large waste of money (Kubo and Barthel 1993). Therefore, shipping companies desire to use harbors where cargo handling is always possible, in turn requiring individual harbors to improve their workability in order to attract more ships.

Table 7.1 Approximate ship costs according to ship type

Ship Type	Ship Cost (US$ per day)	
Pure Car Carrier	16,000 – 32,000	(US$)
LPG Ship	40,000	(US$)
LNG Ship	137,000 – 145,000	(US$)
Container vessels	21,800 – 24,200	(US$)
Bulk carrier: VLCC[*1]	32,000	(US$)
130,000DWT	24,200	(US$)
Panamax[*2]	16,000	(US$)

*1 very large crude oil carrier
*2 maximum size of ship that passes through the Panama Canal

Research on the reasons behind cargo handling interruptions, the duration of interruptions and the related weather conditions, has produced the following results.

Based on the frequency distribution of the interruption time, over 50% of cargo handling interruptions are caused by rain and 20% - 30% are caused by swells. The average duration of a cargo interruption is 5 - 6 hours. It has been pointed out by cargo handling traders that even during fine weather, ships can be moved and cargo handling interrupted due to swells caused by typhoons and other long period waves, especially in harbors facing the Pacific Ocean.

7.1.2 Critical condition of cargo handling

The critical condition of cargo handling depends on (1) cargo packaging, (2) type of ship, and (3) cargo handling machinery. According to research regarding the relationship between the state of cargo and the reasons for cargo handling interruptions, it is seen that interruptions due to cargo falling from a sling occur with box and bag cargo, and interruptions due to breakage of cargo lots or due to difficulty in passing cargo through a hatch is a problem common among all types of packaged cargo. Cargo that has become wet is the most frequent reason for handling interruptions. In addition, interruptions due to the cargo being dispersed by wind often occur with bulk cargo.

However, the acceptable limits of ship motion for cargo handling vary depending on the type of ship (Sawaragi and Kubo 1983). Table 7.2 shows the acceptable motion mode limits for each type of ship (refer to Chapter 2) (Brunn et al. 1981). The limit is smaller for container carriers compared to general cargo carriers. Cargo handling is sometimes interrupted by cargo swing. When a ship is moving, the swing of the cargo suspended by the ship's crane is amplified. Even when using a shore crane, the cargo moves relative to the hold. The limits of ship motion during crane operation will be discussed in the following section.

Table 7.2 Allowable ship movements

Ship Type	Surge (m)	Sway (m)	Heave (m)	Roll (deg)	Yaw (deg)
Tankers	±2.3	±1	±0.5	±4	±3
Ore carriers	±1.5	±0.5	±0.5	±4	±2
(Crane operation using clamshell)					
Grain Carriers	±0.5	±0.5	±0.5	±1	±1
(Elevator or suction)					
Container	±0.5	±0.3	±0.3	±3	±2
L_o/L_o (normal locks)					
Container	±0.2	±0.2	±0.1	nil	nil
R_o/R_o (side)					
Container	±0.1	nil	±0.1	nil	nil
R_o/R_o (bow or stern)					
General cargo	±1	±0.5	±0.5	±3	±2
LNG	±0.1	±0.1	nil	nil	nil

after Per Brunn 1981

(1) Limit of ship motion when using a deck crane

We assume that cargo is unloaded by a deck crane under sway and roll conditions. In this case, as the cargo swings in a plane, it is possible to analyse the swing using the two-dimensional notations defined in Fig. 7.1.
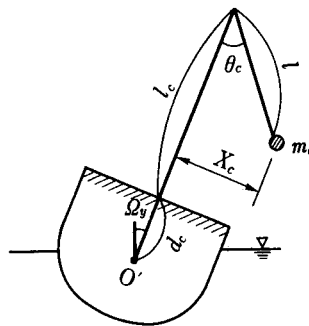
Fig. 7.1 Cargo swing

Here O′ is the center of ship rotation, d_c is the distance from O′ to a plane for cargo handling and l_c is the distance from the plane for cargo handling to the tip of the crane. Using θ_c as the swinging angle of the cargo, m_c for the cargo mass, l for the length of cargo fall, g for gravitational acceleration, and assuming the winding up speed $V = \dot{l}$ to be constant, then a displacement of cargo swing X_c is given as follows by solving the equation for cargo motion under the assumption of infinitesimal movement

$$X_c = l\theta_c = P_1\xi_0 J_1(\xi_0) + P_2\xi_0 Y_1(\xi_0)$$
$$- \frac{\pi V}{4g}\left\{\xi_0 J_1(\xi_0)\int_o^l F_1\xi_0 Y_1(\xi_0)\,\mathrm{d}t - \xi_0 Y_1(\xi_0)\int_o^l F_1\xi_0 J_1(\xi_0)\,\mathrm{d}t\right\}$$

$$(7.1)$$

$$F_1 = \left\{g + (l_c + d_c - l)\sigma^2\right\}\left|\hat{\Omega}_y\right|\sin(\sigma t + \delta_R) + 2V\sigma\left|\hat{\Omega}_y\right|\cos(\sigma t + \delta_R) + \left|\hat{X}\right|\sigma^2\sin(\sigma t + \delta_{sw})$$

$$\xi_0 = 2\sqrt{gl/V^2}$$

where $|\hat{X}|$, $|\hat{\Omega}_y|$ are sway and roll amplitudes, respectively, σ is the angular frequency of the motion, δ_{sw} and δ_R are phase delays, J_1 is the Bessel function of first order, and Y_1 is the Neumann function of first order. P_1 and P_2 are integral constants that are decided by initial conditions of X_c and $\dot{X}_c$.

Figure 7.2 is obtained by calculating Eq. 7.1 for various sway periods T_{sw}. The figure shows the normalized locus of a swinging cargo by the sway amplitude $|X|$. We use T_F for the natural period when $l = l_0$ (l_0: length of rope at the initial winding up stage). When $T_{sw} < T_F$, the swing becomes a maximum at the initial winding up stage. Attention should be paid to this phenomenon in regards to safe cargo handling in the hold. When $T_{sw} = T_F$, a resonance occurs and the swing becomes larger due to the winding up, and when $T_{sw} > T_F$, the swing becomes smaller.
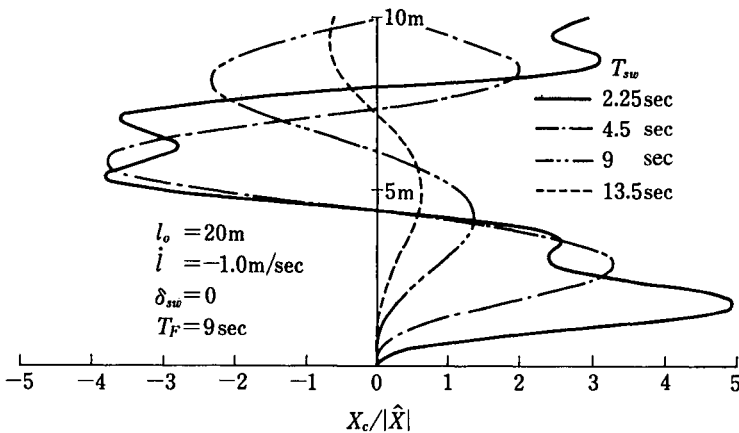
Fig. 7.2 Effect of sway period T_{sw} on cargo swing

Fig. 7.3 shows the swing due to roll movements of the ship. Figures 7.2 and 7.3 show that the natural period of the cargo suspended by the deck crane is approximately 8s, while the natural period of the rolling motion T_{Rn} is given as

$$T_{Rn} = \frac{0.8 B}{\sqrt{\overline{GM}}}$$ (7.2)

where $\overline{GM}$ is the metacentric height and B is the breadth of the ship. $\overline{GM}$ depends on the length and draft of the ship. Setting $\overline{GM} = 3$m in light conditions and $B = 20$m, then $T_{Rn} = 9$s. Thus the natural period of roll in light conditions for a general cargo carrier is nearly equal to the natural period of pendulum for suspended cargo. Accordingly, we can see that ship movements, especially roll, affect the cargo handling performed by the crane.
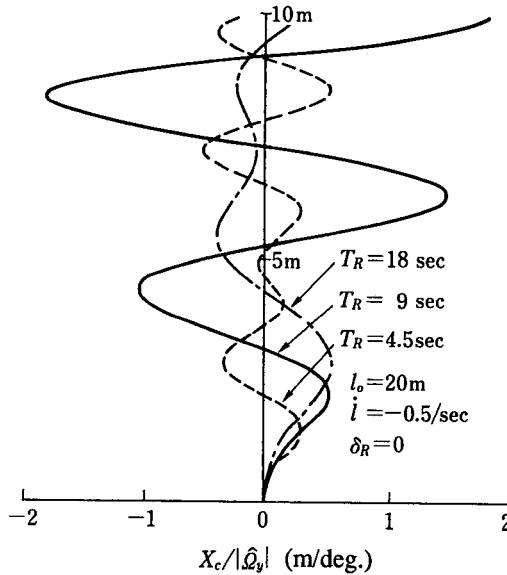
Fig. 7.3   Effect of roll period T_R on cargo swing

Using the relation between ship movements and cargo swing clarified above, we can obtain an acceptable limitation of ship movements for cargo handling.

Table 7.3 shows acceptable limitations of cargo swing that were obtained from field observations of crane operations (Sekita and Taniyama 1976). Although these limitations depend on various kinds of operations, we have chosen 1m as the horizontal limitation amplitude of cargo swing, from which the limitation amplitude d_0 for sway and roll can be obtained.

Table 7.3 Limit of ship movement from the standpoint of crane operation

Kinds of Operation	Horizontal Movement	Vertical Movement
pitching of pile		
82m pile	±0.5~1.5m	±10~15cm
50m pile	±1.0~1.5m	±10~20cm
22m pile	±1.0~2.0m	±10~25cm
setting of pile driving	±0.5~1.0m	±10~20cm
driving pile operation	±0.5~1.5m	±15~25cm
valuable cargo (deck)	~0.20m	±5~6cm
small cargo (valuable)	~0.25m	±5~10cm
small cargo (general)	±1.0~2.0m	±1m

after Sekita and Taniyama 1976

As shown in Figs. 7.4 and 7.5, which give the relations between the period of motions and the limitation of motions for some kinds of l_0 and winding up distances Δl, the limitations of motion are very small. Furthermore, the limitations depend on the cargo fall length l_0. So it is useful, for the safety of cargo handling, to not only decrease the wave height inside the harbor but to also consider the length of cargo fall.
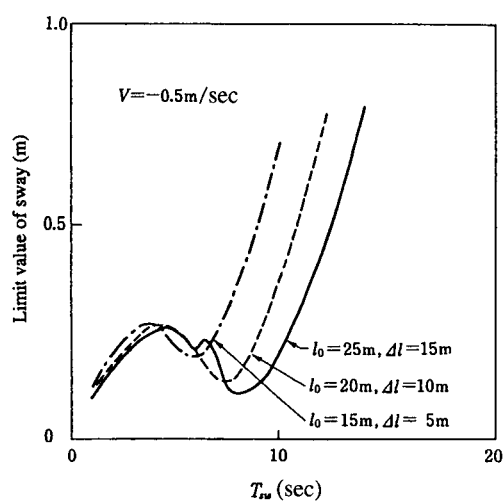
Fig. 7.4 Limit value of sway from the standpoint of cargo swing
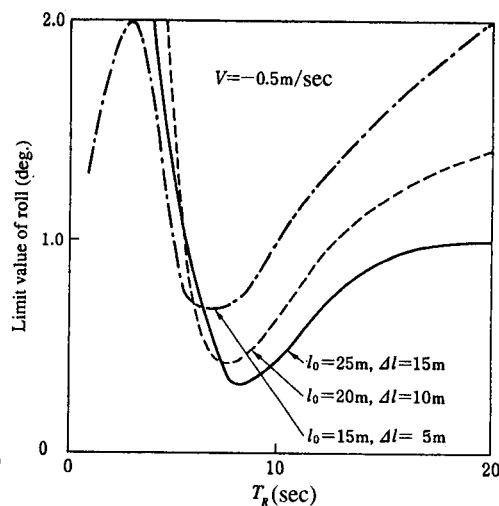
Fig. 7.5 Limit value of roll from the standpoint of cargo swing

(2) Limit of ship motions when using a shore crane
    In the case of a shore crane, even if a ship moves, the ship and the suspended cargo are not directly connected, so the cargo does not swing resonantly, but the cargo does swing relative to the ship's movements. In this case, the safety of the workers in the hold becomes a problem.

Roll motions also cause horizontal movement, so we must consider both sway and roll for cargo handling. Using $|\hat{\Omega}_y|$ for roll amplitude, d_c for the distance from the center of rotation to a cargo handling plane, then the horizontal movement at the plane by roll is given by $2 \cdot d_c \cdot |\hat{\Omega}_y|$. Let us consider the distance d_c for the general cargo carrier. In light conditions such as when cargo is handled near the bottom of the hold, d_c is obtained by subtracting the height of the double bottom (approx. 1m) from the height of the center of gravity. We express d_{cL} as d_c in light conditions. In a full load condition, as cargo is handled near the upper deck, d_c is obtained by subtracting the height of the center of gravity in a full load condition from the depth of the ship. We express d_{cF} as d_c in a full load condition. Figure 7.6 shows the relation between d_{cL}, d_{cF} and L_{pp}. In light conditions, roll motions are apt to resonate to swells and d_{cL} is also large, so the roll motions strongly affect cargo handling.

In general, during the loading stage, cargo is suspended 1m above the already loaded cargo and workers try to move the cargo by adjusting the setting position. Therefore, if the position moves with the amplitude $|X|$ and period T_{sw}, as shown in Fig. 7.7, then the workers must also move the cargo simultaneously to set it on a fixed position. The force F that the workers need to move the cargo is given using the following equations for cargo motion.
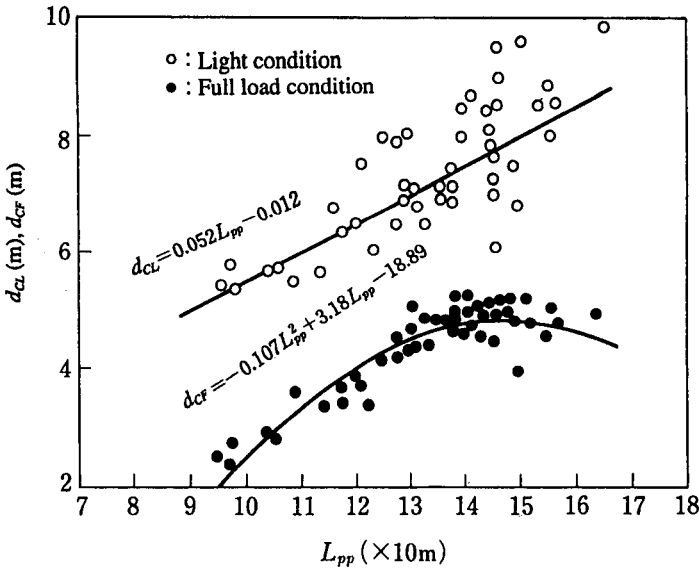
Fig. 7.6 Distance between the center of rotation and the cargo handling plane

$$F = m_c \ddot{X} + m_c g \theta_c = \frac{m_c |\hat{X}| g}{l} \left\{ 1 - \left(\frac{T_F}{T_{sw}} \right)^2 \right\} \cos \sigma t \tag{7.3}$$

$$X = |\hat{X}| \cos \sigma t, \ \theta_c = \frac{|\hat{X}|}{l} \cos \sigma t, \ \sigma = 2\pi / T_{sw}$$
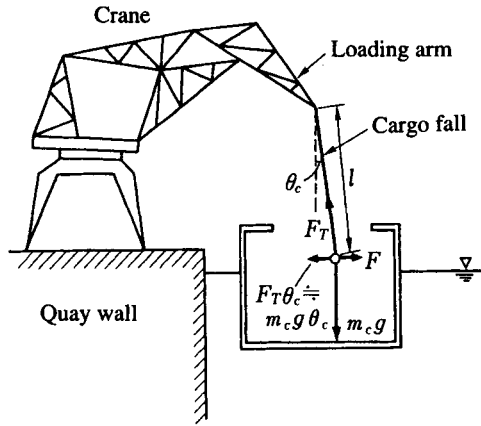
Fig. 7.7   Force acting to workers in the hold
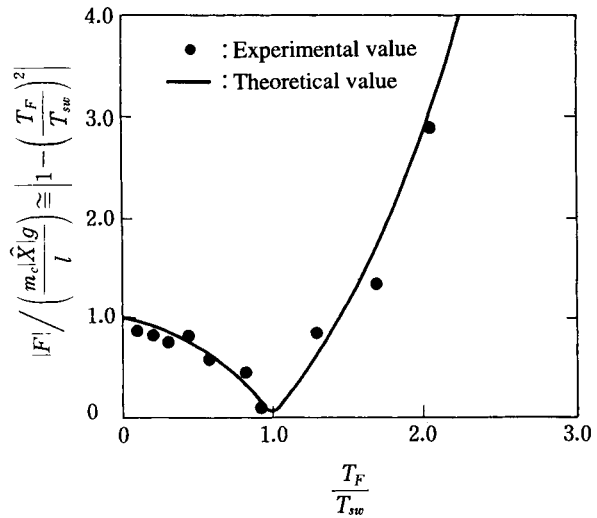
Fig. 7.8   Frequency characteristics of force F acting to workers in the hold

Figure 7.8 shows a comparison between theoretical and experimental values for $|F|$. From this figure, when the period of the ship's horizontal movement T_{su} is equal to the natural period of a pendulum, the workers scarcely require the force, but when the periods are different from each other, the workers need a large force. A limit force pushing horizontally in the hold is approximately 20 kgf because of bad footing. Thus, the limit amplitude of the horizontal ship movement is given by

$$\left|\hat{X}\right|_{LIM} = \frac{0.02l}{m_c\left\{1-\left(T_F/T_{sw}\right)^2\right\}} \; , \quad T_F = 2\pi\sqrt{l/g} \tag{7.4}$$

(3) Operational conditions for cargo handling

So far, a limit of harbor tranquility has been given as 0.5m of the wave height. However, as mentioned above, harbor tranquility should be defined by a limit of ship motion. As an example, we obtained the limit of incident wave height for cargo handling in the case of a ship (length 175m, breadth 27.6m and depth 8.4m) moored along a vertical quay wall.

The limit of wave height when the limit of heave is 0.5m is shown in Fig. 7.9 by using a theory of ship motions, where θ is the angle of the incident wave, in other words, θ is zero for beam waves. H_V is the limit only for heave motions, and it becomes smaller when θ becomes 90°. Namely, when the ship receives head waves, the limit of the wave height becomes large and the influence on cargo handling becomes small.
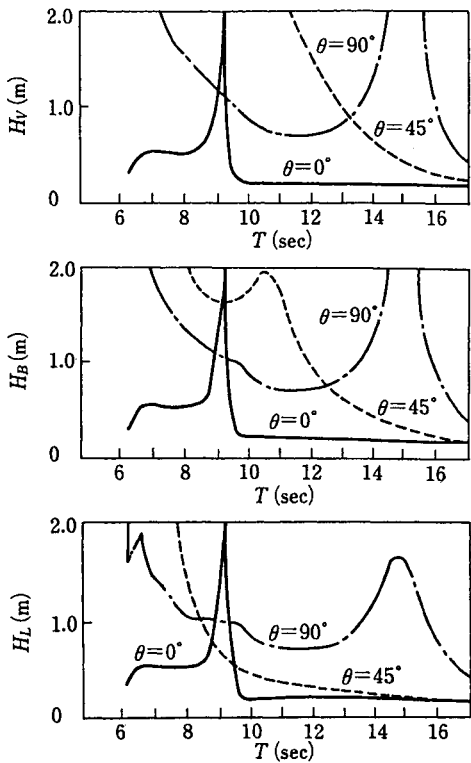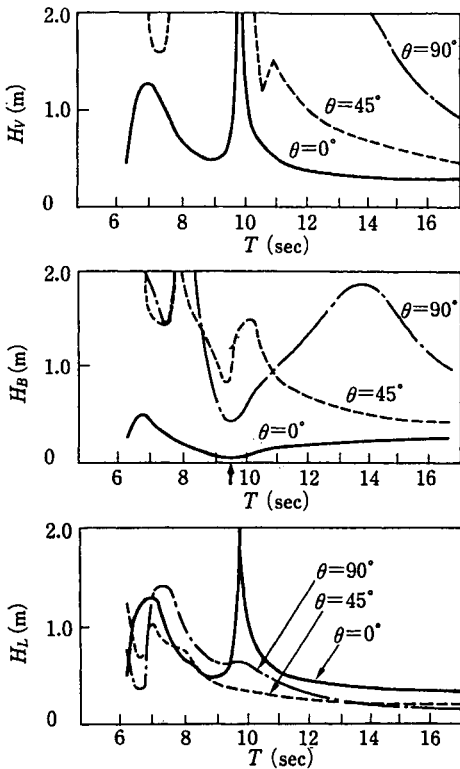
Fig. 7.9 Limit of incident wave height when the acceptable vertical motion for cargo handling is assumed to be 0.5m

Fig. 7.10 Limit of incident wave height when the acceptable horizontal motion for cargo handling is assumed to be 0.5m

Roll motions include a vertical motion on the ship side. So if we take into account the roll and heave motions, the limit of incident wave height is given by H_B. When $\theta = 0°$, H_B becomes very small near the resonance which is shown as an up arrow (Sawaragi and Kubo 1983).

Pitch motions induce a vertical motion at the bow and stern. So if we take into account the pitch and heave motions, the limit is given by H_L. In this case, as the natural period of pitch is 13s the limit of wave height becomes 0.2 ~ 0.3m at the wave period larger than 10s. Thus the limit of the wave height when the heave limit is 0.5m depends on the wave period and the incident wave angle. On the whole, the whole, tranquility from the standpoint of ship motion can be improved by arranging the quay at $\theta = 90°$ rather than $\theta = 0°$.

Figure 7.10 shows the limit of wave height when the whole horizontal amplitude of ship movement is 0.5m. In this case, a beam wave arrangement ($\theta = 0°$) is not as suitable as a head wave arrangement ($\theta = 0°$). Especially at the long-wave period of more than 10s, the limit of wave height becomes 0.2m in the case of a beam wave arrangement.

From the above, we can understand that the limit of wave height depends upon the wave period and the incident wave angle and we should take notice of the mooring direction to improve the limit of wave height.

7.1.3 Survival conditions for mooring

As ship motions increase, mooring accidents sometimes occur and may require immediate departure. If we consider these situations as the limit of mooring, the corresponding limit of the wave height is usually larger than that which is needed for safe cargo handling (Kubo and Barthel 1993). Therefore, it is necessary to consider the relation between an external force and the mooring limit.

At first, the external force is divided into a wave force and a wind force. The external force of waves is composed of two kinds of wave forces, the first being a wind wave or swell whose period is about 10s (these will be referred to as "short waves" hereafter), and an infragravity wave whose period is about one minute (these will be referred to as "long waves" hereafter). When a ship receives these waves, short-period ship motions are induced by short-period waves and long-period ship motions are induced by long period waves. Besides this, extreme asymmetrical mooring where, for example, a fender's spring constant is 100 times that of a mooring line's spring constant (Sawaragi and Kubo 1983) and grouping waves also cause long-period ship motions even if the incident wave period belongs to a short period range (Sawaragi et al. 1978). These phenomena will be described in detail in **7.4**. The large amplitude of ship motions usually happens in long-period ship motions, so long-period ship motions are more important than short-period ship motions when considering the limit of mooring. In fact, it is reported that the mooring ship sometimes runs due to a swell in a harbor facing the ocean. According to these reports, the ship's movements attain to 10~20m and sway movement is usually smaller than the surge movement.

Because of the large surge movement of 10~20m in storm conditions, we should think about these phenomena when we decide the clearance of ships moored along a quay, and the distance from the ship end to the slip end.

On the other hand, when sway motions increase, ship collisions with fenders can become severe, and breakage of fenders (the limit of fender deflection is 50-60%) and a ship's hull cause a limit to ship moorings.

Once a mooring line is broken, the remaining mooring lines receive a stronger force, so the remaining lines are also likely to break. Meanwhile, the ship must correspond to the urgent situation by changing the broken line with a new line. If this can not be preformed,

it must quickly depart from the berth. If the ship is unable to depart, it may drift inside the harbor, land on the quay or become shipwrecked. Typhoon "Muroto" in 1934, and "Jean" in 1950, were valuable learning experiences regarding mooring accidents.

7.2 Numerical Methods for the Prediction of a Wave Field in a Harbor

7.2.1 Governing equations and boundary conditions

In this section, we will show some numerical methods based on the linear potential theory. Although most of these methods are described for regular waves, it is possible to predict an irregular wave field by superposing the solutions for regular waves with different frequencies. As mentioned in **1.2.8**, if we assume the velocity potential Φ as in Eq. (7.5), the governing equation of the function $\tilde{\phi}(x,y)$ reduces the mild slope equation (7.6)

$$\Phi(x, y, z, t) = \tilde{\phi}(x,y)\frac{\cosh k(z+h)}{\cosh kh}e^{-i\sigma t} \tag{7.5}$$

$$\nabla(cc_g\nabla\tilde{\phi}) + k^2 cc_g\tilde{\phi} = 0 \tag{7.6}$$

where c, c_g and k are the phase velocity, the group velocity, and the wave number, respectively. In particular, when the water depth is constant in the whole region of interest, Eq. (7.6) becomes

$$\nabla^2\tilde{\phi} + k^2\tilde{\phi} = 0 \tag{7.7}$$

Let us now think about a harbor as shown in Fig. 7.11. Since Eqs. (7.6) and (7.7) are elliptic type second-order partial differential equations, boundary conditions must be given on all the boundaries of the semi-finite region. Boundary conditions of partial absorption are given on both the harbor boundary Γ_1 and the coastline Γ_3. At infinity, the radiation condition is imposed on the scattered waves by the harbor.
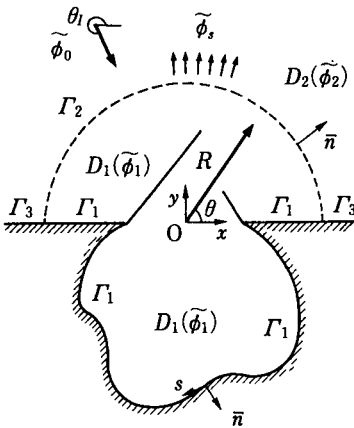
Fig. 7.11 Calculation region and coordinate system
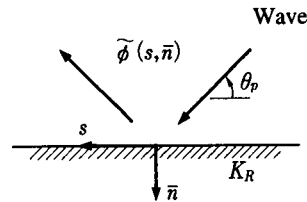
Fig. 7.12 Wave reflection by a partially absorbing boundary

(1) Boundary condition of partial absorption

Let us consider the partial reflection of oblique incident waves on a straight boundary with a reflection coefficient K_R, as shown in Fig. 7.12. If we call the velocity potential of the partial standing waves $\tilde{\phi}(s, \bar{n})$, we have the following equations satisfied on the boundary (Engquist and Majda 1977)

$$\frac{\partial \tilde{\phi}}{\partial \bar{n}} = ik \frac{1 - K_R}{1 + K_R} \sin \theta_p \cdot \tilde{\phi} \quad : \bar{n} = 0 \tag{7.8}$$

where the reflection coefficient K_R is a complex number defined as $K_R = |K_R| e^{i\varepsilon}$, by using the phase difference ε between incident and reflected waves. This equation, however, is not suitable for a boundary condition because it can be used only as long as the angle of incidence θ_p is known beforehand. It is usually difficult to determine θ_p, especially for multidirectional waves commonly seen inside a harbor.

Let us give an approximate expression for Eq. (7.8) that is linear to the angle of incidence (Engquist and Majda 1977; Behredent 1985). If we let $k_n = k \sin\theta_p$ and $k_s = k \cos\theta_p$, then k_n is expressed as

$$k_n = k \sqrt{1 - \left(\frac{k_s}{k}\right)^2} = k \left\{ 1 - \frac{1}{2}\left(\frac{k_s}{k}\right)^2 - \frac{1}{8}\left(\frac{k_s}{k}\right)^4 - \cdots \right\} \tag{7.9}$$

Assuming $k_s/k \ll 1$ and neglecting the order terms higher than $(k_s/k)^2$, Eq. (7.8) is rewritten as an equation of the second-order partial absorption condition

$$ik \frac{\partial \tilde{\phi}}{\partial \bar{n}} + \alpha k^2 \tilde{\phi} + \frac{\alpha}{2} \frac{\partial^2 \tilde{\phi}}{\partial s^2} = 0 \tag{7.10}$$

by using Eq. (7.9) and the relations: $\sin\theta_p = k_n/k$ and $\partial^2 \tilde{\phi}/\partial s^2 = -k_s^2 \tilde{\phi}$, where α is the absorption coefficient defined as

$$\alpha = \frac{1 - K_R}{1 + K_R} \tag{7.11}$$

The rate of energy loss due to reflection K_L^2 is given as $K_L^2 = 1 - K_R^2 = \alpha (1 + K_R)^2$ when K_R is a real number. If we omit the third term of the left hand side of Eq. (7.10), we obtain the first-order partial absorption condition

$$\frac{\partial \tilde{\phi}}{\partial \bar{n}} = ik\alpha \tilde{\phi} \tag{7.12}$$

which has been commonly used in numerical calculations.

The influence of using Eq. (7.10) or Eq. (7.12) instead of Eq. (7.8) can be estimated as a change of the reflection coefficient (Behrendt 1985). Figure 7.13 shows the apparent reflection coefficients, K_{R1} and K_{R2}, that correspond to the first- and second-order partial absorption conditions, respectively, where the real reflection coefficient is 0 (i.e., perfect absorption: $\alpha = 1$). A negative reflection coefficient means that the phase difference ε between incident and reflected waves is π. As seen in this figure, the absolute values of the apparent reflection coefficients are increasing with decreases in θ_p. In order to satisfy the condition $|K_R| < 0.1$, θ_p must be larger than 55° for Eq. (7.12) and larger than 30° for Eq. (7.10).
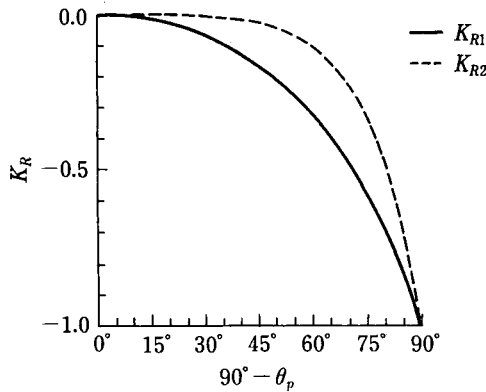
Fig. 7.13 Apparent reflection coefficient

(2) Radiation condition

Let us divide the velocity potential $\tilde{\phi}_2$ in the outside region of the harbor, D_2, into two components

$$\tilde{\phi}_2 = \tilde{\phi}_o + \tilde{\phi}_s \tag{7.13}$$

where $\tilde{\phi}_0$ represents the combination of incident waves and their reflected waves by the coastline, and $\tilde{\phi}_s$ represents the scattered waves by the harbor. The following radiation condition is imposed on $\tilde{\phi}_s$ at infinity

$$\lim_{R \to \infty} \sqrt{R} \left(\frac{\partial \tilde{\phi}_s}{\partial R} - ik\tilde{\phi}_s \right) = 0 \tag{7.14}$$

where R represents the horizontal distance from the origin of the coordinates, i.e. $R = \sqrt{x^2 + y^2}$. The radiation condition implies that only the outgoing scattered waves can exist on the boundary distant from the harbor.

7.2.2 Strict methods

We here use the term "strict method" to indicate the numerical method which does not employ any approximation except for the discretizing a calculated field or time. The finite difference method (FDM), the finite element method (FEM) and the boundary integral equation method (BIEM) are representative strict methods. A method which combines two or more of these methods is called a hybrid method. In this section, we will explain the FEM and the BIEM that are very applicable to a harbor with complex configurations.

(1) The finite element method (FEM)

As mentioned in **1.2.7**, the calculation region is divided into small elements in the FEM. However, it is impossible to divide the whole of the semi-infinite region shown in Fig. 7.11. Assuming that the water depth outside the boundary Γ_2 shown in Fig. 7.11 is constant or sufficiently deep, the following methods are proposed to satisfy the infinity condition (Zienkiewicz et al. 1978):

(i)   Applying the radiation condition Eq. (7.14) on Γ_2 at finite distance,

(ii) Matching the inner solution to the outer solution on Γ_2, where the scattered wave potential $\tilde{\phi}_s$ in the outer region is expressed as a series of analytical solutions of Eq. (7.7) that satisfy Eq. (7.14) (Mei 1983),

(iii) Same as (ii) except that $\tilde{\phi}_s$ in the outer region is expressed by sources or doublets distributed on the Γ_2 (Berkhoff 1972), and

(iv) Using the "infinte" elements with an exponential shape function (Bettes and Zienkiewicz 1977).

We now adopt the method (ii) and assume that the boundary Γ_3 is on the x-axis and fully reflective. The scattered wave potential $\tilde{\phi}_s$ can be expressed as

$$\tilde{\phi}_s = \sum_{n=0}^{\infty} H_n^{(1)}(kR) \cdot \beta_n \cos(n\theta) \tag{7.15}$$

where β_n is an unknown complex coefficient, $H_n^{(1)}$ is the n-th order Hankel function of the first kind, and R and θ are indicated in Fig. 7.11. According to the variational principle, the solution that satisfies Eq. (7.6) in D_1, Eq. (7.10) on Γ_1, and also $\tilde{\phi}_1 = \tilde{\phi}_0 + \tilde{\phi}_s$ and $\partial \tilde{\phi}_1 / \partial \bar{n} = \partial / \partial \bar{n} \, (\tilde{\phi}_0 + \tilde{\phi}_s)$ on Γ_2 is obtained by minimizing the functional $F(\tilde{\phi}_1, \tilde{\phi}_s)$

$$F(\tilde{\phi}_1, \tilde{\phi}_s) = \iint_{D1} \frac{1}{2} \left[cc_g \left(\nabla(\tilde{\phi}_1) \right)^2 - \frac{c_g \sigma^2}{c} \tilde{\phi}_1^2 \right] dS - \int_{\Gamma_1} \left[\frac{1}{2} i \alpha \sigma c_g \tilde{\phi}_1^2 + \frac{i\alpha}{4k} cc_g \left(\frac{\partial \tilde{\phi}_1}{\partial s} \right)^2 \right] ds$$

$$+ \int_{\Gamma_2} cc_g \left[\frac{1}{2} \tilde{\phi}_s - \left(\tilde{\phi}_1 - \tilde{\phi}_o \right) \frac{\partial}{\partial \bar{n}} \left(\tilde{\phi}_o + \tilde{\phi}_s \right) \right] ds - \int_{\Gamma_2} \frac{1}{2} cc_g \tilde{\phi}_s \frac{\partial \tilde{\phi}_o}{\partial \bar{n}} ds \tag{7.16}$$

Behrendt (1985) fully studied the accuracy of this method and the influence of the absorption coefficient. Sawaragi et al. (1988) investigated the applicability of the method by comparing model tests and pointed out that the computation predicts much larger wave heights in a harbor than those in the experiments when the boundaries in a harbor are fully reflecting. These differences, however, can be reduced by adding a small absorption coefficient such as $\alpha = 0.03$ ($K_R = 0.94$) to the boundaries in a harbor, which indicates the importance of energy loss estimation. Since the FEM can be easily used for the complex region and since the treatment of boundary conditions is also straightforward, it is usually

more applicable than the FDM. When calculating a wave field in a large region or for short periodic waves, however, the FEM requires a lot of work in preparing input data, a lot of memory on a computer as well as a lot of computing time.

(2) The boundary integral equation method (BIEM)

We here take Eq. (7.7) as a governing equation and take Eqs. (7.12) and (7.14) as boundary conditions. We choose the 0th-order Hankel function of the first kind, $H_0^{(1)}$, as Green's function, which is a solution of Eq. (7.7) and satisfies Eq. (7.14). Applying Green's formula to the region D_1 and by using the relation: $\lim_{kr \to 0} H_0^{(1)}(kr) = (2i/\pi) \ln(kr)$, we obtain the boundary integral equation

$$\tilde{\phi}_1(x,y) = e \int_{\Gamma_1+\Gamma_2} \left[\tilde{\phi}_1(\overline{X},\overline{Y}) \frac{\partial}{\partial n} \{H_o^{(1)}(kr)\} - H_o^{(1)}(kr) \frac{\partial \tilde{\phi}_1(\overline{X},\overline{Y})}{\partial n} \right] ds(\overline{X},\overline{Y}) \quad (7.17)$$

where a point $(\overline{X},\overline{Y})$ is on the boundary Γ_1 or Γ_2, and r is a distance between (x, y) and $(\overline{X},\overline{Y})$. The coefficient e takes $-i/4$ when the point (x, y) is inside the region and takes $-i/2$ when on the boundary. Furthermore, applying Green's formula to the region D_2 with respect to $\tilde{\phi}_s$, we have

$$\tilde{\phi}_s(x,y) = e \left(\int_{\Gamma_3+\Gamma_\infty} ds - \int_{\Gamma_2} ds \right) \left[\tilde{\phi}_s(\overline{X},\overline{Y}) \frac{\partial}{\partial n} \{H_o^{(1)}(kr)\} - H_o^{(1)}(kr) \frac{\partial \tilde{\phi}_s(\overline{X},\overline{Y})}{\partial n} \right] \quad (7.18)$$

where Γ_∞ indicates the boundary at infinity. By using Eqs. (7.12) and (7.14), Eqs. (7.17) and (7.18) yield

$$\tilde{\phi}_1(x,y) = e \int_{\Gamma_1} \left[\frac{\partial}{\partial n} \{H_o^{(1)}(kr)\} - ik\alpha H_o^{(1)}(kr) \right] \tilde{\phi}_1(\overline{X},\overline{Y}) ds(\overline{X},\overline{Y}) + e \int_{\Gamma_2} \left[\tilde{\phi}_1(\overline{X},\overline{Y}) \frac{\partial}{\partial n} \{H_o^{(1)}(kr)\} \right.$$
$$\left. - H_o^{(1)}(kr) \frac{\partial \tilde{\phi}_1(\overline{X},\overline{Y})}{\partial n} \right] ds(\overline{X},\overline{Y}) : \quad (x,y) \in D_1 \quad (7.19)$$

$$\tilde{\phi}_s(x,y) = e \int_{\Gamma_3} \left[\frac{\partial}{\partial n} \{H_o^{(1)}(kr)\} - ik\alpha H_o^{(1)}(kr) \right] \tilde{\phi}_s(\overline{X},\overline{Y}) ds(\overline{X},\overline{Y}) - e \int_{\Gamma_2} \left[\tilde{\phi}_s(\overline{X},\overline{Y}) \frac{\partial}{\partial n} \{H_o^{(1)}(kr)\} \right.$$
$$\left. - H_o^{(1)}(kr) \frac{\partial \tilde{\phi}_s(\overline{X},\overline{Y})}{\partial n} \right] ds(\overline{X},\overline{Y}) : \quad (x,y) \in D_2 \quad (7.20)$$

If we put (x, y) on Γ_1, Γ_2 and Γ_3 in Eqs. (7.19) and (7.20) and use the matching conditions on Γ_2: $\tilde{\phi}_1 = \tilde{\phi}_0 + \tilde{\phi}_s$ and $\partial \tilde{\phi}_1/\partial n = \partial/\partial n (\tilde{\phi}_0 + \tilde{\phi}_s)$, Eqs. (7.19) and (7.20) reduce to the integral equations with respect to $\tilde{\phi}_1$ on Γ_1, $\tilde{\phi}_s$ and $\partial \tilde{\phi}_s/\partial n$ on Γ_2, and $\tilde{\phi}_s$ on Γ_3. Dividing the boundaries Γ_1, Γ_2 and Γ_3 into small segments and rewriting these integral equations to a set of linear algebraic equations, we can obtain the solutions as a discrete point on the

boundaries. By using the solutions on the boundaries, the velocity potentials inside and outside the harbor are readily calculated from Eqs. (7.19) and (7.20), respectively.

Lee (1971) investigated harbor oscillation problems by using equations similar to Eqs. (7.19) and (7.20). He assumed a straight coastline and fully reflecting boundaries, and put the boundary Γ_2 at the harbor mouth. In this case, we do not need to divide Γ_3 as long as we calculate only the solution inside the harbor. Ijima and Chou (1975) treated a case where a part of Γ_1 or Γ_3 is fully absorbing, but their absorption condition is different from Eq. (7.12). Kusaka (1983) shows the numerical method in which Eq. (7.15) is used instead of Eq. (7.20).

Since $H_0^{(1)}(kr)$ and $\partial/\partial \overline{n} H_0^{(1)}(kr)$ represent a two-dimensional source and a doublet, respectively, when $kr \rightarrow 0$, Eqs. (7.19) and (7.20) indicate that the velocity potentials inside the boundaries are expressed by the sources and the doublets distributed on the boundaries. According to the source distribution method shown in **2.3.2**, the potential $\tilde{\phi}$ in the region D_1 and D_2 can be expressed only by the sources distributed on Γ_1 and Γ_2 (Mei 1978)

$$\tilde{\phi}(x,y)=\tilde{\phi}_o(x,y)+\int_{\Gamma_1+\Gamma_3} f_D(\overline{X},\overline{Y})H_o^{(1)}(kr)\mathrm{d}s(\overline{X},\overline{Y}) \tag{7.21}$$

where $f_D(\overline{X},\overline{Y})$ represents a strength of source. Hwang and Tuck (1970) solved a harbor oscillation problem by applying Eq. (7.21) to the boundary conditions on Γ_1 and Γ_3.

The BIEM, the method that transforms the governing equation to the boundary integral equation by applying Green's formula, has the advantage that the number of unknowns is much less than for the FEM, because the unknowns are restricted to those on the boundaries. As we take Eq. (7.7) as a governing equation, however, it is complicated to extend the BIEM for the varying depth region. Ijima and Chou (1975) and Kusaka (1983) dealt with this problem by dividing the harbor region into portions of constant depth. Mattioli (1978) proposed a method that numerically composes Green's function in which the variance of the water depth is taken into account.

Some other useful methods that employ the FDM and calculate in the time domain have been proposed (Tanimoto and Kobune 1975; Warren et al. 1985). These methods, however, sometimes require particular attention to the treatment of boundary conditions, and moreover it is sometimes difficult to find a steady-state solution in such a region surrounded by fully reflecting boundaries.

7.2.3 Approximate methods

Although the strict methods give us accurate solutions of the governing equations under the boundary conditions, they are not suitable for calculating for a large harbor compared with the wavelength or for multidirectional irregular waves, even if we use the BIEM. Furthermore, as mentioned above, additional energy loss should sometimes be required in the strict methods to explain experimental results. Thus we here show some methods that can be readily used and provide a fairly good approximate solution. These methods are useful for practical design although their applicable range is not clear.

(1) SOGREAH method

Biesel and Ranson (1961) proposed a practical method by employing Kirchhoff's diffraction theory in optics. Take the case of a harbor with a convex configuration as shown in Fig. 7.14, where a harbor boundary is Γ_1 has a reflection coefficient K_R. Water depth is assumed to be constant in the whole harbor region, which indicates that the governing equation reduces to Eq. (7.7). Let us consider expressing the velocity potential $\tilde{\phi}(x, y)$ at a point in the harbor as

$$\tilde{\phi}(x,y) = -e\int_{\Gamma_1+\Gamma_2} G(x,y;\overline{X},\overline{Y})\frac{\partial\phi(\overline{X},\overline{Y})}{\partial\overline{n}}ds(\overline{X},\overline{Y}) \qquad (7.22)$$

where boundary Γ_2 denotes the harbor mouth as shown in Fig. 7.14. If the function G satisfies the condition: $\partial G/\partial\overline{n} = 0$ on Γ_1 and Γ_2, we can easily obtain Eq. (7.22) by applying Green's theorem to the harbor region. However, it is difficult to obtain such a function for an arbitrary configuration of a harbor.
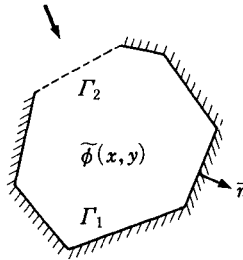
Fig. 7.14 Harbor with a convex configuration

A semi-infinite region bounded by an infinite straight boundary C is a particular case where we can compose the function G which satisfies $\partial G/\partial\overline{n} = 0$ on C

$$G(x,y;\overline{X},\overline{Y}) = H_0^{(1)}(kr) + H_0^{(1)}(kr') \qquad (7.23)$$

where $r' = \sqrt{(x'-\overline{X})^2 + (y'-\overline{Y})^2}$ represents the distance between the mirror image point of $P(x',y')$, which is $P'(x',y')$, and $(\overline{X},\overline{Y})$. Thus the potential $\tilde{\phi}(x,y)$ in the semi-infinite region is expressed by applying Green's theorem as

$$\tilde{\phi}(x,y) = -e\int_c 2H_o^{(1)}(kr)\frac{\partial\tilde{\phi}(\overline{X},\overline{Y})}{\partial\overline{n}}ds(\overline{X},\overline{Y}) \qquad (7.24)$$

This equation implies that the wave field is expressed by sources distributed on the boundary, the strength of which is proportional to normal velocity $\partial\tilde{\phi}/\partial\overline{n}$ on the boundary. Since the source $H_0^{(1)}(kr)$ represents a cylindrical wave, this expression corresponds to Huygens' principle of superposition optics.

For a harbor with a convex configuration as shown in Fig. 7.14, cylindrical waves originating from the boundary Γ_2 propagate directly onto the boundary Γ_1, and the incident waves to Γ_1 can be calculated from Eq. (7.24) by assuming Γ_2 as a part of the infinite boundary C shown in Fig. 7.15.

The incident waves to Γ_1 are reflected by the boundary and scattered inward again. Such reflected waves can also be computed from Eq. (7.24) by dividing Γ_1 into several straight lines and by assuming each line as a part of the infinite boundary. Thus, in the SOGREAH method, the velocity potential in a harbor is expressed by cylindrical waves originating from all surrounding boundaries as:
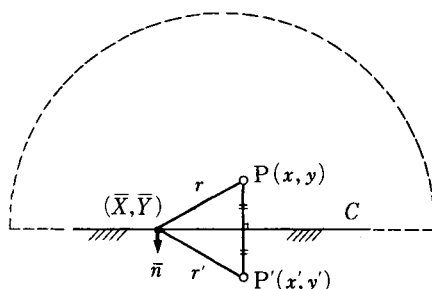
Fig. 7.15 Composition of Green's function in a semi-infinte region

$$\tilde{\phi}(x,\,y) = -e \int_{\Gamma_1+\Gamma_2} 2H_o^{(1)}(kr) \frac{\partial \tilde{\phi}(\overline{X},\,\overline{Y})}{\partial \overline{n}} ds(\overline{X},\,\overline{Y}) \tag{7.25}$$

where $\partial \tilde{\phi}(\overline{X},\overline{Y})/\partial \overline{n}$ represents a velocity component only in the inward direction. In an actual computation, we first put the following initial boundary conditions:

$$\frac{\partial \tilde{\phi}}{\partial \overline{n}} = 0 \qquad : \text{on } \Gamma_1 \tag{7.26}$$

$$\frac{\partial \tilde{\phi}}{\partial \overline{n}} = \frac{\partial \tilde{\phi}_I}{\partial \overline{n}} \qquad : \text{on } \Gamma_2 \tag{7.27}$$

where $\tilde{\phi}_I$ represents the velocity potential of incident waves. After differentiating Eq. (7.25) with respect to $\overline{n}(x,\,y)$, we substitute Eqs. (7.26) and (7.27) into this equation and compute the value of $\partial \tilde{\phi}/\partial \overline{n}$ on Γ_1. If we let this value be $(\partial \tilde{\phi}/\partial \overline{n})'$, the velocity due to the reflected waves from Γ_1 is expressed as

$$\frac{\partial \tilde{\phi}}{\partial \overline{n}} = -K_R \left(\frac{\partial \tilde{\phi}}{\partial \overline{n}} \right)' \tag{7.28}$$

In the next step, we again calculate $\tilde{\phi}$ and $\partial \tilde{\phi}/\partial \overline{n}$ on Γ_1 from Eq. (7.25) by substituting Eqs. (7.27) and (7.28) into it. In the following step, we repeat this process until we obtain a steady-state wave field in a harbor, i.e., until $\partial \tilde{\phi}$ and $\partial \tilde{\phi}/\partial \overline{n}$ converge to certain values on the boundary. For a harbor with concave configuration, we can still apply this method by dividing the harbor region into several convex regions and regarding the imaginary boundaries between these sub-regions as harbor mouths.

As shown above, in the SOGREAH method, a wave field in a harbor is calculated by taking harbor boundaries for wave source lines on the infinite straight boundary of a semi-infinite region. Since the method requires much less memory on a computer than the strict methods such as the FEM and the BIM do, it can be applied to a large harbor compared with the wavelength. However, there remain some problems such as the validity of Eq. (7.25) and an occasional divergence of a solution. Barailler and Gaillard (1967) modified this method so as to take the variance of water depth into account.

(2) Takayama's method

Takayama (1985) proposed a practical method that can be applied to multidirectional irregular waves. In this method, wave transformation in a harbor is classified into diffraction and reflection by breakwaters and quays. The analytical solutions of diffraction by a semi-infinite breakwater and of reflection by a breakwater of finite length are used to calculate diffraction and reflection coefficients, which are superposed on an energy basis. Wave directions in a harbor are determined geometrically as shown in Fig. 7.16. Takayama's method is commonly used in Japan in designing harbors and its applicability has been investigated by comparing many model tests and field measurements. Prediction error of this method is said to be within 30%.

(3) Wave ray method

Larsen (1978) calculated a wave field by tracing wave rays in a harbor, where wave transformation is classified into diffraction and reflection as used in Takayama's method. As shown in Fig. 7.17, wave rays reaching a certain point P consist of incident (η^I), reflected (η^R) and diffracted (η^D) rays. The incident and reflected waves are determined geometrically and the diffracted rays are originated from the breakwater tips or discontinuity points of harbor boundaries. The wave field is calculated as a sum of the contribution of these rays

$$\eta(P)=\eta^I(P)+\sum_i \eta_i^R(P)+\sum_i \eta_i^D(P) \tag{7.29}$$

Larsen used the analytical solutions for wedge diffraction derived by Kouyoumjian and Pathak (1971) when calculating diffraction coefficients.
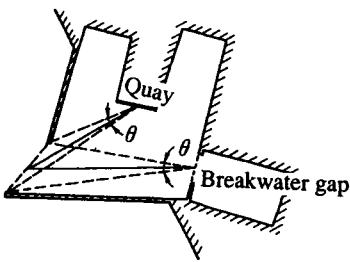
Fig. 7.16 Diffraction and reflection in a harbor   Fig. 7.17 Wave rays reaching point P
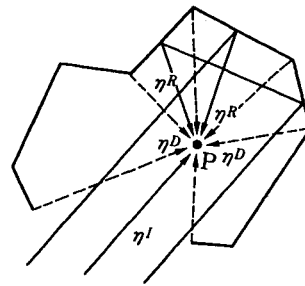
The wave ray method was originally developed for regular waves but can easily be extended for irregular waves. Moreover, this method is suitable for the calculation of wave direction in a harbor. However, it is difficult to account for refraction due to depth variance in contrast with the "wave ray method" shown in 1.2.

In this section we have shown approximate methods, the basic ideas of which are similar to those in optics. The accuracies of these methods, therefore, generally increase as the relative wavelength to a representative dimension of a harbor becomes shorter. Remember that strict methods are not suitable for short relative wavelength, and we know that a method that stands between strict and approximate methods should be developed. Combined use of strict and approximate methods, however, seems to be the best way at present.

7.3 Numerical Methods for the Prediction of Ship Motions in a Harbor

As mentioned in **2.4.2**, ship motions under the excitation of regular waves are obtained by solving the equation of motion, Eq. (2.194). In order to solve this equation, we need to calculate the wave forces, i.e. the Froude-Krylov force $F^{(F)}$, the diffraction force $F^{(D)}$, and the radiation force $F^{(R)}$ represented by the added mass $M_{lm}^{(A)}$ and the damping coefficient $N_{lm}^{(D)}$. We now consider a ship located in a harbor as shown in Fig. 7.18. The Froude-Krylov force is a hypothetical force calculated by integrating the pressure corresponding to the velocity potential of incident waves which are not influenced by the presence of a ship. For a ship in a harbor, however , the incident wave potential must be calculated by numerical methods as shown in **7.2**. Since both diffraction and radiation forces correspond to the waves radiating from the ship, these forces are strongly influenced by harbor boundaries located in the vicinity of the ship. In the following sections, we show numerical methods for calculating wave forces, which take harbor boundaries into account, and the influence of harbor boundaries on wave forces.

7.3.1 Calculation of wave forces under consideration of harbor boundaries

Oortmerssen (1976) and Sawaragi et al. (1982, 1983, 1989, 1991) investigated the influence of harbor boundaries on wave forces. Here we show the numerical method by Sawaragi et al. (1989, 1992), which can be applied to a ship and a harbor with arbitrary configurations. This method is based on the source-doublet distribution method in the BIEM. We show only the equations for the radiation problem, i.e., for the radiation potential ϕ_R, because the diffraction problem is its straightforward extension.

We use coordinate systems as shown in Fig. 7.19 and define the six components of ship motion with respect to the coordinates $G_s x_s y_s z_s$, where G_s is the center of gravity of the ship. Motions parallel to the x_s, y_s and z_s axes are termed sway (X), surge (Y) and heave (Z), and angular motions about these axes are termed pitch (Ω_x), roll (Ω_y) and yaw (Ω_z), respectively. These motions are expressed as

$$X = \hat{X} e^{-i\sigma t}, \, Y = \hat{Y} e^{-i\sigma t}, \, \cdots, \, \Omega_z = \hat{\Omega}_z e^{-i\sigma t} \qquad (7.30)$$
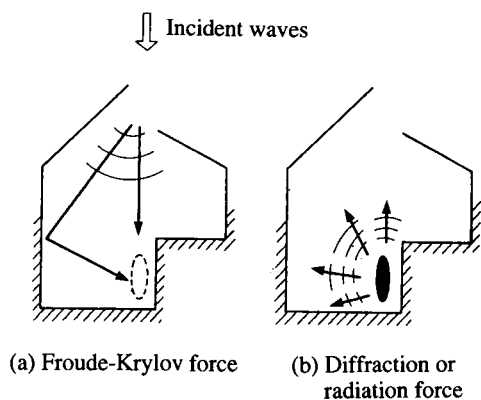
(a) Froude-Krylov force   (b) Diffraction or radiation force

Fig. 7.18 Wave forces and corresponding wave patterns
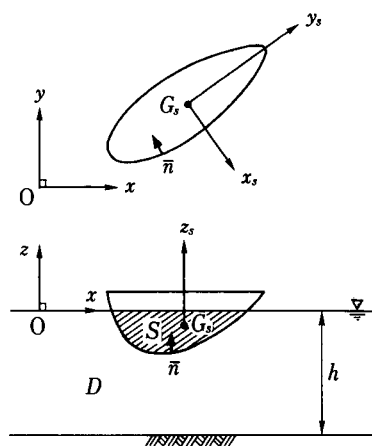
Fig. 7.19 Definition sketch for ship and coordinate systems

by means of complex amplitude $\hat{X}, \hat{Y}, ..., \hat{\Omega}_z$, respectively. If we let normalized radiation potentials be $\phi_R = (\phi_{R1}, \phi_{R2}, ...\phi_{R6})$ (see Eq. (2.182)), and assume that water depth is constant and no other boundaries exist except for the ship, governing equations and boundary conditions are as follows:

$$\nabla^2 \phi_{Ri} = 0 \qquad : \text{in } D \tag{7.31}$$

$$\frac{\partial \phi_{Ri}}{\partial z} - \frac{\sigma^2}{g} \phi_{Ri} = 0 \qquad : \text{at } z = 0 \tag{7.32}$$

$$\frac{\partial \phi_{Ri}}{\partial z} = 0 \qquad : \text{at } z = -h \tag{7.33}$$

$$\frac{\partial \phi_{Ri}}{\partial \bar{n}} = \bar{\xi}_i \qquad : \text{on } S \tag{7.34}$$

$$\sqrt{R} \left(\frac{\partial \phi_{Ri}}{\partial R} - ik\phi_{Ri} \right) = 0 \quad \text{when } R \to \infty \tag{7.35}$$

where R denotes the radial distance from the origin O and $\bar{\xi}_i$ represents the normalized velocity due to the ship motion in the normal direction to wetted surface S (N.B.: $\bar{\xi}_i$ is different from ξ_i in Eq. (2.129) in its sign). If we let the components of the unit normal vector $\bar{n}$ on S be $(\bar{n}_x, \bar{n}_y, \bar{n}_z)$, with respect to the coordinate system $G_s x_s y_s z_s$, $\bar{\xi}_i$ is given as

$$\left. \begin{array}{lll} \bar{\xi}_1 = \bar{n}_x, & \bar{\xi}_2 = \bar{n}_y, & \bar{\xi}_3 = \bar{n}_z \\ \bar{\xi}_4 = y_s \bar{n}_z - z_s \bar{n}_y, & \bar{\xi}_5 = z_s \bar{n}_x - x_s \bar{n}_z, & \bar{\xi}_6 = x_s \bar{n}_y - z_s \bar{n}_x \end{array} \right\} \tag{7.36}$$

By using John's Green's function $G(P,Q)$, the velocity potential at point P is expressed by surface integration over the wetted surface of the ship as follows, because G satisfies similar equations to Eqs. (7.31) through (7.34)

$$\phi_{Ri}(P) = e' \iint_s \left\{ \phi_{Ri}(Q) \frac{\partial}{\partial \bar{n}} G(P,Q) - \bar{\xi}_i(Q) G(P,Q) \right\} dS(Q) \tag{7.37}$$

where e' takes $-1/4\pi$ when the point P is inside the region D and takes $-1/2\pi$ when P is on S. This integral equation can be transformed to a set of algebraic equations by discretizing the surface S into small facets.

When any reflective boundary is placed around the ship, another boundary condition is added to Eqs. (7.32) through (7.35). If Green's function G also satisfies this condition, we can still use Eq. (7.37). In the following subsections, we first show the case where such a Green's function can be easily composed and then show a numerical method for a ship in a basin of an arbitrary configuration.

(1) The mirror image method

For a ship near a wedge-shaped, fully-reflecting boundary as shown in Fig. 7.20, the following boundary condition is added:

$$\frac{\partial \phi_{Ri}}{\partial \bar{n}} = 0 : \text{on } \Gamma_1, \Gamma_2 \tag{7.38}$$

In order to let Green's function G satisfy the condition $\partial G/\partial \bar{n} = 0$ on Γ_1 and Γ_2, we employ the method of images and put singular points at a mirror image point P_i' with respect to the boundary. This method can be applied only when the number of mirror image points is finite and no mirror image points appear in the fluid region. The wedge angle that satisfies these conditions is only π/n ($n = 1,2, ...$). For example, five mirror image points P_1', P_2', ..., P_5' are necessary as shown in Fig. 7.20 when the angle is $\pi/3$, and the modified Green's function G' that satisfies the boundary condition of impermeability on Γ_1 and Γ_2 is expressed as

$$G'(P, Q) = G(P, Q) + G(P_1', Q) + \cdots + G(P_5', Q) \tag{7.39}$$

As shown above, although the method of images is very useful, it has the weakness that boundary the shapes are very restricted and partial reflection on the boundary cannot be taken into account.
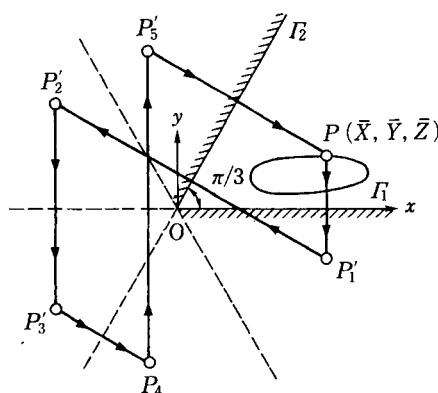
Fig. 7.20 Arrangement of mirror image points

(2) Analysis for a ship in a basin of arbitrary configuration

Consider a ship in a basin of arbitrary configuration with straight coastlines and constant depth as shown in Fig. 7.21. All the boundaries of the basin are assumed vertical and have an arbitrary reflection coefficient, K_R. Two coordinate systems $Oxyz$ and $G_s x_s y_s z_s$ are used as shown in the figure. The system $Oxyz$ is fixed with its origin at the still water level and at the entrance of the basin. The system $G_s x_s y_s z_s$ is fixed at the center of gravity of the ship in its mean position. As mentioned above, if we can develop Green's function to satisfy

in its mean position. As mentioned above, if we can develop Green's function to satisfy the boundary conditions on the harbor boundaries, the numerical procedure becomes the same as that for the ship in open sea by using Eq. (7.37). However, the numerical method to compose such a Green's function has not been developed. Thus, in order to solve the whole region of the basin, the domain of interest is divided into three regions as shown in Fig. 7.21: the semi-infinite ocean (region I), the basin excluding the vicinity of the ship (region II), and the region around the ship (region III). B_1 and B_2 are imaginary vertical boundaries between the regions, and the direction of the normal vector $\bar{n}$ for each region is defined as shown in Fig. 7.21.
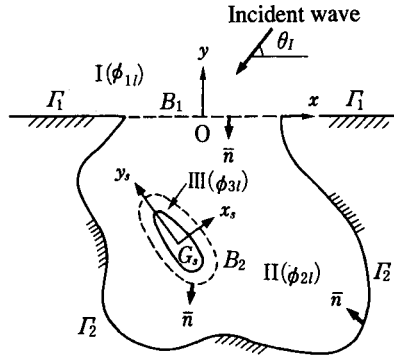
Fig. 7.21 Definition sketch for ship in basin of arbitrary configuration

We let the velocity potentials in each region be f_{R1i}, f_{R2i} and f_{R3i} ($i=1, 2, ..., 6$), respectively, and express f_{R1i} and f_{R2i} as a series of eigenfunctions

$$\phi_{Rli} = f_{li}^{(0)}(x, y)\frac{\cosh k(z+h)}{\cosh kh} + \sum_{n=1}^{\infty} f_{li}^{(n)}(x, y)\frac{\cos k_n(z+h)}{\cos k_n h} \tag{7.40}$$
$$(l = 1, 2)$$

where k and k_n are derived by solving the equations

$$k\,h\tanh kh = -k_n h \tan k_n h = \sigma^2 h / g \tag{7.41}$$

From Eq. (7.31), $f_{li}^{(0)}, f_{li}^{(n)}$ and ϕ_{R3i} satisfy the following equations:

$$\frac{\partial^2 f_{li}^{(0)}}{\partial x^2} + \frac{\partial^2 f_{li}^{(0)}}{\partial y^2} + k^2 f_{li}^{(0)} = 0 \tag{7.42}$$

$$\frac{\partial^2 f_{li}^{(n)}}{\partial x^2} + \frac{\partial^2 f_{li}^{(n)}}{\partial y^2} - k_n^2 f_{li}^{(n)} = 0 \tag{7.43}$$

$$\frac{\partial^2 \phi_{r3i}}{\partial x^2} + \frac{\partial^2 \phi_{R3i}}{\partial y^2} + \frac{\partial^2 \phi_{R3i}}{\partial z^2} = 0 \tag{7.44}$$

In region III, the boundary conditions Eqs. (7.32), (7.33) and (7.34), are imposed on ϕ_{R3i}. In the regions I and II the following conditions apply:

$$\frac{\partial f_{1i}^{(0)}}{\partial \bar{n}} = \frac{\partial f_{1i}^{(n)}}{\partial \bar{n}} = 0 \; : \; \text{on } \Gamma_1 \tag{7.45}$$

$$\frac{\partial f_{2i}^{(0)}}{\partial \bar{n}} = -ik\alpha f_{2i}^{(0)}, \frac{\partial f_{2i}^{(n)}}{\partial \bar{n}} = 0 \; : \; \text{on } \Gamma_2 \tag{7.46}$$

where Γ_1 and Γ_2 are shown in Fig. 7.21. The first equation in Eq. (7.46) corresponds to Eq. (7.12) and indicates the condition of partial absorption. For the function $f_{2i}^{(n)}$, which represents the evanescent mode waves. the boundary condition of full reflection was imposed since the absorption condition for the evanescent mode waves is not clear. Furthermore, the following continuity conditions are given at the imaginary boundaries:

$$\frac{\partial f_{1i}^{(0)}}{\partial \bar{n}} = \frac{\partial f_{2i}^{(0)}}{\partial \bar{n}}, \frac{\partial f_{1i}^{(n)}}{\partial \bar{n}} = \frac{\partial f_{2i}^{(n)}}{\partial \bar{n}}, \tag{7.47}$$

$$f_{1i}^{(0)} = f_{2i}^{(0)}, f_{1i}^{(n)} = f_{2i}^{(n)} : \quad \text{on } B_1$$

$$\frac{\partial \phi_{R2i}}{\partial \bar{n}} = \frac{\partial \phi_{R3i}}{\partial \bar{n}}, \phi_{R2i} = \phi_{R3i} : \quad \text{on } B_2 \tag{7.48}$$

In order to solve the Eqs. (7.42), (7.43) and (7.44) under the conditions of Eqs. (7.45) through (7.48), we employ the boundary integral equation method. For regions I and II, we choose the Hankel function of the first kind and the 0th order $H_0^{(1)}(kr)$ and the modified Bessel function of the second kind and the 0th order $K_0(k_n r)$ as Green's functions of Eq. (7.25) and Eq. (7.25) respectively, where r is the distance between the points P and Q in the regions. By applying Green's formula to the regions I and II and using the boundary conditions Eqs. (7.45) and (7.46), we obtain the functions $f_{1i}^{(0)}$, and $f_{1i}^{(n)}$ at the point P in each region through boundary integration. For example, $f_{2i}^{(0)}(P)$ and $f_{2i}^{(n)}(P)$ are given as

$$f_{2i}^{(0)}(P) = e\int_{\Gamma_2 + B_1 + B_2} \left[f_{2i}^{(0)}(Q)\frac{\partial}{\partial \bar{n}}\left\{H_o^{(1)}(kr)\right\} - H_1^{(0)}(kr)\frac{\partial}{\partial \bar{n}}f_{2i}^{(0)}(Q) \right] ds(Q) \tag{7.49}$$

$$f_{2i}^{(n)}(P) = e\int_{\Gamma_2 + B_1 + B_2} \left[f_{2i}^{(n)}(Q)\frac{\partial}{\partial \bar{n}}\left\{K_o(k_n r)\right\} - K_o(k_n r)\frac{\partial}{\partial \bar{n}}f_{2i}^{(n)}(Q) \right] ds(Q) \tag{7.50}$$

where e is the same as Eq. (7.17). For the region III, John's Green's function $G(P,Q)$ is used and $\phi_{R3i}(P)$ on the boundaries is expressed as

$$\phi_{R3i}(P) = e\iint_{S+B_2} \left[\phi_{R3i}(Q)\frac{\partial}{\partial \bar{n}}G(P,Q) - G(P,Q)\frac{\partial}{\partial \bar{n}}\phi_{R3i}(Q) \right] ds(Q) \tag{7.51}$$

The unknown functions, $f_{li}^{(0)}$, $f_{li}^{(n)}$ and ϕ_{R3i}, are obtained by solving these integral equations together under the continuity conditions, Eqs. (7.47) and (7.48).

To solve these integral equations, the boundaries B_1, Γ_2 and B_2 are divided into line segments numbered N_1, N_2, and N_3, respectively. Moreover, the surface boundaries B_2 and S are divided into rectangular facets of the number $N_C = N_3 \times N_D$ and N_S, respectively. In order to make the number of the unknowns coincide with that of equations, the number of facets in the vertical direction on B_2, N_D, must be equal to $1 + N_F$, where N_F represents the number of components of evanescent mode waves.

7.3.2 Influences of harbor boundaries on wave forces
(1) Wave forces on a ship near wedge-shaped boundaries

We first show the added mass and damping coefficient of a rectangular ship located near four types of quays with angles of 180°, 90°, 60° and 45° as shown in Fig. 7.22, compared with those for a ship in open sea. Figures 7.23 (a) - (c) show the frequency responses of added mass, damping coefficient and wave exciting force in the surge mode, where L_S and ζ_0 denote the ship length and the amplitude of incident waves, respectively. As seen from these figures, the response curves in the case of the existence of a quay are considerably different from those in the open sea and highly dependent on the configuration of the quay as well as the frequencies.
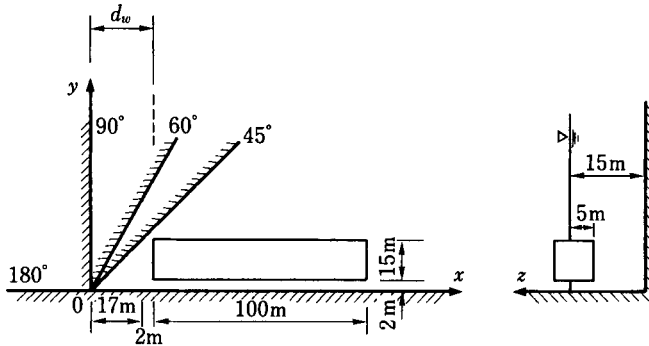
Fig. 7.22   Dimensions and location of the tested ship

Moreover, in order to investigate how far the influence of the quays extends, calculations were carried out in the case of a 90° quay by changing the distance d_w between the ship and the quay parallel to the y-axis. These results are compared with those in the case of 180° quay in Fig. 7.24 for the sway and surge modes. In these figures, $M_{ii}^{(A)90}/M_{ii}^{(A)180}$ and $N_{ii}^{(D)90}/N_{ii}^{(D)180}$ are the ratios of added mass and damping coefficient in the case of a 90° quay to those of a 180° quay and L is wavelength. These figures show that the values of these ratios asymptotically approach 1.0 in the region $D/L > 1.0$. It means that the quay located within a one-wavelength distance from the ship does influence the added mass and the damping coefficients of the ship.

(a) Added mass

(b) Damping coefficient

(c) Wave exciting force
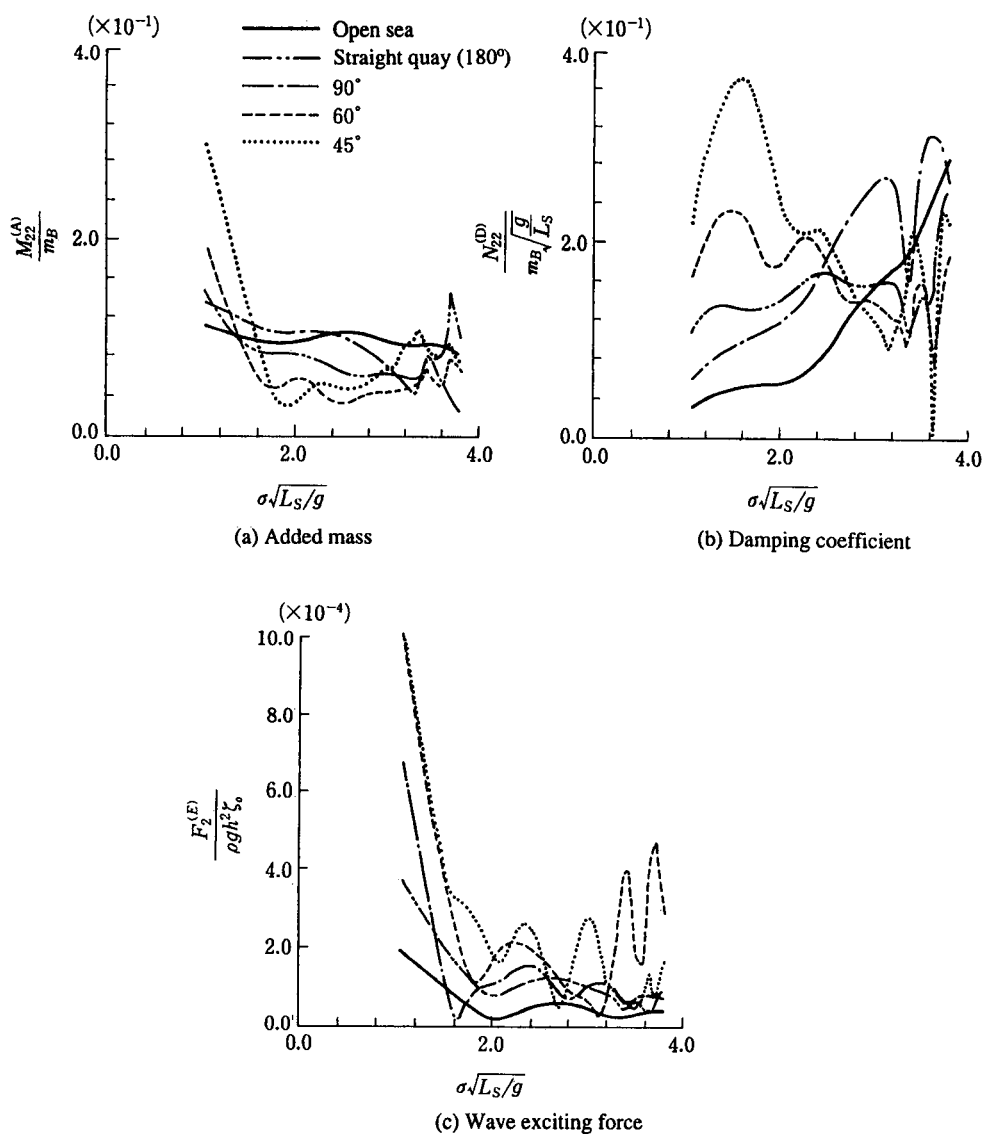
Fig. 7.23 Dependence of wave forces on boundary configuration
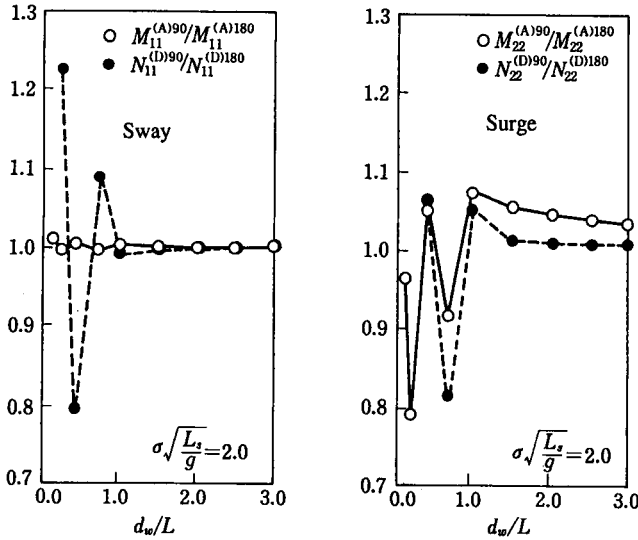
Fig. 7.24 Dependence of added mass and damping coefficients on distance between ship and quay

(2) Wave forces on a ship in a slip

The solid and broken lines in Fig. 7.25 show the frequency response of the added mass $M_{11}^{(A)}$ and the damping coefficient $N_{11}^{(D)}$ in the sway mode, respectively, for a rectangular ship in a rectangular slip shown in this figure. The dotted lines in the figure show those for the same ship in the open sea. The added mass and the damping coefficient corresponding to the slip show some large peaks in their response curves compared with those of the open sea. The frequencies $\sigma\sqrt{L_s/g}=0.7$ and 1.6, where the large peaks appear, correspond to the resonance frequencies of transverse oscillation in the ship, which indicates that characteristics of fluid oscillation in a basin strongly influence the added mass and damping coefficient.

(3) Influence of partial reflection on a boundary

Figure 7.26 shows the dependence of the added mass and the damping coefficient on the absorption coefficient α of all the boundaries of the slip at $\sigma\sqrt{L_s/g}= 0.7$ where the damping coefficient shows a large peak in its response curve as shown in Fig. 7.25. In this figure, the added mass and the damping coefficient strongly depend on α in the region $0\leq \alpha \leq 0.2$ ($0.67 \leq K_R \leq 1$) and asymptotically approach to the value for open sea represented by dotted lines in Fig. 7.25. The damping coefficient, in general, increases with increasing α since the damping energy consists of the energy radiating outward from the harbor and the energy absorbed in a harbor. However, as shown in Fig. 7.26, the damping coefficient may decrease at a particular frequency where the damping coefficient shows a large value. In **7.5.1**, we show the effects of partially-reflecting quays on ship motions, where the condition of the boundary absorption is treated more precisely.
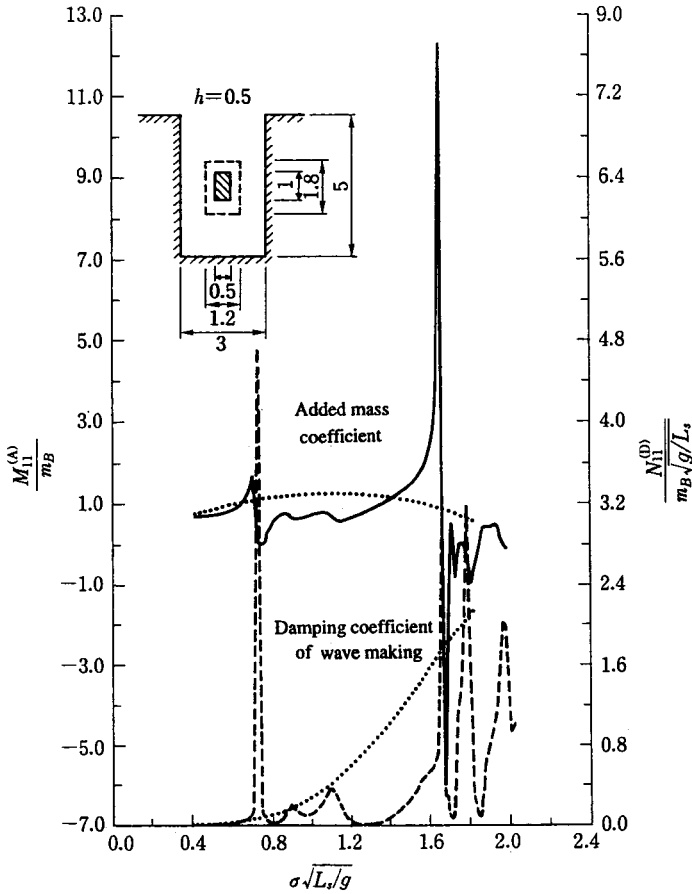
Fig. 7.25 Added mass and damping coefficient for a ship in a rectangular slip

7.3.3 Solution of equation of motion

If we let $X_m = \hat{X}_m e^{-i\sigma t}$ and $F_1^{(E)} = F_1^{(E)} e^{-i\sigma t}$ in the equation of motion (2.140) in Chapter 2 and let, $\hat{X} = (\hat{X}_1, \hat{X}_2, ..., \hat{X}_6)$ and $\hat{F}^{(E)} = (\hat{F}_1^{(E)}, \hat{F}_2^{(E)}, ..., \hat{F}_6^{(E)})$ the equation reduces to

$$\hat{X} = \left[-\sigma^2 \left(M^{(B)} + M^{(A)} \right) - i\sigma N^{(D)} + K \right]^{-1} \hat{F}^{(E)} = H^S(\sigma) \hat{F}^{(E)} \tag{7.52}$$

where $M^{(B)}$, $M^{(A)}$, $N^{(D)}$ and K represents the mass, added mass, damping coefficient and restoring force coefficient matrices. This equation indicates that ship motions are expressed by the frequency response function of motion $H^S(\sigma)$ and the wave exciting force $\hat{F}^{(E)}$. Furthermore, $\hat{F}^{(E)}$ can be expressed as

$$\hat{F}^{(E)} = H^E(\sigma, \theta_I) \hat{\zeta}_I \tag{7.53}$$
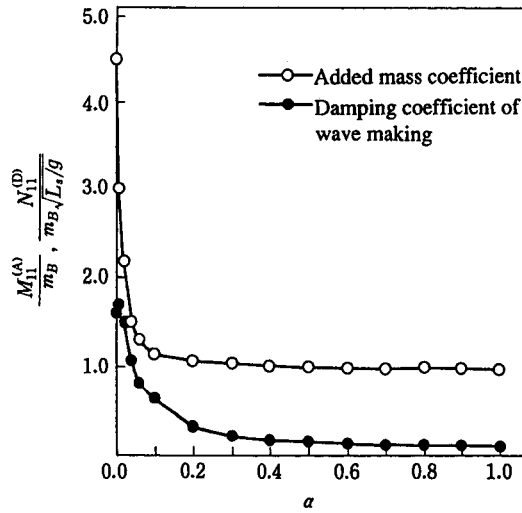
Fig. 7.26 Dependence of added mass and damping coefficient on absorption coefficient

by using the complex amplitude of incident waves entering the harbor, $\hat{\zeta}_I$, where $H^E(\sigma, \theta_I)$ represents the response function of the wave exciting force and θ_I is the angle of incidence. Substituting Eq. (7.53) into Eq. (7.52), the ship motions are given by

$$\hat{X} = H^S(\sigma) H^E(\sigma, \theta_I) \hat{\zeta}_I \tag{7.54}$$

This equation indicates that the ship motions in a harbor are expressed by two response functions H^S and H^E, which represent the oscillation systems of a ship and water, respectively. As mentioned in **2.4.2**, the ship motions cannot be simply expressed in terms of such frequency response functions when the equation of motion is nonlinear. In this case, we must solve the equation by integrating it in the time domain.

7.3.4 Strip method in presence of a quay wall

In Chapter 2, as the practical calculation method, we described the strip method for the floating body moored in waters of a constant depth and without a quay wall. In the case of ship motions in a harbor, however, there are quay walls and slopes as mentioned above, so the treatment of the strip method is different from that of the open waters. Of course, even if there is the quay wall, ship motions can be estimated approximately by using the radiation force and the diffraction forces (which are given by the total forces due to the incident waves and the reflected waves) in the open waters (Ueda 1984). We do not use this approximation method. In the following, a different part of the treatment with and without the quay wall is mainly described (Kubo et al. 1990).

Ships in a harbor are moored along such various berths as an open jetty, solid jetty and slope. In this case, since the depth is sometimes not constant, we use the most basic function $G(r)=(1/2\pi) \ln(r)$ as Green's function shown in **2.4.1**. Here r shows the distance between two points in the fluid. The motions of the floating body are explained with the

coordinate system in Fig. 7.27. This Green's function does not satisfy a free surface condition and a bottom condition, so we must set the calculation points on the free surface and the bottom beside the wetted surface of the body, and set an imaginary boundary at $x = l_D$ far from the origin. If we set the boundary at the position where the evanescent waves of the first mode decrease to the one-hundredth, l_D is given by

$$l_D = \frac{ln\,100}{k_1} + a \tag{7.55}$$

where k_1 is the eigenvalue of $n = 1$ in Eq. (7.41) and a is a half breadth shown in Fig. 7.27.
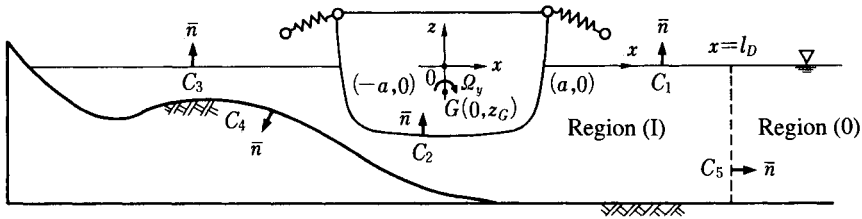
Fig. 7.27   Notation for two-dimensional analysis and coordinate system

Because the evanescent waves can be neglected outside of the imaginary boundary, the radiation potential is given as follows:

$$\phi_{Ri}^{(o)} = \frac{g}{\sigma^2} K_{Ri}\, e^{ikx}\, \frac{\cosh k(h+z)}{\cosh kh} \tag{7.56}$$

Here K_{Ri} is equivalent to the coefficient of a progressive wave and is the unknown complex coefficient of radiated waves caused by the i-th mode body motion. Then, the radiation velocity potential on the boundary is given by solving the simultaneous equations composed by the boundary conditions and Green's formulas

$$\left.\begin{aligned}
\frac{\partial \phi_{Ri}}{\partial \bar{n}} &= \frac{\sigma^2}{g}\phi_{Ri} \;:\; \text{on}\; C_{1,}\, C_{3,} & \frac{\partial \phi_{Ri}}{\partial \bar{n}} &= \bar{\bar{\xi}}_i & :\; \text{on}\; C_2 \\
\frac{\partial \phi_{Ri}}{\partial \bar{n}} &= 0 \;:\; \text{on}\; C_{4,} & \frac{\partial \phi_{Ri}}{\partial \bar{n}} &= \frac{\partial \phi_{Ri}^{(o)}}{\partial \bar{n}},\; \phi_{Ri} = \phi_{Ri}^{(o)} & :\; \text{on}\; C_5
\end{aligned}\right\} \tag{7.57}$$

$$\phi_{Ri}(P) = 2\int_{C1+C2+C3+C4+C5} \left\{ \phi_{Ri}(Q)\frac{\partial G(P,Q)}{\partial \bar{n}} - G(P,Q)\frac{\partial \phi_{Ri}(Q)}{\partial \bar{n}} \right\} dC(Q) \tag{7.58}$$

Here $\bar{\xi}_i$ is given by Eq. (7.36) and we should take care that its direction is opposite to that of the source distribution method in Chapter 2. P and Q are the points on the boundary.

When ϕ_{Ri} ($i = 1,3,5$) is obtained, the pressure p_{Ri} ($i = 1, 3, 5$) is also obtained. In the case of a quay wall, the symmetry and anti-symmetry of the velocity potential and boundary condition as shown in Fig. 2.19 disappear by the reflected wave from the wall, and the body motions of all modes are coupled with one another. Figure 7.29 shows the added mass and the damping coefficients for three kinds of walls shown in Fig. 7.28. Here L_s is the length of the body and B is the breadth. The figure shows us that $M_{13}^{(A)}$ and $N_{13}^{(A)}$ are zero for the open jetty, but not zero for the slope and the solid jetty. Moreover, the other hydrodynamic coefficients are considerably different by the structure of the wall.

(a) Slope

(b) Solid jetty (vertical wall)

(c) Open jetty (transmitted wall) unit;cm
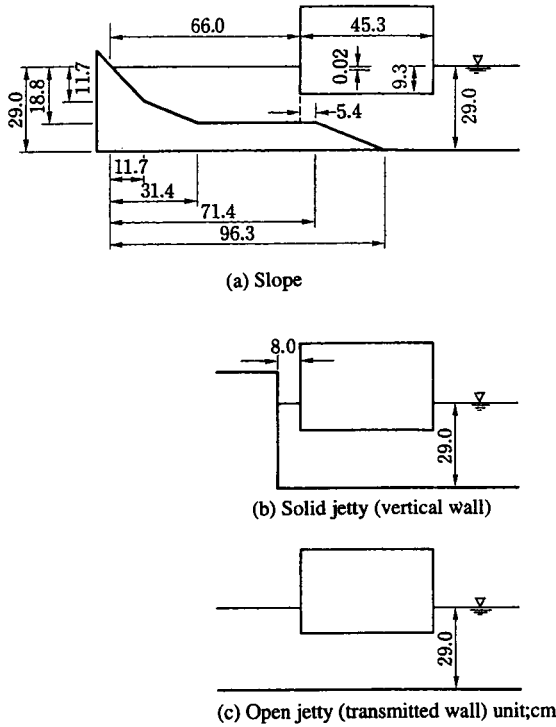
Fig. 7.28   Three kinds of quay walls and floating bodies

Considering the above, in the same manner as Eq. (2.202), the radiation force is obtained as follows:

$$dF_i^{(R)} = \int_{Cs} \left(p_{R1} + p_{R3} + p_{R5} \right) \overline{\xi}_i dC, \qquad (i = 1,3,5)$$

$$= -dM_{i1}^{(A)} \dot{u}_R - dN_{i1}^{(D)} u_R - dM_{i3}^{(A)} \dot{w}_R - dN_{i3}^{(D)} w_R$$

$$-dM_{i5}^{(A)} \ddot{X}_5 - dN_{i5}^{(D)} \dot{X}_5 \qquad\qquad (7.59)$$

$$u_R = \dot{X}_1 - z_G \dot{X}_5 - y\dot{X}_6, \quad w_R = \dot{X}_3 + y\dot{X}_4$$

$(L_S/B=5.27)$
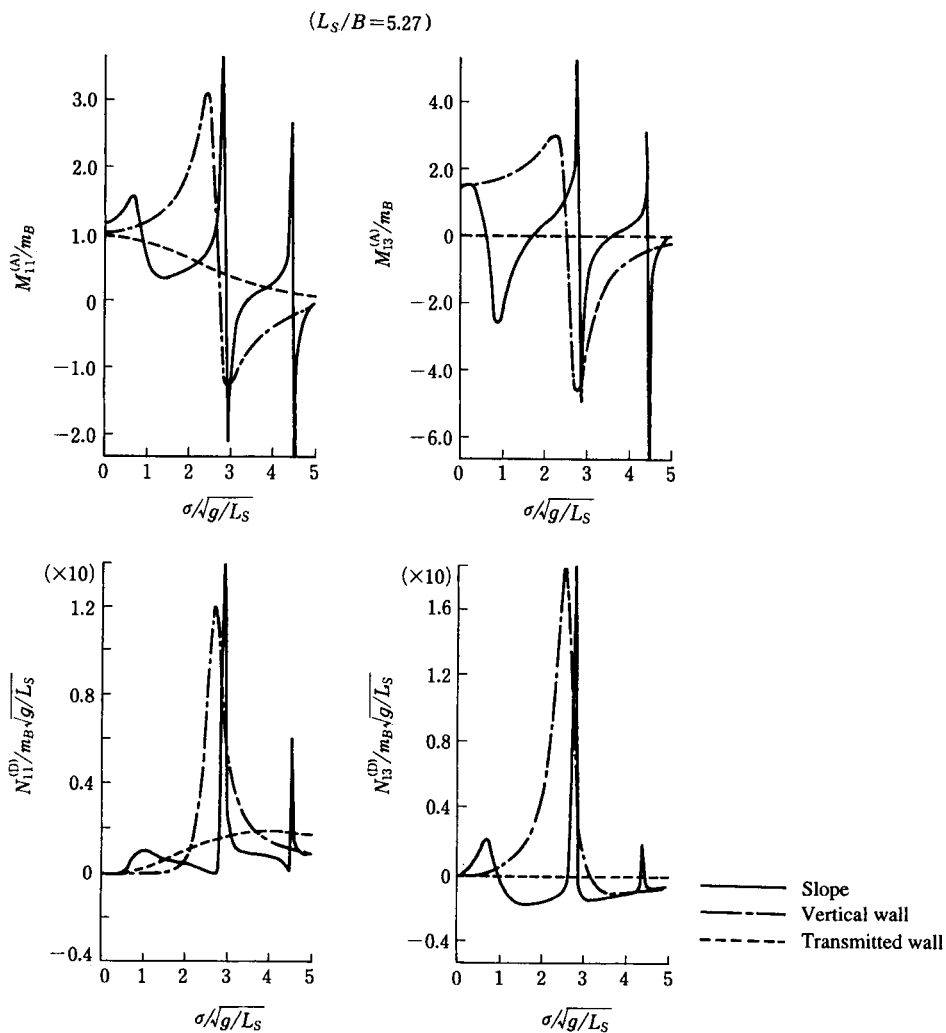
Fig. 7.29　Effect of form difference of quay wall on hydrodynamic coefficient

As $M_{13}^{(A)} = M_{53}^{(A)} = 0$, $N_{13}^{(D)} = N_{53}^{(D)} = 0$ for the open sea, the right hand side was simplified, but in the case of the solid jetty and slope, all of these terms do not disappear. Furthermore, this relationship is still kept in case of diffraction force calculation with the Haskind relation. From Eq. (2.151)

$$dF_i^{(D)} = dM_{i1}^{(A)}\dot{u}_I + dN_{i1}^{(D)}u_I + dM_{i3}^{(A)}\dot{w}_I + dN_{i3}^{(D)}w_I \quad (i = 1, 3, 5)$$

$$u_I = \left.\frac{\partial\left(\Phi_I + \Phi_R\right)}{\partial x}\right|_{x=0,\ z=-d/2}, \quad w_I = \left.\frac{\partial\left(\Phi_I + \Phi_R\right)}{\partial z}\right|_{x=0,\ z=-\zeta(y)/B,} \quad (7.60)$$

Here Φ_I and Φ_R are the velocity potentials of incident waves and reflected waves, respectively. Being different from Fig. 2.19, u_I and w_I must contain the incident and reflected waves as shown above. Three-dimensional radiation and diffraction forces can be obtained by integrating the forces using Eq. (2.149).

7.4 Long-Period Ship Motions

When a ship is moored in stormy weather, large amplitude ship motions with a period of one to two minutes occur, and when not moored it does not have the restoring forces of sway, surge, and yaw, but has a natural period of one to two minutes when moored. Figure 7.30 shows the relation between the ship displacement and the natural periods of surge and sway (Sawaragi and Kubo 1982; Wilson 1951). From this figure, we can understand that the natural period is about 1~2 minutes and is not so much related to the displacement. As the natural period is long enough not to make the radiated waves by the ship motions, the wave making damping coefficient becomes zero. For this reason, small exciting forces make large ship movement, which prevents shipping activities in a harbor such as safe ship mooring and efficient cargo handling. In the following, we describe the causes of long-period ship motions from four standpoints.
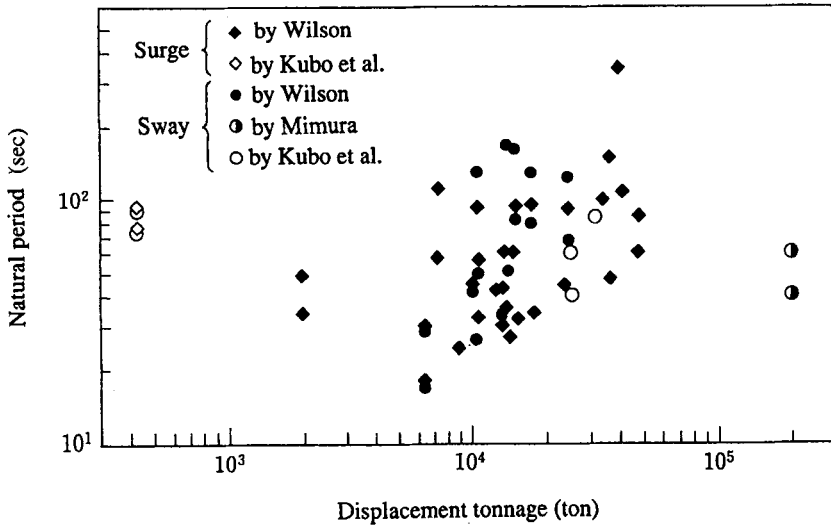
Fig. 7.30   Relation between natural period of surge and sway and displacement tonnage

7.4.1 Asymmetrical mooring

In the case of a moored ship in the field, the restoring force $F^{(M)}$ for sway is composed of the mooring line force and the repelling fender force. Figure 7.31 shows the characteristics between extension and load of various ropes. From this, we understand that the loads are proportional to the extension to the second power.

On the other hand, two kinds of fenders, namely, the pneumatic type and buckling type,
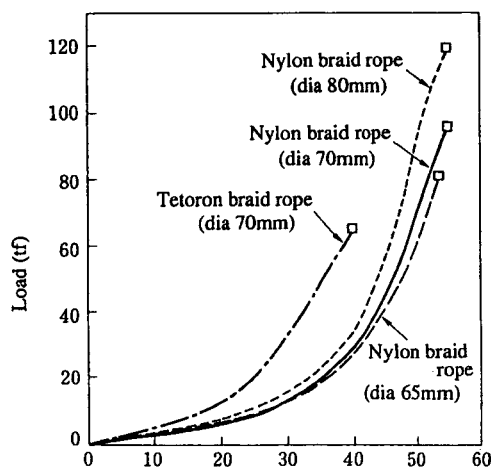
Fig. 7.31 Relation between mooring line extension and load
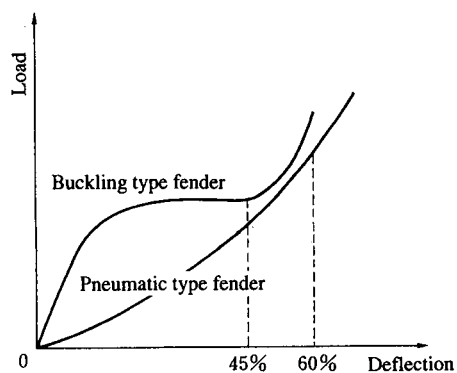
Fig. 7.32 Characteristics of deflection and load on the fender

are used as shown in Fig. 7.32. For the pneumatic type, there are pneumatic fenders and cylinder type fenders. For the buckling type, there are V and H shaped rubber fenders that produce constant repelling forces by buckling deformation. In the case of the buckling fender, approximating the characteristics of the restoring forces near the origin, the relation between load and sway motions is shown in Fig. 7.33. Here C_L and C_F are the spring constants of mooring lines and fenders, respectively. In the prototype mooring, the ratio of both spring constants amounts from 1:100 to 1:1000, and we call them asymmetrical mooring. Ignoring the coupling terms according to Eq. (2.140), the equation of sway motion of a ship moored along the vertical wall is represented by

$$\left(m_B + M_{11}^{(A)}\right)\ddot{X} + N_{11}{}'\dot{X} + F_1^{(M)} = \left(m_B + M_{11}^{(A)}\right)\dot{U} + N_{11}{}'U \qquad (7.61)$$

Here $\dot{U}$ is the average acceleration of the wet body and is given by the following equation in case of beam sea:

$$\dot{U} = \frac{H_I g}{d} \frac{\sin^2(kB/2)}{kB/2} \frac{\sinh kh - \sinh k(h-d)}{\cosh kh}$$

$$\times \frac{\cos k(r_w - B/2) - \cos k(r_w + B/2)}{2\sin^2(kB/2)} \sin \sigma t \qquad (7.61a)$$

where m_B is the mass of the ship, $M_{11}^{(A)}$ is the added mass of sway, N_{11}' is the total damping coefficient, which contains viscous damping, and it is obtained by a free oscillation test. H_I is the amplitude of the incident wave, d is the draft, B is the breadth of ship and r_w is the distance from the center of ship to the quay wall (Lean 1971). In the case of Eq. (7.61), by obtaining the individual solutions for the linear equations in each region I and II of Fig, 7.33, and determining the constants in free oscillation terms with the initial conditions $X=0$ and $\dot{X}$ of the former region, the solution can be determined (Sawaragi and Kubo 1983). Figure 7.34 shows the wave profile at the wall and the sway motions of a model ship with a ship length 2.4m, breadth 0.455m, draft 0.098m in a water depth of 0.211m. The lower figure shows flat peaks, which mean that the ship makes contact with the fender. As one contact occurs for m_d waves, we call them the motions of m_d mode. As shown above, the sway motions at the asymmetrical mooring consist of the short- and long-period ship motions. The long-period motions are named subharmomic motions (Lean 1971). Accordingly, at the asymmetrical mooring, even if the wave period is around 10s, the long-period ship motion of around one minute occurs.
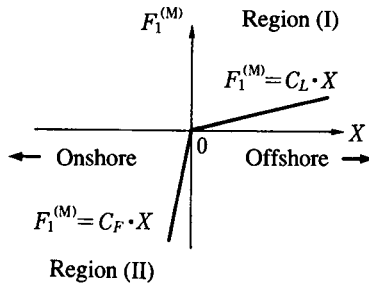
Fig. 7.33   Restoring force for sway
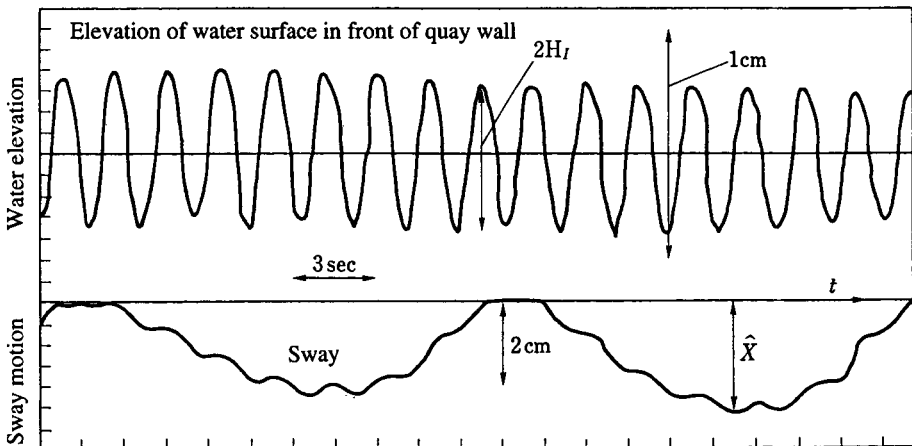
Fig. 7.34   Profile of Sway motion at asymmetrical mooring (model test)

7.4.2 Slow drift oscillations

We assume that the floating body is moored by equal spring constants from both sides. We refer to this as a symmetrical mooring. Applying the beating waves shown in Fig. 7.35 to the body, it moves not only with the wave period but also with the long period of the beat. The external force causing such motions is called drift force (Hsu and Blenkarn 1970). The drif force working per unit length of the body moored along the wall in the finite depth of Fig. 7.36 can be obtained with the conservation of momentum in the same manner as in Chapter 2.
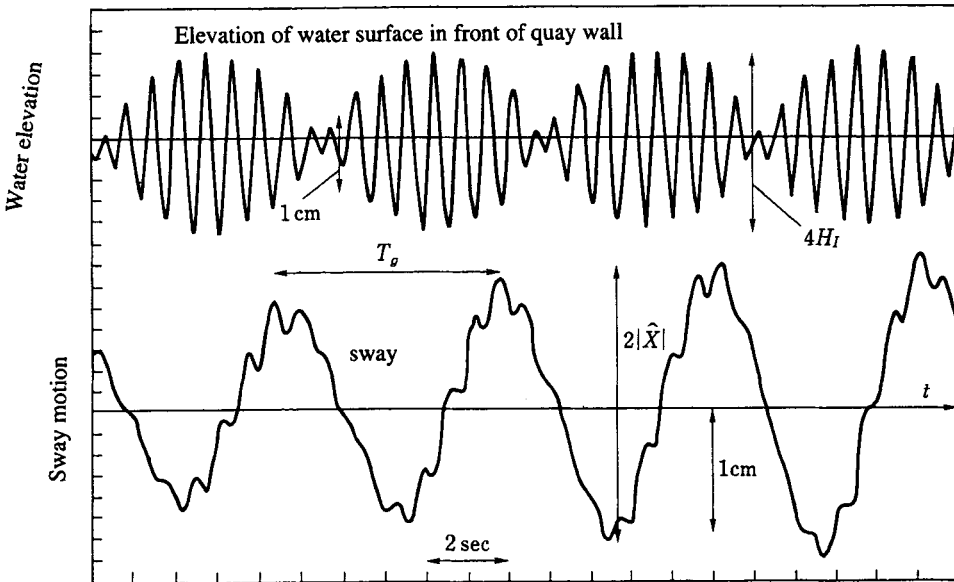
Fig. 7.35   An example of long-period sway motion due to two-component waves
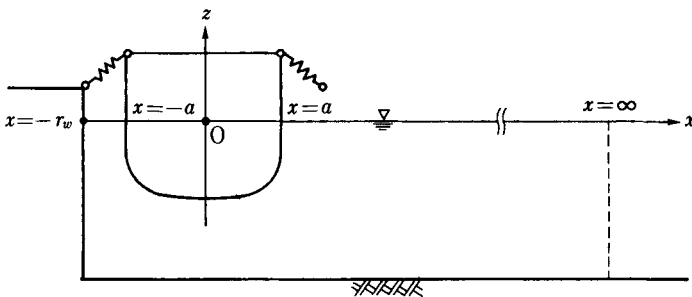
Fig. 7.36   Notation for drift force of a ship moored along a quay wall

The velocity potentials of incident waves, reflected waves and waves between the ship and quay namely, Φ_I, Φ_R and Φ_J (Sawaragi et al. 1980) are given as follows:

$$\Phi_I = \frac{ig\zeta_o}{\sigma} \cdot \frac{\cosh k(h+z)}{\cosh kh} \cdot e^{-ikx-i\sigma t}$$

$$\Phi_R = \frac{ig\zeta_R}{\sigma} \cdot \frac{\cosh k(h+z)}{\cosh kh} \cdot e^{-ikx-i\sigma t},$$

$$\Phi_J = \left\{ G_o \frac{\cos k(r_w+x)}{\cos k(r_w-a)} \cdot \frac{\cosh k(h+z)}{\cosh kh} \right.$$
$$\left. + \sum_{n=1}^{\infty} G_n \frac{\cosh k_n(r_w+x)}{\cosh k_n(r_w-a)} \cdot \frac{\cos k_n(h+z)}{\cos k_n h} \right\} e^{-i\sigma t}$$

(7.62)

where k and k_n are given by Eq. (7.63) and ζ_0 is the amplitude of incident waves. The unknown values ζ_R, G_n ($n = 0, 1, 2, ...$) in the velocity potentials are determined by solving the simultaneous equations relating the boundary conditions and the equation of motions, after that, all velocity potentials are decided.

Setting the control surfaces at the origin of incoming waves $x = \infty$ and at the quay wall $x = -r_w$ and averaging the change of momentum over a period, then we can get the drifting force. The positive direction of the force is the same as the propogating direction of incident waves

$$\hat{F}_{dx} = \frac{1}{2}\rho \int_{-h}^{0} \left\{ \overline{\left(\frac{\partial \Phi_{I+R}}{\partial x}\right)_{\infty}^2} - \overline{\left(\frac{\partial \Phi_{I+R}}{\partial z}\right)_{\infty}^2} + \overline{\left(\frac{\partial \Phi_J}{\partial z}\right)_{-r_w}^2} \right\} dz$$

$$\left\{ -\rho \left\{ \overline{\eta_{\infty}\left(\frac{\partial \Phi_{I+R}}{\partial t}\right)_{\infty}} - \overline{\eta_{-r_w}\left(\frac{\partial \Phi_J}{\partial t}\right)_{-r_w}} \right\}_{z=0} - \frac{1}{2}\rho g\left(\overline{\eta_{\infty}^2} - \overline{\eta_{-r_w}^2}\right) \right.$$

(7.63)

where the subscript shows the x axis. The velocity, pressure and surface elevation shown in Eq. (7.63) are given using the decided velocity potential in Eq. (7.62). Furthermore, we have already used the boundary condition $(\partial \Phi_J / \partial X)_{-r_w} = 0$ in Eq. (7.63). Thus, by rearranging them with Φ_I, Φ_R, and Φ_J, the drift force is presented as follows:

$$\hat{F}_{dx} = \frac{\rho g}{4}\left(1 + \frac{2kh}{\sinh 2kh}\right)\left(1 + \left|\frac{\zeta_R}{\zeta_0}\right|^2\right) \cdot \zeta_0^2$$

$$- \frac{\rho\sigma^2}{4}\left\{ \frac{1}{\cos^2 k(r_w-a)} \cdot \frac{1}{2} \cdot \left(1 + \frac{2kh}{\sinh 2kh}\right) \cdot |G_0|^2 \right.$$

$$\left. + \sum_{n=1}^{\infty} \frac{1}{\cos^2 k_n(r_w-a)} \cdot \frac{1}{2} \cdot \left(1 + \frac{2k_n h}{\sin 2k_n h}\right) \cdot |G_0|^2 \right\}$$

(7.64)

Now, we take the coefficient of drift force D_R as

$$D_R = \hat{F}_{dx}\bigg/\frac{1}{2}\rho g\zeta_0{}^2 \tag{7.65}$$

The relationship between D_R and L/B is obtained as illustrated in Fig. 7.37. The solid line shows the theoretical results and the small circles are the experimental results. We find the negative drift force according to the wavelength. It is a different point compared with the case of the open jetty.
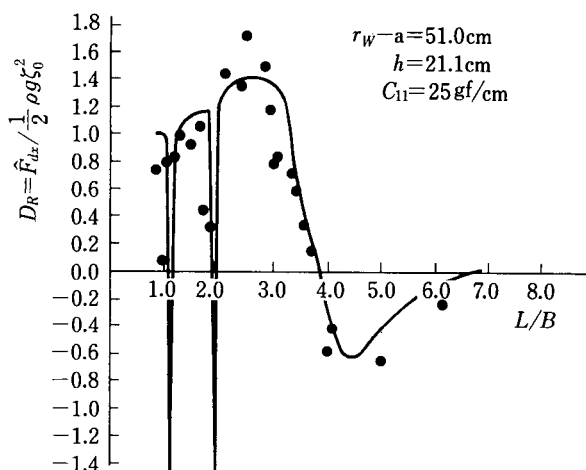
Fig. 7.37 Coefficient of drift force when the spring constant of the mooring system is small and clearance between the ship and the wall is wide

When the wave height gradually varies wave by wave, the drift force also varies slowly and generates the long-period ship motions. Now, for simplicity, supposing two-component waves beating as shown in Fig. 7.35, the slowly-varying drift force $F_{dx}^{(2)}$ is given by

$$F_{dx}{}^{(E)} = \rho g D_R \zeta_0{}^{(1)}\cdot\zeta_0{}^{(2)}\cdot L_s\cdot\cos(\Delta\sigma\cdot t+\delta) \tag{7.66}$$

Here $\zeta_0{}^{(1)}$, $\zeta_0{}^{(2)}$ are the amplitudes of the component waves, respectively, L_s is the ship length, Δk and $\Delta\sigma$ represent the difference of wave numbers and periods of two-component waves. Supposing the symmetrical linear mooring and the uncoupled equation of motion, then the equation of motion is the same as Eq. (7.61)

$$\ddot{X} + 2\varepsilon_{11}\dot{X} + n_{11}^2 X = F_{dx}^{(2)}\bigg/\left(m_B + M_{11}^{(A)}\right) \tag{7.67}$$

where $2\varepsilon_{11} = N'_{11}/(m_B+M_{11}{}^{(A)})$, $n_{11}{}^2 = C_{11}/(m_B+M_{11}{}^{(A)})$, and C_{11} is the coefficient of restoring force due to mooring lines. Substituting $F_{dx}^{(2)}$ of Eq. (7.66) into the above, we can get the long-period ship motions shown in Fig. 7.35. The force amplitude $\hat{F}$ of the mooring line due to the slow drift oscillations is obtained by solving Eq. (7.67) and using $\hat{F} = C_{11} \cdot \hat{X}$, then we get the next equation:

$$\frac{\hat{F}}{\hat{F}_{dx}^{(2)}} = \frac{n_{11}^2}{\sqrt{\left(n_{11}^2 - \Delta\sigma^2\right)^2 + 4\varepsilon_{11}^2\Delta\sigma^2}} \tag{7.68}$$

where $\hat{F}_{dx}^{(2)}$ is the amplitude of $F_{dx}^{(2)}$. The solid line in Fig. 7.38 is the theoretical curve of Eq. (7.68) for the above model ship. T_{swn} in the abscissa is the natural period of sway of the moored ship, T_g is the period of the envelope of a wave group as shown in Fig. 7.35. The solid small circles are the experimental values which are obtained by the wave groups resulting from the superposition of a 1.5 Hz fixed wave frequency and 1.6Hz - 1.8 Hz varying wave frequency. And the open small circles are also experimental ones that are given by the wave group by 1.0 Hz fixed wave frequency and 1.08 Hz - 1.25 Hz varying wave frequency. The coefficient of drift force for the two-component waves is given by the corresponding value for the average frequency according to Hsu's assumption (Hsu et al. 1970). These experimental values agree fairly well with the theoretical values, so the long-period ship motions by the varying drift force can be explained by the above method.
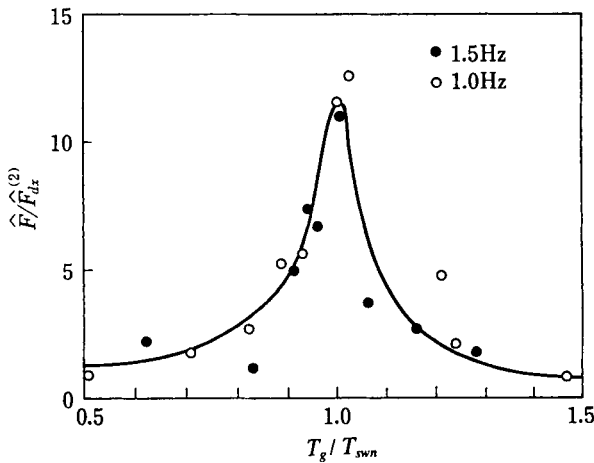
Fig. 7.38   Resonant characteristics of force acting to mooring lines by drift force

7.4.3 Long-period ship motions by harbor oscillations

As the natural period of a moored ship motion is around one minute, such motions as sway, surge and yaw resonate and become large when the long-period waves of about one minute apply to the ship. Since heave, pitch and roll have rather short natural periods, these ship motions are not so large under the long-period waves. So we will not deal with them here. When long-period

waves enter a harbor, the waves sometimes resonate inside the harbor and the height becomes large depending on the size of the harbor (Lee 1971). The Froude-Krylov force in this case can be obtained by integrating the pressure given by the velocity potential in 7.2 over the wetted surface of the ship. Because ship motions hardly make any waves in the long-period motions, the damping force by wave making can be neglected for long-period ship motions. For a rectangular ship, average acceleration in x and y directions $\dot{U}_1$ and $\dot{U}_2$, and angular acceleration $\ddot{\Theta}$ are represented using the Froude-Krylov forces $F_1^{(F)}, F_2^{(F)}, F_6^{(F)}$ as follows:

$$\dot{U}_1 = \frac{F_1^{(F)}}{m_B}, \; \dot{U}_2 = \frac{F_2^{(F)}}{m_B}, \; \ddot{\Theta} = \frac{3 \cdot F_6^{(F)}}{m_B\left((B/2)^2 + (L_s/2)^2\right)} \tag{7.69}$$

Assuming linear and symmetrical mooring, and neglecting the wave making damping coefficient in Eq. (7.61), namely $N'_{11} = N'_{22} = N'_{66} = 0$, then the equations of motions are given by:

$$\left(m_B + M_{11}^{(A)}\right)\ddot{X} + N_{11}^L \dot{X} + C_{11}X = \left(m_B + M_{11}^{(A)}\right)\dot{U}_1 \tag{7.70}$$

$$\left(m_B + M_{22}^{(A)}\right)\ddot{Y} + N_{22}^L \dot{Y} + C_{22}Y = \left(m_B + M_{22}^{(A)}\right)\dot{U}_2 \tag{7.71}$$

$$\left(I_{66} + M_{66}^{(A)}\right)\ddot{\Omega}_z + N_{66}^L \dot{\Omega}_z + C_{66}\Omega_z = \left(I_{66} + M_{66}^{(A)}\right)\ddot{\Theta} \tag{7.72}$$

Here I_{66} is the inertial moment of yaw, $M_{11}^{(A)}, M_{22}^{(A)}$ and $M_{66}^{(A)}$ are the added masses and moment of inertia of sway, surge and yaw, respectively, superscript L shows the factors by the mooring lines. In the above equations, letting

$$2\varepsilon_{11}^L = \frac{N_{11}^L}{m_B + M_{11}^{(A)}}, \; 2\varepsilon_{22}^L = \frac{N_{22}^L}{m_B + M_{22}^{(A)}}, \; 2\varepsilon_{66}^L = \frac{N_{66}^L}{I_{66} + M_{66}^{(A)}},$$

$$n_{11}^2 = \frac{C_{11}}{m_B + M_{11}^{(A)}}, \; n_{22}^2 = \frac{C_{22}}{m_B + M_{22}^{(A)}}, \; n_{66}^2 = \frac{C_{66}}{I_{66} + M_{66}^{(A)}}, \tag{7.73}$$

then, solving Eqs. (7.70) - (7.72), the amplitudes of sway, surge and yaw are given by the following:

$$\left|\hat{X}\right| = \frac{\left|\dot{U}_1\right|}{\sqrt{\left(n_{11}^2 - \sigma^2\right)^2 + \left(2\varepsilon_{11}^L\sigma\right)^2}}, \; \left|\hat{Y}\right| = \frac{\left|\dot{U}_2\right|}{\sqrt{\left(n_{22}^2 - \sigma^2\right)^2 + \left(2\varepsilon_{22}^L\sigma\right)^2}}$$

$$\left|\hat{\Omega}_z\right| = \frac{\left|\ddot{\Theta}\right|}{\sqrt{\left(n_{66}^2 - \sigma^2\right)^2 + \left(2\varepsilon_{66}^L\sigma\right)^2}} \tag{7.74}$$

As an example, Fig. 7.39 shows the amplification factor $\hat{Y}/\zeta_0$ of surge when the ship is moored at the position ①. Here d_s is the length of the ship and L is the wavelength. Though the damping coefficient obtained by the free oscillation test is $\varepsilon_{22}^L = 0.094(\text{sec}^{-1})$, the amplification factors near the resonance show nearly the same results as $\varepsilon_{22}^L = 0$. Thus we still have the problem of the damping coefficient, but we can approximately explain the floating body motion in the long-period range using the natural period obtained by the free oscillation test.
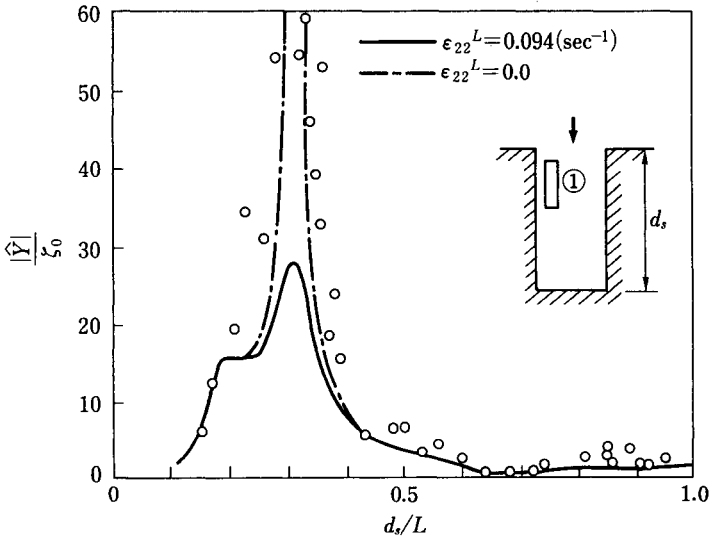
Fig. 7.39 Surge of ship moored at berth 1

7.4.4 Free oscillation as transient phenomenon

In the same way as when we carry out the free oscillation in the experimental basin, when a steady force is suddenly removed from a ship in the field, long-period free oscillations occur. On the contrary, from the state where the steady force does not apply, when the forces suddenly act, the free oscillations also occur (Sawaragi et al. 1978). As an example, the equation of free oscillation is obtained by setting the external forces to zero in the right hand side of Eq. (7.71). By solving this equation under the initial conditions, $Y = Y_0$, $\dot{Y} = 0$ for $t = 0$, the following free oscillations can be obtained.

$$Y = Y_o e^{-\varepsilon_{22}^L t} \sin\left(\sigma_{22} t + \delta\right),$$

$$\sigma_{22} = \sqrt{n_{22}^2 - \left(\varepsilon_{22}^L\right)^2}$$

(7.75)

where Y_0 and δ are the constants determined by the initial conditions. The free oscillations in the above decrease exponentially as shown in Fig. 7.40 and the time T_d when the tangent at $t = 0$ crosses the time axis is given by

$$T_d = 1/\varepsilon_{22}^L \tag{7.76}$$

We need a time longer than T_d to decrease perfectly. Even if we consider T_d the time for extinction, the wave making damping force for the long-period motion is very small and the damping force by the mooring system is also small, and thus it takes a long time to extinguish the long-period free oscillations.
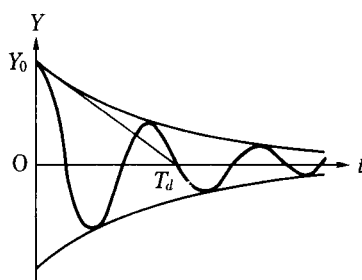
Fig. 7.40 Curve of damping

7.5 Countermeasures for Harbor Tranquility

7.5.1 Reduction of ship motions by harbor improvement
(1) Reduction method by perforated quay wall (Sawaragi et al. 1980)
   In 7.3, we show the calculation method of a wave force considering the reflection coefficient of the harbor boundary, but it was not enough to treat the evanescent mode waves. Here, even through two-dimensional treatment, we calculate the motions of the ship moored along a perforated quay wall by using the strict analytical method and discussed the effect of such a wall on the reduction of ship motions. There are two kinds of low reflection quay walls from the standpoint of hydraulic resistance. One is proportional to the velocity and the other is proportional to the velocity squared. Figure 7.41 shows the ship motions where the hydraulic resistance is proportional to the velocity. Here T is wave period, T_{Rn} is the natural period for roll, l_w is the half breadth of the perforated wall, a is the half breadth of the ship, λ is the ratio of porosity, $r_2 - l_w$ is the breadth of the free water region and we set the resistance coefficient through the wall $\mu_d = 4\pi/T$. The body motions before the low-reflection wall are expressed using the following potentials for the five regions:

$$\Phi_n(x, z, t) = \phi_n(x, z)e^{-i\sigma t} \quad : (n = \mathrm{I} \sim \mathrm{V}) \tag{7.77}$$

$$\phi_1 = \left\{A_o e^{ik(x_1+a)} + B_o e^{-ik(x_1+a)}\right\}\frac{\cosh k(h+z)}{\cosh kh} + \sum_{n=1}^{\infty} A_n e^{k_n(x_1+a)}\frac{\cos k_n(h+z)}{\cos k_n h}$$

$$\phi_{II} = C_0\frac{x_1}{a} + D_0 + \sum_{n=1}^{\infty}\left(C_n \cdot \frac{\sinh\dfrac{n\pi x_1}{h-d}}{\sinh\dfrac{n\pi a}{h-d}} + D_n \cdot \frac{\cosh\dfrac{n\pi x_1}{h-d}}{\cosh\dfrac{n\pi a}{h-d}}\right)$$

$$\cdot\cos\left(n\pi\frac{h+z}{h-d}\right) - \frac{i\sigma\hat{Z}}{h-d}\left\{\frac{x_1^2}{2} - \frac{(h+z)^2}{2} + \frac{(h-d)^2}{6}\right\}$$

$$-\frac{i\sigma\hat{\Omega}_y x_1}{h-d}\left\{\frac{x_1^2}{2} - \frac{(h+z)^2}{2} + \frac{(h-d)^2}{6}\right\}$$

$$\phi_{III} = \left\{E_o e^{-ik(x_1-r_1)} + F_o e^{ik(x_1-r_1)}\right\}\frac{\cosh k(h+z)}{\cosh kh}$$ (7.78)

$$+\sum_{n=1}^{\infty}\left\{E_n e^{-k_n(x_1-r_1)} + F_n e^{k_n(x_1-r_1)}\right\}\frac{\cos k_n(h+z)}{\cos k_n h}$$

$$\phi_{IV} = \sum_{n=0}^{\infty}\left(G_n\frac{\cos \bar{k}_n x_2}{\cos \bar{k}_n l_w} + H_n\frac{\sin \bar{k}_n x_2}{\sin \bar{k}_n l_w}\right)\frac{\cosh \bar{k}_n(h+z)}{\cosh \bar{k}_n h}$$

$$\phi_V = I_0\cos k(r_2 - x_2)\frac{\cosh k(h+z)}{\cosh kh}$$

$$+\sum_{n=1}^{\infty} I_n\cosh k_n(r_2 - x_2)\frac{\cos k_n(h+z)}{\cos k_n h}$$

where A_0, A_n, B_0, B_n,..., I_0, and I_n are the complex constants, k and k_n are given by Eq. (7.41) and $\bar{k}_n$ is the complex eigenvalue determined by the following equation:

$$\bar{k}_n h\tanh \bar{k}_n h = \left(1 - i\frac{\lambda\mu_d}{\sigma}\right)\frac{\sigma^2 h}{g}$$ (7.79)

Furthermore, there are two coordinate systems, that is, the origin of the (x_1, z) system is at the center of the body of the still water line, and the origin of the (x_2, z) system is at the center of the perforated wall. Considering the velocity potential in the perforated wall, we assume Darcy flow. Then the boundary conditions at the free surface and sea bottom are given by

$$\frac{\partial\phi_{IV}}{\partial z} = \left(1 - i\frac{\lambda\mu_d}{\sigma}\right)\frac{\sigma^2 \phi_{IV}}{g} \;:\; z = 0, \quad \frac{\partial\phi_{IV}}{\partial z} = 0 \;:\; z = -h$$ (7.80)

The other boundary conditions are given in the same manner as those in Chapter 2.
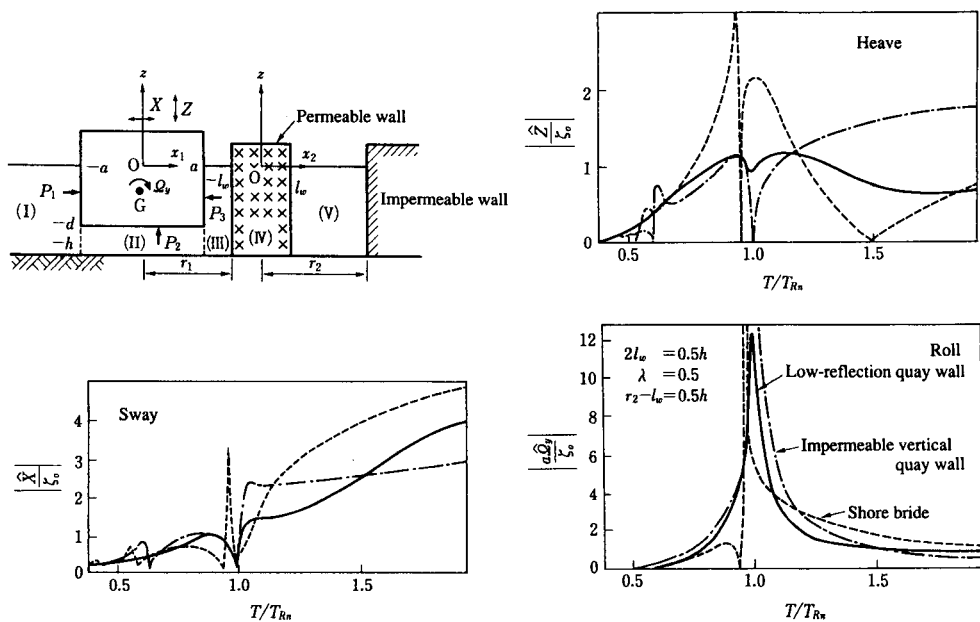
Fig. 7.41   Reduction of ship motion by the structure of the quay wall

Letting horizontal wave forces be P_1, P_3, vertical wave force P_2 and horizontal, vertical, and rotational restoring forces R_H, R_U, R_M, then the equations of motion are expressed as

$$\left.\begin{aligned}
m_B\ddot{X} &= P_1 - P_3 + R_H \\
m_B\ddot{Z} &= P_2 - \rho g B L_s Z + R_v \\
I_{55}\ddot{\Omega}_y &= M_{P1} + M_{P2} + M_{P3} - \rho g B d L_s \overline{GM}\,\Omega_y + R_M
\end{aligned}\right\} \tag{7.81}$$

Here M_{Pi} is the moment by P_i. By solving the simultaneous equations composed by the above boundary conditions and equations of motions, the unknown constants of ship motions and velocity potentials are decided. As an example, the motions of a ship under the conditions of $B = 0.45$m, $d = 0.09$m and $h = 0.211$m, are shown in Fig. 7.41. In the same figure, the ship motions before an impermeable wall are also shown for the sake of comparison. From Fig. 7.41, we can see that roll and sway for a low-reflection wall become smaller than those for an impermeable wall around the wave period less than 1.5 times of the roll natural period, but these relations are reversed at the longer wave periods, while heave is nearly the same at the wave period less than 1.2 T_{Rn}, but over this period, heave becomes very small.

From these results, we can understand that the low-reflection quay wall is more effective than the impermeable quay wall from the standpoint of moored ship motions. But in the case of a ship moored a breadth off the quay wall (equivalent to mooring to a shore bridge), it is impossible to attenuate all ship motions, different from the low-reflection quay wall as shown in Fig. 7.41.

Figure 7.42 shows the response of ship motions in which the permeable resistance of the perforated wall is proportional to the velocity squared. In this case, the water body is divided into four regions. In the perforated wall, the velocity potential does not exist, but for the other domain, the velocity potentials are the same as above. The following relations are obtained as the condition of continuity of velocity and pressure at $x_2 = \pm l_w$:

$$\left(\frac{\partial \phi_{\mathrm{III}}}{\partial x_2}\right)_{x_2 = -l_w} = \left(\frac{\partial \phi_{\mathrm{IV}}}{\partial x_2}\right)_{x_2 = l_w} \tag{7.82}$$

$$-\left(\frac{\partial \phi_{\mathrm{III}}}{\partial t}\right)_{x_2 = -l_w} + \left(\frac{\partial \phi_{\mathrm{IV}}}{\partial t}\right)_{x_2 = l_w} = 2l_w \left\{\frac{\partial V}{\partial t} + \frac{f}{2D_h}|V| \cdot V\right\} \tag{7.83}$$
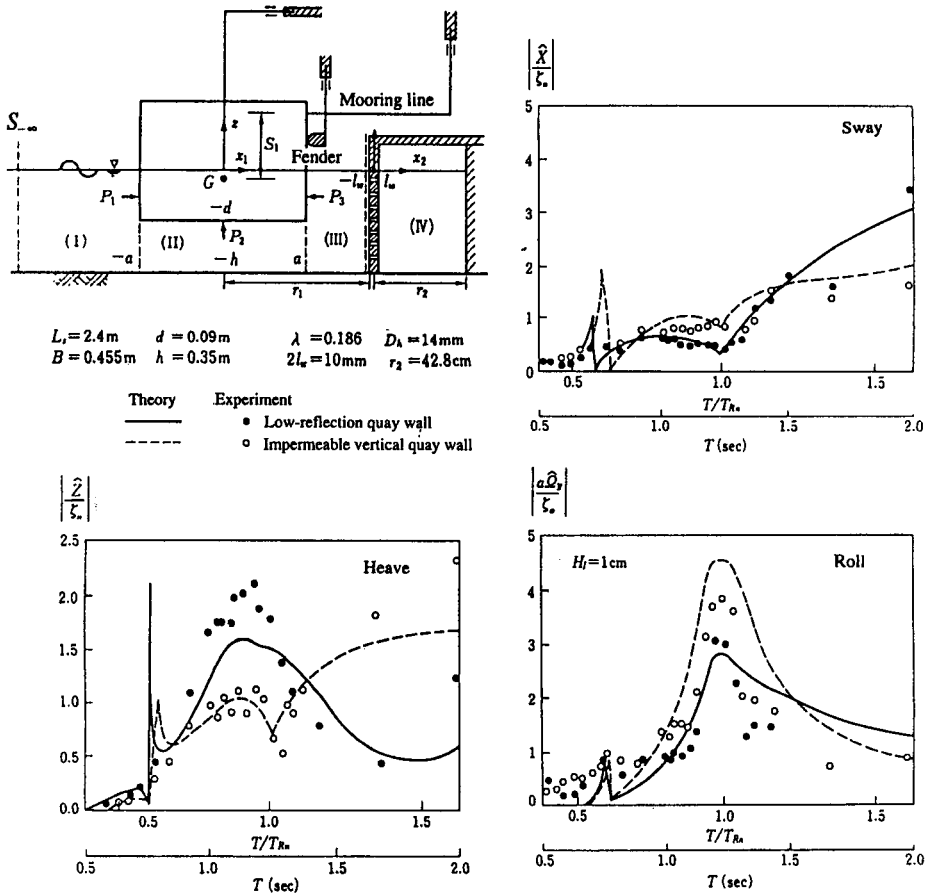
Fig. 7.42 Ship motion moored along a low-reflection quay wall where the permeable resistance is proportional to the velocity squared

Here f is the coefficient of energy loss, D_h is the diameter of the hole, V is the velocity through the perforated wall. V is decided by the velocity potential and Eq. (7.83) contains V squared, so the simultaneous equations become nonlinear. Accordingly, we must find out the solution satisfying the continuity condition of pressure by the iteration method, then the ship motions can be obtained. Comparing the ship motions with those of the impermeable quay wall, roll and sway become smaller at the range of wave period less than $1.2\ T_{Rn}$ but heave becomes larger. When the wave period becomes larger than $1.2\ T_{Rn}$, then the relations become the reverse.
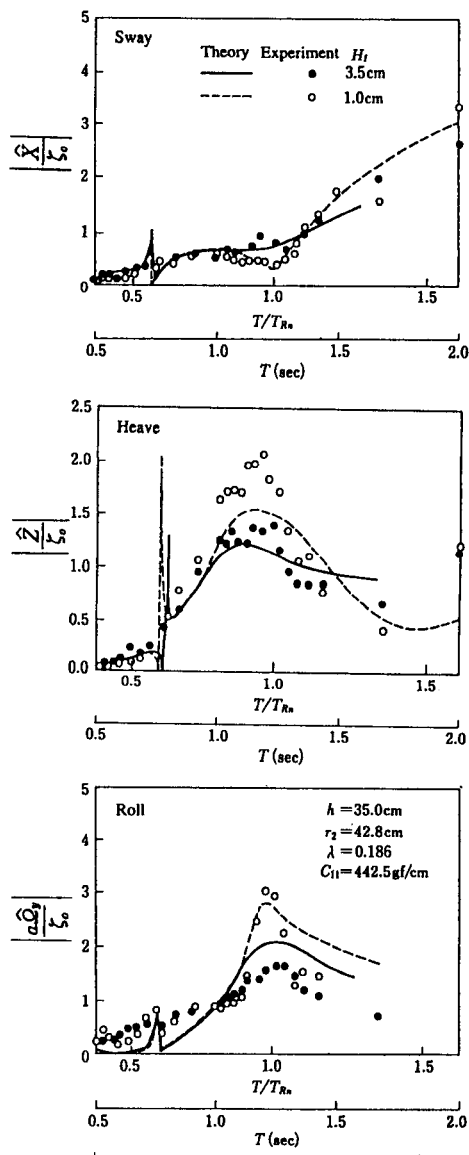
Fig. 7.43   Effect of incident wave height on ship motions

Figure 7.43 shows the nonlinearity of the ship motions for the two incident wave heights, 1cm and 3.5cm. The bigger the incident wave height becomes, the larger nonlinear resistance becomes. So the response of roll and heave normalized by the incident wave height becomes small near the resonance of roll. In other words, the efficiency of reduction of ship motions by the perforated low-reflection wall is small when the incident wave height is small.

In the above, we discussed the reduction of ship motions by two kinds of low-reflection walls. Assuming the wave height in a harbor to be rather small, the quay wall whose resistance is proportional to the velocity is preferable because the efficiency is still high even at the small wave height.

(2) Reduction method by berth selection (Sawaragi and Kubo 1982)

Since the long-period wave has the long wavelength, ship motions are changed by the mooring position. Moreover, the period of long-period ship motions is sometimes similar to that of harbor oscillations, so we consider the reduction method by the different berths in the slip. The mooring positions are shown in Fig. 7.44, namely, berths ①, ② and ③. When the incident waves enter normally, it is clarified from the experiment that surge predominates and sway and yaw are very small at berths ① and ②, while at berth ③, sway predominates and other motions hardly occur. So we show the surge for berths ① and ②, and sway for berth ③ in Fig. 7.45. Here we assume symmetrical moorings for all ships. In the figure, d_s is the ship length, L is the wavelength, $|\hat{Y}|$ $|\hat{X}|$ and ζ_0 are the amplitudes of surge, sway, and the incident waves, respectively. From this figure, we can see that the surge at berth ① is larger than at berth ②, while sway at berth ③ is very small. Judging from the results, the most suitable berth in the slip is berth ③.
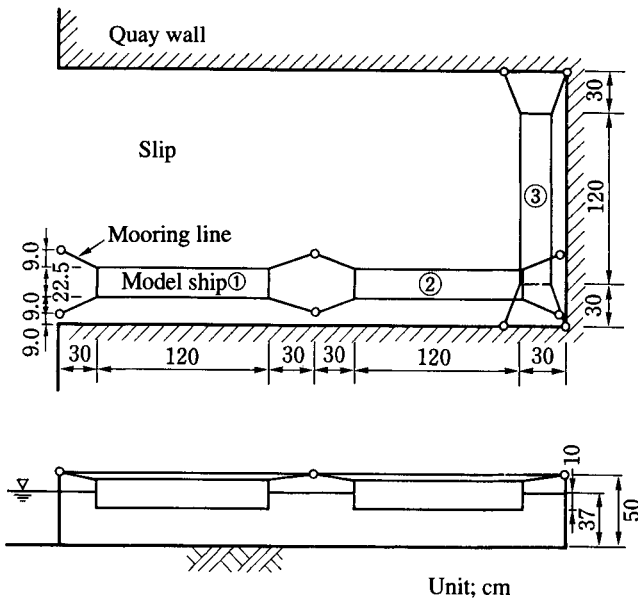
Fig. 7.44 Arrangement of the moored ship inside the slip
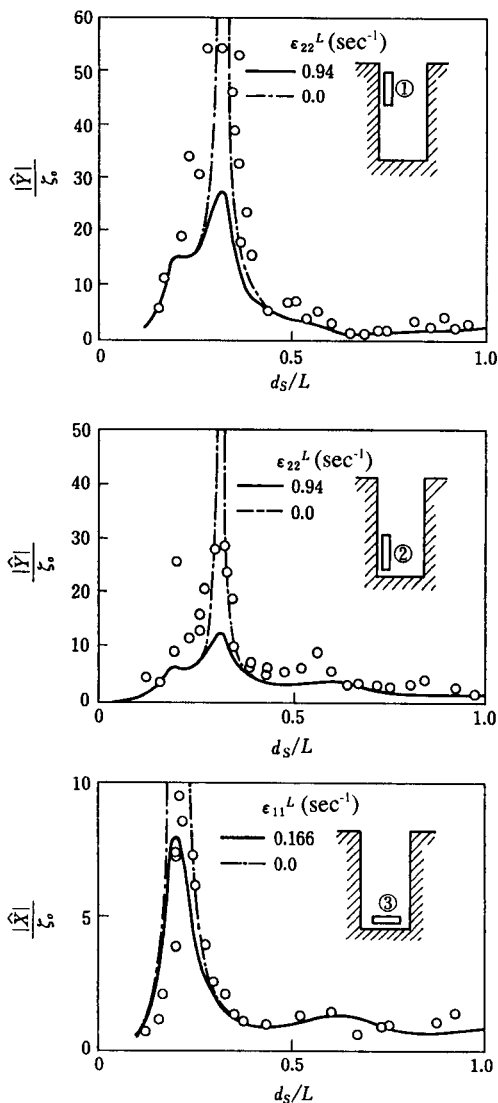
Fig. 7.45 Reduction of long-period ship motions by berth selection inside the slip

(3) Attenuation of ship motions by breakwaters

Sawaragi and Aoki (1992) numerically investigated the effects of narrowing the harbor mouth and constructing inner breakwaters for a rectangular ship (60m x 15m) in an L-shaped harbor as shown in Fig. 7.46, where the water depth and the draft of the ship are 21m and 4.9m, respectively, and the ship is assumed to be moored 19m distant from the nearest quay by four linear springs with spring constants of 9.35 tf/m.
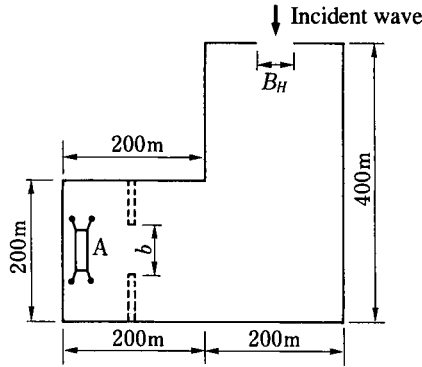
Fig. 7.46   Harbor used in numerical simulation

Figures 7.47 and 7.48 show the absolute values of the response functions in the sway mode in two cases with different widths of harbor entrance B_H, where L/L_S represents the ratio of wavelength (L) to the ship length (L_S) and H_I^E and H_{11}^S are nondimensionalized by multiplying and dividing by $\rho g h^2$ respectively. The peaks of the response function of the wave exciting force H_I^E is reduced by narrowing the harbor entrance, although the response functions of motion H_{11}^S in both cases are almost the same. This tendency is also found in other modes of motion, and thus the construction of a longer breakwater at the entrance has the effect of reducing the response function of the wave exciting force H^E, because the change at the harbor entrance, located far from the ship, has less influence on the added mass and damping than on the wave exciting force.
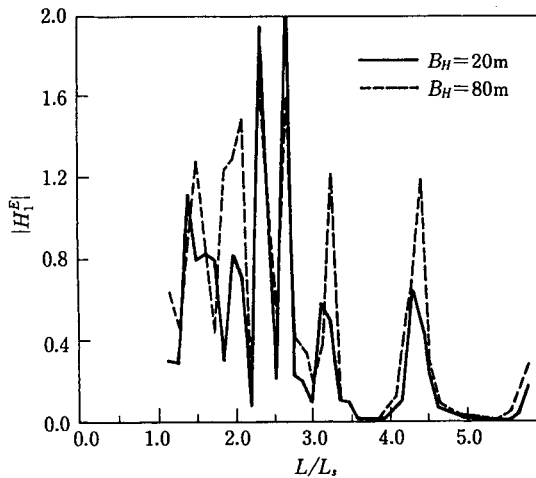
Fig. 7.47   Dependence of H^E on harbor width (sway)
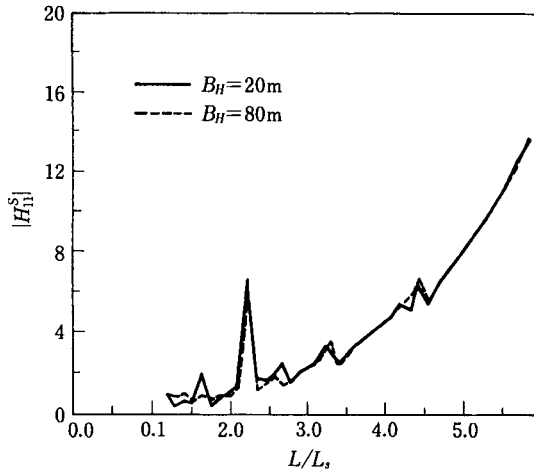
Fig. 7.48   Dependence of H^S on harbor width (sway)

Figures 7.49 and 7.50 show H_1^E and H_{11}^S for the cases both with and without the inner breakwaters represented by the broken lines in Fig. 7.46. A little change can be seen in H_{11}^S, but it is not particularly significant, while the curve for H_1^E changes its form and does not show an overall reduction. This means that, in considering the construction of inner breakwaters near the ship, careful attention must be given to the frequency range of incoming waves, and to the effect on other modes of ship motion.
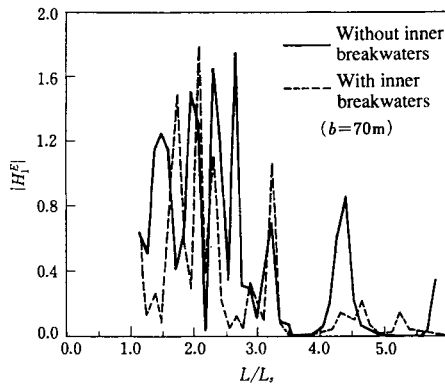
Fig. 7.49   Influence of inner breakwaters on H^E (sway)
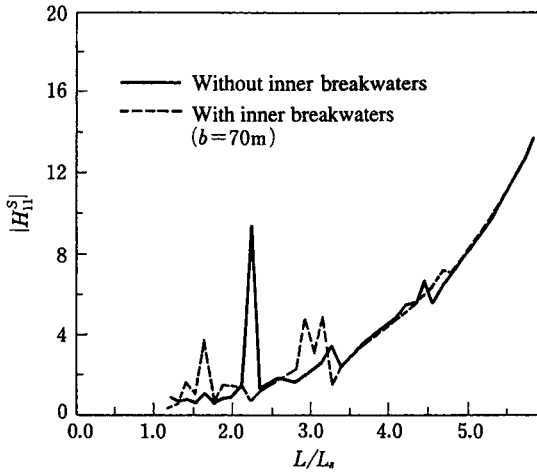
Fig. 7.50 Influence on inner breakwaters on H^S (sway)

7.5.2 Reduction of ship motion by the mooring system

(1) Reduction of short-period ship motions

(a) Reduction method by the spring characteristics of the mooring systems (Sawaragi and Kubo, 1983)

It is clarified in **7.4.1** that an asymmetrical mooring ship receives waves, then it produces subharmonic motions. Figure 7.51 shows the response of sway over the wide range of wave periods. The experimental results (solid circles) and numerical results (solid line) are shown in the figure. T_{sn} in the abscissa obtained by the free oscillation test is the ship colliding interval against the fenders, and X_{max} in the ordinate is the maximum value of distance off the quay wall. The response curve shows many peaks and these peaks occur at the wave period which satisfies the relation $m_d \times T = T_{sn}$. These are the above mentioned subharmonic motions. When the mode number m_d becomes larger than 10 in Fig. 7.51, then the amplification factor of sway suddenly becomes small and the mode number also decreases to 1. From this fact, we can see that the mode number is limited within certain finite numbers. Now, we assume that the ship is moored symmetrically with only fenders or only mooring lines, then their natural periods of sway , T_{SF} and T_{SL} are given:

$$T_{SF} = 2\pi\sqrt{\frac{m_B + M_{11}^{(A)}}{C_F}} = 10 \text{ sec} \quad \text{(field scale)}$$

$$T_{SL} = 2\pi\sqrt{\frac{m_B + M_{11}^{(A)}}{C_L}} = 156 \text{ sec} = 2T_{sn} \quad \text{(field scale)} \tag{7.84}$$

Using these periods, the maximum mode number can be established approximately by the next equation:

$$\max(m_d) = \left(\frac{T_{SL} + T_{SF}}{2}\right)\bigg/ T_{SF} = \frac{T_{sn}}{T_{SF}} + 0.5 \tag{7.85}$$
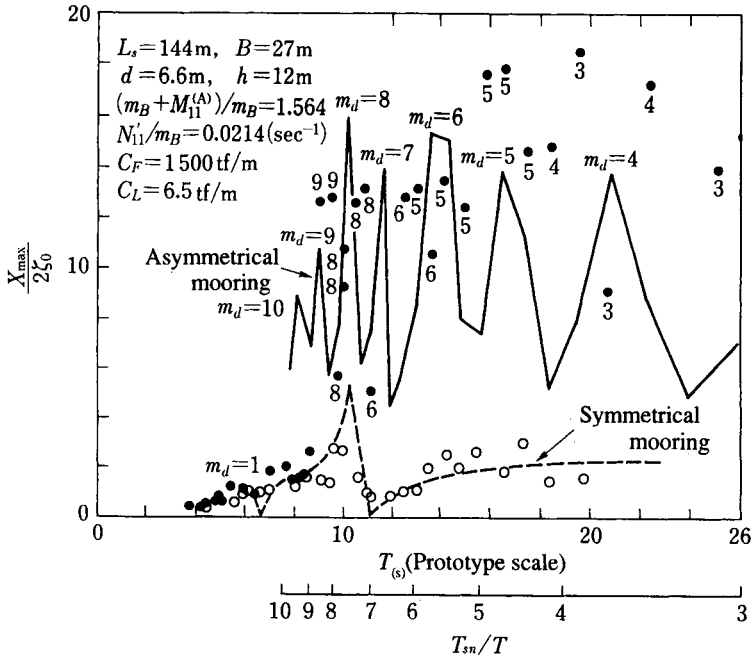
Fig. 7.51 Reduction of subharmonic motions of sway by symmetrizing the spring constants of the mooring system

It is clear from the above that sway in asymmetrical mooring occurs when the subharmonic motions are over the wide range between T_{SF} and T_{Sn}. So the bigger the ratio of C_F to C_L is, the wider the range is. On the contrary, C_F and C_L become close, then the subharmonic motions in the short-period range disappear and the amplification factor also becomes smaller. The small circles and the interrupted line in Fig. 7.51 express the amplification factor of sway in the symmetrical mooring, which are one-order smaller than the asymmetrical one.

(b) Reduction method by dash-pot (Sawaragi and Kubo 1982)

Including dash-pots in the mooring system can be very useful for damping ship motions. Figure 7.52 shows the dash-pot used in our experiment and the set up of the model ship. Giving each velocity potential for the region in the same manner as the above low-reflection quay wall and matching these potentials at the boundaries, the ship motions can be obtained. Figure 7.53 shows the comparison of ship motions with and without dash-pots. Also from this figure we can understand that all ship motions can be decreased throughout the wave period by applying the dash-pots. These results suggest to us that the dash-pots system is more useful than the low-reflection quay wall from the stand point of the ship motion reduction described in **7.5.1**.
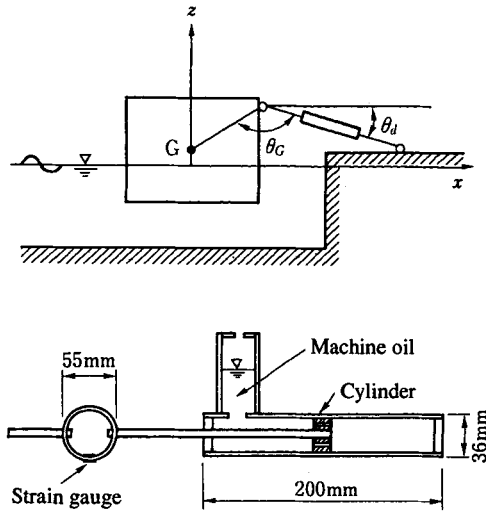
Fig. 7.52 Model dash-pot and installation to a moored ship

(2) Reduction of long-period ship motions
(a) Reduction method by changing mooring system from asymmetrical to symmetrical (Sawaragi and Kubo et al. 1984, 1992)

We described above (1) that the subharmonic sway motions happened in the asymmetrical mooring system and the motions could be removed by changing to symmetrical mooring. If we wish to realize the symmetrical mooring, we have two different methods. At first, we should reduce the stiffness of the fender. By using an ordinary pneumatic fender, we can realize the symmetrical mooring considerably. Secondly, the stiffness of the mooring line should be strengthened. According to this idea, nylon tail rope which combines a piece of nylon rope with wire rope is presented to make the spring constant large. These two methods are useful for the reduction of subharmonic motions.

(b) Reduction method by changing the spring constants of mooring lines (Kubo and Barthel, 1993)

Here we consider the effect of the spring constant of the symmetrical mooring upon the long-period ship motions. Now for an example, we calculate the sway motions of a rectangular ship, length 144m, breadth 27m and draught 6.6m, and two kinds of spring constants are set 6.5 tonf/m and 108.4 tonf/m. The results are shown in Fig. 7.54, T_{swn} is the natural period of sway. From this, by changing the spring constants, we can surprisingly change the sways corresponding to the wave periods 30 ~ 120s.

In the same figure, the ship motions moored along shore bridge (where the ship is moored 30m off the vertical wall) are also shown. It can be pointed out that the ship motions become larger than those close along the vertical quay wall, in other words, a shore bridge is not so desirable for moored ship motion.

Figure 7.55 expresses the short-period ship motions under the above spring constant of the mooring lines. Even if we change the spring constants, it is clear that it is very difficult
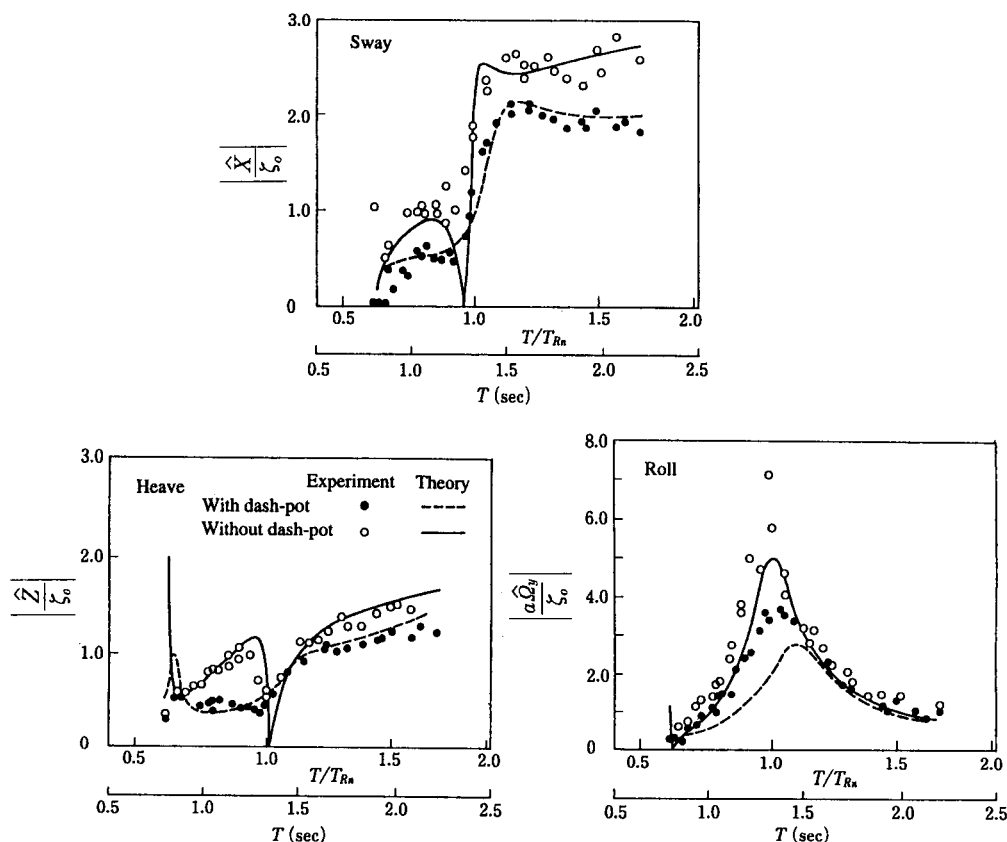
Fig. 7.53   Reduction of ship motion by dash pot

to reduce the short-period ship motions. So if we strengthen the spring constant to avoid matching the natural period of sway with the period of seiche in a basin and to decrease the long-period ship motions, we must also pay enough attention to the mooring line strength. As the mooring lines receive a force which is equal to the spring constant multiplied by the line extension due to short-period ship motions, the force will become strong under the stiff mooring lines.

(c) Reduction method by the damping force (Kubo 1975)

Next , we will consider the motions of moored ships that become large in around one minute, such as surge and sway.

As an example, we investigate surge motions. In the same manner as Eq. (7.67), the uncoupled surge equation of motion can be expressed as

$$\ddot{Y} + 2\varepsilon_{22}\dot{Y} + n_{22}^2 Y = H_I A_{22} \sin \sigma t \tag{7.86}$$
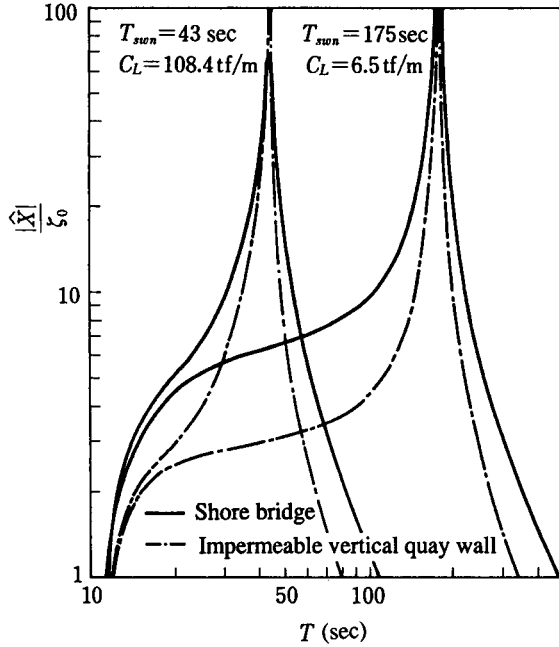
Fig. 7.54 Resonant characteristics of sway at the range of long-period

where ε_{22} is the damping coefficient, n_{22} is the natural angular frequency, A_{22} is the amplitude of external force normalized by the incident wave height H_I and σ is the angular frequency of external force. Then the amplitude of stationary ship motions $|\hat{Y}|$ is given by

$$\frac{|\hat{Y}|}{H_I} = \frac{A_{22}}{\sqrt{\left(n_{22}^2 - \sigma^2\right)^2 + \left(2\varepsilon_{22}\sigma\right)^2}} \tag{7.87}$$

Now, using ε'_{22} for the damping coefficient without dash-pots, ε''_{22} for the one with dash-pots and ε_{22} for the total, we can get the equation

$$\frac{|Y_d|_{max}}{|Y_0|_{max}} = \frac{\varepsilon'_{22}}{\varepsilon_{22}} = \frac{1}{\beta_{22}} \tag{7.88}$$

Here the subscripts d and 0 correspond to with and without dash-pots, β_{22} shows the ratio of ε_{22} to ε'_{22}. The ship's own damping coefficient can be estimated by the free oscillation test of real ship as

$$2\varepsilon'_{22} = \frac{2}{T_{sun}} \tag{7.89}$$

where T_{sun} is the natural period of surge.
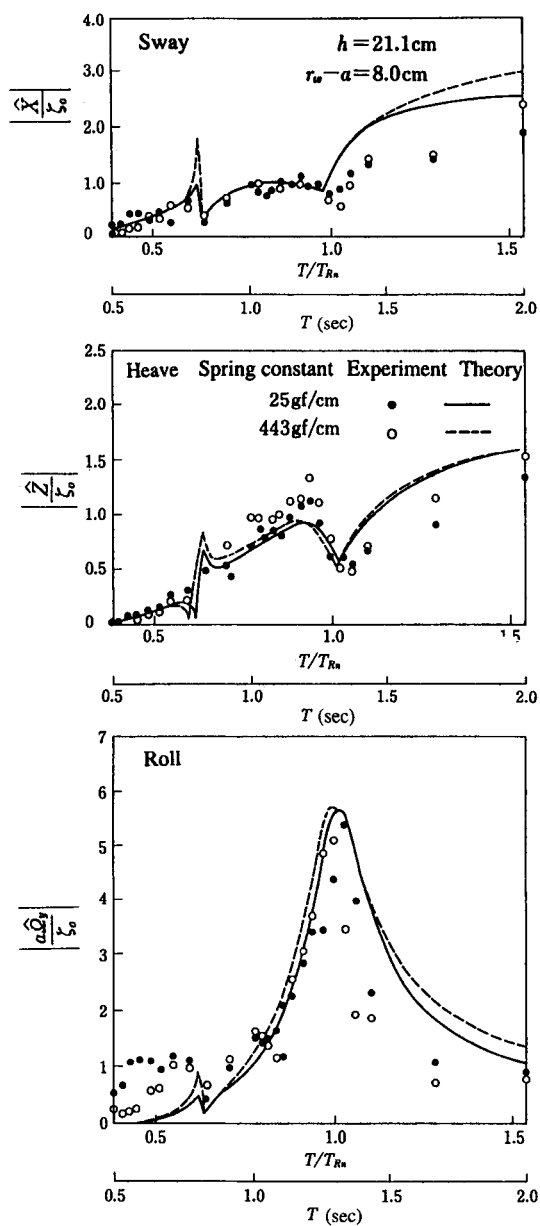
Fig. 7.55 Effect of spring constant of mooring line on short-period ship motions

As shown in Fig. 7.56, bow and stern lines and spring lines are supposed to be moored with angle δ_m to the water line. Using k_d (= damping force / velocity) for the damping coefficient of the dash-pot equipped to the lines, the damping force for surge is given by $(2\,k_d\cos^2\delta_m\,)\dot{Y}$. From this, the additional damping coefficient ε_{22}'' by dash-pots is given as

$$2\varepsilon_{22}'' = \frac{2\,k_d\cos^2\delta_m}{M_B + M_{22}^{(A)}} \tag{7.90}$$

Then, using k_d for the coefficient which decreases the surge to $1/b_{22}$ and F_{22} for the maximum tension on the mooring line, these are presented

$$k_d = \frac{(\beta_{22}-1)\left(m_B + M_{22}^{(A)}\right)}{T_{sun}\cos^2\delta_m}$$

$$F_{22} = k_d n_{22} \frac{|\hat{Y}_0|_{max}}{\beta_{22}}\cos\delta_m \tag{7.91}$$

In the same manner, k_d and F_{11} for sway are given by

$$k_d = \frac{(\beta_{11}-1)\left(m_B + M_{11}^{(A)}\right)}{T_{swn}\sin^2\delta_m}$$

$$F_{11} = k_d n_{11} \frac{|\hat{X}_0|_{max}}{\beta_{11}}\sin\delta_m \tag{7.92}$$

Now setting $\beta_{22} = \beta_{11} = 5$, $M_{22}^{(A)} = 0.1 m_B$, $M_{11}^{(A)} = m_B$, $T_{sun} = T_{swn} = 60$ sec, $\delta_m = 30°$, $|\hat{X}_0|_{max} = |\hat{Y}_0|_{max} = 1m$, m_B = full load displacement, the relation between the gross tonnage and the maximum tension of the line is shown in Fig. 7.57. In the same figure, the mooring line strength by the Japan Maritime Association, and the strength of the bitt by the [Technical Standard of Harbor Structure] are shown. It can be seen that possibilities for improving safety and efficiency of cargo handling exist by applying the dash-pot mooring lines to the mooring system.
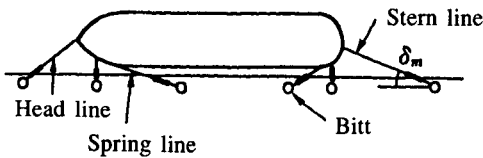
Fig. 7.56 Arrangement of mooring lines

7.6 Problems Associated with Relative Motions of Two Adjacently-Moored Floating Bodies

It is not rare that two or more floating bodies are moored adjacently in a harbor. Ships moored along a floating pier, ships handling cargoes with a barge, fishing boats in a fishery harbor, and pleasure boats in a marina, are examples of floating bodies moored adjacently. When considering the motions of two floating bodies, it is important to know the hydrodynamic interaction between them. However only a few investigations have been done on the interactive motions of two floating bodies. Ohkusu (1976), and Kim and Fang (1985) discussed the relative motions between two ships by means of the strip theory. Kubo and Saito (1990) investigated the motions between two floating bodies by the boundary integral equation method, which can deal with arbitrary shapes of the floating body, the sea bottom and also the quay wall. In this section, the analysis by Kubo and Saito (1990) is introduced.
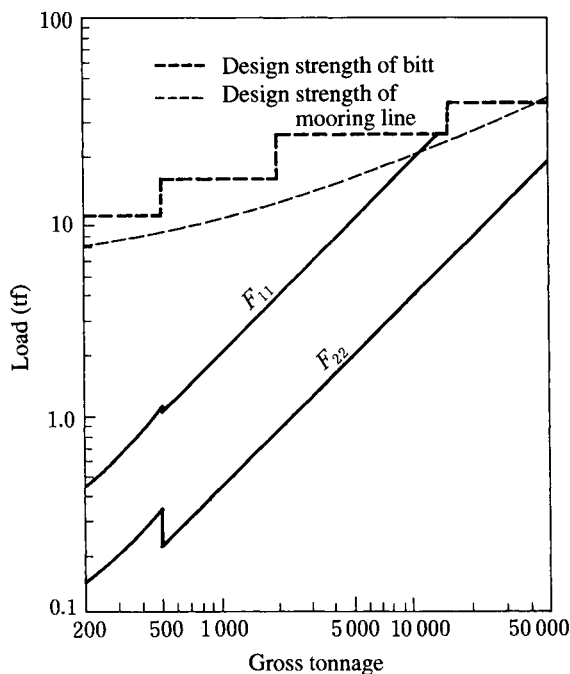
Fig. 7.57 Relation between the strength of bitt and mooring line force when the long-period ship motions are decreased by one-fifth.

7.6.1 Calculation method of the interactive motions of two floating bodies

Two floating bodies are assumed to be oscillating harmonically in regular waves with angular frequency σ. Then, the motions can be expressed by Eq. (7.30) for each body. The two- and three-dimensional calculation methods are explained below.

(1) Two-dimensional calculation method

Let us consider the situation that two floating bodies, "a" and "b", are moored in linear mooring systems, as shown in Fig. 7.58. The fluid is assumed to be incompressible and inviscid, and the fluid motion is treated to be irrotational. The cross section of floating bodies, the sea bottom or quay wall are arbitrary. The velocity potential Φ in the region (I) around the two floating bodies (see Fig. 7.58) is given by

$$\Phi(x, z; t) = \frac{gH_I}{2\sigma} \phi(x, z) e^{-i\sigma t} \tag{7.93}$$
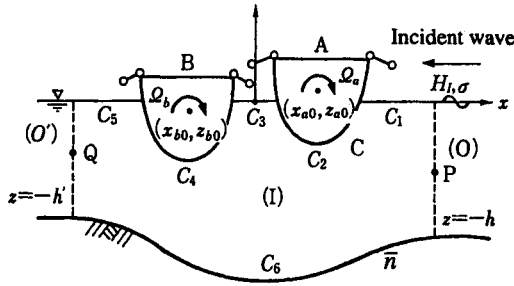
Fig. 7.58 Two-dimensional definition sketch for two floating bodies

where g is the gravitational acceleration and ϕ is the nondimensional potential function that must satisfy the Laplace equation.

In the regions (O) and (O') which are set far away from two floating bodies, nondimensional potential functions ϕ and ϕ' are given by

$$\phi(x, z) = \left(e^{-ikx} + \tilde{K}_R e^{-ikx} \right) \frac{\cosh k(h + z)}{\cosh kh} \tag{7.94}$$

$$\phi'(x, z) = \tilde{K}_T e^{-ik'x} \frac{\cosh k'(h' + z)}{\cosh k'h'} \tag{7.95}$$

where $\tilde{K}_R$ and $\tilde{K}_T$ are the reflection and transmission coefficients of waves, k and k' are the wave numbers corresponding to the region (O) and (O'), respectively.

On the boundary C that covers the region (I), the potential function $\phi(x, z)$ can be expressed by using Green's formula:

$$\phi(x, z) = \frac{1}{\pi} \int_C \left[\phi(x', z') \frac{\partial}{\partial \bar{n}} \left\{ l_n \left(\frac{r}{h_0} \right) \right\} - l_n \left(\frac{r}{h_0} \right) \frac{\partial \phi(x', z')}{\partial \bar{n}} \right] ds \tag{7.96}$$

where, $l_n(r/h_0)$ is the fundamental solution of two-dimensional Laplace equation, (x', z') is the coordinate of a source point, r denotes the distance between (x', z') and (x, z), h_0 is the representative length, $\bar{n}$ is the outward normal on the boundary C.

In Eq. (7.96), the free surface condition is applied on C_1, C_3, and C_5, the fixed solid boundary condition on C_6, the kinematical boundary condition of the floating bodies on C_2 and C_4. The continuity conditions of fluid particle velocity and pressure are applied at the points P and Q.

Solving the simultaneous equation composed of the equations of motions of two floating bodies, Eq. (7.96) and the boundary conditions, the potential function ϕ (x, z) on C, $\bar{K}_R$, $\bar{K}_T$, and the amplitude of motions of the two floating are obtained in a complex form.

(2) Three-dimensional calculation method

The motions are calculated by the three-dimensional boundary integral method using Green's function. In the case of a single floating body, the calculation method has been described in **7.3.1**. The following is a simple extension to the case of two floating bodies.

As shown in Fig. 7.59, the normalized radiation potential around the two floating bodies can be separated as ϕ_{Ra} and ϕ_{Rb}, where subscripts a and b indicate the quantities caused by of the floating bodies "a" and "b", respectively. The basic equations and the boundary conditions are Eqs. (7.31), (7.32), (7.33), (7.35) and (7.38), and both ϕ_{Ra} and ϕ_{Rb} have to satisfy them. The kinematic boundary conditions of the two floating bodies are given as follows:

$$\frac{\partial \phi_{Ria}}{\partial \overline{n}} = \overline{\xi}_{ia}, \quad \frac{\partial \phi_{Ri'b}}{\partial \overline{n}} = 0 \qquad : \text{on } S_a \qquad (7.97)$$

$$\frac{\partial \phi_{Ria}}{\partial \overline{n}} = 0, \quad \frac{\partial \phi_{Ri'b}}{\partial \overline{n}} = \overline{\xi}_{i'b} \qquad : \text{on } S_b \qquad (7.98)$$

where $\overline{\xi}_{ia}$ and $\overline{\xi}_{i'b}$ are normalized velocities of the i-mode of floating body "a" and i'-mode of floating body "b," respectively.

The radiation potentials at point P corresponding to Eq. (7.37) are shown as follows:

$$\phi_{Ria}(P) = e' \left[\iint_{S_a} \left\{ \phi_{Ria}(Q) \frac{\partial}{\partial \overline{n}} G(P, Q) - \overline{\xi}_{ia}(Q) \, G(P, Q) \right\} ds(Q) \right.$$
$$\left. + \iint_{S_b} \left\{ \phi_{Ria}(Q) \frac{\partial}{\partial \overline{n}} G(P, Q) ds(Q) \right\} \right] \qquad (7.99)$$

$$\phi_{Ri'b}(P) = e' \left[\iint_{S_a} \left\{ \phi_{Ri'b}(Q) \frac{\partial}{\partial \overline{n}} G(P, Q) \, ds(Q) \right\} \right.$$
$$\left. + \iint_{S_b} \left\{ \phi_{Ri'b}(Q) \frac{\partial}{\partial \overline{n}} G(P, Q) - \overline{\xi}_{i'b}(Q) \, G(P, Q) \right\} ds(Q) \right] \qquad (7.100)$$

7.6.2 Characteristics of the relative motions of two floating bodies

(1) The influence of an adjacent floating body on hydrodynamic force

(a) The relations of the hydrodynamic coefficients between two floating bodies

We discuss here the situation that the floating bodies "a" and "b" oscillate under the l-mode and m-mode respectively. Using the similar manner to that for a single body, the relations between hydrodynamic coefficients of two floating bodies are given as follows, in spite of the existence of the quay wall and the adjacent floating body
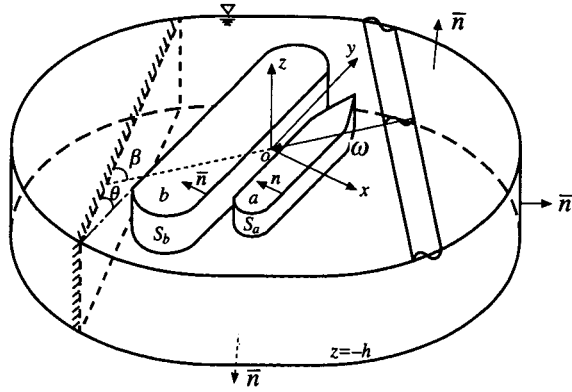
Fig. 7.59 Three-dimensional definition sketch of two floating bodies

$$M_{lama} = M_{mala}, N_{lama} = N_{mala} \atop M_{lbmb} = M_{mblb}, N_{lbmb} = N_{mblb} \Biggr\} \qquad (7.101)$$

$$M_{lamb} = M_{mbla}, N_{lamb} = N_{mbla} \qquad (7.102)$$

where M is the added mass, N is the damping coefficient and the subscript $_{lamb}$ indicates the effect of the m-mode motion of floating body "b" on the l-mode of floating body "a".
(b) The influence of adjacent floating body on hydrodynamic coefficients
Figure 7.60 shows the hydrodynamic coefficients of sway. The hydrodynamic interaction between a floating body and a quay wall is not negligible. The interaction between two
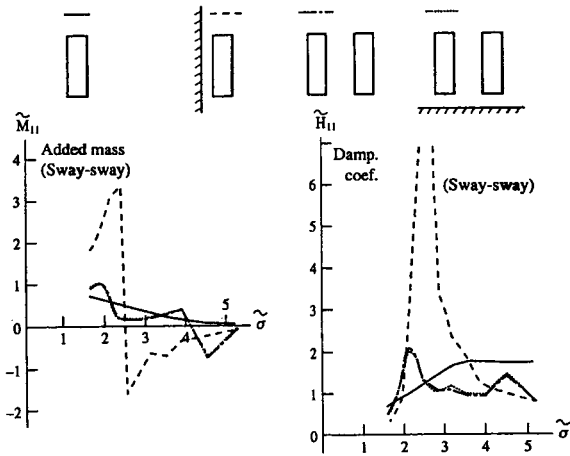
Fig. 7.60 The influence of an adjacent floating body on hydrodynamic coefficients

floating bodies is not also negligible as shown in Fig. 7.60. In some special cases, the influence of a quay wall on the hydrodynamic coefficients can be neglected as shown by the dotted lines and dashed-and-dotted lines.

(2) The influence of mooring systems on relative motions between two floating bodies

It is considered that the relative motions between two floating bodies are influenced by the mooring systems. Figures 7.61 (a) – (d) show the relative horizontal and vertical motions $|X/\zeta_0|$ and $|Z/\zeta_0|$ calculated by using the two-dimensional method with varying R, S, and K shown in Fig. 7.61 (a), where R is the clearance between two floating bodies, S is the distance from the quay wall, K is the spring constant of the mooring line between two floating bodies, and M is the weight of the floating body. Figure 7.61 shows that (i) the influence of clearance R on the relative motions is small, (ii) the relative vertical motions $|Z/\zeta_0|$ are affected significantly by the distance S, and (iii) the stronger spring can effectively reduce the relative horizontal motions, because it forces the two floating bodies to move in phase.
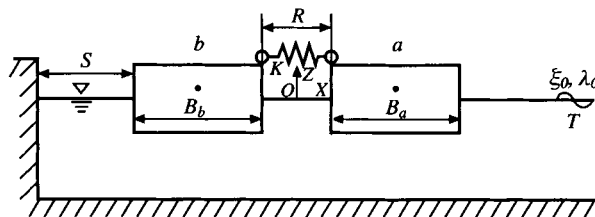
Fig. 7.61(a) Calculation conditions to clear the characteristics of relative motions
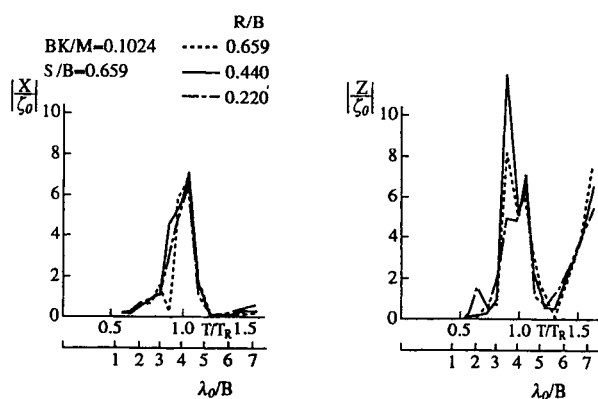
Fig. 7.61(b) The influence of clearance between two floating bodies
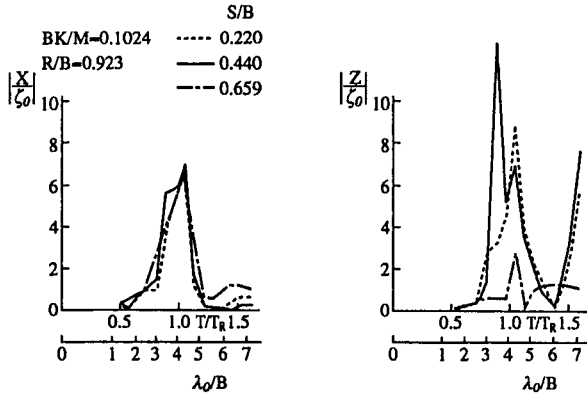
Fig. 7.61(c) The influence of distance from a quay wall
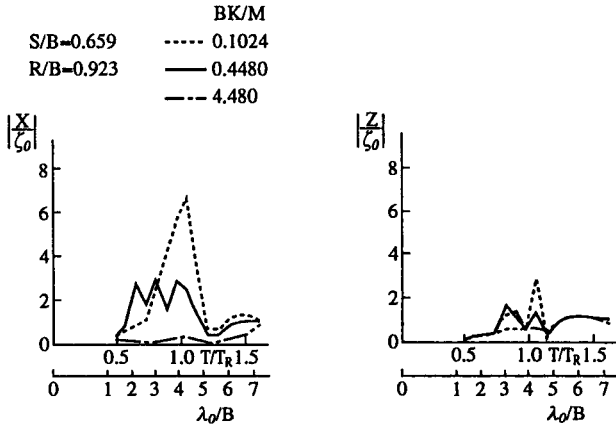
Fig. 7.61(d) The influence of the spring constant of the mooring line

Figure 7.62 shows the relative motions between two floating bodies calculated by the three-dimensional method with varying the mooring angle θ when the incident wavelength λ_0 and the angle β between the wave direction and a quay wall face are constant. The relative motions are significantly affected by the mooring angle θ as shown in Fig. 7.62. This indicates that the mooring angle θ should be carefully determined in relation to the angle of the incident wave.

$\lambda_0/L = 0.314$
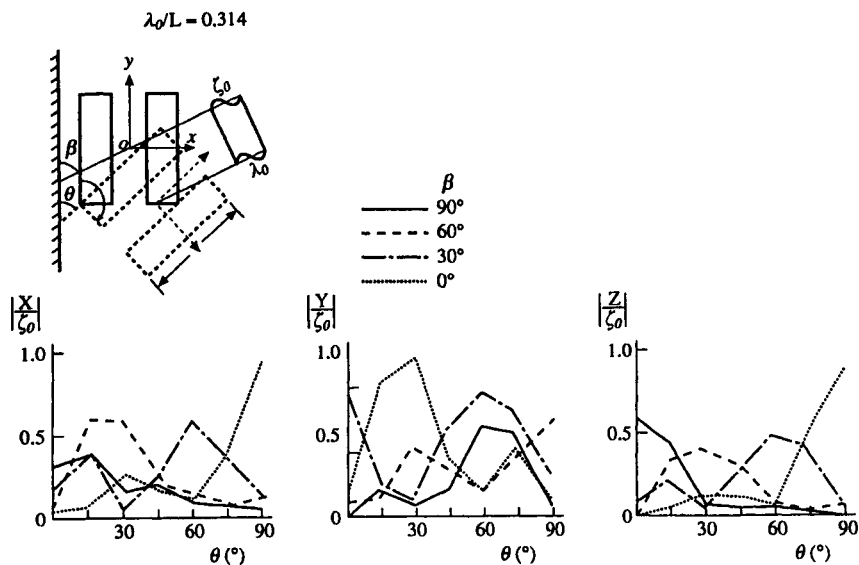
Fig. 7.62 The influence of mooring angle on relative motions

7.6.3 Harbor tranquility problem from the standpoint of the relative motions between two floating bodies

(1) Ability of cargo handling on floating pier

When the cargo is handled in a harbor by using a crane on the floating pier, the operation may be interrupted by large motions of the floating pier or the moored ship. The critical condition of a cargo handling depends on the relative motions between the ship deck and the swinging cargo caused by the motions of the floating pier.

Here, the motions of two floating bodies moored along a slope are investigated by using the two-dimensional method. A floating container terminal, as shown in Fig. 7.63, is treated as an example. The cargo swing and relative motions between ship and cargo are calculated. The cargo swing becomes large when the natural periods of roll of the floating pier and cargo swing are close to the wave period as shown in Fig. 7.64. Therefore, we must carefully decide the breadth and center of gravity for the floating pier, and the length of the cargo fall, which depend on the height of the crane on the floating pier, by taking the predominant waves in the harbor. Figure 7.65 shows the relative motions between swinging cargo and the ship deck varying the distance S from the slope to the floating pier. The cargo handling ability can be significantly improved by selecting the best location of the floating pier.
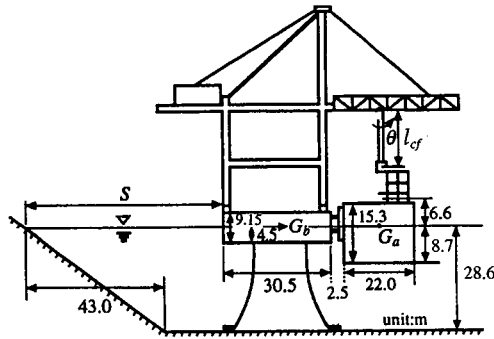
Container ship (a)
M_0=191.40 ton/m
I_{YZ}=9.771×10^3 ton m^2/m

Floating pier (b)
M_0=191.40 ton/m
I_{YZ}=1.0874×10^3 ton m^2/m

Fig. 7.63   An example of a floating container terminal
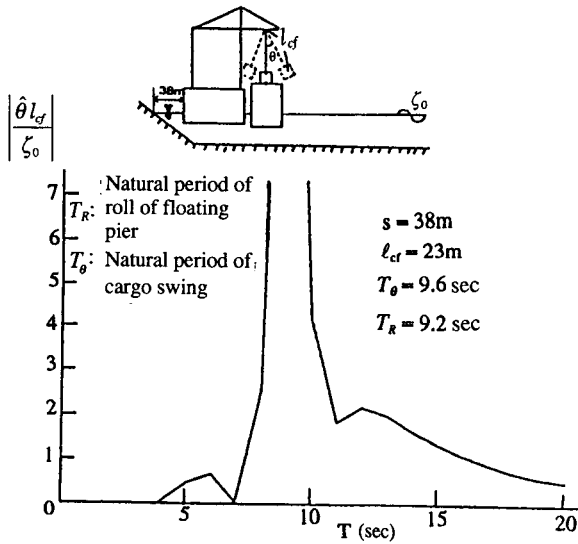
Fig. 7.64   The characteristics of cargo swing
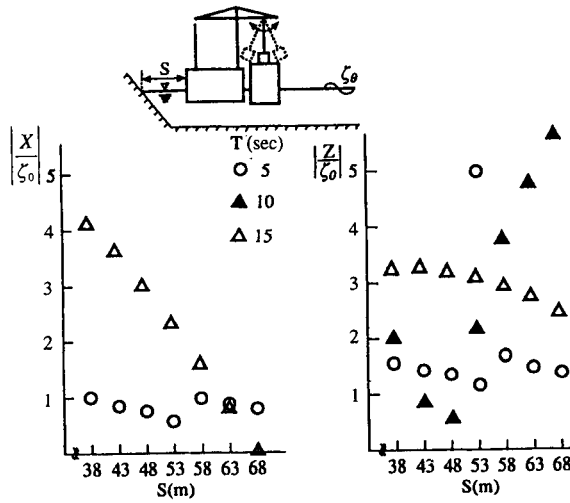
Fig. 7.65 The relative motions between swinging cargo and the ships deck

(2) Evaluation of the clearance of yachts moored in a marina

It is necessary to keep the proper clearance so that hulls and masts of two adjacent yachts do not make contact, in order to attain safe mooring of yachts in the marina.
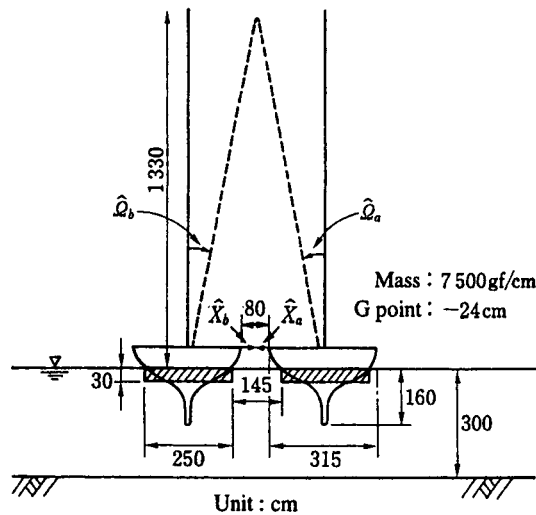
Fig. 7.66 The mean arrangement for mooring yachts

Here, considering the relative motions between the two floating bodies, a method to evaluate the minimal clearance is proposed. Figure 7.66 shows the representative arrangement of mooring yachts. The calculations of the motions of the two floating bodies in a beam sea (see Fig. 7.66) by the two-dimensional method are shown in Fig. 7.67. It can be judged whether or not the hulls and masts make contact with each from Fig. 7.67. For an example, as the most dangerous condition is when two ships oscillate out of phase with each other, the sum of the amplitudes of sway motions of two ships should be less than the clearance between the two ships. And the critical condition of the mast contact can be also estimated in the same manner using the horizontal movements of the top of the mast.
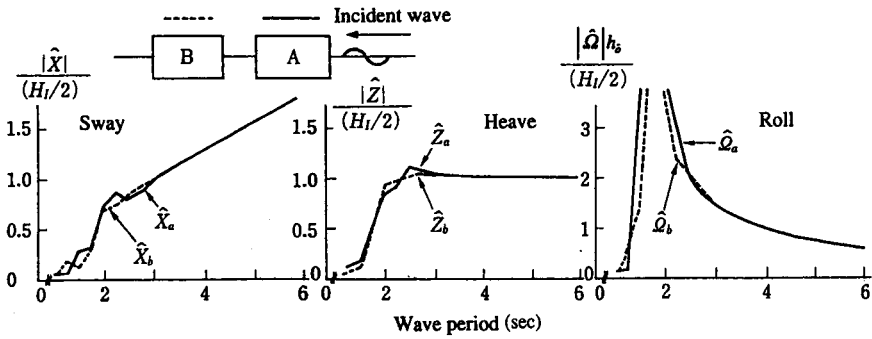
Fig. 7.67 The calculation results of two floating body motions

References

Barailler, L. and P. Gaillard (1967): Evolution recente des models mathematiques d'agitation due a la houle, Calcul de la diffraction en profondeur non uniforme, La Houille Blanche, No.8, pp.861-869.

Behrendt, L. (1985): Finite element model for water wave diffraction including boundary absorption and bottom friction, Paper 37, Inst. of Hydrodynamics and Hydraulic Eng., Technical Univ. of Denmark, 188p.

Berkhoff, J.C.W. (1972): Computation of combined refraction-diffraction, Proc. 13th Int. Conf. on Coastal, ASCE, Vol.1, pp.471-490.

Bettes, P. and O.C. Zienkiewicz (1977): Diffraction and refraction of surface waves using finite and infinite elements, Int. J. for Numerical Methods in Engineering, Vol.11, pp.1271-1290.

Biesel, F. and B. Ranson (1961): Calcul de la diffraction de la houle, Proc. 9th Cong. IAHR, Dubrovnik, pp.688-699.

Bruun, P. (1981): Breakwater of Mooring System, Dock and Harbor Authority, pp.126-129.

Engquist, B. and A. Majda (1985): Absorbing boundary conditions for the numerical simulation of waves, Mathematics of Computation, Vol.31, No.139, pp.629-651.

Hsu, F.A. and K.A. Blenkarn (1970): Analysis of peak mooring forces by slow drift oscillation in random seas, Proc. Offshore Tech. Conf., Paper OTC 1159, pp.135-146.

Hwang, L.S. and E.O. Tuck (1970): On the oscillations of harbours of arbitrary shape, J. Fluid Mech., Vol.42, Part 3, pp.447-464.

Ijima, T. and C.R. Chou (1975): Wave-induced oscillation in harbors with various boundary conditions, 1st and 2nd reports, Tech. Rept. of Kyushu Univ., Vol.48, No.5, pp.587-602 (in Japanese).

Kim, C.H. and M.C. Fang (1985): Vertical relative motion between two adjacent platforms in oblique waves, J. Energy Resources Tech., Vol.107, pp.455-460.

Kouyoumjian, R.G. and P.H. Pathak (1974): A uniform geometrical theory of diffraction for an edge in a perfectly conducting surface, Proc. of IEEE, Vol.62, No.11, pp.1448-1461.

Kubo, M. (1975): Basic research of applicational feasibility of dash-pots in the ship's mooring system, J. Japan Inst. of Navigation, No.73, pp.163-172 (in Japanese).

Kubo, M. and K. Saito (1990): Relative motions between two floating bodies moored along quay wall, Proc. Techno-Ocean '90, pp.442-447.

Kubo, M., K. Saito and S. Sakakibara (1990): Analytical method of ship motions moored along quay walls using a singularity-distribution method, Proc. Techno-Ocean '90, pp.434-441.

Kubo, M., and S. Sakakibara (1992): Advance in safety mooring and operation efficiency at exposed piers, Proc. Techno-Ocean '92, pp.547-552.

Kubo, M. and V. Barthel (1993): Enlarged Concept of Harbor Tranquility, Advances in Hydro-Science and Engineering, Vol.1, Univ. of Mississippi Press, pp.1608-1611.

Kusaka, T., M. Tatsumoto and A. Iwasaki (1983): Wave-induced oscillations in harbours with arbitrary interior reflectivity and variable depth, Proc. of the 30th Japanese Conf. Coastal Eng., JSCE, pp.128-132. (in Japanese)

Larsen, J. (1978) Harbour theory for wind-generated waves based on ray methods, J. Fluid Mech., Vol.87, Part 1, pp.143-158.

Lean, G.H. (1971): Subharmonic motions of a moored ship subjected to wave action, Trans. Roy. Inst. Naval Architects, London, 113, pp.387-399.

Lee, J.J. (1971): Wave-induced oscillations in harbors of arbitrary geometry, J. Fluid Mech., Vol.45, No.2, pp.375-394.

Mattioli, F. (1978): Wave-induced oscillations in harbours of variable depth, Computers and Fluids, Vol.6, pp.161-172.

Mei, C.C. (1978): Numerical methods in water-wave diffraction and radiation, Ann. Rev. Fluid Mech., pp.393-416.

Mei, C.C. (1983): The Applied Dynamics of Ocean Surface Waves, John Wiley & Sons, pp.168-182.

Ohkusu, M. (1976): Ship motions in vicinity of a structure, Proc. Int. Conf. on Behaviour of Offshore Structures, The Norwegian Inst. of Tech., Vol.1, pp.284-306.

Oortmerssen, G. van (1976): The motions of a moored ship in waves, Netherland Ship Model Basin, Publication No.510, 138p.

Sawaragi, T., M. Kubo and T. Kyotani (1978): Study on the long period motions of moored ship, Navigation, No.58, Japan Inst. of Navigation, pp.1-8. (in Japanese)

Sawaragi, T. and M. Kubo (1980): Short and long-period motions of a moored ship in a harbor basin, Proc. of 27th Japanese Conference on Coastal Engineering, JSCE, pp.307-311. (in Japanese)

Sawaragi, T., M. Kubo and T. Kyotani (1980): Motions of a moored ship along the perforated quay wall, Coastal Engineering in Japan, JSCE, Vol.23, pp.277-288.

Sawaragi, T. and M. Kubo (1982): Long-period motions of a moored ship induced by harbor oscillations, Coastal Engineering in Japan, JSCE, Vol.25, pp.261-275.

Sawaragi, T. and M. Kubo (1982): The motions of a moored ship in a harbor basin, Proc. of 18th Int. Conf. on Coastal, ASCE, pp.2753-2762.

Sawaragi, T. and M. Kubo (1983): Some considerations on port planning for security of ships in a harbor basin, Proc. 8th Int. Harbor Cong., pp.2.21-2.28.

Sawaragi, T., M. Kubo and S. Aoki (1984): New mooring system to reduce ship motions and berthing energy, Coastal Engineering in Japan, JSCE, Vol.27, pp.303-313.

Sawaragi, T., S. Aoki and A. Yamamoto (1988): Applicability of a finite element model for the prediction of harbor agitation, Proc. Civil Eng. in the Ocean, Vol.4, JSCE, pp.153-158. (in Japanese)

Sawaragi, T., S. Aoki and A. Yamamoto (1989): Analyses of hydrodynamic forces due to waves acting on a ship in a harbor of arbitrary geometry, Proc. 8th Int. Conf. on Offshore Mech. and Arctic Eng., pp.117-123.

Sawaragi, T. and S. Aoki (1991): Prediction and attenuation of wave-induced ship motion in a harbor, Coastal Eng. in Japan, JSCE, Vol.34, No.2, pp.243-265.

Sakakibara, S. and M. Kubo (1992): Influence of fender type on operational efficiency of cargo handling, Proc. 10th Int. Harbor Cong., pp.4.19-4.23.

Sekita, K. and M. Taniyama (1976): Operational limit of derrick barge on construction of large scale marine structure, Proc. 23rd Japanese Conf. on Coastal Eng., JSCE, pp.45-48. (in Japanese)

Takayama, T. (1985): Computation of wave height distribution inside a harbour, Proc. Int. Conf. of Numerical and Hydraulic Modelling of Ports and Harbours, pp.295-302.

Tanimoto, K., K. Kobune and K. Komatsu (1975): Numerical analysis of wave propagation in harbours of arbitrary shape, Rept. Port and Harbour Res. Inst., Vol.14, No.3. (in Japanese)

Ueda, S. (1984): Analytical method of ahip moored to quay walls and the applications, Note of Port and Harbour Res. Inst., No.504, pp.90-95. (in Japanese)

Warren, R., J. Larsen and P.A. Madsen (1985): Application of short wave numerical methods to harbor design and future development of the model, Proc. Int. Conf. on Numerical and Hydraulic Modelling of Ports and Harbours, pp.303-308.

Wilson, B.W. (1951): Ship response to range action in harbor basins, Trans., ASCE, Vol.116, pp.1129-1157.

Zienkiewicz, O.C., P. Bettes and D.W. Kelly (1978): The finite element method for determining fluid loadings on rigid structures two- and three-dimensional formulations, Numerical Methods in Offshore Engineering, John Wiley & Sons, pp.141-193.

This Page Intentionally Left Blank

Chapter 8 Fishery Structures

8.1 Classification and Function of Aquacultural Propagation Facilities

8.1.1 Artificial fish reef

An artificial fish reef (AFR) is one of the aquacultural propagation facilities to improve the productivity of coastal fisheries. An AFR is usually placed on the sea floor at a depth of about 10m to 200m in order to gather fish.

Although the reasons why and how an AFR can gather fish have not been adequately clarified yet, Japanese fishery researchers have built up the following hypothesis: the thigmotaxis of fish to an object is stimulated by extrinsic factors (i.e., emitted sound of attached epiphytes on an AFR, the sound generated by vortices formed at the AFR, the change of flow, the image of an AFR) and fish gather around the AFR. As the habitat of fish (i.e., feeding behavior, spawning behavior, escaping behavior) is satisfied, the fish live in that place. It is hard to judge under the above mentioned hypothesis whether the change of flow around an AFR is an important factor to the aggregate of fish. Hence, referring to a Japanese study report on not only the relation between the gathering behavior of fish and a current but also the feeding behavior of fish around an AFR, the effect of vortices formed at an AFR and their shedding behind the AFR on gathering fish are discussed in this section.

The gathering behavior of fish to an AFR in various current velocities was experimentally investigated by using a small circulation tank. As a result of this investigation, it has been concluded that fish swim selectively in a low velocity zone formed behind an AFR during an increasing velocity of current and avoid the high velocity zone above an AFR. The averted velocity is larger than the ordinary swimming speed at which fish can swim continuously for long time. Furthermore, from field observations on the relation between the moving behavior of fish and the direction of coastal currents, it has been reported that fish are inclined to move in the direction of the current and approach an AFR. Therefore, it may be found from these studies that changes in the direction and velocity of currents are closely related to the gathering behavior of fish.

The feeding behavior of fish around an AFR consists of a predator-prey relationship; i.e., fish of larger size catch fish of a smaller size, with the latter fish feeding on oceanic microorganisms such as algae attached to an AFR and plankton. The distribution of plankton trapped behind an AFR has been clarified through a diving survey as shown in Fig. 8.1. The distribution shape of plankton is found to be remarkably similar in appearance to the wake region formed behind an AFR, which is described in **8.2.** Therefore, it is considered that the vortex formation behind an AFR significantly affects the prehension of plankton. Recently, it has been indicated that the upwelling generated in front of an AFR has an effect on the improvement of the productive capacity of plankton, because such upwelling flings up highly nutritious salt water from the bottom layer.

From the above mentioned ecological investigations on the gathering behaviors of fish to an AFR, it can be concluded that changes in the fluid flow around an AFR have been pointed out to be one of the important factors on the gathering behavior of fish. Therefore, in order to clarify the effect of the shape of an AFR and the gaps on its surface on the spatial expansion of the wake region formed by vortices, the hydraulic characteristics of an AFR should be investigated. Furthermore, it is necessary to study the interval of an AFR that optimizes its effect on gathering fish.
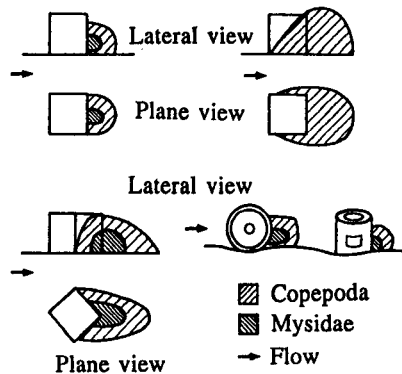
Fig. 8.1 Distribution of plankton around reefs

8.1.2 Moored artificial habitat for fish enhancement

In many field observations, an artificial habitat for fisheries has been found to have functions for the convergence of dispersed fish and the promotion of secondary production. They not only grow fish, shellfish and seaweed, but also help them to survive in the ocean environment. Various kinds of artificial structures have been constructed as marine fish aquacultures along the coast of Japan. They have been anchored to the ocean floor for fishery resources enhancement and management, environmental mitigation and restoration. Generally they are grouped into two categories:
(1) submerged mooring habitats,
(2) floating habitats on the sea surface.
The following sections provide the fundamental concepts on several moored fish cultures.

(1) Submerged habitats for fish
Submerged artificial habitats:
Early floating artificial habitats were made from low cost and readily available materials such as bamboo and wood to gather Yellowtail or Dolphins in the ocean. However, such structures had not sufficient durability in the ocean environment, and as a result many artificial habitats were destroyed or disappeared shortly after deployment. In the last two decades, submerged artificial habitats have improved and some new types consisting of fiber-reinforced plastic members, nets, buoys and mooring facilities, have been moored in deepwater areas for extended periods. Figure 8.2 shows typical examples of moored artificial habitats that have been submerged along the coast of Japan in the Sea of Japan and the Pacific ocean.
Submerged buoy-cable system for shellfish farming:
This structure aims at proliferating shellfish by using baskets suspended from a main cable. About forty baskets are suspended at 5m intervals from the main cable that is 200m long as shown in Fig. 8.3. For buoyancy, a few buoys are attached to each basket.
Figure 8.4 shows the cylindrical shellfish baskets made of plastic nets that are used to breed shellfish. The baskets are 2m in length and 0.5m in diameter and are hung from the main cable 15m deep.
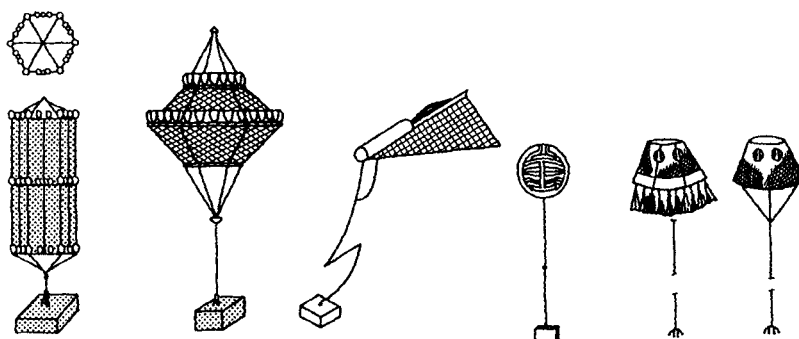
Fig. 8.2 Examples of moored artificial habitats
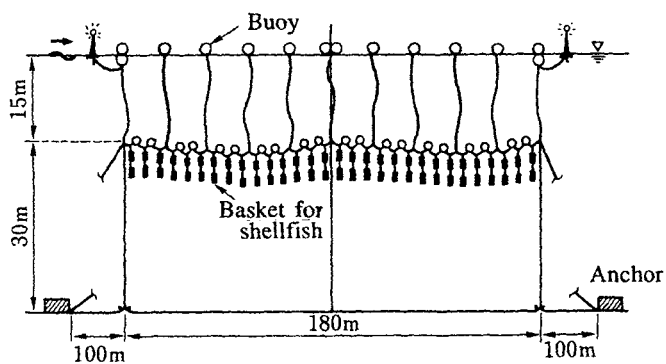
Fig. 8.3 Schematic view of the buoy-cable system
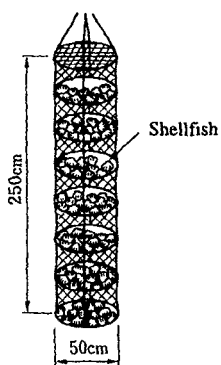
Fig. 8.4 Baskets for the aquaculture

(2) Floating habitats for fish
(i) Floating fishery cages:
  This aims to breed fish, such as Yellowtail, Seabream and Flatfish, in floating cages that consist of an upper steel frame, a bottom, four side wall nets, floats, mooring wires and anchors. The cage resembles a cube and measures about 10m wide and deep. Usually several units of cages are coupled and moored in a bay area. Recently bigger cages have been developed and moored for testing in an offshore area.
(ii) Floating fishery rafts:
  In bay areas and inland sea zones of Japan, a large number of fishery rafts have been constructed to breed shellfish such as oysters, pearl oysters or other kinds of bivalves for commercial management. It consists of a raft made of wood or steel pipe, baskets to contain the shellfish suspended from the rafts, floats, mooring lines and anchors. Over one hundred of the baskets are hung down from a raft. Shellfish cultures utilizing floating rafts have been one of the major fishery industries in Japan.

8.2 Artificial Fish Reef (AFR)

8.2.1 Layout of AFR for coastal fishing ground
(1) Hydraulic investigation on the interval of AFRs in a multi-AFR system
  A multi-AFR system in which AFRs are usually arrayed with a constant interval along in the direction of the dominant flow in a planned sea area has been adopted to activate the properties of the AFR as mentioned in **8.1**. In Japan, the distance between separately arrayed AFRs has been designed in conformity with the following basic construction scheme; the space formed between the AFRs is related to the gathering behavior of fish from the point of view of biology and hydraulics. If the AFR is quite densely accumulated, work of the system on gathering fish may not be demonstrated sufficiently and the AFR produces no economic effect. If the AFRs are arrayed in a long interval, individual AFRs are almost independent and the anticipated effect of the multi system may not be realized fully. Although the basic construction scheme for coastal fishing grounds seems to take into account the relation between the flow pattern around a multi-AFR system and the gathering behavior of fish, the concrete interval between AFRs has been empirically determined mainly by such conventional methods as biological investigation. Hence, while referring to conventional information on the gathering behavior of fish and the above mentioned basic construction scheme for fishing grounds, the approach with an emphasis on the hydraulic point of view for obtaining the optimum interval of the AFR in the multi system will be the focus of this section.
  Based on the AFR arrangement procedure in Japan, a rational project for planning the fishing grounds with an AFR must be established by extracting the fundamental factor through investigation on both the natural environmental conditions in the planned sea area and the economic conditions of fish produced in its area. The flowchart of this planning process is shown in Fig. 8.5. Firstly, after individual items in the investigations on the natural environmental conditions (i.e., the sea and weather conditions, the sea bottom condition and biological condition) and the fishery condition (i.e., the fishery method and fish catches) are clarified, the size of the fishing ground in the planned sea area and the shape of the AFR are determined under consideration of the administrative condition (i.e., budget). Secondly, the optimum arrangement of AFRs which activate the system most has to be surveyed and investigated on the basis of the above mentioned conditions, and the stability of the system against wave actions is evaluated simultaneously. Lastly, the project of the fishing ground is put into practice. The conditions of determining the optimum interval of the AFR consist of four factors that prescribe the rational arrangement of the

Natural Environmental Conditions | Fishery Conditions | Administrative Condition

Research of designed sea area | Research of fishery structure and production | Budget

Sea and weather conditions:
Direction of wind, waves and currents
* Estimation of days for fishing work
* Basic informations on layout of FAD
* Informations on analysis of FAD's stability
Sea bottom conditions:
Characteristics of materials
* Informations on scouring and burying
Biological conditions:
* Distribution density and ecology of focused fishes

Fishery method
Fishery catches

Determination on size of planning fish ground and shape of AFR

Optimum arrangement of AFR | Stability design of AFR

Execution of fishing ground with AFR

Fig. 8.5 Flowchart of the planning for the fishing ground with AFR

AFR as shown in Fig. 8.6. By sufficiently clarifying these factors, the optimum interval may be determined. Figure 8.6 shows the flowchart to clarify the optimum arrangement of the AFRs mainly with hydraulic validity. Accordingly, the factors of No.2 and No.3 in this flowchart have been linked to the science of fisheries, since it seems that these factors should be investigated from the viewpoint of the science of fisheries. The factor of No.1 involves the function of the AFR in gathering fish. This factor should be clarified by relating the ecology of fish to both hydraulic and biological environments around the AFR. However, since these relations have not been sufficiently clarified yet, the factor of No.1 is divided into two parts; i.e., the hydraulic environment and the biological environment.

The substance of studies on the biological environment mainly involves the investigation of the effect of feeds induced by an AFR (i.e., the epiphytes on it, the plankton trapped behind it and the prey-predator relationship between larger and smaller fish) and the relation between the instincts of fish (i.e., thigmotactic and rheotaxitic behaviors) and a change of flow around it. On the other hand, in the study on the hydraulic environment around an AFR, firstly the characteristics of the flow pattern around a single AFR (i.e., the effect of the shape and porosity of the AFR on the spatial expansion of the wake region formed behind it and the intensity of vortices) must be clarified from viewpoint of gathering plankton and the rheotaxis of small fish. Secondly, the effect of an AFR interval in a multi-AFR system on the change of the flow pattern around the multi-AFR system is evaluated from research on the systematic change of the interval and the relationship between the AFR interval and the size of the wake region behind the individual AFR is

put into the form of a graph. Lastly, by using this graph, the optimum interval of the AFR that activates the multi-system most is decided. The above mentioned optimal interval between AFRs is derived from hydraulic studies. The true optimum arrangement of AFRs should be clarified through coupling each investigation on the biological and hydraulic environment around an AFR.
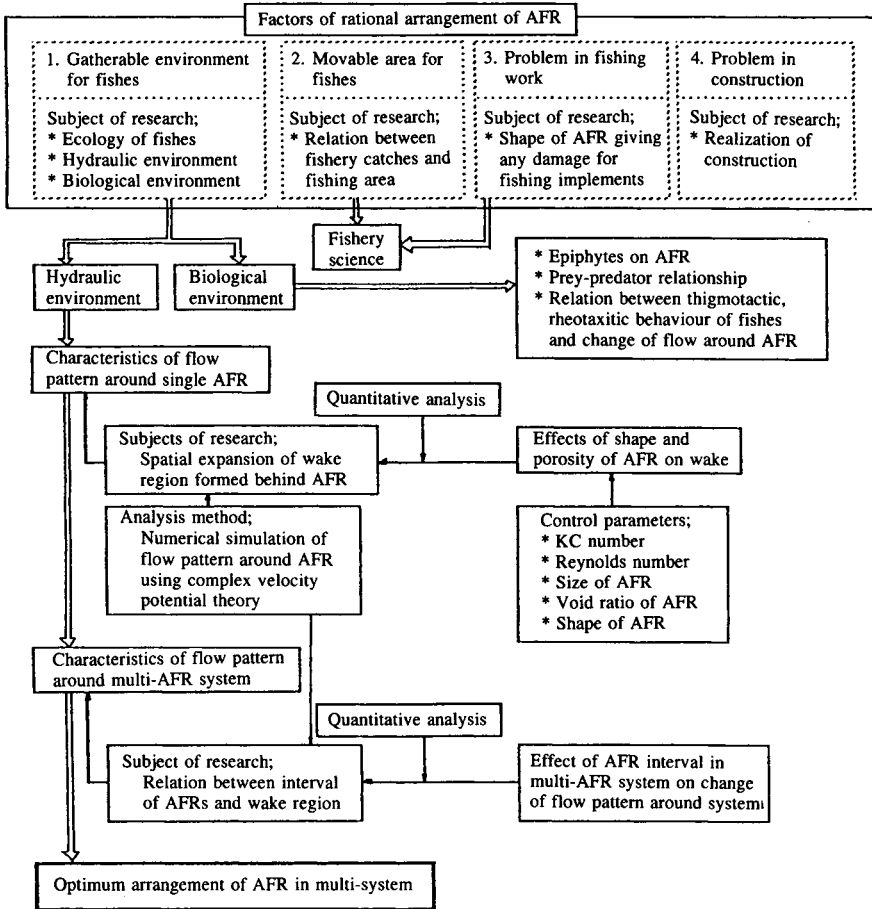
Fig. 8.6 Flowchart of the optimum arrangement of AFR

(2) Characteristics of flow pattern behind a single AFR

Based on experiments and numerical analysis (Sawaragi et al. 1984) on the flow pattern around a single AFR, the hydraulic characteristics of vortices generated behind the single AFR are discussed in this paragraph. The AFR model treated in this study consisted of four rectangular pieces, and the experiments were carried out by using a U-shaped oscillatory flow tank.

(a) Characteristics of vortices behind a single AFR

Figure 8.7 shows the schematic flow patterns that are visualized by using the hydrogen bubble method and taking photographs with a 16mm camera. A large single vortex and a counter flow region (called a wake region) induced by this vortex are generated behind the AFR. The wake region formed behind the AFR is defined as the region where the direction of the horizontal velocity component is reverse to that of the main flow as shown in Fig. 8.7. The area and length of the wake region have been considered as the indices that quantitatively evaluate the wake. The length of the wake region is defined by the distance from the downstream side of the AFR model to the downstream edge of the wake region.
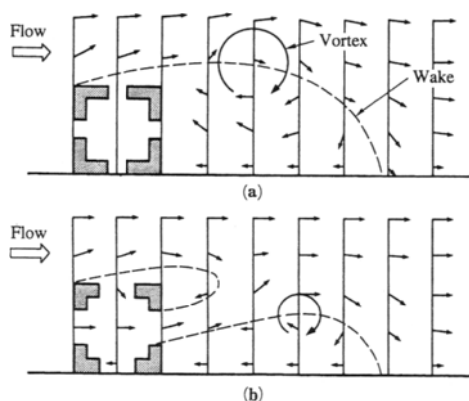
Fig. 8.7 Schematic flow patterns behind AFR

The wake region changes with a change in the main flow velocity in the oscillatory flow, and the angular frequency changes when the wake region becomes a maximum considerably later than that ($\sigma t = \pi/2$) which the main flow velocity becomes a maximum, and it is in the range of the angular frequency $\sigma t = 5\pi/6$ to $\sigma t = 17\pi/18$.

From the results of the experiments, it is found that the wake region formed behind the AFR model may be classified into two patterns by the void ratio of the AFR models (see Fig. 8.7). There is a single wake region in the case of a small void ratio, while the wake is separated into two regions in the case of a large void ratio, due to the efflux of water through the gap that is similar to a jet stream with the same velocity as the main flow. The two kinds of flow patterns depend not only on the void ratio of the AFR but also depend very much on the KC number (Keulengan-Carpenter number). D of the KC number ($= UT/D$) is the typical length of an AFR model, twice the length of one side of the AFR model is adopted as the value of D. In the case of a split of the wake region, the size of the upper region becomes so large that it can be disregarded when compared to the lower region with an increase of the KC number.

It may be considered that the intensity of the vortex formed behind the AFR is a very important hydraulic amount for the purpose of trapping the plankton behind the AFR and relieving the strong flow around it, thereby providing a habitable environment to small fish. Then, through experimental investigation of the circulation of vortices behind the AFR model, it has been clarified that the circulation of vortices changes with the void ratio of the AFR and the values of the circulation become a minimum at the void ratio of about 60%.

Considering a cubic shaped concrete AFR with a void ratio of about 60% has been most frequently used in the present, so now let us discuss the optimum void ratio of an AFR from the mentioned characteristics of the flow pattern around a single model. The circulation of vortices generated behind the AFR with the void ratio of the order of about 60% is less affected by the change of the void ratio in the range of this order. However, when the spatial expansion of the wake region is affected by the change of the void ratio, its value area begins to decrease very quickly at the void ratio above 60%. Although it has not yet been sufficiently clear whether the effect of a vortex on gathering fish is evaluated by the spatial expansion of the wake region or its intensity, if the circulation of the vortices is weak, the small fish with a slow swimming speed may easily catch the plankton trapped behind the AFR. Also, for the sake of an abundant catch of plankton, the large expansion of the wake region may be necessary. As a result of these considerations, it can be concluded that the optimum void ratio of the AFR is in the order of about 60%.

(b) Numerical flow simulation technique around AFR

In the near future, the relationship between the change of the flow pattern around the AFR and the gathering behavior of fish to it will be clarified from a biological standpoint. In order to evaluate the optimum void ratio of the AFR which creates the most suitable flow pattern for the habitable condition of fish, a numerical flow simulation technique including the vortex effect around the AFR must be developed. This paragraph explains the outline of the numerical simulation model developed by Sawaragi and Matsumi (1984). In this model the discrete vortex approximation (explained in detail in 2.7) has been used for the simulation of the vortex formation behind the AFR.

This simulation technique approximates the influx and the efflux of water through gaps in the hollow AFR with the sink and the source points respectively. Then, the appropriate complex velocity potential for the flow around the AFR can be determined by using the Schwartz-Christoffel transformation to project the exterior region in the z-plane into the upper half of the ω-plane with the boundary along the real axis (see Fig. 8.8). The ω-plane is transformed into the physical z-plane by the function
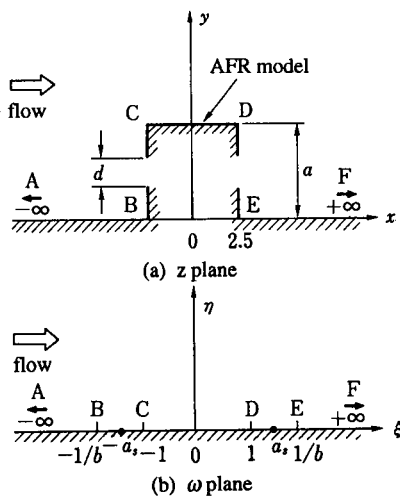
Fig. 8.8 Explanation of Schwartz-Christoffel transformation

$$z = x + iy = l_M\left(b - \frac{1}{b}\right)F(b,\omega) + \frac{l_M}{b}E(b,\omega) + c \tag{8.1}$$

where $\omega = \xi + i\eta$, $i = \sqrt{-1}$, l_M and b are the constants that are determined by the height and shape of the AFR respectively, $F(b,\omega)$ and $E(b,\omega)$ are the elliptic integrals of the first and second kinds with the modulus b respectively, and c is the integral constant. Making a the length of one side of the AFR model proposed here, the constants in Eq. (8.1) b, l_M and c are determined by the following boundary conditions.

$$\begin{array}{lll} z = ia & : & \omega = 0 \\ z = a/2 + ia & : & \omega = 1 \\ z = a/2 & : & \omega = 1/b \end{array} \tag{8.2}$$

When the flow model in the transformed ω-plane consists of an oscillatory main flow with spatially uniform velocity U, N vortices with some circulation created from P separation points, and n sink points and n source points, the complex velocity potential W_ω is given by

$$\begin{aligned} W_\omega = U_\omega &+ \frac{i}{2\pi}\sum_{j=1}^{P}\sum_{k=1}^{N}\Gamma_{jk}\left\{\log(\omega - \omega_{jk}) - \log(\omega - \overline{\omega}_{jk})\right\} \\ &+ \sum_{s=1}^{n}m_s\left\{\log(\omega - a_s) - \log(\omega + a_s)\right\} \end{aligned} \tag{8.3}$$

where Γ_{jk} and ω_{jk} are the circulation and complex coordinates of the k-th vortex created from the j-th separation point respectively. The circulation is defined as positive clockwise, and m_s and a_s are the strength and the position of the sink and source points, and the over bar denotes the complex conjugate. U is given by $U = U_m\sin(\sigma t)$ in which U_m is the amplitude of the main flow velocity. In Eq. (8.3), the first term of the right-hand side indicates the complex velocity potential for the irrotational flow around the AFR model, the second term shows the discrete vortices in the main flow and the imaginary discrete vortices which are necessary in order to maintain the boundary condition of zero flow across the real axis in the ω-plane and the third term presents the influence of the influx and the efflux of water through the gaps in the AFR model.

Figure 8.9 shows an example of the calculated flow pattern around the AFR model with gaps (the void ratio $\lambda = 63\%$) in which the arrows and the symbols indicate the velocity vectors and the positions of the discrete vortices. The solid line shows the circulated wake region and the dotted line represents the wake region measured at the experiments. It is found that the calculated result can simulate the characteristics where the wake region becomes split between upper and lower regions. As a result of these investigations (Sawaragi et al. 1984), it may be concluded that in the case of KC number = 10-20 the flow pattern around a cubic model with a void ratio less than 63% can be estimated by the mentioned numerical simulation method.
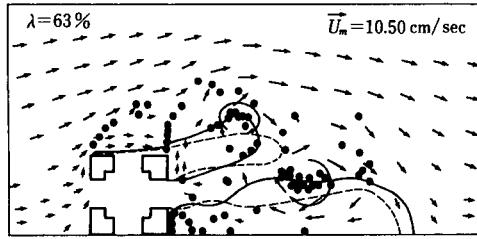
Fig. 8.9 Example of calculated flow patterns around AFR (KC number = 11.86)

(3) Characteristics of flow pattern around multi-AFR system

The multi-AFR system in which the AFRs are usually arrayed with a constant interval along a direction of the dominant flow in the planned sea area has been adopted in order to fully activate the effect of the AFR in gathering fish. The AFR supplies fish not only a hiding place but also nourishing materials which are flung up from the sea bed by the vortex induced. Therefore, the larger an area of the vortex shedding becomes the more the effectiveness of the AFR may be improved. As for the optimum interval of AFRs at which the system is activated most, individual AFRs must be arrayed so that the total wake region of the multi-AFR system is larger than the simple sum of the wake regions of single AFRs in the system. Therefore, based on the numerical simulation method (developed by Matsumi) on the flow pattern around three equally spaced AFRs arrayed in the direction of the flow, the major subjects in this paragraph are to clarify the interaction effect on the flow pattern around the system from the neighboring AFR and the optimum interval of the AFR in the multi system which makes the wake region formed behind an individual AFR become a maximum.

(a) Interaction effect of neighboring AFR on flow pattern

When the flow around the multi-AFR system consists of a periodic incident wave, N discrete vortices with some circulations generated from P separation points and the flow from the source points distributed on the AFR surface for the formulation of a boundary condition on the AFR surface, the complex velocity potential W_z is given by using the Schwartz-Christoffel transformation and the imaginary method as the following equation.

$$W_z = \frac{\sigma H}{2k \sinh kh} \sin\{k(ih+z)-\sigma t\} + \sum_{j=1}^{P}\sum_{k=1}^{N} \frac{i\Gamma_{jk}}{2\pi}\left\{\log\left(e^{\hat{c}z_{jk}} - e^{\hat{c}z}\right) - \log\left(e^{\hat{c}\bar{z}_{jk}} - e^{\hat{c}z}\right)\right\}$$
$$+ \frac{i}{2\pi}\oint_s f_D(z_s)\left\{\log\left(e^{\hat{c}z_s} - e^{\hat{c}z}\right) + \log\left(e^{\hat{c}\bar{z}_s} - e^{\hat{c}z}\right)\right\} ds \tag{8.4}$$

where $\hat{c} = \pi/h$, and h, H and k are the water depth, wave height and wave number respectively, $f_D(z_s)$ is a strength of the source point at the point z_s on the AFR surface. In the numerical calculation of Eq. (8.4), the surface of the AFR is divided into many sections of length, and the source point is set on the center of the individual section.

Figure 8.10(a) shows an example of the simulated flow pattern around three AFR models (the void ratio $\lambda = 63\%$, KC number = 7.5), in which the solid line shows the calculated wake region. The flow pattern induced by the discrete vortices clustered around each AFR

model simulates the dominant features of the flow around the system in the experiments as shown in Fig. 8.10(b). Also, from the investigations on the change of the flow velocity between AFR models concerning the change of the AFR interval, it is found that when the AFR interval is about twice the length of one side of the AFR, the interaction effect of the neighboring AFR on the expansion of the wake region around the multi-system becomes a maximum.
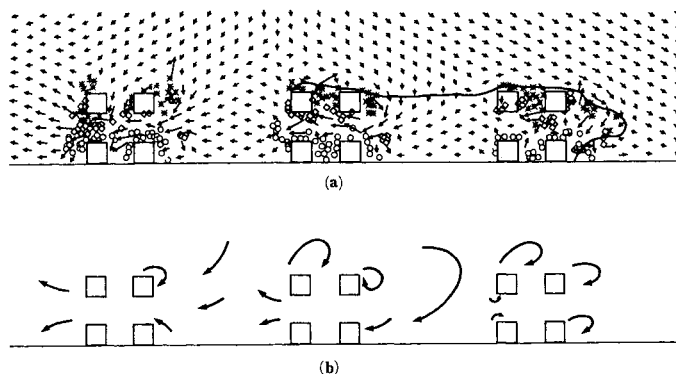
Fig. 8.10 Example of calculated flow patterns around three AFR models (KC number = 7.13)

(b) Optimum arrangement of AFRs

It seems to be possible from a hydraulic standpoint that the area of the wake region formed behind the AFR is used as an important parameter to determine the optimum interval between AFRs, because the gathering of plankton, which has been pointed out to be one of factors of an AFR that the gathering of fish depends on in the wake region. Figure 8.11 shows a comparison between the area of calculated wake region (A_G) behind the center the AFR model of a multi system and that of the single AFR model (A_S), in which l_f/a is the normalized interval between individual AFRs. It can be found that the AFR interval which makes the wake region behind individual AFRs a maximum is twice the side length of the AFR in the region of KC number > 7. When the KC number < 5, however, the optimum interval between the AFRs is the side length of the AFR. In the case of the uniform flow shown in this figure, the area of the wake region formed behind individual AFRs is less affected by these intervals.

8.2.2 Stability design of AFR

(1) Summary of stability design of AFR

In general, the service life of an AFR is estimated to be 30 years. An AFR must be designed to fulfill the intended function during its service life. The ordinary stability design procedure is carried out in conformity with the design criteria of structures for the arrangement and development of projects of coastal fish grounds in Japan. The subject matter of the design is to evaluate the durability of the AFR against the impulsive force at landing on the sea bottom when setting it on a fishing ground, the stability of it against the wave force and the local scour of the sandy bottom around the AFR. This section will introduce the summary of the stability design of an AFR in consideration of problems of the above mentioned design criteria.
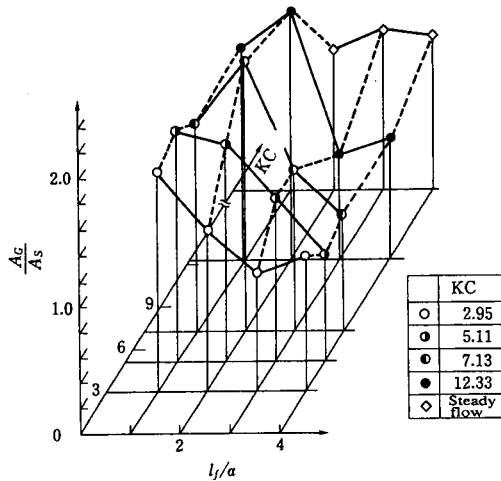
Fig. 8.11 Relation between A_G/A_S, l_f/a and KC number

The items evaluated in the stability design of the AFR are classified into the following three parts.
1) strength of the AFR (before setting up)
    external forces: force at lifting the AFR with a deck crane to throw from a ship, impulsive force at landing on the sea bottom,
2) stability of the AFR (after setting up)
    external forces: fluid force induced by waves and current, local scour around the AFR,
3) accurate setting method (at settling up)
    external force: drift force exerted on the settling AFR.
The investigation on 1) and 3) is carried out according to the flowchart shown in Fig. 8.12. As for the strength of members of the AFR which must be considered at designing, there are the two following kinds of strength: the strength given by treating the sum of two external forces (i.e., the additional force exerted when lifting it with the deck crane by the motion of ship and the dead load of the AFR) as the concentrated load and the strength given from the impulsive force at landing on the sea bottom. The larger value of these strengths is adopted in the calculation of the strength of the AFR members. The method that reduces the settled area of the AFR on the sea floor when thrown down from a ship will be described in **8.2.3**.

The stability of an AFR of 2) is investigated by using the flowchart shown in Fig. 8.13. The stability of an AFR against sliding and overturning is examined by the comparison between the resistance force of the AFR to these motions and the fluid force (i.e., the resultant force composed of the fluid force in the horizontal direction calculated with the Morison formula which is mentioned in **2.5.1** and the fluid force in the vertical direction). When the stability of the AFR is not verified, the dead load of the AFR and the its strength are reinvestigated according to the flowchart shown in Fig. 8.12. In order to evaluate the fluid force exerted on an AFR, when the Morison formula is applied to an AFR that is hollow inside and having a gap, the interaction effects of the AFR members, the neighboring AFR in the multi system and the affect of the bottom on the drag and inertia coefficients should be taken into account. This problem and the vertical component of the fluid force which is not contained in the above mentioned design criteria will be discussed next in (2).
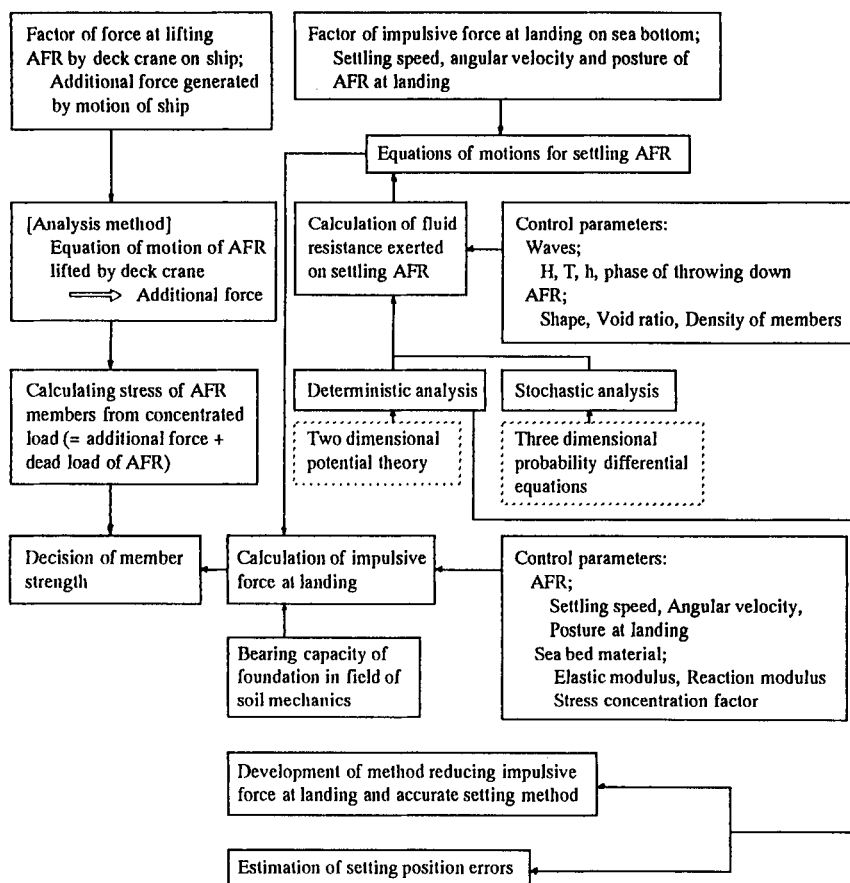
Fig. 8.12 Flowchart of the design of AFR in Japan

Local scour around the AFR is expected since the fish ground is generally a sandy bottom and the AFR causes the flow velocities around it to be accelerated considerably. In the investigation on the stability design of the AFR against the local scour around it, first of all, it must be examined whether or not the sediment transport is generated in designed sea area by using conditions of the incident wave and characteristics of the sea bed material in the designed sea area, because a dynamic scour defined as the scour under condition with sediment transport and a static scour without sediment transport are extremely different in the mechanisms of scour. If the occurrence of sediment transport is verified from this investigation, an examination on the embedding induced by sediment transport must be carried out. On the other hand, in the case of no sediment transport, the local scour is mainly a direct object of the stability design of the AFR.

Figure 8.13 shows the process of the investigation on the stability of the AFR against local scour. The first investigation in this flowchart is to clarify whether or not the local scour occurs by using a criterion for the occurrence of local scour. This criterion is explained in (3) (a) of this section. Secondly, when the scouring hole occurs, the necessity
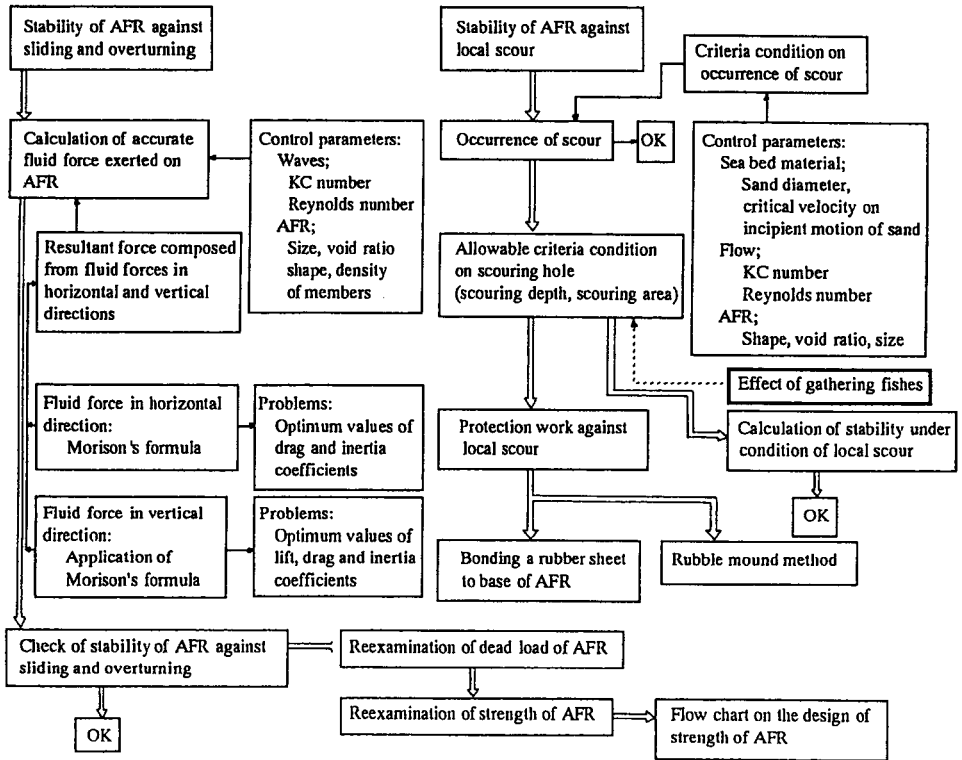
Fig. 8.13 Flowchart on the stability of an AFR

of the protection works against the local scour is investigated by comparing the estimated size of the scour hole (i.e., the depth and the lateral extent of hole) with the allowable criteria. The allowable criteria have not been clarified yet, but it seems that this criteria should be determined by considering the affection of the AFR on gathering fish. Lastly, scour protection methods for the AFR are considered. In this flowchart, two kinds of protection methods are shown. The purpose of the rubber sheet device is to intercept the sediments from the vertices which cause the scour by making a bond from a circular rubber sheet to the base of the AFR, and the purpose of the rubble mound method is to increase the resistant force of sediments to the fluid shear stress by placing rubble around the AFR. The efficiency of these protection methods is clarified in (3) (c) of this section.

(2) Fluid force
(a) Drag and inertia coefficients of AFR

Figures 8.14 and 8.15 show the drag coefficients (C_D) and the inertia coefficients (C_M) of the single AFR in our experiments respectively, the solid lines indicate the mean curves for C_D and C_M from these data. Re in Fig. 8.14 is the Reynolds number defined by UD/ν; D is the representative length of the AFR. As shown in these figures, it is found that the mean curves for C_D and C_M are respectively greater than $C_D = 2$ and $C_M = 2$ in which the values of C_D and C_M are adopted as a design condition of the cubic AFR in the above mentioned design criteria, and the design criteria may underestimate the fluid force exerted on the AFR.
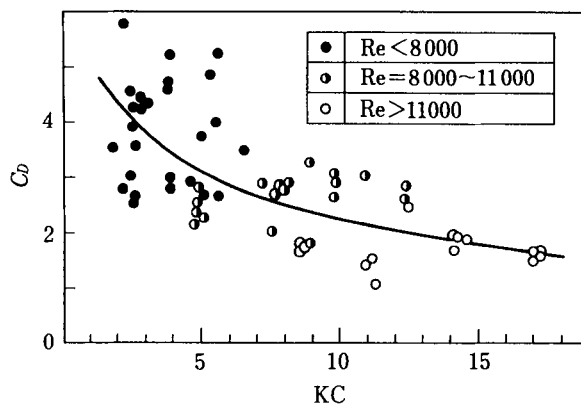
Fig. 8.14 Change of the drag coefficient of the AFR with KC number by experiments ($\lambda = 64\%$)
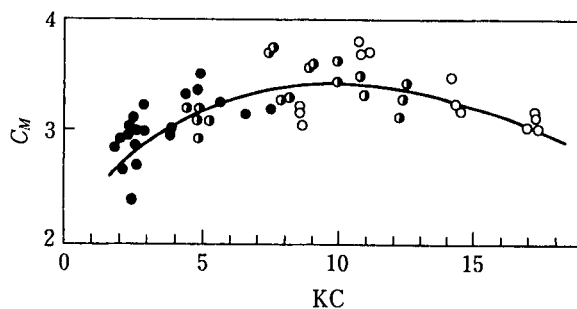
Fig. 8.15 Change of the inertia coefficient of the AFR with the KC number by experiments ($\lambda = 64\%$)

In order to evaluate the bottom effect on the inertia coefficient, the inertia coefficient is analyzed by using the potential theory as the following procedure. It is clear from the potential theory that a flow pattern around an AFR placed on the bottom in a uniform flow becomes equivalent to an irrotational motion of fluid induced by its own movement along the bottom with the velocity of the flow, therefore the analysis is carried out in the latter flow field. The inertia coefficient is composed of the sum of two coefficients of the fluid force. One is the coefficient for the pressure gradient which is induced by the unsteady motion of the fluid and the other is the added mass coefficient. The added mass coefficient of the AFR is evaluated as a coefficient such that the kinetic energy of the fluid induced by the sinusoidal moving AFR in still water becomes equivalent to the kinetic energy of the fluid replaced by the AFR. The inertia coefficient for different values of the void ratio λ of the AFR is shown in Fig. 8.16. The solid line indicates C_M of an AFR, the broken line represents the value of C_M for an infinite fluid field. The difference between the two lines may be caused by the bottom effect. It is seen that C_M decreases with increasing values of λ for $\lambda < 50\%$ whereas C_M is less effected by λ for $\lambda > 50\%$ and the value of C_M approaches 2.67 in this region.
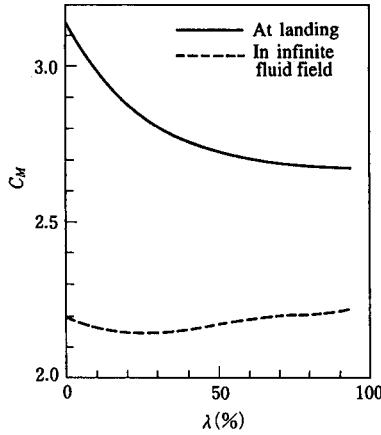
Fig. 8.16 Effects of sea bottom on the inertia coefficient of the AFR

Figure 8.17 shows the change of the inertia coefficient C_M' calculated from the above mentioned technique for the multi-AFR system with respect to the relative interval of the AFR l_f/a. The broken line in the figure represents the values of the single AFR. It is found that the inertia coefficients of the multi system depend on l_f/a and in general the effect of the neighboring AFR on the coefficient is to decrease dramatically the value of the coefficients for the smaller void ratio.
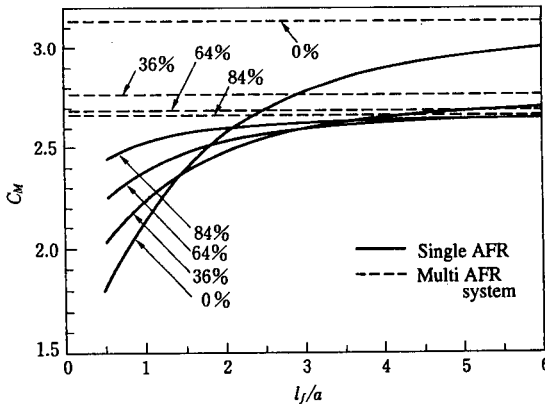
Fig. 8.17 Effect of interaction of the multi-AFR system for the inertia coefficient

Figure 8.18 shows the drag coefficients C_D' obtained in experiments for four kinds of AFR interval l_f of the multi system, in which the solid lines in these figures are the mean curve for C_D of the single AFR and the symbols are equal to these in Fig. 8.14. It is found that C_D' becomes less than C_D of the single case, and the magnitude of this decrease

appears remarkably in the smaller interval. It can be concluded from the data presented here that the values of C_D and C_M which consider the interaction effect of the neighboring AFR and the bottom effect must be adopted as a design condition of the stability design.
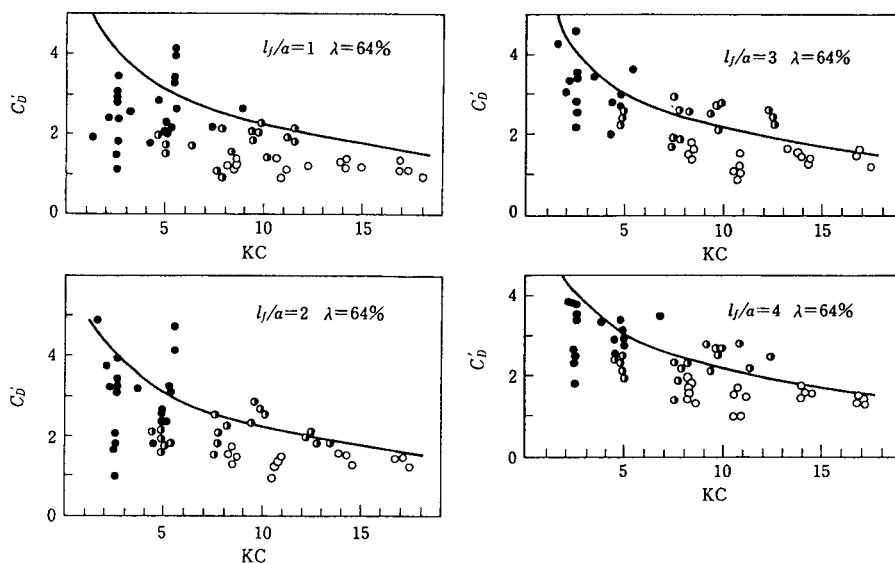
Fig. 8.18   Drag coefficient for the multi-AFR system ($\lambda = 64\%$)

(b) Fluid force in vertical direction

When the maximum value of the fluid force in the vertical direction is so much that it can be disregarded compared to the weight of the AFR, it is not necessary to consider the vertical fluid force in the design condition. Also, even if the maximum force in the vertical direction is approximately equivalent to that in the horizontal direction, when the stability of the AFR against these forces is discussed with static equilibrium equations, the vertical force can be ignored in the design except when there is little difference between both phases when each fluid force becomes a maximum. In this paragraph, in order to clarify the necessity of introducing the vertical force into stability design, the magnitude of the maximum vertical forces taken upward to the bottom and the relation between the phase of these and that of the maximum horizontal forces are investigated from the measurements of the fluid force acting on the AFR in a laboratory wave tank.

The maximum vertical and maximum horizontal forces (F_{Vm}, F_{Hm}) are shown in Fig. 8.19 while their phases (θ_{Vm}, θ_{Hm}) are given in Fig. 8.20. As clearly seen in Fig. 8.19, the magnitude of vertical forces is 0.6 times above that of the horizontal forces. Also, it is found from Fig. 8.20 that the phase difference between both forces is smaller than $\pi/3$, the maximum vertical and horizontal forces are generated at the near phase respectively.

The vertical force exerted on the AFR is pointed out to be important force in stability design calculations. However, the convenient equation to calculate the vertical force and the resultant force combined with the vertical and horizontal forces has yet to be elucidated.
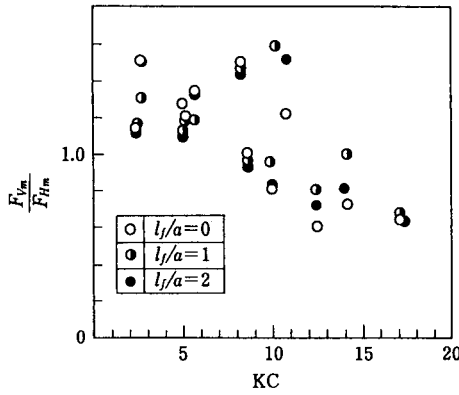
Fig. 8.19 Comparison of vertical and horizontal force for AFR ($\lambda = 64\%$)
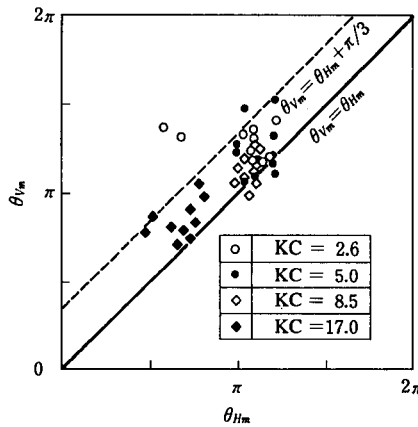
Fig. 8.20 Relation of occurrence phase for maximum vertical and horizontal force ($\lambda = 64\%$)

(3) Local scour and scour protection

Based on the results of the laboratory model experiments in the oscillatory flow, this paragraph considers the following points; the criteria on conditions at which the local scour begins occurring due to the accelerated flow and the vortices generated around the AFR, the mechanisms of the scour by associating the flow pattern around the AFR and the sediment movements, and the effects of the scour protection.

(a) Criteria condition on scour occurrence

Figure 8.21 shows the nondimensional stress obtained by the above mentioned experiments to investigate the relationship between the main flow velocity (u_c^λ) at which the sand around the AFR moves and the critical velocity (u_c^f) is defined as the main flow velocity at the incipient motion of sand under the condition without the AFR (described as the flat bed under here). In the figure, the abscissa shows the ratio l_w/d in which l_w is the
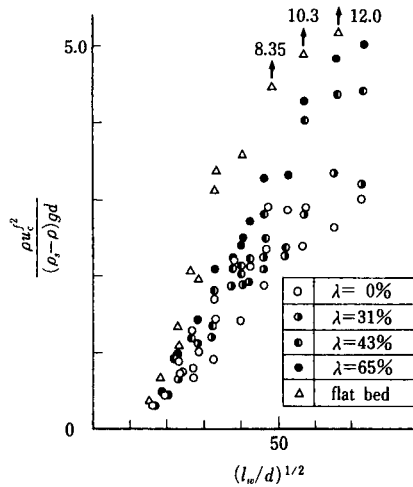
Fig. 8.21 Nondimensional stress of critical velocity at the incipient motion of bed material

orbital diameter and d is the sand diameter, the numerical values indicate the values of the nondimensional stress. The nondimensional stress of the main flow with the AFR is found to become remarkably smaller than the values in the flat bed. Therefore, even if the main flow velocity is smaller than the critical velocity, this result confirms that scour will occur due to placing the AFR. As clearly seen in this figure, the characteristic of change of the nondimensional stress in the flat bed is very similar to those in each void ratio of the AFR. Therefore, it can be assumed that a linear relationship given by the following equation is established between u_c^{λ} and u_c^{f}.

$$u_c^{\lambda} = K_{\lambda} u_c^{f} \tag{8.5}$$

where K_{λ} is the ratio of the critical velocity of the main flow for the case with the AFR to that without it. The values of K_{λ} obtained in the experiments are shown versus the KC number in Fig. 8.22. The region above each curve indicates that the local scour around the AFR occurs. It is found that the main flow velocity which induces the sediment movement around the AFR decreases with increasing KC and approaches about 0.4 times the critical velocity of that without the AFR.

(b) Mechanisms of local scour

It is found from the flow visualization that the local scour around the AFR is characterized by two kinds of sand movements; one is the movement of sand washed downstream by the interaction between flows directed downward along the upstream surface of the AFR and contraction flow (i.e., accelerated flow adjacent to the AFR), the other is the movement of sand suspended and transported downstream by the vortices with the vertical rotation axis to the bottom which are formed at corners of the AFR. The shape of the scour hole is that of an inverted cone at the corners of the AFR, and the depositions of sand suspended by the vortices occur in both sides of the AFR. The bottom profiles
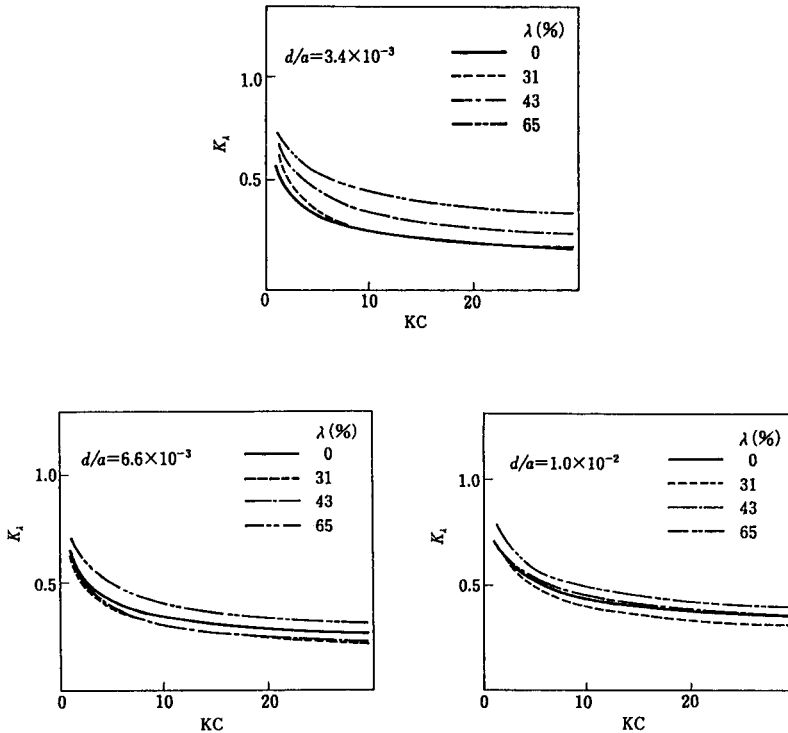
Fig. 8.22   Relation between K_λ and KC

around the AFR induced by these sand movements are illustrated schematically in Fig. 8.23. The pattern of bottom profile is classified into two patterns by void ratio of the AFR (see Fig. 8.23). In the case of the AFR with a large void ratio, the sands transported from the scour hole enter in the hollow inside of the AFR through a gap in the base of it with a developing scour in the corners, and these sand movements produce the clearance between the corners of the AFR and the bottom.

The magnitudes of maximum settlement of the AFR (Δh_m) and the values of the maximum scour depth (h_{sm}) are found to depend on the KC number and void ratio of the AFR (λ) as shown in Fig. 8.24. In the case of AFR with $\lambda = 60\%$ in which this void ratio has been most frequently used in the present, the maximum settlement of the AFR and the maximum scour depth are respectively estimated to be about 10 per cent and 15 per cent of the one side length of the AFR.

(c) Protection works against scour

Since the scour around the AFR is caused by the contraction flow and the vortices as mentioned above, in order to prevent the occurrence of these flows, an improvement of the AFR shape is imagined as scour protection. However, this method will result in an adverse effect from the viewpoint of the gathering effect of fish. Thus, the rubble mound method and the rubber sheet device are developed as scour protection to intercept the sand around
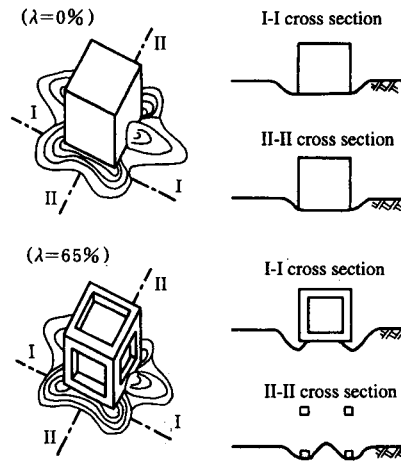
Fig. 8.23 Sketch of bottom profile around AFR
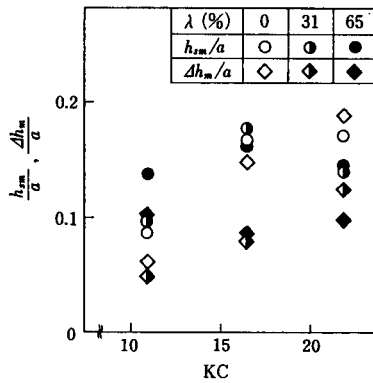
Fig. 8.24 Relation between the maximum settlement, the maximum scouring depth and the KC number

the AFR from the above mentioned flows, and the laboratory model experiments are performed to investigate the efficiency of the following protection method.

      method I   : covering area under the AFR with rubble

      method II : I + placing rubble around the AFR

      method III : bonding circular rubber sheet to base of the AFR

  The purpose of methods I and II is to increase of the resistance force of sediments to the fluid shear stress by placing the rubbles around the AFR. The settlement of the AFR caused by the compaction of rubbles with the rocking motion of the AFR can be predicted in method I. In method II, therefore, rubbles around the AFR are added to method I in order to reduce the rocking of the AFR. On the other hand, the purpose of method III is to intercept the sand from the flows which cause the scour by bonding the rubber sheet to the base of the AFR. Flexible rubber is chosen as the rubber material because the attachment of rigid rubber may cause a second scour.

Figure 8.25 shows the comparison between the settlement of the AFR with the scour protection (Δh_p) and that without these (Δh_m) in order to clarify the efficiency of the scour protection methods. Both experiments are carried out under conditions of same sand size. The values of $\Delta h_p/\Delta h_m$ in every protection method are less than unity and the efficiency of the protection is distinctly confirmed. The protection method of scour with the rubber sheet in particular is highly efficient. Also, by comparing method I and method II, it is found that the settlement of the AFR caused by the compaction of rubbles can be prevented to some degree by reducing the rocking motion of the AFR.
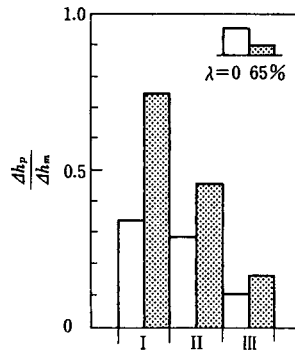
Fig. 8.25 Experimental results on the scour protection works

8.2.3 Accuracy of setting arrangement and impulsive force at landing on sea bottom

(1) Behavior of settling AFR and reducing method of setting position errors

In general, an AFR is constructed by throwing it down from a ship to lay out on the fish ground. Since the settling motion of an AFR consists of three complex motions (i.e., an oscillatory motion in a horizontal direction, a rotational motion and vertical drop), it is difficult to set up an AFR in the right position. As a result of position errors induced in the set up, the work of the multi-AFR system on gathering fish may not be demonstrated sufficiently. The position errors are the important problem in this construction method. The oscillatory motion of a settling AFR in a periodic wave is induced by the instantaneous fluctuations of the pressure distribution around it, which is induced by the vortices generated around it and the wave motion.

It can be estimated that the behavior of a settling AFR is closely related to the initial condition of posture of the AFR at throwing, because the change of the initial angle from the still water surface at throwing may cause a change in the pattern of vortice formations around it and this change directly effects the settling behavior. Hence, to investigate the effective initial posture of an AFR at throwing to reduce the settled area on the sea floor most, systematic calculations for changing the initial angle at throwing were carried out by using the simulation technique (Matsumi et al. 1988) which was developed to analyze the behavior of a settling AFR in consideration of the oscillatory motion in horizontal direction and the rotational motion.

(a) Summary of simulation technique for settling behavior of AFR

In the numerical simulation of the settling AFR, the fluid resistance exerted on the settling AFR is estimated firstly by the integrating the pressure distribution around its

surface. This surrounding pressure distribution is numerically analyzed with both the discrete vortex approximation method for the simulation of the vortex formation behind the AFR and the source distribution method for the formulation of the boundary condition on the surface of it. Secondly, the oscillatory motion of the settling AFR at every moment is numerically calculated from the equations of motions for settling. Referring to Fig. 8.26, the equations of horizontal, vertical and rotational motion for the settling AFR are given as

$$M_a \frac{du_G}{dt} = \sum_{i=1}^{4} F_{xi}$$

$$M_a \frac{dw_G}{dt} = \sum_{i=1}^{4} F_{zi} - (M_a - M_w)g \qquad (8.6)$$

$$I_r \frac{d\omega_r}{dt} = \sum_{i=1}^{4} \left(x_i' F_{zi} - z_i' F_{xi} \right)$$

where M_a and M_w are the mass of an AFR per unit thickness and the fluid replaced by the unit thickness of the AFR, I_r is an inertia moment of an AFR around the gravitational center axis of the AFR, u_G and w_G are the x and z components of the speed of the settling AFR, ω_r is an angular velocity defined as positive anti-clockwise. F_{xi} and F_{zi} are the x and z components of the fluid resistance exerted on an i-th piece ($i = 1$-4) as illustrated in Fig. 8.26, x_i' and z_i' are the distance from the center axis of the AFR cross section to the center of the i-th piece in the x and z direction, and g is the gravitational acceleration.
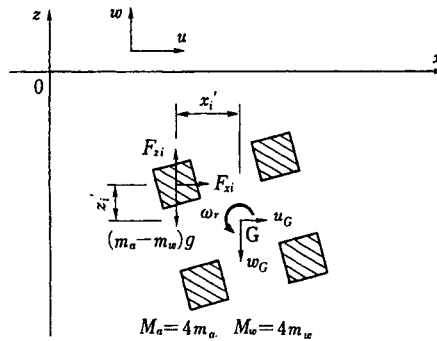
Fig. 8.26 Sketch of the settling AFR

Figure 8.27 shows the calculated behaviors of the settling AFR with the void ratio $\lambda = 64\%$ for three kinds of the initial angles, $\theta_0 = 0°$, $22.5°$, $45°$. D_x/D_z indicates the ratio of a horizontal fluctuation of the settling AFR to a settling distance between each simulated position. From these figures, it is found that the direction of horizontal fluctuation which is recognized from the values of D_x/D_z corresponds to the change of its rotational direction, and the simulation method can successfully simulate the fluctuation of a settling AFR in the horizontal direction with rotational motion.
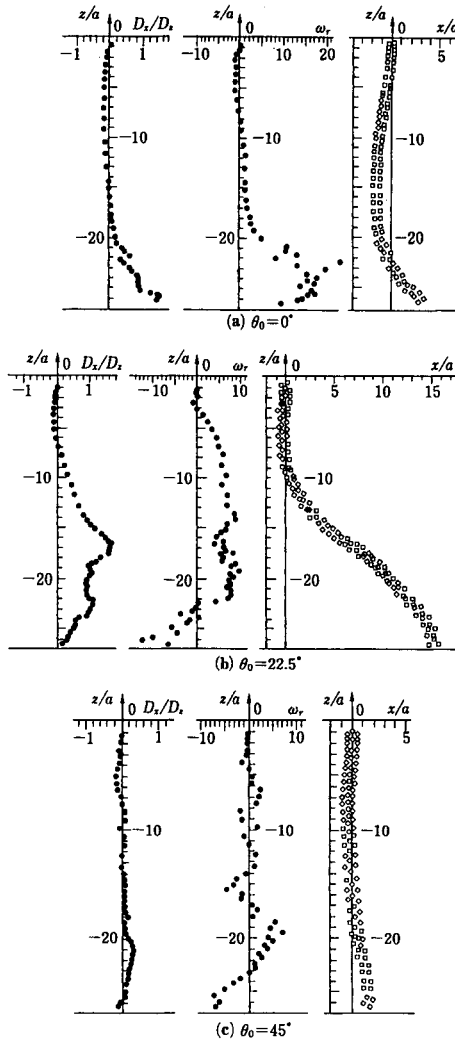
Fig. 8.27 Calculated results of the settling AFR

(b) Relation between initial posture of AFR at throwing and settling behavior

In the case of initial angle $\theta_0 = 0°$ and 22.5° as shown in Fig. 8.27(a) and (b), the rotational direction takes the same direction for the major part of the water depth, the horizontal fluctuation on one side direction becomes very large. When $\theta_0 = 45°$, the period of the change in the rotational direction is shortest among these three cases, and the horizontal fluctuation becomes very small. This situation for the settling AFR becomes the most stable; i.e., less oscillation may take place. From these investigations on the systematic calculations for the change of the initial angle at throwing, it can be concluded that the posture of the AFR at throwing with the angle of 45° from the still water surface reduces the settling area on the sea floor most.

(2) Impulsive force at landing on sea bottom

The design criteria of structures for arrangement and development projects of coastal fish grounds in Japan gives an equation to evaluate the impulsive force exerted on an AFR at landing on the sea bottom. That equation involves the added mass coefficient and the drag coefficient of the AFR, the effect of the bottom on these coefficients is not considered yet. In general, the added mass coefficient of the settling body is affected by the distance between the body and the bottom. Therefore, in order to evaluate the stability of the AFR at landing, the effect of the sea bottom on the added mass coefficient should be taken into account when we determine the design impulsive force of the AFR. Hence, this paragraph discusses the bottom effect on these hydraulic coefficients and the impulsive force of the AFR which is calculated by using these coefficients with the effect of the bottom.

(a) Effect of bottom on added mass and drag coefficient

In general, the added mass coefficient of a moving body in the fluid field has been calculated by utilizing the fluid force exerted on the moving body calculated on the base of the potential theory or by using the kinetic energy of the fluid induced by the moving body. Based on the latter method, the added mass coefficient of the settling AFR in the still water filled bottom were calculated. In the numerical techniques, the source distribution method and the mirror image method are applied to the formulation of the boundary condition on the AFR surface and the bottom respectively.

Figure 8.28 shows the change of the added mass coefficient of the settling AFR with respect to the relative distance h_q/a from the sea bottom. The value of C_A of $\lambda = 0\%$ in the infinite fluid field ($h_q/a = \infty$) is 1.19, and this value is equal to a certain value of the added mass coefficient of a rectangular cylinder. From this result, it is confirmed that the added mass coefficient of the AFR may be evaluated by this analysis technique with sufficient accuracy. As is clearly seen in Fig. 8.28, the shorter the relative distance becomes, C_A is affected by the bottom effect, C_A starts to increase very quickly in the order of increasing the void ratio of the AFR. Furthermore, from the table, it can be found that C_A at landing on the sea bottom ($h_q/a = 0.5$) reaches about 1.4 to 2.3 times of that in the infinite fluid field ($h_q/a = \infty$).

On the other hand, the drag coefficient of the settling AFR was calculated by applying the values of the added mass coefficient mentioned above and the Morison formula to the vertical component of its fluid resistance obtained from the results of its settling behavior mentioned in (1). The bottom effect on the drag coefficient has not been quantitatively clarified yet, because of the wide scatter in the calculations of the drag coefficient. However, the bottom effect involved in the drag coefficient on the impulsive force at landing will be clarified next (2).

(b) Evaluation of impulsive force at landing

Figure 8.29 shows the influence of sea bottom effect on the impulsive force at landing. In this figure, R' indicates the impulsive force at landing under consideration of the bottom effect on C_A and C_D, R is the impulsive force which is calculated by putting $C_A = 1$ and $C_D = 2$. K is the modulus of sea-bed reaction and θ_f is the angle between the AFR surface and the bottom. C_D was varied from 0.1 to 4 in these calculations. It is found form this figure that all values of R'/R are more than unity in spite of the values of C_D, and the design criteria may underestimate the impulsive force exerted on the AFR at landing on the sea bottom. Furthermore, the values of R'/R in each θ_f decrease with the increase of C_D and the magnitudes of decrease (i.e., about 0.02 to 0.03) are not so much. Therefore, it is reasonable that the value of the drag coefficient described in the design criteria is used as that in the calculation of the impulsive force. In the case of coefficient of the added mass, however, the added mass coefficient which considers the bottom effect should be used.

λ (%)	0	30.5	55.5	75.0	88.9
C_A ($h_q/a=\infty$)	1.19	1.15	1.18	1.22	1.24
C_A ($h_q/a=0.5$)	2.74	2.08	1.84	1.82	1.78

λ= 0.0%
λ=30.5%
λ=55.5%
λ=75.0%
λ=88.9%
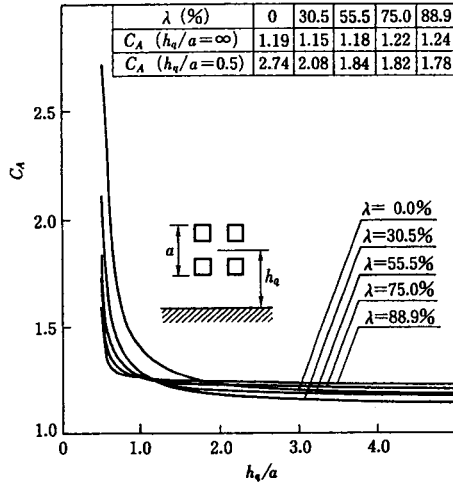
Fig. 8.28 Change of the added mass coefficient of the AFR with relative water depth

$\theta_J=0°$

K	(kg/cm²)
——	1.0×10^5
-----	3.0×10^5
—·—	7.0×10^5

$\theta_J=22.5°$

$\theta_J=45°$
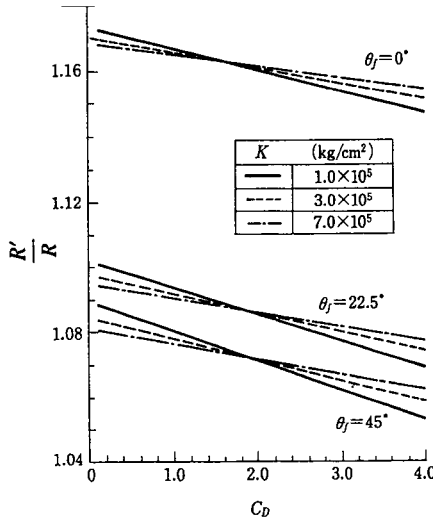
Fig. 8.29 Influence of sea bottom effect on the impulsive force at the landing

8.3 Submerged Moored Artificial habitat

8.3.1 History of the submerged habitat

In this decade so many artificial habitats have been constructed in the deepwater area to concentrate migratory fish. The depth of the submersion sites ranges from 50m to over 1000m. In the earliest submersion of artificial habitats in 1981, most of the constructed structures had been carried away or broken down by storm waves or currents in the offshore areas.

Table 8.1 Number of disappeared artificial habitats in 1981-1985, Japan

Construction Year	1981	1983	1984	1985
Deployment Depth (m)	500-1000	300-1000	300-1000	300-1000
Total Number of the Deployed AH	31	6	7	10
Number of Breakdown AH in 60 Days	25	5	2	0
Number of Breakdown AH in 150 Days	31	5	2	2
(AH: Artificial Habitat)				

Table 8.1 (Ikemoto and Kuroiwa 1987) lists examples of a number of the disappeared artificial habitats in 1981 - 1985. From such field tests, it was found that the rate of breakdown of the structures increased as the submergence was shallower. In order to brace such structures at the submersion location in the long term, it is important to assess correctly their dynamic response to ocean waves. Some theoretical studies have been done relating the dynamic response of submerged mooring structures or cables to surface waves, but there has been almost no verification of the results through comparisons with laboratory or field observations. In the following sections, the dynamic behavior of artificial habitat caused by waves will be discussed.

8.3.2 Dynamic response of a submerged artificial habitat due to waves

In general, a submerged fish culture is installed into the sea bottom by single point mooring. Figure 8.30 shows the notation with respect to a moored cylindrical habitat anchored to the bottom by a tension line. It is assumed that the buoy motions are respected to a vertical plane parallel to the direction of wave propagation, and the mooring line is always straight under the wave action. Therefore, the displacements (x_l, z_l) of the infinitesimal element dM are expressed as follows:

$$x_1 = l\sin\theta_1 + s\sin(\theta_1 + \theta_2) \tag{8.7}$$

$$z_1 = l\cos\theta_1 + s\cos(\theta_1 + \theta_2) \tag{8.8}$$

where l is the mooring line length, s is the arm length of the element, θ_1 and θ_2 are the mooring line and buoy rotation angle respectively. If it is assumed that both angles are small, then the kinetic energy of the element dE is given by

$$dE = \left(\frac{1}{2}\right)dM\left(\dot{x}_1^2 + \dot{z}_1^2\right) \tag{8.9}$$

By integrating Eq. (8.9) with respect to the arm lengths from 0 to L_a, then total energy is obtained as follows:

$$E = \left(\frac{1}{2}\right)l\left\{\left(3r^2 + 3r + 1\right)\dot{\theta}_1^2 + (3r+2)\dot{\theta}_1\dot{\theta}_2 + \dot{\theta}_2^2\right\} \tag{8.10}$$
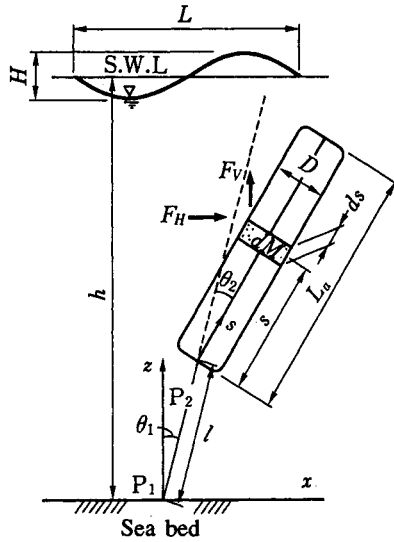
Fig. 8.30 Coordinate of a moored cylindrical habitat

in which L_a is the buoy length, I is the moment of inertia about point P_1 and r is the ratio of the mooring line length to buoy length l/L_a. By substituting Eq. (8.10) into the Lagrange equation, the equations of motion are given by

$$I\left(3r^2 + 3r + 1\right)\ddot{\theta}_1 + I(1.5r + 1)\ddot{\theta}_2 = Q_1 \qquad (8.11)$$

$$I(1.5r + 1)\ddot{\theta}_1 + I\ddot{\theta}_2 = Q_2 \qquad (8.12)$$

in which Q_1 and Q_2 represent the generalized forces related to θ_1 and θ_2 respectively. Q_1 and Q_2 are considered the moments by the pressure gradient forces, imaginary mass forces, drag forces and gravitational forces act to the mass element. Finally, the equations of motion of the submerged reef for θ_1 and θ_2 are expressed as follows:

$$\left(I + C_{A1}J\right)R_1\ddot{\theta}_1 + IR_2\ddot{\theta}_2 + C_1\left(1/3 + r^2\right)L_a^2\dot{\theta}_1 + \left(\rho - \rho_0\right)VgL_a(r + 1)\theta_1$$
$$= \rho(1 + C_{A1})A_s\int_0^{La}(l + s)\mathrm{d}u\Big/\mathrm{d}t\mathrm{d}s + (\rho/2)C_DD\int_0^{La}(l + s)\,u\,|u|\,\mathrm{d}s \qquad (8.13)$$

$$IR_2\ddot{\theta}_1 + (I + C_{A2}J)\ddot{\theta}_2 + C_2(1/2 + r)L_a^2\dot{\theta}_2 + \left(\rho - \rho_0\right)VgL_a\theta_2/2$$
$$= \rho(1 + C_{A2})A_s\int_0^{La}s\,\mathrm{d}u\Big/\mathrm{d}t\mathrm{d}s + (\rho/2)C_DD\int_0^{La}su\,|u|\,\mathrm{d}s \qquad (8.14)$$

$$J = \rho VL_a^2/3, \quad R_1 = 3r(r + 1) + 1, \quad R_2 = 3r/2 + 1$$

in which C_D, C_{Ai} and C_i (i=1,2) are the drag, the added mass and the damping coefficients of the submerged reef, respectively, V and A_s are the volume and cross sectional area of it, ρ and ρ_0 are the mass density of water and reef, g is the gravitational acceleration. From the solutions of the above simultaneous equations, the mooring line force is determined by the equilibrium equation.

Figure 8.31 shows the relationship between the oscillatory amplitude of moored habitat in the case of C_1= 0.014 and C_2=0.045. In this figure, the maximum values of θ_1 and θ_2 appear near the values of ω = 2 in both theoretical and experimental results in which solid and chain lines demonstrate the numerical values of θ_1 and θ_2 respectively. In the resonance frequency, the displacements of the reef are found to increase sharply.
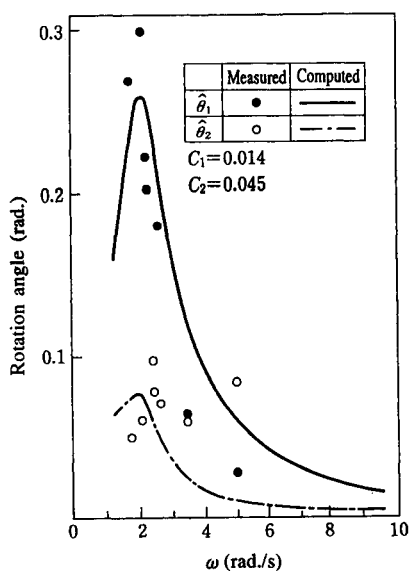
Fig. 8.31   Response characteristics of moored habitats

Figure 8.32 represents the time history of the wave surface, mooring line angle, buoy rotating angle and mooring line force. The experimental values of θ_1 and θ_2 show some fluctuation and the experimental results depart from the numerical results, but the computed mooring line tension agrees with the experimental results.

Figure 8.33 shows the variation of maximum mooring line forces with wave steepness for various values of the ratio of depth to the wavelength. It appears that line forces increase with the increase of the wave steepness and they also increase with the decrease of the ratio of h/L for constant values of wave steepness. Comparison between estimated results and experimental values show good agreement.

Since artificial reefs are composed of fishery nets, pipes and buoys, many kinds of reefs with arbitrary and complex shapes have been developed. In analyzing the dynamic movement of such structures, another sophisticated analytical procedure must be introduced.

458
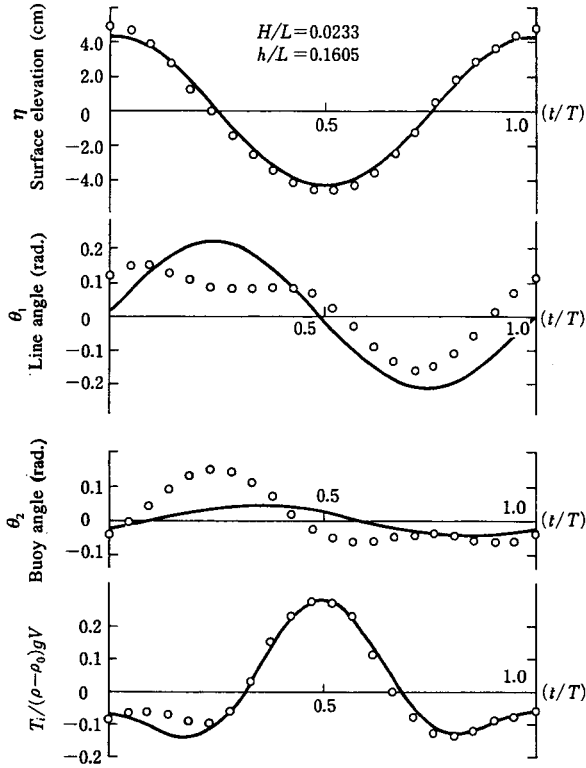
Fig. 8.32 Time history of dynamic motion of habitat
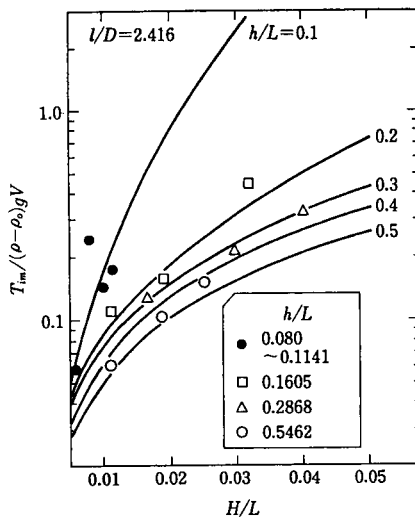
Fig. 8.33 Plots of maximum mooring line force to wave steepness
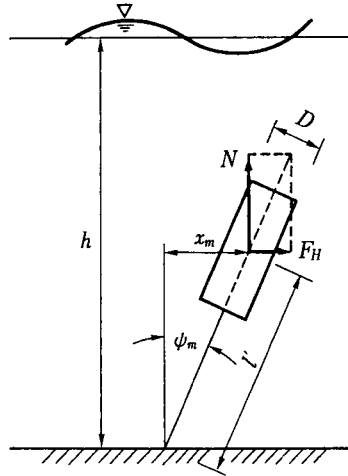
Fig. 8.34 Submerged reef anchored at bottom

Figure 8.34 shows an artificial reef with arbitrary shape anchored to the bottom. Suppose that the maximum line angle of a buoy ψ_m is related to the ratio of horizontal wave forces F_H to net buoyancy N, that is,

$$\psi_m \doteq F_H/N \tag{8.15}$$

Then, the maximum displacement of the center of the gravity of the buoy is expressed in a nondimensional form as follows:

$$\frac{\psi_m l'}{h} = \left\{ \left(C_M \frac{U_0 T}{D} \frac{D}{L_a} \frac{du^*}{dt^*} \right) + C_D \left(\frac{U_0 T}{D} \right)^2 \frac{D}{L_a} u^* |u^*| \right\} \Big/ (1 - \rho/\rho_0) \tag{8.16}$$

where C_M is the added mass coefficient, T is the wave period, U_0 is the maximum horizontal velocity at the depth of center of the gravity, $u^* = u_m/U_0$, $t^* = t/T$, u_m is the maximum velocity of a water particle.

The maximum line force T_{im} in Eq. (8.16) is rewritten in a nondimensional form by

$$\frac{T_{im}}{N} \frac{SgD}{U_0^2} = \left[\left\{ \frac{w_m}{u_m} \left(\frac{D\sigma}{u_m} \right) + \frac{SgD}{u_m^2} \right\}^2 + \left\{ \left(\frac{2C_D}{\pi} \right)^2 + \left(\frac{D\sigma C_M}{u_m} \right)^2 \right\}^2 \right]^{1/2}$$

$$+ C_M \ddot{\psi}_m^2 \left(\frac{D\sigma}{u_m} \right)^2 \frac{l'}{D} - \frac{SgD}{u_m^2} \tag{8.17}$$

where $S = (\rho - \rho_0)$, w_m is a vertical component of the water particle velocity.

Equations (8.16) and (8.17) suggest that the maximum displacement of the reef and mooring line force are related to the three parameters SgD/U_0^2, D/L_a and U_0T/D as follows:

$$\frac{\psi_m l'}{h} = f_1(D/L_a, U_0T/D), \quad \frac{T_{im}}{N}\frac{SgD}{U_0^2} = f_2(D/L_a, U_0T/D) \tag{8.18}$$

SgD/U_0^2 is a parameter of the cylinder Froude number (Emori and Churing 1981). The term U_0T/D is a parameter as well known as the Keulegan-Carpenter number and the ratio of reef length to the buoy diameter D/L_a is a parameter which defines the shape factor of the buoy; slenderness ratio.

Figure 8.35 shows an example of results of a model test for the variation of the maximum displacements of pillar models. There exits an obscure relationship between maximum displacements and U_0T/D.
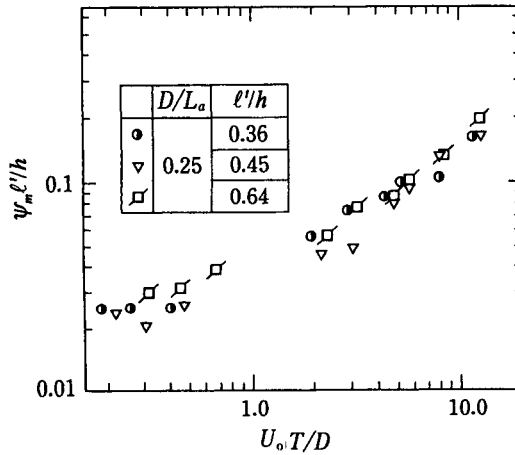
Fig. 8.35 Maximum displacement of reef

Figure 8.36 demonstrates the relationship between nondimensional maximum mooring line forces and U_0T/D. It is found that the nondimensional maximum line forces decrease linearly with an increase of U_0T/D in logarithmic plots. It is clear that the maximum mooring line force is expressed as a function of U_0T/D and D/L_a. Silvester (1974) showed that U_0T/D and D/L_a are important parameters in estimating the wave force for a submerged rigid structure. Those parameters are also predominant in evaluating the wave force acting on submerged artificial habitats.

8.4 Submerged Buoy-Cable System for Shellfish Farming

8.4.1 Response of the buoy-cable system to ocean waves

A great number of buoy-cable structures have been constructed to cultivate and proliferate the shellfish resources in deepwater areas. In order to stabilize such structures
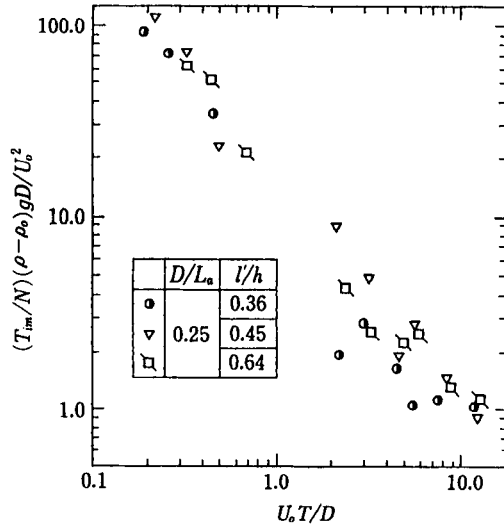
Fig. 8.36   Maximum mooring line force
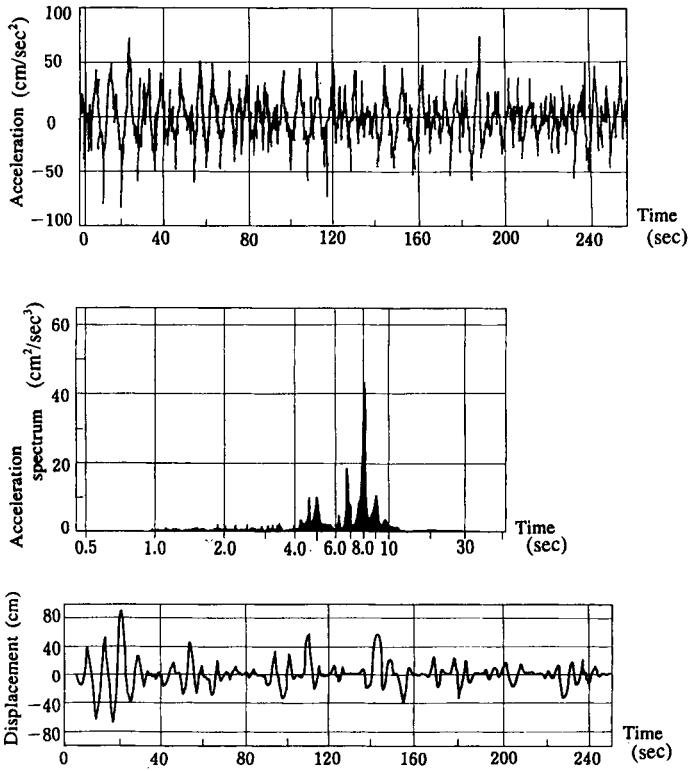
Fig. 8.37   Field observation data of the displacements of the buoy-cable system

in the long term, it is very important to assess correctly their dynamic response to ocean waves. Some theoretical studies have been done relating the dynamic response of submerged cables to ocean currents or waves, but there has been almost no verification of the results through comparisons with laboratory or field tests.

Figure 8.37 presents example data of the dynamic response of the buoy-cable system to waves which was obtained by field observations on Jan. 26 1987 in the Sea of Japan (Matsubara and Noda 1989). Time variations of the acceleration data, the power spectrum and the displacements converted by numerical integration are presented. The significant wave height and wave period at that time were 5.4m and 7.5s, respectively. The accelerations of the movement of the structure are found to vary irregularly but the spectrum shows that the predominant period of acceleration was about 8s. It may be noticed that the predominant period is very close to the significant wave period. The amplitude of the oscillation of the structure is about 1.5m.

While Fig. 8.38 shows an example of the wave data obtained from the field observations, vertical acceleration of the buoy-cable structure and the simulation results were computed using wave data at each interval. The acceleration of the system enlarges sharply in the earlier stages of the storm and decreases gradually in its decaying stage. It should be noted that the numerical results are overestimated slightly but still show quite a similar tendency to the measured results.
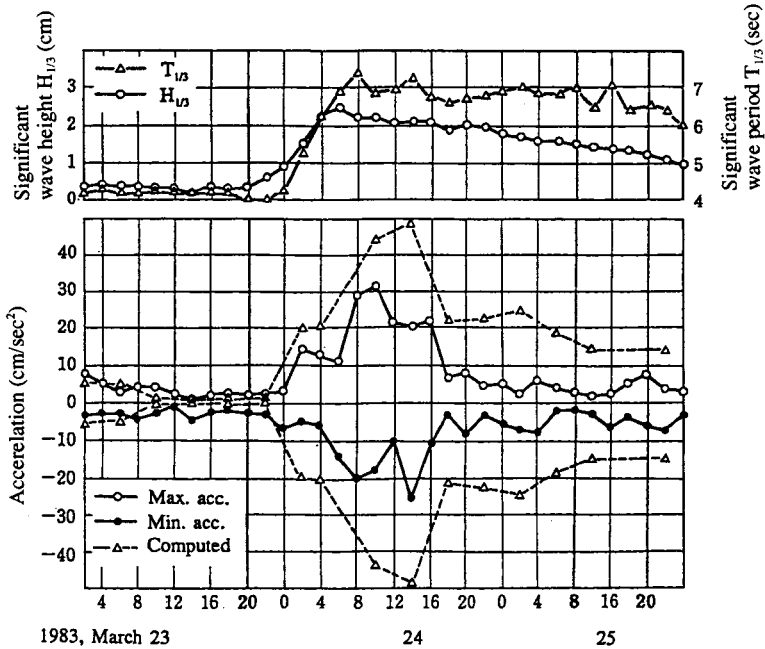
Fig. 8.38 Comparison of numerical results with field data

8.4.2 Equation of motion for the system

Figure 8.39 illustrates the numerical model of the artificial buoy-cable structure moored in the Sea of Japan. The following restrictions are introduced to simplify the mathematical treatment in obtaining equations of motions of the structure under the wave action.
(i)   The motions of the buoys and the cable are restricted to the vertical plane.
(ii) The buoys at both ends of the main cable are treated as fixed.
(iii) Interconnected cables are always straight and not extendible.
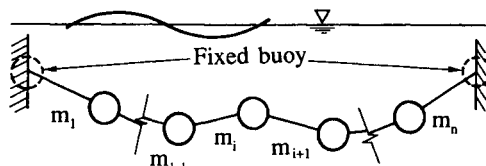
Fig. 8.39   Numerical model of the buoy-cable system
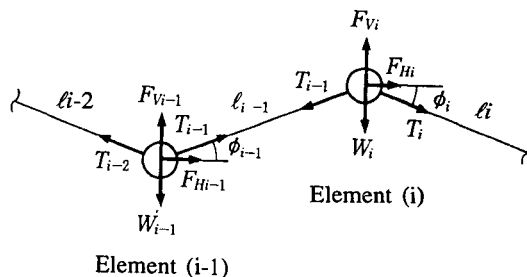
Fig. 8.40   Forces acting on masses

If the baskets and buoys can be considered as discrete lumped masses connected with straight cables, then the structure can be converted to a simple lumped mass model. Similar numerical models have been used by Nath and Felix (1970), Rupe and Thresher (1974) to compute the movement of submerged cables. A similar and simpler model to estimate the dynamics of a submerged buoy-cable structure has been proposed in this decade.

Figure 8.40 depicts the forces acting on mass elements. Summation of forces yields the following equations of mass motion.

$$m_i \ddot{x}_i = F_{Hi} + T_i \cos \phi_i - T_{i-1} \cos \phi_{i-1} \tag{8.19}$$

$$m_i \ddot{z}_i = F_{vi} + T_i \sin \phi_i - T_{i-1} \sin \phi_{i-1} - W_i \tag{8.20}$$

in which x and z are the horizontal and vertical distances to be described by cartesian coordinates, respectively, with z positive upward and x positive shoreward. m_i and W_i are the mass and the volume of the i-th mass element respectively. T_i and ϕ_i are the cable tension and the cable angle with horizontal axis.

Wave forces on the i-th mass element, F_{Hi} and F_{vi} are expressed as follows:

$$F_{Hi} = C_{Mi}\rho V_i \dot{u}_i - C_{Ai}\rho V_i \ddot{x}_i + \left(\frac{1}{2}\right) C_{Dxi}\rho A_{xi}\left|u_i - \dot{x}_i\right|\left(u_i - \dot{x}_i\right) \qquad (8.21)$$

$$F_{vi} = C_{Mi}\rho V_i \dot{w}_i - C_{Ai}\rho V_i \ddot{z}_i + \left(\frac{1}{2}\right) C_{Dzi}\rho A_{zi}\left|w_i - \dot{z}_i\right|\left(w_i - \dot{z}_i\right) \qquad (8.22)$$

where C_{Mi} is the inertia coefficient of the i-th mass element, A_{xi} and A_{zi} are the cross sectional areas of the i-th element projected in x and z directions, respectively. Water particle kinematics are determined by small amplitude wave theory. As the length of the cable segment S_i is taken to be a constant from the foregoing assumption (3),

$$\left(x_{i+1} - x_i\right)^2 + \left(z_{i+1} - z_i\right)^2 = l_i^2 \qquad (8.23)$$

Equations (8.19) and (8.20), together with Eq. (8.23), consist of a set of nonlinear ordinary differential equations which must be solved simultaneously and numerically in an implicit manner to obtain the displacements of the elements and the cable tension. The boundary condition is such that buoys at both ends are always fixed under the wave actions. The initial state of the system for the numerical calculation is the static equilibrium configuration and the initial velocity of all elements is zero at time $t=0$. Wave-induced movement of the buoy-cable system may be solved as initial value problems.

Figure 8.41 demonstrates the relationship between the nondimensional displacement of the center buoy Z/H and the relative wavelength L/l_s for various wave steepnesses H/L in which H, L and l_s are the wave height, wavelength and the span length of the main cable, respectively. It is found that the experimental results of the vertical buoy motions show
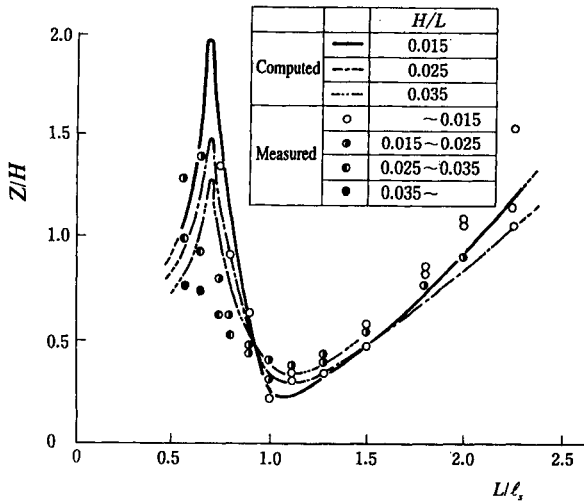
Fig. 8.41 Plots of buoy displacement to wavelength

great variations with an increase in L/l_s and have a tendency to reach a maximum at L/l_s = 0.7. The large amplification of the displacement of the structure can be explained as a resonance phenomenon, occurring when the natural frequency of free vibration of the buoy-cable system corresponds to the frequency of the wave. The numerical results are in good agreement with the experimental results.

Figure 8.42 depicts the variations of the movement of the main cable at each phase within a wave period. It is clear that the response of the main cable is similar to that of a string fixed at both ends. The pattern of the curve varies with the wave conditions and the nodes and loops appear in the movement of the cable. Computational results coincide with the experimental results.
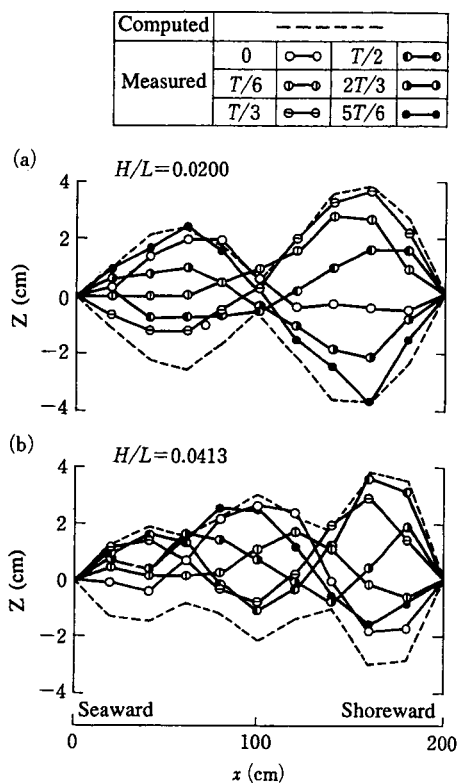
Fig. 8.42   Movement of the main cable

8.4.3 Countermeasure works against motion of longlines

As mentioned above, the submerged buoy-cable system is oscillated by surface waves. Especially under the resonance condition, the displacement increases rapidly. Such movement of the structure extended over a long time has been considered the cause of dead and deformed shellfish in the baskets. Thus, some artificial gadget to diminish the movement of the buoy-cable system by the wave is required from commercial management. Figure 8.43 shows the experimental results of the stabilizing system by using

resisting plates, which are attached to the bottom of the baskets, where Zp is the ratio of the movement of the main cable with resisting plates to that without these, D and dr are the diameter of the plate and buoys, respectively. The effect becomes more and more noticeable when the diameter of the stabilizing plate D increases.
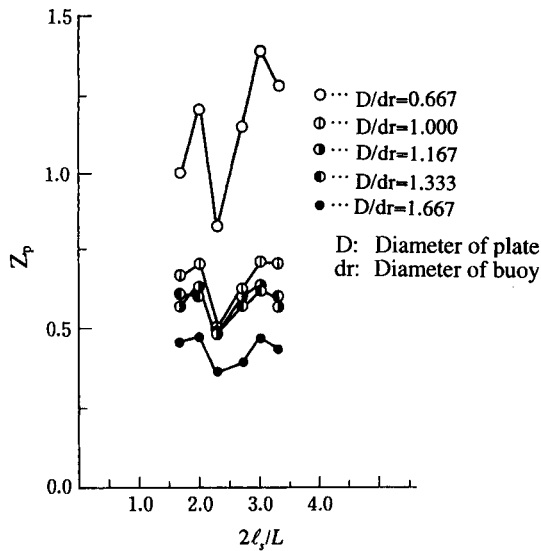
Fig. 8.43 Change of the vertical displacements by stabilizing plates

8.5 Floating Fishery Cages

8.5.1 Drag coefficient of a wire net

Since the fishery cage floats on the surface of the ocean, it pitches and rolls as the waves progress. For derivation of the motion of a cage in waves, the most important point is to estimate the fluid force acting on the wire net that surrounds the whole cage. The inertia force acting on the net may be neglected because the total mass of wire net of the fish cage is not so large, while the drag force should be considered because the cross sectional area of the mesh net amounts to a certain quantity. The drag coefficient may be evaluated by the towing tests of the plain net in sill water. Figure 8.44 shows the relationship between drag force coefficients of a plain wire net and the Reynolds number (UD/v, U and D are the towing velocity and diameter of the net, respectively, and v is the kinematic viscosity) obtained from laboratory tests. The drag coefficients of the net decreases linearly with the increment of the wire net Reynolds number, and its empirical equation is expressed by

$$C_D = 9.84 \text{Re}^{-0.36} \tag{8.24}$$
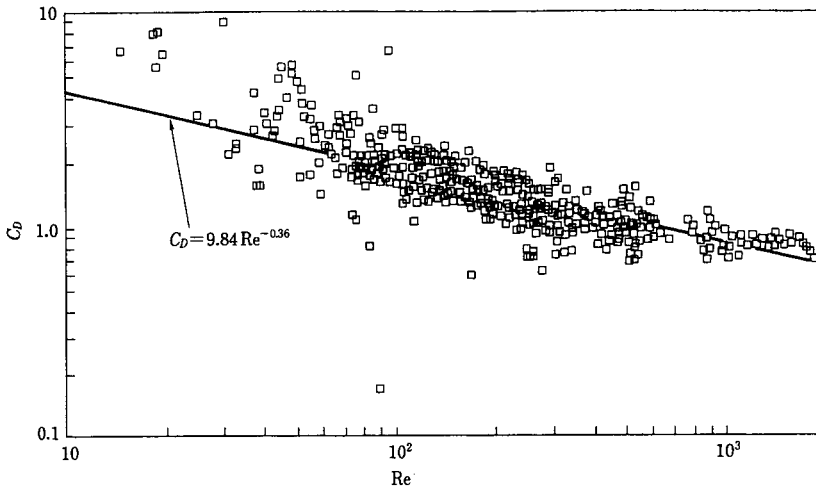
Fig. 8.44 Relationship between drag force coefficients and Reynolds number

8.5.2 Dynamic response of the floating cage to waves

The equations of two-dimensional motion for a cage in regular waves are derived in the same manner as already discussed in Chapter 2 as follows:

$$m\ddot{x} = F_H + T_{HC} - T_H$$
$$m\ddot{z} = F_V - T_{VC} - T_V - (\rho - \rho_0)gV$$
$$I\ddot{\theta} = M_1 - M_2 + M_3$$

$$(8.25)$$

where m and V are the mass and the volume of the cage, and F_H and F_V are wave forces in horizontal and vertical directions respectively. T_H and T_V are vertical and horizontal components of the shoreward mooring line forces. T_{HC} and T_{VC} are also horizontal and vertical components of the seaward mooring line forces, respectively. I is the inertia moment about the center of gravity of the cage, M_1 and M_2 are the moments by the seaward and shoreward mooring line forces, M_3 is the moment by the wave forces about the center of gravity. If wave forces acting on the mooring lines are evaluated in Eq. (8.25), some numerical methods such as a lumped mass model have to be applied to compute the mooring line forces.

Figure 8.45 shows the relationship between experimental results and numerical results of the horizontal and vertical displacements by waves. There are some discrepancies between the computed and measured profiles, and computational results underestimate the heaving and swaying displacements of a cage. However, the phases of simulated displacements are in good agreement with the experimental results.

Figure 8.46 demonstrates the comparison of numerical results of pitching movement with the experimental results within one wave period. There is good agreement between the computed and experimental displacements. These simulation results provide a fair verification of the evaluation of wave-induced loads on the plain net and numerical model of a floating fishery cage.
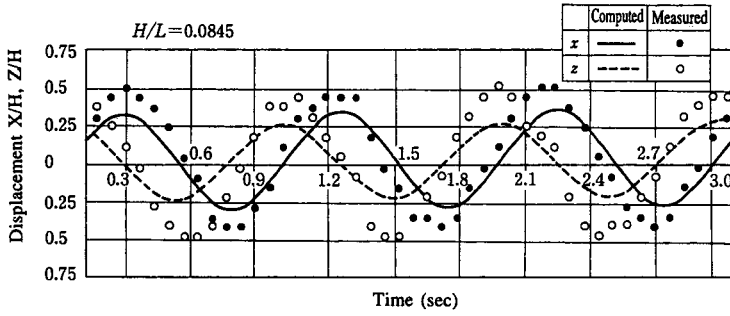
Fig. 8.45 Comparison of calculated displacements with experimental results
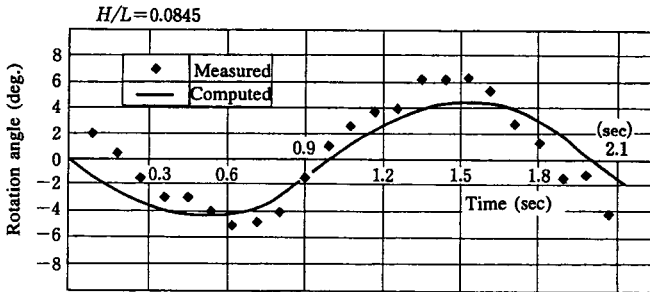
Fig. 8.46 Comparison of numerical results of pitching with measured data

References

Ikemoto H. and T. Kuroiwa (1987): Structural problems of artificial habitat, Fisheries Engineering, Vol.23, No.2, pp.43-50. (In Japanese)

Emori, I. and D. J. Schuring (1981): Theories and applications of laboratory tests, Gihoudo, 246p.

Matsubara, Y. and H. Noda (1989): Dynamic behavior of a submerged buoy-cable structure by ocean waves, Proc. of 23rd Cong., IAHR, Ottawa, Vol.C, pp.493-500.

Matsumi, Y. and A. Seyama (1988): The fundamental study to reduce the settled area of the fish aggregation devices on the sea floor thrown from a ship, Proc. 21st Int. Conf. on Coastal Eng., ASCE, Vol.III, pp.2937-2951.

Nath, J. H. and M.P. Felix (1970): Dynamics of single point mooring in deepwater, J. Waterways, Harbors and Coastal Eng. Div., Proc. ASCE, Vol.96, No.WW4, Paper 7700, pp.815-833.

Rupe, R.C. and R.W. Thresher (1974): The anchor-last deployment problem for inextensible mooring lines, J. Eng. for Industry, Transaction of ASME, Paper No.74-WA/OCT-5.

Sawaragi, T., Y. Matsumi and K. Hayashi (1984): Numerical simulation of flow pattern around a fish aggregation device, Coastal Eng. in Japan, JSCE, Vol.27, pp.109-118.

Silvester, R. (1974): Coastal Engineering 1, Elsevier, 455p.

This Page Intentionally Left Blank

Index

This Page Intentionally Left Blank